GEOLOGIJA

2025 | št.: **68/2**

GeoZS
Geološki zavod Slovenije

ISSN
Tiskana izdaja / Print edition: 0016-7789
Spletna izdaja / Online edition: 1854-620X

GEOLOGIJA

68/2 – 2025

GeoZS
Geološki zavod Slovenije

GEOLOGIJA	2025	68/2	89-354	Ljubljana

GEOLOGIJA
ISSN 0016-7789

Izdajatelj: Geološki zavod Slovenije, zanj direktor **dr. Miloš Bavec**
Publisher: Geological Survey of Slovenia, represented by Director **dr. Miloš Bavec**
Financirata Javna agencija za raziskovalno in inovacijsko dejavnost Republike Slovenije in Geološki zavod Slovenije
Financed by the Slovenian Research and Innovation Agency and the Geological Survey of Slovenia

Naslov uredništva / Editorial Office: GEOLOGIJA Geološki zavod Slovenije / Geological Survey of Slovenia
Dimičeva ulica 14, SI-1000 Ljubljana, Slovenija
Tel.: +386 (01) 2809-700, Fax: +386 (01) 2809-753, e-mail: urednik@geologija-revija.si
URL: https://www.geologija-revija.si/

GEOLOGIJA izhaja dvakrat letno. / GEOLOGIJA is published two times a year.
GEOLOGIJA je na voljo tudi preko medknjižnične izmenjave publikacij. /
GEOLOGIJA is available also on exchange basis.

Izjava o etičnosti
Izdajatelji revije Geologija se zavedamo dejstva, da so se z naglim naraščanjem števila objav v svetovni znanstveni literaturi razmahnili tudi poskusi plagiatorstva, zlorab in prevar. Menimo, da je naša naloga, da se po svojih močeh borimo proti tem pojavom, zato v celoti sledimo etičnim smernicam in standardom, ki jih je razvil odbor COPE (Committee for Publication Ethics).

Publication Ethics Statement
As the publisher of Geologija, we are aware of the fact that with growing number of published titles also the problem of plagiarism, fraud and misconduct is becoming more severe in scientific publishing. We have, therefore, committed to support ethical publication and have fully endorsed the guidelines and standards developed by COPE (Committee on Publication Ethics).

Baze, v katerih je Geologija indeksirana / Indexation bases of Geologija: Scopus, Directory of Open Access Journals, GeoRef, Zoological Record, Geoscience e- Journals, EBSCOhost

Cena / Price

Posamezni izvod / Single Issue	Letna naročnina / Annual Subscription
Posameznik / Individual: 15 €	Posameznik / Individual: 25 €
Institucija / Institutional: 25 €	Institucija / Institutional: 40 €

Tisk / Printed by: TISKARNA JANUŠ d.o.o.

Slika na naslovnici: Meteorit Jesenice, ki je 9. aprila 2009 padel na Mežaklo, izvira iz asteroidnega pasu med Marsom in Jupitrom in je uvrščen med kamnite hondrite. Slika prikazuje makro vzorec na levi (foto: Miha Jeršek) in del poliranega zbruska na desni (Ambrožič s sod., članek v tej številki).

Cover page: The Jesenice meteorite, which fell on 9 April 2009 on the Mežakla Plateau, originates from the asteroid belt between Mars and Jupiter and is classified as a stony chondrite. The image shows a hand specimen on the left (photo: Miha Jeršek) and a portion of a polished thin section on the right (Ambrožič et al., paper in this issue).

GEOLOGIJA 68/2, 89-354, Ljubljana 2025

VSEBINA – CONTENTS

Članki - Articles

Podatkovni članki – Data Articles

Poročila in ostalo - Reports and More

Nekrolog - In Memorium

GEOLOGIJA 68/2, 95-111, Ljubljana 2025

https://doi.org/10.5474/geologija.2025.001

Article

Geokemične lastnosti podstrešnega, stanovanjskega in cestnega prahu v okolici cementarne v Anhovem, Slovenija

Geochemical properties of attic, household and street dust in the vicinity of the cement plant in Anhovo, Slovenia

Mateja GOSAR* & Martin GABERŠEK

Geološki zavod Slovenije, Dimičeva ulica 14, SI-1000 Ljubljana, Slovenija; *corresponding author: mateja.gosar@geo-zs.si

Prejeto / Received 23. 1. 2025; Sprejeto / Accepted 14. 2. 2025; Objavljeno na spletu / Published online 28. 2. 2025

Ključne besede: podstrešni prah, stanovanjski prah, cestni prah, onesnaženje, geokemija, Anhovo
Key words: attic dust, household dust, street dust, contamination, geochemistry, Anhovo

Izvleček

Na širšem območju Anhovega smo vzorčili in analizirali stanovanjski, podstrešni ter cestni prah. Namen dela je ugotoviti geokemične lastnosti treh tipov prahu, ki so posledica geogenih dejavnikov, preteklih in sedanjih vplivov cementarne ter tudi drugih dejavnikov. Z raziskavo smo zajeli naselja Anhovo, Morsko, Deskle, Ložice, Gorenje Polje, Goljevica, Ravna, Krstenica, Kanal in Bodrež. V presevkih (< 0,063 mm) obravnavanih vzorcev so bile po razklopu z zlatotopko določene vsebnosti arzena (As), kadmija (Cd), kobalta (Co), kroma (Cr), bakra (Cu), živega srebra (Hg), mangana (Mn), molibdena (Mo), niklja (Ni), svinca (Pb), antimona (Sb), talija (Tl) in cinka (Zn).

Sestava prahu se močno razlikuje med posameznimi tipi in med vzorčnimi mesti. Razponi med najmanjšimi in največjimi vsebnostmi elementov so večinoma veliki, kar kaže na deloma različne vire v različnih predelih obravnavanega območja in na antropogene vplive. Rezultati kažejo, da so za celotno raziskovano območje značilne relativno visoke vsebnosti Hg v vseh treh tipih prahu. Vsebnosti Hg so izrazito večje tako v primerjavi z Mariborom, kot slovenskim podeželjem in večjimi slovenskimi urbanimi kraji. Glede na predstavljene podatke lahko sklepamo, da na vsebnosti Hg v prahu oz. v okolju vplivajo antropogeni viri, ki so bili aktivni v preteklosti in viri, ki so aktivni še danes. Za raziskovano območje so v primerjavi z drugimi podatki za Slovenijo značilne tudi nekoliko večje vsebnosti Tl in Mn.

Abstract

Household, attic, and street dust were sampled and analysed in the influential area of cement plant located in Anhovo, Slovenia. The aim of the work is to determine the geochemical properties of the three types of dust, which are the result of geogenic factors, past and current influences of the cement plant, and other factors. The study covered the settlements of Anhovo, Morsko, Deskle, Ložice, Gorenje Polje, Goljevica, Ravna, Krstenica, Kanal and Bodrež. The levels of arsenic (As), cadmium (Cd), cobalt (Co), chromium (Cr), copper (Cu), mercury (Hg), manganese (Mn), molybdenum (Mo), nickel (Ni), lead (Pb), antimony (Sb), thallium (Tl) and zinc (Zn) were determined in the sieved dust samples (<0.063 mm) after agua regia digestion.

The composition of dusts varies greatly between the three dust types and also between sample sites. The ranges between the minimum and maximum levels are mostly large, which indicates different sources in different parts of the studied area and anthropogenic influences. The results show that the studied area is characterized by relatively high Hg levels in all three types of dust. The Hg levels are significantly higher compared to town of Maribor, the Slovenian countryside and Slovenian urban areas. Based on the presented data, we can conclude that the levels of Hg in the studied three dust types and in the environment is influenced by anthropogenic sources that have been active in the past and sources that are still active today. The studied area is also characterized by slightly higher Tl and Mn levels compared to other data for Slovenia.

Uvod

Dimni plini iz cementarn in (so)sežigalnic ter potencialno strupeni elementi

Proizvodnja cementa ima lahko več negativnih vplivov na okolje, med katerimi so najpomembnejši emisije CO_2, CO, NO_x, SO_x, dioksinov, furanov, hlapnih organskih spojin in prašnih delcev, manjše količine odpadkov, hrup, posegi v prostor (npr. kamnolomi) ter uporaba hladilne vode (Mishra et al., 2022; Mohamad et al., 2022). Cementarne pogosto kot gorivo uporabljajo tudi različne odpadke, kar lahko ob neustreznih ukrepih povzroča dodatne izpuste plinov in trdnih delcev v okolje.

Obnašanje glavnih in slednih elementov med zgorevanjem odpadkov je odvisno od njihove naravne hlapljivosti, njihove vsebnosti in pojavne oblike v gorivu ter od kemičnih reakcij, ki potečejo z žveplom ali drugimi hlapljivimi komponentami.

Ob zgorevanju odpadkov večina prvin ostane v obliki trdnih delcev v elektrofiltrskem pepelu ali pepelu in žlindri, ki ostane v kotlu, nekatere prvine pa preidejo v plinasto fazo oz. dimne pline. Večina kovin (npr. Cd, Cr, Cu, Ni, Pb, Zn, V) se sprošča iz sistema v obliki trdnih delcev (žlindre/pepela). Samo Hg, As in Se so vsaj delno prisotni tudi v plinasti fazi, podobno kot pri zgorevanju premoga (Shuqin et al., 2006). Sproščanje elementov je odvisno od lastnosti in velikosti delcev. Med zgorevanjem so delci podvrženi kompleksnim spremembam, ki vodijo do izhlapevanja hlapljivih elementov (Senegačnik, 2019).

Ocenjene emisije Hg v zrak iz antropogenih virov so leta 2015 znašale 2220 ton, pri čemer je proizvodnja cementa predstavljala približno 11 % globalnih antropogenih emisij (UNEP, 2019). Industrija cementa je eden od treh največjih virov antropogenih emisij Hg v Evropi (UNEP, 2019). Antropogene emisije predstavljajo približno 30 % vseh emisij Hg v ozračje. V istem poročilu ugotavljajo, da so ocenjeni globalni antropogeni izpusti Hg v ozračje za leto 2015 za približno 20 % večji, kot so bili v ocenah za leto 2010, večinoma na račun povečanja emisij v Aziji.

Po podatkih Pacyna in sodelavcev (2006) so emisije Hg iz cementarn znatne in so bile za leto 2000 ocenjene na približno 5,6 % skupnih emisij Hg iz svetovnih antropogenih virov in na približno 12,6 % v Evropi (brez Rusije) (Pacyna et al., 2006). Cementarne Hg izpuščajo v ozračje v dimnih plinih, klinkerju in prahu, ki ga večinoma odstranijo iz dimnih plinov (Kogut et al., 2021; Ljubič Mlakar et al., 2010). Živo srebro v dimnih plinih cementarn prihaja iz surovin, ki se uporabljajo za proizvodnjo cementa, kot tudi iz goriv, ki se dovajajo v rotacijsko peč (Kogut et al., 2021). Razširjanje emisij Hg (ali kateregakoli onesnaževala) od točkovnega vira do območij odlaganja je odvisno predvsem od smeri in jakosti vetra oz. meteoroloških pogojev (Croxford et al., 1996). Med zgorevanjem se Hg lahko sprosti v treh oblikah – v oksidirani obliki (Hg^{2+}), v elementarni obliki (Hg^{0}) in v obliki, ki se veže na trdne delce. V plinasti in trdni fazi Hg hitro oksidira, navadno s halogeni (Cl, Br), ki so prisotni v gorivu ali v dimnih plinih. Živo srebro, ki se veže na trdne delce in oksidirano Hg je preprosto zajeti s čistilnimi sistemi (Senegačnik, 2019). Težje pa je zajeti elementarno Hg, ki je lahko prisotno v večjih koncentracijah v dimnih plinih (Senegačnik, 2019).

Elementarno živo srebro se v atmosferi zadrži relativno dolgo (več mesecev) in se zato lahko transportira zelo daleč (Lindqvist & Rodhe, 1985). Oksidirane oblike se v atmosferi zadržijo precej krajši čas, v odvisnosti od topnosti v vodi, ki se nahaja v atmosferi. Trdni delci, ki vsebujejo Hg pa se odložijo najbližje izvora. S suhim in mokrim odlaganjem Hg in njegovih spojin se atmosfersko Hg vključuje v biosfero in vstopa v vodno-biološko kroženje. Zaradi tega je atmosferska pot Hg pomemben del biogeokemijskega kroženja živega srebra in njegovih spojin v naravi.

V cementarnah uporabljajo posebne sisteme za odstranjevanje Hg iz dimnih plinov, ki temeljijo na njegovih specifičnih lastnostih. Tudi vrečasti filtri, elektrostatični odpraševalniki in mokri pralniki, ki so namenjeni odstranjevanju kislih komponent, kot so SO_x, HCl in HF, odstranijo del emisij Hg (Senegačnik, 2019).

Edina še delujoča cementarna v Sloveniji je cementarna v Anhovem, ki je pričela delovati leta 1921. Do leta 1996 so proizvajali cementno-azbestne izdelke. Pri svoji dejavnosti že vrsto let uporabljajo tudi alternativna goriva oz. različne vrste odpadkov. V cementarni v Anhovem lahko istočasno uporabljajo različna goriva, ki morajo biti posebej pripravljena in prilagojena sistemu za doziranje. Tako kot vsaj 200 cementarn v Evropski uniji, ki uporabljajo odpadke kot vir alternativnih goriv, morajo tudi v Anhovem izpolnjevati predpisano zakonodajo (Internet 1). Masni tok živega srebra skozi procese cementarne v Anhovem so preučevali Ljubič Mlakar in sodelavci (2010). Izvedene so bile periodične točkovne meritve, s čimer so spremljali povečanje vsebnosti Hg in obnašanje dimnih plinov v različnih delih procesa izdelave cementa. Nadaljevali so z raziskavo (Ljubič Mlakar et al., 2011), ki je bila osredotočena na razumevanje onesnaževanja s Hg, ki ga povzroča cementarna. Aktivni in pasivni biomonitoring z epifitskimi lišaji so združili z drugimi instrumentalnimi meritvami emisij Hg, vsebnosti Hg v surovinah, koncentracije elementarnega Hg v zraku, količine prašnih oblog, temperatur, padavin in drugih meritev iz rednega programa monitoringa cementarne. Speciacija Hg v dimnih plinih je pokazala, da je glavna oblika izpuščenega Hg reaktivno plinasto Hg^{2+}, kar je značilno za cementarne. Koncentracije elementarnega Hg v zraku so merili v različnih meteoroloških pogojih in so bile relativno nizke, povprečno manj kot 10 ng/m^3) (Ljubič Mlakar et al., 2011). Glede na visok delež Hg^{2+} v plinasti fazi je bil lokalen vpliv sedimentiranega Hg ocenjen kot pomemben. Koncentracije Hg v lišajih in situ niso pokazale pomembnega vpliva, presajeni (transplantirani) lišaji pa so pokazali povečanje koncentracije Hg, še posebno na eni lokaciji v bližini cementarne. Zanimivo je, da so opazili, da je bila vitalnost lišajev prizadeta v daljšem obdobju

biomonitoringa, kar so povezali z nekaterimi elementi v prašnih delcih in njihovo alkalnostjo ter vplivi ostalih emisij. Koncentracije Hg izmerjene v presajenih lišajih, ki so bili v dobrem stanju, so bile v dobri korelaciji z delovnim časom peči v cementarni (tj. izpuščeno količino Hg) (Ljubič Mlakar et al., 2011). Nadalje so ocenili skupne letne emisije Hg iz cementarne na povprečno 10 kg in največ 24 kg (Ljubič Mlakar et al., 2011). Ljubič Mlakar in sodelavci (2011) zaključujejo študijo z ugotovitvijo, da je cementarna edini pomemben vir Hg na območju raziskav in da naravne surovine vsebujejo zelo majhne vsebnosti Hg. Glede na to, je mogoče sklepati, da je onesnaženje, ki ga povzroča cementarna, majhno. Nadalje so zapisali, da bi lahko visokotemperaturni industrijski procesi pomembno prispevali k onesnaženosti zraka s potencialno strupenimi elementi. Opozarjajo, da vsaka sprememba v uporabi goriv, surovin ali tehnologije lahko povzroči spremembe in da bo v prihodnje to zelo pomembno zaradi povečane uporabe alternativnih goriv ter sekundarnih surovin v cementarni (Ljubič Mlakar et al., 2011).

V okviru magistrske naloge z naslovom »Ugotavljanje onesnaženosti zraka v srednji soški dolini z izbranimi vrstami mahov« (Mavrič, 2020) so s pomočjo usedanja zračnih delcev na površino mahov ter s filtriranjem zraka skozi filtre z zračno črpalko preučevali onesnaženost zraka v srednji Soški dolini. Za vzorčenje so uporabili štiri vrste mahov, ki so jih izpostavili po dva meseca na štirih izbranih vzorčnih mestih (Gorenje Polje, Zagabrca, Ložice in Markiči – kontrolno vzorčno mesto) v času kurilne sezone ter izven kurilne sezone. Elementno sestavo mahov pred in po izpostavitvi so določili s tehnikama XRF in ICP-MS. Po izpostavitvi so vse vrste mahov zelo dobro akumulirale Cl. Večina je slabo privzemala Br, Cr in Ni, saj so se ti elementi iz vzorcev izpirali. Vsebnosti akumuliranih elementov so se razlikovale tako med različnimi vrstami mahov, kot med različnimi vzorčnimi mesti. V Soški dolini, na lokacijah v bližini cementarne, so bile koncentracije Hg in Tl višje kot na vzorčnem mestu na pobočju sosednje doline. Na vseh vzorčnih mestih je tako med kurilno in nekurilno sezono večina vrst mahov akumulirala Al, Si, S, K, Ca, Ti, Mn in Fe. V obeh sezonah se je akumuliral tudi Cl. V kurilni sezoni so vse vrste mahov dodatno akumulirale še Pb na vzorčnem mestu Gorenje Polje, tri vrste pa Cr. Na Zagabrci so tri vrste mahu akumulirale Rb, Ag in Hg, v Ložicah pa Rb in Tl. V nekurilni sezoni so vse vrste mahov (poleg že omenjenih elementov) akumulirale Hg in Tl na vzorčnem mestu Gorenje Polje. Po tri vrste mahov so nakazovale povečanje vsebnosti Sr na vseh štirih vzorčnih mestih. Rubidij je bil prisoten na vseh vzorčnih mestih razen v Markičih. Povečanje vsebnosti Zn je bilo zaznano na vzorčnem mestu Markiči, povečanje Hg pa na vzorčnem mestu Zagabrca in Ložice (Mavrič, 2020). Dodatno so z zračno črpalko vzorčili trdne delce v zraku po dva dni v kurilni in izven kurilne sezone (na istih vzorčnih mestih), pri čemer so s pomočjo separatorja trdne zračne delce ločili glede na njihovo velikost (2,5–10 μm – inhalabilna frakcija, < 2,5 μm – respirabilna frakcija). Filtre (polikarbonatni membranski filtri s premerom 47 mm) z ujetimi trdnimi delci so analizirali z LA-ICP-MS in jih pregledali z vrstičnim elektronskim mikroskopom (SEM-EDX) ter delcem določili elementno sestavo. Na pregledanih filtrih so prevladovali delci saj, ki so se združevali v večje skupke. Zapisali so tudi, da so našli delce podobne azbestnim vlaknom. Koncentracija trdnih delcev je bila med kurilno sezono v povprečju višja kot izven kurilne sezone (Mavrič, 2020). Avtorica poudarja, da so za zanesljive zaključke potrebne dodatne raziskave (Mavrič, 2020).

Namen raziskave je bil določiti geokemično sestavo treh tipov prahu v okolici cementarne v Anhovem. Želeli smo ugotoviti ali na podlagi raziskave lahko opazimo morebitne pretekle in sedanje vplive cementarne v Anhovem na geokemične lastnosti prahu in tudi okolja na splošno.

Materiali

Na vplivnem območju cementarne v Anhovem smo vzorčili tri tipe prahu: stanovanjski (sl. 1) podstrešni (sl. 2) in cestni prah (sl. 3). Stanovanjski prah je tip prahu, ki se odlaga na ravnih površinah (npr. tla, pohištvo) v bivalnih delih hiš oz. stanovanj. Sestavljajo ga organski in anorganski delci naravnega ter antropogenega izvora, ki prihajajo predvsem iz notranjih virov in v manjši meri iz zunanjih. Notranji viri so odvisni od aktivnosti in navad stanovalcev ter lastnosti stanovanj, zato se med posameznimi stanovanji močno razlikujejo (Morawska & Salthammer, 2003; Rasmussen, 2004; Turner & Ip, 2007; Gaberšek, 2020; Gaberšek & Gosar, 2021). Stanovanjski prah je indikator trenutnih virov onesnaženja in, ker je človek z njim v vsakodnevnem stiku, je študij stanovanjskih prahov pomemben tudi z vidika zdravja ljudi.

Podstrešni prah je tip prahu, ki se odlaga na neposeljenih in neizoliranih podstrešjih. Večinoma izvira iz naravnih in antropogenih zunanjih virov (Cizdziel & Hodge, 2000; Šajn, 2003; Gosar et al., 2006; Davis & Gulson, 2005). Neprekinjeno in nemoteno odlaganje delcev ter njihova dolgotrajna stabilnost na podstrešjih omogoča posredno oceno

Sl. 1. Stanovanjski prah: prerezana polna vrečka iz sesalca in sejanje (foto: M. Gaberšek).

Fig. 1. Household dust: cut vacuum cleaner bag and sieving its content (photo: M. Gaberšek).

Sl. 2. Vzorčenje podstrešnega prahu (foto: M. Gosar).

Fig. 2. Attic dust sampling (photo: M. Gosar).

zgodovinske obremenjenosti zraka z onesnaževali, od izgradnje stavbe do časa vzorčenja (Gosar & Šajn, 2001; Ilacqua et al., 2003; Šajn, 2003; Davis & Gulson, 2005; Gosar et al., 2006; Völgyesi et al., 2014; Miler & Gosar, 2019; Gaberšek, 2020; Gaberšek & Gosar, 2021; Gaberšek et al., 2022).

V primeru cestnega prahu gre za prah oziroma trdne delce, ki se odlagajo in kopičijo na zunanjih asfaltiranih in betonskih površinah (Gunawardana et al., 2012; Denby et al., 2018). Cestni prah predstavlja mešanico materialov, delcev naravnega in antropogenega izvora (Taylor, 2007; Amato

Sl. 3. Vzorčenje cestnega prahu (foto: M. Gosar).

Fig. 3. Street dust sampling (photo: M. Gosar).

et al., 2009; Gunawardana et al., 2012; Žibret et al., 2013; Ali et al., 2019; Teran et al., 2020; Gaberšek, 2020; Gaberšek & Gosar, 2021). Eden izmed pomembnejših antropogenih virov je promet, tako zaradi izgorevanja goriv, kot zaradi obrabe gum, zavor in ostalih delov vozila (Grigoratos & Martini, 2015; Hwang et al., 2016; Ali et al., 2019). Seveda na sestavo cestnega prahu pomembo vplivajo vsi antropogeni viri, ki so aktivni v času pred vzorčenjem. Odlaganje in zadrževalni čas cestnega prahu je močno odvisen od vremenskih pogojev (sušno, dež, veter) in lastnosti površin (prisotnost por in razpok, kjer se prah lahko zadrži). Cestni prah torej odraža razmere v zunanjem okolju v relativno bližnji preteklosti (nekaj dni, tednov ali mesecev).

Metode dela

Načrt vzorčenja različnih vrst prahov smo pripravili skupaj s sodelavci iz Biotehniške fakultete (BF), ker so oni v istem letu raziskovali tla na obravnavanem območju. Vzorčenje prahov smo izvedli spomladi leta 2023. Pri vzorčenju podstrešnega in stanovanjskega prahu smo imeli tudi izjemno dragoceno pomoč in podporo Občine Kanal ob Soči in občanov, ki so nam omogočili vstop v njihova stanovanja oz. podstrehe in s tem vzorčenje.

Vzorčenje

Vzorčili smo stanovanjski, podstrešni in cestni prah na vplivnem območju cementarne v Anhovem (sl. 4). Stanovanjski prah (vrečke iz sesalcev) smo pridobili na 16 lokacijah (oznaka HD), podstrešni prah na 11 lokacijah (oznaka AD; na eni lokaciji smo vzeli 2 vzorca) in cestni prah na 14 lokacijah (oznaka SD). Stanovanjski prah smo vzorčili s pridobitvijo polnih vrečk iz sesalcev. Sodelujoči stanovalci so ob tem izpolnili vprašalnik o njihovem življenjskem slogu in navadah ter lastnostih stanovanj, ki bi lahko vplivale na kemično sestavo stanovanjskega prahu. Slika 1 prikazuje pripravo vzorca stanovanjskega prahu v laboratoriju. Podstrešni prah smo vzorčili z uporabo najlonskih krtač oz. s krtačenjem prahu z lesenih površin na podstrešjih (predvsem tramov), ki so bila zgrajena pred najmanj 50 leti. Pri vzorčenju se je izkazalo, da se zaradi načina gradnje tipičnih hiš na teh podstrehah sedimentira relativno malo prašnih delcev. Na nekaterih podstrehah, ki smo jih obiskali ni bilo dovolj prahu in zato nismo uspeli pridobiti vzorca. Na sliki 2 je prikazano vzorčenje podstrešnega prahu. Cestni prah smo vzorčili s krtačenjem z najlonskimi krtačami iz primernih (asfaltiranih ali betoniranih) površin. Na sliki 3 so predstavljene fotografije vzorčenja cestnega prahu.

Vse tri tipe prahu smo pridobili v sledečih naseljih v širši okolici Anhovega oz. cementarne: Krstenica, Anhovo, Gorenje Polje, Deskle, Deskle – Rodež, Bodrež, Morsko, Ložice in Kanal, samo stanovanjski prah pa tudi v naseljih Ravna in Goljevica. Na sliki 4 so prikazane lokacije vzorcev posameznega tipa prahu. Zaradi zavarovanja anonimnosti stanovalcev, ki so nam omogočili vzorčenje stanovanjskega in podstrešnega prahu, lokacije vzorčnih mest niso centrirane na mesto vzorčenja, ampak so naključno nekoliko premaknjene, tako da sledenje do hiše/stanovanja, kjer smo vzorčili ni mogoče.

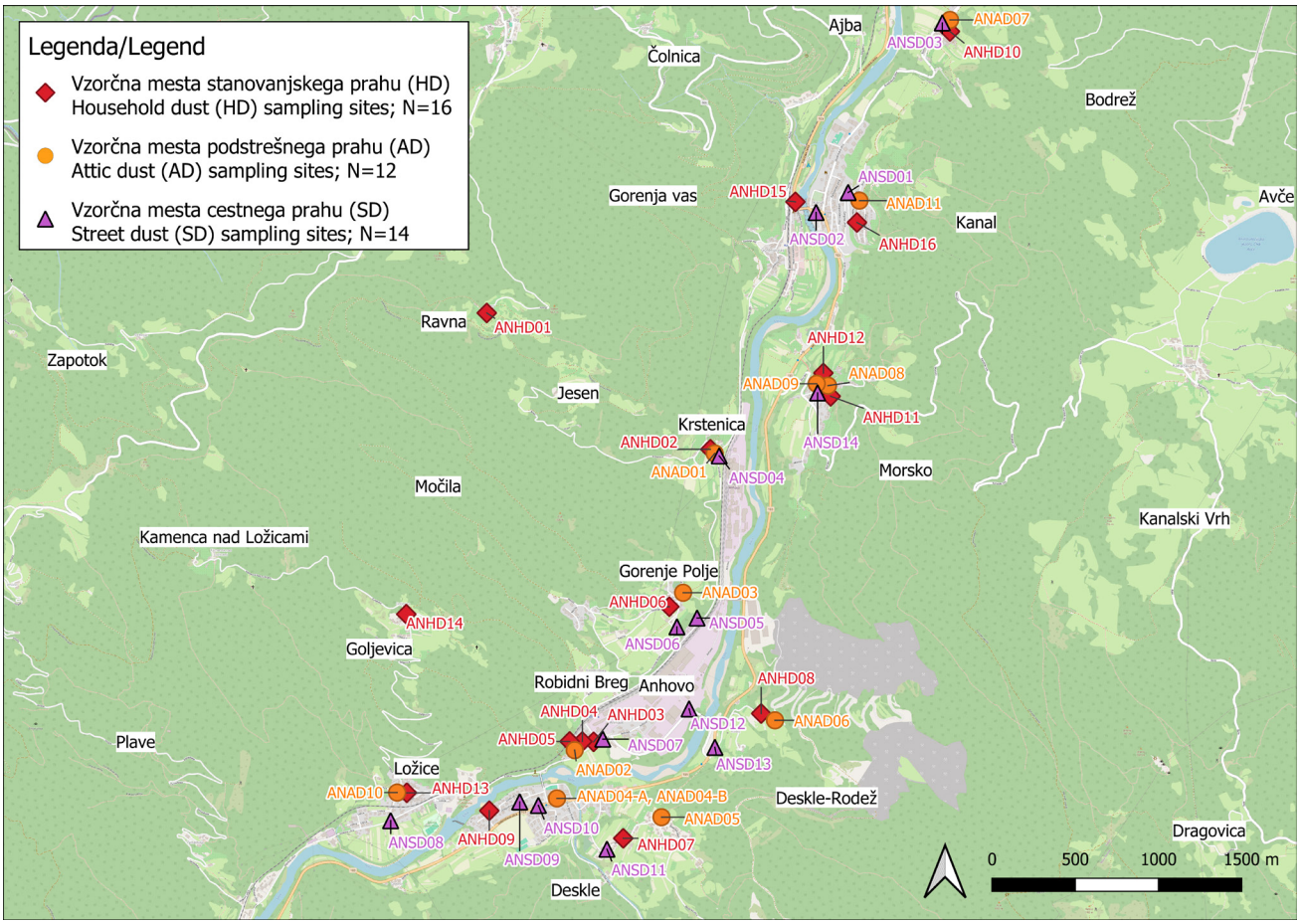

Sl. 4. Prikaz vzorčnih mest stanovanjskega, podstrešnega in cestnega prahu.
Fig. 4. Sampling sites of household, attic and street dust.

Priprava vzorcev in analitika

V laboratoriju Geološkega zavoda Slovenije smo vzorce prahov po sušenju na 35 °C presejali na frakcijo < 0,063 mm. Ta frakcija je bila analizirana. Kemična analiza vzorcev je bila opravljena v laboratoriju Bureau Veritas Mineral Laboratories (mednarodna akreditacija ISO/IEC 17025:2017), v Vancouvru v Kanadi. Za določitev multi-elementne sestave vključujoč vsebnosti As, Cd, Co, Cr, Cu, Hg, Mo, Mn, Ni, Pb, Sb, Tl in Zn je bilo 0,5 g vzorca prelitega z modificirano zlatotopko (mešanica kislin HCl in HNO_3 ter vode v razmerju 1:1:1), eno uro segrevano na 95 °C in potem primerno razredčeno z destilirano vodo. Vsebnosti elementov v raztopini so bile določene z induktivno sklopljeno plazemsko (ICP) masno spektrometrijo (MS). Na podlagi ponovitev analiz devetih vzorcev (po tri vsakega tipa prahu) in analize standardov (BCR 146R, OREAS 45e, OREAS 151b) je bila kakovost analitike ocenjena kot ustrezna za vse obravnavane elemente.

Rezultati in razprava

V tabeli 1 so podani osnovni podatki neparametrične statistike, ki je v tovrstnih raziskavah, z relativno malo vzorci, najbolj smiselna (Min – najmanjša vsebnost, Md – mediana, Max – največja vsebnost) o vsebnostih As, Cd, Co, Cr, Cu, Hg, Mn, Mo, Ni, Pb, Sb, Tl in Zn v vseh treh tipih prahu na preiskovanem območju. V nadaljevanju podrobneje opisujemo njihove vsebnosti, ki so primerjalno prikazane na slikah od 5 do 7, in njihove prostorske porazdelitve.

Kemična sestava stanovanjskega prahu

Vsebnosti arzena (As) v stanovanjskem prahu so v območju od 1,6 do 6,7 mg/kg. Vsebnosti kadmija (Cd) so večinoma od 0,56 do okoli 3 mg/kg. Odstopa le vsebnost v stanovanjskem prahu iz Bodreža, ki vsebuje 6,48 mg/kg kadmija. Glede na podatke iz vprašalnika o navadah stanovalcev kaže, da v stanovanju prebivalci ne kadijo, večji vpliv zunanjega okolja je možen zaradi sesanja predpražnikov. Vsebnosti kobalta (Co) se večinoma gibajo od 3,5 do 10 mg/kg. Z vsebnostjo 29,8 mg/kg izstopa samo vzorec iz Rodeža pri Desklah. Iz vprašalnika ni videti kakšnih posebnosti v navadah stanovalcev ali v lastnostih stanovanja. Tudi pri vsebnostih kroma (Cr), molibdena (Mo), niklja (Ni), bakra (Cu) navzgor odstopa vzorec iz Rodeža. Vsebuje na primer 195 mg/kg Cr, kar je skoraj 4-kratna vsebnost mediane in je izjemno bogat tudi z bakrom

Tabela 1. Osnovne statistike za stanovanjski, podstrešni in cestni prah.
Table 1. Basic statistics for household, attic and street dust.

	ENOTA UNIT	LD	STANOVANJSKI PRAH HOUSEHOLD DUST HD (N=16)			PODSTREŠNI PRAH ATTIC DUST AD (N=12)			CESTNI PRAH STREET DUST SD (N=14)		
			Min	Md	Max	Min	Md	Max	Min	Md	Max
As	mg/kg	0,1	1,6	2,8	6,7	5,1	7,6	36,7	1,7	2,9	4,5
Cd	mg/kg	0,01	0,56	0,95	6,48	1,34	2,26	7,38	0,35	0,46	1,39
Co	mg/kg	0,1	3,5	5,8	29,8	5,0	7,2	48,2	3,3	6,0	10,8
Cr	mg/kg	0,5	26	50	195	34	55	245	25	45	660
Cu	mg/kg	0,01	76	183	2800	75	110	306	19	49	232
Hg	mg/kg	0,005	0,345	1,497	6,502	0,003	3,703	17,419	0,395	1,911	5,721
Mn	mg/kg	1	292	432	697	400	660	1441	379	622	3820
Mo	mg/kg	0,01	1,12	1,94	24,43	1,50	2,61	10,10	0,95	2,47	11,46
Ni	mg/kg	0,1	25	47	131	26	42	71	19	27	58
Pb	mg/kg	0,01	37	67	246	79	195	315	14	32	215
Sb	mg/kg	0,02	1,3	3,0	72,2	1,2	3,5	9,2	0,6	1,3	15,5
Tl	mg/kg	0,02	0,06	0,14	0,41	0,12	0,50	6,87	0,06	0,14	1,63
Zn	mg/kg	0,1	332	556	1054	231	550	839	99	221	605

LD-meja detekcije uporabljene analitske metode / detection limit; N-število vzorcev / number of samples; Min-najmanjša vsebnost / minimum level; Md-mediana / median; Max-največja vsebnost / maximum level

(2800 mg/kg). Pri vsebnostih bakra (Cu) opazimo nadalje tudi, da od mediane (183 mg/kg) navzgor nekoliko odstopa vzorec (830 mg/kg) iz Bodreža. Posebnosti v navadah prebivalcev, ki bi lahko pojasnile visoke vsebnosti, nismo opazili. Vsebnosti mangana (Mn) ne odstopajo močno od mediane (432 mg/kg) in se gibljejo od 292 do 697 mg/kg. Vsebnosti molibdena (Mo) so blizu mediane (1,94 mg/kg), odstopa že prej omenjeni vzorec iz Rodeža z vsebnostjo 24,4 mg/kg. Podobno je pri vsebnostih niklja (Ni). Poleg vzorca iz Rodeža od mediane (47 mg/kg) navzgor odstopa tudi eden izmed vzorcev iz Anhovega (131 mg/kg). Visoke vsebnosti Mo, Ni, Co, Cr in Cu v stanovanjskem prahu v Rodežu morda lahko pripišemo vplivu bližnjega kamnoloma fliša oz. laporovca, ki ga uporabljajo v cementarni. Za potrditev te domneve bi bilo potrebno določiti geokemično sestavo fliša. Glede na podatke o geokemičnih ozadjih in pragovih (Gosar et al., 2019) je v tem delu Slovenije pričakovati nekoliko višje vsebnosti naštetih elementov, z izjemo molibdena (Mo). Pri vsebnostih svinca (Pb) od mediane (67 mg/kg) navzgor odstopa samo vzorec iz Raven (246 mg/kg). Pri vsebnosti antimona (Sb) od mediane (2,96 mg/kg) navzgor zelo močno odstopa samo eden izmed dveh vzorcev iz Kanala (72 mg/kg). Pri vsebnostih talija (Tl) je zanimivo, da od mediane (0,14 mg/kg) navzgor pomembneje odstopata predvsem dva vzorca iz Anhovega (0,41 in 0,40 mg/kg) nekoliko manj tudi vzorec iz Gorenjega Polja (0,28 mg/kg). Vsebnosti cinka (Zn) so od 332 do 1054 mg/kg, mediana je 556 mg/kg. Največ Zn je v vzorcih iz Bodreža in Kanala.

Vsebnosti živega srebra (Hg) v stanovanjskem prahu se gibljejo od 0,345 do 6,502 mg/kg, mediana je 1,497 mg/kg. Glede na to, da prebivalci v stanovanjih, kjer smo pridobili stanovanjski prah ne kadijo, so vrednosti razmeroma visoke. Izrazito odstopa največja vrednost, ki smo jo določili v stanovanjskem prahu v Goljevici, zahodno od Anhovega.

Primerjava s podatki o elementi sestavi stanovanjskih prahov iz Maribora (Gaberšek 2020; Gaberšek & Gosar, 2021), Idrije (Bavec et al., 2017), slovenskega podeželja in urbanih okolij (Teran, 2020) kaže (sl. 8), da so vsebnosti Hg na obravnavanem območju med 4 in 6-krat večje kot v Mariboru (Gaberšek 2020; Gaberšek & Gosar, 2021) in na slovenskem podeželju ter v urbanih krajih Slovenije (Teran, 2020). Mediana v Idriji (20,9 mg/kg, Bavec et al., 2017) je 13,9-krat večja kot na obravnavanem območju v okolici Anhovega (1,5 mg/kg). To je glede na zelo močno obremenjeno okolje v Idriji (Baptista Salazar et al., 2017; Bavec & Gosar 2016; Gosar & Teršič, 2015; Gosar et al., 2006; Gosar et al., 2016; Gosar & Teršič, 2012 in tam našteti viri) zaradi več stoletij pridobivanja Hg povsem razumljivo.

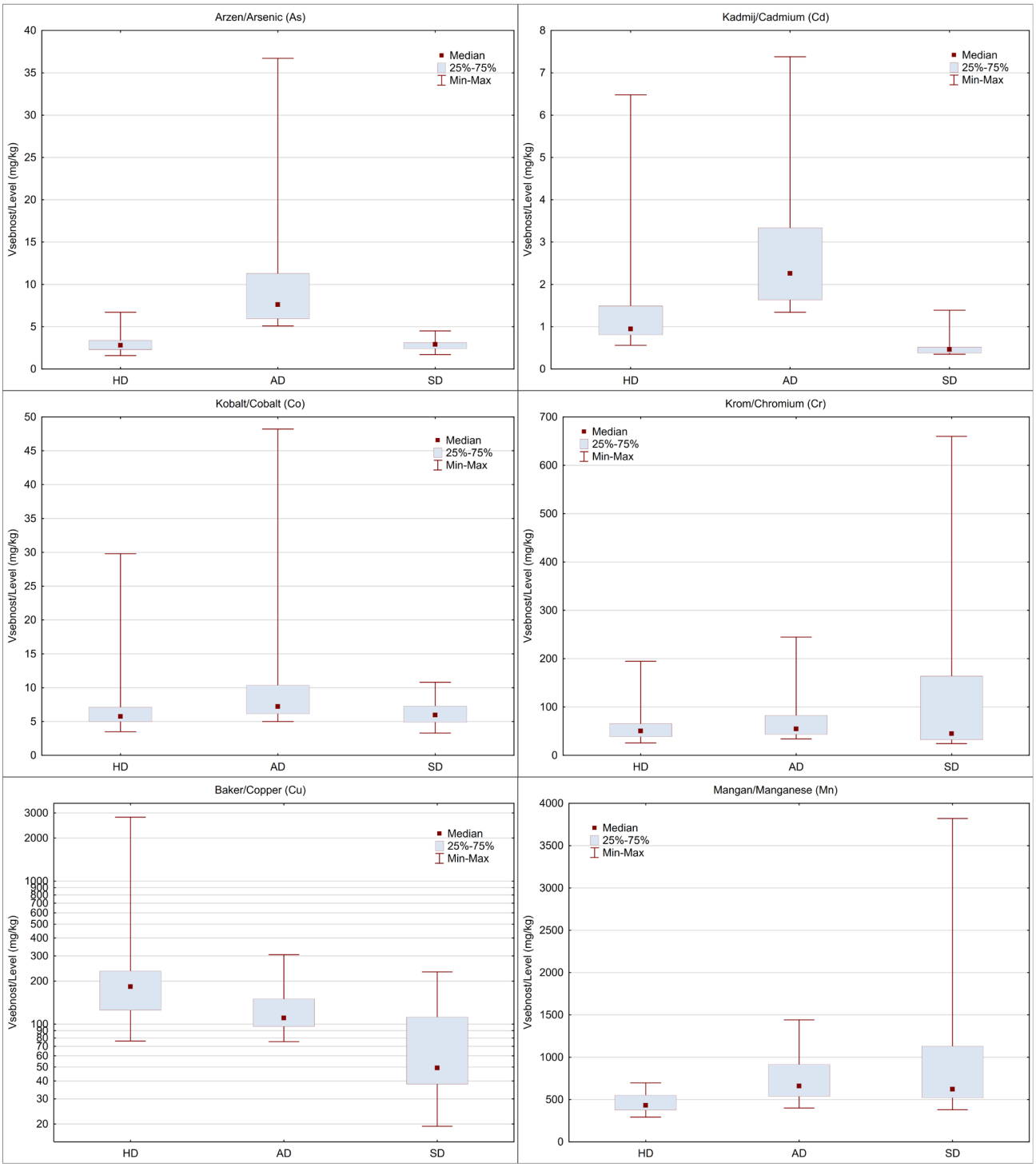

Sl. 5. Primerjava osnovnih statističnih parametrov v stanovanjskem (HD), podstrešnem (AD) in cestnem (SD) prahu za As, Cd, Co, Cr, Cu, Mn.
Fig. 5. Comparison of basic statistical parameters in household (HD), attic (AD) and street (SD) dust for As, Cd, Co, Cr, Cu, Mn.

Razmerja med medianami ostalih obravnavanih elementov v stanovanjskem prahu med raziskovanim območjem in Mariborom (Gaberšek 2020; Gaberšek & Gosar, 2021), slovenskim podeželjem in urbanimi okolji v Sloveniji (Teran, 2020) so prikazane na sliki 8. Mediane za Tl, Mn, Cu in Ni so na obravnavanem območju večje kot v Mariboru. Glede na slovensko podeželje so mediane na obravnavanem območju večje za večino obravnavanih elementov; za več kot 1,5-krat za Tl in Cu, do 1,5-krat večje so mediane za Mn, Ni in Pb. Tudi primerjava median z urbanimi območji kažejo na večje vsebnosti Tl, Mn in Cu na širšem območju Anhovega.

Kemična sestava podstrešnega prahu

Vsebnosti As v podstrešnem prahu so v območju od 5,1 do 36,7 mg/kg, z mediano pri 7,6 mg/kg. Od mediane navzgor izrazito odstopa eden izmed dveh vzorcev iz naselja Morsko (36,7 mg/kg).

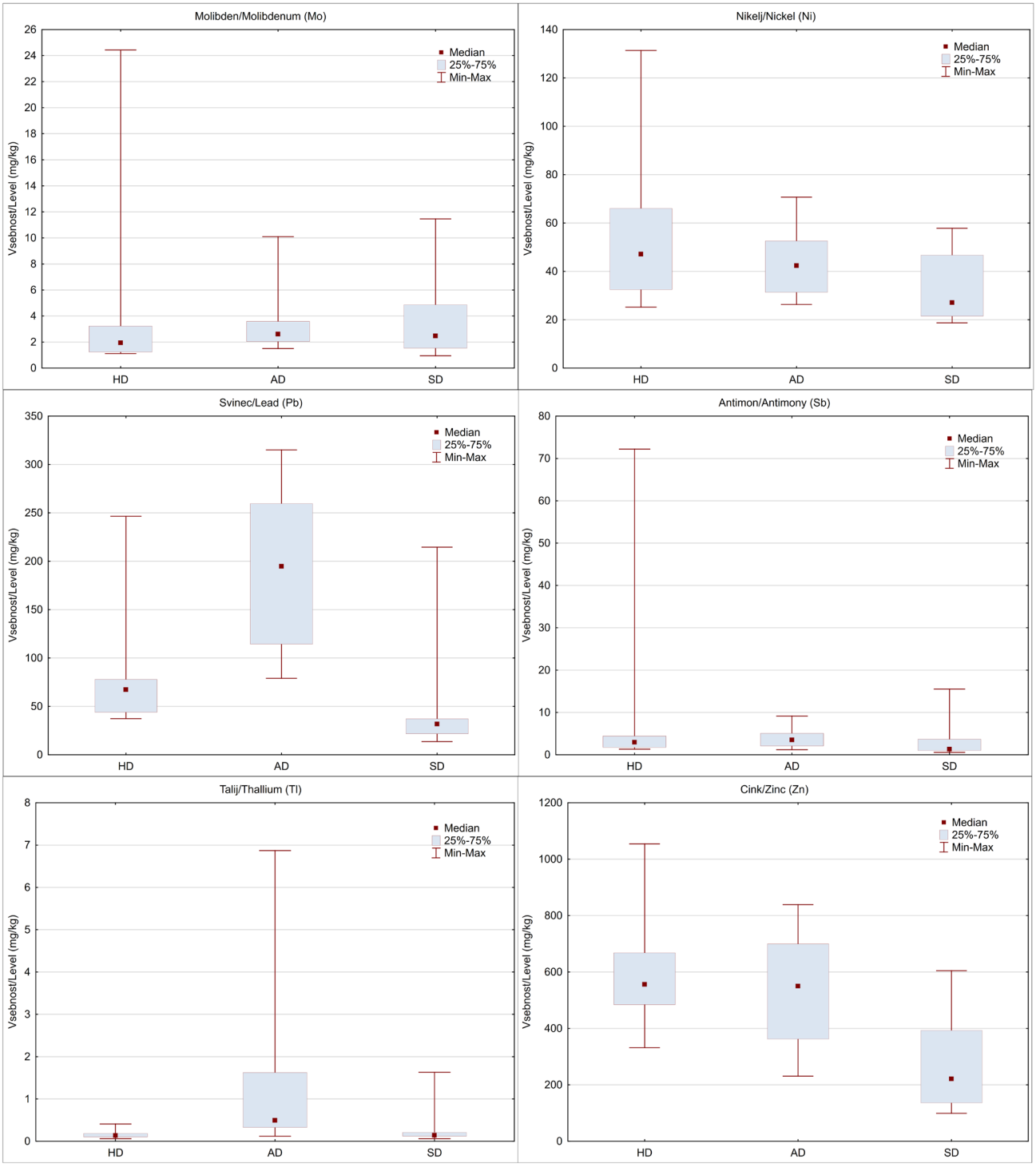

Sl. 6. Primerjava osnovnih statističnih parametrov v stanovanjskem (HD), podstrešnem (AD) in cestnem (SD) prahu za Mo, Ni, Pb, Sb, Tl, Zn.
Fig. 6. Comparison of basic statistical parameters in household (HD), attic (AD) and street (SD) dust for Mo, Ni, Pb, Sb, Tl, Zn.

Drugi dve največji vsebnosti, ki pa od mediane ne odstopata močno, sta bili ugotovljeni v Desklah. Vsebnosti Cd so od 1,34 do 7,38 mg/kg, mediana je 2,26 mg/kg. Največjo vsebnost Cd smo ugotovili v podstrešnem prahu iz Gorenjega Polja. Vsebnosti Co se večinoma gibajo od 5 do 48 mg/kg. Samo vzorec iz Rodeža pri Desklah izrazito odstopa od mediane, ki znaša 7,2 mg/mg. Pri vsebnostih Cr navzgor močno odstopa vzorec iz Kanala, ki vsebuje 245 mg/kg kroma, kar je 4,5-kratna vsebnost mediane (55 mg/kg). Pri vsebnostih Cu opazimo, da od mediane (110 mg/kg) z vsebnostjo 306 mg/kg navzgor odstopa isti vzorec iz Kanala, ki vsebuje tudi veliko Cr. Vsebnosti Mn ne odstopajo močno od mediane (660 mg/kg) in se gibljejo od 400 do 1000 mg/kg, z izjemo vzorca iz Anhovega, kjer je vsebnost 1441 mg/kg. Vsebnosti Mo so blizu mediane (2,61 mg/kg), močno odstopa le vzorec iz Rodeža pri Desklah z vsebnostjo 10,1 mg/kg. V Rodežu smo ugotovili tudi največjo vsebnost Mo

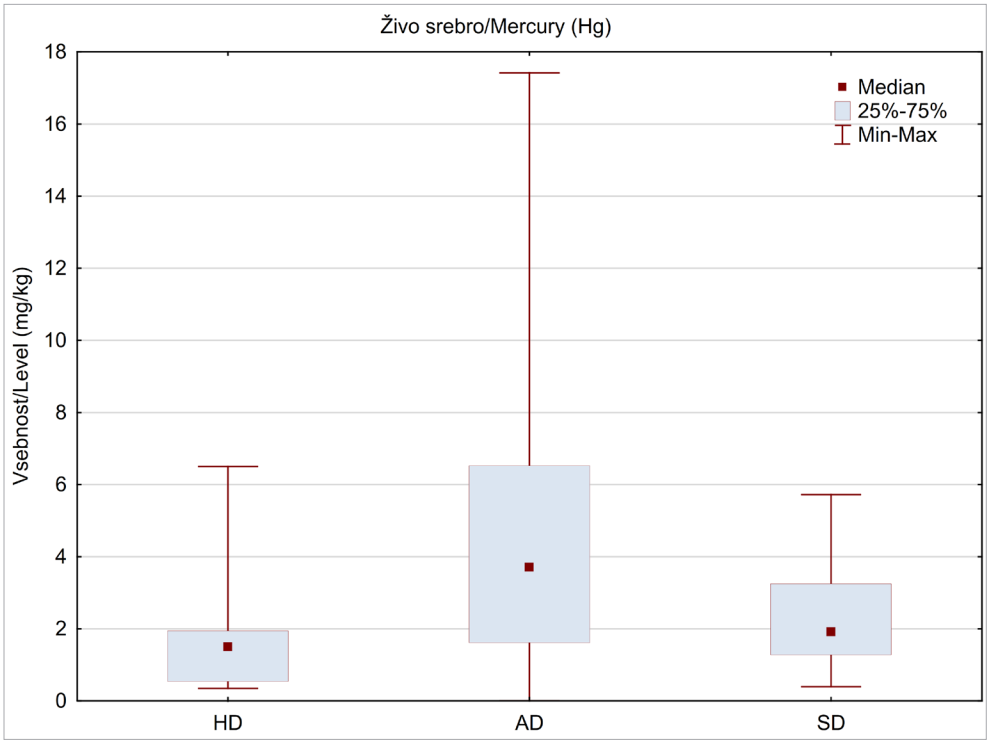

Sl. 7. Primerjava osnovnih statističnih parametrov v stanovanjskem (HD), podstrešnem (AD) in cestnem (SD) prahu za živo srebro (Hg).

Fig. 7. Comparison of basic statistical parameters in household (HD), attic (AD) and street (SD) dust for mercury (Hg).

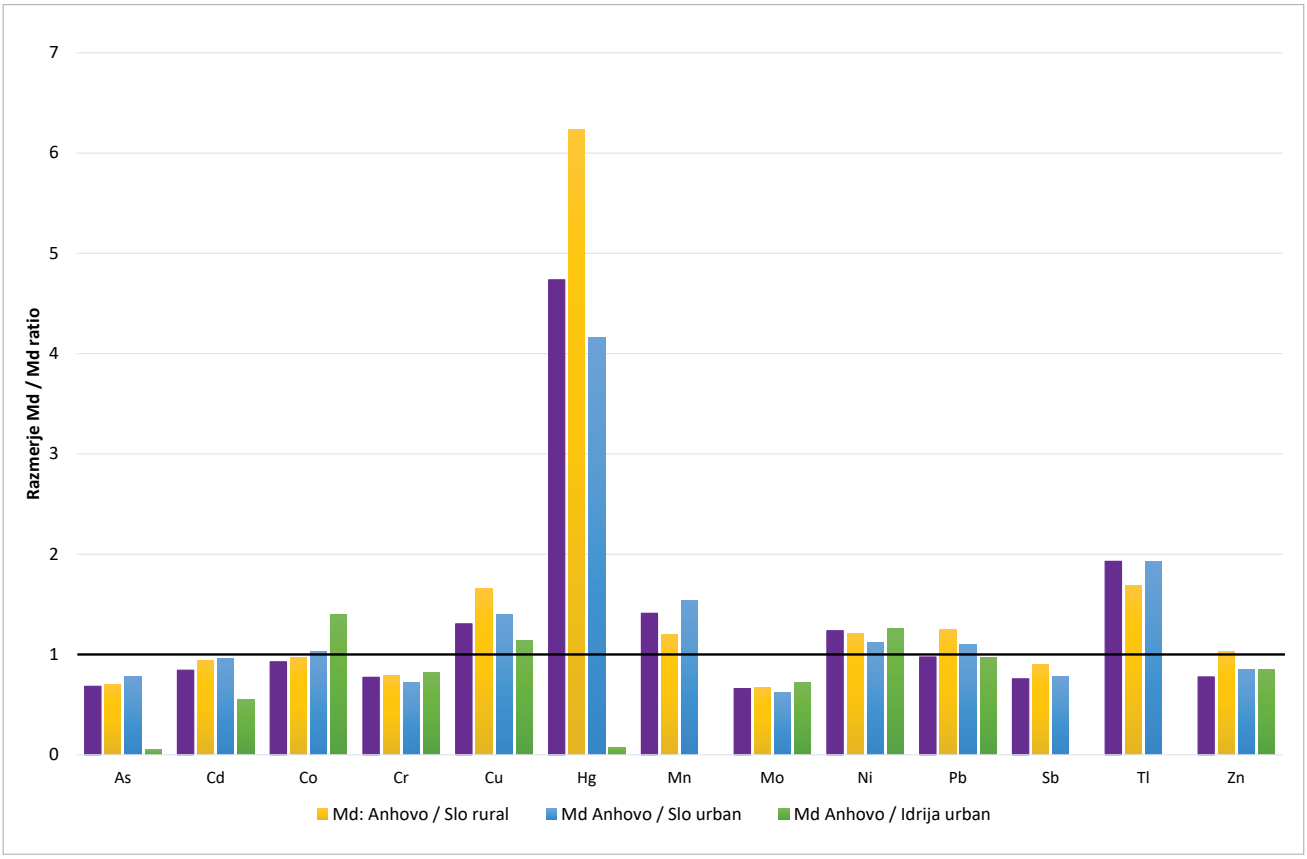

Sl. 8. Razmerja med medianami v stanovanjskem prahu za obravnavane elemente med raziskovanim območjem (Anhovo) in vrednostmi v Mariboru (Mb; Gaberšek & Gosar, 2021), na slovenskem podeželju (Slo rural) in v urbaniziranih okoljih (Slo urban) v Sloveniji (Teran, 2020) ter v Idriji (Bavec et al., 2017; za Mn, Sb in Tl ni podatkov za Idrijo).

Fig. 8. Ratios of medians in houshold dust for the considered elements between the study area (Anhovo) and values in Maribor (Mb; Gaberšek & Gosar, 2021), in the Slovenian countryside (Slo rural) and in urbanized environments (Slo urban) in Slovenia (Teran, 2020) and in Idrija (Bavec et al., 2017; for Mn, Sb and Tl there are no data for Idrija).

v stanovanjskem prahu. Tudi pri vsebnostih Ni od mediane (42 mg/kg) navzgor nekoliko odstopajo vzorci iz Deskel, Gorenjega Polja in Rodeža pri Desklah. Pri vsebnostih Pb od mediane (195 mg/kg) navzgor nekoliko odstopajo vzorci iz Deskel, Bodreža in kraja Morsko. Pri vsebnostih Sb od mediane (3,49 mg/kg) navzgor odstopata vzorca iz Deskel (vsebnosti 7,67 in 9,17 mg/kg). Pri vsebnosti Tl od mediane (0,50 mg/kg) navzgor močno odstopa vzorec podstrešnega prahu iz Gorenjega Polja (6,87 mg/kg). V istem kraju smo določili tudi visoke vsebnosti Tl v stanovanjskem prahu. Vsebnosti Zn so od 231 do 839 mg/kg, mediana je 550 mg/kg. Največ Zn je v vzorcu iz Kanala. V Kanalu smo ugotovili tudi relativno visoke vsebnosti Zn v stanovanjskem prahu.

Vsebnosti Hg se gibljejo od 0,025 do 17,42 mg/kg, z mediano pri 3,703 mg/kg. Od mediane močno odstopa največja vsebnost Hg v podstrešnem prahu v Krstenici, severno od Anhovega. Druge vsebnosti večje od mediane so bile ugotovljene v krajih Morsko, Bodrež, Kanal (vse severno od Anhovega) in tudi v Ložicah, JZ od Anhovega.

Podatkov o povprečnih vsebnostih elementov v podstrešnem prahu za celotno Slovenijo ni. Zato smo izračunali razmerja med medianami v podstrešnem prahu na vplivnem območju cementarne v Anhovem in vrednostmi v Mariboru (Gaberšek 2020; Gaberšek & Gosar, 2021, Gaberšek et al., 2022) ter v Idriji (Gosar et al., 2006) (sl. 9). Na obravnavanem območju je mediana Hg 11,7-krat večja, kot v Mariboru. Večje vsebnosti kot v Mariboru imata na obravnavanem območju še Tl in Mn. Primerjava median obravnavanega območja z medianami z območja Idrije kaže, da je v Anhovem med 1,4 in 1,7-krat več Co, Cr, Cu, Mn in Ni kot v Idriji. Kljub temu, da so vsebnosti Hg na obravnavam območju v podstrešnem prahu visoke glede na primerjavo z Mariborom, je glede na razmerja median v Idriji 7,2-krat več Hg kot na obravnavanem območju, kar je pravzaprav malo, glede na izjemno obremenjenost Idrije in okolice s Hg.

Kemična sestava cestnega prahu

Vsebnosti As v cestnem prahu so med 1,7 in 4,5 mg/kg, z mediano pri 2,9 mg/kg. Od mediane navzgor nekoliko odstopajo vzorci iz Bodreža, Kanala, Deskel in Rodeža. Vsebnosti Cd so od 0,35 do 1,39 mg/kg, mediana je 0,46 mg/kg. Največjo vsebnost Cd smo ugotovili v cestnem prahu iz Gorenjega Polja, podobno kot v podstrešnem prahu. Vsebnosti Co se večinoma gibajo od 3,3 do 10,8 mg/kg. Vsebnosti v vzorcih iz Bodreža, Deskel in Rodeža pri Desklah so večje od mediane, ki znaša 5,95 mg/mg. Pri vsebnostih Cr navzgor močno odstopa vzorec iz Rodeža pri Desklah, ki vsebuje 660 mg/kg Cr, kar je skoraj 15-kratna vrednost mediane (45 mg/kg). Tudi v Bodrežu, ki leži severno od Kanala, na robu obravnavanega območja, smo ugotovili visoko vsebnost Cr v cestnem prahu (581 mg/kg). Pri vsebnostih Cu opazimo, da od mediane (49 mg/kg) navzgor najbolj odstopa eden izmed vzorcev iz Kanala (232 mg/kg). Vsebnosti nad 100 mg/kg so še v Desklah in Rodežu. Vsebnosti Mn od mediane (622 mg/kg) močno odstopajo v Bodrežu (3820 mg/kg) in Rodežu pri Desklah (3792 mg/kg). Vsebnost Mo od mediane (2,47 mg/kg) močno odstopa v vzorcu iz Rodeža

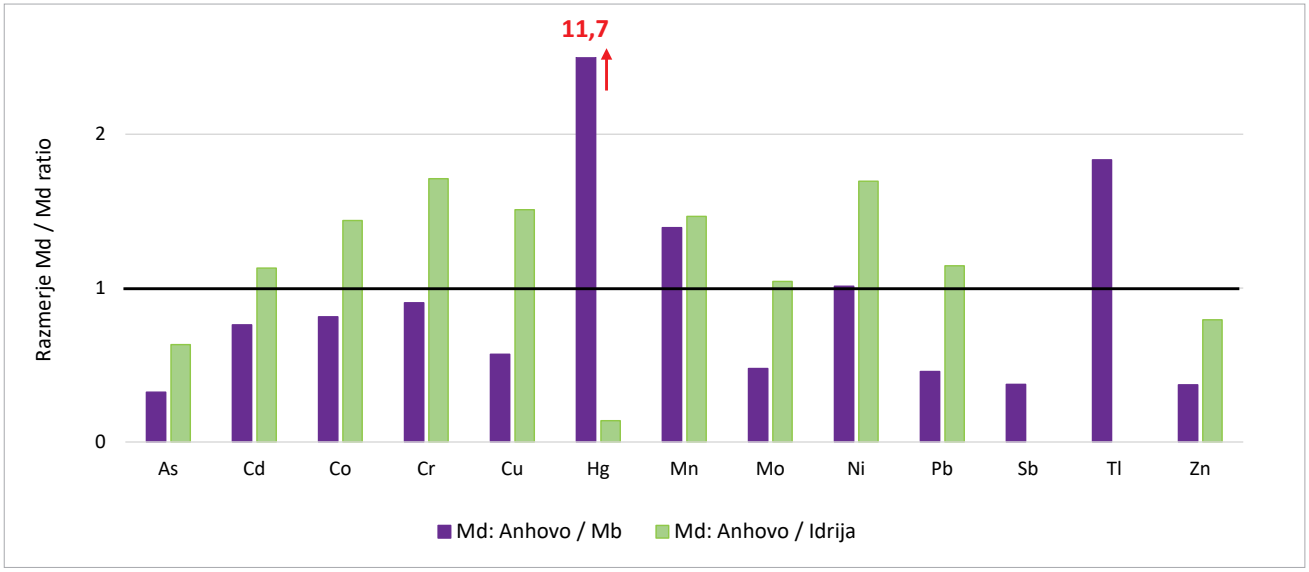

Sl. 9. Razmerja med medianami v podstrešnem prahu za obravnavane elemente med raziskovanim območjem in vrednostmi v Mariboru (Mb; Gaberšek & Gosar, 2022) ter med raziskovanim območjem in urbanim okoljem v Idriji (Gosar et al., 2006; za Sb in Tl ni podatkov za Idrijo).

Fig. 9. Ratios of medians in attic dust for the considered elements between the research area and values in Maribor (Mb; Gaberšek & Gosar, 2022) and between the research area and the urban environment in Idrija (Gosar et al., 2006; for Sb and Tl there are no data for Idrija).

pri Desklah, ki vsebuje 11,5 mg/kg Mo. V Rodežu smo največje vsebnosti Mo odkrili tudi v podstrešnem in stanovanjskem prahu. Visoke vsebnosti Mo v cestnem prahu so tudi v enem od vzorcev v Desklah in v enem od vzorcev v Kanalu. Vsebnosti Ni v cestnem prahu so od 18,7 do 58 mg/kg, z mediano pri 27 mg/kg. Pri vsebnostih Pb od mediane (32 mg/kg) navzgor nekoliko odstopa eden od vzorcev iz Kanala, vsebnosti večje od 100 mg/kg so tudi v dveh vzorcih v Desklah in v Rodežu. Pri vsebnosti Sb od mediane (1,32 mg/kg) navzgor odstopajo isti vzorci kot pri svincu (Pb). Pri vsebnostih Tl od mediane (0,14 mg/kg) navzgor močno odstopa eden od dveh vzorcev cestnega prahu iz Gorenjega Polja (1,63 mg/kg). V istem kraju smo določili tudi visoke vsebnosti Tl v stanovanjskem in podstrešnem prahu. Vsebnosti Zn so od 99 do 605 mg/kg, mediana je 221 mg/kg. Največ Zn je v vzorcih iz Kanala in Rodeža. V Kanalu smo ugotovili tudi relativno visoke vsebnosti Zn v stanovanjskem in podstrešnem prahu.

Vsebnosti Hg se gibljejo od 0,395 do 5,721 mg/kg, z mediano pri 1,911 mg/kg. Od mediane najbolj odstopata vsebnosti v cestnem prahu v krajih Morsko in Ložice, severno in jugozahodno od Anhovega. Druge vsebnosti večje od mediane so bile izmerjene v Kanalu, Desklah in Krstenici. Primerjava median za Hg med raziskovanim območjem in Mariborom (Gaberšek 2020; Gaberšek & Gosar, 2021), slovenskim podeželjem in urbanimi okolji v Sloveniji (Teran, 2020; Teran et al., 2020) jasno kaže, da so vsebnosti na obravnavanem območju precej večje, kot v primerjanih lokacijah (sl. 10). Zelo ilustrativen je tudi prikaz razmerij median Hg na sliki 11. Glede na razmerja median je Hg na vplivnem območju cementarne v Anhovem približno 19-krat več kot v Mariboru, približno 40-krat

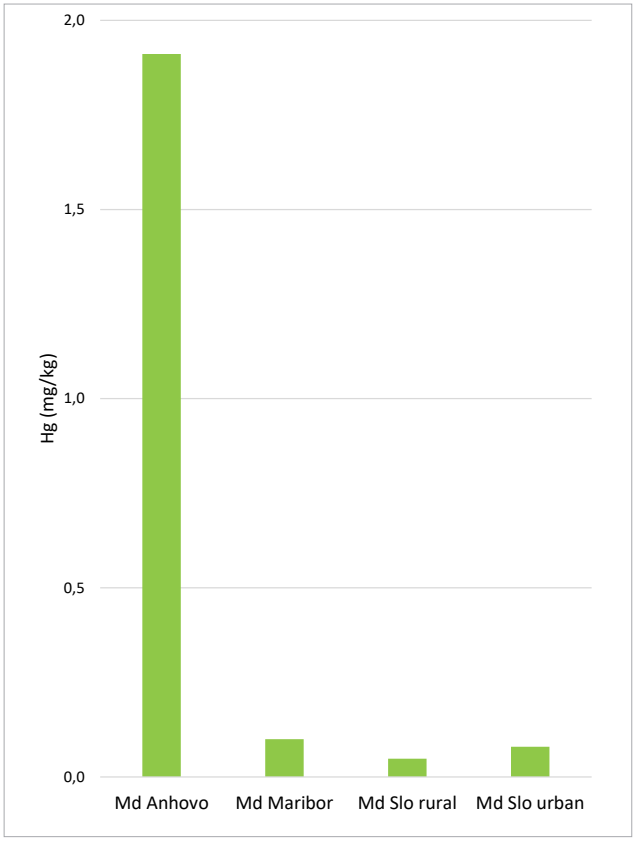

Sl. 10. Primerjava median Hg (mg/kg) v cestnem prahu na obravnavanem območju, v Mariboru (Gaberšek & Gosar, 2021), na slovenskem podeželju in v urbaniziranih okoljih v Sloveniji (Teran, 2020; Teran et al., 2020).

Fig. 10. Comparison of Hg (mg/kg) medians in street dust in the study area, in Maribor (Gaberšek & Gosar, 2021), in the Slovenian countryside and in urbanized environments in Slovenia (Teran, 2020; Teran et al., 2020).

več kot na slovenskem podeželju in približno 24-krat več kot v slovenskih urbanih okoljih (sl. 11).

Razmerja med medianami v cestnem prahu za ostale obravnavane elemente med raziskovanim območjem in vrednostmi v Mariboru (Gaberšek 2020; Gaberšek & Gosar, 2021), slovenskim

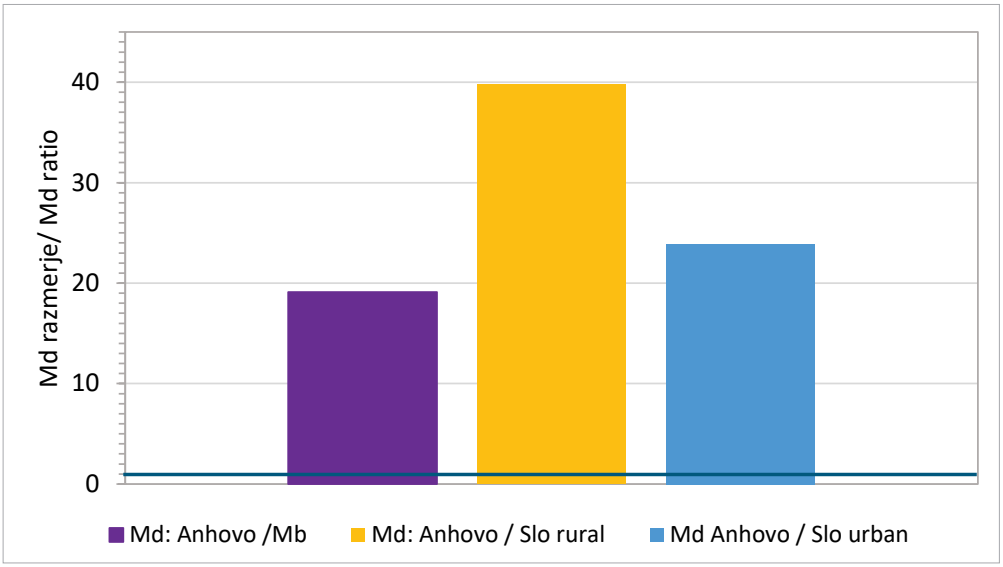

Sl. 11. Razmerja med medianami Hg v cestnem prahu med raziskovanim območjem in vrednostmi v Mariboru (Gaberšek & Gosar, 2021), na slovenskem podeželju in v urbaniziranih okoljih v Sloveniji (Teran, 2020; Teran et al., 2020).

Fig. 11. Ratios of Hg medians in street dust between the study area and values in Maribor (Gaberšek & Gosar, 2021), in the Slovenian countryside and in urbanized environments in Slovenia (Teran, 2020; Teran et al., 2020).

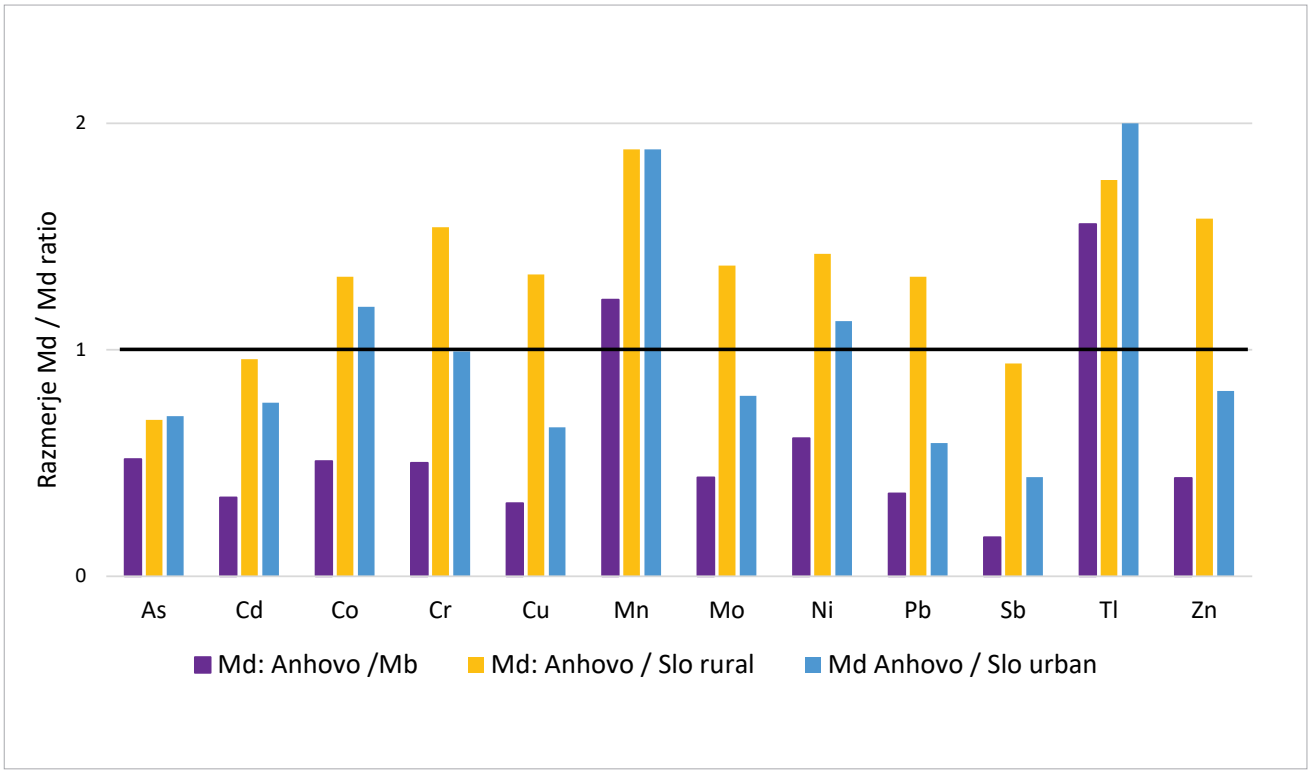

Sl. 12. Razmerja med medianami v cestnem prahu za obravnavane elemente med študijskim območjem in vrednostmi v Mariboru (Gaberšek & Gosar, 2021), na slovenskem podeželju in v urbaniziranih okoljih v Sloveniji (Teran, 2020; Teran et al., 2020).

Fig. 12. Ratios of medians in street dust for the considered elements between the study area and values in Maribor (Gaberšek & Gosar, 2021), in the Slovenian countryside and in urbanized environments in Slovenia (Teran, 2020; Teran et al., 2020).

podeželjem in urbanimi okolji v Sloveniji (Teran et al., 2020; Teran, 2020) so prikazane na sliki 12. Na raziskovanem območju sta samo mediani Tl in Mn večji kot v Mariboru. Glede na slovensko podeželje ugotavljamo, da so mediane na obravnavanem območju večje za večino obravnavanih elementov, od katerih so za Mn, Tl, Zn in Cr večje za več kot 1,5-krat. Tudi razmerja median z urbanimi območji kažejo na večje vsebnosti Tl in Mn na obravnavanem območju.

Interpretacija rezultatov in primerjava vsebnosti obravnavanih elementov v različnih tipih prahu

Stanovanjski (HD), podstrešni (AD) in cestni (SD) prah se razlikujejo v več lastnostih, saj so posledica različnih dejavnikov. Med drugim se razlikujejo v kemični sestavi. Velik vpliv na kemično sestavo imajo različni naravni in antropogeni viri, zadrževalni čas materialov na določenem območju in izpostavljenost vremenskim pogojem. Na sestavo podstrešnega prahu vplivajo predvsem dolgotrajni zunanji viri, na sestavo cestnega prahu sedanji zunanji viri, na sestavo stanovanjskega prahu pa imajo najpomembnejši vpliv gospodinjske dejavnosti stanovalcev, navade stanovalcev in lastnosti stanovanj, značilen pa je tudi doprinos prašnih delcev iz zunanjih virov. Podstrešni prah je precej manj izpostavljen neposrednim vremenskim dejavnikom kot cestni prah in aktivnostim stanovalcev kot stanovanjski prah. V podstrešnem prahu se lahko odvijajo tudi nekateri dolgotrajnejši procesi, kot je npr. kristalizacija sekundarnih mineralov.

Na slikah 5 do 7 so prikazani glavni statistični parametri vsebnosti obravnavanih elementov za vse obravnavane tipe prahu (podatki v tabeli 1). Taka predstavitev rezultatov omogoča dobro primerjavo kemične sestave različnih tipov prahov na preiskovanem območju. Sestava prahov se močno razlikuje med posameznimi tipi. Razponi med najmanjšimi in največjimi vsebnostmi so običajno veliki, kar kaže na različne vire v različnih predelih obravnavanega območja in na antropogen vpliv. V podstrešnem prahu smo izmed vseh prahov ugotovili največje mediane za večino obravnavanih elementov. Navzgor zelo odstopajo vsebnosti Pb. Verjetno je vzrok temu promet zaradi uporabe osvinčenega bencina v preteklosti.

Kot smo predstavili že v prejšnjih poglavjih, so vsebnosti Hg v vseh treh tipih prahu na preiskovanem območju visoke v primerjavi z vsebnostmi v Mariboru in po Sloveniji. Prostorski prikaz vsebnosti Hg v vseh vzorcih vseh treh tipov prahu je prikazan na sliki 13. Seveda so na obravnavanem območju mnogo manjše kot na območju Idrije, ki je zaznamovano z visokimi

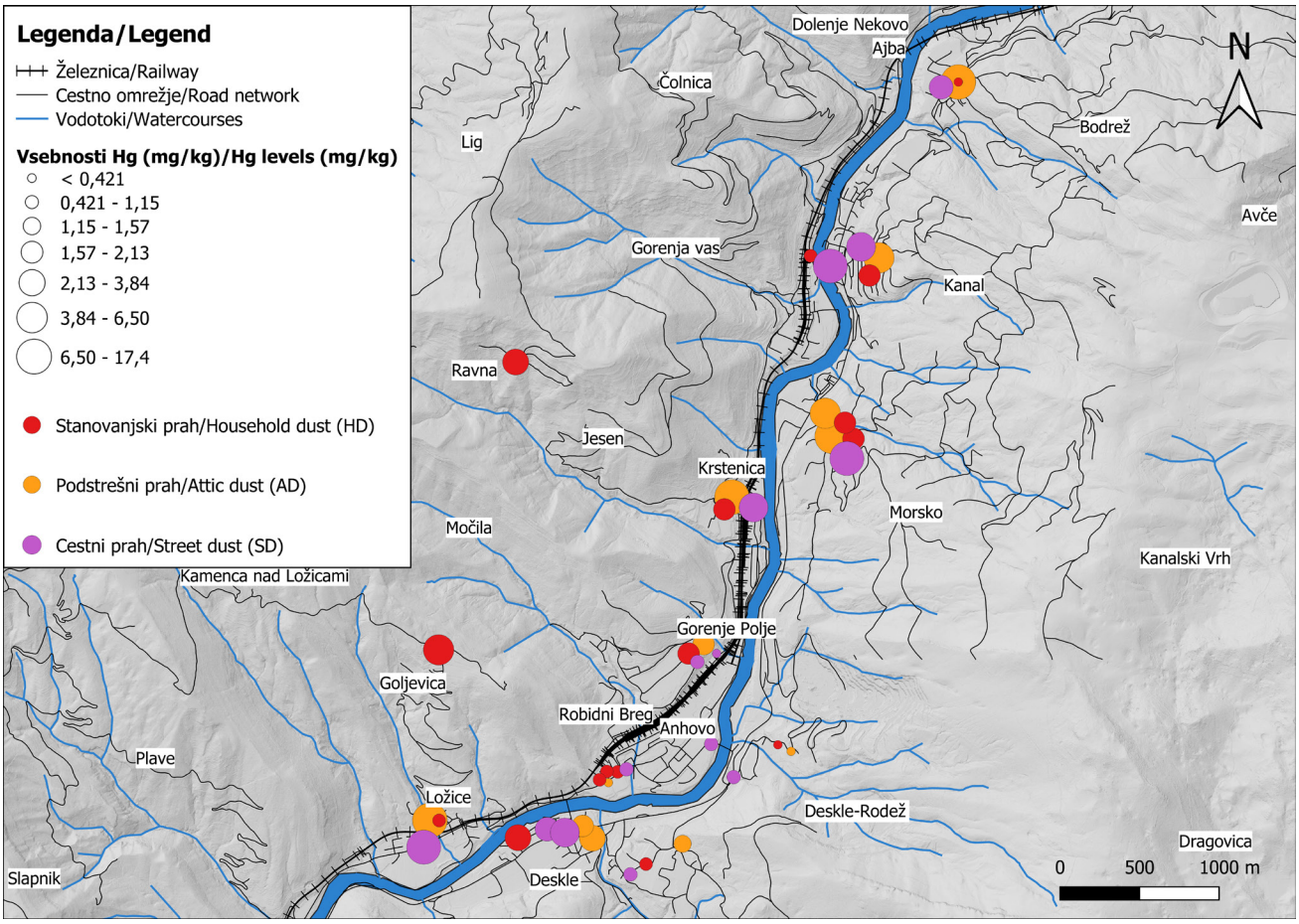

Sl. 13. Prostorski prikaz vsebnosti Hg v vseh vzorcih vseh treh tipov prahu.
Fig. 13. Spatial presentation of Hg levels in samples of all three dust types.

vrednostmi Hg v vseh segmentih okolja zaradi 500-letnega pridobivanja in predelave rude. Mediana Hg na preiskovanem območju v podstrešnem prahu je izrazito največja in znaša 3,703 mg/kg, sledita mediani v cestnem (1,911 mg/kg) in stanovanjskem prahu (1,497 mg/kg). Največjo vsebnost Hg (17,419 mg/kg) smo ugotovili v podstrešnem prahu v Krstenici. Tudi v krajih Morsko (8,573 mg/kg in 4,334 mg/kg), Bodrež (6,542 mg/kg) in Ložice (6,504 mg/kg) ter v Kanalu (4,623 mg/kg) je v podstrešnem prahu več kot 4 mg/kg Hg. V cestnem prahu je največ Hg v kraju Morsko, nadalje so vsebnosti visoke (večje od 3 mg/kg) še v Ložicah in Kanalu. V Krstenici, ki leži severno od Anhovega smo izmerili 2,190 mg/kg Hg, kar je tudi precej. V stanovanjskem prahu smo največjo vsebnost Hg (6,502 mg/kg) ugotovili v Goljevici, zahodno od Anhovega. Druga največja koncentracija Hg v stanovanjskem prahu je v kraju Ravna (3,837 mg/kg) in tretja v Desklah (2,696 mg/kg). Glede na predstavljene podatke lahko sklepamo, da na sestavo prahov vplivajo viri Hg, ki so bili aktivni v preteklosti in tudi tisti, ki so aktivni še danes. Glede na prostorsko porazdelitev Hg v vseh vzorcih vseh treh tipov prahu (sl. 13) so najbolj obremenjeni kraji, ki niso neposredno ob cementarni, ampak kraji, ki so vzdolž doline, gorvodno in dolvodno, ter v stanovanjskem prahu tudi višje ležeči kraji.

Zaključek

Na širšem območju Anhovega smo vzorčili in analizirali stanovanjski, podstrešni ter cestni prah. Zajeli smo sledeča naselja na vplivnem območju cementarne: Anhovo, Morsko, Deskle, Ložice, Gorenje Polje, Goljevica, Ravna, Krstenica, Kanal in Bodrež. V vseh vzorcih smo določili vsebnosti 13 elementov.

Sestava prahu se močno razlikuje med posameznimi tipi. Razponi med najmanjšimi in največjimi vsebnostmi so običajno veliki, kar kaže na različne vire v različnih predelih obravnavanega območja in na antropogen vpliv. Vsebnosti večine elementov v vseh treh tipih prahu so precej enakomerno razporejene med posameznimi vzorci, s posameznimi izstopajočimi visokimi vsebnostmi. Te posamezne visoke vsebnosti se za različne elemente pojavljajo v različnih naseljih in jih zato ne moremo povezati z enim virom.

Primerjava rezultatov s podatki za Maribor, Idrijo, slovensko podeželje in slovenska urbana območja je pokazala, da so vsebnosti Hg v stanovanjskem prahu (mediana je 1,497 mg/kg) na obravnavanem območju med 4 in 6-krat večje kot v Mariboru in na slovenskem podeželju ter v urbanih krajih Slovenije. Večje so tudi mediane Tl, Mn in Cu. Tudi v podstrešnem prahu smo ugotovili relativno visoke vsebnosti Hg, katerega mediana (3,703 mg/kg) je 11,7-krat večja, kot v Mariboru. Od mediane za podstrešni prah močno odstopa največja vsebnost Hg v podstrešnem prahu v Krstenici. Druge vrednosti večje od mediane so bile izmerjene še v krajih Morsko, Bodrež, Kanal in Ložice. Večje vsebnosti kot v Mariboru imata na obravnavanem območju v podstrešnem prahu še Tl in Mn. Tudi v cestnem prahu, ki odraža trenutne zunanje vire trdnih delcev in obravnavanih elementov, smo ugotovili večje vsebnosti Hg kot drugje po Sloveniji. Mediana Hg na raziskovanem območju znaša 1,911 mg/kg, kar je 19-krat več, kot je mediana Hg v Mariboru, skoraj 40-krat več, kot na slovenskem podeželju in skoraj 24-krat več, kot v slovenskih večjih urbanih naseljih. Od mediane najbolj odstopata vsebnosti v cestnem prahu v krajih Morsko in Ložice, severno in jugovzhodno od Anhovega. Druge vsebnosti večje od mediane so bile izmerjene v Kanalu. Nekoliko večje kot drugod so tudi vsebnosti Tl in Mn.

Rezultati kažejo, da so za raziskovano območje značilne relativno visoke vsebnosti Hg v vseh treh tipih prahu. Vsebnosti so izrazito večje tako v primerjavi z Mariborom, kot slovenskim podeželjem in večjimi slovenskimi urbanimi kraji. Glede na predstavljene podatke lahko sklepamo, da na vsebnosti Hg v prahu oz. v okolju vplivajo viri, ki so bili aktivni v preteklosti in viri, ki so aktivni še danes. Glede na prostorsko porazdelitev Hg v vzorcih vseh treh tipov prahu so najbolj obremenjeni kraji, ki niso neposredno ob cementarni, ampak kraji, ki so vzdolž doline, gorvodno in dolvodno, ter v stanovanjskem prahu tudi višje ležeči kraji. Za raziskovano območje so v primerjavi z drugimi podatki za Slovenijo značilne tudi nekoliko večje vsebnosti Tl in Mn.

Zahvala

Raziskavo sta financirala Javna agencija za znanstvenoraziskovalno in inovacijsko dejavnost (ARIS) in Ministrstvo za okolje podnebje in energijo RS v okviru raziskovalnega projekta Ciljnega raziskovalnega programa „CRP 2022“ z naslovom »Ocena potencialnega vpliva sežiga in sosežiga odpadkov na zdravstvene posledice pri ljudeh: modelna študija na primeru cementarne Salonit Anhovo« in ARIS v okviru Raziskovalnega programa Podzemne vode in geokemija (P1-0020), ki se izvaja na Geološkem zavodu Slovenije. Finančno pomoč je nudila tudi Slovenska nacionalna komisija za UNESCO, Nacionalni odbor Mednarodnega programa za geoznanost in geoparke (IGGP).

Literatura

Ali, M.U., Liu, G., Yousaf, B., Ullah, H., Abbas, Q. & Munir, M.A.M. 2019: A systematic review on global pollution status of particulate matter-associated potential toxic elements and health perspectives in urban environment. Environ. Geochem. Health, 41: 1131–1162. https://doi.org/10.1007/s10653-018-0203-z

Amato, F., Pandolfi, M., Viana, M., Querol, X., Alastuey, A. & Moreno, T. 2009: Spatial and chemical patterns of PM10 in road dust deposited in urban environment. Atmos. Environ. 43: 1650–1659. https://doi.org/10.1016/j.atmosenv.2008.12.009

Bavec, Š. & Gosar, M. 2016: Speciation, mobility and bioaccessibility of Hg in the polluted urban soil of Idrija (Slovenia). Geoderma, 273: 115–130. https://doi.org/10.1016/j.geoderma.2016.03.015

Bavec, Š., Gosar, M., Miler, M. & Biester, H. 2017: Geochemical investigation of potentially harmful elements in household dust from a mercury-contaminated site, the town of Idrija (Slovenia). Environ Geochem Health, 39: 443–465. https://doi.org/10.1007/s10653-016-9819-z

Baptista Salazar, C., Richard, J.H., Horf, M., Rejc, M., Gosar, M. & Biester, H. 2017: Grain-size dependence of mercury speciation in river suspended matter, sediments and soils in a mercury mining area at varying hydrological conditions. Applied geochemistry, 81: 132–142. https://doi.org/10.1016/j.apgeochem.2017.04.006

Cizdziel, J.V. & Hodge, V.F. 2000: Attics as archives for house infiltrating pollutants: trace elements and pesticides in attic dust and soil from southern Nevada and Utah. Microchem. J., 64: 85–92, https://doi.org/10.1016/S0026-265X(99)00018-1

Croxford, B., Penn, A. & Hillier, B. 1996: Spatial distribution of urban pollution: civilizing urban traffic. Sci. Total Environ., 189–190: 3–9. https://doi.org/10.1016/0048-9697(96)05184-4

Davis, J.J. & Gulson, B.L. 2005: Ceiling (attic) dust: A “museum” of contamination and potential hazard. Environ. Res., 99: 177–194. https://doi.org/10.1016/j.envres.2004.10.011

Denby, B.R., Kupiainen, K.J. & Gustafsson, M. 2018: Review of Road Dust Emissions. In: Amato, F. (eds.): Non-Exhaust Emissions-An Urban Air Quality Problem for Public Health; Impact and Mitigation Measures. Elsevier, 183–203. https://doi.org/10.1016/B978-0-12-811770-5.00009-1

Gaberšek, M. 2020: Celostna obravnava geokemije trdnih anorganskih delcev v urbanem okolju. Doktorska disertacija. Fakulteta za gradbeništvo in geodezijo, Ljubljana: 215 p.

Gaberšek, M. & Gosar, M. 2021: Towards a holistic approach to the geochemistry of solid inorganic particles in the urban environment. Science of the total environment, 763: 144214. https://doi.org/10.1016/j.scitotenv.2020.144214

Gaberšek, M., Watts, M.J. & Gosar, M. 2022: Attic dust: an archive of historical air contamination of the urban environment and potential hazard to health? Journal of Hazardous Materials, 432: 128745. https://doi.org/10.1016/j.jhazmat.2022.128745

Gosar, M. & Šajn, R. 2001: Mercury in soil and attic dust as a reflection of Idrija mining and mineralization (Slovenia). Geologija, 44: 137–159. https://doi.org/10.5474/geologija.2001.010

Gosar, M. & Teršič, T. 2012: T. Environmental geochemistry studies in the area of Idrija mercury mine, Slovenia. Environ Geochem Health, 34 (Suppl 1): 27–41. https://doi.org/10.1007/s10653-011-9410-6

Gosar, M. & Teršič, T. 2015: Contaminated sediment loads from ancient mercury ore roasting sites, Idrija area, Slovenia. Journal of geochemical exploration, 149: 97–105. https://doi.org/10.1016/j.gexplo.2014.11.012

Gosar, M., Šajn, R. & Teršič, T. 2016: Distribution pattern of mercury in the Slovenian soil: geochemical mapping based on multiple geochemical datasets. Journal of geochemical exploration, 167: 38–48. https://doi.org/10.1016/j.gexplo.2016.05.005

Gosar, M., Šajn, R. & Biester, H. 2006: Binding of mercury in soils and attic dust in the Idrija mercury mine area (Slovenia). Science of The Total Environment, 369: 1/3: 150–162. https://doi.org/10.1016/j.scitotenv.2006.05.006

Gosar, M., Šajn, R., Bavec, Š., Gaberšek, M., Pezdir, V. & Miler, M. 2019: Geochemical background and threshold for 47 chemical elements in Slovenian topsoil. Geologija, 62/1: 7–59. https://doi.org/10.5474/gologija.2019.001

Grigoratos, T. & Martini, G. 2015: Brake wear particle emissions: a review. Environ. Sci. Pollut. Res. 22: 2491–2504. https://doi.org/10.1007/s11356-014-3696-8

Gunawardana, C., Goonetilleke, A., Egodawatta, P., Dawes, L. & Kokot, S. 2012: Source characterisation of road dust based on chemical and mineralogical composition. Chemosphere, 87: 163–170. https://doi.org/10.1016/j.chemosphere.2011.12.012

Hwang, H.M, Fiala, M.J., Park, D. & Wade, T.L. 2016: Review of pollutants in urban road dust and stormwater runoff: part 1. Heavy metals released from vehicles. Int. J. Urban Sci., 20: 334–360. https://doi.org/10.1080/12265934.2016.1193041

Ilacqua, V., Freeman, N.C.J., Fagliano, J. & Lioy, P.J. 2003: The historical record of air pollution as defined by attic dust. Atmos. Environ., 37: 2379–2389. https://doi.org/10.1016/S1352-2310(03)00126-2

Kogut, K., Gorecki, J. & Burmistrz, P. 2021: Opportunities for reducing mercury emissions in the cement industry. J. Clean. Prod., 293: 126053. https://doi.org/10.1016/j.jclepro.2021.126053

Lindqvist, O. & Rodhe, H. 1985: Atmospheric Mercury - A review. Tellus, 37B: 136–159.

Ljubič Mlakar, T., Horvat, M., Kotnik, J., Jeran, Z., Vuk, T., Mrak, T. & Fajon, V. 2011: Biomonitoring with epiphytic lichens as a complementary method for the study of mercury contamination near a cement plant. Environmental Monitoring and Assessment, 181/1: 225–241. https://doi.org/10.1007/s10661-010-1825-5

Mavrič, A. 2020: Ugotavljanje onesnaženosti zraka v srednji Soški dolini z izbranimi vrstami mahov = Air pollution monitoring in the middle Soča valley by selected moss species. Magistrsko delo. Univerza v Ljubljani, Biotehniška fakulteta, Študij ekologije in biodiverzitete, Ljubljana: 79 p.

Miler, M. & Gosar, M. 2019: Assessment of contribution of metal pollution sources to attic and household dust in Pb-polluted area. Indoor Air, 29: 487–498. https://doi.org/10.1111/ina.12548

Mishra, U.C., Sarsaiya, S. & Gupta, A. 2022: A systematic review on the impact of cement industries on the natural environment. Environmental Science and Pollution Research, 29: 18440–18451, https://doi.org/10.1007/s11356-022-18672-7

Mohamad, N., Muthusamy, K., Embong, R., Kusbiantoro, A. & Hashim, M.H. 2022: Environmental impact of cement production and Solutions: A review. Materials Today: Proceedings, 48/4: 741–746. https://doi.org/10.1016/j.matpr.2021.02.212

Morawska, L. & Salthammer, T. 2003: Fundamentals of Indoor Particles and Settled Dust. In: Morawska, L. & Salthammer, T. (eds.): Indoor Environment, Airborne Particles and Settled Dust. Wiley-VCH, 3–46.

Pacyna, E.G., Pacyna, J.M., Steenhuisen, F. & Wilson, S. 2006: Global anthropogenic mercury emission inventory for 2000. Atmospheric Environment, 40/22: 4048–4063. https://doi.org/10.1016/j.atmosenv.2006.03.041

Rasmussen, P.E. 2004: Elements and their compounds in indoor environments. In: Merian, E., Anke, M., Ihnat, M. & Stoeppler, M. (eds.): Elements and their compounds in the environment: occurrence, analysis and biological relevance. Weinheim: 215–234. https://doi.org/10.1002/9783527619634.ch11

Senegačnik, A. 2019: Sežig in sosežig odpadkov: osnovne značilnosti energijske izrabe odpadkov. In: Brvar, M. (ed.): Vpliv sežiganja odpadkov na okolje in zdravje. 8. srečanje o kemijski varnosti, Slovensko zdravniško društvo, Sekcija za klinično toksikologijo: Univerzitetni klinični center Ljubljana, Center za klinično toksikologijo in farmakologijo, Interna klinika. Zbornik prispevkov, 9–25.

Shuqin L., Yongtao W. & Li Y.J.: 2006: Oakey, Volatilization of mercury, arsenic and selenium during underground coal gasification. Fuel, 85/10–11: 1550–1558. https://doi.org/10.1016/j.fuel.2005.12.010

Šajn, R. 2003: Distribution of chemical elements in attic dust and soil as reflection of lithology and anthropogenic influence in Slovenia. Journal de Physique, IV/107: 1173–1176. https://doi.org/10.1051/jp4:20030509

Taylor, K. 2007: Urban environments. In: Perry, C. & Taylor, K. (eds.): Environmental Sedimentology. Department of Environmental and Geographical Sciences, Manchester Metropolitan University. Blackwell Publishing: 190–222.

Teran, K. 2020: Household and road dust as indicators of airborne particulate matter elemental composition: dissertation. Nova Gorica: 155 p.

Teran, K., Žibret, G. & Fanetti, M. 2020: Impact of urbanization and steel mill emissions on elemental composition of street dust and corresponding particle characterization. Journal of hazardous materials, 384: 120963. https:/doi.org/10.1016/j.jhazmat.2019.120963

Turner, A. & Ip, K.H. 2007: Bioaccessibility of Metals in Dust from the Indoor Environment: Application of a Physiologically Based Extraction Test. Environ. Sci. Technol., 41: 7851–7856. https://doi.org/10.1021/es071194m

United Nations Environment Programme (UNEP), 2019: Global Mercury Assessment 2018. Chemicals and Health Branch, Geneva: 59 p.

Völgyesi, P., Jordan, G., Zacháry, D., Szabó, C., Bartha, A. & Matschullat, J. 2014: Attic dust reflects long-term airborne contamination of an industrial area: A case study from Ajka, Hungary. Appl. Geochemistry, 46: 19–29. https://doi.org/10.1016/j.apgeochem.2014.03.010

Žibret, G., Van Tonder, D. & Žibret, L. 2013: Metal content in street dust as a reflection of atmospheric dust emissions from coal power plants, metal smelters, and traffic. Environ. Sci. Pollut. Res., 20: 4455–4468. https://doi.org/10.1007/s11356-012-1398-7

Electronic sources:

Internet 1: https://alpacem.si/trajnostni-razvoj/ekologija/ (dostop 22. 4. 2024)

GEOLOGIJA 68/2, 113-121, Ljubljana 2025

https://doi.org/10.5474/geologija.2025.003

Article

Revision of *Xanthopsis bodracus* Makarenko, 1956 (Crustacea: Decapoda) from the Palaeogene of Ukraine

Revizija *Xanthopsis bodracus* Makarenko, 1956 (Crustacea: Decapoda) iz paleogena Ukrajine

Vitaly DERNOV

Institute of Geological Sciences, National Academy of Sciences of Ukraine, 55 b, Oles Honchar Str., Kyiv, 01601, Ukraine; National Museum of Natural History, National Academy of Sciences of Ukraine, 15, Bohdan Khmelnytskyi Str., Kyiv, 01054, Ukraine, e-mail: vitalydernov@gmail.com

Prejeto / Received 23. 1. 2025; Sprejeto / Accepted 4. 4. 2025; Objavljeno na spletu / Published online 30. 7.2025

Key words: decapod crustaceans, *Harpactoxanthopsis, Xanthopsis*, Lutetian, taxonomy
Ključne besede: deseteronožni raki, *Harpactoxanthopsis, Xanthopsis*, lutecij, taksonomija

Abstract

The present article constitutes a revision of the decapod crustacean species *Xanthopsis bodracus* Makarenko, 1956 from the early Lutetian (Eocene, Palaeogene) of the Crimean Peninsula, southern Ukraine. The distinctive morphological characteristics of *Xanthopsis bodracus* enable its classification within the genus *Harpactoxanthopsis* Via Boada, 1959, as the type series of *Xanthopsis bodracus* precisely aligns with the diagnostic criteria of this genus. Of the five species in the genus *Harpactoxanthopsis*, *Xanthopsis bodracus* is morphologically closest to *Harpactoxanthopsis quadrilobatus* (Desmarest, 1822). However, there are currently insufficient grounds to confidently synonymise *Xanthopsis bodracus* with *Harpactoxanthopsis quadrilobatus*, as the poorly preserved type material, of which only a part has been preserved, does not allow this. In view of this, *Xanthopsis bodracus* has been revised as *Harpactoxanthopsis* sp. The Palaeogene decapod assemblages of Crimea consist of five genera including *Coeloma* A. Milne-Edwards, 1865, *Protocallianassa* Beurlen, 1930, *Arcticocarcinus* Shweitzer et al., 2016, *Xanthopsis* M'Coy, 1849, and *Harpactoxanthopsis* Via Boada, 1959.

Izvleček

Pričujoči članek predstavlja revizijo vrste deseteronožcev *Xanthopsis bodracus* Makarenko, 1956 iz zgodnjega lutecija (eocen, paleogen) Krimskega polotoka v južni Ukrajini. Izrazite morfološke značilnosti vrste *Xanthopsis bodracus* omogočajo njeno uvrstitev v rod *Harpactoxanthopsis* Via Boada, 1959, saj se tipska serija vrste *Xanthopsis bodracus* natančno ujema z diagnostičnimi znaki tega rodu. Od petih vrst v rodu Harpactoxanthopsis je *Xanthopsis bodracus* morfološko najbližje *Harpactoxanthopsis quadrilobatus* (Desmarest, 1822). Vendar trenutno ni dovolj razlogov za zanesljivo sinonimizacijo *Xanthopsis bodracus* s Harpactoxanthopsis quadrilobatus, saj slabo ohranjen tipski material, od katerega se je ohranil le del, tega ne omogoča. Glede na to je bil *Xanthopsis bodracus* revidiran kot *Harpactoxanthopsis* sp. Paleogensko dekapodno združbo Krima sestavlja pet rodov. Med njimi so *Coeloma* A. Milne-Edwards, 1865, *Protocallianassa* Beurlen, 1930, *Arcticocarcinus* Shweitzer et al., 2016, *Xanthopsis* M'Coy, 1849, in *Harpactoxanthopsis* Via Boada, 1959.

Introduction

In Ukraine, Palaeogene decapod crustaceans (order Decapoda Latreille, 1802) occur in the Kanivian (Ypresian) and Kyivian (late Lutetian–Bartonian) regional stages of the Dnipro River basin (Radkevich, 1900; Chernyshev, 1949), the Kyivian regional stage in the Donets Basin (Likharev, 1917; Chernyshev, 1949), the Danian, Thanetian, Ypresian, Lutetian, and Rupelian of the Crimean Peninsula (Makarenko, 1956; Birshtein, 1960; Levitsky, 1974; Korobkov, 1975; Ilyin, 2005; Dernov & Udovychenko, 2023), the Oligocene of the Ukrainian Carpathians (Gorbach, 1956; Hyžný et al., 2022), and the Nikopol Basin (Griaznov, 1956; Selin, 1964). However, recently this group has not attracted much attention of Ukrainian palaeontologists, despite the fact that its study is of great palaeogeographic importance.

The most diverse assemblages of Ukrainian Palaeogene decapods were recorded from Crimea and consists of at least five genera, *Coeloma* A. Milne-Edwards, 1865, *Protocallianassa* Beurlen, 1930, *Arcticocarcinus* Shweitzer et al., 2016, *Xanthopsis* M'Coy, 1849, and *Harpactoxanthopsis* Via Boada, 1959 (Levitsky, 1974; Ilyin, 2005; Dernov & Udovychenko, 2023).

In 1956, Ukrainian palaeontologist Dr. Dmytro Yelyseyovych Makarenko (1925–2008) described a new crab species, *Xanthopsis bodracus,* from the "crab horizon", a local marker stratigraphic level containing decapod remains, which occurs in the early Lutetian limestone succession (Vassilenko, 1952; Muratov & Nemkov, 1960; Zernetsky, 1962; Ilyin, 2005; Zernetsky et al., 2015). Unfortunately, Makarenko (1956) did not define the holotype of this species and the place of storage of the examined material. This work is devoted to the revision of the surviving part of the type material of *Xanthopsis bodracus* Makarenko, 1956, which was found by the present author in the collections of late Dr. Makarenko.

Material and methods

The study is based on a small collection (NMNH-G 8607) of moderately preserved remains of *Xanthopsis bodracus* Makarenko, 1956, consisting of six carapace fragments and their inner moulds preserved in limestone. Of the four specimens of *Xanthopsis bodracus* carapaces figured by Makarenko (1956: figs 1–4; see also Fig. 1), only one specimen (NMNH-G 8607/11) was found in the collection NMNH-G 8607. The carapace mould figured by Makarenko (1956: Fig. 1), the carapace mould with a right claw (Fig. 2 in Makarenko, 1956), and an isolated claw (Fig. 3 in Makarenko, 1956) are absent (probably lost). The images provided by Makarenko (1956) are the only feature that allows us to identify the type series of

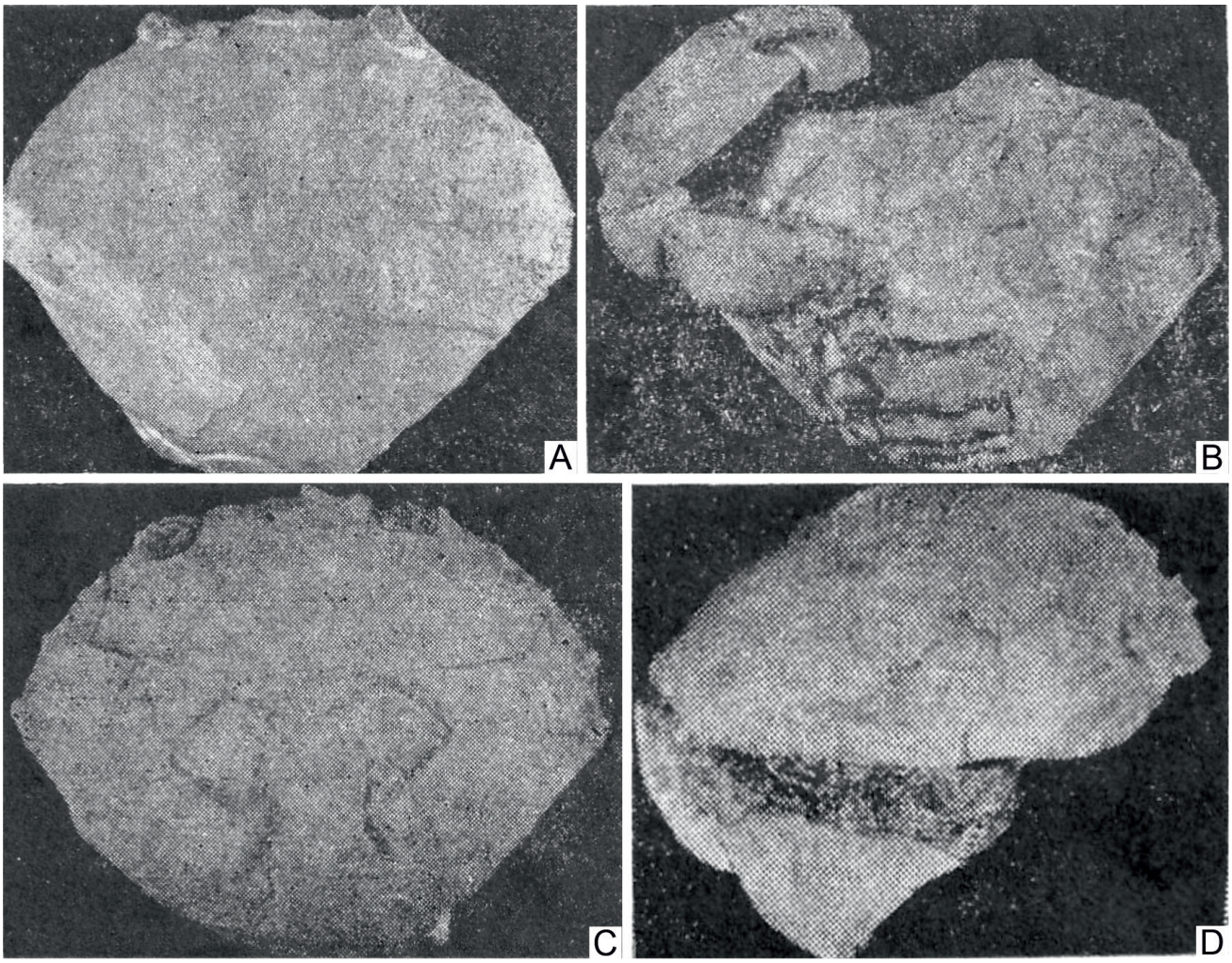

Fig. 1. Specimens of the type series of *Xanthopsis bodracus* Makarenko, 1956, as figured in the protologue (Makarenko, 1956: Figs. 1–4). A – "The mould of the carapace of an adult male (dorsal view)" (Makarenko, 1956: Fig. 1); hereinafter translated from Ukrainian by the author. B – "The mould of the carapace with the right claw and abdomen pressed to the ventral surface; ventral view" (Makarenko, 1956: Fig. 2). C – "The cephalothorax mould, which well showing the ornamentation; female individual in dorsal view" (Makarenko, 1956: Fig. 4). D – "The damaged right claw of a large crab specimen; ventral view' (Makarenko, 1956: Fig. 3). Remark: Makarenko (1956) did not indicate the specimen numbers and did not provide data that would allow to determine their size.

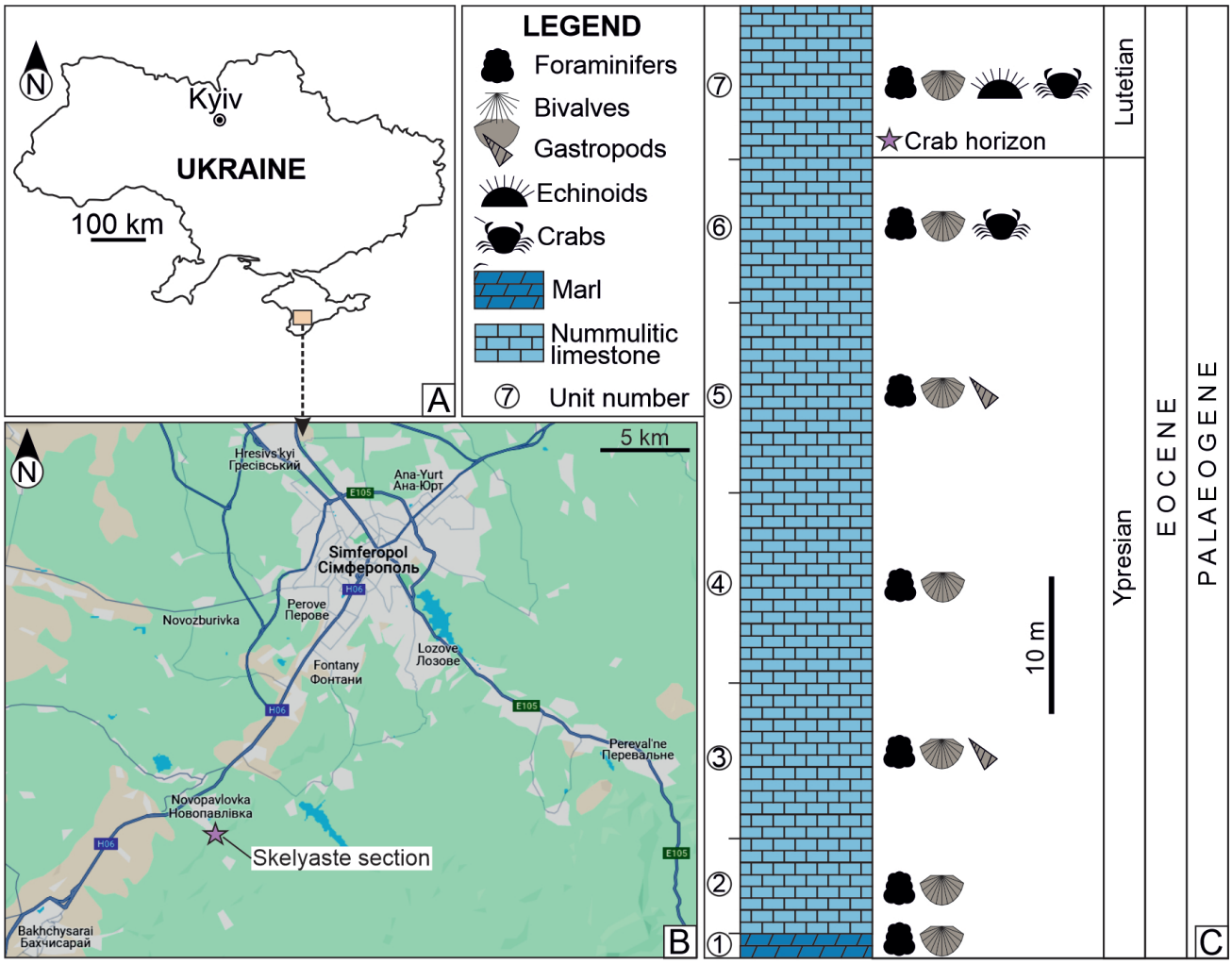

Fig. 2. Geographical location (A, B) and stratigraphic position (C) of the type locality of *Xanthopsis bodracus* Makarenko, 1956 (marked with a purple asterisk). Lithological column of the Skelyaste section (Fig. 2C) modified after Zernetsky (1962: p. 196).

Xanthopsis bodracus, since the total amount of the studied material and a holotype are not specified in the protologue.

The material examined was collected by the Dr. Makarenko from the lower Lutetian (Eocene) limestones exposed as a steep cliff on the right bank of the Bodrak River near the village of Skelyaste, Autonomous Republic of Crimea, Ukraine (Fig. 2) during an excursion of a meeting on the Palaeogene stratigraphy of the southern part of the former USSR in 1955.

In 1956, these decapod remains, represented by at least seven specimens, were described as a new species *Xanthopsis bodracus* Makarenko, 1956. The type material of *Xanthopsis bodracus* was considered lost until it was found in November 2023 in the Makarenko's collection stored in the Department of Stratigraphy and Palaeontology of Cenozoic Sediments, Institute of Geological Sciences, National Academy of Sciences of Ukraine, Kyiv. The research was also greatly aided by Dr. Makarenko's notes taken during the 1955 excursion. Now, the studied collection (NMNH-G 8607) is stored in the Department of Geology, National Museum of Natural History, National Academy of Sciences of Ukraine, Kyiv.

The collection NMNH-G 8607 consists of 15 specimens (NMNH-G 8607/01 to NMNH-G 8607/15). The fossil-bearing rock is a white limestone with small shell debris. In addition to decapod remains, the collection NMNH-G 8607 contains tests of unidentified nummulitids, steinkerns of the bivalves *Thracia* sp. and *Chlamys* sp., burrows ?*Palaeophycus* isp., and a fragment of the steinkern of the nautiloid *Aturia* sp. bearing a poorly preserved external mould of a serpulid tube and burrows.

The specimen NMNH-G 8607/07 bears the trace fossils assigned to the ichnogenus *Arachnostega* Bertling, 1992, preserved on the surface of the crab carapace inner mould (see Fig. 4A, C). This ichnogenus is usually interpreted as a domichnia or feeding structure in a consolidated soft- to firmground substrate, produced by detritus- or deposit-feeding polychaetes (Bertling, 1992; Fatka et al., 2011; Zatoń, 2020; Dernov, 2023).

This paper uses the decapod taxonomy proposed by Schweitzer et al. (2010) and morphological terminology and methods of describing fossil decapods summarized by Schweitzer et al. (2024).

Geological setting

The Skelyaste section is represented by a sequence of predominantly white and grey nummulitic non-laminated limestones of the Bakhchisarai and Simferopol formations ascribed to the Ypresian and lower Lutetian (Zernetsky et al., 2015) (see Fig. 2C). Based on foraminifer studies, the Ypresian/Lutetian boundary in this section is located at the base of Unit 7 (personal communication of Dr. Tamara S. Ryabokon, Institute of Geological Sciences of the NAS of Ukraine, February 2024).

Numerous foraminifers, such as *Nummulites distans* Deshayes, 1838, *N. atacicus* Leymerie, 1846, *Discocyclina archiaci* (Schlumberger, 1903), *D. sella* (d'Archiac, 1850), *Assilina spira* (Roissy, 1805), *A. exponens* (Sowerby, 1840), *Operculina gigantea* Mayer, 1876, as well as bivalves *Pycnodonta rarilamella* (Deshayes, 1864), *Spondylus* cf. *tenuispina* Sandberger, 1863, *Chlamys* cf. *opia* Vassilenko, 1952, *Cardium* cf. *gigas* Defrance, 1817, *Chama calcarata* Lamarck, 1806, gastropods *Strombus* sp., *Cerithium* sp., *Rostellaria ampla* Rutot, 1876, and echinoids *Conoclypeus conoides* Agassiz , 1839 occur in the Ypresian part of the limestone succession (Units 1 to 6 – see Fig. 2C) (Zernetsky, 1962; Vyalov, 1975).

The foraminifers *Nummulites polygyratus* Deshayes, 1838, *N. distans* Deshayes, 1838, *Assilina exponens* (Sowerby in Sykes, 1840), *A. irregularis* Carter, 1853, bivalves *Spondylus* cf. *eichwaldi* Fuchs, 1870, *Pseudamussium solea* (Deshayes, 1830), and echinoids *Conoclypeus conoides* Agassiz, 1839 were found in Unit 7, i.e. in the Lutetian part of the limestone succession (Zernetsky, 1962; Vyalov, 1975).

According to Makarenko (1956), the specimens of *Xanthopsis bodracus* was found in a limestone interlayer, about 0.4-m-thick, wich lies in the lower part of Unit 7 (Fig. 2C). Numerous foraminifers, shells of bivalves, and moulds of the gastropods, up to 0.45 m long, as well as trace fossils co-occurring with crabs (Makarenko, 1956).

The lower part of the Lutetian in some sections of the Crimea contains the so-called "crab horizon", which is a local correlation marker (Vassilenko, 1952; Muratov & Nemkov, 1960). In addition to *Xanthopsis bodracus*, *Harpactoxanthopsis lutugini* (Likharev, 1917) and *H.* cf. *lutugini* (Likharev, 1917) also occur in the "crab horizon" (Ilyin, 2005). It should be noted, however, that in the Ypresian–Lutetian interval of Crimea, crabs are known both in the highest part of the Ypresian and in the lowest part of the Lutetian (Vassilenko, 1952; Zernetsky, 1962; Vyalov, 1975), but the specimens described by Makarenko (1956: p. 74) come from the basal part of the Lutetian.

The Ypresian-Lutetian nummulitic limestone sequence in the Crimea probably accumulated in the distal part of the inner ramp above the base of wind waves at fast sedimentation rates and high hydrodynamics (Lygina et al., 2010; Zernetsky et al., 2015). Similar environmental conditions have been recorded for the genus *Harpactoxanthopsis* Via Boada, 1959, to which *Xanthopsis bodracus* belongs (see the section "Systematics"), in the Eocene of Croatia and Slovenia (Mikuz, 2002; Gašparič et al., 2015; Križnar & Gašparič, 2019).

Systematics

Makarenko (1956) did not provide a formal diagnosis of *Xanthopsis bodracus*, but briefly described the morphology of the type specimens in detail. Makarenko (1956: p. 75–76; translated from Ukrainian by the author) notes, that "The posterior part of the carapace resembles a trapezoid, the lateral sides of which converge at an angle of 80–83° outside the small base. The posterolateral margins are almost straight, rounded. The abdomen is small, flattened, consists of four segments, bent under the cephalothorax and is located in the longitudinal depression of the ventral surface. The dorsal side of the finger is wedge-shaped. The cutting edge of the pollex bears small teeth. The surface of the carpus is rounded and smooth below; above, on the keel projection, there are 5–6 small pointed tubercles. Other four pairs of pereiopods are not preserved. The surface of the carapace is evenly convex and no separate regions are distinguished. The carapace is evenly covered with dense, small, round pits. The same pits are present on the claws. Symmetrically arranged diamond-shaped depressions with branches extending posteriorly are present in the most convex part of the carapace. An adult specimen is 41 mm long, 50 mm wide, and has a maximum height of 18 mm".

Only the material figured by Makarenko (1956: Figs. 1–4) allows us to get an an idea of the morphology of *Xanthopsis bodracus*, since the unfigured specimens from the collection NMNH-G 8607 (Fig. 4), although referred to *Xanthopsis bodracus* here, are not part of the type series.

Specimen NMNH-G 8607/11 (Fig. 3A–C) is a moderately-preserved carapace inner mould in

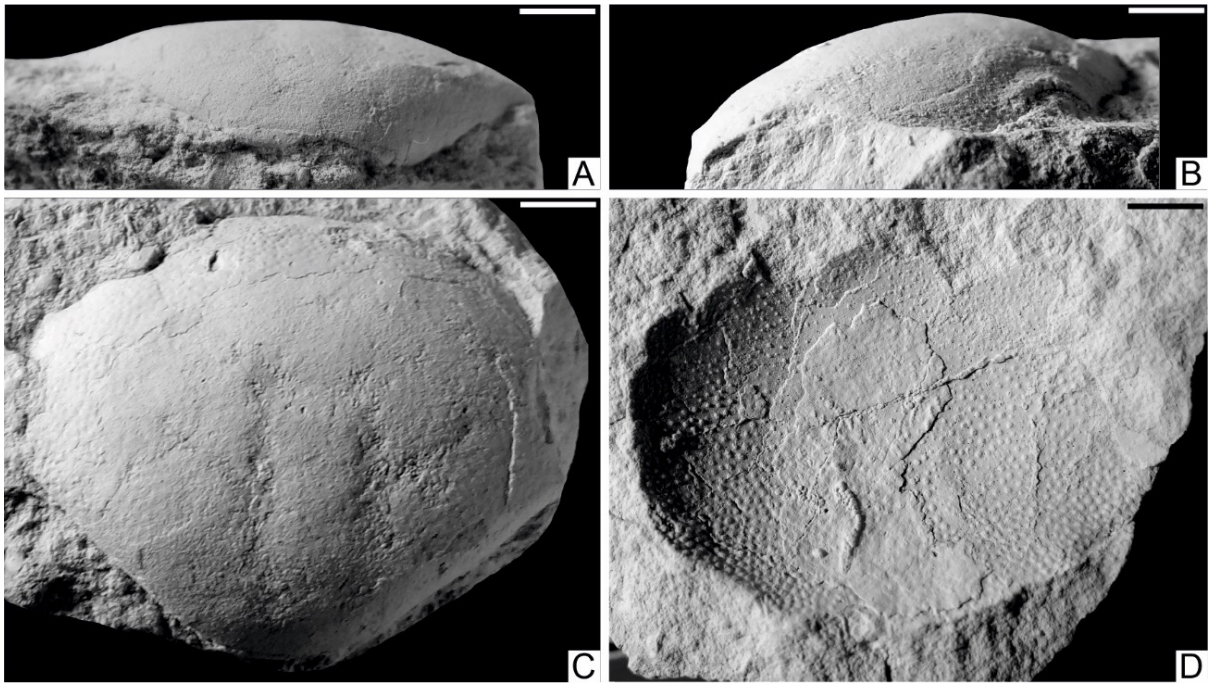

Fig. 3. Specimens of *Xanthopsis bodracus* Makarenko, 1956 of the type series. A–C – specimen NMNH-G 8607/11 (A – posterior view, B – lateral view, C – dorsal view). D – specimen NMNH-G 8607/12 (counterpart of NMNH-G 8607/11) in dorsal view. Scale bars = 5 mm.

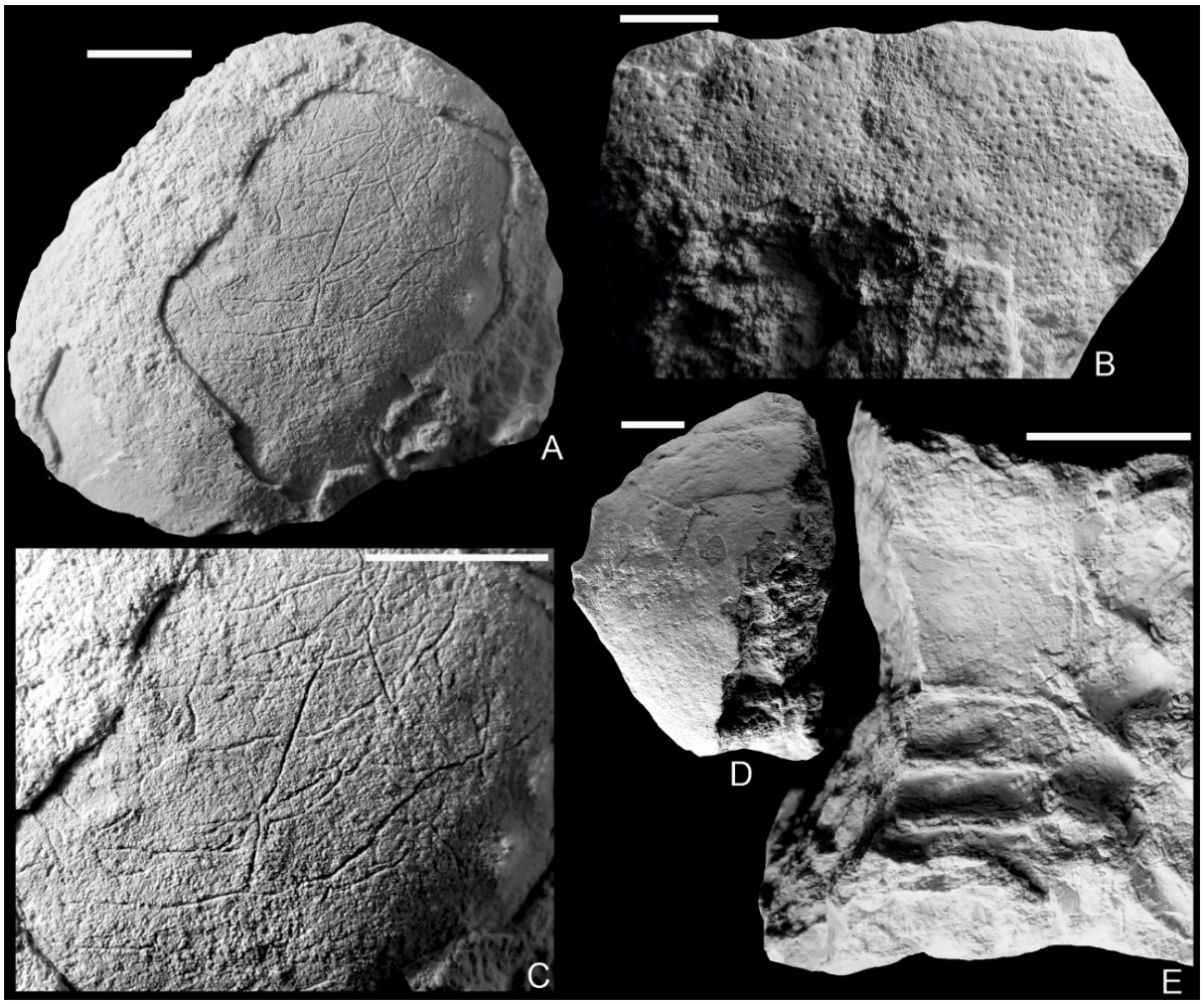

Fig. 4. Decapod specimens from the collection NMNH-G 8607. A, C – carapace fragment of *Xanthopsis bodracus* bearing trace fossils *Arachnostega* (specimen NMNH-G 8607/07: A – general view, C – enlarged part of the carapace with *Arachnostega* burrows). B – carapace fragment of *Xanthopsis bodracus* in dorsal view (specimen NMNH-G 8607/08). D – carapace fragment of *Xanthopsis bodracus* in dorsal view (specimen NMNH-G 8607/09). E – carapace fragment of *Xanthopsis bodracus* in ventral view (specimen NMNH-G 8607/10). Scale bars = 5 mm

the dorsal aspect. Specimen NMNH-G 8607/12 is a counterpart impression of the dorsal surface of NMNH-G 8607/11 with a preserved cuticle. The carapace is rounded-hexagonal almost ovate in outline (Fig. 3C), narrowing considerably posteriorly with poorly defined regions, strongly convex longitudinally (Fig. 3B) and moderately convex transversely (Fig. 3A), 34 mm wide and 27 mm long, and almost as wide as long (length/width = 0.79). The greatest width of the carapace is approximately in the middle of its length. The front is slightly convex, almost straight, approximately 12 mm wide (about 33 % of the total carapace width); fronto-orbital width is 23 mm. Almost circular orbits, 4 mm wide and 2.5 mm deep, are poorly preserved (see Figs. 3B, C). The anterolateral margins are not preserved. The posterolateral margins are very slightly convex, almost straight; the posterior margin is narrow, straight, 10 mm wide. The base of a low spine is preserved on the right posterolateral margin in the specimen NMNH-G 8607/11.

On the dorsal surface of the carapace mould, there are weak branchiocardial shallow grooves, which limit the slightly convex cardiac region in the transverse aspect. The ventral surface and pereiopods in NMNH-G 8607/11 and NMNH-G 8607/12 are not preserved.

The dorsal surface of the carapace NMNH-G 8607/11 is poorly preserved; only in front, near the frontal margin, small pits occur. Numerous rounded pits are present on the carapace counterpart with a partially preserved cuticle (NMNH-G 8607/12).

Discussion and concluding remarks

The morphological description of *Xanthopsis bodracus* given above does not contradict its description presented by Makarenko (1956). However, he noted some morphological details that cannot be observed on the specimen NMNH-G 8607/11, although their reliability is not in doubt, as they are confirmed by the images (Makarenko, 1956: figs. 1–4). For example, Makarenko (1956: p. 75) reports that the carapace front is divided by four spines, of which the two outer ones form the inner orbital spines; three spines are present on each of the anterolateral margins (see Fig. 1).

The characteristic morphological features of *Xanthopsis bodracus* allow to place it to the genus *Harpactoxanthopsis* Via Boada, 1959 (type species: *Cancer quadrilobata* Desmarest, 1822). The material described above, as well as the images of the type series of *Xanthopsis bodracus* given by Makarenko (1956), fully correspond to the diagnosis of this genus given by Schweitzer (2003: p. 1119), namely: "Carapace about 80 percent as long as wide, ovate; regions poorly defined; branchiocardiac groove usually well-defined along lateral margins of urogastric region. Front with four blunt spines including inner orbital spine; anterolateral margin convex, with five spines excluding outer orbital spine".

According to Schweitzer et al. (2010), the genus *Harpactoxanthopsis* includes five species, *H. bittneri* (Lőrenthey, 1898), *H. lutugini* (Likharev, 1917), *H. quadrilobatus* (Desmarest, 1822), *H. souverbei* (A. Milne-Edwards, 1862), and *H. villaltae* Vía Boada, 1959. Of all these species, *H. lutugini* and *H. quadrilobatus* are the most morphologically similar to *Xanthopsis bodracus*.

No morphological differences were found between the crabs described by Makarenko (1956) and *H. quadrilobatus* described from other localities (e.g., Desmarest, 1822; A. Milne Edwards, 1862; Bittner, 1875; Lőrenthey and Beurlen, 1929; Vía, 1969; Beschin et al., 1994; Hyžný, 2014; Gašparič et al., 2015). In Ukraine, *Harpactoxanthopsis quadrilobatus* previously was recorded by Chernyshev (1949) from the Kyiv Formation (late Lutetian–Bartonian) of the vicinity of the city of Kyiv. However, there are currently insufficient grounds to confidently synonymise *Xanthopsis bodracus* with *Harpactoxanthopsis quadrilobatus*, as the poorly preserved type material, of which only a part has been preserved, does not

Table 1. Palaeogene decapods of Crimea (modified after Dernov and Udovychenko, 2023, table 1).

Taxa	Age	References
Coeloma vigil Milne-Edwards, 1865	Rupelian	Ilyin, 2005
Harpactoxanthopsis sp.	Early Lutetian	This study
Harpactoxanthopsis cf. *lutugini* (Likharev, 1917)	Late Lutetian	Ilyin, 2005
	Ypresian	
Harpactoxanthopsis lutugini (Likharev, 1917)	Late Ypresian or early Lutetian	Levitsky, 1974
Xanthopsis nodosa McCoy, 1849	Early Ypresian	Ilyin, 2005
Protocallianassa sp.	Danian	Levitsky, 1974
Arcticocarcinus cf. *insignis* (Segerberg, 1900)	Early Danian	Dernov & Udovychenko, 2023

allow this. In view of this, *Xanthopsis bodracus* has been revised as *Harpactoxanthopsis* sp. Thus, taking into account the data obtained, the Palaeogene decapod assemblages of Crimea consist of five genera (Table 1). These records often have an unclear stratigraphic position and therefore it is difficult to analyse the stratigraphic distribution of taxa.

Acknowledgements

The author is grateful to Dr. Tamara S. Ryabokon for her advice on the Skelyaste section and assistance with the collection of the late Dr. Dmytro Makarenko. The author is sincerely grateful to anonymous reviewers, whose comments and suggestions improved the quality of the final version of the manuscript. The research was carried out within the framework of the scientific theme "Late Precambrian and Phanerozoic biota of Ukraine: biodiversity, revision of systematic composition and phylogeny of leading groups" (No. 0122U001609).

References

Agassiz, L. 1839: Description des Echinodermes fossiles de la Suisse. 1. *Spatangoides* et *Clypeasteroides*. Nouveau Mémoire de la Société Helvétique des Sciences naturelles, 3: 1–101.

d'Archiac, E.J.A.D. 1850: Description des fossiles du groupe nummulititique recueillis par M. S.-P. Pratt et M.J. Delbos aux environs de Bayonne et de Dax. Mémoires de la Société géologique de France, deuxième série, 3: 397–456.

Bertling, M. 1992: *Arachnostega* n. ichnog. – burrowing traces in internal moulds of boring bivalves (late Jurassic, Northern Germany). Paläontologische Zeitschrift, 66: 177–185. https://doi.org/10.1007/BF02989487

Beschin, C., Busulini, A., de Angeli, A. & Tessier, G. 1994: I Crostacei Eocenici della cava "Boschetto" di Nogarole Vicentino (Vicenza-Italia settentrionale). Lavori Società Veneziana di Scienze Naturali, 19: 159–215.

Beurlen, K. 1930: Vergleichende Stammesgeschichte, Grundlagen, Methoden und Probleme unter besonderer Berücksichtigung der hoheren Krebsen. Fortschritte der Geologie und Palaeontologie, 8: 317–586.

Birshtein, J.A. 1960: Order Decapoda. In: Orlov, Yu.A. (ed.): Fundamentals of Palaeontology, 8. Arthropods: trilobites and crustaceans. State Scientific and Technical Publishing House of Literature on Geology and Protection of Subsoil, Moscow: 439–456.

Bittner, A. 1875: Die Brachyuren des vicentinischen Tertiärgebirges. Denkschriften der Kaiserlichen Akademie der Wissenschaften. Mathematisch-Naturwissenschaftliche Classe, 34: 63–106.

Carter, H.J. 1853: Descriptions of some of the larger forms of fossilised Foraminifera in Scinde; with observations on their internal structure. Annals and Magazine of Natural History, 11/63: 161–177. https://doi.org/10.1080/03745485609496239

Chernyshev, B.I. 1949: Subclass Malacostraca. Order Decapoda. In: Ryabinin, A.N. & Korobkov, I.A. (eds.): Atlas of the reference forms of the fossil fauna of the USSR. Vol. 12. Palaeogene. State Publishing House of Geological Literature, Moscow: 289–294.

Defrance, J.L.M, 1817: Cardites (foss.). In: Cuvier, F. (ed.): Dictionnaire des Sciences Naturelles. Vol. 7. Levrault, Strasbourg & Le Normant, Paris: 87–91.

Derenyuk, N.Ye. 1984: Geological Map of the Crimean Mountains. Scale 1:200 000. Krymgeologiya, Sevastopol.

Dernov, V.S. 2023: *Ichtyocoprus affectatus* Makarenko, 1993 is a bivalve boring rock cast, not a coprolite. Collection of scientific works of the Institute of Geological Sciences of the NAS of Ukraine, 16/1: 70–80. https://doi.org/10.30836/igs.2522-9753./12023.295187

Dernov, V. & Udovychenko, M. 2023: The first record of the genus *Arcticocarcinus* Shweitzer et al., 2016 (Decapoda, Brachyura) in the Danian of Crimea (Ukraine) and its palaeobiogeographical significance. Bulletin of Taras Shevchenko National University of Kyiv. Geology, 101/2: 5–14. https://doi.org/10.17721/1728-2713.101.01

Deshayes, G.P. 1824–1837: Description des coquilles fossiles des environs de Paris. Published by the author, Paris: 393 p. https://doi.org/10.5962/bhl.title.52303

Deshayes, G.P. 1838: Description des coquilles fossiles recueillies en Crimée par M. de Verneuil, et observations générales à leur sujet. Mémoires de la Société géologique de France. Série 1, 3: 37–69.

Deshayes, G.P. 1864–1865: Description des animaux sans vertèbres découverts dans le bassin de Paris pour servir de supplément à la Description des coquilles fossiles des environs de Paris comprenant une revue générale de toutes les espèces actuellement connues. Tome troisiéme. Mollusques céphalés, deuxième partie. Mollusques céphalopodes. Baillière, Paris: 667 p.

Desmarest, A.G. 1822: Les crustacés proprement dits. In: Brongniart, A. & Desmarest, A.G. (eds.): Histoire naturelle des crustacés fossiles, sous les rapports zoologiques et géologiques. F.-G. Levrault, Paris: 67–142.

Fatka, O., Mikuláš, R., Szabad, M., Micka, V. & Valent, M. 2011: *Arachnostega* Bertling, 1992 in the Drumian (Cambrian) sediments of the Teplá-Barrandian region (Czech Republic). Acta Geologica Polonica, 61/4: 367–381.

Fuchs, T. 1870: III. Beiträge zur Kenntniss fossiler Binnenfaunen. III. Die Fauna der Congerienschichten von Radmanest im Banate. Jahrbuch der Kaiserlich Königlichen Geologischen Reichsanstalt, 20: 343–364.

Gašparič, R., Fraaije, R.H.B., Van Bakel, B.W.M., Jagt, J.W.M. & Skupien, P. 2015: Mesozoic–Cenozoic crustaceans preserved within echinoid tests and bivalve shells. Bulletin of Geosciences, 90/3: 601–611. https://doi.org/10.3140/bull.geosci.1551

Gorbach, L.P. 1956: On the crabs from the Menilite shales of the Eastern Carpathians. Transactions of the Lviv Geological Society, 2/3: 30–42.

Griaznov, V.I. 1956: On the confinement of finds of the crabs *Coeloma vigil* M.-Edw. to Oligocene manganese-ore facies. Reports of the Academy of Sciences of the USSR, 106: 717–719.

Hyžný, M. 2014: *Harpactoxanthopsis quadrilobatus* (Desmarest, 1822) from the Eocene of Slovakia and Italy: the phenomenon of inverted images of fossil heterochelous crabs. Bulletin of the Mizunami Fossil Museum, 40: 23–27. https://doi.org/10.5474/geologija.2002.008

Hyžný, M., Kovalchuk, O., Świdnicka, E., Barkaszi, Z., Berezovsky, A., Dumitriu, S., Grădianu, I. & Stefaniak, K. 2022: Revisiting brachyuran crabs (Malacostraca: Decapoda) from Oligocene and Miocene fish beds of Europe. Geologica Carpathica, 73/6: 579–597. https://doi.org/10.31577/geolcarp.73.6.3

Ilyin, I.V. 2005: Cretaceous and Palaeogene decapod crustaceans (Crustaceamorpha, Decapoda) of the western part of Northern Eurasia. Moscow University Press, Moscow: 295 p.

Korobkov, I.A. 1975: Decapod crustaceans. In: Grossheim, V.A. & Korobkov, I.A. (eds.): Stratigraphy of the USSR. Palaeogene System. Nedra, Moscow: 433–435.

Kriźnar, M. & Gašparič, R. 2019: Eocene of Slovenian Istria and Lutetian "Transitional beds with Crabs". Book of abstracts, 7th Symposium on Mesozoic and Cenozoic decapod crustaceans (Ljubljana, 17–21 June 2019). Tiskarna Oman, Kranj: 116–123.

Lamarck, J.P. 1806: Memoire sur les fossiles des environs de Paris. Annales du Museum d'Histoire naturelle de Paris, 8: 156–166.

Latreille, P.A. 1802: Histoire Naturelle, Générale et Particulière des Crustacés et des Insectes. Ouvrage Faisant suite à l'Histoire Naturelle Générale et Particulière, Composée par Le-Clerc de Buffon, et Rédigée par C.S. Sonnini, Membre de Plusieurs Sociétés Savantes. Vol. 3. Dufart, Paris: 468 p. https://doi.org/10.5962/bhl.title.60678

Levitsky, E.S. 1974: Fossil decapod crustaceans of the city of Bakhchisarai area. Bulletin of the Moscow Society of Naturalists. Geology, 49: 101–119.

Leymerie, A. 1846: Mémoire sur le terrain à *Nummulites* (épicrétacé) des Corbières et de la Montagne Noire. Mémoires de la Société Géologique de France, serie 2, 1: 337–372.

Likharev, B.K. 1917: Crab remains from the lower Tertiary of the Pridonetskii Krai. Yearbook of the Russian Palaeontological Society, 1: 13–24.

Lőrenthey, E.: 1898. Beiträge zur Decapodenfauna des ungarischen Tertiärs. Természetrajzi Füzetek, 21: 1–133. https://doi.org/10.5962/bhl.title.10253

Lőrenthey, E. & Beurlen, K. 1929: Die fossilen der Länder der Ungarischen Krone. Geologica Hungarica, Series Palaeontologica, 3: 1–420.

Lygina, Ye.A., Kopaevich, L.F., Nikishin, A.M., Shalimov, I.V. & Yakovishina, Ye.V. 2010: Lower and middle Eocene deposits of the Crimean Penninsula: facies features and depositional environments. Bulletin of the Moscow University. Series 4. Geology, 6: 11–22.

Makarenko, D.Ye. 1956: Crab remains from the Palaeogene deposits of the Crimea. Geological Journal (Ukraine), 16: 74–76.

Mayer, C. 1876: Description de Coquilles fossiles des terrains tertiaires supérieurs (suite). Journal de Conchyliologie, 24: 168–180.

M'Coy, F. 1849: On the classification of some British fossil Crustacea, with notices of new forms in the university collection at Cambridge. Annals and Magazine of Natural History, 4/23: 161–179, 330–335, 392–414. https://doi.org/10.1080/03745486009494843

Mikuž, V. 2002: Nova najdba rakovice *Harpactoxanthopsis quadrilobata* (Desmarest) v eocenskem flišu pri Gračišću blizu Pazina v Istri (Hrvaška). Geologija, 45/1: 97–102. https://doi.org/10.5474/geologija.2002.008

Milne-Edwards, A. 1865: Description de quelques Crustacés Nouveaux appartment à la tribu des Maiens. Annales De La Société Ento-

mologique De France, 4: 133–147. https://doi.org/10.5962/bhl.title.10083

Muratov, M.V. & Nemkov, G.I. 1960: Palaeogene deposits of the Bakhchisarai area and their significance for Palaeogene stratigraphy of the southern part of the USSR. In: Yanshin, A.L., Vyalov, O.S., Dolgopolov, N.N. & Menner, V.V. (eds.): Palaeogene deposits of the southern part of the European part of the USSR. Publishing of the Academy of Sciences of the USSR, Moscow: 15–23.

Quayle, W.J. & Collins, J.S.H. 1981: New Eocene crabs from the Hampshire Basin. Palaeontology, 24: 733–758.

Radkevich, G.O. 1900: On the lower Tertiary deposits in the vicinity of Kaniv. Transactions of the Kyiv Society of Naturalists, 16: 1–45.

de Roissy, F. 1805: Histoire naturelle générale et particulière des Mollusques; livre faisant suite aux œuvres de Buffon, et partie du cours complet d'Histoire naturelle rédigé par C. S. Sonnini. Tome 5. Dufart, Paris: 590 p.

Rutot, A. 1876: Note sur quelques fossiles recueillis dans le diluvium des environs de Tongres. Annales de la Société Malacologique de Belgique, 10: 7–20.

Sandberger, C.L.F. 1858–1863: Die Conchylien des Mainzer Tertiärbeckens. Kriedel und Niedner, Wiesbaden: 458 p. https://doi.org/10.5962/bhl.title.13953

Schlumberger, C. 1903: Troisieme note sur les Orbitoides. Bulletin de la Societe Geologique de France. Serie 4, 3: 273–289.

Schweitzer, C.E. 2003: Utility of proxy characters for classification of fossils: an example from the fossil Xanthoidea (Crustacea: Decapoda: Brachyura). Journal of Paleontology, 77/6: 1107–1128. https://doi.org/10.1666/0022-3360(2003)077<1107:uopcfc>2.0.co;2

Schweitzer, C.E., Feldmann, R.M., Audo, D., Charbonnier, S., Fraaije, R.H.B., Franţescu, O.D., Hyžný, M., Karasawa, H., Klompmaker, A.A., Luque, J., Robins, C.M., Schram, F.R., Schweigert, G. & Tshudy, D. 2024: Treatise online. Part R, Revised, Volume 1: Generalized external adult Decapoda morphology. The University of Kansas Press, Lawrence: 125 p.

Schweitzer, C.E., Feldmann, R.M., Garassino, A., Karasawa, H. & Schweigert, G. 2010: Systematic list of fossil decapod crustacean species. Crustaceana monographs, 10. Brill, Leiden and Boston: 222 p. https://doi.org/10.1163/193724012x626575

Schweitzer, C.E., Karasawa, H., Luque, J. & Feldmann, R.M. 2016: Phylogeny and classification of Necrocarcinoidea Förster, 1968 (Brachyura: Raninoida) with description of two new genera. Journal of Crustacean biology, 36/3: 338–372. https://doi.org/10.1163/1937240X-00002432

Selin, Y.I. 1964: Oligocene stratigraphy and molluscs of the Bolshe-Tokmaksky manganese-ore district. Nedra, Moscow: 240 p.

Sowerby, J. de C. 1834–1843: The mineral conchology of Great Britain; or Coloured figures and descriptions of those remains of testaceous animals or shells, which have been preserved at various times and depths in the earth. Vol. 7. Privately published by author, London: 80 p.

Sykes, W.H. 1840: A notice respecting some fossils collected in Cutch, by Capt. Walter Smee, of the Bombay Army. Transactions of the Geological Society of London, 2/5: 715–719. https://doi.org/10.1144/transgslb.5.3.715

Vassilenko, V.K. 1952: Eocene stratigraphy and mollusk fauna of Crimea. Proceedings of the All-Union Research Geological Exploration Institute, 59: 1–128.

Vía, L. 1969: Crustacéos Decápodos del Eoceno español. Pirineos, 91–94: 1–479.

Via Boada, L. 1959: Decápodos fósiles del Eoceno español. Boletín del Instituto Geológico y Minero de España, 70: 331–402.

Vyalov, O.S. 1975: The Bakhchisarai Palaeogene section. 2. Main outcrops of Eocene and Oligocene deposits. Geology and geochemistry of fossil fuels, 47: 80–88.

Zatoń, M. 2020: No evidence for fungal infection of Upper Jurassic horseshoe crabs: A comment on Błażejowski et al. (2019). Palaeogeography, Palaeoclimatology, Palaeoecology, 554: article 109142. https://doi.org/10.1016/j.palaeo.2019.03.043

Zernetsky, B.F. 1962: Crimea. Eocene. In: Bondarchuk, V.G. (ed.): Stratigraphy of the Ukrainian SSR. Palaeogene. Publishing House of the Academy of Sciences of the Ukrainian SSR, Kyiv: 183–202.

Zernetsky, B.F., Ryabokon, T.S. & Lulyeva, S.A. 2015: Issue of studying of the Eocene sedimentary succession of the Crimean and Kerch peninsulas. Collection of scientific works of the IGS of the NAS of Ukraine, 8: 33–62. https://doi.org/10.30836/igs.2522-9753.2015.145320

GEOLOGIJA 68/2, 123-145, Ljubljana 2025

https://doi.org/10.5474/geologija.2025.006

Article

Evaluation of cut slope stability in the Lesser Himalaya of Nepal

Ocena stabilnosti vkopnih brežin v Nizki Himalaji v Nepalu

Krishna Kumar SHRESTHA[1], Kabi Raj PAUDYAL[1], Dinesh PATHAK[1], Alessandro FRANCI[2] & Prem Bahadur THAPA[3]*

[1]Central Department of Geology, Tribhuvan University, Kirtipur, Kathmandu, Nepal
[2]International Center for Numerical Methods in Engineering (CIMNE), Universitat Politècnica de Catalunya (UPC), Carrer Gran Capitán, UPC Campus Nord, Barcelona, Spain
[3]Department of Geology, Tri-Chandra Multiple Campus, Tribhuvan University,
*Corresponding author's e-mail: prem.thapa@trc.tu.edu.np

Prejeto / Received 9. 5. 2025; Sprejeto / Accepted 6. 6. 2025; Objavljeno na spletu / Published online 30. 7.2025

Key words: cut slope, slope stability, numerical modelling, evaluation and validation, Lesser Himalaya, Nepal
Ključne besede: vkopna brežina, stabilnost pobočja, numerično modeliranje, vrednotenje in potrjevanje, Nizka Himalaja, Nepal

Abstract

A spatial inventory of cut slopes in the central and western Lesser Himalaya of Nepal was prepared and characterised to evaluate their stability. The stability of these cut slopes is governed by the geotechnical properties of rock/soil together with slope geometry, groundwater conditions and human interventions. Numerous cut slope failures were observed in areas where slope geometry is modified for engineering developments such as roads, dams, powerhouses, industrial development, etc. Two modelling sites were evaluated using the Limit Equilibrium Method (LEM), Finite Element Method (FEM), and Particle Finite Element Method (PFEM). Pre-failure analyses using LEM and FEM under dry and saturated conditions revealed that the stability of the Lesser Himalayan hillslopes with considerable soil thickness is predominantly controlled by the depth of groundwater level (GWL). Slopes remain stable with a factor of safety (FoS)>1.3 when the GWL lies below 7 m from the surface and gradually become unstable as it approaches the surface. This trend for both slopes confirms that elevated groundwater during the rainy season is the major cause of frequent cut slope failures in the Himalayan regions. The comparison of FoS from LEM and Strength Reduction Factor (SRF) from FEM showed a strong cross-correlation (90–99 %), revealing minimal variation which affirmed the validity of the adopted modelling techniques used in this study. Post-failure simulations of these sites were further analysed using an innovative approach, the robust PFEM modelling technique, to compute the dynamic failure mechanism. Sensitivity analysis of both modelled sites showed that friction angle and cohesion are the most significant parameters for slope stability evaluation. Moreover, forward and back analyses indicated that computed results are in good agreement, thus depicting reliability and performances along with the model validation.

Izvleček

Za oceno stabilnosti vkopnih brežin v osrednjem in zahodnem delu Nizke Himalaje v Nepalu je bil pripravljen in karakteriziran prostorski popis. Stabilnost teh brežin je odvisna od geotehničnih lastnosti kamnin in tal, geometrije pobočja, hidrogeoloških razmer ter človekovih posegov v prostor. Na območjih, kjer je bila zaradi inženirskih posegov, kot so gradnja cest, jezov in elektrarn, spremenjena geometrija pobočja, so bila opažena številna porušenja vkopnih brežin. Z uporabo metode mejnega ravnotežja (LEM), metodo končnih elementov (FEM) in metodo delnih končnih elementov (PFEM) sta bili izbrani dve lokaciji modeliranja. Analize, izvedene z metodama LEM in FEM v suhih in nasičenih pogojih so pokazale, da je stabilnost pobočij v Nizki Himalaji, prekritih z večjo debelino tal, pretežno odvisna od globine nivoja podzemne vode (GWL). Pobočja ostajajo stabilna s faktorjem varnosti (FoS) >1,3 kadar gladina podzemne vode (GWL) leži več kot 7 m pod površjem in postopoma postajajo vedno bolj nestabilna, ko se nivo vode približuje površju. Ta trend je opazen pri obeh izbranih pobočjih in potrjuje, da je povišana gladine podzemne vode v obdobju deževne dobe glavni vzrok pogostih porušitev pobočij v himalajski regiji. Primerjava faktorjev varnosti izračunanih z metodo LEM ter faktorja zmanjšane trdnosti (SRF) pridobljenega z metodo FEM je razkrila močno medsebojno korelacijo (90–99 %), kar kaže na minimalne razlike in potrjuje zanesljivost uporabljenih modelirnih tehnik v tej študiji. Simulacije po porušitvi na teh območjih so bile dodatno analizirane z uporabo inovativnega robustnega pristopa z PFEM modeliranjem za izračun dinamičnega mehanizma porušitve. Analiza občutljivosti obeh modeliranih območij je pokazala, da sta trenje in kohezija ključna parametra za oceno stabilnosti pobočij. Poleg tega so druge izvedene analize pokazale dobro ujemanje pridobljenih rezultatov, kar potrjuje zanesljivost modela, njegovo učinkovitost ter veljavnost.

Introduction

Mass movements such as landslides, debris flow and cut slope failures are significant hazards and risks in the Lesser Himalaya of Nepal, particularly during the rainy season. These events are exacerbated by weak and fractured lithologies, intense seasonal rainfall, active tectonics and increasing human interventions. Average altitudes of this region vary from 300 to 3500 m (Groppo et al., 2023), and it is the most populated region in the Himalaya that comprises sedimentary and less metamorphosed rocks (Upreti, 1999). Impacts of active tectonics, extensive human intervention and rapidly growing infrastructure development in this region are extremely exacerbating the landslides and cut slope failures. Most of the infrastructures concentrated near the road, which declines as a function of distance from the road network, justifies the significance of the road in terms of socio-economic development (Rawat & Sharma, 1997).

The occurrence of cut slope failures to large-scale landslides is frequent in the Lesser Himalayan Terrain of Nepal (e.g., Hasegawa et al., 2009; Phuyal et al., 2022; Thapa et al., 2023; Phuyal et al., 2025). Major highways in Nepal often traverse through river valleys and steep mountainous regions where numerous cut slopes of varying geometries are highly susceptible to failure during rainfall and earthquakes. About 46 % of the Prithvi Highway (NH04) runs through hillsides with multiple cut slopes. The Krishnabhir landslide (83 km west of Kathmandu) in 2000 blocked the Prithvi Highway for over two weeks, causing a shortage of daily commodities (Maskey, 2016) in the capital city. Similarly, the Jogimara landslide (90 km west of Kathmandu) also obstructed the highway for 10 days (Upreti & Dhital, 1996). These locations were recurrently affected by landslides for almost a decade, and the annual blockages during the monsoon season caused repeated disruptions to public and local transportation networks. The Jure landslide in 2014 along the Araniko Highway killed 156 people and damaged 2 km of road (Panthi, 2021). Over 4,000 landslides and cut slope failures occurred between 1971 and 2020, causing 5,000+ deaths, averaging 111 annually (Adhikari & Gautam, 2022). In 2023, 45 deaths were recorded, while in 2024, 343 deaths and 48 missing cases occurred by the end of the monsoon. Unusual intense rainfall from 26 to 28 September 2024 triggered more than 500 landslides and cut slope failures along the Prithvi Highway alone, causing severe disruptions and 35 fatalities in a single incident. These data indicate the vulnerability of highways to slope failures in mountainous regions underscoring the urgent need for comprehensive slope stability assessment to reduce the socio-economic impacts.

Geological structures, active seismic zones, steep topography, seasonal rainfall (hydro-meteorological), and increasing anthropogenic activities are the major causes of mass movement in weak areas like in the Lesser Himalaya (Varnes, 1958; Gerrard, 1994; Upreti, 1999; Shrestha et al., 2004; Dahal et al., 2006; Dahal & Hasegawa, 2008; Singh, 2009; Haigh & Rawat, 2011; Devkota et al., 2013; Regmi et al., 2013; Rahman et al., 2014; Dahal, 2014; Pathak, 2016; Marc et al., 2019; Dikshit et al., 2020; Shrestha et al., 2023). These appear in the form of earth flow, debris, bulging, rock fall, avalanches and so on (Varnes, 1978; Cruden & Varnes, 1996; Hungr et al., 2014). Infrastructure development in this region requires natural slopes subject to cutting to create space for roads, hydropower facilities, industries, railways, airports and canals, resulting in cut slopes of varying scales (DoR, 2007; Sutejo & Gofar, 2015). Geo-environmental factors like slope geometry, lithology, soil depth, weak band, groundwater condition, drainage density and proximity to faults are the key factors to control the stability of excavated cut slopes (Wyllie & Mah, 2004; Singh et al., 2020).

Defective engineering techniques in changing the slope geometry, torrential rainfall (Dahal et al., 2006), long exposure to the atmosphere, the presence of weak bands, rapid weathering, shallow groundwater, lack of surface drainage and dynamic loading frequently cause roadside failures. Various incidents of landslides from small to large scales along the major highways of Nepal were reported (Schuster & Hubl, 1995; Upreti & Dhital, 1996; Martin, 2001; Bhattarai et al., 2004; Hearn, 2011; Dahal, 2014; Thapa, 2015; Regmi et al., 2016; Hearn & Shakya, 2017; Vuillez et al., 2018; Pant and Acharya, 2021; Pradhan et al., 2022; Robson et al., 2022; Pudasaini et al., 2024; Shrestha et al., 2023; Pokhrel et al., 2024; Robson et al., 2024; Sapkota & Timilsina, 2024; Phuyal et al., 2025, etc.). Within the different road sections in the Lesser Himalaya terrain of Nepal, various methods of analytical, conventional and numerical modelling techniques have been used to analyse the cut slope stability on soil and rock by different researchers (Ray & Smedt, 2009; Pathak, 2014; Dhakal & Acharya, 2019; Shrestha et al., 2023; Acharya & Dhital, 2023; Poudyal et al., 2024).

Cut slope stability evaluation utilises various conventional and numerical modelling approaches through the Limit Equilibrium Method (LEM)

and the Finite Element Method (FEM). LEM often uses the "method of slices" to calculate the Factor of Safety (FoS) based on driving and resisting forces (Morgenstern & Sangrey, 1978; Nian et al., 2012; Burman et al., 2015; Deng et al., 2017). FEM, on the other hand, offers a more complex approach which incorporates stress-strain behaviour and material properties to analyse slope stability (Griffiths & Lane, 1999; Burman et al., 2015). The majority of cut slope stability assessments in the Nepal Himalaya have relied on field investigations, rock mass classification and calculation of FoS by conventional techniques. However, few studies have attempted to evaluate cut slope stability in Nepal using numerical modelling techniques for comprehensive analyses (e.g., Kharel & Acharya, 2017; Khatri & Acharya, 2019; Shrestha et al., 2023). Thus, the present study has integrated computational techniques of numerical modelling in evaluating the cut slope stability within the Himalayan terrain. Based on the spatial inventory of cut slopes in the Lesser Himalaya of central and western Nepal, two cut slopes have been chosen for detailed study, as they represent typical slides in their respective regions and have seriously impacted the socio-economic conditions of the community that depends entirely on the roads passing through them. The modelling approaches of LEM, FEM and the particle finite element method (PFEM) have been implemented to compute the pre-failure and post-failure mechanisms of the respective slopes. The results obtained through these techniques were validated based on the field evidence and simulated results of the computed models.

Study area

The study area is situated in the western and central Nepal Himalaya, bounded by latitudes 27°48'52" N to 27°49'12" N and longitudes 83°17'33" E to 86°13'11" E (Fig. 1). The areal coverage of the study area is about 17,500 km^2 and lies in the adjoining regions of the major cities Pokhara and Kathmandu, with elevations ranging from 230 m to 3,780 m. However, the actual investigation is focused primarily along the road corridors, as the majority of cut slopes are located adjacent to road alignments. The total length of road sections assessed in this study is approximately 2000 km, encompassing both primary and secondary highway networks. The geomorphology of this region is largely shaped by metamorphic and meta-sedimentary rocks of the Lesser Himalaya. The area has experienced significant uplift and erosion, which has shaped a complex geo-environment, forming various geomorphic landforms. The major physiographic divisions, namely the Mahabharat Range and Midland Zone, are the major landform units in this region. The Mahabharat Range is a distinct high mountain belt north of the Indo-Gangetic Plain, while the Midland Zone features a relatively subdued landscape typically covered with residual, colluvial and alluvial deposits. The characteristics of landform conditions combined with extensive anthropogenic activities predispose the region to frequent landslides and slope failures during the summer monsoon season.

Geological setting and spatial distribution

Geologically, the study area lies within the Lesser Himalayan Zone of Nepal and is bounded by two major thrust sheets of the Himalaya: the Main Boundary Thrust (MBT) to the south and the Main Central Thrust (MCT) to the north (Fig. 1). This region consists of two distinct metamorphic zones that include the low-grade Lesser Himalayan metasediments and the high-grade Lesser Himalayan Crystallines (Gansser, 1974). This zone features abundant faulting and folding as its primary geological structures (Upreti, 1999; Dhital, 2015). The main rock types in this area comprise slate, phyllite, schist, quartzite, dolomite and limestone, with some intrusions of granites and meta-basic rocks. The differential strengths of rock strata with highly folded and faulted geo-environments make the region particularly susceptible to landslides and cut slope failures. The prediction of slope failures and landslides together with assessment of mitigative measures becomes essential because of the complex slope failure process and limited understanding of underlying mechanisms which are typical problems in mountainous regions, especially along the hill-cut slope of the Lesser Himalaya (Singh et al., 2008; Hasegawa et al., 2009).

A cut slope inventory database has been developed from various road sections of major highways within the study area of central and western Nepal. Two specific sites were selected for further detailed investigations, as they are the recurring slope failures annually and have considerable socio-economic impacts: the Kokhe Slide in Gorkha District (Site-1: 28°01'35"N, 84°40'13"E) along the Gorkha-Arughat rural road and the Udipur Slide in Lamjung District (Site-2: 28°10'51"N, 84°25'43"E) along the Dumre-Besishahar-Chame Highway (NH25) of Nepal (Fig. 1). Both slides are recurrently triggered during the monsoon season, influenced by shallow groundwater tables, weak and weathered lithology typical of slopes in the

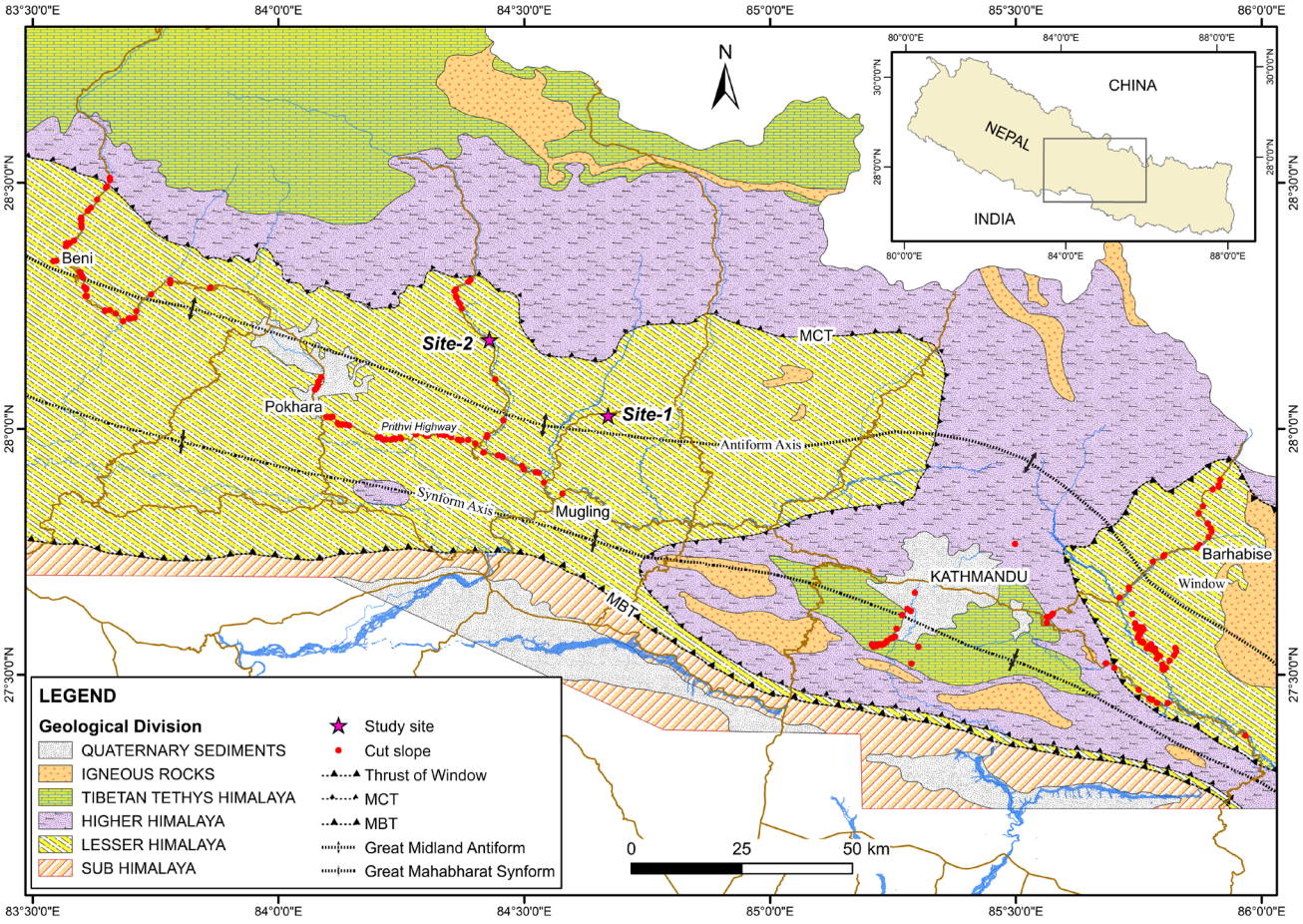

Fig. 1. Geological setting (modified after Dhital, 2015) and spatial distribution of cut slopes in the study area.

Lesser Himalaya, inadequate drainage, and various anthropogenic disturbances. The slide at Site-1 initiated before 2009 and is still posing threats to public transport during the monsoon of every year as progressive sliding occurs annually. The major failure at Site-2 occurred in July 2022 and swept away the 90 m road section downhill and is reactivating during the monsoon of every year. Detailed investigations are based on typical slope geometries, rapidly rising groundwater tables and recurrent failures with a documented history that have a direct impact on public transportation. Findings from these slopes can be applied to many other slides with similar features in terms of geometry, lithology, groundwater conditions, precipitation patterns and socio-economic impacts.

Cut slopes and site characteristics

The characteristics of cut slopes in the Lesser Himalaya are influenced by slope geometry, lithology, weathering and hydrogeological conditions (Upreti & Dhital, 1996; Wyllie & Mah, 2004; Dahal et al., 2008; Phuyal & Thapa, 2023; Shrestha et al., 2023). Cut slope failures in the study area are often observed on higher and steeper slope gradients experiencing more gravitational forces that have increased the shear stress exceeding the soil strength (Fig. 2a). Improper and non-engineered methods of excavation during construction without due consideration of local geology are significant contributors to slope failures.

Many steep and high cut slopes formed in heavily weathered rocks are in a marginal stable state even under dry conditions. During rainfall, these materials become saturated and fail due to excessive pore pressure development (Fig. 2b). Failures often occur in areas with highly jointed, fractured, folded or faulted rock masses within the Lesser Himalaya (Fig. 2c, d).

Every year, high and prolonged precipitation during the monsoon saturates the soil and increases pore water pressure therein. This reduces the effective stress and shear strength of the soil and leads to instability (Terzaghi, 1943; Craig, 2004; Duncan & Wright, 2005). Tensional cracks developed at the crown of the slope create a path for water to percolate easily into the slope and aggravate the failure mechanism (Fig. 2e). Residual soil found along the road section with unprotected higher slope height and steeper gradient is susceptible to failure during the wet season (Fig. 2f).

Fig. 2. Cut slope characteristics in the Lesser Himalayan Zone of western and central Nepal: (a) weak rock exposure and steep cut slope failed during heavy rainfall along the Prithvi Highway, Tanahun, (b) completely weathered high slope along the Kanti Lokpath, Lalitpur, (c) rock blocks over loose materials failed along the Pushpalal Highway, Kaski, (d) folded rock showing numerous discontinuities prone to failure at Dolakha, (e) a translational slide along the Kathmandu-Melamchi Highway, Sindhupalchowk, and (f) a failed residual soil slope due to slope modification for highway expansion along the Prithvi Highway, Dhading.

The cut slopes failure at Site-1 consists of the residual soil formed from the phyllite rock of the Kuncha Formation. The lithology in this area is psammitic phyllite, which is characterised by alternating layers of crenulated micaceous material comprising microfolds and a quartz-rich layer embedded within the fine-grained matrix of well-foliated mica minerals. This type of phyllite consists of quartz, K-feldspar, and muscovite as primary minerals, whereas tourmaline, biotite, opaque minerals, oxides and clay minerals as accessory minerals (Silwal et al., 2024). Sericitisation and

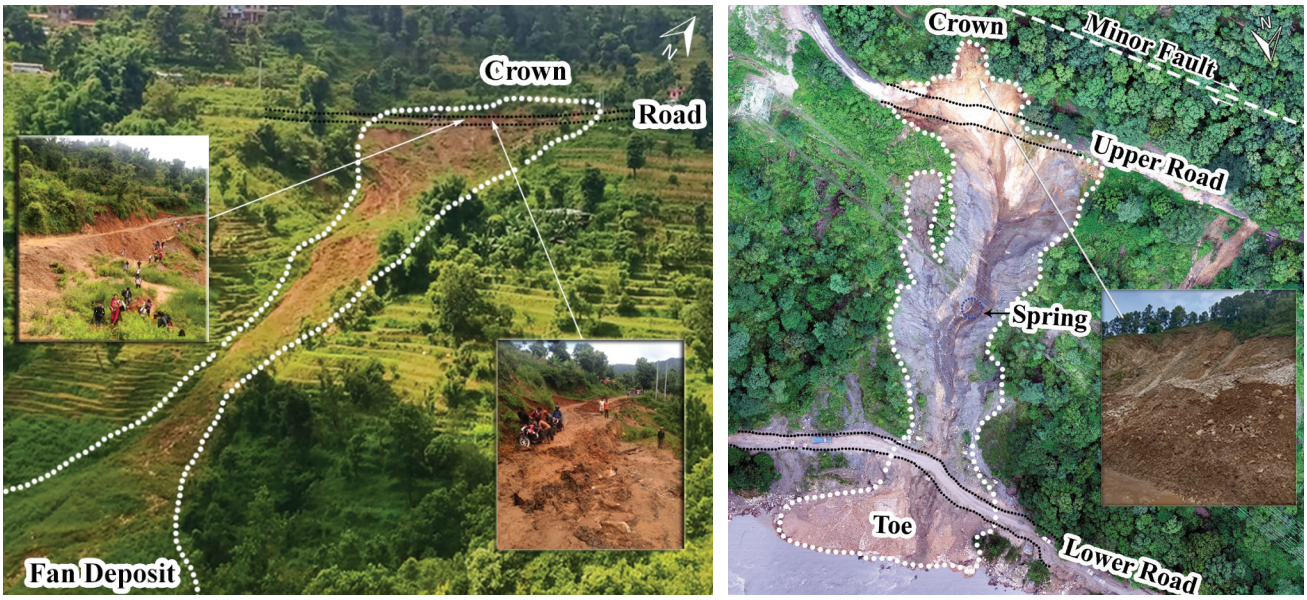

Fig. 3. Characteristic features of the modelling sites: (a) Site-1, the Kokhe Slide, inset shows the road conditions within the slide-affected section, (b) Site-2, the Udipur Slide, inset shows the slope section above the road.

alteration effects are very common in this type of rock and are well observed in the slope materials (Fig. 3a). Mineral composition and textural features (e.g., foliation, cracks, alterations) aid in classifying rock strength and weathering grades, which in turn help estimate geotechnical parameters (e.g., unit weight, Young's modulus, Poisson's ratio). Furthermore, the presence of micaceous minerals (e.g., sericite, clay) indicates weak rock mass that are associated with observed failure mechanisms.

The cut slope failure at Site-2 lies under the Fagfog Quartzite of the Lower Nawakot Group, which is highly fractured and thinly foliated with poor rock mass quality (Panthi, 2006). The section above the road is characterized by highly fractured and weathered quartzite, and the lower section contains thick colluvium. A minor fault is expected in this area, as seen by the high fracture frequency observed in the quartzite rock (Fig. 3b).

Data and methodology

Representative soil and rock samples from the slope failure scarp and adjacent exposures of the selected sites 1 and 2 were collected for laboratory testing to determine geotechnical properties. Unit weight (γ), cohesion (c), friction angle (ϕ), Young's modulus (E), Poisson's ratio (ν) and density (d) are the required input parameters for slope stability evaluation (Table 1).

Table 1.Geotechnical parameters of Site-1 and Site-2.

Parameters	Site-1				Site-2			
	Soil		Rock mass		Soil		Rock mass	
	DC*	SC**	DC	SC	DC	SC	DC	SC
Unit weight (γ), kN/m^3	17.2	18.4	26	22.81	17.0	19.6	26	27.5
Cohesion (c), kPa	16	4	42	35.8	40	20	200	185
Friction Angle (φ), °	22	14	38	32	28	14	35	31
Young's Modulus (E), kPa	40,000	40,000	52,000×10^3	52,000×10^3	400,000	400,000	36,000×10^3	36,000×10^3
Poisson's Ratio (ν)	0.4	0.4	0.23	0.23	0.30	0.30	0.25	0.25
Density (d) (kg/m^3)	1753	2331	-	-	1733	2180	-	-

***Note**: *DC = Dry condition, **SC = Saturated condition*

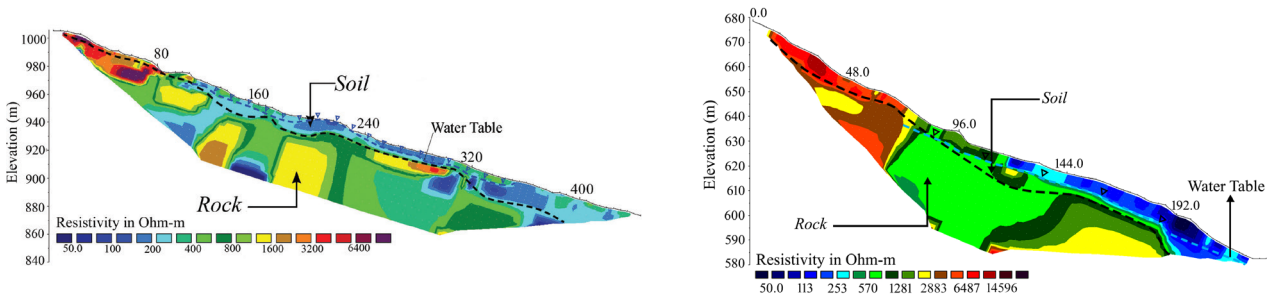

Fig. 4. Geophysical survey for subsurface investigation by electrical resistivity tomography: (a) Site-1 and (b) Site-2.

Field investigation of each specific site was carried out in detail using a Total Station (TS) survey for generating the hill slope profiles and a geophysical survey using Electrical Resistivity Tomography (ERT) for delineating sub-surface geological layers and identifying groundwater positions, which are important controlling factors in model development and slope stability analysis (Loke, 2004; Loke et al., 2013; Cardarelli & Fischanger, 2006; Panda et al., 2023). The interpretation of ERT correlates the variations in resistivity with different subsurface materials and conditions, such as lithology, moisture content and the groundwater level (Singh et al., 2014). Interpretative models derived from the processed tomograms of the slopes at sites 1 and 2 were integrated into slope-section profiles to evaluate cut slope stability (Fig. 4).

Modelling methods

Numerous advanced numerical techniques, encompassing continuum, discontinuum, and hybrid methods, are available for soil and rock slope stability analyses (Griffiths & Lane, 1999; Cheng et al., 2007; Zheng et al., 2014; Sharma et al., 2017). Numerical modelling of two cut slope failures (Kokhe and Udipur) was evaluated using Slide v.6.0 and Phase2 v.8.0, followed by a comparative analysis of Factor of Safety (FoS) under varying input conditions. Moreover, both sites were simulated utilising the multi-physics simulation framework "GiD" interface equipped with the Kratos platform. Input parameters for these simulations were also determined in the laboratory as per ASTM standards.

The numerical modelling processes involved a series of analytical computation workflows: defining problems based on site conditions, selecting the method, creating numerical models, computing outcomes and interpreting & validating results (Fig. 5). LEM and FEM modelling have evaluated the pre-failure state of cut slopes, and their post-failure mechanism has been analysed by Particle Finite Element Method (PFEM).

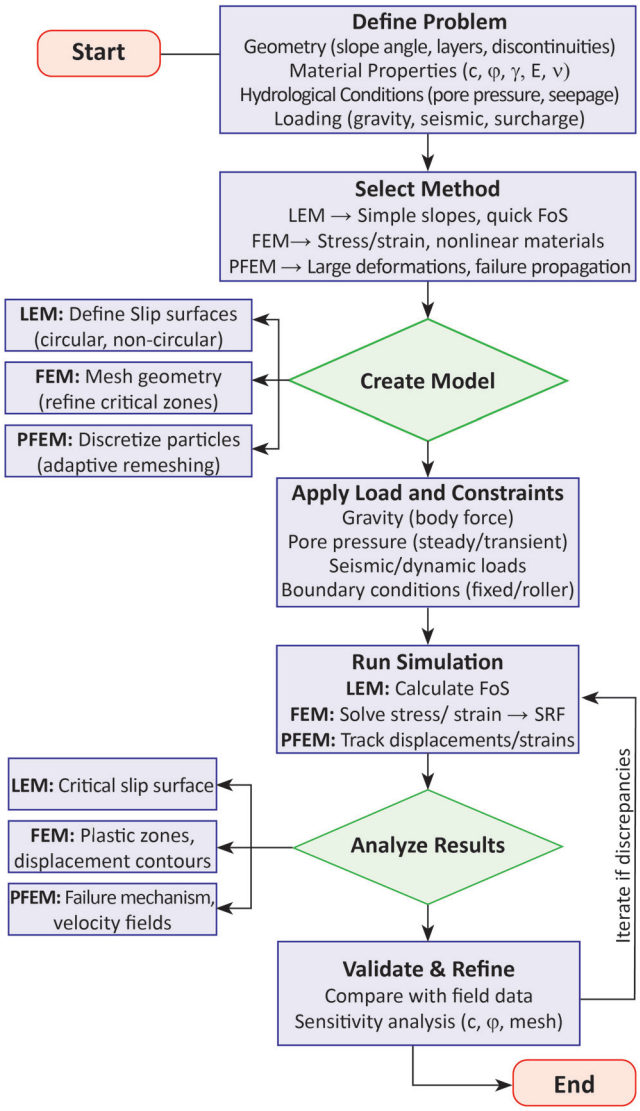

Fig. 5. Methodological framework for cut slope stability evaluation.

Model setup and computation

Numerical modelling of cut slopes involves slope behaviour simulation under various conditions to assess stability and failure modes (Singh et al., 2008). The model setup was performed by defining the geometry of the slope, assigning material properties, and applying boundary conditions (Fig. 6). The model geometry has encompassed the

actual slope, including its height and angle. Triangulated meshes were generated throughout the slope model with finer meshes around high-stress gradients and failure slip surfaces.

The GLE/Morgenstern-Price method (Slide v.6.0) was used in the LEM model to determine the safety factors in both dry and saturated conditions for evaluating the slopes in two different geo-environments. In addition, the same slope was computed by the FEM technique using Phase^2 v.8.0. The FEM model was discretised using six-noded triangular meshes of 3,000 elements under gravitational loading for dry and saturated conditions. Boundary conditions significantly influence slope stability analyses in numerical modelling (Chugh, 2003). Therefore, appropriate selection of boundary conditions is essential for reliable numerical modelling, which has been considered in this study.

After model setup with defined boundary conditions, assigned material properties and hydraulic parameters, simulations were conducted for varying groundwater levels. The variation of the FoS was evaluated in terms of fluctuating groundwater levels to identify the critical failure surface due to pore water pressure during rainy seasons. A plane strain analysis was further applied by selecting metric units and using the Gaussian elimination solver for accuracy purposes. The stress analysis was performed with a maximum of 500 iterations and a tolerance level of 0.001 to ensure convergence. The gravity loading was applied to the created model, and meshes were generated using a six-noded graded triangle as recommended by Komadja et al. (2020). Before running the simulation, the base and the right boundary of the model were restrained in both horizontal (X) and vertical (Y) directions to prevent movement. The model slope face was kept unrestrained to allow free deformation during numerical modelling.

The Limit Equilibrium Method (LEM) is a method of slices widely used for assessing slope stability because of its simplicity and user-friendliness. It derives FoS with respect to force and moment equilibrium. LEM analyses a slope by cutting it into fine slices and applying appropriate equilibrium equations (equilibrium of forces and/or moments) to calculate the FoS (Matthews et al., 2014). The common methods of LEM analysis are Ordinary/Fellenius (Fellenius, 1936), Bishop simplified (Bishop, 1955), Lowe and Karafiath (Lowe & Karafiath, 1965), GLE/Morgenstern-Price (Morgenstern & Price, 1965), Spencer (Spencer, 1967), Janbu Simplified and Janbu Corrected (Janbu, 1954), and Corps of Engineer #1 and #2 (USACE, 2003). Among these, the Morgenstern-Price (M-P) method (1965) and Sarma's method (1973) are advanced ones that account for both force and moment equilibrium and improve the accuracy of FoS on a factual basis. The M-P method involves complex equations, and different forms can be found depending on the assumptions made. The FoS in the Morgenstern-Price method is expressed as (Eq. 1) (Fan et al., 2021):

$$FoS = \frac{\int (c' + (\sigma - \mu)\tan\phi')\sec\alpha d_x}{\int \tau d_x} \qquad (1)$$

where, c' = effective cohesion, ϕ= effective angle of internal friction, σ = total normal stress on the base of the slice, μ = pore water pressure on the base of the slice, α= inclination of the base of the slice, and τ= shear stress on the base of the slice

The Finite Element Method (FEM) is an advanced computational technique which enhances traditional LEM by providing a higher degree of realism and deformation visualisations of materials (Matthews et al., 2014). FEM provides insights into stress, strain and displacement, which makes it a fundamental tool for analysing the deformation behaviour of slope materials (Cheng

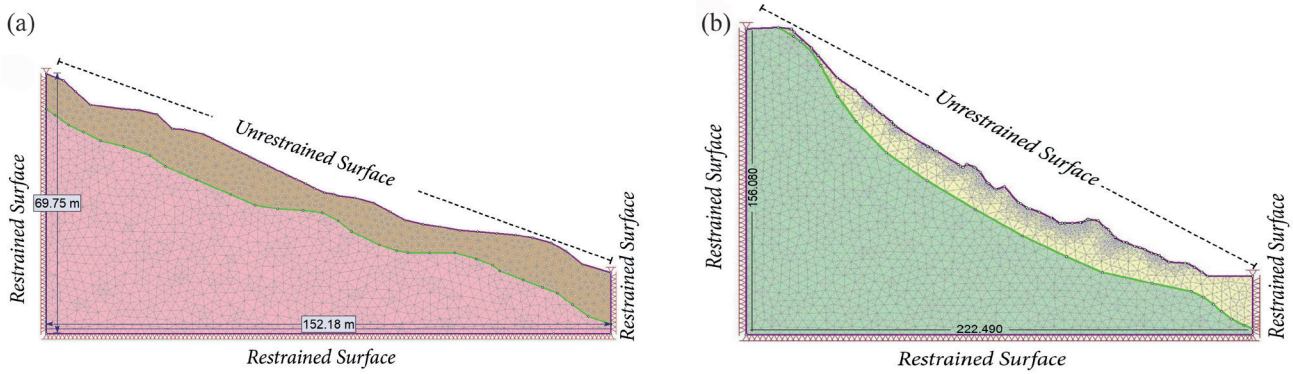

Fig. 6. Numerical model setup with mesh and boundary conditions: (a) Site-1 and (b) Site-2.

et al., 2007; Burman et al., 2015). FEM offers several advantages over LEM in slope stability analysis (Griffiths & Lane, 1999) as it does not require prior assumptions regarding the shape and location of the failure surface (Dawson et al., 1999). In this method, failure naturally emerges along a surface where material strength is deficient of resisting applied shear stresses. In FEM, the Shear Strength Reduction (SSR) technique has been applied to the Mohr-Coulomb criterion using Phase^2 to determine the Strength Reduction Factor (SRF).

The Particle Finite Element Method (PFEM) is a robust numerical technique which enables the solution of multi-physics problems involving extensive domain deformations (Oñate et al., 2004; Oñate et al., 2011). The PFEM model enables domain particles to move through space using Lagrangian dynamics while nodal variables determine their physical properties (e.g., density and viscosity) throughout the entire simulation period. The algorithm generates dynamic meshes through Delaunay triangulation and alpha shape scheme processes to prevent mesh distortion (Oñate et al., 2011).

The Navier–Stokes equations describe the fluid body motion and are governed by (Eq. 2 & 3). These equations relate the velocity u = u(x, t) and the Cauchy stress tensor σ = σ(x, t) through principles of momentum balance and mass conservation (Cremonesi et al., 2020) by:

$$\rho \frac{D\mathrm{u}}{Dt} = \mathrm{div}\,\sigma + b \quad \text{in } \Omega_t \times (0,T) \tag{2}$$

$$\frac{D\rho}{Dt} + \rho\,\mathrm{div}\,\mathrm{u} = 0 \quad \text{in } \Omega_t \times (0,T) \tag{3}$$

where, ρ(x) represents the fluid density, b(x, t) denotes external body forces per unit mass, and D/Dt is the material time derivative. A Lagrangian technique reduces the total time derivatives to a local time derivative and vanishes the convective factor in the governing equations. This characteristic is inherent in Lagrangian methods like the Particle Finite Element Method (Idelsohn et al., 2008; Idelsohn & Oñate, 2010; Franci et al., 2020).

The PFEM is capable of solving complex fluid-solid interaction problems and deformation mechanics. It is particularly useful in post-failure landslide analysis as it efficiently deals with extensive deformations, fragmentation and fluid-solid interactions. Both modelling sites (Site-1 and Site-2) were simulated in PFEM in terms of two-phase system based on distinct layers of materials identified from ERT and borehole data. The upper soil layer shows plastic behaviour under saturated conditions, whereas the underlying solid rock mass serves as a rigid and non-deforming base in the model. For Site-1, the saturated soil mass was modelled with a density (d) of 2331 kg/m^3, an internal friction angle (ϕ) of 14°, and cohesion (c) of 4 kPa, which were used as input parameters for the numerical computations.

Results and discussion

Limit Equilibrium Method (LEM)

The rigorous M-P method is an advanced and highly reliable method that satisfies both force and moment equilibrium (Zheng, 2012; Fan et al., 2021; Shrestha et al., 2023). This method has been adopted in the present modelling process. The safety factors of Site-1 were calculated under different conditions by considering fluctuations in the groundwater level of this area using this method, which is appropriate for analysing circular slip surfaces (Fig. 7). The analysis yielded a FoS of 1.42 under normal dry conditions (Fig. 7a), which is above the recommended minimum FoS of 1.25 for cut slopes, indicating a stable slope. Three different groundwater scenarios were analysed with varying depths of 7.0 m, 1.5 m and 0.5 m below the existing groundwater level (GWL). The calculated FoS values for these three different GWLs are 1.25, 0.97 and 0.87, respectively (Fig. 7b, c, d). Higher FoS values were observed with deeper GWL, and FoS decreased under elevated GWL, which corroborates the frequent cut slope failures observed during the rainy seasons.

According to the precipitation records from the Department of Hydrology and Meteorology (DHM, 2024), Nepal, the average annual precipitation at Site-1 is 254.88 mm. A transient analysis of this site for 24 hours with 250 mm of rainfall calculated a FoS of 1.18 after the implementation of gabion walls along with a three-stage drainpipe installation, representing the critical situation of slope during heavy rainfall (Fig. 7e). Considering the same rainfall condition with added static loading of 20 kN/m^2 and seismic loading of 0.17 g (horizontal) and 0.08 g (vertical), the calculated FoS is 1.10, which is still above the unity, indicating the marginal stability of slope (Fig. 7f) in the extreme conditions of loading too. There is a 42.98 % variation in FoS for Site-1 while transitioning from dry to saturated conditions.

The LEM analysis by M-P method for Site-2 has shown that the FoS in dry condition is 1.18

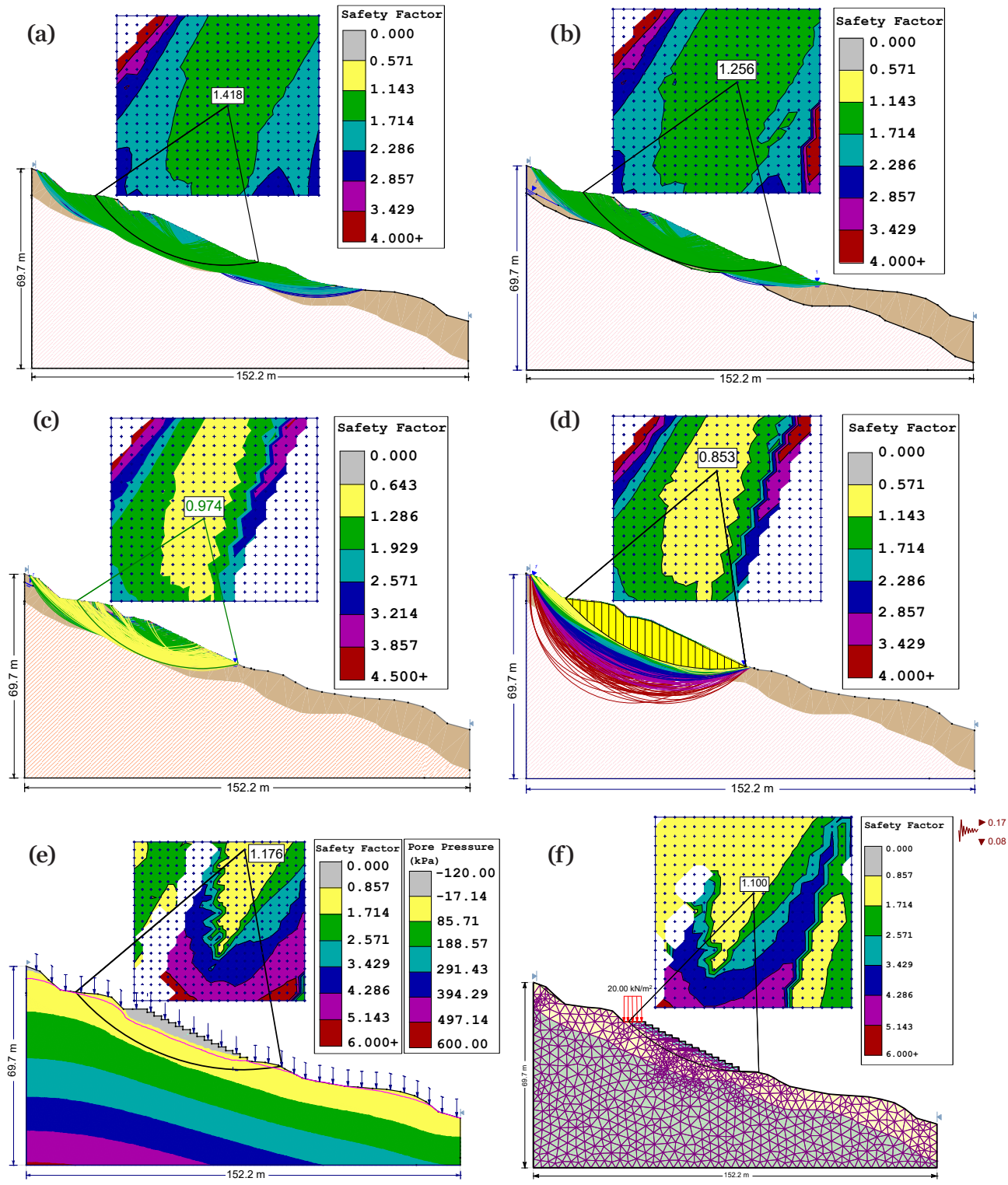

Fig. 7. Limit equilibrium stability analysis of Site-1: (a) dry condition, (b) GWL at 7 m, (c) GWL at 1.5 m, (d) GWL at 0.5 m, (e) transient analysis for 24 hours with 250 mm rainfall, (f) transient analysis with static loading of 20 kN/m^2 and seismic loading of 170 g (horizontal) and 80 g (vertical). (Note: The scale for all figures is same as given in Fig. 7a)

(Fig. 8a), which significantly declines to 0.41 under saturated condition (Fig. 8b). This slope exhibits marginal stability under dry conditions and ultimately transitions into an unstable state in saturated conditions. A variation of 66 % is found in the FoS for this slope when changing from dry to saturated conditions.

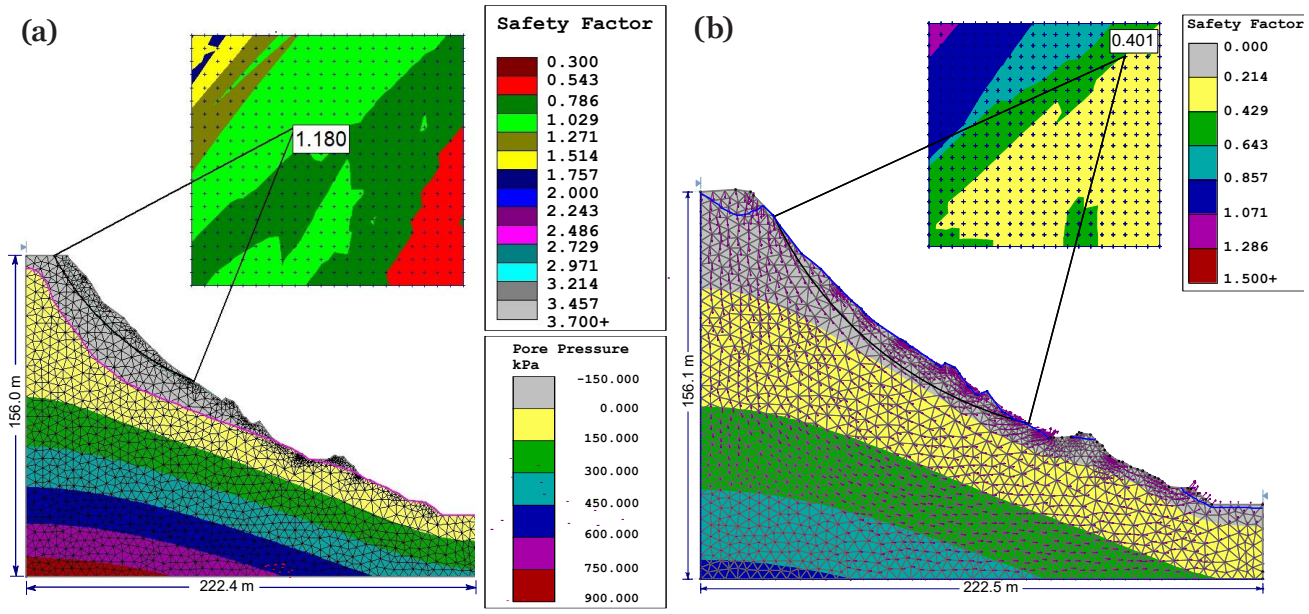

Fig. 8. Limit equilibrium stability analysis of Site-2: (a) dry condition, (b) saturated condition.

Finite Element Method (FEM)

The FEM analysis for Site-1 calculated an SRF of 1.45 under dry conditions, indicating a stable slope state. In saturated conditions, the SRF decreased to 0.82 (Fig. 9a-d), which has predicted the critical failure probability. These two conditions for Site-1 clearly show a 43.44 % change in safety factor when the slope gets saturated. Similarly, for Site-2, SRF under dry conditions is 1.15, showing a marginal stability of slope. This safety factor changes to 0.39 under saturated conditions. This change in FoS between two conditions is 66.08 %, which is very critical in terms of slope instability.

The maximum shear strain values at both slope sites have shown that elevated pore water pressure strongly influences slope materials to destabilise. The maximum shear strain at Site-1 increased from 0.0105 to 0.0315 on changing the scenario from dry to saturation, thereby showing a 57.5 % increase in slope material deformation (Fig. 9a, c). Likewise, Site-2 experienced a maximum shear strain of 0.00386 under dry and 0.009 under

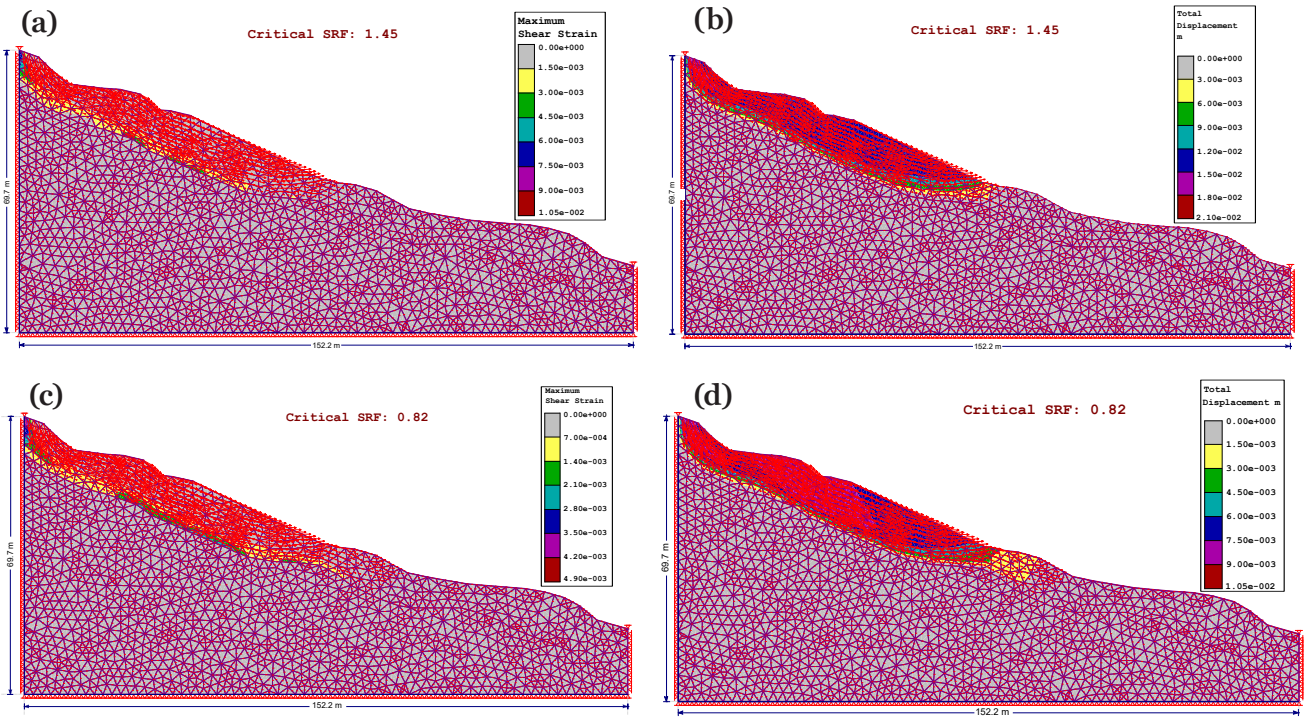

Fig. 9. Maximum deformation vectors at Site-1 under dry conditions: (a) shear strain, (b) total displacement and saturated conditions: (c) shear strain, (d) total displacement.

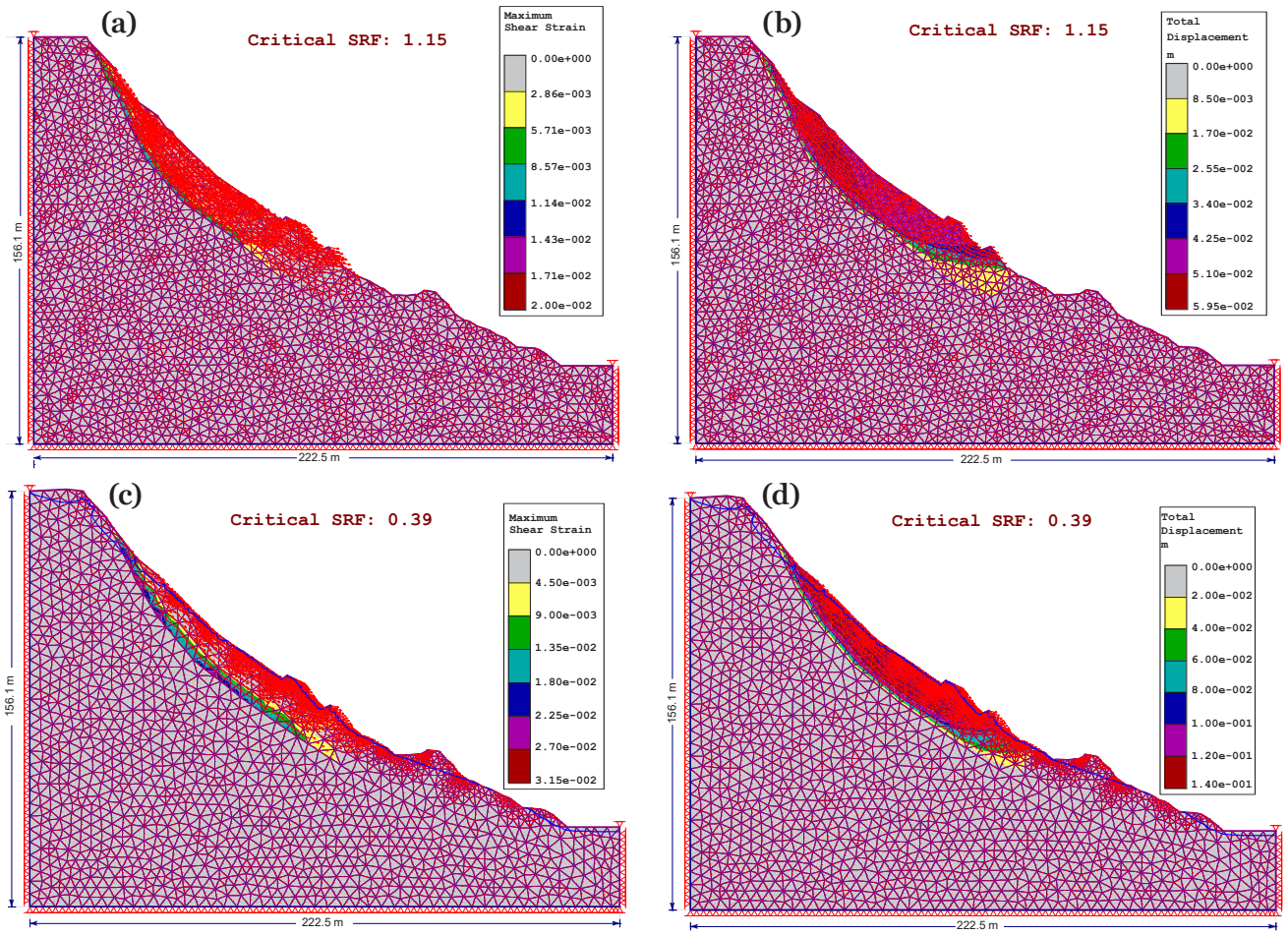

Fig. 10. Maximum deformation vectors at Site-2 under dry conditions: (a) shear strain, (b) total displacement and under saturated conditions: (c) shear strain, (d) total displacement.

saturated conditions (Fig. 10a, c) indicating a 133 % increase in shear strain due to increased pore water pressures within the slope debris mass.

Total displacement contours with deformation vectors from FEM results show the zone of failure, its distribution and intensity, thereby expressing deformation behaviour across the slope. At Site-1, the magnitude of displacement contours illustrates that maximum displacement occurs at the top portion of the free face and gradually diminishes downwards. The maximum displacements for Site-1 and Site-2 under dry conditions are 19.6 mm and 140 mm, respectively (Fig. 9d & Fig. 10d).

Particle Finite Element Method (PFEM)

To ensure the reliability of the numerical results, a series of mesh convergence tests were performed for different mesh sizes of 4.0 m, 3.0 m, 2.0 m, 1.0 m and 0.5 m consecutively to compare the resulting sediment deposition heights (Fig. 11a).

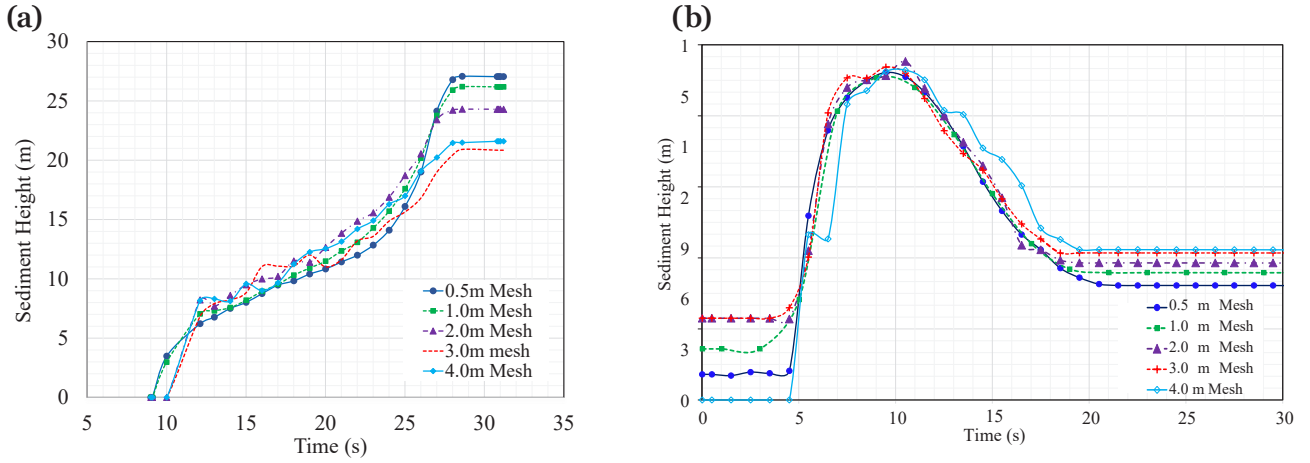

Fig. 11. Temporal variation of sediment deposition height simulated using different mesh sizes in PFEM analysis: (a) at the base of the slope for Site-1 and (b) at the lower road section for Site-2.

The simulation results showed that mesh sizes of 1.0 m and 0.5 m produced nearly identical results, indicating that a 1.0 m mesh provides sufficient resolution for accurately capturing the dynamic debris flow and deposition patterns of the sliding mass, thereby maintaining computational efficiency.

For Site-2, the density, internal friction angle and cohesion of the saturated material were determined to be 2180 kg/m³, 14° and 6 kPa, respectively. A 2D mesh sensitivity analysis was conducted to assess the numerical accuracy of the simulations. By comparing sedimentation height profiles across varying mesh sizes (4.0 m, 2.0 m, 1.0 m and 0.5 m), it was observed that mesh sizes of 0.5 m and 1.0 m yielded nearly identical results (Fig. 11b). The results have confirmed the adequacy of the 1.0 m mesh for optimising the runout dynamics and flow morphology without hindering computational efficiency, which aligns with the recommendations from similar PFEM studies by Cremonesi et al. (2011) and Oñate et al. (2014).

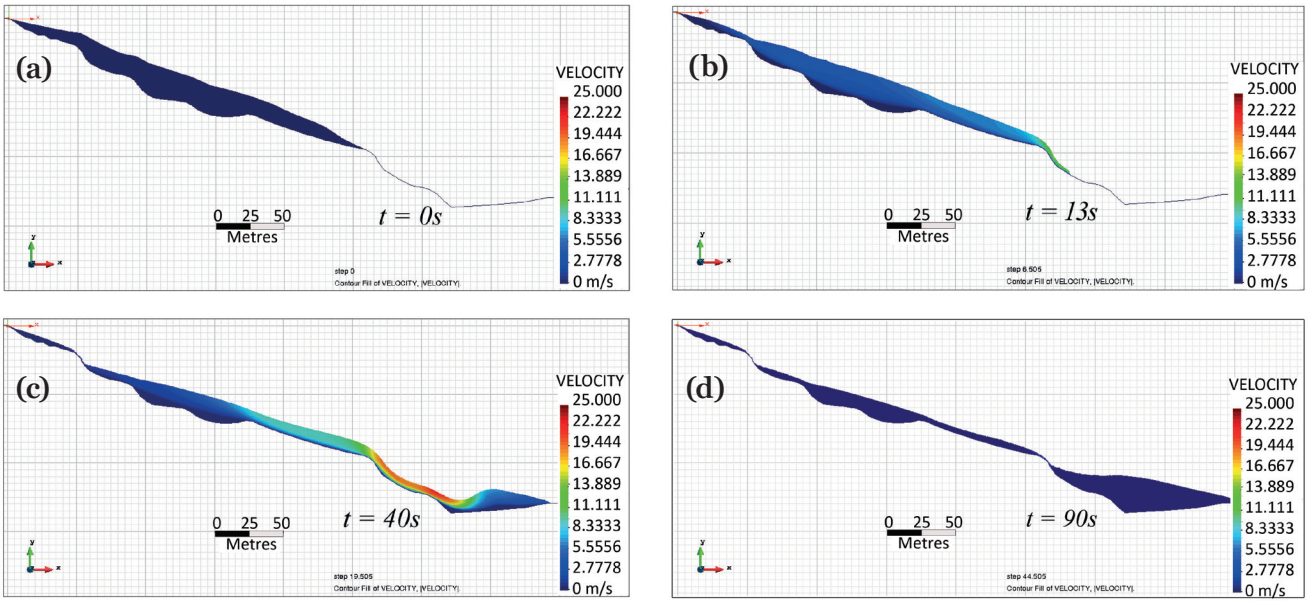

Fig. 12. Progressive post-failure flow stages at Site-1 simulated using 2D-PFEM: (a) t = 0s (b) t = 13s, (c) t = 40s, and (d) t = 90s.

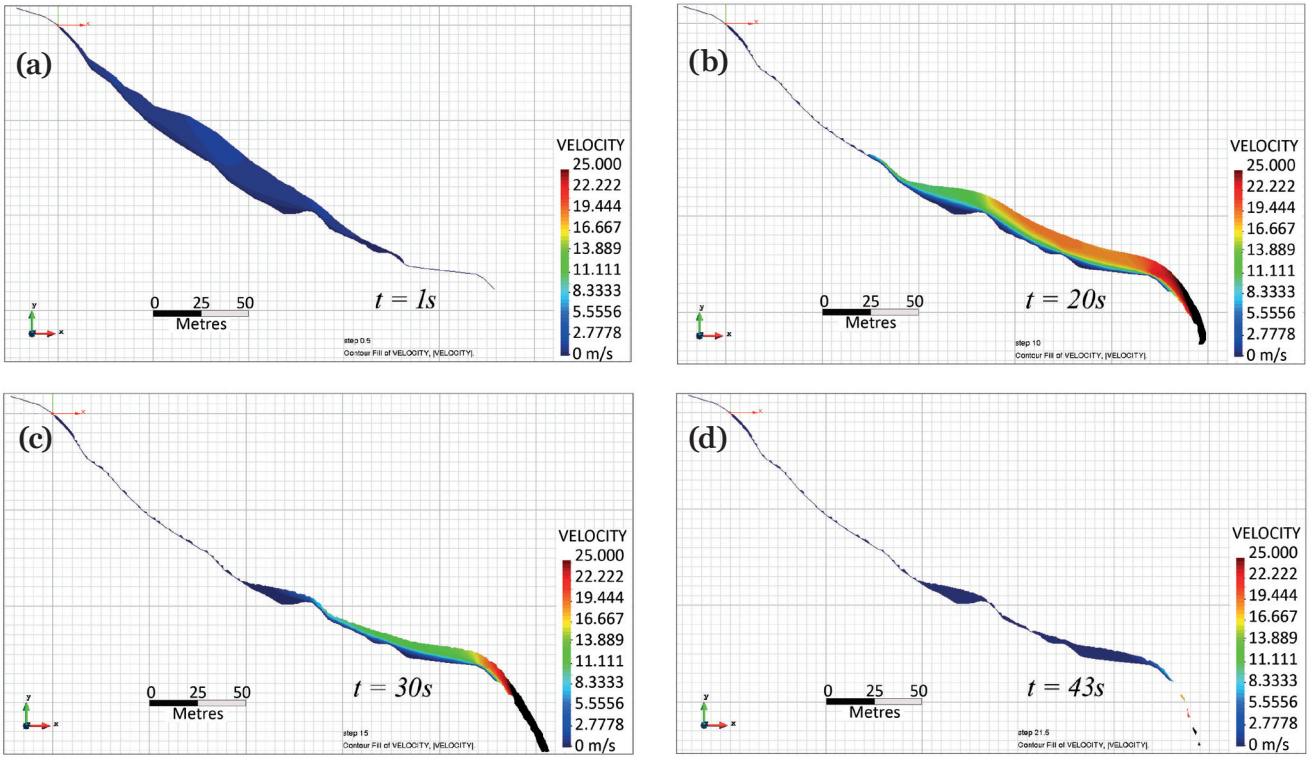

Fig. 13. Progressive post-failure stages at Site-2 simulated using 2D-PFEM: (a) t = 1s, (b) t = 20s, (c) t = 30s, and (d) t = 43s.

The PFEM simulation at Site-1 has assessed both the initiation of failure and the subsequent transport of residual soil with particular emphasis on the Lesser Himalaya of central and western Nepal, where annual rainfall averages approximately 254 mm. The numerical result for this site has provided insights into the landslide dynamics under debris-fluid flow conditions. The debris mass progressively accelerated downslope, reaching a peak velocity of 19.6 m/s before impacting the slope base. The computed runout distance is approximately 425 m from the roadway at the slope crest, which reflects the mobility and energy of the sliding mass. The final deposition profile shows a maximum sediment thickness of 26.1 m at the base of the slope (Fig. 12).

The PFEM analysis for Site-2 was performed in both 2D and 3D configurations, which displayed a realistic simulation of the post-failure conditions. Fig. 13 and Fig. 14 illustrate the time-evolved

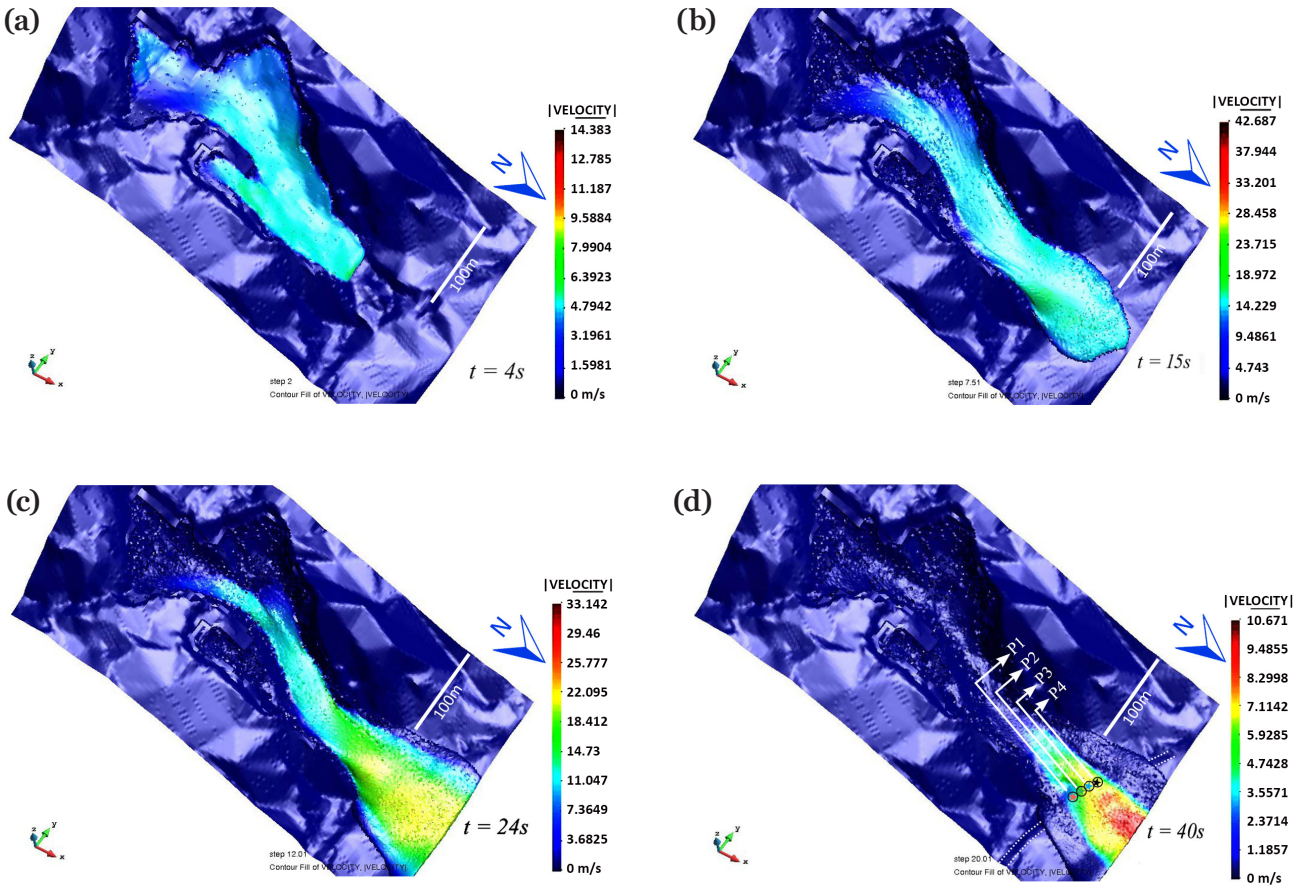

Fig. 14. Progressive post-failure stages at Site-2 simulated using 3D-PFEM: (a) t = 4s, (b) t = 15s, (c) t = 24s and (d) t = 40s.

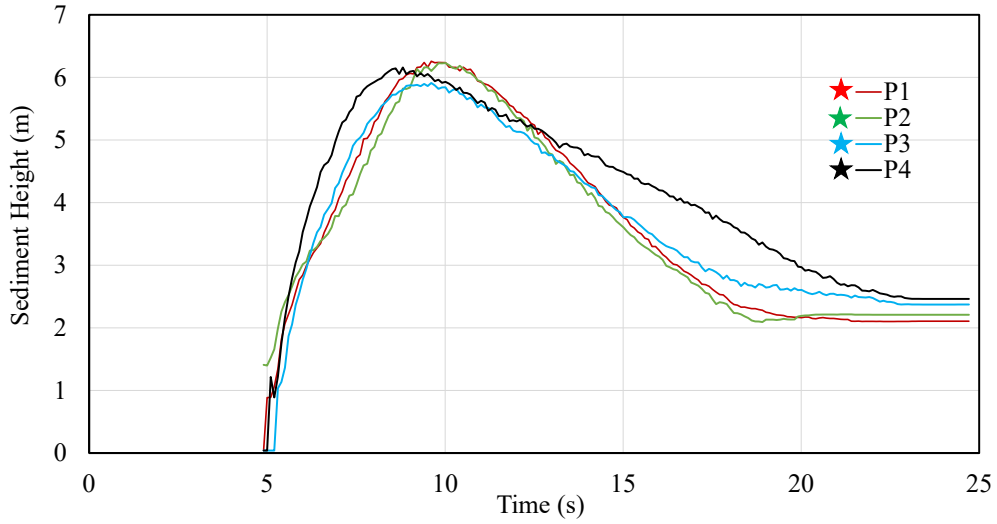

Fig. 15. Temporal evolution of sediment accumulation at four locations along the lower road section of Site-2, based on computed results from the 3D PFEM simulation. (*Notations P1 to P4 correspond to observation points indicated in Fig. 14d*)

progression of the sliding mass, from initial detachment to eventual deposition and spreading at the lower end. A significant accumulation of failed material was observed at the base of the slope where a motorable road was blocked by the debris mass. The simulation results indicated a maximum deposition thickness of approximately 6.2 m at the point of observation along the lower road section (Fig. 15).

Model performance and sensitivity

The cut slope modelling approach effectively predicted FoS and identified potential slip surfaces under varying geological and hydrological conditions using pre-failure analyses via LEM and FEM. The quick estimations from LEM were refined through FEM, which accounted for stress–strain behaviour and complex slope geometries. Post-failure conditions simulated through PFEM successfully reconstructed deformation patterns using site-specific geotechnical inputs. The consistency between pre- and post-failure results aligns well with field observations, validating the reliability and robustness of the adopted modelling techniques.

The results from LEM and FEM analyses demonstrate that changes in GWL have a significant impact on slope stability at both sites. The slopes remained unstable when the GWL was 1.0 m below the surface but became marginally stable between 2.0 and 6.0 m and reached a stability condition when the GWL dropped below 7.0 m with FoS exceeding 1.25. The observed pattern was uniform for both methods at Site-1; however, FEM results at Site-2 remained unstable even when the GWL was below 2.0 m (Fig. 16). The analysis showed that FoS/SRF values increased steadily with groundwater levels lowering down at both locations, which suggests that deeper groundwater levels increase the stability of slopes. Conversely, a rise in GWL due to infiltration during rainfall led to a reduction in FoS. The rise in GWL induces seepage forces which also align in the direction of potential slope movement and augment the contributing factors causing instability (Fredlund et al., 2012). At both sites, increased saturation leads to the loss of matric suction, causing the soil to weaken and become more susceptible to failure (Lu & Godt, 2013). FEM results further indicated that Site-2 is more susceptible to groundwater fluctuations than Site-1.

Site-1 undergoes FoS changes of 40.78 % in LEM and 46.47 % in FEM when transitioning from dry to saturated conditions. Similarly, Site-2 undergoes a change of 61.18 % in LEM and 65.81 % in FEM under the same conditions. The changes in FoS from dry to saturated conditions in both LEM and FEM methods are high and range from 40.78 % to 65.81 % across both sites. Under dry conditions, a change of 3.79 % and 27.32 % occurred in FoS by LEM and FEM at Site-1 and Site-2, respectively, which are dependent on the site-specific geo-material properties (Table 2). Similarly, in saturated conditions, the change in FoS in LEM and FEM for Site-1 and Site-2 are 13.04 % and 36 %, respectively.

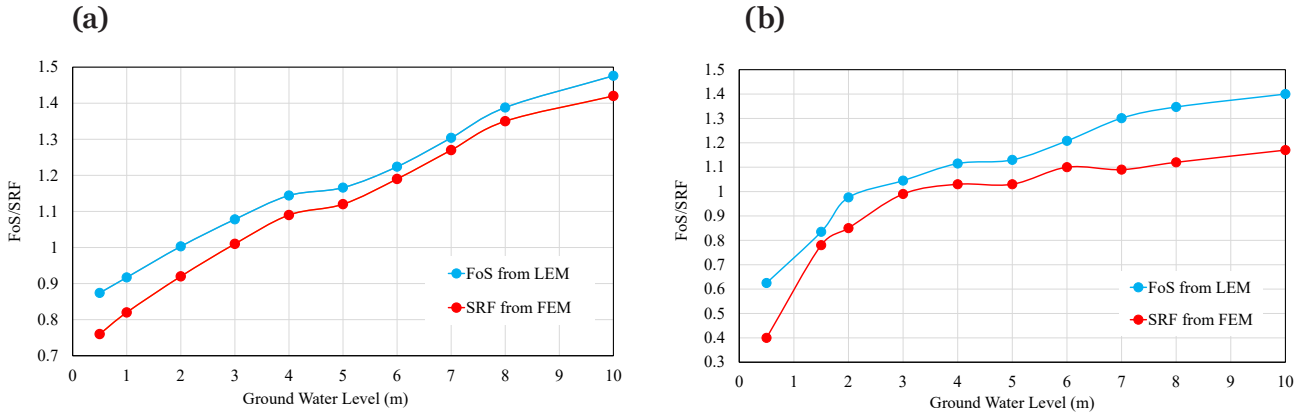

Fig. 16. Comparison of safety factors obtained from LEM and FEM at varying groundwater levels: (a) Site-1 and (b) Site-2.

Table 2. Variation in FoS under dry and saturated conditions for both sites using LEM and FEM methods.

Location	LEM (dry)	LEM (sat.)	% change in LEM (dry & sat.)	FEM (dry)	FEM (sat.)	% change in FEM (dry & sat.)	% change in LEM (dry) & FEM (dry)	% change in LEM (sat.) & FEM (sat.)
Site-1	1.476	0.874	40.78	1.42	0.76	46.47	3.79	13.04
Site-2	1.610	0.625	61.18	1.17	0.40	65.81	27.32	36.00

A comparison of LEM and FEM results under dry conditions revealed a minimal variation of 2.54 % in the safety factor, demonstrating strong agreement between the two methodologies in the absence of groundwater influence. This variation increased slightly to 2.74 % under saturated conditions, indicating that both methods consistently capture the effects of saturation on slope stability. This marginal increase can be attributed to the more complex hydro-mechanical processes accounted for in FEM, including stress redistribution and strain localisation, which are not addressed in LEM (Dawson et al., 1999; Sheng et al., 2003).

Sensitivity analyses of the slopes at both sites were performed to identify the slope parameters that significantly influence the slope stability (Fig. 17). This analysis helps in understanding failure mechanisms, evaluating model robustness, supporting design decisions and optimising the monitoring stages of a slope.

The sensitivity analyses for Site-1 (Fig. 17a) and Site-2 (Fig. 17b) showed that the friction angle (φ) has the most significant influence on slope stability and that an increase in friction angle significantly increases the FoS. Cohesion (c) also has a positive influence on stability, but to a lesser extent. On the other hand, unit weight (γ) has a negative correlation, where an increase in unit weight results in a decrease of FoS. This implies that reducing the soil weight or increasing the frictional resistance can greatly enhance the slope stability at Site-1. From these two analyses, it is observed that the change in FoS is non-linear for friction angle and unit weight but is linear for cohesion. The variation in FoS in both analyses is less than 1 %, indicating a strong agreement.

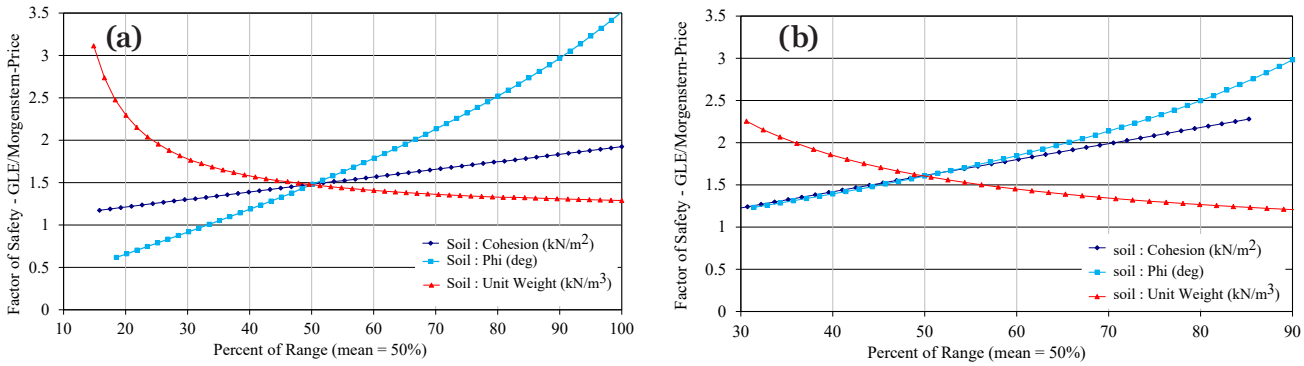

Fig. 17. Sensitivity analysis of slope stability parameters: (a) Site-1 and (b) Site-2.

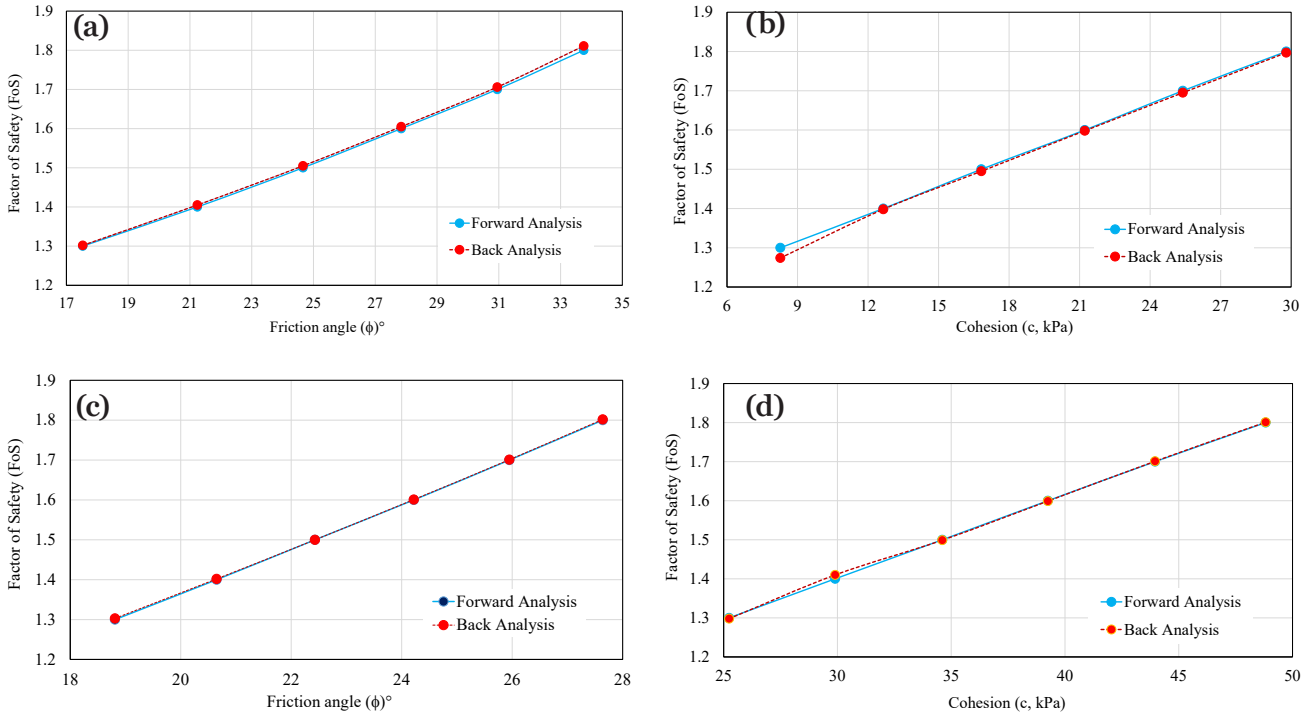

Fig. 18. Evaluation of model consistency through forward and backward analyses under parameter variation: (a) Site-1 with constant cohesion, (b) Site-1 with constant friction angle, (c) Site-2 with constant cohesion and (d) Site-2 with constant friction angle.

The close agreement between forward and back analyses for both modelling sites demonstrated the robustness and reliability of the numerical models (Fig. 18), confirming that the selected geotechnical parameters (c, φ, γ) are well-calibrated and effective in predicting slope stability behaviour under varying conditions.

The maximum shear strain for both slopes was found to be confined at the slip surface, which diminishes gradually towards the ground surface. This shear strain achieved its maximum value under saturated conditions for both slopes and was lower in dry conditions. The increase in shear strain is attributed to elevated pore water pressures that decrease the effective stress within the slope materials. The higher strain values under dry conditions at Site-1 as compared to Site-2 indicated that the soil profile at Site-1 exhibits weaker deformation characteristics, possibly due to lower stiffness and higher water retention or finer soil grains. Site-2 showed lower strain values under dry conditions, which signifies the stable and stiff material behaviour, likely due to its coarse-grained structure and dense packing. Thus, the present study highlights the importance of integrating advanced numerical methods such as FEM for slope stability evaluations, particularly in Lesser Himalayan regions which experience seasonal groundwater fluctuations. The capability of FEM to simulate both stress and deformation makes it well suited for analysing residual soil slopes, which often exhibit progressive failure under saturated conditions.

The pre-failure evaluation of cut slope sites was further simulated using PFEM, with results showing a maximum deposition thickness of 26.1 m at the base of Site-1 and approximately 6.2 m at the lower road section of Site-2. These results are in close agreement with field observations and the damage reports provided by the Department of Roads (DoR), Nepal, thereby validating the model's performance. The consistency between the numerical results and field evidence reinforces the reliability and potential of PFEM for modelling real-world slope failures. Previous researchers have also successfully simulated comparable failure mechanisms in their studies on rapid landslides, debris flows and earth dam failures (Llano-Serna et al., 2016; Zabala & Alonso, 2011).

Validation of model

Validation is essential for establishing the reliability of numerical models in slope stability assessments (e.g., Trucano et al., 2006; Xiong et al., 2009; Fawaz et al., 2014; Kaczmarek & Popielski, 2019). It involves comparing model predictions with field observations or established analytical solutions to ensure the accuracy and reliability of the model outputs (Kaczmarek & Popielski, 2019). This process is crucial for confirming the suitability of models in evaluating slope stability and predicting potential failures. In this study, the validity of the results was enhanced through a comparative analysis of outcomes from LEM, FEM, and PFEM applied to two slides with similar geological settings. The convergence of results among these methods strengthens the overall validity. A similar comparative validation approach was employed by Pradhan & Siddique (2020), using numerical outputs from different methods. The use of slope sections with comparable material properties and boundary conditions across different locations has also been recognised as an effective validation strategy (e.g., Fredlund & Krahn, 1977; Xing, 1988; Griffiths & Marquez, 2007; Mekonnen, 2021). A similar validation approach has been adopted in the present study using a Slide, Phase^2 and PFEM simulations with the same material and boundary conditions.

The safety factors obtained from LEM and FEM for varying groundwater levels at Site-1 and Site-2 were cross-plotted to assess their correlation. The correlation coefficient of the best-fit line quantifies the degree of agreement between the two methods, demonstrating the reliability of the results. A strong correlation reinforces the validity of the derived safety factors (Fig. 19), while discrepancies may indicate methodological limitations or site-specific influences. The findings underscore the importance of implementing complementary analytical approaches in geotechnical solutions.

The computed correlation coefficients of the safety factors derived from the Limit Equilibrium Method (LEM) and the Finite Element Method (FEM) for Site-1 and Site-2 are 0.99 and 0.91, respectively. These values indicate a very strong positive linear relationship between the outputs of the two methodologies. For Site-1, the near-perfect correlation coefficient (R^2=0.99) demonstrates that the safety factors calculated by FEM align closely with those obtained from LEM. This implies that under the given boundary conditions, soil properties, and groundwater regimes, the simplified assumptions in LEM are sufficiently representative of the slope's actual stability conditions captured by FEM, which accounts for more complex stress–strain behaviour and material deformation.

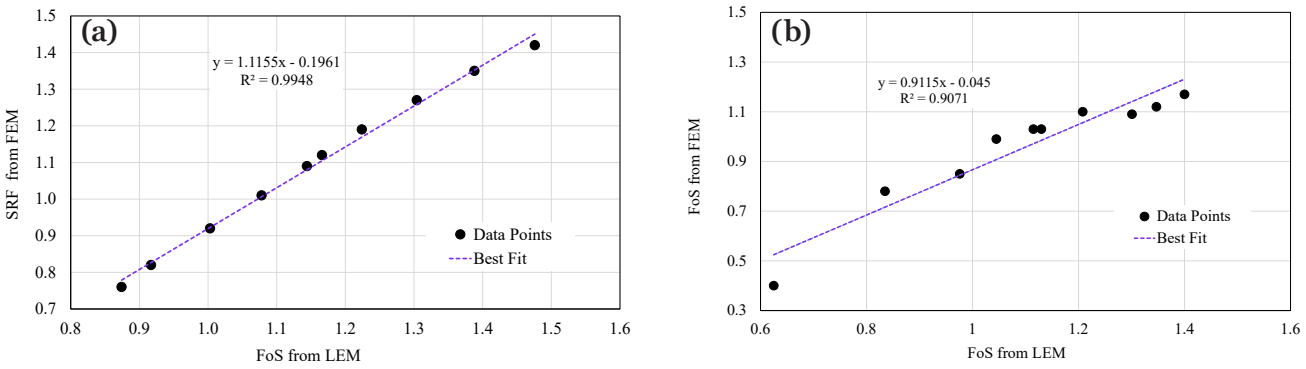

Fig. 19. Correlation between the safety factors derived from the Finite Element Method (FEM; Phase^2) and the Limit Equilibrium Method (LEM; Slide) for (a) Site-1 and (b) Site-2. Linear regression lines and coefficients of determination (R^2) demonstrate the strong consistency between the two modelling approaches.

The correlation coefficient (R^2 = 0.91) at Site-2 is slightly lower than that of Site-1 but still indicates a robust agreement between the two methods. The observed difference could be attributed to site-specific geotechnical complexities such as heterogeneity of material layering, anisotropy, or non-linear deformation behaviour which are better represented in FEM due to its continuum-based formulation. FEM's capability to simulate progressive failure mechanisms, pore pressure redistribution, and localised yielding makes it especially sensitive to such conditions, thereby leading to slight deviations from LEM predictions. Nevertheless, the high correlation coefficients at both sites confirm the mutual consistency and validation of the two modelling approaches in evaluating slope stability. This supports the application of LEM for preliminary assessments or parametric studies while highlighting FEM's strength for more detailed and deformation-based analyses, particularly under complex geological or hydrological conditions.

Conclusions

This study has evaluated the cut slopes in the Lesser Himalaya of Nepal that are often influenced by groundwater saturation together with slope geometry and triggering factors. Pre-failure analyses using the Limit Equilibrium Method (LEM) and Finite Element Method (FEM) revealed that saturation substantially reduces the shear strength of slope material, causing safety factors to attenuate by 40.78–65.81 % when transitioning from dry to saturated conditions. The analysis of the modelling sites showed that slopes remained unstable when groundwater levels were within 1.0 m from the surface, became marginally stable between 2.0 m and 6.0 m, and achieved stable conditions below 7.0 m depths with a factor of safety exceeding 1.3. Closely aligned results from both LEM and FEM results (<10 % variation) and the good agreement between forward and back analyses (<1 % deviation) validate the robustness and reliability of the adopted numerical modelling techniques. The post-failure Particle Finite Element Method (PFEM) simulations quantified the dynamic failure behaviour which computed the debris velocities of 19.6–23 m/s and runout distances of 305–425 m, thereby providing insights into potential impact zones and downstream risks.

An integrated LEM-FEM-PFEM framework has proven to be a suitable approach for analysing slope stability under varying groundwater conditions and identifying critical slope sections. The findings of this research not only decipher failure mechanisms of cut slopes in the Lesser Himalaya but also provide a validated multi-method evaluation in similar geo-environmental settings. The results also deliver valuable scientific and practical insights for designing resilient infrastructure and reducing cut slope failure hazards.

Acknowledgements

We are grateful to the Centre for Numerical Methods in Engineering (CIMNE), Spain for providing an opportunity of a research stay to the first author in acquiring the knowledge of numerical modelling techniques under the Marie Skłodowska-Curie Actions (MSCA) Staff Exchange Project ("LOC3G") funded by the European Commission.

References

Acharya, A. & Dhital, M.R. 2023: Rock mass qualitative stability aspects of cut-slopes in the Lesser Himalaya of central Nepal. Bulletin of Nepal Geological Society, 40: 93–100.

Adhikari, B. R. & Gautam, S. 2022: A review of policies and institutions for landslide risk management in Nepal. Nepal Public Policy Review, 2: 93–112.

Bhattarai, P., Tiwari, B., Marui, H. & Aoyama, K. 2004: Quantitative slope stability mapping with ArcGIS: prioritize highway maintenance. In: Proceedings of ESRI's 24th Annual International User's Conference, San Diego. ESRI.

Bishop, A.W. 1955: The use of the slip circle in the stability analysis of slopes. Géotechnique, 5/1: 7–17. https://doi.org/10.1680/geot.1955.5.1.7

Burman, A., Acharya, S., Sahay, R. & Maity, D. 2015: A comparative study of slope stability analysis using traditional limit equilibrium method and finite element method. Asian Journal of Civil Engineering, 16/4: 467–492.

Cardarelli, E. & Fischanger, F. 2006: 2D data modelling by electrical resistivity tomography for complex subsurface geology. Geophysical Prospecting, 54/2: 121–133.

Cheng, Y.M., Lansivaara, T. & Wei, W.B. 2007: Two-dimensional slope stability analysis by limit equilibrium and strength reduction methods. Computers and geotechnics, 34/3: 137–150.

Chugh, A.K. 2003: On the boundary conditions in slope stability analysis. International journal for numerical and analytical methods in geomechanics, 27/1: 905–926.

Craig, R.F. 2004: Craig's Soil Mechanics (7th ed.). Spon Press, 460 p.

Cremonesi, M., Franci, A. & Perego, U. 2011: A Lagrangian finite element approach for the simulation of the extrusion process in hot metal forming. Computer Methods in Applied Mechanics and Engineering, 200/13-16: 867–882.

Cremonesi, M., Franci, A., Idelsohn, S. & Oñate, E. 2020: A state of the art review of the particle finite element method (PFEM). Archives of Computational Methods in Engineering, 27/5: 1709–1735.

Cruden, D.M. & Varnes, D.J. 1996: Landslide types and processes. In: Turner, A.K. & Schuster, R.L. (eds.): Landslides investigation and mitigation. Transportation research board, US National Research Council. Special Report 247, Washington, DC, Chapter 3: 36–75.

Dahal, R.K. & Hasegawa, S. 2008: Representative rainfall thresholds for landslides in the Nepal Himalaya, Geomorphology, 100/3-4: 429–443. https://doi.org/10.1016/j.geomorph.2008.01.014

Dahal, R.K. 2014: Regional-scale landslide activity and landslide susceptibility zonation in the Nepal Himalaya. Environmental Earth Sciences, 71: 5145–5164. https://doi.org/10.1007/s12665-013-2917-7

Dahal, R.K., Hasegawa, S., Masuda, T. & Yamanaka, M. 2006: Roadside slope failures in Nepal during torrential rainfall and their mitigation. Disaster mitigation of debris flows, slope failures and landslides: 503–514.

Dahal, R.K., Hasegawa, S., Nonomura, A., Yamanaka, M., Dhakal, S. & Paudyal, P. 2008: Predictive modelling of rainfall-induced landslide hazard in the Lesser Himalaya of Nepal based on weights-of-evidence. Geomorphology, 102/3-4: 496–510. https://doi.org/10.1016/j.geomorph.2008.05.041

Dawson, E.M., Roth, W.H. & Drescher, A. 1999: Slope stability analysis by strength reduction. Géotechnique, 49/6: 835–840. https://doi.org/10.1680/geot.1999.49.6.835

Deng, D.P., Li, L. & Zhao, L.H. 2017: Limit equilibrium method (LEM) of slope stability and calculation of comprehensive factor of safety with double strength-reduction technique. Journal of Mountain Science, 14/11: 2311–2324. https://doi.org/10.1007/s11629-017-4537-2

Department of Hydrology & Meteorology (DHM), 2024: Climate Services. Government of Nepal. https://www.dhm.gov.np/climate-services/climate%20reports/monthly-reports

DoR, 2007: Roadside Geotechnical Problems: A Practical Guide to their Solution. Road Maintenance and Development Project, Department of Road (DoR), Government of Nepal: 217 p.

Devkota, K.C., Regmi, A.D., Pourghasemi, H.R., Yoshida, K., Pradhan, B., Ryu, I.C., Dhital, M.R. & Althuwaynee, O.F. 2013: Landslide susceptibility mapping using certainty factor, index of entropy and logistic regression models in GIS and their comparison at Mugling–Narayanghat road section in Nepal Himalaya. Natural hazards, 65: 135–165.

Dhakal, D. & Acharya, I.P. 2019: Slope Stability Analysis of Hill Side Steep Cut Slope and Its Stabilization by the Method Soil Nailing Technique, A Case Study of Narayanghat-Mugling Road Section. In: Proceedings of Institute of Engineering (IOE) Graduate Conference, Nepal.

Dhital, M.R. 2015: Geology of the Nepal Himalaya: regional perspective of the classic collided orogen. Springer: 498 p.

Dikshit, A., Sarkar, R., Pradhan, B., Segoni, S. & Alamri, A.M. 2020: Rainfall induced landslide studies in Indian Himalayan region: a critical review. Applied Sciences, 10/7: 2466. https://doi.org/10.3390/app10072466

Duncan, J.M. & Wright, S.G. 2005: Soil Strength and Slope Stability. John Wiley & Sons Inc., 309 p.

Fan, Q., Lin, J., Sun, W., Lu, J. & Chen, P. 2021: Analysis of Landslide Stability Based on the Morgenstern-Price Method. In E3S Web of Conferences, 299: 02019.

Fawaz, A., Farah, E. & Hagechehade, F. 2014: Slope stability analysis using numerical modelling, American Journal of Civil Engineering, 2/3: 60–67. https://doi.org/10.11648/j.ajce.20140203.11

Fellenius, W. 1936: Calculation of the stability of earth dams. In: Proceedings, 2nd Congress, International Society of Soil Mechanics and Foundation Engineering: 445–462.

Franci, A., Cremonesi, M., Perego, U. & Oñate, E. 2020: A Lagrangian nodal integration method for free-surface fluid flows. Computer Methods in Applied Mechanics and Engineering, 361: 112816.

Fredlund, D.G. & Krahn, J. 1977: Comparison of slope stability methods of analysis. Canadian Geotechnical Journal, 14/3: 429–439. https://doi.org/10.1139/t77-045

Fredlund, D.G., Rahardjo, H. & Fredlund, M.D. 2012: Unsaturated Soil Mechanics in Engineering Practice. John Wiley & Sons: 926 p.

Gansser, A. 1974: Himalaya. Geological Society, London, Special Publications, 4/1: 267–278.

Gerrard, J. 1994: The landslide hazard in the Himalayas: geological control and human action. Geomorphology and Natural Hazards, 10: 221–230. https://doi.org/10.1016/B978-0-444-82012-9.50019-0

Griffiths, D. V. & Marquez, R. 2007: Three-dimensional slope stability analysis by elasto-plastic finite elements. Geotechnique, 57/6: 537–546.

Griffiths, D.V. & Lane, P.A. 1999: Slope stability analysis by finite elements. Géotechnique, 49/3: 387–403. https://doi.org/10.1680/geot.1999.49.3.387

Groppo, C., Rolfo, F., Tamang, S. & Mosca, P. 2023: Lithostratigraphy, Petrography Lesser and Metamorphism Himalayan Sequence. Himalaya, Dynamics of a Giant 2: Tectonic Units and Structure of the Himalaya: 157–188.

Haigh, M. & Rawat, J.S. 2011: Landslide causes: Human impacts on a Himalayan landslide swarm. Belgeo, Revue belge de géographie, 3–4: 201–220.

Hasegawa, S., Dahal, R.K., Yamanaka, M., Bhandary, N.P., Yatabe, R. & Inagaki, H. 2009: Causes of large-scale landslides in the Lesser Himalaya of central Nepal. Environmental Geology, 57: 1423–1434. https://doi.org/10.1007/s00254-008-1420-z

Hearn, G.J. 2011: Slope engineering for mountain roads. Geological Society of London: 223 https://doi.org/10.1144/EGSP24

Hearn, G.J. & Shakya, N.M. 2017: Engineering challenges for sustainable road access in the Himalayas. Quarterly Journal of Engineering Geology and Hydrogeology, 50/1: 69–80.

Hungr, O., Leroueil, S. & Picarelli, L. 2014: The Varnes Classification of Landslide Types, an Update. Landslides, 11: 167–194. https://doi.org/10.1007/s10346-013-0436-y

Idelsohn, S.R., Marti, J., Limache, A. & Oñate, E. 2008: Unified Lagrangian formulation for elastic solids and incompressible fluids: application to fluid–structure interaction problems via the PFEM. Computer Methods in Applied Mechanics and Engineering, 197/19–20: 1762–1776.

Idelsohn, S.R. & Onate, E. 2010: The challenge of mass conservation in the solution of free-surface flows with the fractional-step method: Problems and solutions. International Journal for Numerical Methods in Biomedical Engineering, 26/10: 1313–1330.

Janbu, N. 1954: Application of composite slip surfaces for stability analysis. European Conference on Stability of Earth Slopes, 3: 43–49.

Kaczmarek, L.D. & Popielski, P. 2019: Selected components of geological structures and numerical modelling of slope stability. Open Geosciences, 11/1: 208–218.

Kharel, G. & Acharya, I.P. 2017: Stability Analysis of Cut-slope: A case study of Kathmandu-Nijgadh Fast track. In: Proceedings of Institute of Engineering (IOE) Graduate Conference, 5: 171–174.

Khatri, S. & Acharya, I. P. 2019: Stability Analysis of Road-Cut slope: A Case Study of Kanti Lokpath. In: KEC Conference: 205–208.

Komadja, G.C., Pradhan, S.P., Roul, A.R., Adebayo, B., Habinshuti, J.B., Glodji, L.A. & Onwualu, A.P. 2020: Assessment of stability of a Himalayan road cut slope with varying degrees of weathering: A finite-element-model-based approach. Heliyon, 6/11. https://doi.org/10.1016/j.heliyon.2020.e05297

Llano-Serna, M.A., Oñate, E. & Idelsohn, S. 2016: Particle finite element method for the simulation of large deformation landslides. Computers and Geotechnics, 74: 118–126.

Loke, M.H. 2004: Tutorial: 2-D and 3-D electrical imaging surveys. Geotomo Software, Res2dinv 3.5 Software. 136 p.

Loke, M.H., Chambers, J.E., Rucker, D.F., Kuras, O. & Wilkinson, P.B. 2013: Recent developments in the direct-current geoelectrical imaging method. Journal of Applied Geophysics, 95: 135–156.

Lowe, J. & Karafiath, L. 1965: Slope stability analysis by the moment method. Proceedings of the American Society of Civil Engineers, 91: 1–27.

Lu, N. & Godt, J.W. 2013: Hillslope hydrology and stability. Cambridge University Press: 458 p.

Marc, O., Behling, R., Andermann, C., Turowski, J.M., Illien, L., Roessner, S. & Hovius, N. 2019: Long-term erosion of the Nepal Himalayas by bedrock landsliding: The role of monsoons, earthquakes and giant landslides. Earth Surface Dynamics, 7/1: 107–128. https://doi.org/10.5194/esurf-7-107-2019

Martin, R.P. 2001: The design of remedial works to the Dharan–Dhankuta road, East Nepal. Geological Society, London, Engineering Geology Special Publications, 18/1: 197–204 https://doi.org/10.1144/GSL.ENG.2001.018.01.28

Maskey, S. 2016: A Case Study of the Krishna Bhir slope failure disaster: past and present scenario at a glance. International journal of Rock engineering and Mechanics, 2: 1–11.

Matthews, C., Farook, Z. & Helm, P. 2014: Slope stability analysis–limit equilibrium or the finite element method. Ground Engineering, 48/5: 22–28.

Mekonnen, F.A. 2021: Performance evaluation of geometric modification on the stability of road cut slope using FE Based plaxis software. In Landslides. IntechOpen. https://doi.org/10.5772/intechopen.99633

Morgenstern, N.R. & Price, V.E. 1965: The analysis of the stability of general slip surfaces. Geotechnique, 15/1: 79–93.

Morgenstern, N.R. & Sangrey, D.A. 1978: Methods of stability analysis. Landslides: analysis and control, Transportation Research Board Special Report, 176, Washington, D.C.: 155–171.

Nian, T.K., Huang R.Q., Wan, S.S. & Chen, G.Q. 2012: Three-dimensional strength-reduction finite element analysis of slopes: geometric effects. Canadian Geotechnical Journal, 49/5: 574–588. https://doi.org/10.1139/t2012-014

Oñate, E., Celigueta, M.A., Idelsohn, S.R., Rossi, R. & Suárez, B. 2011: Advances in the particle finite element ethod (PFEM) for solving fluid–soil–structure interaction problems in engineering. Advances in Computational Mechanics: 1–30.

Oñate, E., Franci, A. & Carbonell, J.M. 2014: A particle finite element method (PFEM) for coupled thermal analysis of quasi and fully incompressible flows and fluid-structure interaction problems. In Numerical Simulations of Coupled Problems in Engineering, Springer International Publishing: 129–156.

Oñate, E., Idelsohn, S.R., Del Pin, F. & Aubry, R. 2004: The particle finite element method–an overview. International Journal of Computational Methods, 1/2: 267–307.

Panda, S.D., Kumar, S., Pradhan, S.P., Singh, J., Kralia, A. & Thakur, M. 2023: Effect of groundwater table fluctuation on slope instability: a comprehensive 3D simulation approach for Kotropi landslide, India. Landslides, 20/3: 663–682.

Pant, J.R. & Acharya, I.P. 2021: Stability Analysis of Road-cut Slope: A Case Study of Jiling Landslide along the Galchi-Trishuli-Mailung-Syaprubeshi Rasuwagadi Road. In: Proceedings of 9th Institute of Engineering (IOE) Graduate Conference, Institute of Engineering, Tribhuvan University, Nepal, 9: 9–15.

Panthi, K.K. 2006: Analysis of engineering geological uncertainties related to tunnelling in Himalayan rock mass conditions (PhD dissertation), Trondheim, Norway: Department of Geology and Mineral Resources Engineering, Norwegian University of Science and Technology.

Panthi, K.K. 2021: Assessment on the 2014 Jure Landslide in Nepal – a disaster of extreme tragedy. IOP Conference Series: Earth and Environmental Science. 833. 012179. https://doi.org/10.1088/1755-1315/833/1/012179

Pathak, D. 2014: Geohazard assessment along the road alignment using remote sensing and GIS: Case study of Taplejung-Olangchunggola-Nangma road section, Taplejung district, east Nepal. Journal of Nepal Geological Society, 47/1: 47–56.

Pathak, D. 2016: Knowledge based landslide susceptibility mapping in the Himalayas. Geoenvironmental Disasters, 3: 1–11. https://doi.org/10.1186/s40677-016-0042-0

Phuyal, B. & Thapa, P.B. 2023: Failure mechanism of large-scale landslide in the central Nepal Himalaya. Journal of Nepal Geological Society,

66: 37–52. https://doi.org/10.3126/jngs.v66i01.57921

Phuyal, B., Acharya, M.S. & Thapa, P.B. 2025; Landslide Size-Frequency Distribution and Factor Effects on Susceptibility Modelling in the Himalayan Region, Central Nepal. Geotechnical and Geological Engineering, 43/1: 55. https://doi.org/10.1007/s10706-024-03014-w

Phuyal, B., Thapa, P.B. & Devkota, K.C. 2022: Characterization of large-scale landslides and their susceptibility evaluation in central Nepal Himalaya. Journal of Nepal Geological Society, 63/01: 109–122. https://doi.org/10.3126/jngs.v63i01.50846

Pokharel, R.P., Khanal, N.R. & Paudel, B. 2024: Landslide Susceptibility Analysis in Kaski District, Nepal: Using Remote Sensing Technique with Intensive Field Verification. https://doi.org/10.21203/rs.3.rs-4687294/v1

Poudyal, A., Dahal, A., Shrestha, J. & Timilsina, M. 2024: Cut Slope Stability Analysis on Terrain with Slope at Besishahar, Lamjung. International Journal on Engineering Technology, 1/2: 230–249.

Pradhan, S., Toll, D.G., Rosser, N.J. & Brain, M.J. 2022: An investigation of the combined effect of rainfall and road cut on landsliding. Engineering Geology, 307, 106787. https://doi.org/10.1016/j.enggeo.2022.106787

Pradhan, S.P. & Siddique, T. 2020: Stability assessment of landslide-prone road cut rock slopes in Himalayan terrain: a finite element method based approach. Journal of Rock Mechanics and Geotechnical Engineering, 12/1: 59–73.

Pudasaini, S.P., Mergili, M., Lin, Q. & Wang, Y. 2024: Dynamic simulation of rock-avalanche fragmentation. Journal of Geophysical Research: Earth Surface, 129(9), e2024JF007689.

Rahman, A.U., Khan, A.N. & Collins, A.E. 2014: Analysis of landslide causes and associated damages in the Kashmir Himalayas of Pakistan. Natural Hazards, 71: 803–821. https://doi.org/10.1007/s11069-013-0918-1

Rawat, D.S. & Sharma, S. 1997: The development of a road network and its impact on the growth of infrastructure: a study of Almora District in the Central Himalaya. Mountain Research and Development: 117–126.

Ray, R.L. & De Smedt, F. 2009: Slope stability analysis on a regional scale using GIS: a case study from Dhading, Nepal. Environmental Geology, 57, 1603–1611.

Regmi, A.D., Dhital, M.R., Zhang, J.Q., Su, L.J. & Chen, X.Q. 2016: Landslide susceptibility assessment of the region affected by the 25 April 2015 Gorkha earthquake of Nepal. Journal of Mountain Science, 13: 1941–1957.

Regmi, A.D., Yoshida, K., Dhital, M.R. & Devkota, K. 2013: Effect of rock weathering, clay mineralogy, and geological structures in the formation of large landslide, a case study from Dumre Besei landslide, Lesser Himalaya Nepal. Landslides, 10: 1–13. https://doi.org/10.1007/s10346-011-0311-7

Robson, E., Agosti, A., Utili, S. & Milledge, D. 2022: A methodology for road cutting design guidelines based on field observations. Engineering Geology, 307, 106771. https://doi.org/10.1016/j.enggeo.2022.106771

Robson, E., Pradhan, S. & Toll, D. 2024: A field study on the stability of road cut slopes in Nepal. In: Geo-Resilience 2023 Conference, Cardiff, Wales, ISSMGE Online Library. https://doi.org/10.53243/Geo-Resilience-2023-1-8

Sapkota, B. & Timilsina, M. 2024: Road Side Slope Stabilization Using Ground Water Management at Far-Western Nepal. Asian Journal of Engineering Geology, 1 (Special Issue):17–18.

Sarma, S.K. 1973: Stability analysis of embankments and slopes. Geotechnique, 23/3: 423–433.

Schuster, M. & Hübl, J. 1995: Impact of road construction on the Pokhara-Baglung highway, Kaski district, Nepal. Sustainable reconstruction of highland and headwater regions: 175–182.

Sharma, L.K., Umrao, R.K., Singh, R., Ahmad, M. & Singh, T.N. 2017: Geotechnical characterization of road cut hill slope forming unconsolidated geo-materials: a case study. Geotechnical and Geological Engineering, 35: 503–515.

Sheng, D., Smith, D.W., W. Sloan, S. & Gens, A. 2003: Finite element formulation and algorithms for unsaturated soils. Part II: Verification and application. International Journal for Numerical and Analytical Methods in Geomechanics, 27/9: 767–790.

Shrestha, D.P., Zinck J.A. & Van, R.E. 2004: Modelling land degradation in the Nepalese Himalaya. Catena, 57/2: 135–156. https://doi.org/10.1016/j.catena.2003.11.003

Shrestha, K.K., Paudyal, K.R. & Thapa, P.B. 2023: Numerical modelling of cut-slope stability in the Lesser Himalayan terrain of west-central Nepal. Journal of Nepal Geological Society, 66: 75–90. https://doi.org/10.3126/jngs.v66i01.57933

Silwal, B.R., Gyawali, B.R. & Yoshida, K. 2024: Geochemical and mineralogical analysis of low-

grade metamorphic rocks and their response to shallow landslide occurrence in Central Nepal. Geoenvironmental Disasters, 11/1: 37.

Singh, A.K. 2009: Causes of slope instability in the Himalayas. Disaster Prevention and Management: An International Journal, 18/3: 283–298. https://doi.org/10.1108/09653560910965646

Singh, H.O., Ansari, T.A., Singh, T.N. & Singh, K.H. 2020: Analytical and numerical stability analysis of road cut slopes in Garhwal Himalaya, India. Geotechnical and Geological Engineering, 38: 4811–4829. https://doi.org/10.1007/s10706-020-01329-y

Singh, R., Umrao, R.K. & Singh, T.N. 2014: Stability evaluation of road-cut slopes in the Lesser Himalaya of Uttarakhand, India: conventional and numerical approaches. Bulletin of Engineering Geology and the Environment, 73: 845–857.

Singh, T.N., Gulati, A., Dontha, L. & Bhardwaj, V. 2008: Evaluating cut slope failure by numerical analysis–a case study. Natural Hazards, 47: 263–279. https://doi.org/10.1007/s11069-008-9219-5

Spencer, E. 1967: A method of analysis of the stability of embankments assuming parallel interslice forces. Géotechnique, 17: 11–26. https://doi.org/10.1680/geot.1967.17.1.11

Sutejo, Y. & Gofar, N. 2015: Effect of area development on the stability of cut slopes. Procedia Engineering, 125: 331–337.

Terzaghi, K. 1943: Theoretical Soil Mechanics. John Wiley & Sons: 526 p.

Thapa, P.B. 2015: Occurrence of landslides in Nepal and their mitigation options. Journal of Nepal Geological Society, 49: 17–28. https://doi.org/10.3126/jngs.v49i1.23138

Thapa, P.B., Phuyal, B. & Shrestha, K.K. 2023: Spatial variability of slope movements in central and western Nepal Himalaya: Evaluating large-scale landslides to cut-slopes. Journal of Nepal Geological Society, 65: 183–194. https://doi.org/10.3126/jngs.v65i01.57777

Trucano, T.G., Swiler, L.P., Igusa, T., Oberkampf, W.L. & Pilch, M. 2006: Calibration, validation, and sensitivity analysis: What's what. Reliability Engineering & System Safety., 91/10-11: 1331–1357. https://doi.org/10.1016/j.ress.2005.11.031

Upreti, B.N. & Dhital, M. 1996: Landslide studies and management in Nepal. ICIMOD, Nepal: 87 p.

Upreti, B.N. 1999: An overview of the stratigraphy and tectonics of the Nepal Himalaya. Journal of Asian Earth Sciences, 17/5–6: 577–606. https://doi.org/10.1016/S1367-9120(99)00047-4

USACE, 2003: Engineering and Design: Slope stability, Engineer Manual 11102-2-1902.

Varnes, D.J. 1958: Landslide types and processes. Landslides and engineering practice, 24: 20–47.

Varnes, D.J. 1978: Slope movement types and processes. Special report, 176: 11–33.

Vuillez, C., Tonini, M., Sudmeier-Rieux, K., Devkota, S., Derron, M.H. & Jaboyedoff, M. 2018: Land use changes, landslides and roads in the Phewa Watershed, Western Nepal from 1979 to 2016. Applied Geography, 94: 30–40.

Wyllie, D.C. & Mah, C. 2004: Rock Slope Engineering. 4th Ed. The Institution of Mining and Metallurgi London, 456 p.

Xing, Z. 1988: Three dimensional stability analysis of concave slopes in plan view. Journal of Geotechnical Engineering, 114/6: 658–671.

Xiong, Y., Chen, W., Tsui, K-L. & Apley, D.W. 2009: A better understanding of model updating strategies in validating engineering models. Computer methods in applied mechanics and engineering, 198/15–16: 1327–1337. https://doi.org/10.1016/j.cma.2008.11.023

Zabala, F. & Alonso, E.E. 2011: Progressive failure of Aznalcóllar dam using the finite element method. Géotechnique, 61/9: 795–808.

Zheng, H. 2012: A three-dimensional rigorous method for stability analysis of landslides. Engineering Geology, 145: 30–40.

Zheng, W., Zhuang, X., Tannant, D.D., Cai, Y. & Nunoo, S. 2014: Unified continuum/discontinuum modeling framework for slope stability assessment. Engineering Geology, 179: 90–101.

GEOLOGIJA 68/2, 147-200, Ljubljana 2025

https://doi.org/10.5474/geologija.2025.007

Article

Mesozoic stratigraphy of Dinaric successions at the Dinarides – Southern Alps boundary, Sava Folds region, Slovenia

Stratigrafija dinarskih mezozojskih zaporedij na meji med Dinaridi in Južnimi Alpami, območje Posavskih gub, Slovenija

Benjamin SCHERMAN[1]*, Ágnes GÖRÖG[2], Boštjan ROŽIČ[3], Szilvia KÖVÉR[4,1] & László FODOR[4,1]

[1]ELTE Eötvös Loránd University, Institute of Geography and Earth Sciences, Department of Geology, Pázmány Péter sétány 1C, 1117 Budapest, Hungary; *corresponding author: benjaminscherman@gmail.com
[2]Hantken Miksa Foundation, H–1022 Budapest, Detrekő utca 1/b, Hungary
[3]University of Ljubljana, Faculty of Natural Sciences and Engineering, Department of Geology, Aškerčeva 12, SI–1000 Ljubljana, Slovenia
[4]HUN–REN Institute of Earth Physics and Space Science, Csatkai E. u. 6–8, 9400 Sopron, Hungary

Prejeto / Received 27. 4. 2025; Sprejeto / Accepted 8. 8. 2025; Objavljeno na spletu / Published online 29. 8. 2025

Key words: Triassic, Jurassic, Cretaceous, Aptian–Albian calpionellids, Dinarides, Southern Alps, Sava Folds
Ključne besede: trias, jura, kreda, aptijsko-albijske kalpionelide, Dinaridi, Južne Alpe, Posavske gube

Abstract

In central Slovenia, on the border between Southern Alpine derived units and Dinaric units in the northern part of the Sava Folds, detailed field observations and reambulation-type mapping were conducted. The research aimed to clarify the distribution of Mesozoic formations and the palaeogeographical and tectonic position of the studied area.

Based on field observations, lithofacies, microfacies, and biostratigraphic studies (including benthos and planktonic foraminifers, dinocysts, acritarchs, chitinoidellids, calpionellids, green algae, microproblematica, calcareous nannofossils and ascidians), the following successions characterize the northern limb of the Trojane Anticline and the Tuhinj–Motnik Syncline: upper Anisian to lowermost Ladinian platform carbonates (Mendole Formation) are overlain by Ladinian siliciclastic successions including volcanoclastic resediments (Pseudozilian Formation). These either interfinger or are overlain by the Ladinian to lower Carnian platform limestone (Schlern Formation); in the upper part of this formation, the deep–marine siliciclastics and/or carbonates are locally intercalated. Following a significant stratigraphic gap, the lower Tithonian to lower Valanginian pelagic limestone and carbonate resediments (Biancone Formation s.l.) were deposited. The Biancone limestone is covered by upper Aptian–upper Albian (Cenomanian?) marlstone with occasional calcarenite (calciturbidite) interlayers (Lower Flyschoid/Gora Formation). The succession ends with Upper Cretaceous pelagic and resedimented limestones (Volče/Krško Formation).

The age and spatial distribution of these successions often differ from that depicted on the existing geological maps. This succession resembles the Transition Zone between the External and Internal Dinarides. Our study indicates the presence of similar transitional Mesozoic Dinaric successions north of the previously proposed Southern Alpine thrust front.

Izvleček

V severnem delu Posavskih gub osrednje Slovenije, na meji med južnoalpskimi in dinarskimi enotami, je bila izdelana stratigrafska reambulacija z namenom dopolnitve razumevanja paleogeografskega in tektonskega razvoja raziskanega območja.

Na podlagi natančnih in dobro dokumentiranih terenskih opazovanj, litofaciesov, mikrofaciesov in biostratigrafije (vključno z bentoškimi in planktonskimi foraminiferami, dinocistami, akritarhi, hitinolidelidi, kalpionelami, zelenimi algami, različno mikroproblematiko in kalcitnim nanoplanktonom) je bil proučen naslednji razvoj Trojanske antiklinale in Tuhinjsko–Motniške sinklinale: zgornjeanizijski do spodnjeladinijski platformni apnenci (Mendolska formacija), katere prekriva ladinijsko siliciklastično zaporedje s presedimentiranimi vulkaniti (Psevdoziljska formacija), še višje pa ladinijski do spodnjekarnijski platformni apnenci in dolomiti (Schlernska formacija), ki se lahko v zgornjem delu formacije prepletajo z globljemorskimi siliciklastičnimi in/ali apnenčastimi vključki. Po dolgi stratigrafski vrzeli sledijo spodnjetithonijski do spodnjevalanginijski pelagični apnenci z redkejšimi plastmi presedimentiranih apnencev (Biancone formacija s.l.). Biancone apnenec prekriva zaporedje laporovcev in kalkarenitov (kalciturbiditov) zgornjeaptijske do zgornjealbijske (?cenomanijske) starosti (Spodnja flišoidna/Gora formacija). Zaporedje se konča z zgornjekrednimi pelagičnimi in presedimentiranimi apnenci (Volčanski apnenec/Krška formacija). Starosti in prostorsko razširjanje navedenih formacij se pogosto razlikujeta od tistih, prikazanih na obstoječih geoloških kartah.

Ta zaporedja so primerljiva zaporedjem Prehodne cone med Notranjimi in Zunanjimi Dinaridi. V tem prispevku so prvič objavljeni dokazi za obstoj dinarskih razvojev severno od predhodno predlagane Južnoalpske narivne meje. Tovrstne odnose med mezozojskimi paleogeografskimi in recentnimi geotektonskimi enotami je možno razložiti s kompleksnim terciarnim tektonskih razvojem širšega ozemlja.

Introduction

The Southern Alpine Thrust Front (SATF) constitutes the tectonic boundary between the Dinarides and the Southern Alps, and has been studied in western Slovenia, where it is defined by the base of the Tolmin Thrust Sheet in the foothills of the Julian Alps (e.g., Placer, 1998b, 2008; Schmid, 2008, 2020). The Slovenian Basin's (SB) deep-marine Middle Triassic to Cretaceous sedimentary succession, encompassed by this thrust sheet, has been the subject of investigation since the 1970s. The paleogeographic location, while presumed narrow and relatively deep, remains a point of contention amongst scholars (Cousin, 1970, 1973; Caron & Cousin, 1972; Haas, 1995; Buser, 1989, 1996; Rožič, 2005, 2006, 2009, 2016, Rožič et al., 2013, 2014, 2017, 2022, 2024). Its southern and southwestern borders, however, were defined by the Dinaric (Adriatic, Friuli) Carbonate Platform (DCP), situated in what is now the External Dinarides. East of the Quaternary Ljubljana Basin, the exact position of the SATF is still debated (e.g., Placer, 1998b, 2008; Schmid et al., 2020). Prior research indicates that the SATF traverses the central Slovenian Sava Folds region east of Ljubljana. The ambiguity primarily stems from the less-defined stratigraphic subdivision of deeper marine (SB) and shallow marine (DCP) successions within the Sava Folds, which serve as indicators of structural subdivision. The southward migration of deeper marine successions of the SB resulted from Mesozoic paleogeographic and sedimentary conditions on the slopes of the adjacent carbonate platform. This is evident in the Upper Jurassic and Cretaceous deeper marine successions, comparable to those of the SB, deposited over the Triassic and/or Lower Jurassic carbonate platform successions (Aničič et al., 2002; Rižnar, 2006; Poljak, 2017; Reháková & Rožič, 2019; Gerčar et al., 2023). The transition area between the External and Internal Dinarides is defined by this succession (Placer, 1998b, 2008). For brevity, we will refer to this paleogeographic zone as the Dinaric Transition Zone (DTZ). Notably, the Sava Folds contain continuous Ladinian to Late Cretaceous deep-marine sequences within the Sloveni-

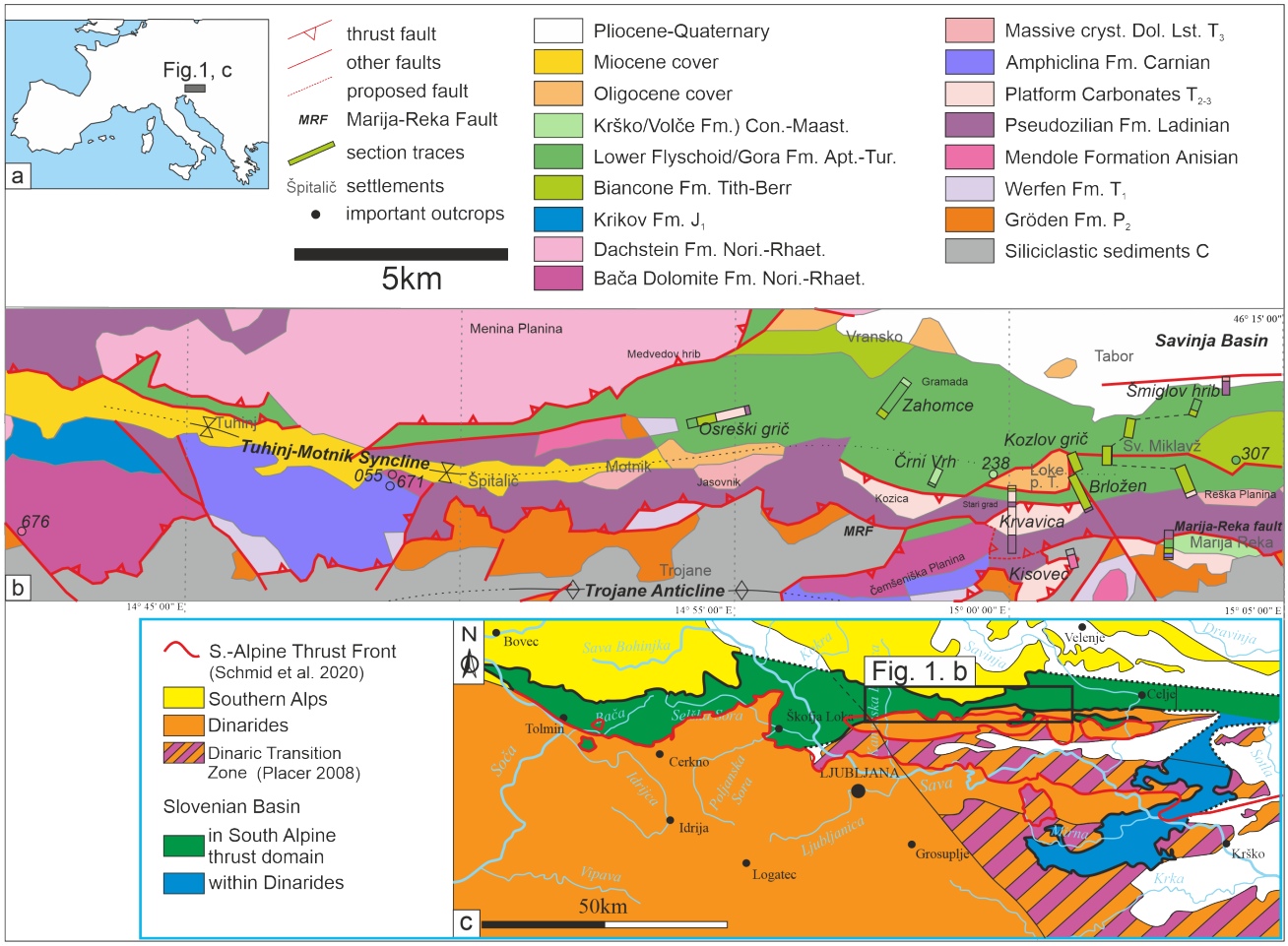

Fig. 1. a) Geographical position of the research area, b) the Trojane Anticline and the Tuhinj-Motnik Syncline of the Sava Folds. Locality of the sections and observation points on the geological map (after Buser, 2010). Modified MRF see dashed line. c) Research area located between the Dinarides and the Southern Alps (map modified after Rožič et al., 2019), the Dinaric Transition Zone marked according to Placer (2008) and the South Alpine Thrust-front according to Schmid et al. (2020).

an Basin, presumably as erosional remnants of a significant thrust-sheet (Buser, 1989, 1996, 2010; Rožič, 2016). Studies from the Mirna River Valley revealed that this succession is characteristic of the southernmost SB (originally nearest to DCP) which comprises coarse Middle Jurassic carbonate breccia megabeds (Ogorelec & Dozet, 1997; Rožič et al., 2019, 2022).

The existence of correlative Jurassic deeper-marine successions in the northern Sava folds has been confirmed recently; this is more precisely on the northern limb of the Trojane Anticline near Celje (Scherman et al., 2023). Alternatively, geological fieldwork conducted in this region indicates the presence of a DTZ succession, structurally consistent with the underlying thrust unit. Consequently, our research plans included expanding our study of Mesozoic successions along the northern branch of the Trojane Anticline and the Tuhinj–Motnik Syncline. The substantial stratigraphic heterogeneity evident in geological maps produced over the last 120 years additionally influenced our area of study (Teller, 1907; Winkler, 1923; Grad, 1969; Lapanje & Šribar, 1973; Buser, 1977, 2010; Premru, 1983a; Placer, 1998b, 2008). This discrepancy can also be attributed to the lack of detailed sedimentological and biostratigraphical research in the area, as only two such studies have been conducted to date. Grad (1969) performed a microfacies analysis of the formations he classified as the Triassic Pseudozilian Formation, finding no fossils other than indeterminate radiolarians. The Upper Cretaceous age of resedimented limestone layers in the study area was determined by Lapanje & Šribar (1973) through foraminiferal analysis of formations near Marija Reka. Their subsequent work in Sveti Miklavž revealed *Clypeina jurassica*, consistent with an Upper Jurassic to Lower Cretaceous age. The accompanying explanatory texts to the geological maps of Buser (1979) and Premru (1983b) only allude to inconsistencies and inaccuracies within these publications without offering a viable resolution. These booklets contain only taxon lists of conodonts, molluscs, benthic and planktonic foraminifers, and nannofossils found in the different formations. This data refers to specific localities or smaller areas, but the exact stratigraphic position is not revealed. We correlated sections of observation points based on sedimentological, biostratigraphical, and palaeoenvironmental data gathered from detailed field observations. We describe nine sections, six of which underwent detailed study, and three more which are included because this data helps to map the sedimentary evolution of the region through the Mesozoic Era. The combination of this study results with previously presented SB succession (Scherman et al., 2023) will serve the basis for ongoing structural geological studies of the region, thereby advancing comprehension of the Dinarides–Southern Alps Border Zone in eastern Slovenia.

Geological setting

The research area is located in Central Slovenia, between Kamnik to the west and Celje to the east, north of the Sava River. It comprises the southern border of the Menina Plateau, the southern end of the Savinja Basin, and the northern Posave Hills (Fig. 1).

According to the tectonic subdivision of Placer (2008), the research area is situated in the northern part of the Sava Folds, namely its northernmost members, the Trojane Anticline and the Tuhinj–Motnik Syncline. It lies on the boundary between the Southern Alps and the Dinarides. Mesozoic successions are partially covered by the sediments of the Pannonian Basin. Important tectonic features in the area are the Sava Fault Zone, Marija Reka Fault, and the Southern Alpine Thrust Front. These faults run west to east across the northern part of the studied area and intersect with each other. The axes of the Sava Folds are also east–west trending. Placer (1998, 2008) distinguished three tectono–stratigraphic units: the Palaeozoic successions named "Palaeozoic Soft Beds", the Dinaric Transition Zone, and the Slovenian Basin.

The main formations of both the northern Dinarides and the Southern Alpine units are briefly described below. In both tectonic units, the successions start with Carboniferous to Permian siliciclastic sediments. This sequence has been divided into three members, Ca, Cb, and Cc, by Mlakar (1985, 2003). The lowest Ca member is grey to black shale, siltstone, and fine sandstone. Its estimated thickness is 300 m. The Cb member is an upward–coarsening quartz sandstone and an overlying quartz conglomerate with an estimated thickness of 1,100 m. The Cc member is composed of fine–grained shale, with occasional interbeds of sandstone or conglomerate, estimated to be approximately 250 m thick (Novak & Skaberne, 2009). It is followed by the Middle Permian Gröden Formation, a terrigenous fluvial deposit. It is composed of red quartz sandstones and sometimes quartz conglomerates with a thickness of 400 to 900 m (Buser, 1979). The youngest Palaeozoic formation is the bedded dolomite of the Upper Permian "Karavanke Formation". These few-meter-thick dolomite beds resulted from the marine transgression (Buser, 1989).

In the Trojane Anticline, the Upper Permian carbonates transition to the Lower Triassic Werfen Formation, which consists of limestones and/or dolomites intercalated by clay, siltstone, marl and marly or oolitic limestone. Its relatively rich fossil content suggests that it was deposited in a shallow subtidal – supratidal marine environment (Ramovš et al., 2001). This succession gradually transitions into carbonates, known as the Anisian Platform Carbonates in Slovenian literature, equivalent to the Serla and/or Contrin Formation of the Central Southern Alps (e.g., Gianolla et al., 1998; Celarc et al., 2013). In the southern part of the Sava folds a term Mendole Formation is used for these beds (Poljak, 2017) and we accept it in this paper. It is composed of bedded or massive grey dolomites and limestones, with an approximate thickness of 800 m in the Sava Folds region (Premru, 1983; Aničić, 1991; Dozet & Buser, 2009).

The formations of the Dinaric Transition Zone (DTZ) show transition from a platform to a deeper water basin environment. This area has suffered subsidence during the Middle Triassic, resulting in the intercalation of basinal sediments and the carbonate platform (Rožič et al., 2024). Typically, the Ladinian strata begin with the siliciclastics of the Pseudozilian Formation. It consists of shales, greywackes, sandstones, and resedimented volcanoclastics, sometimes with dark limestone layers. It was first described by Teller (1898) in central Slovenia. In the Southern Alps, it is known as the Wengen Formation (e.g., Gianolla et al., 1998; Skaberne et al., 2024). According to Dozet & Buser (2009), this formation marks the opening of the Slovenian Basin during the Ladinian, but it is also present in DTZ successions (Placer, 2008).

Pseudozilian Formation is overlain by the Ladinian to lower Carnian platform carbonates. A stratigraphic inconsistency marks this formation, as it was previously described as Cordevolian (abandoned early Carnian substage) beds (Buser, 1977, Dozet & Buser, 2009) but was later proven to be largely Ladinian in age (for discussion see Celarc, 2004, 2008). From the eastern Southern Alps corresponding beds are known as the Schlern Formation (Celarc et al., 2013). This name was also conditionally used in Dinarides (Čar, 2010). In Dinarides this formation is known also as Diplopora limestone and/or Saharoid dolomite (due to whitish coarse crystalline texture) (Celarc, 2008). Because Diplopora algae were not found during our research, we decided to use the term Schlern Formation. We note that the topmost part of this formation could also be early Carnian in age in our research area (see below) and would therefore correspond partially to the Cassian Dolomite Formation of the Southern Alps. In this paper, we use the term Schlern Formation in the broad sense for the entire, monotonous upper Ladinian to lower Carnian carbonates lying generally above the Pseudozilian Formation. The characteristic of the Ladinian strata is the gradual progradation of the carbonate platform over the basinal deposits (e.g., Fois, 1983). It was described, for example, from the Julian and Kamnik Alps in Slovenia, although late Anisian–early Ladinian (Celarc et al., 2013) as well as in the Dinarides (Šmuc & Čar 2002; Čar, 2010).

In the southern part of the Sava Folds, these deposits are followed by thick succession of the Upper Triassic and Jurassic shallow-marine carbonates (Poljak, 2017). In the northern Sava folds, including our investigated sections, these carbonates are missing, and the Schlern Formation is covered discordantly by the Upper Jurassic–Lower Cretaceous Biancone Limestone (Aničić et al., 2004; Buser, 2010; Reháková & Rožič, 2019). It is followed by deep marine formations equivalent to the Cretaceous Lower Flyschoid (Gora), Volče Limestone (Krško), and Upper Flyschoid (Veliki trn) formations of the Slovenian Basin (Poljak, 2017; Gerčar et al., 2022).

During the Middle Triassic to Maastrichtian, the Slovenian Basin was an inter–platform basin between the Dinaric (Adriatic) Carbonate Platform to the south and Julian Carbonate Platform (later submarine plateau named Julian High) to the north. The stratigraphy and depositional setting of the SB are well described in the Tolmin nappe system (western Slovenia), in the southern foothills of the Julian Alps (Rožič, 2005, 2009; Rožič & Popit, 2006; Rožič et al., 2009, 2013, 2014, 2017, 2019, 2022; Rožič & Šmuc, 2011; Gale et al., 2012; Goričan et al., 2012a, b). Recently, Rožič et al. (2018, 2019, 2022) described a new occurrence of the SB sequence at Mirna Valley (eastern Slovenia), in the central part of the Sava Folds, south of the investigated area. This succession represents the southern margin of the SB, generally corresponding to that of the Podmelec Nappe, but it contains the thick Middle Jurassic Ponikve Breccia Member, surrounded by prominent gaps. Scherman et al. (2023) have found similar successions along the northern limb of the Trojane Anticline, demonstrating the connection between the western and eastern SB occurrences. In the SB, the deep-water succession starts with the Ladinian–Carnian Pseudozilian–Amphiclina beds. Generally, it is considered that the Pseudozilian Fm. (the composition is the same as that in the DTZ)

transitions into the Amphiclina Beds (Skaberne et al., 2024). It means that the Carnian dark pelagic limestone alternates with sandstone and shale. The latter does not contain volcanites and has more carbonate than the Pseudozilian Fm. However, the separation of the Pseudozilian Formation and the Amphiclina Beds is difficult and needs revision (Skaberne et al., 2024). In the Southern Alps, the Amphiclina Beds can be generally correlated with the San Cassiano Formation (Gianolla et al., 1998).

The Triassic ends with the Norian–Rhaetian Bača Dolomite Formation, a dark grey dolomite with chert layers and nodules. The formation is up to 350 m thick and contains chert-dolomite breccia bodies, occasionally several tens of meters thick (Gale, 2010; Oprčkal et al., 2013). Solely in the northernmost outcrops of the SB (proximal to the Julian Carbonate Platform), the late Norian and Rhaetian part is not dolomitized and occurs as hemipelagic and resedimented limestones of the Slatnik Formation (Gale et al., 2012; Rožič et al., 2009, 2013).

The Jurassic of the SB begins with the Hettangian–Pliensbachian Krikov Formation, composed of well-bedded, dark grey, hemipelagic, and resedimented limestones, often featuring chert nodules and layers. Resediments prevail in the northern part of the SB, whereas they become progressively rarer towards the south. In the southernmost parts the lithology is dominated by hemipelagites (Rožič, 2006, 2009). It is followed by the Toarcian Perbla Formation, which consists of laminated marlstones, mudstones, subordinate micritic limestones, black chert, and limestones with chert (Cousin, 1973; Buser & Dozet, 2009; Rožič, 2009; Rožič et al., 2019, 2022). It is overlain by the Aalenian–lower Tithonian Tolmin Formation, consisting of two pelagic members. The Lower Member consists of thin-bedded, silicified, dark limestones and chert, which in the Bajocian passes into the Upper Member, composed of radiolarite and subordinate shale (Rožič, 2009; Goričan et al., 2012). Close to the boundary of the two members and on top of the Upper Member, resedimented limestones (mainly in the form of calciturbidites) are interstratified. In the southernmost part of the SB, the older resedimented limestones became abundant, thicker, and coarser and were described as the Bajocian–Bathonian (?Callovian) Ponikve Breccia Member of the Tolmin Formation. This member was produced by large–scale debris–flows and subordinate calciturbiditic currents and is usually following and followed by a stratigraphic gap. The Ponikve Breccia contains Late Triassic to Middle Jurassic platform carbonate lithoclasts and platform–derived components, including fossils, ooids, and oncoids (Rožič, 2019, 2022; Scherman et al., 2023).

The following formation is the Tithonian–Berriasian Biancone Limestone Formation (e.g., Rožič & Reháková, 2024). These thin-layered white to yellow and occasionally red pelagic carbonates are very rarely interrupted by resedimented limestone layers. It is followed by the Aptian–Turonian Lower Flyschoid Formation (sensu Cousin, 1981), which often begins with a basal breccia layer and transitions upwards into alternating marlstone, mudstone (sometimes even shale), and calciturbiditic beds. The measured thickness in the western Slovenian Basin is up to 300 m (Schlagintweit et al., 2024; Gerčar, 2024). We note that the upper (upper Cenomanian-Turonian) part of this formation is dominated by reddish marly limestone and was mapped in the western SB as a separate unit (Buser, 1986). It is overlain by the Coniacian–lower Maastrichtian Volče Limestone Formation, a thin–layered or laminated creamy–white micritic limestone (e.g., Ogorelec et al., 1976; Premru, 1983). It is characterized by varying time intervals, from upper Cenomanian to the lower Maastrichtian, and thicknesses (50–200 m) depending on the area (e.g., Ogorelec et al., 1976; Rižnar, 2006; Poljak, 2017; Gerčar et al., 2022). In the Slovenian Basin, the succession overlain by the Maastrichtian Upper Flyschoid Formation, composed predominantly of marlstone and marked by different resedimented layers containing carbonates and thin sandstone beds. The maximal thickness is 400 m. We note that in the southern Sava Folds, different names were used for the Cretaceous formations that generally correspond to those described above. In stratigraphic order, these are the Gora, Krško, and Veliki trn formations (Poljak, 2017). The Mesozoic formations are covered discordantly by the Cenozoic ones and are preserved in the cores of the Tuhinj–Motnik and Laško synclines. The deposition of the Oligocene Pseudosocka (Trbovlje) Formation began in the early Oligocene (Kiscellian) with conglomerates that show upward gradation, followed by coal deposits, which are covered by sandstones, claystones, and other siliciclastic sediments. Andesite, dacite, and their rhyolitic tuffs are interbedding from the middle Kiscellian. (Placer, 1998a; Aničić et al., 2002). Deposition in the Miocene begins with the Laško Formation, characterized by conglomerates covered by Lithotamnium Limestone, followed by a marlstone with varying sand and limestone content (Buser, 1979; Premru, 1983; Aničić et al., 2002).

Materials and methods

Our fieldwork aimed to determine the distribution and relationship of the lithostratigraphic units. Except for a few small (10–20 m) quarries, natural cliffs and road cuts most of the observation points (shortly sites) represent only a few meters of rock outcrops, although some roadcuts offered more continuous observations. Selected from a few hundred sites, 119 of them are discussed in this work. From there, rock samples were collected. Strike and dip data, site numbers, field sketches, field images, notes, and tags with GPS coordinates were documented using the Field MOVE field mapping software. High–quality field photos were taken using a Panasonic DMC–FZ200 camera.

The numbering of the samples corresponds to the site number, and within a site, different samples were also given a letter code. The samples were examined and compared in the laboratory using a magnifying glass (loupe). Finally, 5 × 5 cm–sized thin–sections were made from 64 samples for microfacies and microfossil analyses made by Á Görög. The preservation of the microfossils varies from well to weak due to the post–depositional alterations (e.g., silicification, dolomitization) of the rocks. Petrological analysis was carried out on two samples (614 and 326) by Sándor Józsa (Eötvös University, pers. Communication). Calcareous nannofossils analysis was performed on eight samples where thin–sections did not contain age–determining microfossils. For this study, two smear slides per sample were prepared in the Laboratory of the Hantken Foundation, using standard techniques (samples from sites 238, 299, 301–303, 307, 326, 330, and 549). Except for 301–302 and 326, each yielded a poor nannofossil assemblage, allowing investigation only with the polarizing light microscope. Frequent silicification altered the optical properties of the crystal-units, making determination difficult. For the radiolaria study, 5 samples from sites 629, 632, 636, 643, and 644 were dissolved in diluted HF, following the standard laboratory procedures of Pessagno and Newport (1972), and the same samples in 75 % acetic acid, following methods of Karaminia (2004), but residues yielded no fossils. Samples from site 614 were prepared using the standard palynological processing techniques described by Wood et al. (1996). Two smear–slides were made from each, but none contained fossils.

The thin–sections and smear–slides were studied using an Olympus BH2–BHS microscope, and photomicrographs were taken with a Canon EOS 200D camera of the Hantken Foundation. Additionally, two composite photomicrographs were created using a Zeiss Axioskop 40 microscope with an AxioCam MRc5 (Zeiss) camera at 1x zoom and the AxioVision AxioVs40 V4.8.2.0 software at the MTA–ELTE Geological, Geophysical, and Space Sciences Research Group, Hungarian Academy of Sciences, at Eötvös University.

As the results of the microfacies analysis, the following categories were determined (see Fig. 2). Carbonate–texture system of Dunham (1962) and Folk (1962) are in column 1 and 2. Frequently occurring allochems, observed alterations and visible post depositional fabrics are colour coded in column 3, 4 and 5. In column 6 the relevant fossils are marked with letters. The detailed legend for all microfacies analysis is placed at Figure 2.

During the microfossil analyses, we first provide the occurrence and semiquantitative abundance of different fossil groups such as calcareous nannofossils, calcareous dinocysts (or c–dinocysts) and calcitarchs, calcimicrobes, microproblematica, green algae, terrestrial plants, Calpionella, Radiolaria, benthic Foraminifera, planktonic Foraminifera, Porifera, Stromatoporoidea, Vermes, Gastropoda, fragments of Bivalvia shell, elongated calcite particles ("filaments"), Ostracoda, Bryozoa, Echinodermata and Tunicata. Then, the semiquantitative abundance of the classified taxa (genus and species) of calcareous nannofossils, c–dinocysts, calcitarchs, calcimicrobes, microproblematica, green algae, Calpionella, benthic and planktonic Foraminifera, Porifera, Stromatoporoidea, Vermes and Tunicata are listed. The stratigraphic range and biozones of the most important taxa are indicated in charts (Tables 1–5) and along the lithological columns of the sections. In the text, fossils are listed in order of their frequency. The order of the images of the microfossils belonging to a section follows the systematic order, and within that, the succession of the samples from oldest to youngest. The selected synonymy, taxonomy, stratigraphic range, and ecological requirement of the most important microfossils are enumerated in Appendix 2.

The results of all these investigations helped B. Scherman to give the stratigraphic position of the separated sites and arrange them into sections. The map coordinates of the sites and site numbers, with the determined formation names, are listed in Appendix 3.

Results

Description of the studied sites

In previous studies (Scherman et al., 2023), we have observed Slovenian Basin–type successions along the northern limb of the Trojane Anticline. To understand the contact with the north–lying units, their age and paleogeographic origin had to be determined.

Based on field observations, lithofacies, microfacies, and biostratigraphical studies, several stratigraphical columns could be compiled which can contain hiatus in observation. These can be composed of several sites or sub-sections, which are shifted along the strike of the rock units (see for example Sveti Miklavž section on Fig. 1). In other cases, the section contains tectonic units which belong to different stratigraphical columns (e.g., Marija Reka section the following sections have been compiled and named after nearby mountains, hills, and villages.

We are presenting our observations in composite sections in an order moving northwards from the Palaeozoic core of the Trojane Anticline (Fig. 1) Krvavica section, Marija Reka section, Brložen and Kozlov grič sections, Sv. Miklavž section (composed of four sub-sections), Šmiglov hrib section, Osreški grič section, Zahomce section, and finally, the Črni vrh section. The latter three are positioned north–west from the Krvavica section. In addition, four single observation sites were selected and analysed. These are listed in chronological order from oldest to youngest.

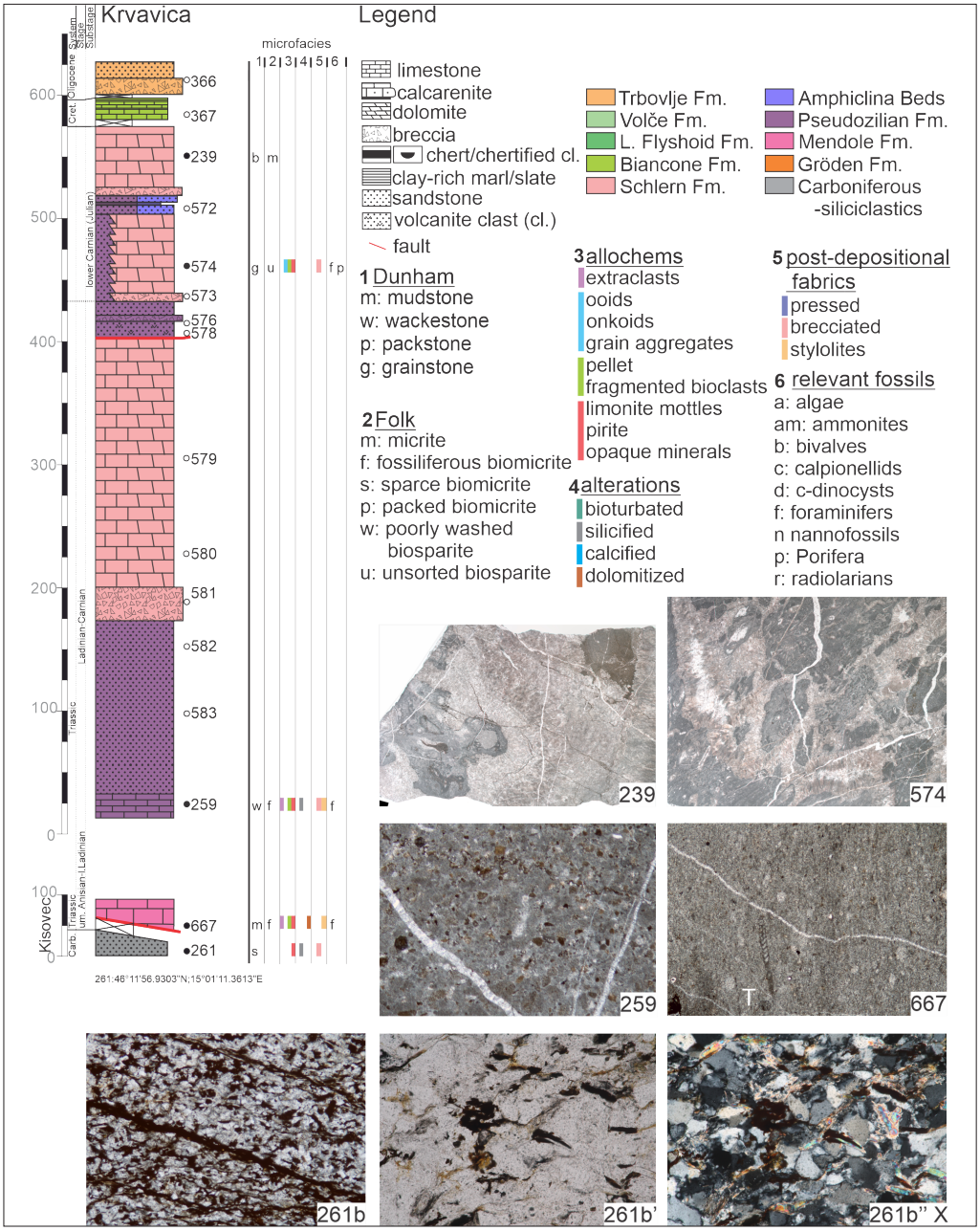

Fig. 2. Stratigraphic column of the Kisovec Hill and Krvavica Mt. sections with the indication of the chronostratigraphic assignments and GPS coordinates (below). Note the lithology and the formations marked by colors (see legend); the studied sites shown with a circle, sites with samples taken for analyses marked with black-filled circles; the results of the microfacies analysis (see legend); photomicrographs of the thin sections made from samples with sample number (right lower corner). See the text and Appendix 1 for the details of the microfacies and microfossil analysis. All of these apply to the stratigraphic column and microfacies images presented in each section of the current paper. Fossils: T: *Turriglomina mesotriassica* (Koehn-Zaninetti) site 667; Calcimicrobe bundstone, sites 574 and 239. The width of the microphotographs is 3mm (sites 261b, 667, and 259); 6 mm (sites 574 and 239), and 0.6 mm (sites 261b' and 261"). X: crossed polarized light. Abbreviations: Carb. (Carboniferous); Cret. (Cretaceous); um. (upper-middle); cl. (clast).

Fig. 3. Lithofacies of the Kisovec Hill and Krvavica Mt. sections. **a** variegated siliciclastic sediments of the Trbovlje Fm., **b** carbonate breccia bed, Schlern Fm., **c** gravitational breccia forming the base of the Schlern Fm., **d** volcanic clasts in the Pseudozilian Fm., **e** Fine-grained sandstone of the Pseudozilian Fm., **f** black pelagic limestone of the Pseudozilian Fm., **g** bedded part of the Mendole Formation, **h** slates of the Carboniferous siliciclastic sediments, **i** massive carbonate body of the Mendole Formation. The letters in the upper right corner are abbreviations for the cardinal directions. Numbers in the lower right corner are site numbers.

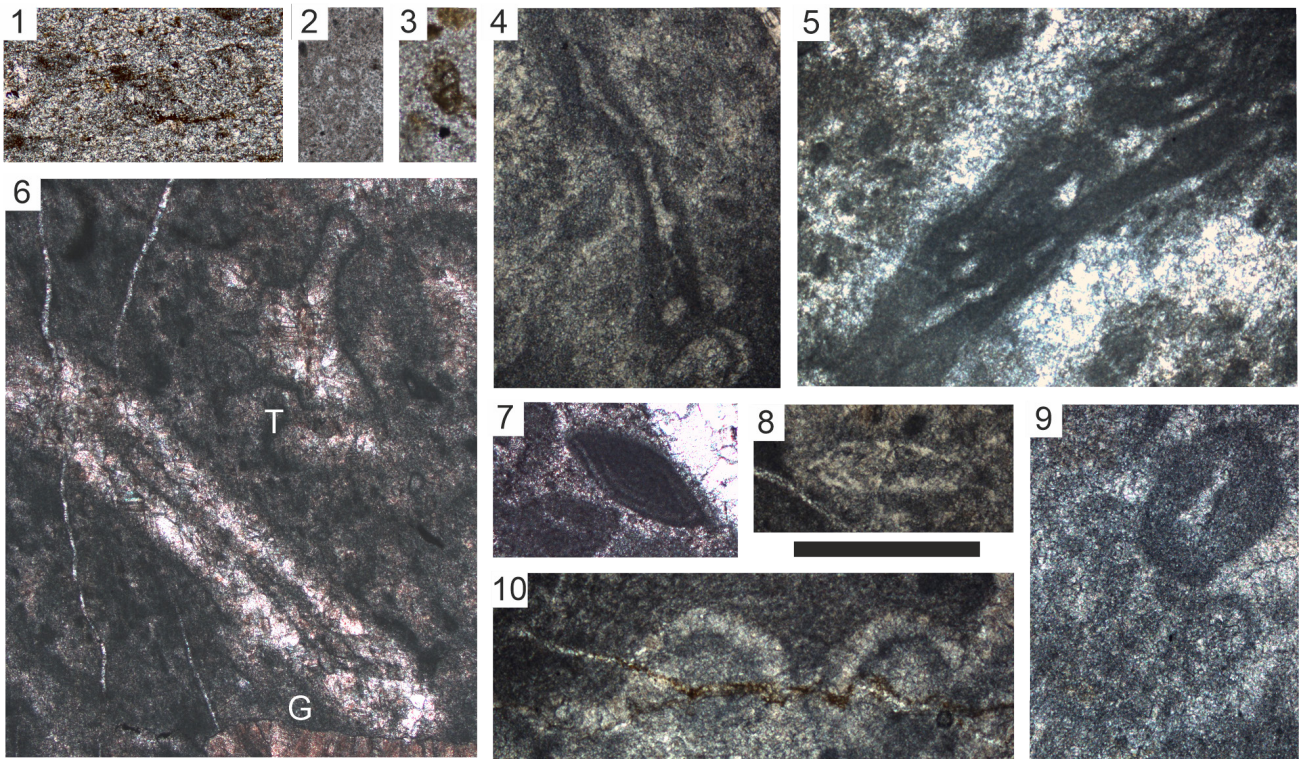

Fig. 4. Microfossils of the Kisovec Hill (1-2) and Krvavica Mt. (4-10) sections. **1-2** sample 667: **1** *Paratriasina* sp., **2** Textulariidae sp., **3** Textulariidae sp., sample 259a, **4-10** sample 574, **4** „*Tubiphytes*" (sensu Senowbari-Daryan) sp., **5** *Palaeonubecularia gregaria* (Wendt), **6** *Nodobacularia vujisici* Urošević & Gaździcki (N) and *Thaumatoporella parvovesiculifera* (Raineri) (T), **7** *Ophthalmidium* sp., **8** *Howchinella woodwardii* (Howchin), **9** *Angulodiscus minutus* (Koehn-Zaninetti), **10** *Salzburgia ?variabilis* Senowbari-Daryan & Schäfer. The scale bar is 200 μm.

Kisovec Hill and Krvavica Mt. sections (Figs. 1–4; Tables 1–2; Appendices 1–2)

Kisovec Hill is located 2 km south of the village Loke pri Taboru. On the eastern side of Kisovec Hill, at site 261, the lowermost part of the section builds up from continental, dark, purplish–brown Carboniferous shale. Based on the petrological analysis, the foliated shale dominantly consists of well–sorted angular quartz grains. Besides them, a few micas and opaque minerals are also present.

Above it, a nearly 20 m high outcrop (site 667) of medium–grey limestone succession appears. The contact between the two formations has not been explored, but based on the literature (e.g., Rainer et al., 2016), an erosional disconformity may exist between them while former maps interpreted a thrust contact (Buser, 1977, 2010). In the lower part, the limestone is massive and thick-bedded (up to 1,8 m), upwards, the beds become thinner at the top, the layers are only 5–10 cm thick. The texture of the rock is mudstone/wackestone, fossiliferous biomicrite, with scattered opaque minerals and partly dolomitized. There are a few intraclast, pellets, benthic foraminifers, ostracods, and fragments of *Thaumatoporella parvovesiculifera*. Among the foraminifers, the upper Anisian–lower Ladinian *Turriglomina mesotriassica,* the uppermost Anisian––Carnian *Paratriasina* sp, and a few textulariids could be recognized. These fossils date the rock to the latest Anisian–early Ladinian interval. The macro– and microfacies of the rock indicate a carbonate platform environment. Most likely, these rocks can be classified as the Mendole Formation.

The Krvavica Mt. section is located 1 km east of Čemšeniška–Planina and 1.5 km south of the village of Loke pri Taboru. This composite section comprises observations made on Kisovec Hill, just south of Krvavica Mt., and extends through Krvavica Mt. The beds dip to the north, the order of sites in the description is from south to north. It begins with observations at site 261, featuring Carboniferous shales, and it is followed by carbonate platform sediments observed at site 667. Site 259 is projected from approximately 1 km east, resembling the limestone member of the Pseudozilian.

Towards the north of the previous sites, southeast of Krvavica Mt. (site 259), dark grey, well–bedded, partly silicified limestone succession can be observed. The texture of the rock is wackestone, fossiliferous biomicrite, with common angular intraclasts and pellets. Fossils are represented only by a few specimens of benthic foraminifers, such as textulariids and nodosariids. Based on the mac-

Table 1. Stratigraphic range of the algae, green algae, porifera, vermes and tunicata in the studied sites.

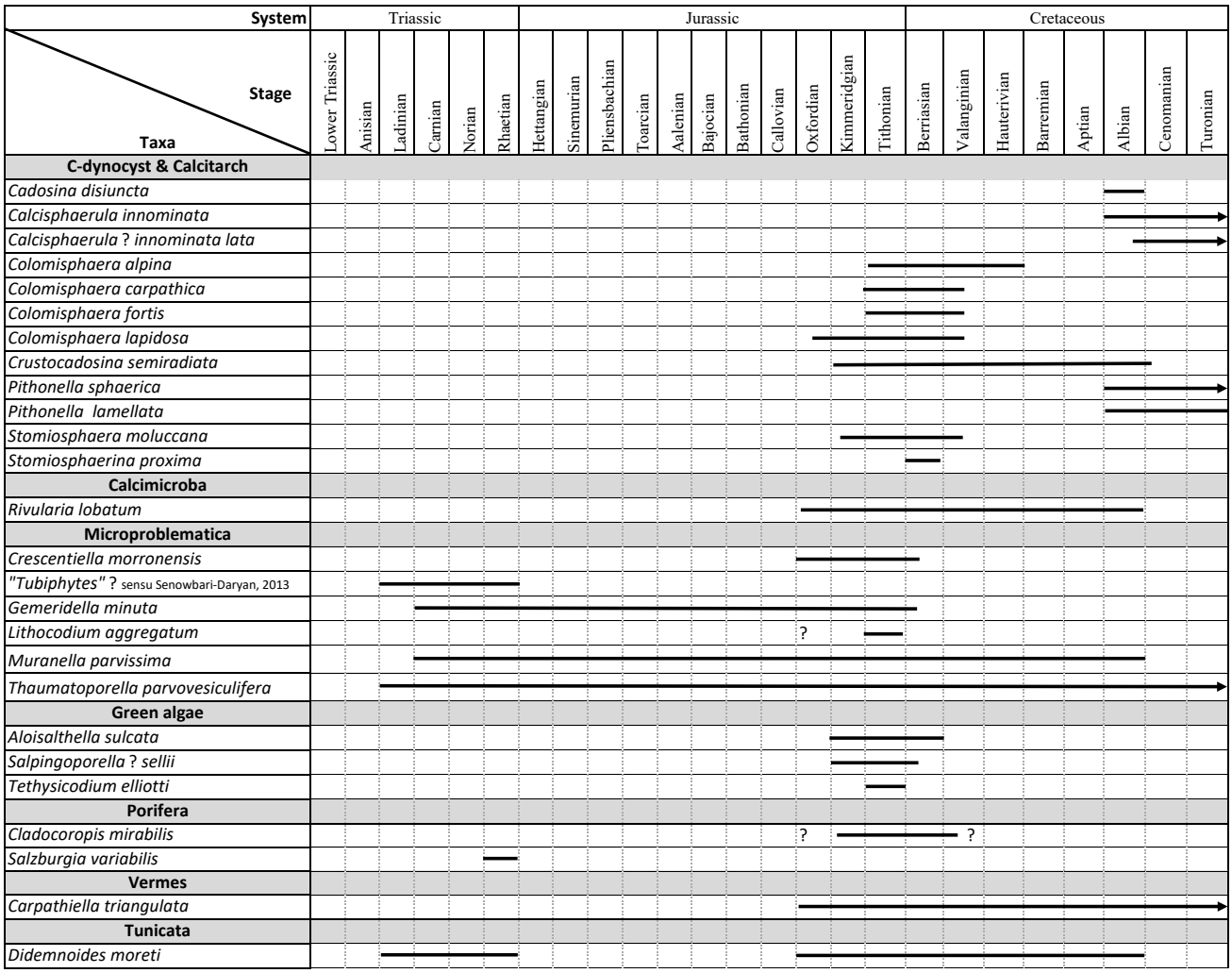

roscopic appearance and the microfacies, the rock most probably belongs to the Ladinian Pseudozilian Formation.

On the southern flank of Krvavica Mt., the classic greywacke development of the Pseudozilian Formation can be studied in several natural outcrops and road cuts (e.g., sites 583 and 582). The estimated thickness is about 150 m. This siliciclastic succession is cut by ~25 m thick, light grey monomictic breccia horizon (site 581). The clasts are composed of carbonate, and the matrix is a brick–red clay, occasionally with light grey calcite cement. Above it in succession, at more than 200 meters (sites 580 and 579), the massive platform carbonate succession of the Ladinian–Carnian Schlern Formation can be traced. The rocks are greyish–white limestones–dolostones.

Above this (sites 578, 576), the Pseudozilian Formation reappears at a thickness of about 30 m. Here, the Pseudozilian Formation is composed of greywacke with volcanoclastic intercalations; upwards, the grain size decreases. At this point our mapping observations indicate a tectonic contact between them, a thrust fault can be projected from the west to the section. Alternatively, this could also represent interfingering of basinal and platform succession, which presumably is the case further north.

At site 573, a thinner, approximately 5–7 m thick breccia horizon occurs, like the one at site 581. Above it, the beds of the Schlern Formation occur again. At site 574, the texture of the rock is pelloidal grainstone, unsorted biosparite with ooids, oncoids, benthic foraminifers, and fragments of the sponge cf. *Salzburgia variabilis*, the microproblematica *Thaumatoporella parvovesiculifera,* and the Dasycladacean algae. Among the foraminifers, the platform–dwelling *Angulodiscus minutus*, *Palaeonubecularia gregaria, Gheorghianina vujisici,* and *Howchinella woodwardii* could be identified. Based on the cooccurrence of the *A. minutus* and *G. vujisici,* the age of the rock is early Carnian–Norian.

More to the north (at site 572), the massive carbonate is overlain by medium–dark grey aleuritic shale. On the field, only debris was observed that

Table 2. Stratigraphic range of the benthic foraminifers in the studied sites.

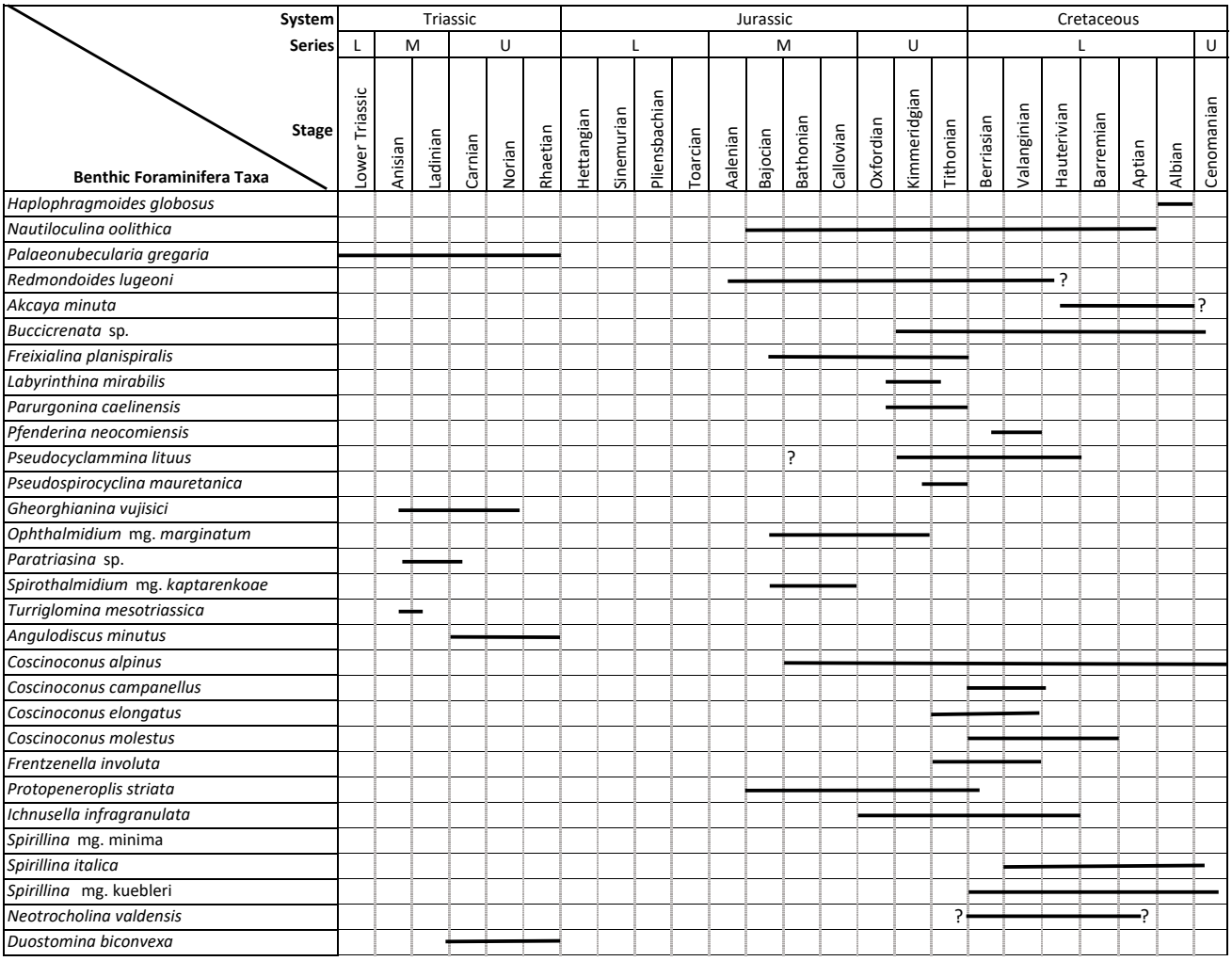

we attributed to the topmost part of the Pseudozilian Formation. Additionally, the geomorphology of the area shows peaks composed of carbonates and intervening saddles formed by clastic rocks, found in scree. Breccia horizons are observed on the bottom of the carbonate bodies. This geometry can be interpreted as the interfingering of the harder limestone beds of the Schlern Formation and the softer siliciclastic Pseudozilian Formation. These phenomena also indicate that the sediments of this interval in the Krvavica Mt. section were deposited in somewhat deeper water than those of the previous ones. The Schlern Formation begins with a breccia horizon, indicating episodical carbonate progradation over the deeper water successions. Another interpretation for the alternation of the Pseudozilian and Schlern Formation would be tectonic stacking. However, these middle carbonate bodies do not continue down the valley, as observed at Krvavica Mt. or the northernmost platform, thus the repetition is at least partly sedimentary in origin.

The appearance of the third monomictic breccia bed (above site 572) and the massive, light grey limestone with a microbial bioherm (site 239) suggest shallowing. The texture is microbial boundstone, with voids filling with radial fibrous cement. This carbonate can belong to the latest prograding toe of the Schlern Formation.

The following outcrop (site 367) is situated on the northern side of Krvavica Mt., where thin-layered (2–4 cm) ochre, cream-white limestone with interlayered clay films and marl crop out. Based on the macroscopic fabric analogy, this could be the Upper Jurassic–Lowermost Cretaceous Biancone Formation with an estimated thickness of 20 m.

On the uppermost part of the section (site 366), variegated grey–ochre siliciclastic sediment crops out. In the lower part, the rock is a fine-grained unsorted breccia composed of rounded and angular clasts (up to 5 cm) derived from older formations, primarily carbonates and shales, as well as cemented sandstones. Upwards, the amount and the size of the clasts decrease, and the sandstone is less cemented. With facies analogy and according to the older maps, this was categorized as the Oligocene Trbovlje Formation.

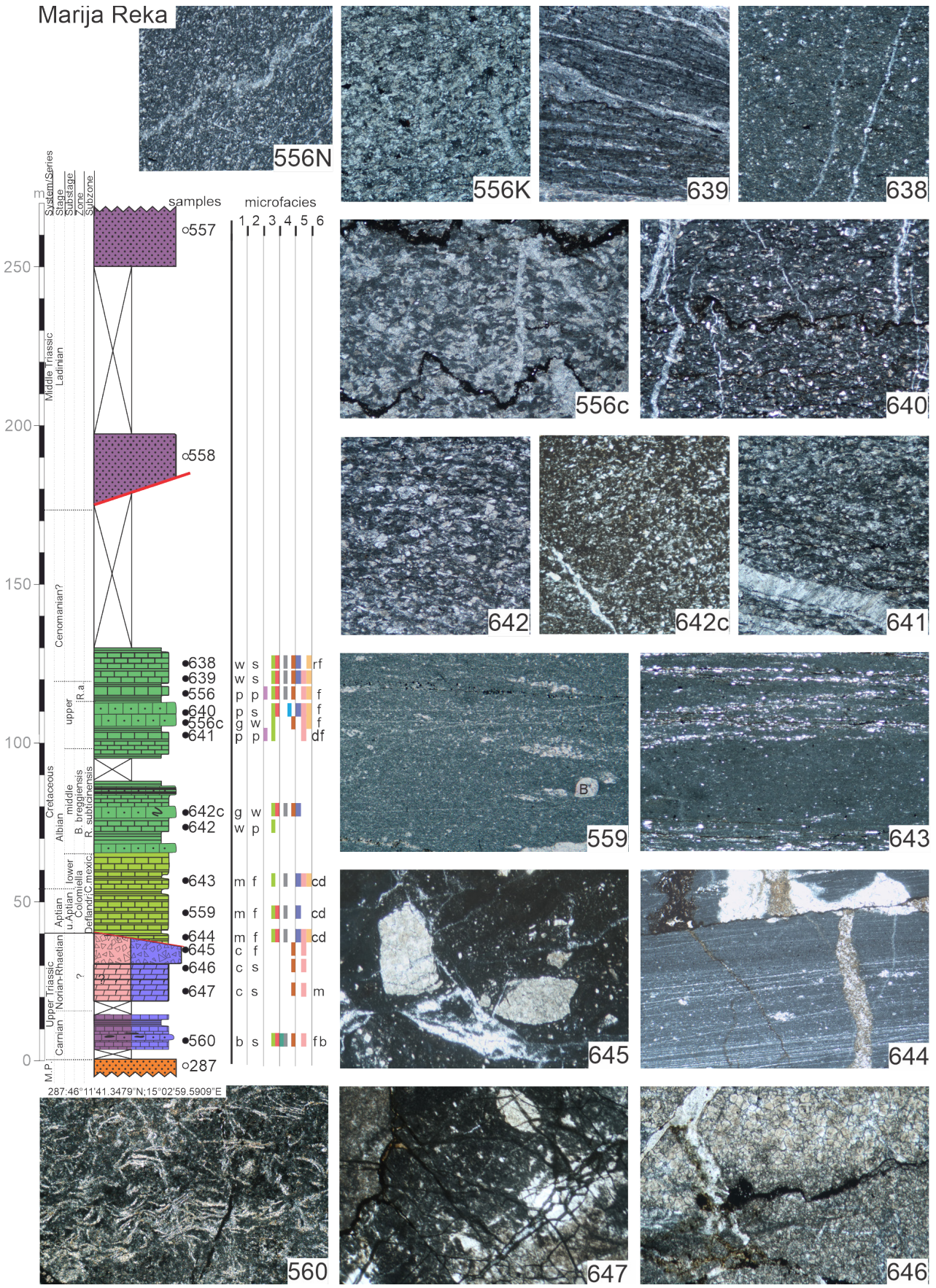

Fig. 5. Stratigraphic column and microfacies of the Marija Reka section. For the legend, see Fig. 2. The width of the photomicrographs is as follows: sites 560, 647, and 646 – 6 mm; sites 645-643, 559, 556c, and 640 – 3 mm; sites 642, 642c, 641, 638, 639, 556K, and 556N – 2 mm. Abbreviations: M.P. (Upper Permian); u. (upper); Deflandr. (*Deflandronella*); C.mexic. (*Colomiella mexicana*); B. breggiensis (*Biticinella breggiensis*); R. (*Rotalipora*); R.a. (*Rotalipora appeninica*) B. (*Bullopora rostrata*).

Fig. 6. Lithofacies and structural features of the Marija Reka section. For the legend, see Fig. 3. **a** calcarenite bodies and thin-layered marl with limestone alternating within the Lower Flyschoid Fm., **b** layers and axial plane foliation within the Pseudozilian Fm., **c** folded chert layers inside a calcarenite body, Lower Flyschoid Fm., **d** thick calcarenite beds between thinly layered marlstone of the Lower Flyschoid Fm., **e** Thin-layered limestone folded in asymmetric folds with steeply NW-plunging fold hinges with stereogram within the Biancone Fm., **f** dark chert layers in calcarenite body within Lower Flyschoid Fm. **g** map view of early joints, veins, and faults and their relation to NW-dipping bedding inside Ladinian-Carnian limestone (Pseudozilian Fm. or Amphiclina Beds), **h** brecciated dolomite, probably Amphiclina Beds.

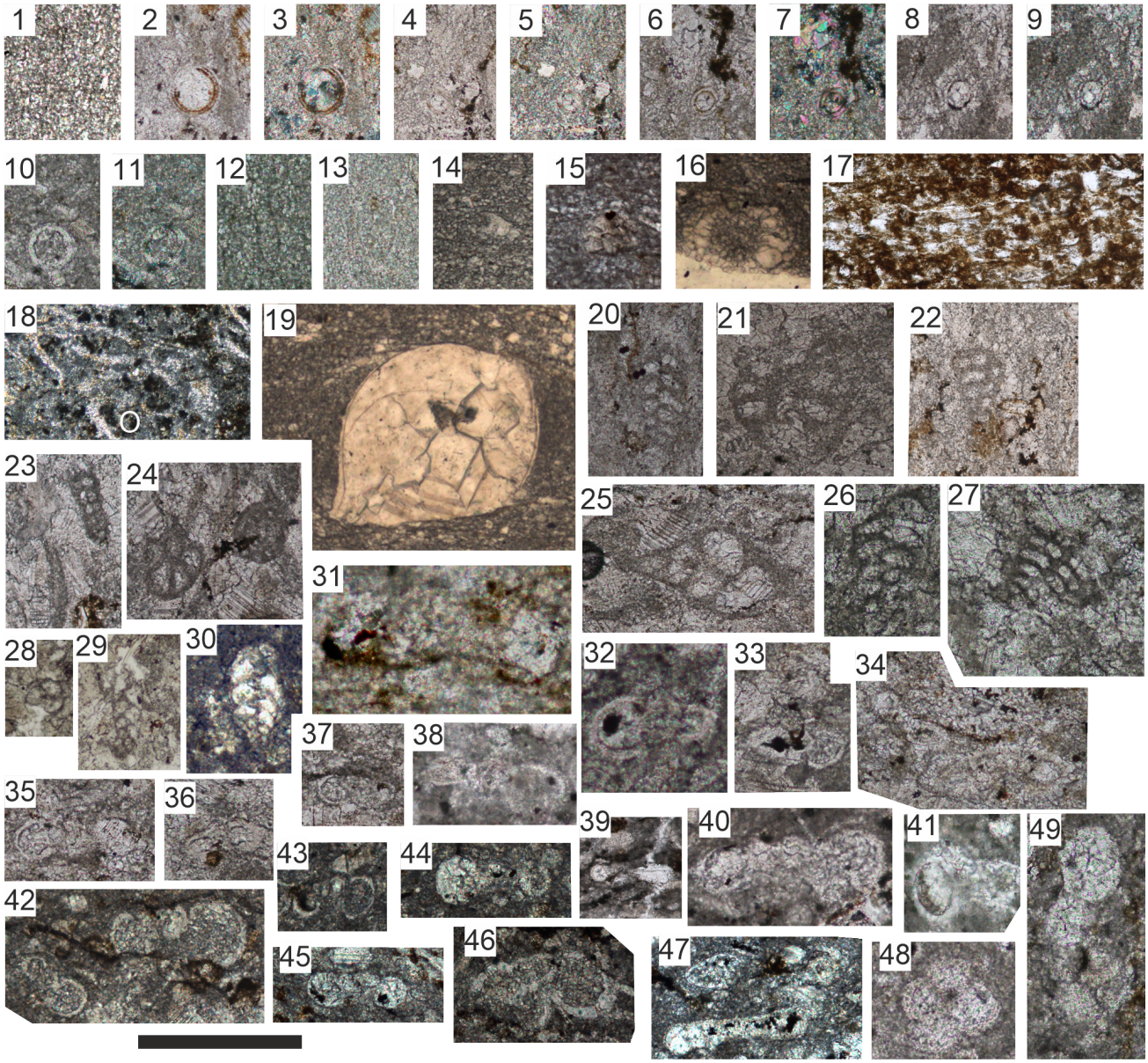

Fig. 7. Microfossils of the Marija Reka succession: **1** *Cadosina disiuncta* Knauer, sample 559, **2-5** sample 642: **2-3** *Pithonella sphaerica* (Kaufmann), (**3**: crossed Nicols), **4-5** *Pithonella* sp. A with three layered wall (**5**: crossed Nicols), **6-9** sample 241: **6-7** *Calcisphaerula? innominata lata* Adams, Khalili and Said, (**7**: crossed Nicols), **8-9** *Praecalcigonellum* sp., **10-11** sample 556N: **10-11** *Calcisphaerula innominata* Bonet, (**11**: crossed Nicols), **12***Parachitinoidella cuvillieri* Trejo, sample 559, **13** *Colomiella recta* Bonet, sample 643, **14-17** sample 559: **14-15** *Gemeridella minuta* Borza & Misik, **16** *Didemnoides moreti* (Durand Delga), **17** *Dasycladacea indet*., sample 642c, **18** oberhauserellid (o) and thin Bivalve valves coated by isopachous rims on both sides, sample 560, **19** *Bullopora rostrata* Quenstedt, sample 559, **20-23** sample 642: **20** *Ammobaculoides* sp., **21** *Voloshinoides* sp., **22** *Vercorsella* sp., **23** *Novolesia* sp., **24-25** sample 641: **24** *Nezzazatinella* sp. and *Haplophragmoides globosus* Lozo, **25** *Verneuilina* sp. **26-27** sample 556c: **26** cf. *Novolesia* sp., **27** cf. *Akcaya minuta* (Hofker), sample 640, **28-30** sample 556K: **28** Verneuilinidae sp., **29** *Bolivinopsis* sp., **30** Bolivinidae? sp., **31** *Coscinoconus* sp., sample 638, **32-34** sample 642: **32** *Biticinella breggiensis* (Gandolfi), **33** *Thalmanninella balernaensis* (Gandolfi), **34** *Ticinella raynaudi* Sigal and *Thalmanninella praebalernaensis* (Sigal), **35-37** sample 641: **35** *Ticinella primula* Luterbacher (Plummer), **36** *Ticinella madecassiana* Sigal**, 37** *Ticinella raynaudi* Sigal, **38-41** sample 640: **38-39** *Clavihedbergella simplex* (Morrow), (Gandolfi), **40** *Ticinella praeticinensis* Sigal, **41** *Ticinella roberti* (Gandolfi), **42-47** sample 556K: **42** *Laeviella bentonensis* (Morrow) and *Microhedbergella rischi* (Moullade), **43** *M. rischi* (Moullade), **44-45** *Muricohedbergella planispira* (Tappan), **46** *Muricohedbergella delrioensis* (Carsey), **47** *P. buxtorfi* (Gandolfi) and *Spirillina* sp., **48-49** sample 556N: **48** *Favusella washitensis* (Carsey), **49** *Pseudothalmanninella subticinensis* (Gandolfi). The scale bar is 500 μm at figures 1-31 and 200 μm at figures 32-49.

The Marija Reka section (Figs. 1, 5–7; Tables 1–4; Appendices 1–2)

The Marija Reka section is located on the eastern side of Štrebenkel Mt., starting 450 m south of the farm Urankar. Our observations were conducted along a 600 m-long stretch of road. The approximate thickness of the section is 270 m. The bedding is dipping to the north, the order of sites in the description is from south to north. In most studied Mesozoic beds, silicification, secondary dolomitization, and other post-depositional fabrics (e.g., micro-breccia, stylolites) could be recognized.

The section begins with the Permian terrestrial, red clastic Gröden Formation, which outcrops at site 287. At site 560, the succession is approximately 15 m thick, composed of grey, well-bedded

micritic limestone and laminated marlstone. The limestone layers, with thicknesses ranging from 5 to 20 cm, are occasionally silicified. A poorly preserved ammonoid with ceratitid sutures was found. The rock is boundstone, packed biomicrite with thin-shelled, pelagic bivalves, primarily their debris. Polycrystalline neomorphic rims grow out syntaxially from both sides of the valves. There are a few recrystallized foraminifera (oberhauserellid?). The rock is brecciated, and the fractures are filled with red-black striped calcite crystals. The rock could belong to the deep-water Ladinian Pseudozilian Formation or Carnian Amphiclina Beds because it is the only formation from when Triassic ammonites and "Bositra" lumachella are known (Ramovš, 1981, 1986, 1997, 1998a; Gale et al., 2017; Rožič et al., 2024).

After a gap brecciated grey and white crystalline, fossil-free dolomites crop out (sites 647, 646, and 645). This approximately 20 m thick dolomite succession may most likely belong to the Amphiclina Beds or Pseudozilian Formation. However, the Ladinian to early Carnian Schlern Formation cannot be excluded. In the next ~25 m, these beds are followed by tectonically folded thin-bedded Biancone-type, light grey–ochre, mottled, cherty limestone, often with thin marly intercalations (sites 644, 559, and 643).

The texture of the rock is mudstone, fossiliferous biomicrite with large amounts of scattered pyrite and other opaque minerals. Due to subsequent silicification, the preservation of the fossils is poor. The bioclasts are radiolarians and a few calpionellids. Additionally, c-dinocysts and calcitarchs such as *Cadosina disiuncta, Crustocadosina semiradiata,* and ascidia *Didemnoides moreti* could be identified, as well as the microproblematica *Gemeridella minuta*. At site 559, the presence of *Parachitinoidella cuvillieri*, characterized by dark microgranular lorica, indicates the late Aptian *Colomiella* Zone, *Deflandronella* Subzone (Trejo, 1975). Higher in the section (site 643), with the appearance of the calcite–hyaline-walled *Colomiella recta,* the existence of the uppermost Aptian–lowermost Albian *Colomiella* Zone, *C. mexicana* Subzone (Trejo, 1975) could be demonstrated. Besides them, a few specimens of *Spirillina italica* and the attached *Bullopora* sp. could be identified. The presence of calpionellids and c-dinocysts, and the almost complete absence of foraminifers imply an oligotrophic hemipelagic/pelagic palaeoenvironment, with occasionally dysoxic conditions.

Further to the north, about 10 m away, a lithological change can be observed. In the dark grey silicified marl succession, grey calcarenite beds occur (e.g., sites 642, 642c, and 641). Chert layers and nodules are commonly intercalated in the latter. At site 642, the texture of the marl is wackestone, packed biomicrite with planktonic and benthic foraminifers and c-dinocysts. The planktonic foraminifers are represented by *Ticinella raynaudi, T.* spp.*, Clavihedbergella simplex, Biticinella breggiensis,* and *Thalmanninella praebalernaensis*. Based on the co-occurrence of the two latter species, this bed belongs to the uppermost middle Albian *B. breggiensis* Zone *R. subticinensis* Subzone. The benthic foraminifera assemblage consists of agglutinated forms such as *Ammobaculoides* sp., *Novolesia* sp., *Voloshinoides* sp., and *Vercorsella* sp. Pithonellids are common, especially *Pithonella sphaerica*, but a few specimens of the three-layer-walled *P. lamellata* also occur. The very fine-grained calcarenite bed at site 642c is a poorly washed grainstone with common fragments of Bivalvia shells and a few agglutinated benthic foraminifera (textulariids). A thallus of Dasycladales indet. also could be recognized. Higher up, after a gap, at site 641, the macroscopic appearance and texture of the rock are very similar to those at site 642 but richer in fossils. Especially c-dinocysts are common, namely *Pithonella sphaerica* and *Calcisphaerula*? *innominata lata*. A few specimens of the calcitarch *Praecalcigonellum* sp. could also be identified. The planktonic foraminifera fauna consists of ticinellids; the following species can be classified as *T. raynaudi, T. primula,* and *T. madecassiana*. Among benthic foraminifers, only agglutinated occur, mainly textulariids indet., additionally *Akaya minuta*, *Haplophragmoides globosus, Nezzazatinella* sp., *Belorussiella* sp., and *Verneuilina* sp. appear. *Calcisphaerula*? *innominata lata* is known from the late Albian thus, this bed can be dated to this age.

Above, in the next 15 m (sites 556c, 640, 556), the calcarenitic limestone beds become gradually thinner and more frequent, and the rock between them is more argillaceous and finely laminated. At site 556c, the microfacies study indicates fine-grained calcarenites with grainstone and poorly washed biosparite texture. In the relatively diverse foraminiferal fauna, the agglutinated forms dominate, such as *Akcaya minuta, Novolesia* sp. *Verneuilina* sp., *Verneuilinidae* sp.*, Nezzazatinella* sp.*, Trochammina* sp., and textulariids indet. Besides them, a few specimens of calcareous-hyaline Lenticulina spp. and nodosarid sp. could also be recognized. Among the planktonic forms, only the *Ticinella primula* could be classified, indicating that this bed is not younger than the late Albian.

Table 3. Stratigraphic range of the planktic foraminifers in the studied sites.

Series	Lower Cretaceous										Upper Cretaceous					
Stage	Aptian			Albian							Cenomanian				Turonian	
Substage	upper			lower			middle		upper		lower	mid	upper		lower	
Planktonic Foraminifera Zones & their beginning (Ma)	Hedbergella infracretacea 118,9	Paraticinella eubeajaouensis = rohri 118	Microhedbergella miniglobularis 113,3	M. renilaevis 113,2	M. rischi 112,9	T. madecassiana 112,3	T. primula 111,8	B. breggiensis 107,3	P. ticinensis 103,9	R. appeninica 102	T. globotruncanoides	H. helvetica	R.cushmani	Whiteinellla archaeocretacea	Helvetoglobotruncana helvetuca	
Planktonic Foraminifera Taxa								T. praeticinensis 107,3	R. subticinensis 107							
Biticinella breggiensis																
Clavihedbergella simplex																
Favusella washitensis																
Laeviella bentonensis																
Muricohedbergella delrioensis																
Muricohedbergella planispira																
Planomalina buxtorfi																
Pseudothalmanninella subticinensis																
Thalmanninella praebalernaensis																
Ticinella madecassiana																
Ticinella praeticinensis																
Ticinella primula																
Ticinella raynaudi																
Ticinella roberti																

Table 4. Stratigraphic range of the calpionellids in the studied sites.

Taxa \ System	Jurassic	Lower Cretaceous					
Stage	Tithonian	Berriasian	Valanginian	Hauterivian	Barremian	Aptian	Albian
Calpionella alpina							
Calpionellopsis oblonga							
Calpionellopsis simplex							
Chitinoidella boneti							
Chitinoidella elongata							
Colomiella recta							
Crassicolaria intermedia							
Lorenziella hungarica							
Parachitinoidella cuvillieri							
Praetintinnopella andrusovi							
Tintinnopsella carpathica							
Tintinnopsella remanei							

At sites 640 and 556, the texture of the marl layers is packestone. The fossil and mud content varies even within a single rock sample; thus, the type of biomicrite can be sparse, packed, or poorly washed. The opaque minerals are common. The bioclasts are mainly planktonic foraminifers. At site 640, the following planktonic foraminifera could be identified: *Ticinella raynaudi, Clavihedbergella simplex, T. roberti, T. praeticinensis,* and *Pseudothalmanninella subticinensis*. Besides them, only a few specimens of *Valvulina* sp. and textulariids occur. Based on species and the stratigraphic position, the age of this bed is late Albian. At site 556, diverse planktonic and benthic foraminifera assemblage appear containing the following taxa: *Muricohedbergella delrioensis, M. planispira, Planomalina buxtorfi, Pseudothalmanninella subticinensis, Thalmanninella praebalernaensis, Ticinella madecassiana, T. praeticinensis, T. primula, Biticinella breggiensis, Favusella washitensis, Laeviella bentonensis,* and *T.* sp. also the agglutinated benthic forms such as *Bolivinopsis* sp., *Ammobaculoides* sp., *Nezzazatinella* sp. *Verneuilinidae* sp., *Akcaya minuta,* and ?Bolivinidae sp. The following c-dinocysts occur: *Calcisphaerula innominata, Calcisphaerula*? *innominata lata,* and *Pithonella sphaerica*. Since *Muricohedbergella delrioensis* and *Planomalina buxtorfi* appeared at the beginning of the *Rotalipora appeninica* Zone and *Biticinella breggiensis*, *Ticinella madecassiana* and *T. praeticinensis* became extinct at the end of this zone, this bed deposited during the uppermost Albian *R. appeninica* Zone.

In the next 12 m, at sites 639 and 638, the calcarenitic limestone beds range from a few cm to 10 cm in thickness, interspersed with marl and shale clay layers. The texture of the limestone is wackestone, sparse biomicrite. The planktonic foraminifers and the c-dinocysts are missing. Besides the very rare aragonitic involutinid foraminifers, such as platform-dwelling *Coscinoconus* sp. and *Frentzenella* sp., only a few calcified radiolarians occur. Since both genera became extinct at the end of the Cenomanian, these beds cannot be younger than this age. This entire upper Aptian (? Cenomanian) succession can be classified as the Lower Flyschoid Formation.

Further north, no rock outcrops were found in the next 75 m of the Marija Reka section, while at site 558, the resedimented volcaniclastics of the Triassic Pseudozilian Formation are present. Further along the section, the dark greenish-grey Triassic formation is easily traceable, and there is a good outcrop north of the farm Urbanek (site 557) ending the section. The Pseudozilian Formation, however, continues towards the Sv. Miklavž composite section (Buser, 1977). This northern part of the section is separated from the southern one, by a major thrust fault which corresponds to the Marija Reka Fault. This fault extends both to the west and east from Krvavica Mt. to Mrzlica Mt. (Grad, 1969; Buser, 1977, 1979; Placer, 1998b, 2008) (Fig. 1). The southern segment of the section represents a separate lithostratigraphic column, which could be truncated by a fault (Fig. 5).

The Brložen section (Figs. 1, 8–10; Tables 1–2, 4; Appendices 1–2)

The Brložen section is located 2 km south of the village Loke on the eastern side of Brložen Mt. It is compiled from almost continuous outcrops interrupted by short, covered segments. The beds are always dipping to the north, gently or very steeply, the order of sites in the description is from south to north.

The succession starts in the volcanoclastic-rich Pseudozilian Formation at outcrop 254. After a short gap in outcrops and stratigraphy, the outcropping succession continues with a significantly younger 60 cm thick brecciated limestone bed with medium grey clasts in an ochre matrix at site 555. The texture of the rock is wackestone, with finely fragmented bioclasts of unknown origin and very rare calpionellids. The lorica of the *Chitinoidella boneti* could be identified, indicating the lowermost upper Tithonian Chitinoidellids Zone, *Boneti* Subzone (sensu Benzaggagh, 2020).

Above it, roughly 30 m higher, the succession continues with alternating marlstones and limestones (sites 625 and 626). The brownish–grey marl is a thin laminated shale. The limestone is mostly just a few centimeters thick, but occasionally, m-thick beds can be observed. The thin-layered limestone beds are fine-grained and vary in colour from light grey to yellow and sometimes pink. The thick layers are coarse-grained calcarenites. The find grade limestones are radiolarian wackestone, sparse, or packed biomicrite. Besides the calcified radiolarians, a few calpionellid, benthic foraminifers, and ostracods occur. The existence of *Calpionella alpina, Chitinoidella boneti, Ch. elongata*, and *Crassicolaria intermedia* indicates the lower upper Tithonian *Crassicolaria* Zone or A Zone, Chitinoidellids/Primitive Calpionellids Subzone or A0 Subzone (sensu Benzaggagh, 2020) or *T. remanei* Zone (sensu Reháková, 2000). Within the foraminifers, *Vercorsella* sp., *Spirillina* mg. *kübleri*, and *Lenticulina* sp. could be recognized. Due to the tectonic influences, the appearance of folds and post-depositional fabrics are common.

After an approximately 20 m thick covered interval, a more than 130 m thick continuous section is exposed. It starts with brecciated limestone (site 627), which is overlain by a relatively homogenous succession consisting of well-bedded grey, pink, and ochre limestones with common grey calcarenite intercalations and occasionally cherty layers and nodules. The limestone beds are 1–10 cm thick and intercalated with clay films or upwards finely layered several cm to dm thick marls (from sites 628 to 251). In the last 20 m, the bedding thickens up to roughly 1 m. At the end of the succession (sites 251, 593 and 634), similar thick brecciated limestone beds occur. In some places (sites 253 and 252), the folding of the thinly layered limestone could be observed. The texture of these limestones is wackestone with varying amounts of fossils, from fossiliferous biomicrite to packed biomicrite. Limonitic mottles and opaque minerals are dispersed in the calcareous matrix. Finely fragmented bioclasts, followed by radiolarians, echinoderm skeletons, and c-dinocysts are the most common components. Besides them, a few calpionellids, benthic and planktonic foraminifers (hedbergellids indet.), and ostracods also could be recognized.

At site 628a, based on the existence of *Praetintinnopsella andrusovi, Calpionella alpina*, and *Tintinnopsella carpathica,* this bed also belongs to the lower upper Tithonian *Crassicolaria* Zone, Chitinoidellids/Primitive Calpionellids Subzone. Among the foraminifers, only a few specimens of *Spirillina* mg. *kuebleri* appear. A relatively large fragment of *Rivularia lissaviensis* is present, indicating that the platform was not far away, as its fragile skeleton would not have been able to withstand prolonged transport.

Higher up in the section (sites 628), besides the relatively common *Colomisphaera carpathica* and *C. fortis,* a few specimens of *Crassicolaria intermedia* and *Tintinnopsella remanei* show that this layer belongs to the *Tintinnopsella Intermedia* Subzone (A1) within the *Crassicolaria* Zone. In the micritic limestone layers of the upper part of the Brložen section (from site 630 to 252), the index fossil content is relatively homogeneous, consisting of c-dinocysts such as *Colomisphaera carpathica, C. alpina,* and *Crustocadosina semiradiata;* calpionellids such as *Tintinnopsella carpathica* and *Calpionella alpina*. Additionally, a few specimens of spirillinids, namely *Spirillina* mg. *kuebleri* and *S.* mg. *minima,* occur. These fossils also suggest the upper Tithonian *Tintinnopsella Intermedia* Subzone.

In the succession, the multiple calcarenite layers appear, for example, at sites 628, 253, 629, 630, 631, 632, and 633. Their thickness ranges from 30 to 70 cm.

At site 630, the thickness of the calcarenite bed varies between 70–200 cm, most probably due to syn-sedimentary or early diagenetic faulting. These calcarenite beds yield fossils primarily of platform origin, including benthic foraminifers, calcimicrobes, microproblematica, green algae, mollusk shell fragments, and sponges. Among the hemipelagic elements, only *Colomisphaera alpina* could be recognized.

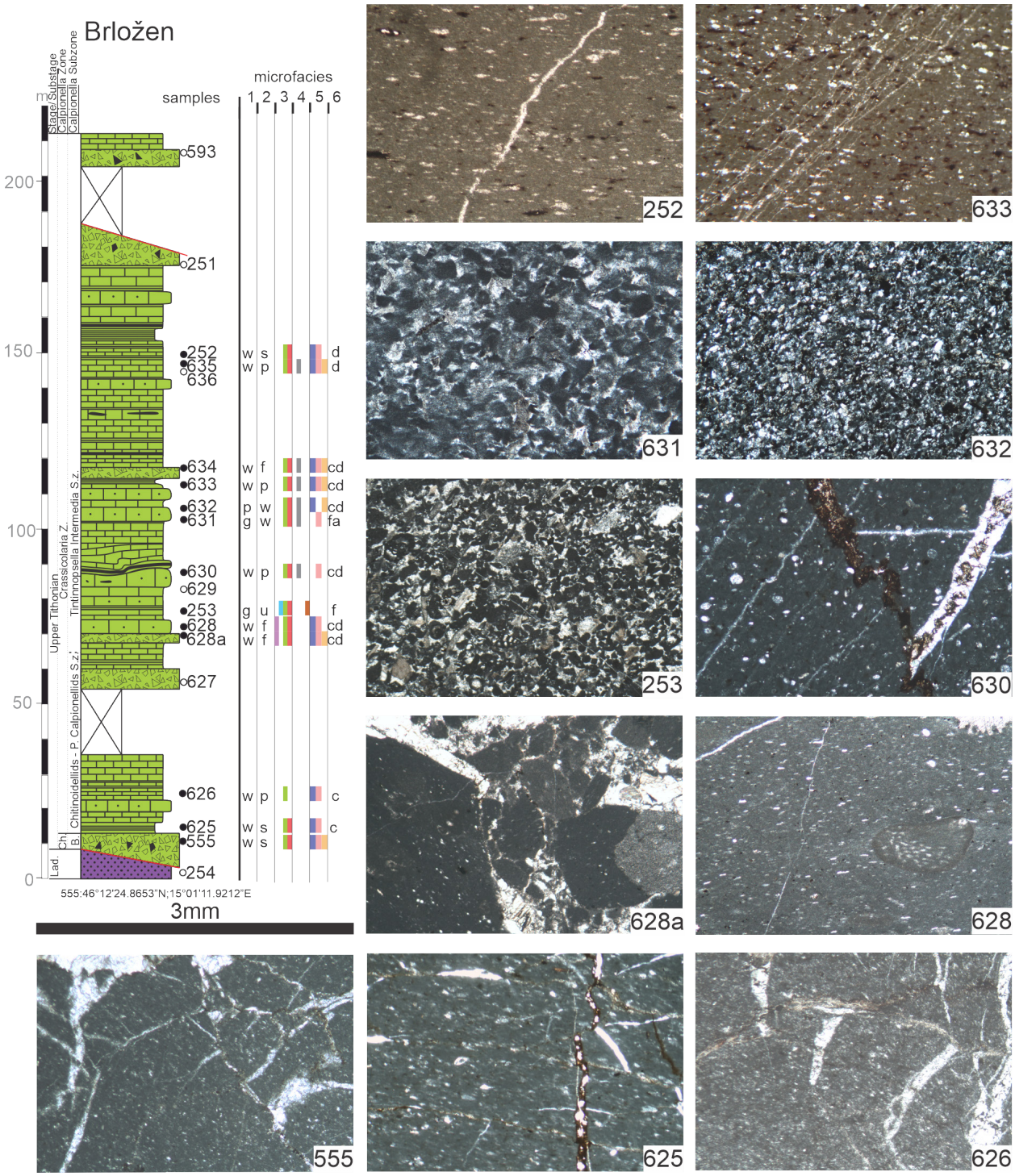

Fig. 8. Stratigraphic column and microfacies of the Brložen section. For the legend, see Fig. 2. The scale bar is 3 mm. Abbreviations: Lad. (Ladinian); Ch. (*Chitinoidella*); B. (*Boneti*); Z. (Zone); P. (Primitive); S.z. (Subzone).

The sample from site 253 contains a diverse fossil assemblage, dominating the agglutinated foraminifers such as *Redmondoides lugeoni, Nautiloculina oolithica, Buccicrenata* sp., *Pseudogaudryina* sp., *Valvulina* sp., *Dobrogeina* sp., and textulariids indet. Involutinids are relatively common, namely *Protopeneroplis striata, Coscinoconus alpinus*, and *Trocholina* cf. *conica*. Besides them, *Mohlerina basiliensis, Neotrocholina valdensis, Lenticulina* spp., and *Istruloculina* sp. could be identified. The microproblematicum *Thaumatoporella parvovesiculifera*, as well as the green algae *Aloisalthella sulcata* (formerly *Clypeina jurassica*) and other Dasycladales sp., also occur. This fossil assemblage indicates the late Tithonian age.

Higher up in the section, in the calcarenite beds (sites 631 and 632), a few pelagic-hemipelagic elements, such as *Colomisphaera alpina, Calpionella alpina*, and *Spirillina* mg. *kuebleri,* could be identified. Their assemblages are poorer in the

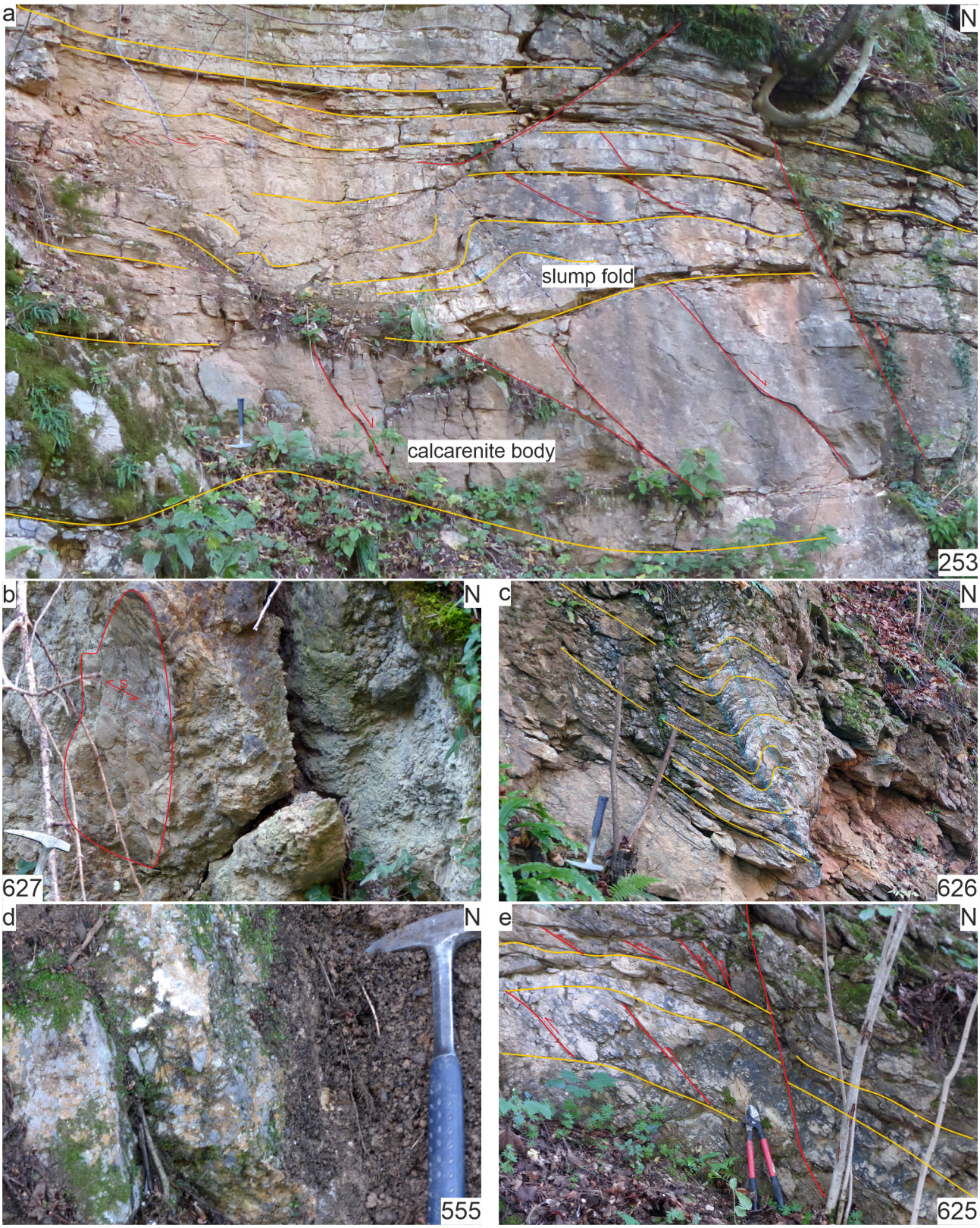

Fig. 9. Lithofacies and structural features of the Brložen section. For the legend, see Fig. 3. **a** calcarenite body with alternating thickness covered with layered limestone slumpfolds is covered with the following strata; thrust joints taper to the bedding, and faults sometimes are covered with following beds inside the resedimented limestones, Biancone Fm., **b** breccia body and sinistral strike-slip fault surface, **c** over calcarenite bed the thin-layered limestone is folded into close folds with oblique fold axial plane, **d** Brecciated limestone on the southern contact of Biancone Fm with Pseudozilian Fm., **e** small thrust joints indicate top-to-S direction these joints only appear to connect clay films between layers, Biancone Fm.

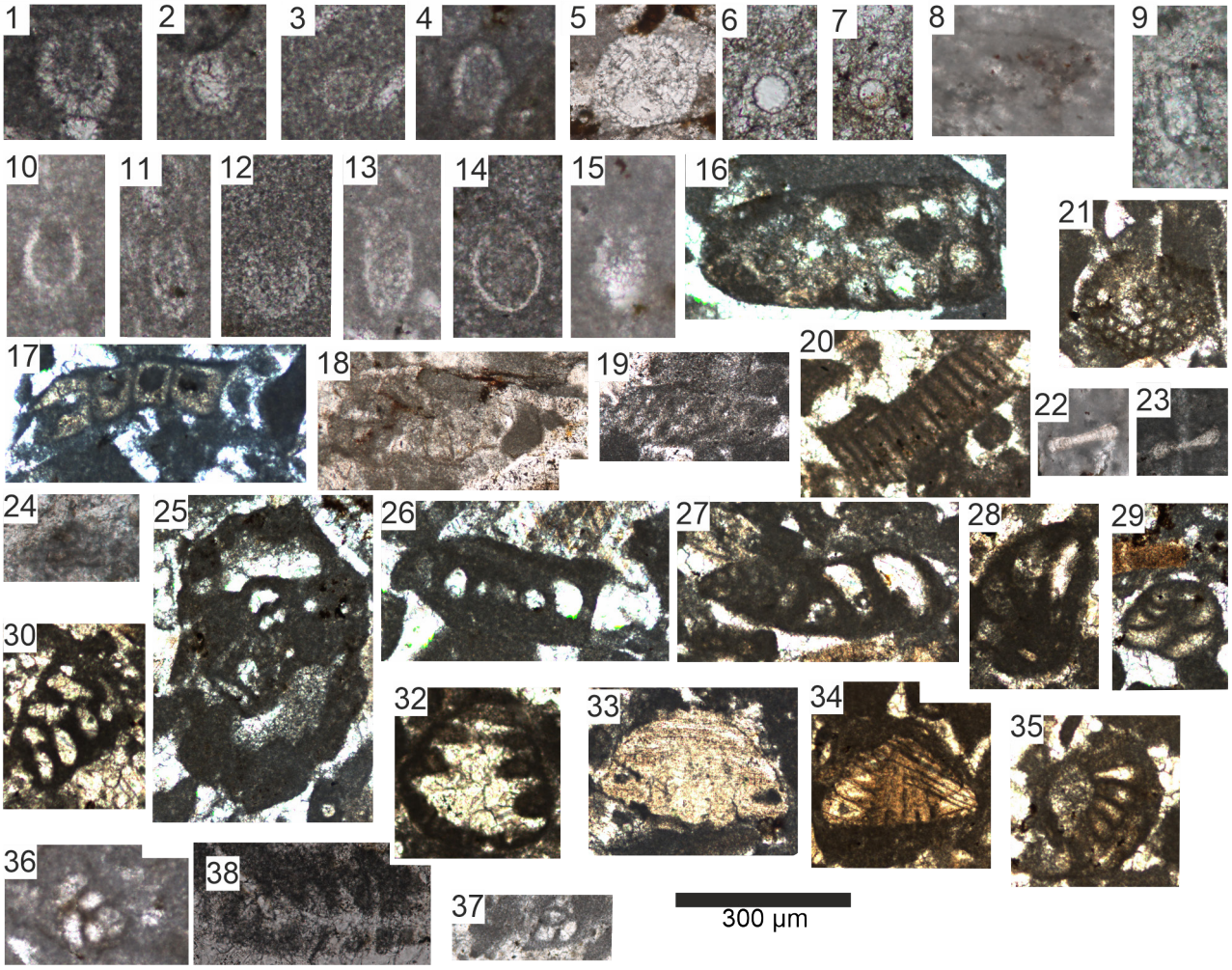

Fig. 10. Microfossils of the Brložen section. **1-3** sample 628: **1-2** *Colomisphaera carpathica* (Borza), **3** *Colomisphaera fortis* Řehánek, **4** *Crustocadosina semiradiata* (Wanner), sample 630, **5** *Colomisphaera alpina* (Leischner), sample 632, **6-7** *C. carpathica* Borza, sample 635, **8** *Chitinoidella elongata* Pop, sample 625, **9** *Chitinoidella boneti* Doben, sample 626, **10-11** *Praetintinnopsella andrusovi* Borza**,** sample 628c, **12-13** sample 628: **12** *Tintinnopsella remanei* Borza, **13** *Crassicolaria intermedia* Duran Delga, **14** *Calpionella alpina* Lorenz, sample 630, **15** Charophyta gyrogonite, sample 628, **16-17** sample 253: **16** Dasycladales sp., **17** *Aloisalthella sulcata* Alth, **18-19** sample 631: **18** ?*Suppiluliumaella* sp., **19** ?*Linoporella* sp., **20-21** *Thaumatoporella parvovesiculifera* (Raineri), sample 253, **22-23** sample 625, **22** *Spirillina minima* Schako, B, **23** *Spirillina* mg. *kuebleri* Danitch, **24** Vercorsella sp., sample 626, **25-35** sample 253: **25** Buccicrenata sp., **26** *Nautiloculina oolithica Mohler,* **27** *Paleogaudryina* sp., **28** *Freixialina planispiralis* Ramalho, **29** *Dobrogelina* sp., **30** *Redmondoides lugeoni* (Septfontaine), **32** *Coscinoconus alpinus* Leupold, **33** *Trocholina* cf. *conica* (Schlumberger), **34** *Neotrocholina valdensis* (Reichel), **35** *Protopeneroplis striata* Weynschenk, **36***Textularia* sp., sample 630, **37-38** sample 631: **37** *Valvulina* sp., **38** *Coscinoconus elongatus* Leupold. The scale bar is 300 µm.

number of species, but among the foraminifers, *Coscinoconus elongatus* and nodosarids, and among the green algae, ?*Linoporella* sp. and ?*Suppiluliumaella* sp. appear as newer taxa. Based on the stratigraphic range of the aforementioned taxa, the age of these calcarenite beds is late Tithonian. The approximately 200 m thick Biancone succession of the Brložen section is late Tithonian in age.

The Kozlov grič section (Figs. 1, 11–14; Tables 1–2, 4; Appendices 1–2)

The Kozlov grič section is located 750 m south of the village Loke and west of Kozlov grič (Kozlov Hill). The nearly 70 m section consists of almost continuous outcrops. Because of the southerly dip, the order of sites in the description is from north to south.

In the northernmost part of the section (site 610), a dark grey brecciated silicified limestone layer is present, which probably resulted from syn-sedimentary brecciation. It is overlain by ~17-m-thick (up to site 613) fine-grained grey marls in which limestone layers occasionally appear (e.g., sites 611 and 612). The composition of the breccia clasts is wackestone and packed biomicrite which contains radiolarians. The radiolarians have been deformed and lie in an oriented manner due to pressure. Fragmented calcareous bioclasts and opaque minerals are also common (Fig. 11). At site 612, the limestone intercalation is wackestone, composed of packed biomicrite with fragmented calcareous bioclasts of unknown origin and filaments.

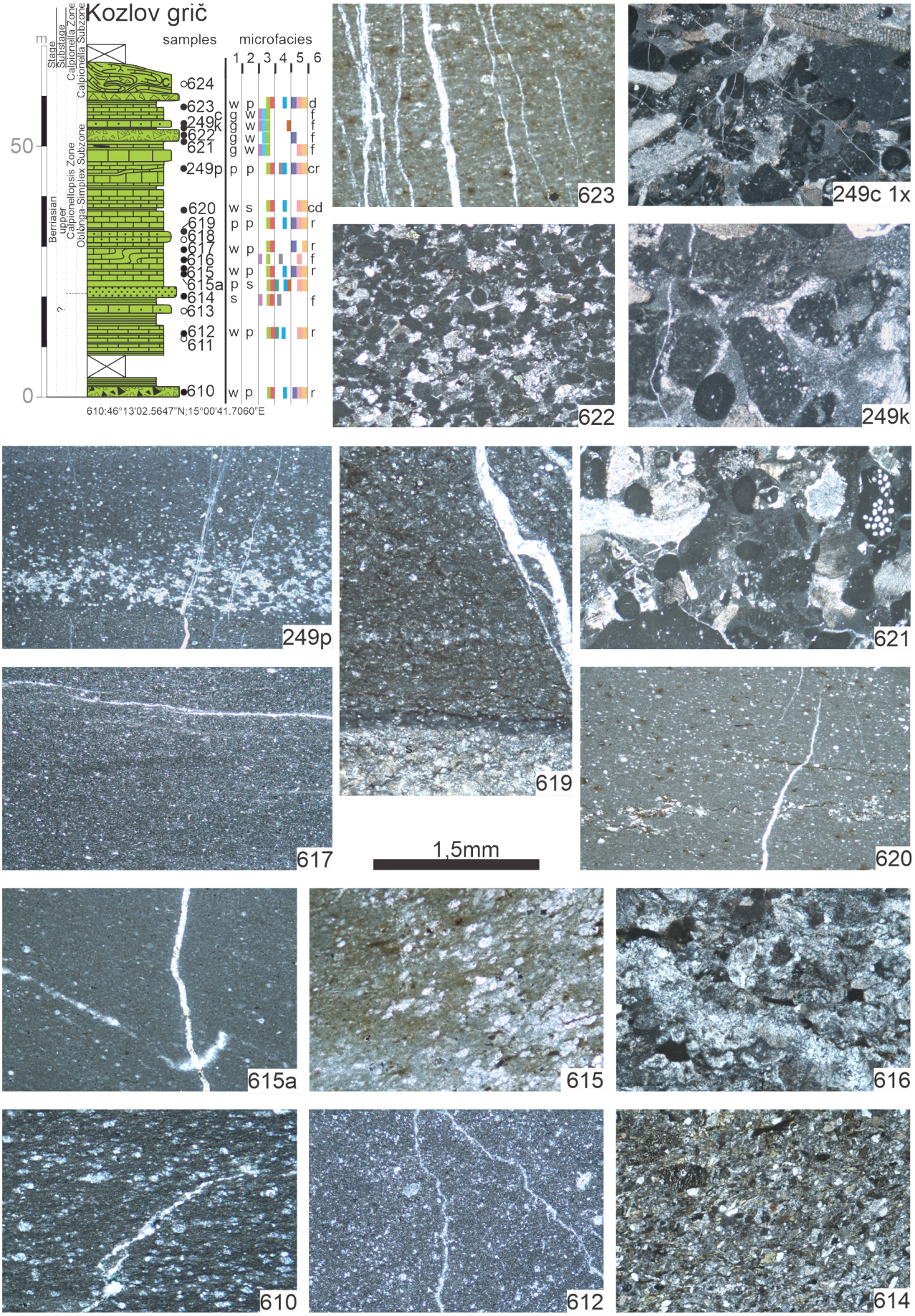

Fig. 11. Stratigraphic column and microfacies of the Kozlov grič section. For the legend, see Fig. 2. The scale bar is 1.5 mm, except for 249c 1×, where it is 3 mm.

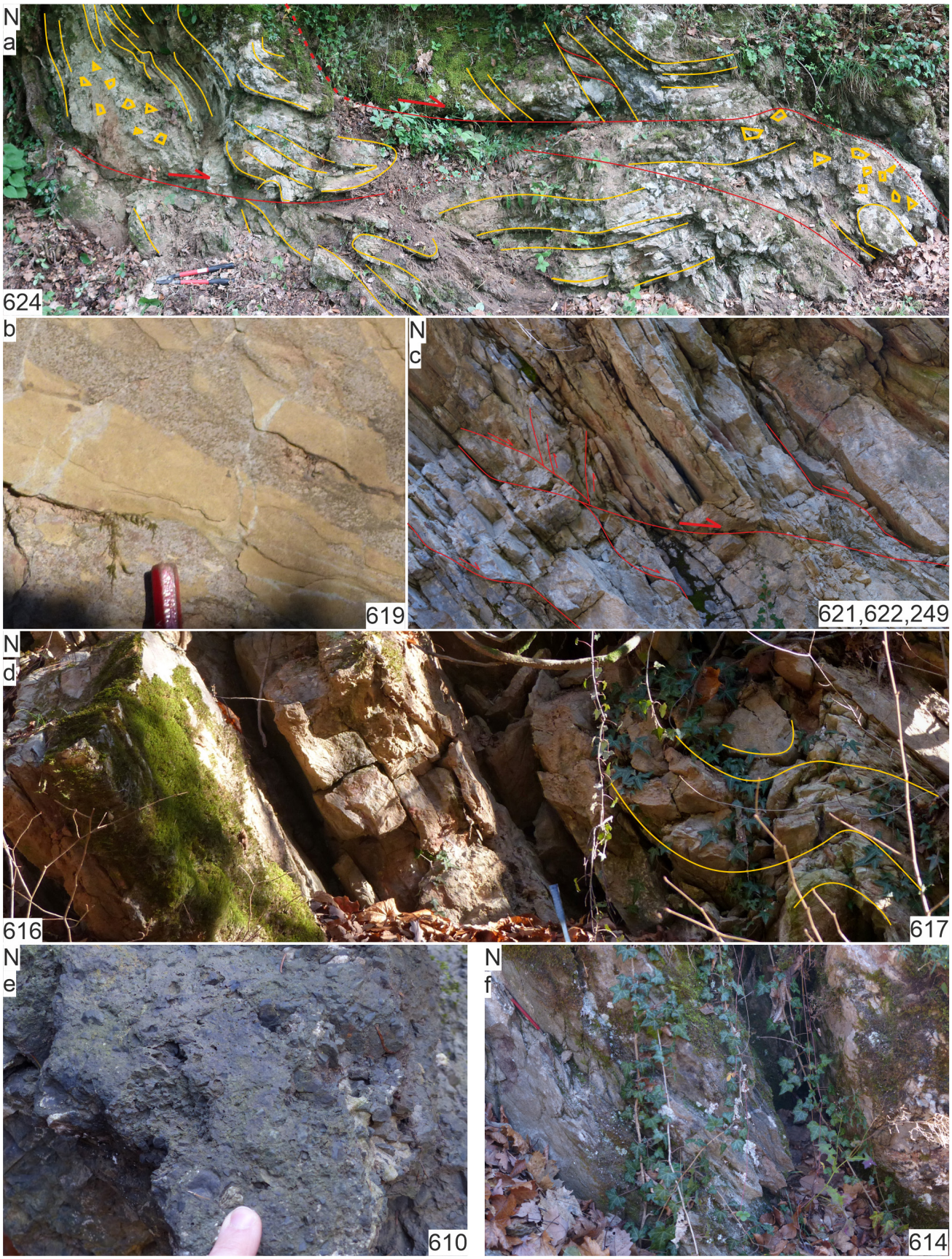

Fig. 12. Lithofacies and structural features of the Kozlov grič section. For the legend, see Fig. 3. **a** breccia bodies and thin layered limestone with marl chaotically folded in a slump fold, Biancone Formation, **b** thin films of clay-rich sediment over the coarse limestone layers, Biancone Fm., **c** limestone layers and calcarenite bodies cut through by pretilt thrust fault pairs that run into the clay richer interlayers, Biancone Fm., **d**: limestone layers and calcarenite beds sandwich almost isoclinally folded layers another sump fold in Biancone Fm. E: Dark chert breccia on the northernmost outcrop in Biancone Fm. F: Coarse sandstone flysch-like layer containing basic volcanic material between limestone beds, Biancone Fm.

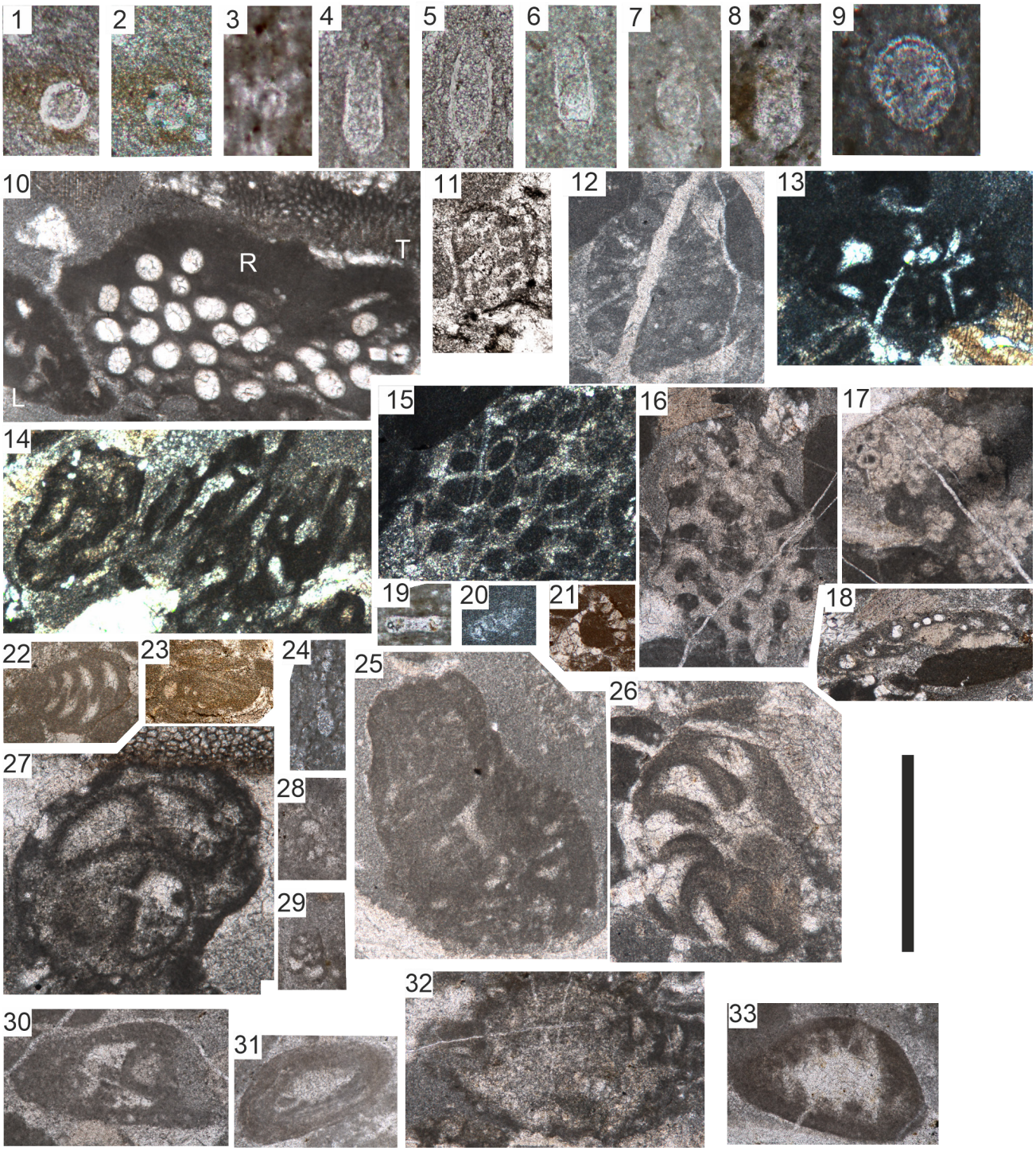

Fig. 13. Microfossils of the Kozlov grič section. **1-2** *Stomiosphaera moluccana* Wanner (**2**: crossed Nicols), sample 620, **3** *Colomisphaera lapidosa* (Vogler), sample 623, **4-7** sample 620: **4-5***Calpionellopsis oblonga* (Cadisch), **6** *Tintinnopsella carpathica* (Murgeanu & Filipescu), **7** *transitional form of Lorenziella plicata Remane and Lorenziella hungarica Knauer & Nagy and,* **8-9** sample 249p: **8** *Calpionellopsis* simplex (Colom), **9** *Stomiosphaerina proxima* Řehánek, **10** *Rivularia lobatum* (Yabe & Toyoma) (R), *Lithocodium aggregatum* Elliott (L) and *Thaumatoporella parvovesiculifera* (Raineri) (T), sample 621, **11** ?*Teutloporella* sp., sample 622, **12-14** sample 249k: **12** Dasycladales (?*Triploporella*) sp., **13** *Clypeina* sp., **14** *Isnella* aff. *misiki* Senowbari-Daryan sensu Schlagintweit & Gawlick, **15-17** sample 249c: **15** microproblematicum tubes with calcareous micritic wall, **16** *Cladocoropis mirabilis* Felix, **17** *Muranella parvissima* (Dragastan), **18** *Mohlerina basiliensis* (Mohler), sample 616, **19** *Spirillina italica* Dieni & Massari, sample 623, **20** silicified textulariids, sample 621, **21-23** sample 622: **21** *Protopeneroplis* sp., **22** *Redmondoides lugeoni* (Septfontaine), **23** *Istriloculina* sp., **24** silicified *Spirillina* sp., sample 249p, **25-26** sample 249k: **25** *Labyrinthina*? sp. A, **26** *Pfenderina neocomiensis* (Pfender), **27-33** sample 249c: **27** Lituolidae indet., **28** *Trochammina* sp., **29** textulariid sp. **30** *Everticyclammina* sp., **31** *Coscinoconus molestus* (Gorbachik), **32** *Frentzenella involuta* (Mantsurova) **33** *Coscinoconus campanellus* (Arnaud-Vanneau et al.). The scale bar is 200 μm at figures 1-9 and 1000 μm at figures 10-33.

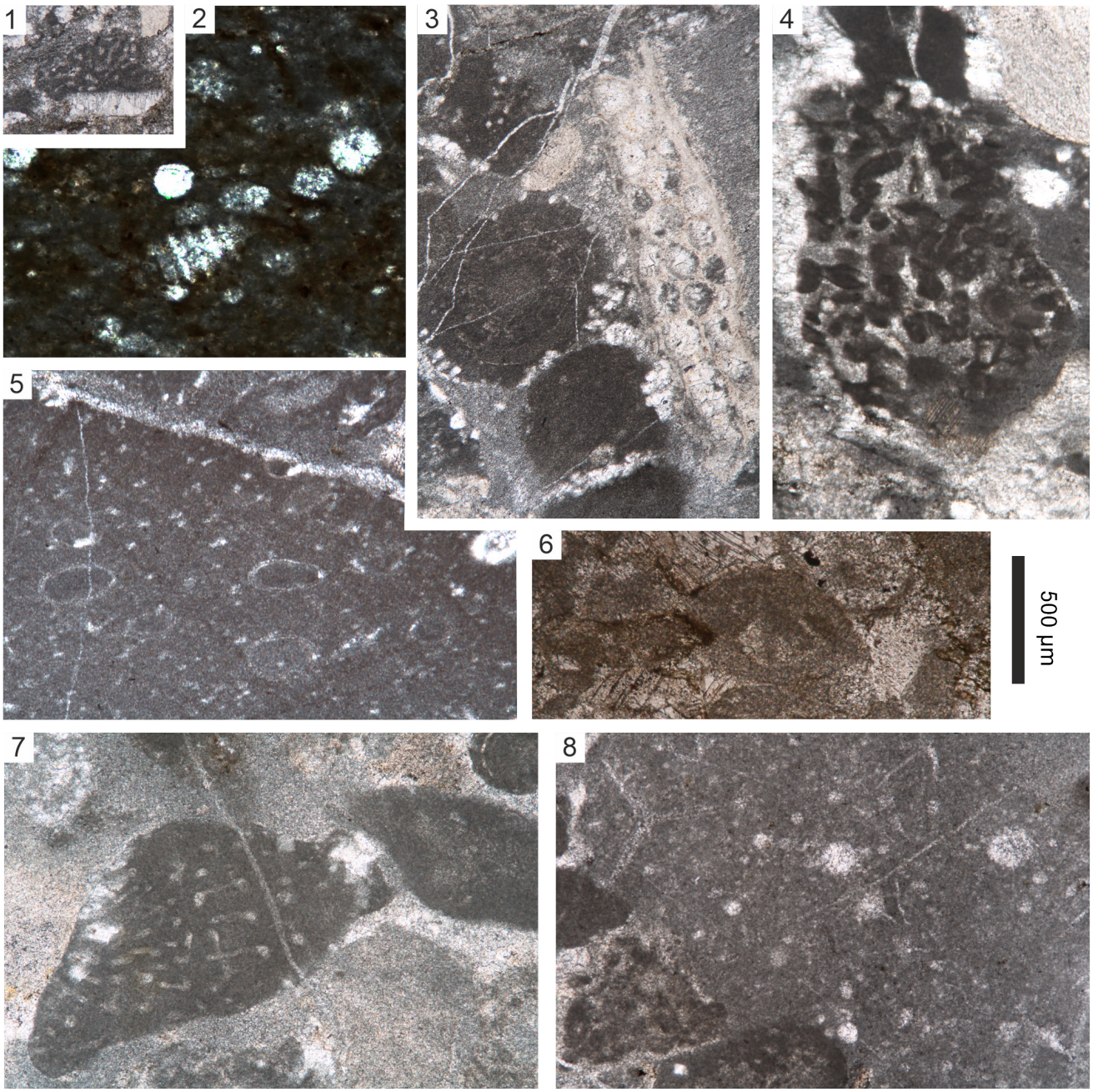

Fig. 14. Microfossils of the Kozlov grič section. **1** Stromatoporoidea sp., sample 616, **2** well-preserved radiolarians, sample 249p, **3-5** sample 621: 3 grainstone with the skeleton of Bryozoa, radial ooid with peloid nucleus, peloid, the latter show the trace of microborer (microbe or fungi), **4** extraclasts, peloidal grainstone with miliolinid foraminifera, **5** extraclasts, wackestone with ostracods, and fine calcitic fragments, **6** *Carpathiella triangulata* Misík, Sotak & Ziegler, sample 622, **7-8** sample 249c: **7** fragment of Porifera skeleton, **8** extraclasts, radiolarian wackestone. The scale bar is 500 µm.

Over the first calcarenite layer (site 613), the marl succession is followed by an approximately 2 m-thick sandstone bed (site 614). The grey sandstone is composed of a silicified matrix and contains various metamorphosed heavy minerals, as well as volcanic and sedimentary rocks. Among the minerals, chrome-spinel with a chlorite coating and secondary opaque minerals, such as ilmenite and magnetite, are the most common. The majority of the rock grains are chlorite, showing a metamorphic appearance; basalt with an equigranular fabric is metamorphosed and calcified; and dolerite, which contains plagioclase mesh and in between pyroxene altered into chlorite. These minerals and rock fragments indicate an ophiolitic provenance of this bed. (petrology by Józsa, personal com., see correlations in the Discussion chapter) There are only a few sedimentary rock fragments, including micritic limestone with poorly preserved benthic foraminifers such as the upper Tithonian–lowermost Aptian *Neotrocholina valdensis*, nodosarid sp., and foraminifera indet.

Above the sand layer, in the next 10 m (sites 615–619), the limestone content dominates and is

separated by just thin clay films. A 30 cm thick medium grey calcarenite bed occurs at site 616.

Rip-up mudclasts were observed at site 619. The light grey-ochre mottled limestones, with tiny terracotta mottles (sites 615a, 615, 617, and 619), are radiolarian wackestone/packestone, packed biomicrite. Besides the limonite mottles, other opaque minerals are also common. The arrangement of the fossils (radiolarian and calcareous fragments) often shows gradation (Fig. 11.). Apart from the calcified radiolarians, only a few sponge spicules and fragments of Echinodermata and thin mollusca shells appeared. The 60 cm thick calcarenite bed (site 616) is a partly silicified grainstone, packed biomicrite with high amounts of opaque minerals. The fossil assemblage consists of Echinodermata, benthic foraminifera, and Stromatoporoidea. Among the foraminifers, *Mohlerina basiliensis*, *Redmondoides lugeoni*, *Lenticulina* sp., nodosarid sp., and *Valvulina* sp. could be identified. The co-occurrence of these species suggests the Kimmeridgian–Valanginian interval. The microfacies indicates that the northern part of the section (up to site 619) was deposited in a pelagic, toe-of-slope environment. This explains the appearance of the layers (at site 617) folded into a slump fold.

From site 620 to site 623, in the thin-bedded fine-grained limestone succession, the calcarenite intercalations become more common and thicker, reaching a maximum thickness of 1 m. It can be observed in a small quarry (sites 249 p, c, k, 621-623). Here, the steeply dipping layers are cut by faults that are formed on low angles compared to the bedding planes (Fig. 12).

The limestone layers are similar in macroscopic appearance to the previous ones, i.e., ochre-grey mottled with terracotta patches (sites 620, 249p, and 623). Their texture is also wackestone-packstone, packed biomicrite with common opaque minerals. The main difference is that in addition to the radiolarians, calpionellids and c-dinocysts are also present, although in smaller numbers.

At sites 620 and 249p, the co-occurrence of *Calpionellopsis oblonga, Tintinnopsella carpathica, C. simplex, Lorenziella plicata-hungarica, Stomiosphaera moluccana,* and *S. proxima* indicate the upper Berriasian substage, *Calpionellopsis* Zone, *Oblonga-Simplex* (D2) Subzone or *Oblonga* Subzone (sensu Allemann et al., 1971). In the upper most studied micritic layer (site 623), only the upper Oxfordian–lower Valanginian *Colomisphaera lapidosa* occurs. Besides these planktonic forms, only a few ostracods and benthic foraminifers, such as *Spirillina italica* and textulariid sp., could be identified.

At site 249c, the texture of the fine to medium-grained calcarenite layers (sites 621, 622, 249k, c) is grainstone, poorly washed biosparite. The intraclasts and extraclasts are common. Each studied sample contained ooids, oncoids, and pellets. Among the bioclasts, the fragments of echinoderms and the benthic foraminifers are the most frequent. Besides them, the remnants of platform-dwelling organisms, such as microproblematica, green algae, Porifera, Stromatoporoides, Vermes, and Bryozoa, form diverse fossil associations. The Foraminifera fauna is dominated by agglutinated species, such as *Redmondoides lugeoni, Trochammina* sp., textulariid spp., and larger foraminifers like *Pfenderina neocomiensis, Everticyclammina* sp., *Labyrinthina*? sp., and Lituolidae indet. Involutinids are relatively diverse, represented by *Coscinoconus molestus, C. alpinus, C. campanellus, Frentzenella involuta,* and *Protopeneroplis* sp. Besides them, specimens of *Mohlerina basiliensis, Neotrocholina valdensis,* and *Istriloculina* sp. also could be identified. The fragments of microproblematica are frequent, such as ?*Crescentiella morronensis*, *Lithocodium aggregatum, Thaumatoporella parvovesiculifera, Isnella* aff. *misiki, Muranella parvissima,* and tubes with calcareous micritic walls. The algae are represented by *Rivularia lobatum, Clypeina* sp., ?*Teutloporella* sp., ?*Triploporella* sp., and Dasycladales sp. The Porifera *Cladocoropis mirabilis* and Vermes *Carpathiella triangulata* could be recognized. These fossils are characteristic of shallow, photic-zone marine environments. The most common extraclasts are the radiolarian wackestone grains. In the semi-consolidated state, the basin sediment was torn up and crumpled by the moving debris. The microfossil assemblages are typical of the Tithonian—Valanginian interval. The *Pfenderina neocomiensis, Coscinoconus campanellus,* and *Frentzenella involuta* narrow down the succession's age to the late Berriasian–Valanginian. The clasts of peloidal grainstone with miliolinid foraminifers or wackestone with ostracods (site 621) may originate from a different environment of the same age as the platform or even from an older formation.

Over the previously described calcarenite layers, limestone and marl succession returns below site 624, where a chaotically folded unit with disrupted carbonate breccia bodies follows. The bedding of the layers turns from steeply dipping to the south into sub-horizontal. The breccia bodies and the slump folds are then cut through by a low-angle fault with top to-the-north movement. (Fig. 12a)

Summing up, similarly to the Brložen section, the Kozlov grič section built-up from the Biancone Limestone, deposited in a proximal hemipelagic toe of slope–slope environment during the late Berriasian, *Calpionellopsis* Zone, *Oblonga-Simplex* (D2) Subzone or *Oblonga* Subzone. The succession is a radiolarian micritic limestone with intercalated calcarenite layers that become more common, thicker, and more proximal upwards.

The Sveti Miklavž section (Fig. 1, 15–19; Tables 1–2, 5; Appendices 1–2)

The composite Sveti Miklavž (or Sv. Miklavž) section was created based on field observations and detailed studies of sites around the former settlement of Sveti Miklavž (46°6′37″N 14°44′39″E). It covers an area of ~3.5 km wide in an E–W direction and ~1.5 km long in an N–S direction. In this studied area, the bedding dip direction is alternating between north and south, dipping steeply to sub-vertical or moderately to gently. These facts make the compilation of a continuous succession impossible and the estimations of thickness and correlation difficult.

The section begins at the south, on the western side of Kukel Mt. (site 352), where layers of the light grey Triassic Platform Limestone are exposed. Above it (sites 346, 347, 349, 554a, b), along a NE–SW section, the ochre-coloured carbonate layers can be followed with a thickness of more than 200 m. The succession consists of limestone beds (site 554a) of variable thickness (5–50 cm), with calcarenite beds (e.g., site 347, 554b) and thin-bedded marl or marly limestone intercalations (e.g., site 349). At site 554a, the texture of the limestone is radiolarian wackestone, sparse

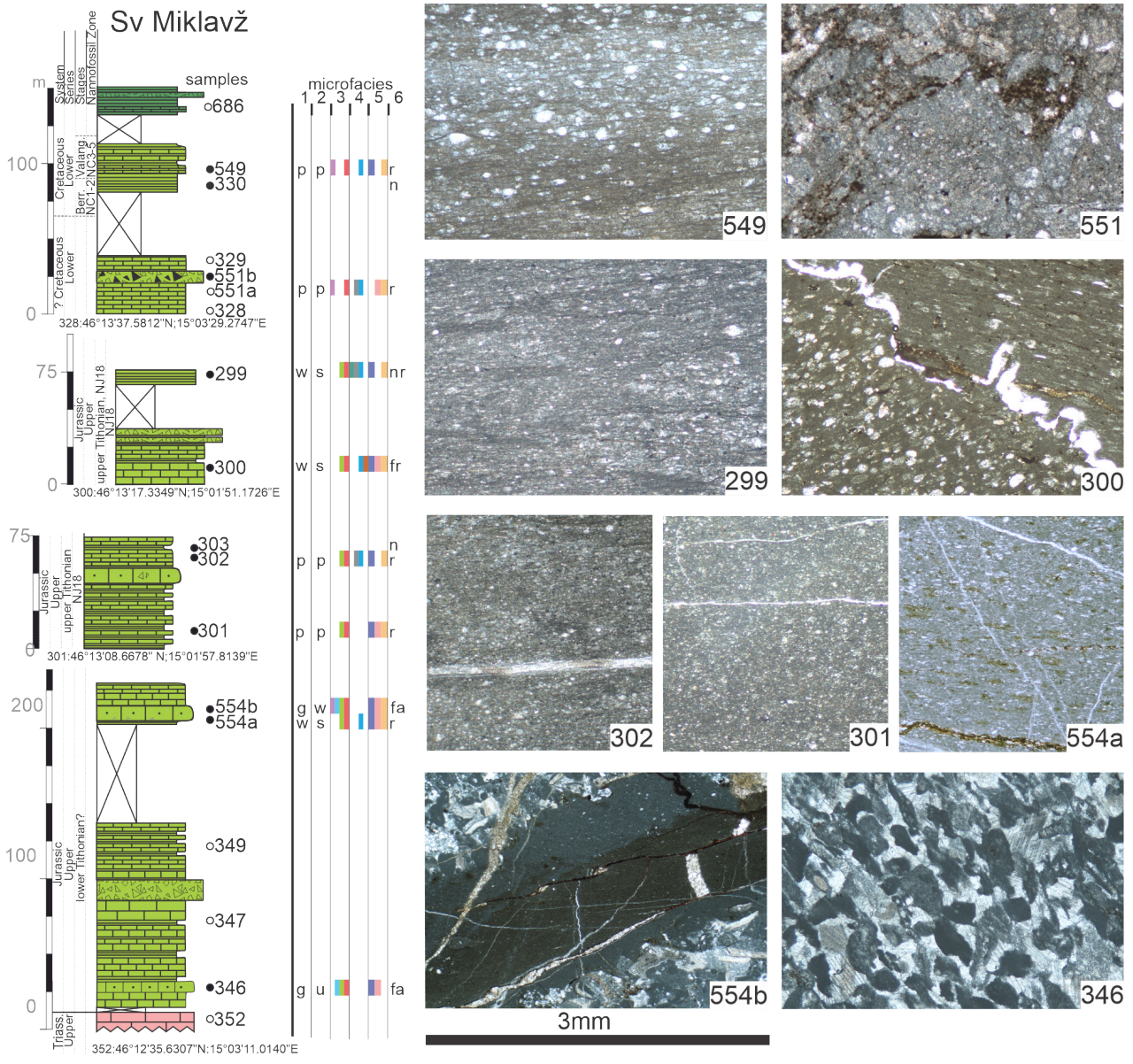

Fig. 15. Stratigraphic column and microfacies of the Sveti Miklavž section. For the legend, see Fig. 2. The scale bar is 3 mm, except for 554b, where it is 6 mm. Abbreviations: Triass. (Triassic); Berr. (Berriasian); Valang. (Valanginian).

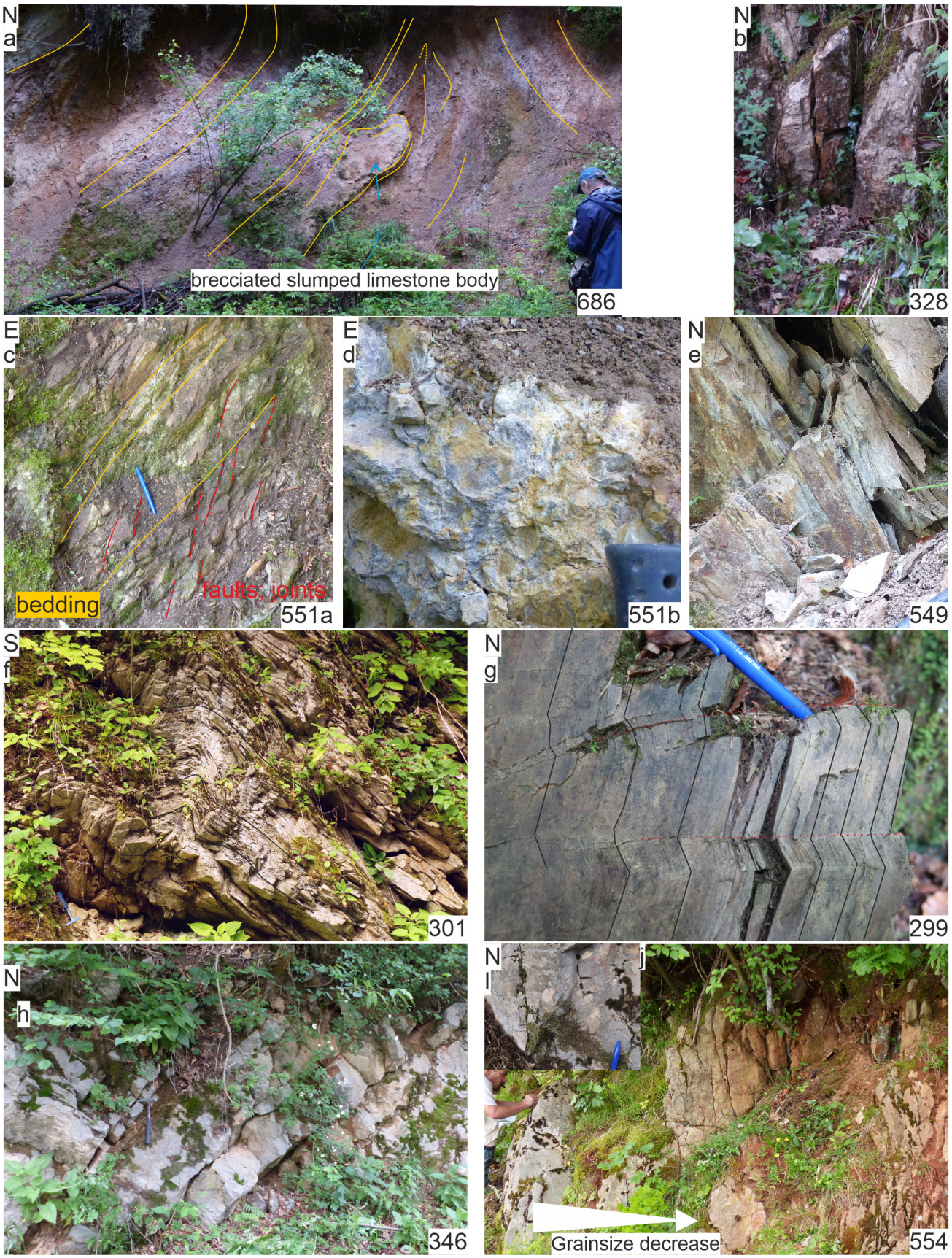

Fig. 16. Lithofacies and structural features of the Sveti Miklavž section. For the legend, see Fig. 3. **a** calcarenitic body slump folded in marl, Lower Flyschoid Fm., **b** *bedded chert between pelagic limestone layers*, Biancone Fm., **c** *chertified pelagic limestone*, Biancone Fm., **d** *l*imestone breccia, Biancone Fm., **e** thin-laminated marl, *Biancone* Fm., **f** close detachment folds in thin layered limey marlstone, Biancone Fm., **g** kink-folds in the thin laminated silicified marl, Biancone Fm., **h** *t*hick-bedded resedimented limestones at the base of *the* Biancone Fm., **i** fine-grained mud-clasts inside *a* calcarenite body of *the* Biancone Fm., **j** calcarenite with mud-clasts following bedded limestone of the Biancone Fm.

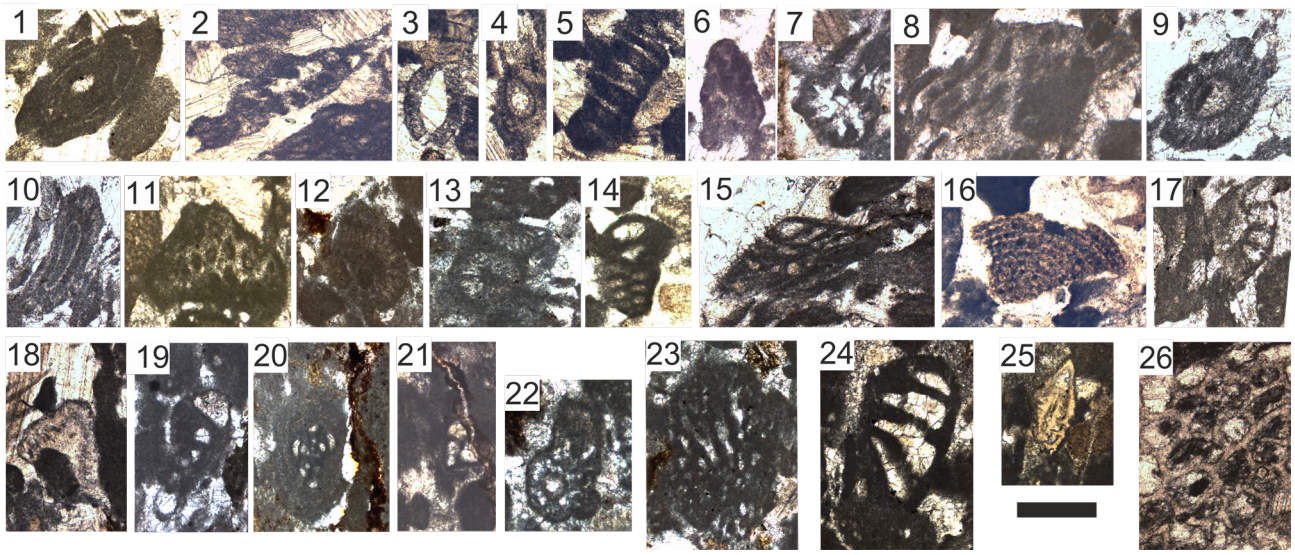

Fig. 17. Microfossils of the Sveti Miklavž section. **1-10** sample 346: **1** *Crescentiella morronensis* (Crescenti), **2** *Acicularia* sp., **3-4** Charophyte gyrogonites, **5** *Anisoporella* sp., **6** *Cylindroporella* sp., **7** *Clypeina* sp., **8** *Salpingoporella* sp., **9-10** *Linoporella* sp., **11-13** sample 554b: **11** *Salpingoporella* sp., **12** *Salpingoporella*? *sellii* (Crescenti), **13** *Tethysicodium elliotti* (Dragastan), **14-19** sample 346: **14** textulariid sp., **15** larger agglutinated indet., **16** *Pseudospirocyclina mauretanica* Hottinger, **17** *Protopeneroplis* sp., **18** *Ichnusella infragranulata* (Noth), **19** *Spirothalmidium* mg. *kaptarenkoae* Danitch, **20-26** sample 554b: **20** *Glomospira* sp. in ooids, **21** *Valvulina* sp., **22** *Labyrinthina mirabilis* Weynschenk, **23** *Parurgonina caelinensis* Cuvillier, Foury & Pignatti Morano, **24** pfenderinid? sp., **25** *Lenticulina* sp., **26** Bryozoa, sample 554b. The scale bar is 200 μm.

biomicrite with fragmented bioclasts of undeterminable origin, and dispersed limonite mottles. The studied calcarenite layers (sites 346 and 554b) are unsorted or poorly washed biosparite, with extra- and intraclasts, ooids, pellets, and limonite mottles. The most common bioclasts are benthic foraminifers, green algae, microproblematica, and fragments of echinoderms. Both calcarenite layers yielded the following taxa: *Mohlerina basiliensis*, *Crescentiella morronensis*, *Thaumatoporella parvovesiculifera*, and *Salpingoporella* sp. A. In the lower layer (site 346), besides the fossils listed above, *Lithocodium aggregatum*, *Acicularia* sp., Charophyte gyrogonite, Dasycladales sp. indet., *Anisoporella* sp., *Clypeina* sp., *Cylindroporella* sp., *Linoporella* sp., textulariids, *Pseudospirocyclina mauretanica, Ophthalmidium* mg. *marginatum*, *Spirothalmidium* mg. *kaptarenkoae*, *Coscinoconus alpinus*, *Protopeneroplis striata*, *Protopeneroplis* sp., *Ichnusella infragranulata* also occur. While in the upper layer (site 554b) among the green algae *Aloisalthella sulcata*, *Salpingoporella*? *sellii*, *Tethysicodium elliotti* could be identified. Here, in the foraminifera association, *Glomospira* sp., *Redmondoides lugeoni*, *Valvulina* sp., *Labyrinthina mirabilis*, *Parurgonina caelinensis*, pfenderinid sp., and *Lenticulina* sp. also appear. Based on the stratigraphic distribution of these taxa, especially the co-occurrence of *Tethysicodium elliotti* and *Labyrinthina mirabilis,* the age of these layers is early Tithonian. It is worth noting that *Spirothalmidium* mg. *kaptarenkoae* appears to have existed during the Tithonian period. The microfacies and fossil association of the succession suggest that these layers were deposited in a hemipelagic basin, where grains produced in the photic zone of a shallow marine environment were supplied. The occurrence of the Charophyte gyrogonites indicates a freshwater inflow. Each studied sample exhibits post-depositional fabrics caused by increased pressure due to burial.

The next outcrop-sequence has a thickness of approximately 75 m and consists of sites 301-303, which are situated in a nearly northeast–southwest direction. The rock is ochre-coloured and thin-layered almost throughout, with only one thicker (~10 m) calcarenite bed appearing. In the older part (site 301), marl and shale layers are dominant, while upward, the limestones become more abundant. The texture of the limestone (sites 301, 302) is radiolarian packstone, packed biomicrite, with fragments of calcareous bioclast of unknown origin, dispersed opaque minerals, and a few specimens of textulariid benthic foraminifera. Nannofossils could not be identified in these samples. The sample from site 303 yielded a moderately preserved, relatively diverse association of a few nannofossil specimens. The genus *Cyclagelosphaera* is the most common, represented by *C. brezae* and *C. deflandrei*. Besides them, *Rotelapillus crenulatus, Hexalithus noeliae, Conusphaera mexicana, Retecapsa schizobrachiata, Truncatoscaphus intermedius, Stradnerlithus* sp., ?*Lithraphidites* sp. and ?*Acadialithus* sp. also occur. Based on the stratigraphic range of these nannofossils, the age of the rock is late Tithonian, NJ18 Nannofossil Zone.

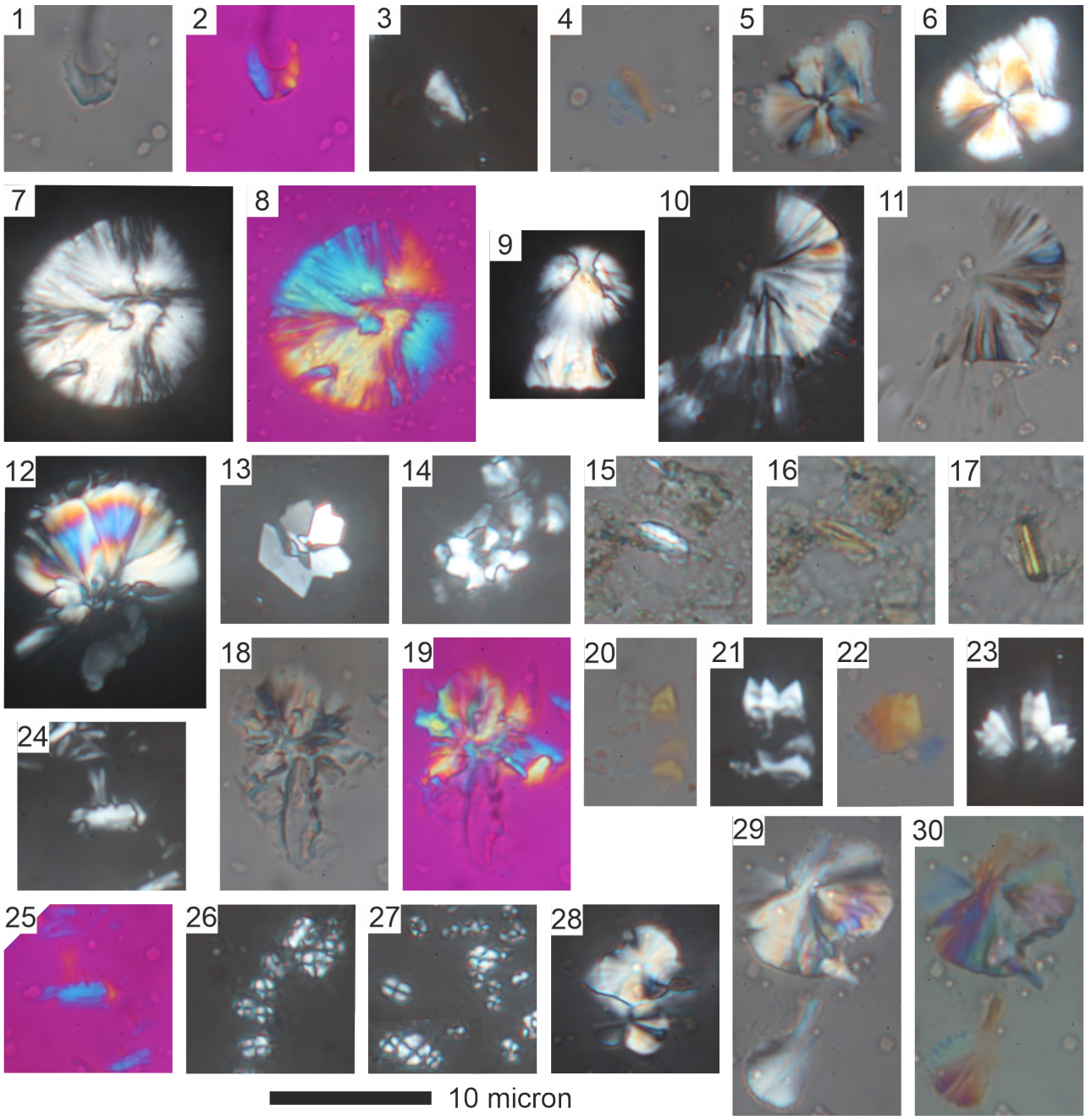

Fig. 18. Upper Tithonian nannofossils from the Sveti Miklavž section. **1-25** sample 303: **1-2** ?*Acadialithus* sp., **3-4** *Conusphaera mexicana* Trejo, **5-9** *Cyclagelosphaera brezae* Applegate & Bergen, **10-12** *C. deflandrei* (Manivit) Roth, **13-14** *Hexalithus noeliae* Loeblich & Tappan, **15-16** ?*Lithraphidites* sp., **17** *Truncatoscaphus intermedius* Perch-Nielsen, **18-19** *Retecapsa schizobrachiata* (Gartner) Grün in Grün & Allemann, **20-23** *Rotelapillus crenulatus* (Stover) Perch-Nielsen, **24-25** *Stradnerlithus* sp., **26-30** sample 299: **26-27** *Conusphaera maledicto* Varol & Bowman, **28-30** *Cyclagelosphaera brezae* Applegate & Bergen. The scale bar is 10 µm. Fossils under plane-polarised light are: 1, 3, 5, 10, 15, 17-18, 20, 22, 30; under cross-polarized light are: 4, 6, 7, 9, 11-14, 16, 21, 23-24, 26-28, 31, under cross-polarized light and gypsum plate are: 2, 4, 8, 19, 25.

Further north, the next succession starts with site 300. Above, the grey-ochre-coloured, fine-grained, thin-bedded limestones are replaced by thicker (varies from 40 cm up to 2 m) breccia layers. The texture of the limestone is radiolarian wackestone-packstone, sparse-packed biomicrite with dispersed opaque minerals and a few fragments of echinoderms and benthic foraminifera. Despite the dolomitization, *Neotrocholina valdensis* could be identified, dating the rock to the late Tithonian to early Aptian interval. *Neotrocholina* is platform-dwelling foraminifera (e.g., Rigaud et al., 2018), its appearance in this pelagic-hemipelagic limestone indicates a nearby platform environment. The sample exhibits post-depositional fabrics resulting from pressure. After the nearly 50 m thick gap, at site 299, grey-ochre mottled, thin-layered marl and shale appear. The texture of the marl is wackestone, sparse biomicrite with tiny fragmented bioclasts and several calcified radiolarians. From the smear slides of the sample, *Conusphaera maledicto* and *Cyclagelosphaera brezae* could be classified. The co-occurrence of

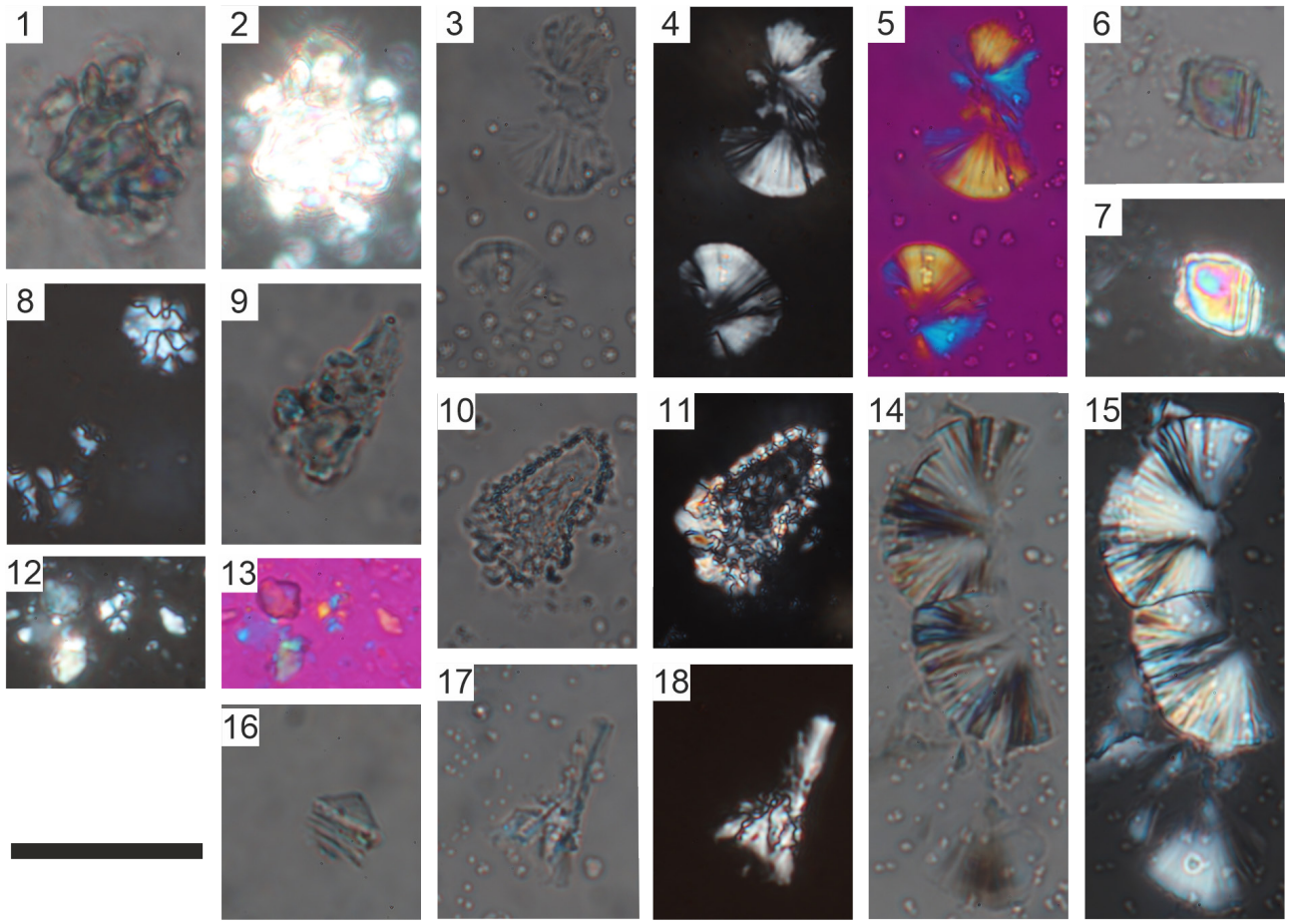

Fig. 19. Lower Cretaceous (Berriasian – Hauterivian) nannofossils from the Sveti Miklavž section. **1-13** sample 330: **1-2** *Assipetra* sp., **3-5** *Cyclagelosphaera brezae* Applegate & Bergen, **6-7** *Nannoconus* gr. *circularis* Deres & Achéritéguy, **8** *Nannoconus* sp., **9** *Nannoconus colomii* (de Lapparent) Kamptner, **10-11** *Nannoconus kamptneri* Brönnimann, **12-13** *Palaeomicula maltica* (Worsley) Varol & Jakubowski, **14-18** sample 549: **14-15** *Cyclagelosphaera deflandrei* (Manivit) Roth, **16** *Conusphaera* sp., **17-18** *Staurolithites pseudocarinolithus* (Applegate & Bergen) Young & Bown. The scale bar is 10 μm. Fossils under plane-polarised light are: 1, 3, 6, 9-10, 14, 16-17; under cross-polarized light are: 2, 4, 7-8, 11-12, 15, 18; under cross-polarized light: and gypsum plate are: 5, 13.

these nannoliths indicates the late Tithonian NJ18 nannofossil zone, and it coincides with the age of the site 300. Based on these, the entire succession is also upper Tithonian (NJ18 Zone).

The next succession was composed based on sites 328, 551a, b, and 329, and above a ~45 m gap on sites 330 and 549. At the lower three sites, the lithology is grey-ochre thin-bedded, silicified limestone with dispersed mm-sized brick-red dots. At site 551b, an about 50 cm thick grey breccia horizon occurs. In the thin section, the rock is microbreccia, the clasts are composed of radiolarian packstone or packed biomicrite with common opaque minerals. Only terrestrial plant remains appeared as fossils, indicating the proximity to the mainland. The upper part of the succession (site 330) starts with grey-ochre thin-layered marl and shale. The genus *Nannoconus* dominates the nannofossil association. The following taxa could be determined: *Nannoconus kamptneri, N.* gr. *kamptneri, N. colomii, N.* gr. *circularis, N.* sp. Besides them, specimens of *Cyclagelosphaera brezae, Palaeomicula maltica,* and *Assipetra* sp. occur. The co-occurrence of these taxa suggests the earliest Berriasian–latest Valanginian (NC1–NC3 zones) interval. Upwards (site 549), the rocks are more calcareous and thin-bedded. Here, the texture of the limestone is radiolarian packstone, packed biomicrite, with a few fragments of terrestrial plants and sponge spicules. The very poor and predominantly fragmented nannofossil assemblage consists of *Nannoconus* sp., *Conusphaera* sp., *Cyclagelosphaera deflandrei*, and *Staurolithites pseudocarinolithus,* indicating an age of Valanginian–Hauterivian (NC3– lower NC5 zones).

More than 100 m north of site 330, at site 686, a few meters-thick layer of purplish-red, shaley marl is exposed. Limestone layers and a 1–2 m thick sedimentary breccia body are intercalated in the marl.

In summary, the layers of the Biancone Formation could be identified in the Sv. Miklavž section, except the northernmost site 686, whose layers are classified as the Lower Flyschoid Formation based on lithology. The age range of the Biancone Formation was determined using calcareous nannofossils, spanning from the earliest Berriasian–latest Valanginian and Valanginian–Hauterivian.

Table 5. Stratigraphic range of the calcareous nannofossils in the studied sites.

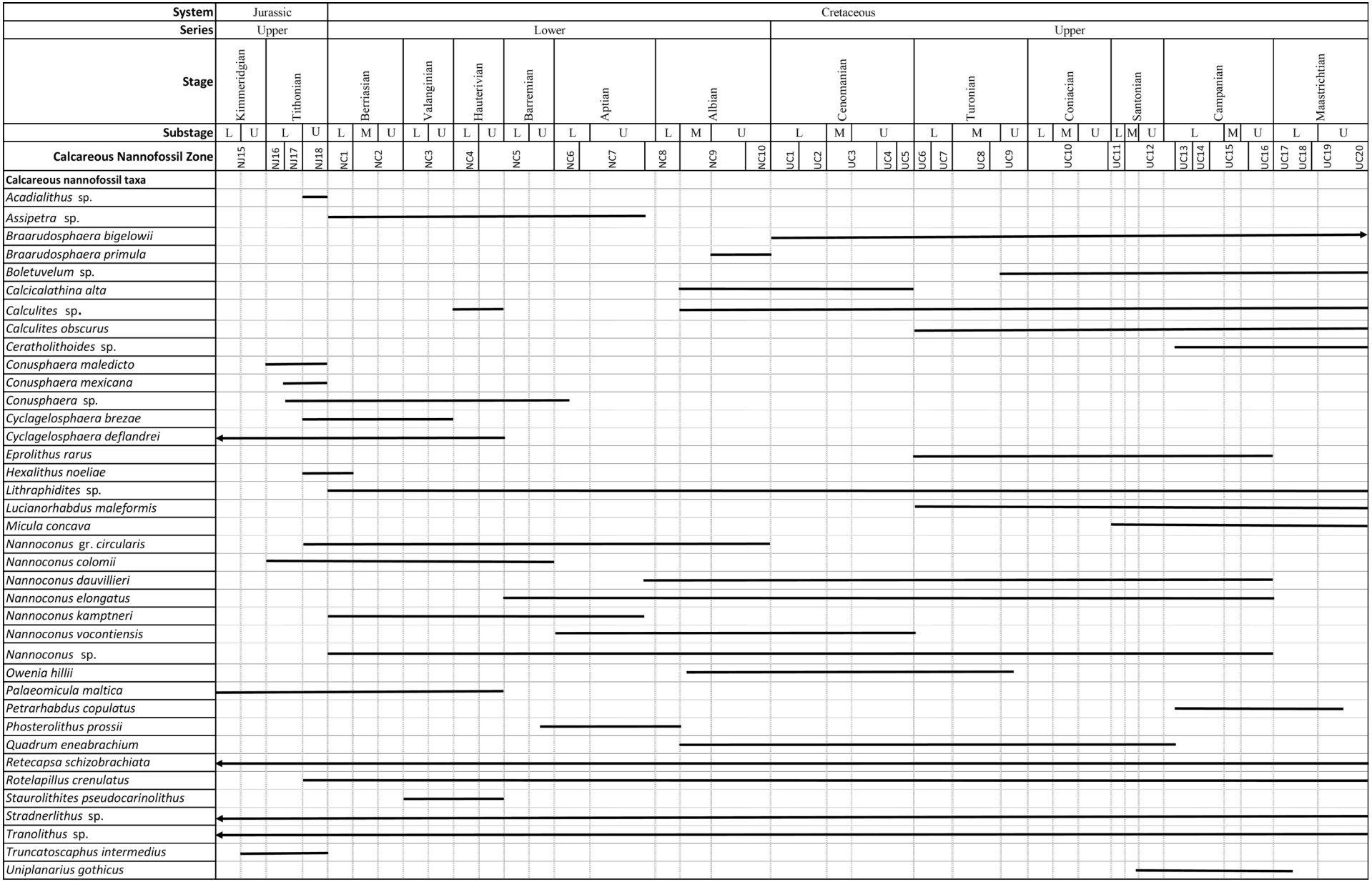

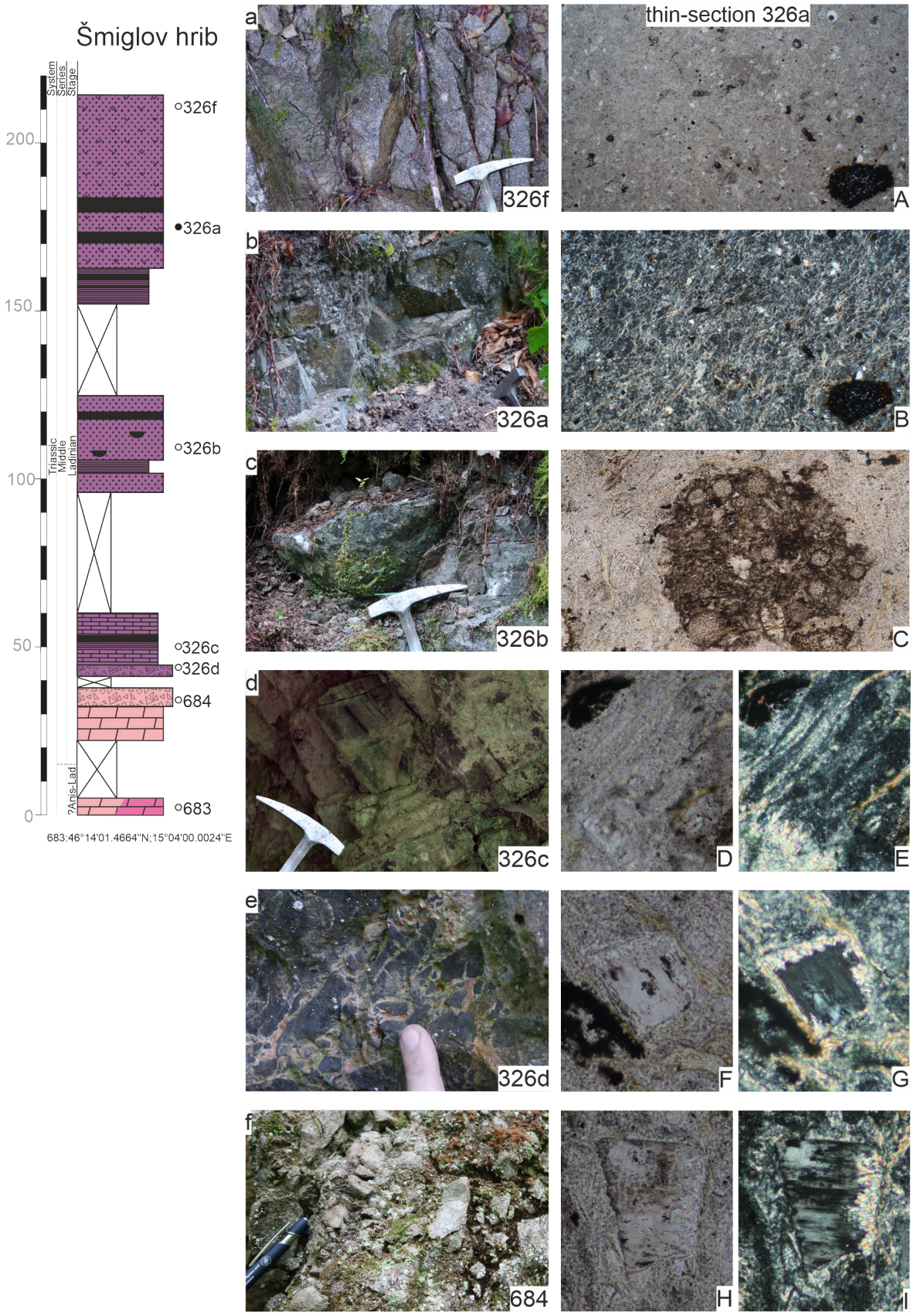

Fig. 20. Stratigraphic column and lithofacies of the Šmiglov hrib section, and microfacies of the sample 326a. **a, b, c** Pseudozilian Formation volcanoclastics in sandstone, **d,** Pseudozilian Formation slate and marl, **e** Pseudozilian Formation limestone breccia, **f** Schlern Formation dolomite breccia. For the legend, see Figs. 2-3. **A-B** fine sandstone with tiny glass shards and fragments of terrestrial plants (bottom right corner), **B** with crossed Nicols, **C** radiolarian packstone grain, **D-E** pumice grain, **E** with crossed Nicols, **F-G** Potassium feldspar (sanidine) with sericite rim, **G** with crossed Nicols, **H-I** plagioclase altered by sericite, **I** with crossed Nicols. The widths of the photomicrographs are: A-B – 3 mm; C – 1,5 mm; D-I – 0,2 mm. Abbreviations: Anis-Lad. (Anisian-Ladinian).

The Šmiglov Hrib section (Figs. 1, 20; Appendix 1)

The north–south Šmiglov hrib section starts 250 m south of Grajska vas village. The bedding is dipping to the south throughout. The succession is continuous but might be overturned in this case the description starts from the youngest formation.

In the northernmost part (site 683), the massive white to light grey fine-grained dolomite is covered by white, grey dolomite breccia (site 684) with a calculated thickness of 40 m. Based on the lithology, these beds presumably belong to the Schlern Dolomite or the Mendole Formation. After a small gap, a several-meter thick, silicified limestone breccia appears (site 326d). The cement is composed of red calcite, and the dark grey carbonate clasts are 3–7 cm in diameter. Above (site 326c), it is followed by a 20 m thick, medium-grey, well-bedded pelagic limestone. Some layers are silicified in a few meters thickness.

After a 30 m gap, alternating dark purple-grey fine-medium-grained sandstones and siltstones are cropping out in a 30 m thick succession (site 326b) while shale was observed in scree. Half-spherical, 30-40 cm large, silicified blocks occur in some places (Fig. 20), and higher up the section, strongly silicified beds appear. After another gap, a 12 m thick, well-bedded, dark greenish-grey, chertified siltstone succession occurs.

This succession is capped by an approximately 65 m thick, medium to coarse grey sandstone with white pumice clasts (1–2 mm) (site 326a, f). The silica content is changing, and the highest volcanic content is located at the top of the site 326f. In the thin-sections from site 326a, components of acidic magmatic origin are the most common, such as glass shards, pumice fragments, resorbed quartz grains, alkali feldspars (sanidine), plagioclases, biotite, and zircon. The presence of sericite and calcite indicates the influence of metamorphism. (S. Józsa personal comment). Besides the mineral constituents, carbonized fragments of terrestrial plants and fragments of benthic foraminifera (*Lenticulina* sp., Foraminifera indet.) could also be recognized. These rock-forming particles refer to a rhyolite tuff that fell into a shallow sea relatively close to the shore.

Based on the results of this study and the principle of superposition, we can classify these rocks as the Schlern Formation (each sub site of 326) and the Ladinian Pseudozilian Formation.

The Osreški grič section (Figs. 1, 21)

The east–west oriented Osreški grič section is situated on the north slope of Osreški Hill and has a westward dip in this area.

The section begins (at site 690b) with a massive shallow marine carbonate, followed by an almost 150 m thick succession of dark grey weathered shales of the Pseudozilian Formation. Its stratigraphic position and lithological features led to the assumption that it is the Ladinian Schlern Dolomite. Below the middle part of the succession (site 690), approximately 15 m thick, well-bedded (7–12 cm thick layers) black pelagic limestone interlayers occur. These beds probably indicate a minor drowning of the platform. About 20 m above the pelagic limestone, a several-meter-thick dolomite breccia interlayer interrupts the monotonous platform depositional sequence again.

These Middle Triassic carbonates are overlain by the 70–90 m thick, characteristic Upper Jurassic–Lower Cretaceous Biancone Formation. In the ochre-grey, thin-layered (2–8 cm) carbonate succession (site 689d), redeposited beds ranging from calcarenite to breccia appear occasionally. The frequency of these resedimented layers and the thickness of the marls increase (up to 10 m) upwards.

In the uppermost 60–80 m of the section, Lower Flyschoid Formation is observed. The lithology changes, becoming more argillaceous. Medium grey, thin-bedded marls, marly limestones with clay intercalation, argillaceous marls, and fine-grained calcarenite and breccia beds alternate frequently. The submarine erosion has created uneven surfaces and channels (site 689c) between the breccia and the underlying marl and limestone layers. Additionally, marly-limestone beds with bed-parallel chert nodules (site 689b) and 30–50 cm silicified blocks in argillaceous marl (site 689a) occur.

The contact of Biancone and Lower Flyschoid is additionally observed at site 315, on the opposite side of the valley. Here, the main outcrop is of Biancone sl., and the systematic appearance of the calcarenite layers is truncating the thin-layered limestone and marl beds.

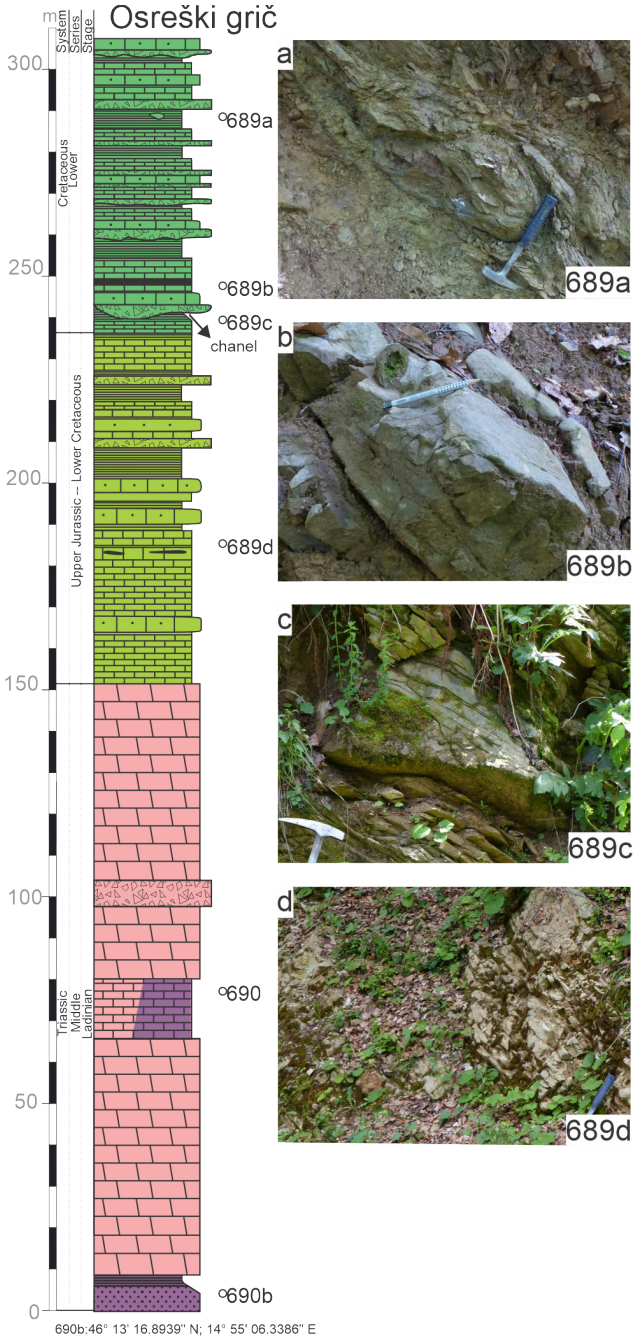

Fig. 21. Stratigraphic column and lithofacies of the Osreški grič section. **a** Lower Flyschoid Formation silicified carbonate body **b** Lower Flyschoid calcarenite with chert layer **c** Lower Flyschoid formation channel and erosional bottom **d** Biancone Formation. For the legend, see Fig. 2.

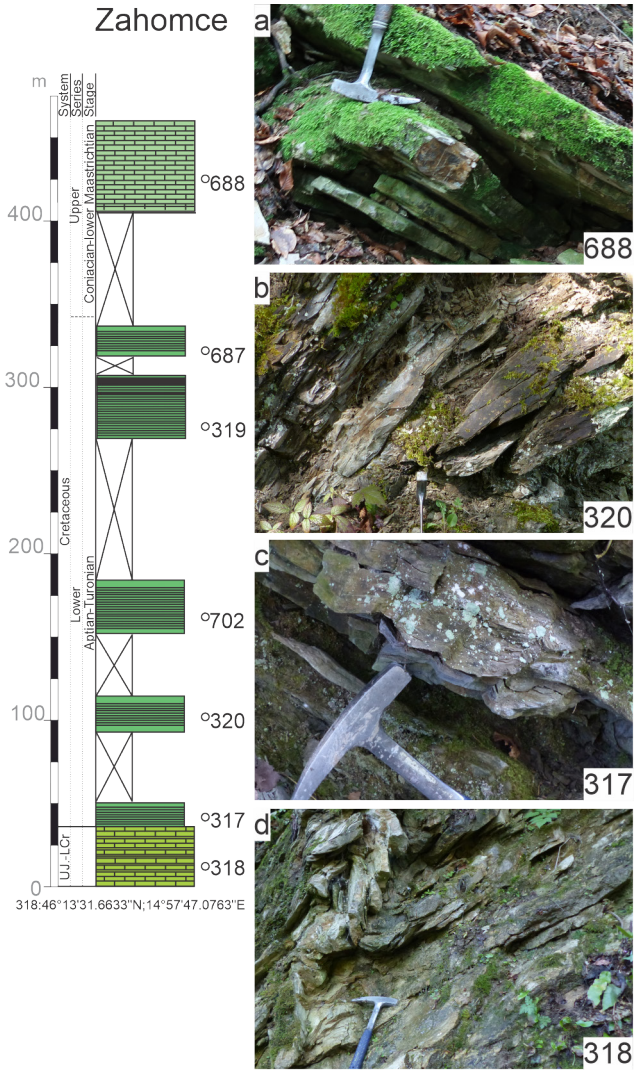

Fig. 22. Stratigraphic column and lithofacies of the Zahomce section. **a** Volče Limestone Formation, **b**, **c** Lower Flyschoid Formation, **d** Biancone Formation folded isoclinally. For the legend, see Fig. 2. Abbreviations: UJ-LCr. (Upper Jurassic – Lower Cretaceous).

The Zahomce section (Figs. 1, 22; Appendix 1)

The south–north Zahomce section runs north from the scattered settlement of Zahomce to Grmada Hill. The strike of the bedding is E–W, although the dip angle changes from shallow to steeply dipping. The dip direction is mostly to the north, but at sites 317 and 320, it is to the south. The section is composed of smaller observed segments. The total thickness was calculated considering the missing section parts.

At the lowermost part of the section (site 318), an ochre-grey folded (anticline) limestone is visible. This thin-bedded limestone is considered the Upper Jurassic–lowermost Cretaceous Biancone Formation.

It is overlain by approximately 10 m thick, grey, finely laminated marl layers (site 317). Black shales with a couple of 10-m thicknesses appear in several places (sites 320, 702, 319, 687) up the section. Sporadically, some 10 cm thick layers of fine-grained calcarenite limestone occur (e.g., site 320). Based on lithological features and stratigraphic position, these beds belong to the Lower Flyschoid Formation with an estimated thickness of 300 m. At the northern end of the section (site 688), ochre – light grey pelagic limestone with chert nodules, the Scaglia-type Upper Cretaceous Volče limestone crops out for 50–60 m.

The Črni Vrh (Zahomce) section (Figs. 1, 23)

The Črni Vrh section is located 1.5 km west of the village of Loke. It runs from the saddle north of Kozica through Črni vrh. The observations of multiple sites are projected into a north–south directed section. The bedding dips gently to the north throughout. The section starts at site 235, which is topographically lower positioned, and thus, it is projected into the section from the north from a 200 m distance. The rock is thin-bedded dark grey marl and slaty marlstone. The same formation is observed at site 706a in the south. The thickness of this marly succession exceeds 50 m and likely continues downwards. Based on the lithology, it can be identified as the Lower Flyschoid Formation.

It is overlain by a ~10 m thick, medium-grey monomict limestone breccia bed. Upwards, the succession consists of cream-white, ochre, thin (2–5 cm) layered pelagic limestones with grey, 2 to 10 m thick allodapic limestone (calcarenite) intercalations (sites 706b and 234).

On the west side of Črni Vrh (site 705, projected 100 m westward), in a thickness of ~20 m, the pelagic limestone mentioned above alternates with beds of calcareous microbreccia or fine-grained calcirudit, ranging in thickness from 10 to 25 cm. The grey calcareous micritic matrix of the resedimented limestones contains dark grey, red, and ochre clasts. The clasts are moderately sorted and subrounded in shape. Based on the lithology (Ogorelec et al., 1976), this approximately 60 m thick rock formation most probably belongs to the Volče Limestone.

Other important sites (Figs. 1, 24–26; Tables 1, 2, 5; Appendices 1–2)

Four sites (sites 676, 671, 307, and 238) could not be fitted into the sections, but they provided new and relevant data for recent and further studies.

Site 676 (46° 12' 07.7225" N, 14° 41' 51.5503" E) is located 500 m west of the Velink Hill, on the small mountain road from Vaserno towards Gradišče. A medium-grey, well-bedded limestone outcrops here, with a thickness of ~2 m. The texture of the rock is dolomitized packstone/wackestone, fossiliferous micrite with pellets, microbial grains, and opaque minerals. The fossil assemblage consists of Echinodermata fragments, benthic foraminifers, ostracods, and microproblematica. The following taxa could be identified as*Thaumatoporella parvovesiculifera*, textulariids, *Turriglomina mesotriassica,* and *Paratriasina* sp. The co-occurrence of the latter foraminiferal taxa indicates the latest Anisian–earliest Ladinian age. Based on the macroscopic and microscopic characteristics of these beds, including fossils, this formation is identical to that in the Kisovec Hill section (site 667) near Krvavica, namely the Mendole Formation.

Site 671 (46° 12' 44.2990" N, 14° 48' 45.4369" E) is near the main road from Špitalič to Tuhinj, southeast of a large quarry (site 055), exposing Bača Dolomite Buser (2010). From the main road a forestry road heads into a small valley where 18–20 m thick layers of dark grey limestone are exposed with a dip angle greater than 70°. The texture of the rock is peloidal-bioclastic wackestone, poorly washed biosparite with benthic foraminifers, Vermes tubes, fragments of Echinodermata, and

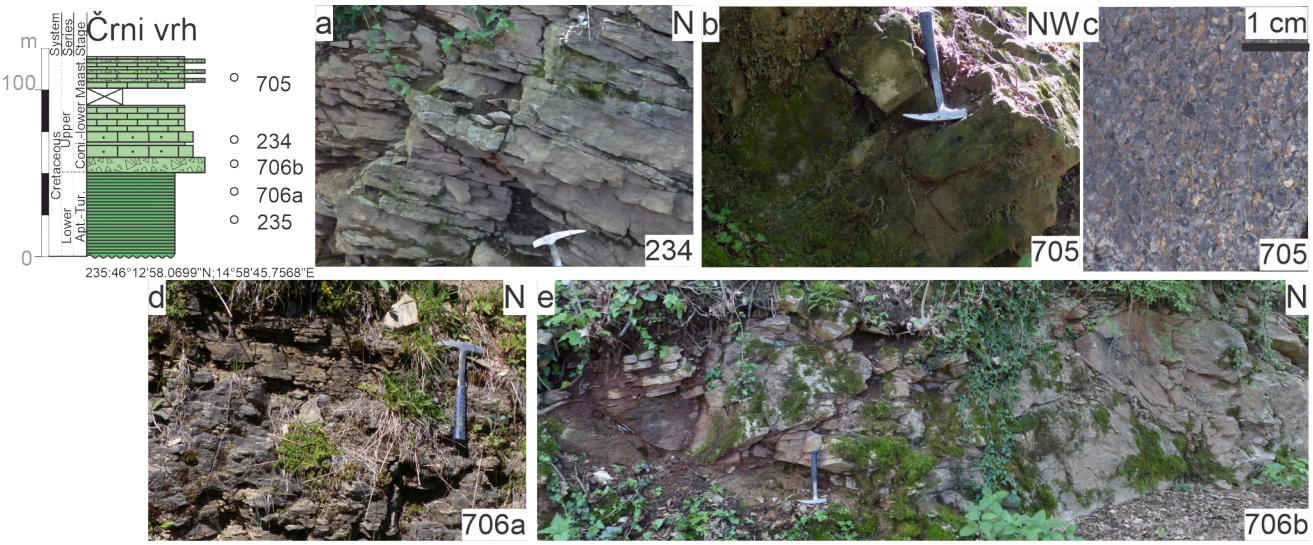

Fig. 23. Stratigraphic column and lithofacies of the Črni vrh section. **a, b, e** Volče Limestone Formation **c** the cut and polished surface of the sample from site 705. **d** Lower Flyschoid Formation. For the legend, see Fig. 2. Abbreviations: Apt.-Tur. (Aptian – Turonian); Coni. – lower Maast. (Coniacian – lower Maastrichtian).

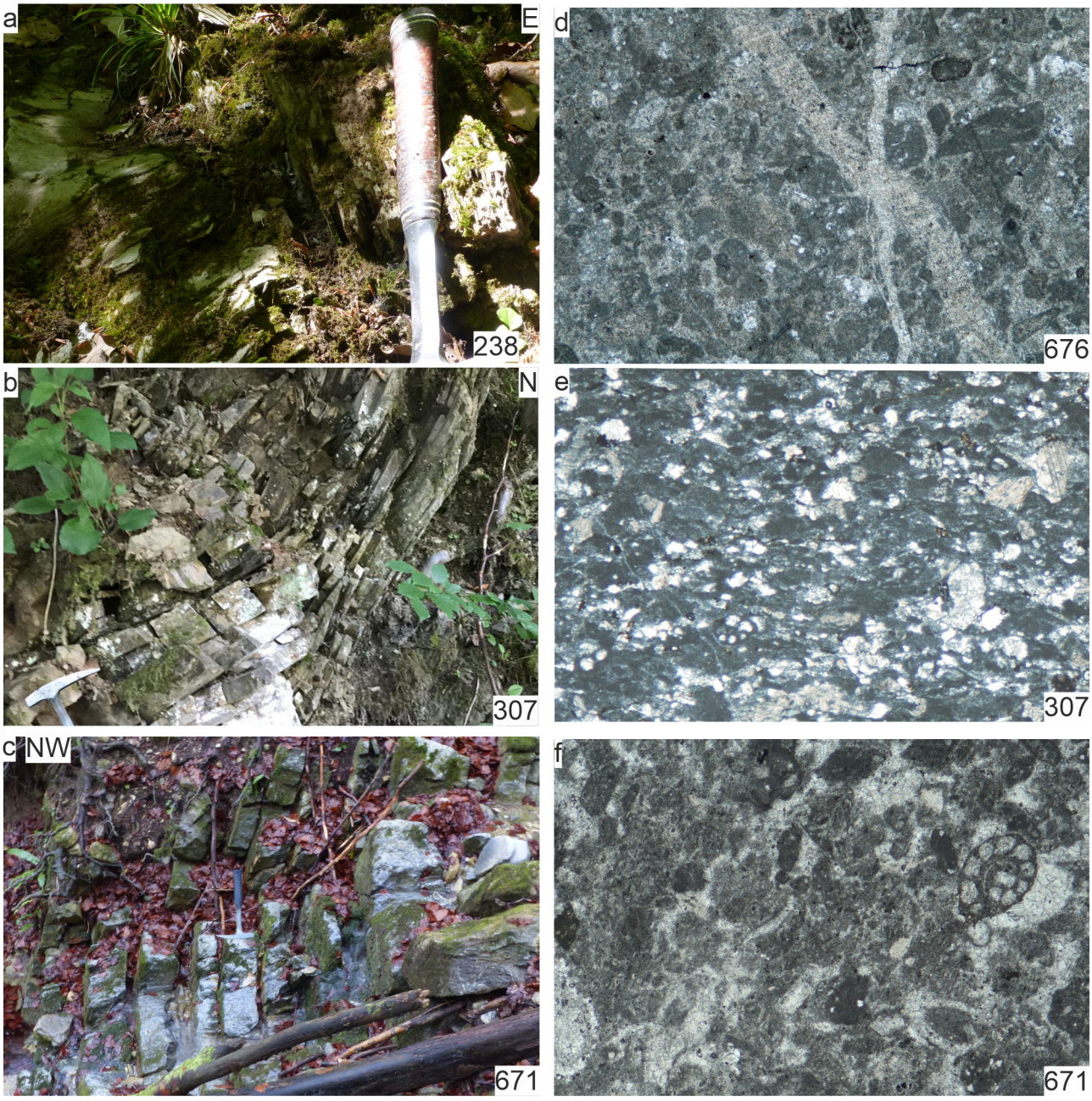

Fig 24. Lithofacies and microfacies of sites. For the legend, see Fig. 3. **a** site 238 =Volče Limestone Formation, **b** and **e** site 307 = Lower Flyschoid Formation; **c** and **f** 671 = Amphiclina Beds; and **d** site 676= Mendole Formation. The width of the photomicrographs is 3 mm.

Bivalvia. Among the foraminifers, the specimens of aragonitic Duostominidae and Oberhauserellidae are the most common. From these groups, the *Duostomina* sp. and the Lower Triassic–Rhaetian *D. convexa* could be identified. Miliolinids are represented by *Agathammina* sp. and miliolinids sp., while the agglutinated ones are by *Ammobaculites* sp. and *Palaeonubecularia gregaria*. A few *Lenticulina* sp. also occur. The microfacies and the fossils indicate a shallow marine environment. Based on the literature (Gale et al., 2017), these rocks can be attributed to the upper part of the Carnian Amphiclina Beds or the transition of this formation to the Bača Dolomite (site 055).

Site 307 (46° 13' 03.4793" N, 15° 04' 09.5071" E) is located in the broader Sv Miklavž area, on the road from the valley of Reka Creek towards Marija Reka, approximately 250 m east of Strnik Hill. The approximately 6 m wide outcrop features thin-bedded (3–15 cm) medium-dark grey calcarenite with thin clay intercalations, some layers contain dark grey cherty nodules. The texture of the rock is peloidic bioclastic grainstone, poorly washed biosparite with benthic foraminifers, and fragments of the Echinodermata. Among the foraminifers, the agglutinated forms such as *Arenobulimina* sp., *Belorussiella* sp., *Nezzazata* sp., *Vercorsella* sp., and textulariid sp. and the

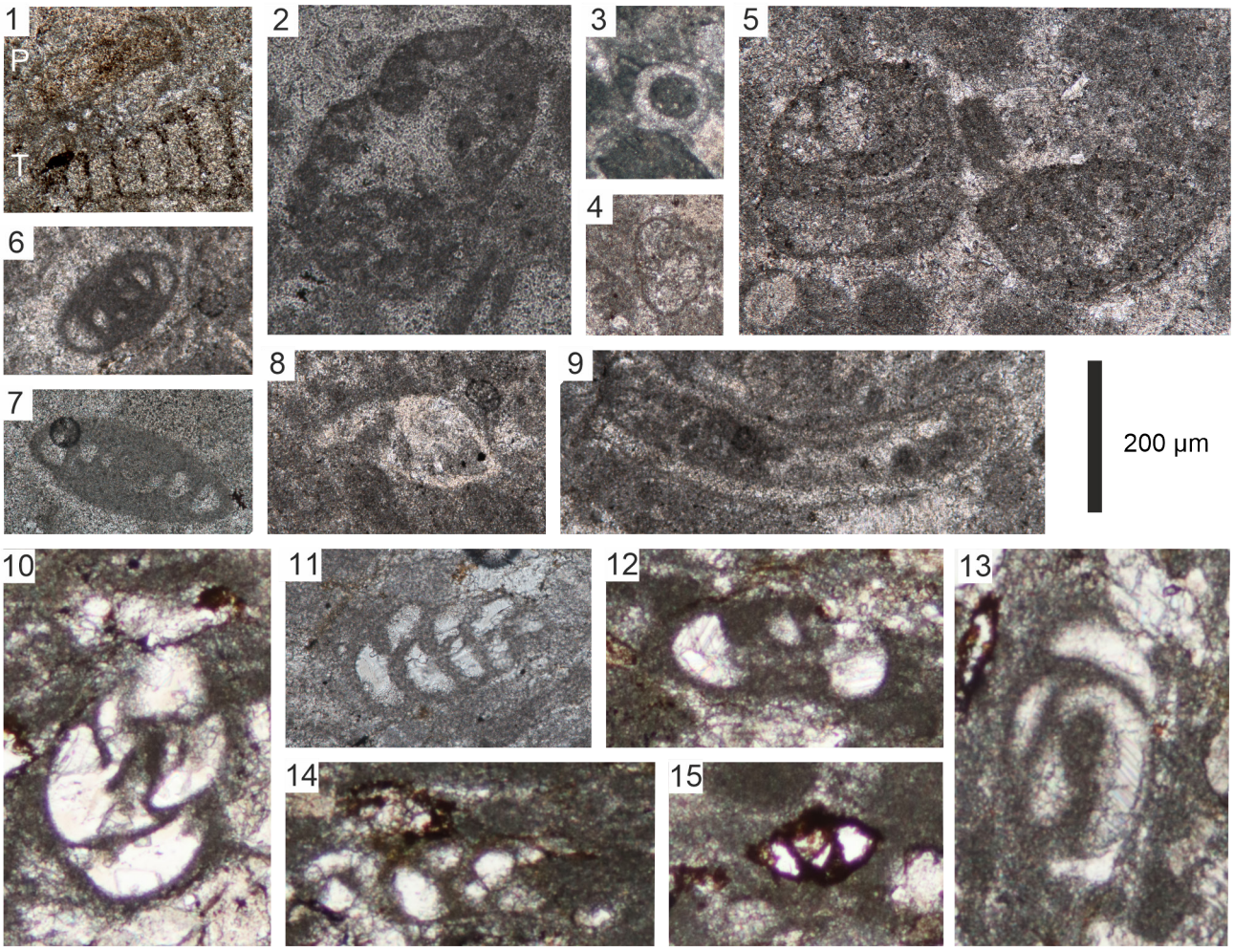

Fig. 25. Microfossils of the sites 676, 671 and 307. **1** *Paratriasina* sp. (P) and *Turriglomina mesotriassica* (Koehn-Zaninetti) (T), sample 676, **2-9** sample 671, **2** *Ammobaculites* sp., **3** *Palaeonubecularia* gregaria (Wendt) on a Vermes tube., **4** *Oberhauserella* sp., **5** *Duostomina biconvexa* Kristan-Tollmann, **6** *Agathammina* sp., **7** *Ophthalmidium* sp., **8** *Lenticulina* sp., **9** Vermes tube, **10-15** sample 307, **10** *Arenobulimina* sp., **11** *Belorussiella* sp., **12** *Nezzazata* sp., **13** *Pseudotriloculina* sp. **14** *Decussoloculina* sp., **15** *Istriloculina* sp. The scale bar is 200 µm.

miliolinids such as *Decussoloculina* sp., *Istriloculina* sp., *Pseudotriloculina* sp., and Miliolina indet. are dominated. A few specimens of nodosariids also occur. The co-occurrence of these genera indicates a late Early Cretaceous (Aptian–Albian) age. In the poor nannofossil association, the *Nannoconus* (*N. vocontiensis, N. elongatus,* and *N.* cf. *dauvillieri)* is the most common taxon. Besides them, *Tranolithus* sp., *Owenia hillii*, *Calcicalathina alta*, *Braarudosphaera primula*, *Quadrum eneabrachium,* and *Phosterolithus prossii* also occur, suggesting a late Albian age (mid NC9–NC10 zones). It is consistent with the age assigned by foraminifera. It means that the platform, from which the calcarenite layers with foraminifera originate is coeval (late Albian) with the deeper marine interlayered marls containing nannofossils. This rock is related to the Lower Flyschoid Formation.

Site 238 (46° 12’ 53.4832” N, 14° 59’ 42.5620” E) is in a roadcut on the road from Loke village towards Črni Vrh, approximately 370 m west of the village Loke, at the second hairpin turn uphill. The rock is brownish-grey, thin-bedded, or laminated calcareous marl. Due to the nature of the rock, it was not possible to make thin-sections, so smear-slides were made for nannofossil examination. The poor and partly silicified nannofossil assemblage provided the following taxa: *Braarudosphaera bigelowii, Micula concava, Lucianorhabdus* aff. *arborius, L. maleformis, Petrarhabdus copulates, Boletuvelum* sp., *Calculites* sp., *C. obscurus, Ceratholithoides* sp., ?*Cylindralithus* sp., *Eprolithus rarus,* and *Uniplanarius gothicus*. These forms indicate the Campanian age, namely the (UC13–UC16) zone, and thus, the rock can be classified as the Volče Limestone Formation.

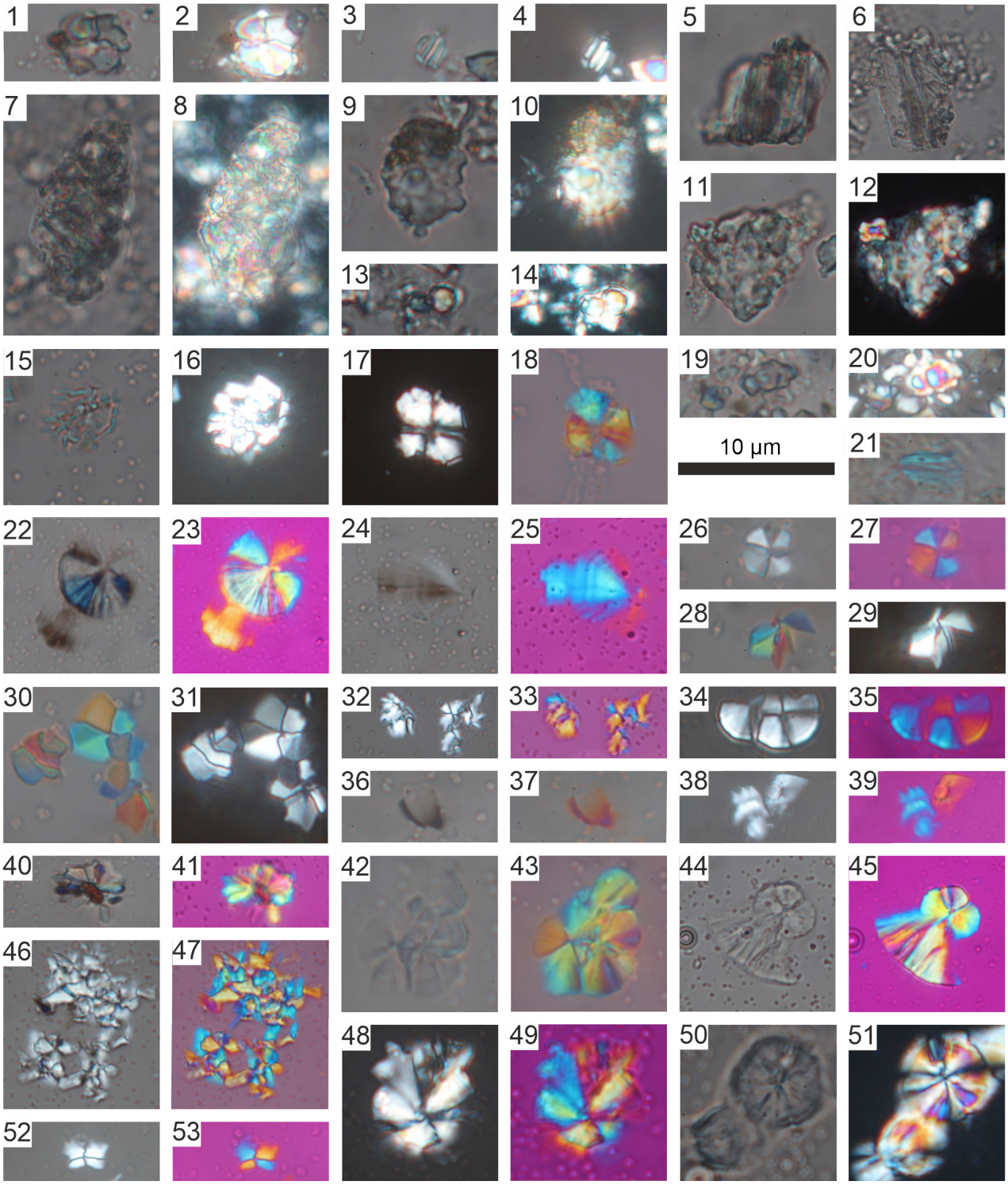

Fig. 26. Cretaceous nannofossils of the sites 307 and 238. **1-20** sample 307: **1-2** *Braarudosphaera primula* Black, **3-6** *Calcicalathina alta* Perch-Nielsen, **7-8** *Nannoconus* cf. *dauvillieri* Deflandre & Deflandre-Rigaud, **9-10** *Nannoconus elongatus* Brönnimann, **11-12** *Nannoconus vocontiensis* Deres & Achéritéguy, **13-14** *Owenia hillii* Crux, **15-16** *Phosterolithus prossii* (Herrle & Mutterlose) Aguado, reworked?, **17-18** *Quadrum eneabrachium* Varol, **19-20** *Tranolithus* sp., **21-40** sample 238: **21** *Lucianorhabdus maleformis* Reinhardt, **22-25** *Boletuvelum* sp., **26-31** *Braarudosphaera bigelowii* (Gran & Braarud), **32-33** *Calculites* sp., **34-35** *Calculites obscurus* (Deflandre) Prins & Sissingh in Sissingh, **36-37** *Ceratholithoides* sp., **38-39** ?*Cylindralithus* sp., **40-41** *Eprolithus rarus* Varol, **42-45** *Lucianorhabdus* aff. *arborius* Wind & Wise in Wise & Wind, **46-47** *Micula concava* (Stradner *in* Martini & Stradner) Verbeek, **48-51** *Petrarhabdus copulatus* (Deflandre) Wind & Wise in Wise, **52-53** *Uniplanarius gothicus* (Deflandre) Hattner & Wise, in Wind & Wise. The scale bar is 10 µm. Fossils under plane-polarised light are 1, 3, 5-7, 9, 11, 13, 15, 19, 21, 22, 24, 26, 28, 30, 36, 42, 44, 50; under cross-polarized light are: 2, 4, 8, 10, 12, 14, 16-17, 20, 29, 31, 32, 34, 38, 40, 46, 48, 51, 52, under cross-polarized light: and gypsum plate are: 18, 23, 25, 27, 33, 35, 37, 39, 41, 43, 45, 47, 49, 53.

Discussion

Based on our study, we present the distribution of formations observed in the area, highlighting new occurrences and biostratigraphical data (Fig.27). For details, see the chapter "Description of the Studied Sites."

The oldest formations, including terrestrial **Carboniferous shale** and the **Middle Permian Gröden Sandstone,** are outcropping at the southernmost points of the studied area, at Kisovec Hill and Marija Reka sections. The formations were identified based on their litho- and microfacies.

After a large gap, the Mesozoic series starts with the so-called **Mendole Formation**. This formation was detected at the westernmost observation point (site 676) and Kisovec Hill (site 667) (Fig.27). Site 676 had different classifications, Lower Triassic basinal carbonate (Premru, 1983a) and Bača Dolomite (Buser, 2010). This paper presents the first microfacies description of this formation at Kisovec Hill. Previous geological maps (Buser, 1977, 2010; Premru, 1983a) described this succession as Middle-Upper Triassic Platform Carbonates. The litho- and microfacies, as well as the foraminiferal fauna of these two sites, are very similar despite their relatively large distance (more than 22 km) and patchy occurrence. The foraminifera fauna (*Turriglomina mesotriassica* and *Paratriasina* sp.) indicates the latest Anisian–early Ladinian interval. At the base of the Šmiglov hrib section, the light-grey dolomite (site 683) may also belong to this formation or to the Ladinian–lower Carnian Schlern Dolomite. Previously, Grad (1969) interpreted this part as Pseudozilian Fm. which was reinterpreted as Jurassic (Buser, 1977) and later, to Cretaceous Lower Flyschoid Formation (Buser, 2010), as indicated by the map (Fig. 1).

The next two formations, namely the Ladinian siliciclastic-volcanoclastic **Pseudozilian** and platform carbonate **Schlern** formations, interfinger in the middle-upper part of Krvavica (Fig. 2, 27) and probably also in the Osreški grič section (Pseudozilian Fm: 690b and 690?; Schlern Fm. sites 690?). In the latter section, previously only the Pseudozilian (Premru, 1983a) or Lower Flyschoid formations were mapped (Buser, 2010;). While, in the Šmiglov hrib section, the Pseudozilian Formation (sites 326 d, c, b, a, f) overlies the Mendole Formation or Schlern Fm. (sites 683 and 684) with a thickness of nearly 200 m (Fig. 20). It means that the entire Šmiglov hrib sequence is Triassic, not Cretaceous as previously thought (Buser, 2010).

The Pseudozilian Formation was identified based on its lithofacies and microfacies, as only a few non-age-indicating benthic foraminifera were found in the Krvavica section. From the Krvavica section in the west to the northern Marija Reka section and further east, the Pseudozilian Formation has been confirmed at the base of the Brložen section (Fig. 8, site 254, Buser, 1977; Premru, 1983a), in several individual sites. It is found in the northern part of the Marija Reka section (Fig. 5, sites 558 and 557), where it lies structurally above the Cretaceous formations. This tectonic contact was postulated by previous authors to be the Marija Reka Fault. Its western continuation is south of the Krvavica Mt. (Grad, 1969, Lapanje & Šribar 1973; Buser, 1977).

The **Schlern Formation** was identified with the help of its lithofacies and microfacies as well as the shallow-water microfossil assemblage of the Krvavica section (Fig. 2, site 574). The age-determining benthic foraminifers, such as *Angulodiscus minutus* and *Gheorghianina vujisici,* suggest lower Carnian–Norian age. It also occurs at the base of the Sveti Miklavž section at the Reška Planina. The map indicates a narrow strike of platform carbonate just east of the section (Fig. 1b) and our new data confirms this. It is important to mention, that the platform carbonate does not form a continuous belt between Pseudozilian and the Biancone formations; it is missing in some cases, for example from the Brložen section.

In the upper part of the Krvavica section (sites 573, 574, and 572), the **Schlern Formation** interfingers with the dark grey pelagic marlstone (only detected from scree), the uppermost **Pseudozilian Formation** or the Amphiclina Beds. At the lower part of the Marija Reka section (site 560), the pelagic limestone with thin-shelled bivalves and ammonite and the fossil-free dolomite above it (sites 647, 646, and 645) most probably belong to this formation or the Amphiclina Beds. It should be noted that dolomite may be part of the Schlern Dolomite or the Norian-Rhaetian Bača Dolomite, so the section could belong either to DTZ or SB succession. At site 671 (at the western part of the studied area), dark grey limestone with rich and diverse Upper Triassic shallow-water fossil assemblage (benthic Foraminifers, Vermes, and Bivalvia) crops out. This rock can be attributed to the upper part of the Carnian **Amphiclina Beds.** Although in general the lithostratigraphic attribution of the Ladinian to Carnian mixed siliciclastic, volcanoclastic and carbonate succession is difficult in this case the continuation of this section to the overlying Bača Dolomite at site 055 may support their classification to the SB succession (Buser, 2010; Placer, 2008).

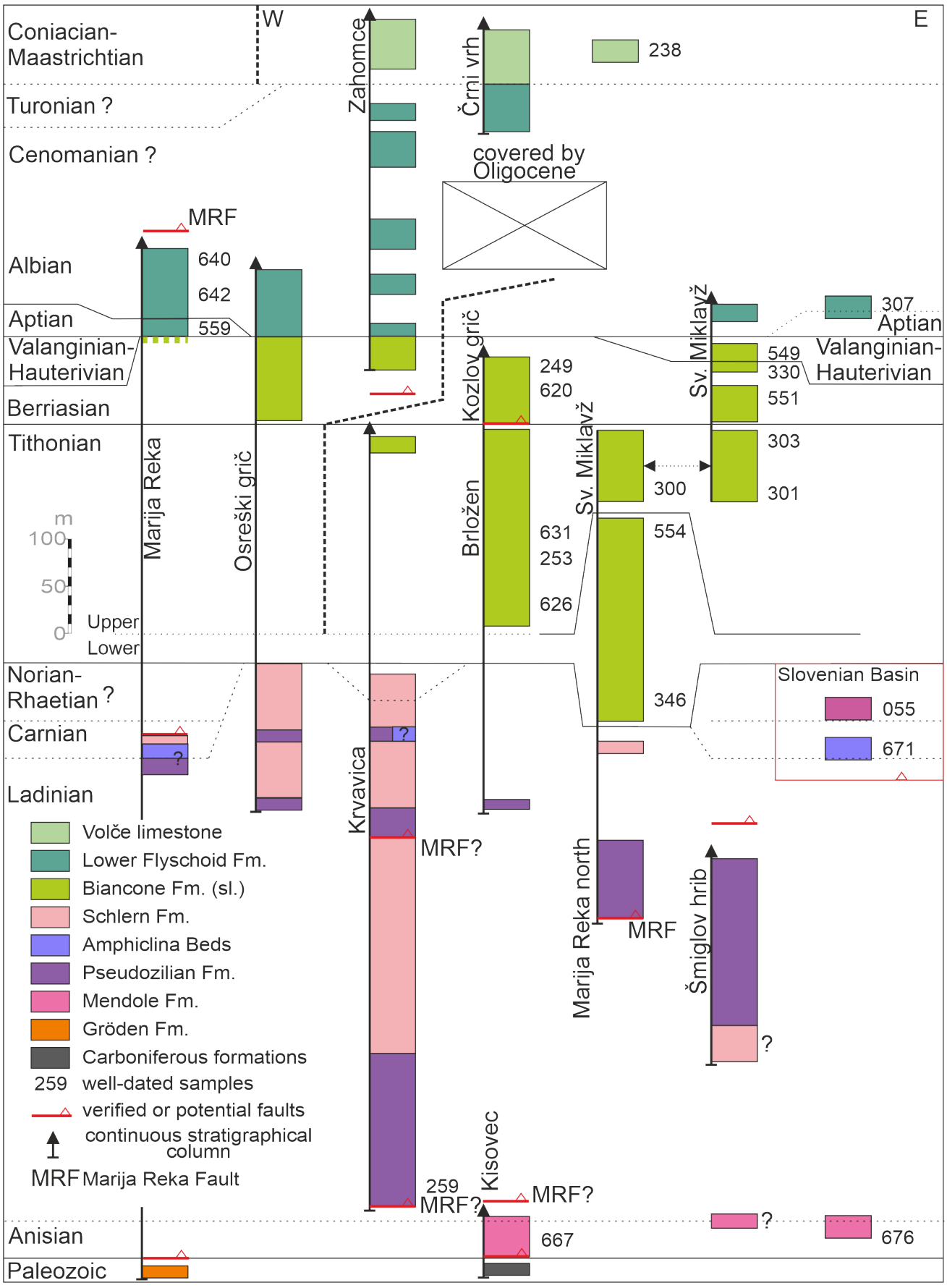

Fig. 27. Correlation of the formations in the discussed composite sections. All of the successions belong to the DTZ, except for the outcrops at 671 and 055, which belong to the SB. Detailed sections are presented in chapter Description of the Studied Sites. Site numbers are shown where age data has been determined in this study. Formation ages at other sections are based on literature. Question mark (?) indicates uncertainties in the determined formation or fault-line. Sections are in a west-east order except the Marija Reka section, which is split by the MRF, for their placement see (Fig. 1) thick dashed line is separating successions visually.

Age distribution of the Biancone Formation

After a major sedimentary gap, the Upper Jurassic–Lower Cretaceous Biancone Limestone appears. The macroscopic appearance of the formation compared to the so far studied sections of the central SB in western Slovenia (Rožič & Reháková, 2024) and the studied area does not match entirely. In the studied sites, chert layers or nodules are almost never found. Their colour is light grey to ochre, mottled and spackled with ochre. In addition, calcarenite interbeds are common in the studied sites, whereas they are almost absent in the SB.

Thus, all rocks with lithofacies resembling this one were classified as the Biancone Formation sensu lato (Fig.27). This thin-bedded micritic limestone, often with marl, shale, and calcarenite intercalations, appears in most sections, except the Marija Reka (where the age of the rock is younger despite the facies), Šmiglov hrib, and Črni Vrh sections. Its thickness varies roughly between 20 m (Kvravica section) and 200 m (Brložen section). The tectonic repetition of layers within a section was not detected. A few age-indicator chitinoidellids, calpionellids, c-dinocysts, calcitarch, and microproblematica occasionally appear in the thin-sections. The ages of four sites (sites 303, 299, 330, and 549 in the Sveti Miklavž section) are based on nannofossils. In the calcarenite layers, mainly the benthic foraminifers and green algae serve as age-diagnostic taxa.

The oldest biostratigraphic data from the Biancone Formation originate from the two calcarenite beds (site 346 and 554b) in the lower part of the ~200 m thick Sveti Miklavž section. The rocks yielded relatively diverse microfossil assemblages dominated by benthic foraminifera and Dasycladales. *Clypeina jurassica* (=*Aloisalthella sulcata*) was also likely identified from this location by Lapanje & Šribar (1973, pl. 2, fig. 1). Based on the co-occurrence of *Tethysicodium elliotti* and *Labyrinthina mirabilis,* the age of these beds is early Tithonian. The oldest known occurrence of the Biancone Limestone in the Southern Alpine–Dinaric Realm dates back to the late Tithonian (e.g., Goričan et al., 2012; Rožič et al., 2014; Rožič & Reháková, 2024). We note that fossils redeposited from the platform can be older than the sediment in which they were buried in a hemipelagic environment. However, this possibility is ruled out by the taphonomic nature of the fossils (e.g., even the most fragile skeletons are preserved, lithoclasts are missing). We assume that these layers correspond to the first sediments after the Early to Middle Jurassic sedimentary gap, which is dated to the late Kimmeridgian–lower Tithonian (Buser, 1986; Rožič et al., 2014). In the western outcrops of the SB, the oldest part of the Biancone Formation is coeval with the uppermost part of the Tolmin Formation. There in the Kimmeridgian–early Tithonian part of the formation, calcarenites are described within the radiolarites (Rožič, 2009; Goričan et al., 2012 a). Those calcarenites have a similar composition to those observed at the Sv Miklavž section.

Upward, the age of the two nearly 75 m thick subsections is late Tithonian, NJ18 Nannofossil Zone based on the co–occurrence of *Cyclagelosphaera brezae, Hexalithus noeliae,* and *Conusphaera mexicana* (Fig. 15, in sites 303 and 299). The appearance of the upper Tithonian–lower Aptian benthic foraminifera, *Neotrocholina valangiana* (site 300), coincides with it (Fig. 27).

The Biancone Limestone of the Brložen section is also late Tithonian in age. With the help of chitinoidellids and calpionellids, it was possible to divide succession into calpionellid zones and subzones. The appearance of the *Chitinoidella boneti* and the absence of other calpionellids verify the lowermost upper Tithonian *Chitinoidellids* Zone, the *Boneti* Subzone (sensu Benzaggagh, 2020) in the lowermost bed of the section (site 555). It is worth mentioning that this is the oldest calpionellid zone demonstrated from the DTZ succession of the Mt. Rudnica, located within the Sava Folds (Reháková & Rožič, 2019). The next 60 m of the section belongs to the lower upper Tithonian *Crassicolaria* Zone or A Zone, Chitinoidellids/Primitive Calpionellids Subzone or A0 Subzone (sensu Benzaggagh, 2020) or *T. remanei* Zone (sensu Reháková, 2000), based on the occurrence of *Calpionella alpina, Chitinoidella boneti, Ch. elongata*, and *Crassicolaria intermedia, Praetintinnopsella andrusovi, Tintinnopsella carpathica* (sites 625, 626 and 628a). This calpionellids zone was also identified by Rožič & Reháková (2024) from the western SB.

In the upper part of the Brložen section (from site 628), *Tintinnopsella carpathica*, *Calpionella alpina, Crassicolaria intermedia,* and *Tintinnopsella remanei* indicate the middle upper Tithonian Tintinnopsella Intermedia Subzone (A1) of the *Crassicolaria* Zone. The calcareous dinoflagellate cysts, such as Colomisphaera carpathica and C. fortis, C. alpina, and Crustocadosina semiradiata, which appear together with the calpionellids, reinforce this age. The microfossil association of the calcarenite bed (site 253), including *Redmondoides lugeoni, Nautiloculina oolithica, Mohlerina basiliensis, Protopeneroplis striata, Neotrocholi-*

na valdensis, Coscinoconus alpinus, *Trocholina* cf. *conica*, *Thaumatoporella parvovesiculifera*, *Aloisalthella sulcata* suggests also a late Tithonian age.

We could not confirm the presence of the uppermost Tithonian and lower–middle Berriasian calpionellid zones in the studied area due to the lack of calpionellids or other age-indicator fossils. We should not assume a lack of sediment in succession but rather explain the lack of finding them by the rarity of calpionellids and the post-diagenetic alteration of the rocks. One possible occurrence of these layers is at Osreški grič (~80 m, site 689d), Krvavica (~25 m, site 367), and Zahomce (~30 m, site 318) sections; however, these sections have not been studied in detail to date. Another possible occurrence of these layers could be the bottom of the Kozlov grič section and the uppermost sub-section of the Sveti Miklavž section.

The lowermost 20 m of the marl succession of the Kozlov grič section did not yield age-determining fossils.

From two micritic layers (sites 620 and 249p) the upper Berriasian, *Calpionellopsis* Zone, *Oblonga-Simplex* (D2) Subzone or *Oblonga* Subzone (sensu Allemann et al., 1971) could be proven based on the *Calpionellopsis oblonga, Tintinnopsella carpathica, C. simplex, Lorenziella plicata-hungarica, Stomiosphaera moluccana,* and *S. proxima*. Higher up (site 623), the appearance of the upper Oxfordian–lower Valanginian *Colomisphaera lapidosa* also supports this age. The microfossil assemblages of the calcarenite beds (sites 616, 621, 622, 249k, c) are diverse, consisting of platform-dweller forms such as benthic foraminifers, Echinodermata, green algae, microproblematica, algae, Porifera, Stromatoporoides, Vermes, and Bryozoa. In the larger foraminifers- and involutinid-dominated foraminifera fauna, the co-occurrence of *Pfenderina neocomiensis, Coscinoconus campanellus,* and *Frentzenella involuta* suggests the late Berriasian–Valanginian age. It is consistent with the late Berriasian age obtained from the calpionellids.

The sample examined from the Sveti Miklavž section (site 551b) did not contain age-indicating fossils. Upwards (site 330), after a gap, the lowermost Cretaceous nannofossils assemblage was found containing *Nannoconus kamptneri, Nannoconus gr. kamptneri, N. colomii, N.* gr. *circularis, N.* sp., *Cyclagelosphaera brezae, Palaeomicula maltica*, and *Assipetra* sp. These taxa indicate the lower Berriasian–upper Valanginian (NC1–NC3 zones). Higher up in the section (site 549), the Valanginian–Hauterivian age (NC3–lower NC5 zones) is plausible based on the nannofossils, such as *Cyclagelosphaera deflandrei* and *Staurolithites pseudocarinolithus*. These latter ages are slightly younger than the late Berriasian (Calpionellopsis Zone, Oblonga Subzone) age established based on previous calpionellid studies (Reháková & Rožič, 2019; Rožič & Reháková, 2024). However, it is worth noting that at the upper boundary of the sections examined in these older studies, the much younger Lower Flyschoid Formation was deposited with disconformity.

Summing up, the stratigraphic range of the Biancone Limestone sensu lato in the studied area is early Tithonian–earliest (?) Valanginian. It means that we have identified layers of this pelagic formation in the Sveti Miklavž section that are slightly older and slightly younger than the generally accepted late Tithonian–late Berriasian age in the SB (e.g., Cousin, 1981; Rožič & Reháková, 2024) as well as DTZ successions (Reháková & Rožič, 2019). It is important to emphasise that classical SB has radiolarites of the Tolmin Formation and above the Biancone Limestone overlain by a sharp contact (Rožič & Reháková, 2024). Whereas in areas closer to DCP, the succession below the typical calpionellid-bearing Biancone limestone is also rich in calcareous content. These are characterized by limestones rich in chert nodules and beds. (Rožič et al., 2014). Similar succession rich in the Upper Jurassic (hemi) pelagic carbonate is reported also from the Bovec Trough from the NW Julian Alps (Šmuc, 2005; Šmuc & Goričan, 2005). In the same area, the Valanginian–Hauterivian nannofossil associations and the upper Valanginian–lower Hauterivian radiolarian zone (UAZ 17–18 of Baumgartner et al., 1995) were mentioned in this formation (Buser, 1979; Goričan & Šmuc, 2004; Šmuc, 2005). Similarly, in the NW Dinarides, the pelagic limestone ranges from the Tithonian to the end of the Hauterivian (e.g., Cadet, 1978; Lužar–Oberiter et al., 2012).

The depositional environment of the Biancone Limestone formation in the studied sites may have been a pelagic-hemipelagic basin above the CCD. Debris from the nearby platform was periodically transported into this basin. Only in the Kozlov grič section were extraclasts of ophiolitic origin found in the calcarenite layers. In the oldest part of the formation (site 346, Sveti Miklavž section, Fig. 15), the Charophyte gyrogonites, while in the youngest part (sites 551b, 549, Sveti Miklavž section), the remnants of terrestrial plants indicate a freshwater influence.

The geographical distribution of the Biancone Limestone formation is much larger within the northern Trojane anticline than what is depicted

on the latest geological map of the area (Buser, 2010). Additionally, without exception, these layers were formerly classified as Lower Flyschoid Formation. In contrast, the occurrence of the Biancone Limestone, as indicated in the easternmost part of the area (site 307), is now attributed to the Lower Flyschoid Formation based on our investigations.

Sandstone bed in the Biancone Formation

In the lowermost 20 m of the marl succession of the Kozlov grič section a nearly 2 m-thick grey, cherty sandstone bed (site 614) occurs. In addition to few fossils, rock fragments and heavy mineral grains typical of sandstones originating from the ophiolite series are present. Sandstone beds in a marl succession with similar composition are known from several gravity-flow dominated successions. Examples include the Berriasian–lowermost Albian Rossfeld Formation of the Eastern Alps (Pober & Faupl, 1988), the Valanginian Studor formation of the Bled Basin (Slovenia, Kukoc et al. 2012), the Oštrc formation in Croatia (Lužar-Oberiter et al., 2012), and the late Berriasian–Hautrivian Bersek Marl in the Gerecse Mountains, Hungary (Császár & Árgyelán, 1994; Árgyelán, 1996). It has been demonstrated that the material of the rock fragments originates from the Dinaric Ophiolite Belt (e.g., Pober & Faupl, 1988; Császár & Árgyelán, 1994; Kukoč et al., 2012; Lužar-Oberiter et al., 2012; Goričan et al., 2018). This work presents the first discovery of these lithofacies within the Biancone Formation of the Sava Folds. Because of the isolated occurrence of this sandstone bed, the palaeogeographic position of the northern Sava Fold area was far from the ophiolite source.

Lower Flyschoid Formation and Volče Limestone Formation

In the studied area, from west to east, we were able to identify the Lower Flyschoid Formation in the following sections: Osreški grič section (sites 689 d, c, a, 80 m), Zahomce section (sites 318, 317, and 320) Črni Vrh section (sites 235 and 706a), Sveti Miklavž section (site 686), Marija Reka section (sites 644, 559, 643, 642, 642c, 641, 556c, 640, 556, 639, 638) and site 307 (Fig.27). In the Osreški grič, Zahomce, and Sveti Miklavž sections, it overlies the Biancone Limestone with disconformity. The Marija Reka section is exceptionally deposited directly on the Triassic strata, which might indicate a tectonic contact in this area.

The identification of the formation was based on the typical lithofacies, except for the Marija Reka section and site 307, where microfacies analysis and nannofossil examination were also performed on the samples. The succession consists of the dense alternation of dark grey or purplish-red thin-bedded marly-limestone, marl or shaley argillaceous marl, with dark-grey calcarenite, breccia and chert layers, or limestone with chert nodules. Upwards, the alternation of different rock lithofacies becomes more frequent, and the marl content increases. The texture of the marly layers is dominantly wackestone, packed biomicrite with planktonic and benthic foraminifers and c-dinocysts. Calcarenite beds have a grainstone, poorly washed biosparite texture and contain mainly benthic foraminifera as fossils.

In the Marija Reka section, the ~25 m sequence overlying the Triassic formations differs from those described above. The rock is light grey, ochre-mottled, cherty limestone with marly intercalations. The texture is mudstone, fossiliferous biomicrite with scattered opaque minerals and poorly preserved radiolarians, c-dinocysts, chitinoidellids, calpionellids, calcitarchs, and benthic foraminifers. The appearance (site 559) of Parachitinoidella cuvillieri indicates a late Aptian age within the *Colomiella* Zone and *Deflandronella* Subzone (Trejo, 1975). Upward (site 643), the occurrence of *Colomiella recta* suggests the younger subzone of the *Colomiella* Zone, the uppermost Aptian–lowermost Albian, *C. mexicana* Subzone (Trejo, 1975). The lithofacies, microfacies, and fossil groups of the rock are very similar to those of the Biancone Formation; however, the age is significantly younger, as indicated by the presence of calpionellids and chitinoidellids, which is also confirmed by the occurrence of *Cadosina disiuncta*. It is important to note that this is the first confirmation of the existence of the upper Aptian layers of the Lower Flyschoid Formation, which several previous authors assumed based on foraminifers (Caron & Cousin, 1972; Caron in Cousin, 1981; Samiee, 1999; Brajkovič et al., 2022; Schlagintweit et al., 2024) or radiolarians (Rožič et al., 2014).

Above this pelagic limestone macroscopically resembling the Biancone s.s Formation, the classic development of the Lower Flyschoid Formation appears in the Marija Reka section. The uppermost middle Albian *R. subticinensis* Subzone of the *B. breggiensis* Zone is indicated by the co-occurrence of the *Biticinella breggiensis* and *Thalmanninella praebalernaensis*. Upwards (from site 641), the existence of the *Calcisphaerula*? *innominata lata* and *Ticinella primula* suggest that layers were deposited in the late Albian. From site 556, the succession belongs to the uppermost Albian *R. appeninica*

Zone, based on the concomitance of *Muricohedbergella delrioensis, Planomalina buxtorfi, Biticinella breggiensis*, *Ticinella madecassiana,* and *T. praeticinensis*. The benthic foraminifera fauna of the calcarenite beds consist predominantly of agglutinated forms, but no orbitolinids were found. Based on the involutinids (*Coscinoconus* sp. and *Frentzenella* sp.) recovered from the uppermost 10 m of the Marija Reka section, the succession cannot be older than Cenomanian.

According to previous geological maps (Buser, 2010), the rocks at the southern part of the Marija Reka section were classified as the Upper Cretaceous Volče Limestone but were previously mapped as Lower Flyschoid or equivalent Cretaceous formations (Lapanje & Šribar, 1973; Buser, 1977). This 90 m thick sequence is likely to belong to the Lower Flyschoid Formation. Their figured orbitolinid fragments (pl. 1, fig. 2; pl. 2, fig. 2) cannot be assigned to a species. Their specimen identified as *Globotuncana* sp. (pl. 1, fig. 1) is likely a rotaliporid and can be attributed to the Albian–Cenomanian genus *Thalmaninella*. Buser (1977) similarly marked the area as Upper Cretaceous limestones, this corresponds with the age of the Lower Flyschoid Formation.

In the eastern observation point (site 307) of the studied area, the benthic foraminifera fauna of the calcarenitic bed indicates an Aptian–Albian age. At the same time, in the marl layer, the appearance of *Braarudosphaera primula* within the nannofossil association narrows down the age of the formation to the late Albian.

The age of the Lower Flyschoid Formation in the studied area is late Aptian–latest Albian (early Cenomanian?).

By comparing the new data with the classification of the latest geological map (Buser, 2010), the following can be established. The Lower Flyschoid Formation occurs at its greatest thickness (300 m) in the Zahomce section, it overlies the Biancone Limestone and is overlain by the Volče Limestone. (see below). The situation is similar in the Osreški grič section (where it is 80 m thick), where the Biancone is underlying, and in the Črni Vrh sections (here 50 m thick), where the Volče Limestone is overlying the formation. While the map of Buser (2010) indicates the Lower Flyschoid Formation throughout the entire area of the Sveti Miklavž section, it is only present at the very top of the section with a thickness of a few meters. As mentioned above, the map indicates the Biancone Formation at site 307. The largest difference was observed in the Marija Reka section, where it appears to be 100 m thick. It was mapped as Triassic Platform Carbonates and the surrounding Cretaceous formations were classified as the Krško beds of late Cenomanian Turonian age (Lapanje & Šribar, 1973; Buser, 2010).

Based on its lithofacies, the Coniacian–lower Maastrichtian Volče Formation is identified in three locations within the studied area: at the top of the Zahomce (site 688) and Črni vrh (sites 706b, 234, 705) sections, as well as east of these sections, at site 238. The nearly 60 m Scaglia-type succession consists of alternating thin-bedded ochre – light grey pelagic limestones and calcarenite, calcirudite, or microbreccia. The thickness of the latter beds can reach 10 meters at the bottom of the sequence, becoming thinner upwards. A nannofossil study was carried out from the marl sample of site 238. The co-occurrence of *Petrarhabdus copulates* and *Eprolithus rarus* refers to the Campanian age (UC13–UC16 zones). However, further detailed studies should be done on this formation to consolidate its stratigraphic frame.

The youngest formation in the studied area is the Oligocene siliciclastic Trbovlje Formation. It was identified only at the uppermost part of the Krvavica section (site 366) and near site 238 based on its lithofacies, namely sandstone, siltstone, conglomerate and breccia. This more than 20 m thick succession covers the Biancone, Lower Flyschoid and Volče Formations and is built up of variegated grey–ochre breccia, siltstone and sandstone beds. Its appearance in the investigated area agrees with the geographical distribution marked on previous maps (Grad, 1969; Buser, 1977, 2010; Premru, 1983).

Summary of the lithostratigraphic results

From the studied sections we reconstructed several lithostratigraphic columns which are marked by arrowhead lines on Fig. 27. Sometimes the successions are probably cut by minor faults like in the Marija Reka section. The continuity of sections into a single column is not always certain, partly because of the presence of structural complications. Although probable tectonic disturbances (folding and/or faulting) are present in the Brložen and Kozlov grič sections, they are considered to form one lithostratigraphic column. Their ages are complementary, Tithonian and Berriasian, respectively. The composite Sv. Miklavž section forms a single stratigraphic column although an overlap can exist in the Tithonian part (Fig. 27). The northern part of the Marija Reka section is the base of the stratigraphy at this succession although the Pseudozilian was not surveyed in detail. At its southern end the Šmiglov hrib section is

separated by a fault and the opposite bedding dip from the Sv. Miklavž section and it is in contact with the Oligocene rocks to the north (Fig. 1). Although a tectonic contact between the Kisovec Hill and Krvavica sections is possible, they can also form a continuous stratigraphical column because the two sections apparently form a youngening succession without repetition or gap. The Črni vrh section can be the continuation of the Krvavica section, although they are shifted along strike and the Oligocene covers the transition (Fig. 1, 27).

All these constructed successions share the same formations, although thickness variations can occur (Fig. 27). They all have a similar Triassic succession with basinal and platform development. Their age can be Ladinian to early Carnian, with a supposed continuation into higher Late Triassic in the Krvavica section. These are followed by the Biancone Formation, with a large hiatus. The pelagic limestone start earliest in the Tithonian. Another specialty is the Aptian thin-layered limestone at the Marija Reka section which is considered as the lower Flyschoid Formation according to its age, but with macroscopic appearance similar to the Biancone Fm. The Lower Flyschoid Formation is unequivocally present, while the Volče Limestone could have been eroded during the Cenozoic from some sections.

All these led to the conclusion that sections described in this paper belong to the palaeogeographic and tectonic unit determined by Placer (1998b, 2008) as the DTZ (Dinaric Transition Zone). From all locations presented in this paper only at one (sites 055 and 671) we could clearly confirm that the formations belong to the SB succession as suggested previously (Buser, 2010; Placer, 1998b, 2008). Other SB successions were identified in the area situated south from the supposed Marija Reka Fault, like on the Čemšeniška Planina (Fig. 1, Scherman et al. 2023). All the studied new sections and stratigraphical columns lie north of this important fault expect for the Marija Reka section itself. The position of the Krvavica section is not clear, could be south or north from the western branch of the MRF or this latter dissects in two the section itself. This shows that the Dinaric successions reappear north of the Slovenian Basin succession, involving the nappe position of this latter, as indicated by previous studies (Placer, 1998b, 2008; Buser 2010, Rozic et al 2019; Fig. 1b).

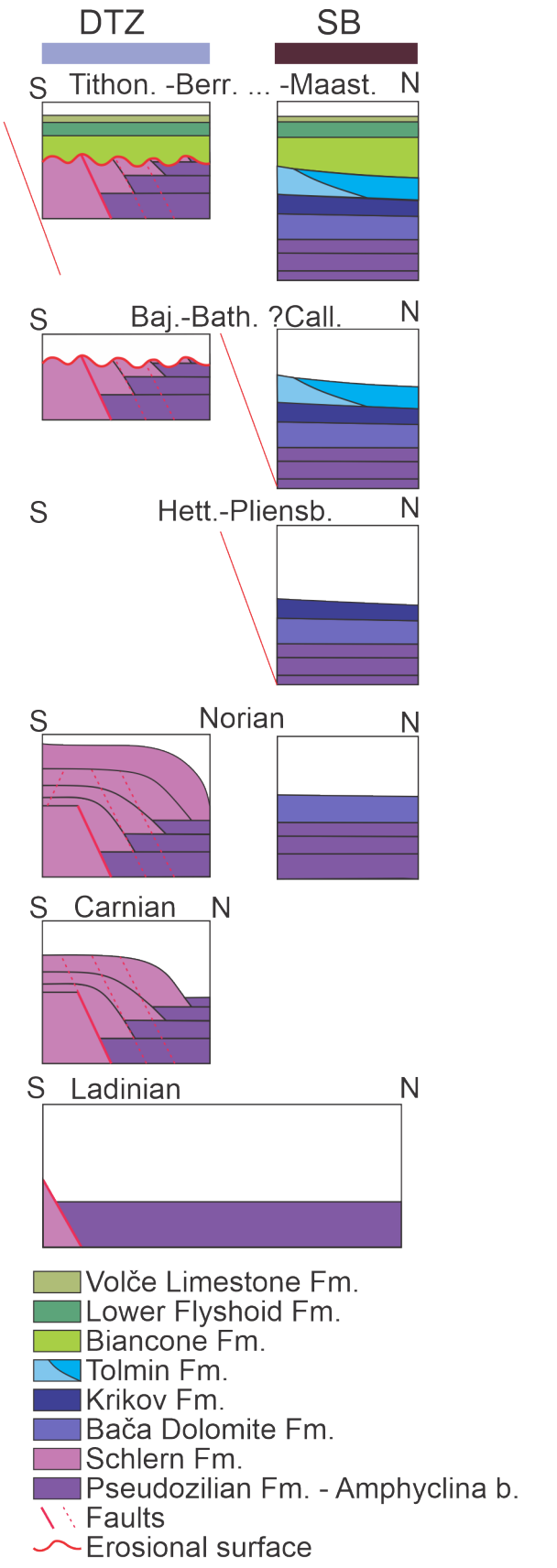

Fig. 28. Comparison of the Mesozoic evolution of the Dinaric Transitional Zone (DTZ) and Slovenian Basin (SB) during the Ladinian – Maastrichtian interval. Abbreviations: Hett.: Hettangian; Pliensb.: Pliensbachian; Baj.: Bajocian; Bath.: Bathonian; Call.: Callovian; Tihon.: Tithonian; Berr.: Berriasian; Maast.: Maastrichtian.

Evolution of the Slovenian Basin and Dinaric Transition Zone

In this paper we presented new stratigraphic and sedimentological findings from the DTZ successions of the northern Sava folds. Combined with previously published studiees of the basinal successions from the same area (Scherman et al., 2023), the paleogeographic evolution of this segment of the Greater Adria margin (Schmid et al. 2020) can be better constrained. The history of the SB and the DTZ began during the Ladinian with the fragmentation of the unified Anisian Mendole Formation (e.g., Rožič et al., 2017). During the Ladinian and early Carnian, a siliciclastic and volcaniclastic deep-marine Pseudozilian formation was deposited in both paleogeographic units. After the main tectonic/volcanic period, the platform prograded above the entire DTZ area, whereas SB remained deep-marine until the end of Cretaceous. A fault-controlled margin of the platform is postulated but not confirmed within the study area (Fig. 28: Ladinian). Namely, solely the two end-member successions are observed here: the DTZ with late Ladinian-early Carnian platform carbonates (Schlern Formation) and the SB with a Carnian deep marine clastic and carbonate sequence (Amphiclyina beds). For this reason, a large thrust displacement is most probable between SB and DTZ successions which covers the gradual palaeogeographical and sedimentologic transitions between these two distinct palaeogeographical domains. At the Krvavica section, we observed the alternation of the platform and deep-water sediments. It could be interpreted as a platform-edge carbonate lobes prograding into the basin. Interestingly, the authors of the earliest works (Teller, 1907; Winkler, 1923) on the Trojane Anticline and the Tuhinj-Motnik Syncline already recognized this sedimentological phenomenon. However, as described before, the interpretation of structurally repeated boundaries between the Pseudozilian and Schlern formations would also be possible, considering the tectonic setting. Further detailed studies of this area should clarify the question. (Fig. 2. Fig. 28: Carnian).

Above the Schlern formation, the long stratigraphic gap marks the DTZ succession and is covered by the already deep marine Biancone Limestone Formation. This gap cannot be univocally explained, but in the neighbouring SB sedimentation continued and the Upper Triassic and Lower Jurassic shows rather distal basinal formations (Fig. 28). These are in sharp contrast to the overlying Middle Jurassic Ponikve breccia member of the Tolmin Formation (Scherman et al., 2023). In the wider area, this limestone megabreccia was recently recognized along the entire margin of the SB, assigned to the Bajocian–Bathonian and is interpreted to have originated during a major collapse of the Dinaric Carbonate Platform margin. Clasts in this breccia belong to the basin, slope as well as Upper Triassic and Lower Jurassic platform-margin carbonates. The collapse of the platform margin led to the first major post–Triassic retread of the platform margin (Rožič et al., 2019, 2022) and could also contribute to the origin of the described gap in the DTZ successions. The Middle Jurassic extensional deformation might have resulted in rift shoulder uplift, and this process could be associated with denudation and/or non-deposition during and just after the Mid-Jurassic extension. The denudation could erase the trace of the latest Triassic to Early Jurassic evolution of this segment of the margin.

Over a minor gap in the southernmost SB and a significant gap in the DTZ successions, a generally uniform sedimentation pattern was established in both paleogeographic entities. However, important differences still occur and are best recorded in the Biancone Limestone formation (Fig. 27: Tithonian). The formation is relatively thin (ranging up to several tens of meters) and composed almost entirely of pelagic limestone, near the Krvavica Section at the northern slope of Čemšeniška Planina (Scherman et al., 2023), but the thickness in DTZ (e.g. Brložen section) can exceed 100 m, and the succession spans a longer time interval. In contrast to the SB, in the study area the Biancone contains quite frequent resedimented limestones due to proximity of active Dinaric Carbonate Platform. Our results provide two other important pieces of information.

The onset of the Biancone Limestone Formation in the DTZ could be a combination of a substantial depression of the CCD (Weissert 1979) and probably a renewed tectonic subsidence, likely of post-rift character (Bertotti et al., 1993; Berra & Carminati 2010). Alternatively, the Tithonian subsidence can be a reflection of the subduction to obduction process along the eastern active Adriatic margin (Picotti & Cobianchi 2017). This tectonic pulse was so far poorly detected in mesoscale structures. In the form of latest Jurassic neptunian dykes From the Dinaric region, in the Julian Alps and the Alpine passive margin (e.g., Šmuc 2005; Črne et al., 2007; Whitmarsch & Manatschal, 2012; Rožič et al., 2018), slumps in the Biancone limestone in other localities (Rožič & Reháková, 2024) and origination of the Bohinj Breccia in the Bled Basin (Kukoč et al., 2012; Goričan et al., 2018).

In the studied Brložen section, syn-sedimentary normal faults were recognized, which caused slope instability associated with slump folds.

The second important information comes from the intercalated sandstone bed of the Kozlov grič section. The documented ophiolitic detritus was deposited in the early Cretaceous foreland basin situated on the thinned Greater Adria margin in front of the advancing obducted Neotethyan ophiolite sheets (Internal Dinarides) (Tari, 1994; Kukoč et al., 2012; Lužar-Oberiter et al., 2012; Goričan et al., 2018). In such a scenario, the studied paleogeographic domains were situated on the forebulge side of the foreland basin where slope instability occurred but was rarely reached by gravity mass flow deposits which derived from the ophiolite. A similar geodynamic-sedimentological situation was proposed for the northern Transdanubian Range segment of the foreland basin (Fodor et al., 2013; Sztanó et al., 2018).

The distinction between the SB and DTZ structural units is based on differences between the stratigraphic units and the overall absence of the Norian–lower Tithonian sediments in the described succession. Our results also indicate that the SB sediments marked in the Trojane Anticline and the Tuhinj-Motnik Syncline on the map of Placer (2008) largely belong to the DTZ palaeogeographic domain and not to the SB. In addition to stratigraphical complexities, the post-Mesozoic deformations largely rearranged the original palaeogeographical situation (Scherman et al., 2023). This calls for a reinterpretation or a redefinition of the Southern Alpine thrust front in this part of Slovenia, as both tectonic interpretations and stratigraphical and palaeogeographical observations should be considered in its definition.

Summary

In the Trojane Anticline and the Tuhinj-Motnik Syncline, located in the northern part of the Sava Folds, revision of selected parts of the Mesozoic successions was conducted. The formations were identified based on their stratigraphic position, litho- and microfacies, and biostratigraphic data.

The paper presents the lithofacies of nearly 120 selected observation sites, of which microfacies analysis and paleontological investigation were performed on ~70. Each litho- and microfacies type as well as all 141 identified microfossil taxa, is shown.

Biostratigraphy is mainly based on benthic (32 species) and planktonic foraminifera (14 species), calpionellids (12 species), and calcareous nannofossils (31 species). We also considered age-indicating forms belonging to other fossil groups, such as c-dinocysts (13 species), calcimicroba (1 species), microproblematica (6 species), Dasycladales (3 species), Porifera (2 species) and Vermes (1 species) (Tables 1–5). The following biozones could be identified in the formations: the calpionellids zones: Chitinoidellids Zone, *Boneti* Subzone, *Crassicolaria* Zone, Chitinoidellids/Primitive Calpionellids and *Tintinnopsella Intermedia* Subzones (from upper Tithonian to lower Valanginian), *Calpionellopsis* Zone, *Oblonga-Simplex* Subzone (upper Berriasian) and *Colomiella* Zone *Deflandronella* and *C. mexicana* subzones (upper Aptian–lower Albian); planktonic foraminifera zones as from *B. breggiensis* Zone *R. subticinensis* Subzone (uppermost middle Albian) to *R. appenninica* Zone (the uppermost Albian); and nannofossil zones: NJ18 (the upper Tithonian), NC1–NC3 (Berriasian–latest Valanginian), NC3– lower NC5 (Valanginian–Hauterivian), NC9–NC10 (upper Albian) and UC13–UC16 (Campanian).

For the palaeoecological interpretation, in addition to the fossil groups listed above, we also utilized semi-quantitative data from charophytes, terrestrial plants, radiolarians, stromatoporoids, gastropods, bivalves, ostracods, bryozoans, echinoderms, and the results of the microfacies analysis (Appendices 1–2).

The Mesozoic successions of the studied area belong to the Dinaric Transition Zone (DTZ), which is underlain by Palaeozoic clastics and Late Permian to Anisian carbonates. However, in the studied area, the Upper Permian and Lower Triassic strata were not recorded. In the Ladinian deep marine volcaniclastites siliciclastics and carbonates were followed by the re-established carbonate platform towards the Upper Triassic. The Ladinian and Carnian heterogenous sequences of deep-marine successions are under- and overlain by several generations of re-established carbonate platform successions. A long stratigraphic gap was followed by end-Jurassic to Cretaceous basinal formations comparable to those of the Slovenian Basin deposited. These include the lower Tithonian–lower Valangian Biancone Limestone s.l., the upper Aptian–upper Albian (Cenomanian?) Lower Flyschoid Formation and the Upper Cretaceous Volče Formation, which closes the sequence. Cretaceous formations correspond to Gora, Krško and Veliki trn formations from the southern Sava Folds.

The present-day geographic distribution of studied stratigraphic units differ from those shown on the existing geological maps. We found that either the spatial extent of units or their litho-

and/or chronostratigraphic definitions of older geological maps have to be updated. Our observations also indicate that vast areas of the northern Trojane Anticline and the Tuhinj–Motnik Syncline composed of the stratigraphic successions of the Dinaric Transition Zone. This indicates that this Dinaric transitional unit is present even north of the previously proposed Southern Alpine thrust front. They appear in this structural position due to north-dipping thrust faults. In consequence in the Sava Folds region, the lower structural boundary of the typical SB successions cannot be considered a clear marker for the Southern Alpine thrust front, which is in a strong contrast to the western Slovenian structural geometry.

Further systematic lithostratigraphic and structural geological studies are necessary to refine the existing geological maps, understand the structural evolution, and redefine the Southern Alpine thrust front.

Acknowledgment

We want to thank Sándor Józsa for the help in the petrographic description of samples (261, 326, 614). We are grateful to Anita Gáspár, Jose Carlos Jiménez-Lopez, Diana Olveczka, Daniela Rehákova, Ramin Samiee, Iryna Suprun, Osman Varol and the Hantken Foundation for their help in obtaining the literature. Thanks to László Szikszai for the technical support. The research was jointly funded by the National Research, Development, and Innovation Office of Hungary (NKFIH OTKA project No. 134873), the Hantken Foundation, and the Slovenian Research Agency (research core funding No. P1-0195). Last but not least, we would like to thank Ryder Van Liew from Quill and Key Society for proof reading the manuscript.

Appendix 1, 2 and 3: Supplementary data as-sociated with this article can be found in the on-line version at https://doi.org/10.5474/geologija.2025.007

References

Allemann, F., Catalano, R., Fares, F. & Remane, J. 1971: Standard calpionellid zonation (Upper Tithonian-Valanginian) of Western Mediterranean Province. In: Proc. Second Plankton Conf., Roma, 1970, 11: 1337-1340.

Aničić, B. 1990: Geological setting of the Orlica mountain. Geologija, 33/1: 233–287. https://doi.org/10.5474/geologija.1990.005

Aničić, B., Ogorelec, B. & Dozet, S. 2004: Geološka karta Kozjanskega 1: 50.000 = Geological map of the Kozjansko (Slovenia) 1: 50.000. Geološki zavod Slovenije, Ljubljana.

Árgyelán, G.B. 1996: Geochemical investigations of detrital chrome spinels as a tool to detect an ophiolitic source area (Gerecse Mountains, Hungary). Acta Geologica Hungarica, 39/4: 341–368.

Baumgartner, P.O., Bartolini, A. Carter, E.S., Conti, M.G., Cortese, T., Danelian, P., De Wever, P. Dumitrica, R. Dumitrica-Jud, Goričan, Š., Guex, J., Hull, D.M, Kito, N., Marcucci, M., Matsuoka, A., Murchey, B., O'Dogherty, L., Savary, J., Vishnevskaya, V., Widz, D. & Yao, A. 1995: Middle Jurassic to Early Cretaceous radiolarian biochronology of Tethys based on Unitary Associations: 1013–1048. In: Baumgartner, P.O., O'Dogherty, L., Goričan, Š., Urquhart, E., Pillevuit, A. & De Wever, P. (eds.): Middle Jurassic to Lower Cretaceous Radiolaria of Tethys: Occurrences, Systematics, Biochronology. Mémoires de Géologie: 23 p.

Benzaggagh, M. 2020: Discussion on the calpionellid biozones and proposal of a homogeneous calpionellid zonation for the Tethyan Realm. Cretaceous Research, 114, 104184.

Berra, F. & Carminati, E. 2010: Subsidence history from backstripping analysis of the Permo-Mesozoic succession of the Central Southern Alps (Northern Italy). Basin Research, 22: 952–975.

Bertotti, G., Picotti, V., Bernoulli, D. & Castellarin, A. 1993: From rifting to drifting: Tectonic evolution of the South-Alpine upper crust from the Triassic to the Early Cretaceous. Sedimentary Geology, 86/1–2: 53–76.

Brajkovič, R., Djurić, B., Gerčar, D., Cvetko Tešović, B., Rožič, B. & Gale, L. 2023: Mid-Cretaceous calcarenite in stone products from the Roman colony of Emona, Regio X (modern Ljubljana, Slovenia). Archaeometry, 65/1: 17–35.

Buser, S. 1977: Basic Geological Map SFRJ, 1:100.000, list Celje, L 33-67. Zvezni geološki zavod, Beograd.

Buser, S. 1979: Basic Geological Map SFRJ 1:100.000. Explanatory Booklet. Sheet Celje. Zvezni geološki zavod Jugoslavije, Beograd: 72 p.

Buser, S. 1986: Basic Geological Map SFRJ 1:100.000. Explanatory Booklet. Sheet Tolmin and Videm (Udine). Zvezni geološki zavod Jugoslavije, Beograd: 103 p.

Buser, S. 1989: Development of the Dinaric and Julian carbonate platforms and the intermediate Slovenian basin (NW Yugoslavia). In: Carulli, G.B., Cucchi, F. & Radrizzani, C.P. (eds.): Evolution of the karstic carbonate

platform: Relation with other periadriatic carbonate platforms. Memorie della Società Geologica Italiana, 40: 313–320.

Buser, S. 1996: Geology of western Slovenia and its paleogeographic evolution. In: Drobne, K., Goričan, Š. & Kotnik, B. (eds.): The role of Impact Processes in the Geological and Biological Evolution of Planet Earth. International workshop, ZRC SAZU: 111–123.

Buser, S. 2010: Geological map of Slovenia 1: 250.000. Geološki zavod Slovenije, Ljubljana.

Buser, S. & Dozet, S. 2009: Jura = Jurassic. In: Pleničar, M., Ogorelec, B. & Novak, M. (eds.): Geologija Slovenije = The geology of Slovenia. Geološki zavod Slovenije, Ljubljana: 215–254.

Cadet, J.P. 1978: Essai sur l'évolution alpine d'une paléomarge continentale; les confins de la Bosnie-Herzegovine et du Monténegro (Yougoslavie): Mémoires de la Société Géologique de France, 133: 83 p.

Čar, J. 2010: Geološka zgradba idrijsko–cerkljanskega hribovja. Tolmač h geološki karti idrijsko – cerkljanskega hribovja med Stopnikom in Rovtami 1: 25.000 – Geological structure of the Idrija–Cerkno hills. Explanatory Book to the Geological map of the Idrija–Cerkljansko hills. Geološki zavod Slovenije, Ljubljana: 127 p.

Caron, M. &Cousin, M. 1972: Le sillon slovene; les formations terrigenes cretacees des unites externes au Nord-Est de Tolmin (Slovenie occidentale). Bulletin de la Société Géologique de France, S7-XIV /1–5: 34–45. https://doi.org/10.2113/gssgfbull.S7-XIV.1-5.34

Celarc, B., Goričan, Š. & Kolar-Jurkovšek, T. 2013: Middle Triassic carbonate-platform breakup and formation of small-scale half-grabens (Julian and Kamnik–Savinja Alps, Slovenia). Facies, 59: 583-610. https://doi.org/10.1007/s10347-012-0326-0

Cousin, M. 1970: Esquisse geologique des confins italo-yougoslaves; leur place dans les Dinarides et les Alpes meridionales. Bulletin de la Société Géologique de France; S7-XII /6: 1034–1047. https://doi.org/10.2113/gssgfbull.S7-XII.6.1034

Cousin M. 1973: Le sillon slovene: les formations triasiques, jurassiques et neocomiennes au Nord-Est de Tolmin (Slovenie occidentale Alpes meridionales) et leurs affinites dinariques. Bulletin de la Société Géologique de France, S7-XV (3-4): 326–339. https://doi.org/10.2113/gssgfbull.S7-XV.3-4.326

Cousin, M. 1981: Les repports Alpes – Dinarides. Les confins de I'talie et de la Yougoslavie. Annales de la Société géologique du Nord, 5/1: 1–521.

Császár, G. & Árgyelán, G.B. 1994: Stratigraphic and micromineralogic investigations on Cretaceous Formations of the Gerecse Mountains, Hungary and their palaeogeographic implications. Cretaceous Research, 15/4: 417–434.

Dozet, S. & Buser, S. 2009: Trias. In: Pleničar, M., Ogorelec, B. & Novak, M. (eds.): Geologija Slovenije. Geološki zavod Slovenije, Ljubljana: 161–214.

Dunham, R.J. 1962: Classification of carbonate rocks according to depositional texture. In: Ham, W.E. (ed.): Classification of Carbonate Rocks, American Association Petrology Geology Memoir, 1: 108–121.

Fodor, L., Sztanó, O. & Kövér, Sz. 2013: Pre-conference field trip: Mesozoic deformation of the northern Transdanubian Range (Gerecse and Vértes Hills). Acta Mineralogica-Petrographica, Field Guide Series: 31, 1–34.

Folk, R.L. 1962: Spectral subdivision of limestone types. In: Ham. W.E. (ed.): Classification of Carbonate Rocks-A Symposium. Am. Assoc. Pet. Geol. Mem., 1: 62–84.

Fois, E., & Jadoul, F. 1983: La dorsale paleocarnica anisica di Pontebba. Rivista Italiana di Paleontologia e Stratigrafia, 89/1: 3–30.

Gale, L. 2010: Microfacies analysis of the Upper Triassic (Norian) "Baca Dolomite": early evolution of the western Slovenian Basin (eastern Southern Alps, western Slovenia). Geologica Carpathica, 61/4: 293–308. https://doi.org/10.2478/v10096-010-0017-0

Gale, L., Kolar-Jurkovšek, T., Šmuc, A. & Rožič, B. 2012: Integrated Rhaetian foraminiferal and conodont biostratigraphy from the Slovenian Basin, Eastern Southern Alps. Swiss Journal of Geosciences, 105/3: 435–462. https://doi.org/10.1007/s00015-012-0117-1

Gale L., Novak, U., Kolar-Jurkovšek, T., Križnar, M. & Stare, F. 2017: Characterization of silicified fossil assemblage from upper Carnian "Amphiclina beds" at Crngrob (central Slovenia). Geologija, 60/1:61–75. https://doi.org/10.5474/geologija.2017.005

Gale, L., Peybernes, C., Mavrič, T., Kolar-Jurkovšek, T. & Jurkovšek, B. 2020: Facies and fossil associations in Ladinian carbonate olistoliths at Dole pri Litiji, Slovenia. Facies, 66: 18 p. https://doi.org/10.1007/s10347-020-00601-0

Gerčar, D., Zupančič, N., Waśkowska, A., Pavšič, J. & Rožič, B. 2022: Upper Campanian bentonite layers in the Scaglia-type limestone of the

northern Dinarides (SE Slovenia). Cretaceous Research, 134, 105158

Gianolla, P., Zanche, V. & Mietto, P. 1988: Triassic sequence stratigraphy in the Soutern Alps (Northern Italy): definition of sequences and basin evolution. SEPM Spec. Publ. 60: 730–751.

Gerčar, D. 2024: Stratigrafija in sedimentologija Spodnje flišoidne formacije Slovenskega bazena. Doktorska disertacija. Univerza v Ljubljani, Fakulteta za gradbeništvo in geodezijo, Ljubljana: 174 p.

Goričan, Š., Rožič, B. & Pavšič, J. 2006: Datacije jurskih radiolarijskih rožencev Tolminskega pokrova. In: Zbornik povzetkov, Slovenski geološki kongres, Idrija, 46–47.

Goričan, Š. & Pavšič, J. & Rožič, B. 2012a: Bajocian to Tithonian age of radiolarian cherts in the Tolmin Basin (NW Slovenia). Bulletin de la Société Géologique de France, 183: 369–382. https://doi.org/10.2113/gssgfbull.183.4.369

Goričan, Š., Košir, A., Rožič, B., Šmuc, A., Gale, L., Kukoč, D, Celarc, B., Crne, A., Kolar-Jurkovšek, T., Placer, L. & Skaberne, D. 2012b: Mesozoic deep-water basins of the eastern Southern Alps (NW Slovenia). Journal of Alpine Geology, 54: 101–143.

Goričan, Š., Žibret, L., Košir, A., Kukoč, D. & Horvat, A. 2018: Stratigraphic correlation and structural position of Lower Cretaceous flysch-type deposits in the eastern Southern Alps (NW Slovenia). International Journal of Earth Sciences, 107/8: 2933-2953. https://doi.org/10.1007/s00531-018-1636-4

Goričan, Š., Đaković, M., Baumgartner, P.O., Gawlick, H.J., Cifer, T., Djerić, N., Horvat, A., Kocjančič, A., Kukoč, D. & Mrdak, M. 2022: Mesozoic basins on the Adriatic continental margin–a cross-section through the Dinarides in Montenegro/Mezozojski bazeni na kontinentalnem robu Jadranske plošče–presek čez Dinaride v Črni gori. Folia biologica et geologica, 63/2: 85–150.

Goričan, Š. & Šmuc, A. 2004: Albian Radiolaria and Cretaceous stratigraphy of Mt. Mangart (Western Slovenia). Razprave IV. razreda SAZU. 45. 29-49. Grad, K. 1969: Pseudo-Zilian beds between Celje and Vransko. Geologija, 12: 91–105.

Grad, K. 1969: Pseudo-zilian beds between Celje and Vransko. Geologija, 12/1: 91–105. Retrieved from https://www.geologija-revija.si/index.php/geologija/article/view/266

Haas, J., Kovács, S., Krystyn, L. & Lein, R. 1995: Significance of Late Permian-Triassic facies zones in terrane reconstructions in the Alpine-North Pannonian domain. Tectonophysics, 242/1–2: 19–40. https://doi.org/10.1016/0040-1951(94)00157-5

Lapanje, V. & Šribar, Lj. 1973: Zgornjekredni sedimenti na območju Posavskih gub. (Upper Cretaceous Deposits in the Sava Folds). Geologija, 16: 237–244.

Loriga, C.B., Masetti, D. & Neri, C. 1982: La Formazione di Werfen (Scitico) delle Dolomiti occidentali: sedimentologia e biostratigrafia. Associato all'Unione stampa periodica italiana, 501–585

Lužar-Oberiter, B., Mikes, T., Dunkl, I., Babić, L. & von Eynatten, H. 2012: Provenance of Cretaceous synorogenic sediments from the NW Dinarides (Croatia). Swiss Journal of Geosciences, 105: 377–399.

Mlakar, I. 1985: A contribution to the knowledge of the geological structure of the Sava Folds and their Southern border. Geologija, 28/1: 157–182.

Mlakar, I. 2003: The problems of Palaeozoic beds and reconstruction of the Middle Permian sedimentary basin in Western Slovenia. Geologija, 46/1: 5–39. https://doi.org/10.5474/geologija.2003.001

Novak, M. & Skaberne, D. 2009: Zgornji Karbon in Spodnji Perm = Upper Carboniferous and lower Permian). In: Pleničar, M., Ogorelec, B. & Novak, M. (eds.): Geologija Slovenije =The geology of Slovenia). Geološki zavod Slovenije, Ljubljana: 99–136.

Oprčkal, P., Gale, L., Kolar-Jurkovšek, T. & Rožič, B. 2012: Outcrop-scale evidence for the Norian-Rhaetian extensional tectonics in the Slovenian Basin (Southern Alps). Geologija, 55/1: 45–56. https://doi.org/10.5474/geologija.2012.003

Ogorelec, B., Šribar, Lj. & Buser, S. 1976: Olitologij in biostratigrafiji volčanskega apnenca = On lithology and Biostratigraphy of Volče limestone. Geologija, 19: 125–151.

Ogorelec, B. & Dozet, S. 1997: Upper Triassic, Jurassic and Lower Cretaceous beds in eastern Sava Folds - Section Laze at Boštanj (Slovenia). RMZ-Materials and geoenvironment, 44/3–4: 223–235.

Pessagno, E.A. & Newport, R.L. 1972: A technique for extracting Radiolaria from radiolarian cherts. Micropaleontology, 18: 231–234. https://doi.org/10.2307/1484997

Picotti, V. & Cobianchi, M. 2017: Jurassic stratigraphy of the Belluno Basin and Friuli Platform: a perspective on far-field compression in the

Adria passive margin. Swiss Journal of Geosciences, 110: 833–850.

Placer, L. 1998a: Structural meaning of the Sava folds. Geologija, 41/1: 191–221.

Placer, L. 1998b: Contribution to the macrotectonic subdivision of the border region between Southern Alps and External Dinarides. Geologija, 41/1: 223–255. https://doi.org/10.5474/geologija.1998.013

Placer, L. 2008: Principles of the tectonic subdivision of Slovenia. Geologija, 51/2: 205–217. https://doi.org/10.5474/geologija.2008.021

Pober, E. & Faupl, P. 1988: The chemistry of detrital chromian spinels and its implications for the geodynamic evolution of the Eastern Alps. Geologische Rundschau, 77: 641–670.

Poljak, M. 2017: Geological map of the Eastern part of the Krško Basin 1: 25.000 (with explanatory booklet). Geološki zavod Slovenije, Ljubljana, Slovenia.

Premru, U. 1983a: Basic Geological Map SFRJ 1:100.000, Sheet Ljubljana, L-33-66. Zvezni Geološki zavod, Beograd.

Premru, U. 1983b: Basic Geological Map SFRJ 1:100.000. Explanatory Booklet. Sheet Ljubljana. Zvezni geološki zavod Jugoslavije, Beograd. 72 p.

Ramovš, A. & Kochansky-Devidé, V. 1981: Permian-Triassic boundary at Brušane village in Velebit Mt. Geologija, 24/2: 327–330.

Ramovš, A. 1986. Globljemorski zgornjetriasni (karnijski) apnenci na loškem ozemlju. Pelagische obertriadische (karnische) Kalksteine im Gebiet von Škofja Loka. Loški razgledi, 33: 111–114.

Ramovš, A. 1997: Two new petalodont teeth (Chondrichthyes, Upper Carboniferous) from the Karavanke Mountains, Slovenia. Geologija, 40/1: 109–112.

Ramovš, A. 1998a. Amoniti na loškem ozemlju. Loški Razgledi, 45: 11–13

Ramovš, A., Aničič, B. & Dozet, S. 2001: Comparison of Lower Triassic developments in Eastern Sava Folds and Northern Julian Alps (Slovenia). RMZ-Mater. Geoenvir. Ljubljana: 48/3: 415–432.

Reháková, D. & Michalík, J. 2000: Calcareous dinoflagellate and calpionellid bioevents versus sea-level fluctuations recorded in the West-Carpathian (Late Jurassic/Early Cretaceous) pelagic environments. Geologica Carpathica, 51/4: 229–243.

Reháková, D. & Rožič, B. 2019. Calpionellid biostratigraphy and sedimentation of the Biancone limestone from the Rudnica Anticline (Sava Folds, eastern Slovenia). Geologija, 62/2: 89–101. https://doi.org/10.5474/geologija.2019.004

Rižnar, I. 2006: Zgodovina raziskav krških in velikotrnskih plasti (revizija krških in velikotrnskih plasti). Razprave IV raz. SAZU XLVII 2, 79–99, Ljubljana.

Rižnar, I. & Jovanović, D. 2006: Stone material of regional provenance from Sirmium. Starinar, 56: 139–152.

Rožič, B. 2005: Albian–Cenomanian resedimented limestone in the Lower Flyschoid Formation of the Mt. Mrzli Vrh Area (Tolmin region, NW Slovenia). Geologija, 48/2: 193–210. https://doi.org/10.5474/geologija.2005.017

Rožič, B. 2006: Sedimentology, stratigraphy and geochemistry of Jurassic rocks in the western part of the Slovenian Basin. Ph.D. thesis, University of Ljubljana, Ljubljana: 148 p.

Rožič, B. 2009: Perbla and Tolmin formations: revised Toarcian to Tithonian stratigraphy of the Tolmin Basin (NW Slovenia) and regional correlations. Bulletin de la Société Géologique de France, 180: 411–430. https://doi.org/10.2113/gssgfbull.180.5.411

Rožič, B. 2016: Paleogeographic units. In: Novak, M. & Rman, N. (eds.): Geological atlas of Slovenia. Geološki zavod Slovenije, Ljubljana: 14–15.

Rožič, B., Kolar-Jurkovsek, T. & Šmuc, A. 2009: Late Triassic sedimentary evolution of Slovenian Basin (eastern Southern Alps): description and correlation of the Slatnik Formation. Facies, 55: 137–155. https://doi.org/10.1007/s10347-008-0164-2

Rožič, B., Gale, L. & Kolar-Jurkovšek, T. 2013: Extent of the Upper Norian-Rhaetian Slatnik formation in the Tolmin nappe, Eastern Southern Alps. Geologija, 56/2: 175–186. https://doi.org/10.5474/geologija.2013.011

Rožič, B., Goričan, Š., Švara, A. & Šmuc, A. 2014: The Middle Jurassic to Lower Cretaceous succession of the Ponikve klippe: The southernmost outcrops of the Slovenian Basin in Western Slovenia. Rivista Italiana di Paleontologia e Stratigrafia, 120: 83–102. https://doi.org/10.13130/2039-4942/6051

Rožič, B., Kolar-Jurkovšek, T. Žvab Rožič, P. & Gale, L. 2017: Sedimentary record of subsidence pulse at the Triassic/Jurassic boundary interval in the Slovenian Basin (eastern Southern Alps). Geologica Carpathica, 68: 543–561. https://doi.org/10.1515/geoca-2017-0036

Rožič, B., Gale, L., Brajkovič, R., Popit, T. & Žvab Rožič, P. 2018: Lower Jurassic succession at

the site of potential Roman quarry Staje near Ig (central Slovenia). Geologija, 61/1: 49–71. https://doi.org/10.5474/geologija.2018.004

Rožič, B., Gerčar, D., Oprčkal, P., Švara, A., Turnšek, D., Kolar-Jurkovšek, T., Udovč, J., Kunst, L., Fabjan, T., Popit, T. & Gale, L. 2019: Middle Jurassic limestone megabreccia from the southern margin of the Slovenian Basin. Swiss Journal of Geosciences, 112/1: 163–180. https://doi.org/10.1007/s00015-018-0320-9

Rožič, B., Gale, L., Oprčkal, P., Švara, A., Popit, T., Kunst, L., Turnšek, D., Kolar-Jurkovšek, T., Šmuc, A., Ivekovič, A., Udovč, J. & Gerčar, D. 2022: A glimpse of the lost Upper Triassic to Middle Jurassic architecture of the Dinaric Carbonate Platform margin and slope. Geologija, 65/2: 177–216. https://doi.org/10.5474/geologija.2022.011

Rožič, B., Kocjančič, A., Gale, L. Zupančič, N., Popit, T., Vodnik, P., Kolar-Jurkovšek, T., Brajkovič, R. & Rožič, P. 2024: Architecture and sedimentary evolution of the Ladinian Kobilji curek basin (External Dinarides, central Slovenia). Swiss Journal of Geosciences, 117/3. https://doi.org/10.1186/s00015-023-00449-w

Rožič, B. & Popit, T. 2006: Resedimented limestones in Middle and Upper Jurassic succession of the Slovenian Basin. Geologija, 49/2: 219–234. https://doi.org/10.5474/geologija.2006.016

Rožič, B. & Reháková, D. 2024: Sedimentology and biostratigraphy of the Biancone Limestone Formation of the Tolmin Basin (Southern Alps, NW Slovenia). Cretaceous Research, 163, 105958.

Rožič, B. & Šmuc, A. 2011: Gravity-flow deposits in the Toarcian Perbla formation (Slovenian basin, NW Slovenia). Rivista italiana di paleontologia e stratigrafia, 117/2.

Samiee, R. 1999: Fazielle und diagenetische Entwicklung von Plattform-Becken-Ubergangen
in der Unterkreide Sloweniens. PhD Thesis, University of Erlangen, 185pp

Scherman, B., Rožič, B., Görög, Á., Kövér, S. & Fodor, L. 2023: Upper Triassic–to Lower Cretaceous Slovenian Basin successions in the northern margin of the Sava Folds. Geologija, 66/2: 205–228. https://doi.org/10.5474/geologija.2023.009

Schlagintweit, F., Gerčar, D. & Rožič, B. 2024: Reworked neritic fauna in the Lower Cretaceous 'Lower Flyschoid Formation'of the Tolmin Nappe (Slovenia): New data on biostratigraphy and palaeogeography. Cretaceous Research, 154: 105746

Schmid, S. M., Bernoulli, D., Fügenschuh, B., Maßenco, L., Schefer, S., Schuster, R., Tischler, M. & Ustaszewski, K. 2008: The Alpine-Carpathian-Dinarideorogenic system: Correlation and evolution of tectonic units. Swiss Journal of Geosciences, 101: 139–183. https://doi.org/10.1007/s00015-008-1247-3

Schmid, S.M., Fügenschuh, B., Kounov, A., Maţenco, L., Nievergelt, P., Oberhänsli, R., Pleuger, J., Schefer, S., Schuster, R., Tomljenović, B., Ustaszewski, K. & van Hinsbergen, D.J.J. 2020: Tectonic units of the Alpine collision zone between Eastern Alps and western Turkey. Gondwana Research, 78: 308–374. https://doi.org/10.1016/j.gr.2019.07.005

Šmuc, A. 2005: Jurassic and Cretaceous stratigraphy and sedimentary evolution of the Julian Alps, NW Slovenia. Založba ZRC.

Smuc, A. & Goričan, S. 2005: The Jurassic sedimentary evolution of a carbonate platform into a deep-water basin, Mt. Mangart (Slovenian-Italian border). Rivista Italiana di Paleontologia e Stratigrafia, 111/1.

Šmuc, A. & Čar, J. 2002: Upper Ladinian to Lower Carnian sedimentary evolution in the Idrija-Cerkno Region, Western Sovenia. Facies, 46: 205–216.

Skaberne, D., Čar, J., Pristavec, M., Rožič, B. & Gale, L. 2024: Middle Triassic deeper-marine volcano-sedimentary successions in western Slovenia. Geologija, 67/1: 71–103. https://doi.org/10.5474/geologija.2024.005

Sztanó, O., Császár, G., Fodor, L. & Budai, T. 2018. Cretaceous. In: Budai, T. (ed.): Geology of the Gerecse Mts. Mining and Geological Survey of Hungary, Budapest ISBN 978-963-671-312-6

Tari, G. 1994: Alpine Tectonics of the Pannonian basin. PhD. Thesis, Rice University, Texas, USA. 501 p.

Teller, F. 1898: Erläuterungen zur Geologischen Spezialkarte der Österr.–Ungar. Monarchie. Eisenkapel und Kanker. Geol. R. A., Wien

Teller, F. 1907: Geologische Karte der Österr.–Ung. Monarchie, SWGruppe, 93, Cilli-Ratschach, Wien.

Trejo, M. 1975. Zonificacion del limite Aptiano—Albiano de Mexico Rev. Inst. Mex. Petr. (Mexico), Revista del Instituto Mexicano del Petroleo, 7: 6–29.

Vrabec, M. 2001: Strukturna anliza cone Savskega preloma med Trstenikom in Stahovnico (Structural analysis of the Sava fault zone between Trstenik and Stahovica) (in Slovenian with English abstract). Unpublished PhD thesis, University of Ljubljana: 94 p.

Vrabec, M. & Fodor, L. 2006: Late Cenozoic tectonics of Slovenia: Structural styles at the northeastern corner of the Adriatic microplate. In: Pinter, N., Grenerczy, Gy., Weber, J., Medak, D. & Stein, S. (eds.): The Adria Microplate: GPS Geodesy, Tectonics, and Hazards. – NATO Science Series, IV, Earth and Environmental Sciences, 61: 151–168.

Weissert, H. 1979. Die Paläoozeanographie der südwestlichen Tethys in der Unterkreide. Mitt. Geol. Inst. Eidg. Tech. Hochsch. Univ. Zürich, 226: 1–174.

Wood, G.D., Gabriel, A.M. & Lawson, J.C. 1996: Palynological techniques – processing and microscopy. In: Jansonius, J. & McGregor, D.C. (eds.): Palynology: Principles and Applications 1. American Association of Stratigraphic Palynologists Foundation, 29–50.

Whitmarsh, R. & Manatschal, G. 2012: Evolution of magma poor continental margins: From rifting to the onset of seafloor spreading. Phanerozoic Passive Margins, Cratonic Basins and Global Tectonic Maps, 303-317. https://doi.org/10.1016/B978-0-444-56357-6.00008-1

Winkler, A. 1923: Über den Bau der östlichen Südalpen. Mitteilungen der geologischen Gesellschaft in Wien. XVI. Bd. S. 1–272.

GEOLOGIJA 68/201-219, Ljubljana 2025

https://doi.org/10.5474/geologija.2025.008

Article

Carbon cycling dynamics in the headwater Radovna stream recharged by Lipnik springs, a carbonate catchment in the Julian Alps, Slovenia, based on stable isotope analysis

Dinamika kroženja ogljika v zgornjem toku potoka Radovna, ki ga napajajo izviri Lipnik, znotraj karbonatnega zaledja v Julijskih Alpah (Slovenija), na podlagi analize stabilnih izotopov

Tjaša KANDUČ[1]*, Timotej VERBOVŠEK[2] & Nataša MORI[3]

[1]Department of Environmental Sciences, Jožef Stefan Institute, Jamova cesta 39, SI-1000 Ljubljana, Slovenia; *corresponding author: tjasa.kanduc@ijs.si
[2]Department of Geology, Faculty of Natural Sciences and Engineering, University of Ljubljana, Aškerčeva 12, SI-1000 Ljubljana, Slovenia; e-mail: timotej.verbovsek@ntf.uni-lj.si
[3]Department of Organisms and Ecosystem Reserach, National Institute of Biology, Večna pot 121, 1000, Ljubljana, Slovenia; e-mail: natasa.mori@nib.si

Prejeto / Received 8. 4. 2025; Sprejeto / Accepted 21. 7. 2025; Objavljeno na spletu / Published online 10. 12. 2025

Key words: total alkalinity, stable isotopes, carbon, pCO_2, headwater stream, Julian Alps
Ključne besede: totalna alkalnost, stabilni izotopi, ogljik, pCO_2, zgornji tok porečja, Julijske Alpe

Abstract

Carbon cycling was investigated monthly (July, August, September, October, November, March and May) from July 2023 to May 2024 in the Radovna stream originating from the permanent Lipnik spring in the Julian Alps, Slovenia using isotopic composition of carbon in dissolved inorganic carbon ($\delta^{13}C_{DIC}$) and particulate organic carbon ($\delta^{13}C_{POC}$). The investigated catchment is composed of massive coarse - crystal dolomite and limestone. Total alkalinity ranged from 2.2 to 2.7 mM and is characteristic for carbonate pristine environments. In-situ parameters e.g. dissolved oxygen ranged from 11.0 to 12.0 mg/L, pH from 7.9 to 8.1 and specific electrical conductivity from 275 to 318 µS/cm, respectively. The values of dissolved oxygen reflect that the water system is well oxygenated. CO_2 presented a source of carbon to the atmosphere during all investigated months. Oversaturation with CO_2 is 1.01 to 4.1 times of atmospheric value. $\delta^{13}C_{DIC}$ ranged from -11.8 to -9.7 ‰. This indicates that dissolved inorganic carbon under different discharge conditions mainly originates from the dissolution of carbonates (from 50.3 % to 57.3 %), followed by the degradation of organic matter (from 42.8 % to 49.7 %). Equilibration with atmospheric CO2 has a negligible impact, ranging from 0.01 % to 0.11 %. $\delta^{13}C_{POC}$ in river water indicate sources such as plant debris, with $\delta^{13}C_{POC}$ of -29.4 ‰, and highly degraded soil organic matter, with $\delta^{13}C_{POC}$ of -24.9 ‰. The $\delta^{13}C_{DIC}$ and $\delta^{13}C_{POC}$ values are typical for a forest stream flowing over a limestone substrate. Strong statistical negative significant correlation was obtained between electrical conductivity and water temperature, mass of total suspended solids (m_{TSS}) and pH.

Izvleček

Ogljikov cikel smo preučevali mesečno (julij, avgust, september, oktober, november, marec, maj) od julija 2023 do maja 2024 v potoku Radovne, ki izvira iz stalnega izvira Lipnik v Julijskih Alpah, Slovenija, z uporabo izotopske sestave ogljika v raztopljenem anorganskem ogljiku ($\delta^{13}C_{DIC}$) in partikulatnem organskem ogljiku ($\delta^{13}C_{POC}$). Raziskano porečje je sestavljeno iz masivnega grobo-kristalnega dolomita in apnenca. Totalna alkalnost se je spreminjala od 2,2 do 2,7 mM in je značilna za karbonatna naravna okolja. In-situ parametri kot je raztopljen kisik so se spreminjali od 11,0 do 12,0 mg/L, pH od 7,9 do 8,1 mg/L, specifična elektroprevodnost pa od 275 do 318 µS/cm. Vrednosti raztopljenega kisika odražajo, da je vodni sistem dobro prezračen s kisikom. CO_2 predstavlja sproščanje ogljika v atmosfero iz potoka v vseh preiskanih mesecih. Prenasičenost s CO_2 je 1,01 do 4,1 krat večja od atmosferske vrednosti. $\delta^{13}C_{DIC}$ se je spreminjala od -11,8 ‰ do -9,7 ‰. To kaže, da raztopljeni anorganski ogljik pri različnih pretokih vode večinoma izvira iz raztapljanja karbonatov (od 50,3 % do 57,3 %), sledi pa razgradnja organske snovi (42,8 % do 49,7 %). Uravnoteženje z atmosferskim CO2 ima zanemarljiv vpliv, v razponu od 0,01 % do 0,11 %. Partikulatni organski material (POC) izvira iz površinskega in podzemnega toka. $\delta^{13}C_{POC}$ v odvzeti vodi je odražal vir iz rastlinskih ostankov z $\delta^{13}C_{POC}$ -29,4 ‰ in razgrajenega preperinskega organskega materiala z $\delta^{13}C_{POC}$ -24,9 ‰. Vrednosti $\delta^{13}C_{DIC}$ in $\delta^{13}C_{POC}$ so tipične za gozdni potok, ki teče po apnenčasti podlagi. Močna, statistično značilna negativna korelacija je bila ugotovljena med elektroprevodnostjo in temperaturo vode, maso celotne suspendirane snovi (m_{TSS}) in pH.

Introduction

Rivers play a pivotal role in the global carbon cycle, acting as conduits that transport carbon between terrestrial, aquatic, and atmospheric systems. They facilitate the movement of dissolved inorganic carbon (DIC), dissolved organic carbon (DOC), and particulate organic carbon (POC), significantly influencing both local and global carbon dynamics (Battin et al., 2008). During high-flow events, rivers can export substantial amounts of DOC and POC through overland runoff, introducing plant-derived organic matter into aquatic environments. Moreover, rivers often serve as sources of carbon dioxide (CO_2) to the atmosphere (Raymond et al., 2013), with concentrations frequently surpassing ambient levels, underscoring their role as net CO_2 sources. Headwater streams (Richardson, 2019) directly reflect carbon input from soils and groundwaters and are important due to their large proportion in global river networks, representing more than 96 % of the total number of streams. As a result, they contribute significant amounts of CO_2 to the atmosphere, accounting for approximately 36 % (i.e., 0.93 Pg C yr–1) of total CO_2 outgassing from rivers and streams globally (Marx et al., 2017). The analysis by Marx et al., (2017) indicated that the global river average pCO_2 of 3100 ppm is more often exceeded by contributions from small streams when compared to rivers with larger catchments (> 500 km^2).

Stable isotopes, such as carbon isotopes (^{13}C and ^{12}C) in dissolved inorganic carbon (DIC), are particularly useful for tracing sources of carbon, understanding processes like photosynthesis, respiration, dissolution of carbonates/precipitation of carbonates within river systems (Kendall & McDonell, 1998; Lyons et al., 2013). Isotopic equilibrium between river water and the atmosphere has been demonstrated to be an exception in most cases (Gammons et al., 2011). Landscape, climate, catchment lithology, and vegetation type influence $\delta^{13}C_{DIC}$ values. In highly turbulent river systems, such as those with a torrential character or those exhibiting Alpine or Alpine – Dinaric flow regimes, photosynthesis can be neglected (Kanduč et al., 2007a). The $\delta^{13}C_{DIC}$ value is determined either by the fractionation that occurs during carbon transformation or by the mixing of carbon from different sources (Atekwana & Krishnamurthy, 1998; Doctor et al., 2008; Karlović et al., 2022; Knoll et al., 2024; Evans et al., 2024). The isotopic composition of particulate organic carbon ($\delta^{13}C_{POC}$) is related to its origin in the terrestrial environment, leaching from the terrestrial sources and in stream processes (Kanduč et al., 2007b; Waldron et al., 2018; Utsumi et al., 2025).

The main objective was to determine CO_2 saturation, and identify biogeochemical processes through carbon mass balance calculations, including organic matter degradation, carbonate dissolution and equilibration with atmospheric CO_2 using $\delta^{13}C_{DIC}$ in a small stream of the Radovna River in the Julian Alps, recharged by the permanent Lipnik Spring (Mori et al., 2015). Additionally, we investigated the origin of carbon in particulate organic carbon (POC) using $\delta^{13}C_{POC}$. The study provides important insights into the poorly understood role of headwater streams (Richardson, 2019) in global carbon dynamics.

Catchment characteristics of the studied headwater stream

The Lipnik spring system lies in the Julian Alps of northwestern Slovenia, at the foot of the Pokljuka plateau (Fig. 1). It consists of two intermittent springs and one permanent spring, with discharge elevations ranging from 665 to 692 m a.s.l. These sources give rise to a short stream that feeds into the Radovna River, which belongs to the upper Sava River catchment. Figure 1 illustrates the investigated small carbonate stream, a tributary of the Radovna River, originating from the permanent Lipnik spring. Located near the glacial valley of Krnica in Julian Alps, the Lipnik spring is a part of the Radovna–Mežakla aquifer system within the broader Sava River Basin. Tectonically, it belongs to the Julian Alps thrust, with the Mesozoic layers of the Kranjska Gora thrust to the north, and separated from the southern Karavanke mountain range and Košuta thrust by the Sava Fault (Fig. 1). The region features sedimentary layers with ages from the Lower Triassic to the Cretaceous, predominantly Upper Triassic carbonates. The catchment area (Fig. 1) comprises various geological formations. These include massive coarse-crystalline dolomite and limestone of Rhaetian and Cordevolian age, (number 84 on the map), platy micritic limestone with chert nodules from the Pokljuka Formation (number 87) and Middle Triassic (Anisian) dolomites (number 91). Additionally, there are Middle Triassic (Ladinian) clastic rocks and tuffs (number 90). Some parts of the massive and bedded Dachstein limestones transition into Main dolomites (number 76). The floor of the Radovna valley is covered with Quaternary fluvial deposits (number 12) and sections of unconsolidated moraine (number 14) are present (Fig. 1).

Hydrogeologically, the catchment is characterized by extensive, moderately to highly productive karst fracture aquifers, with smaller, localized

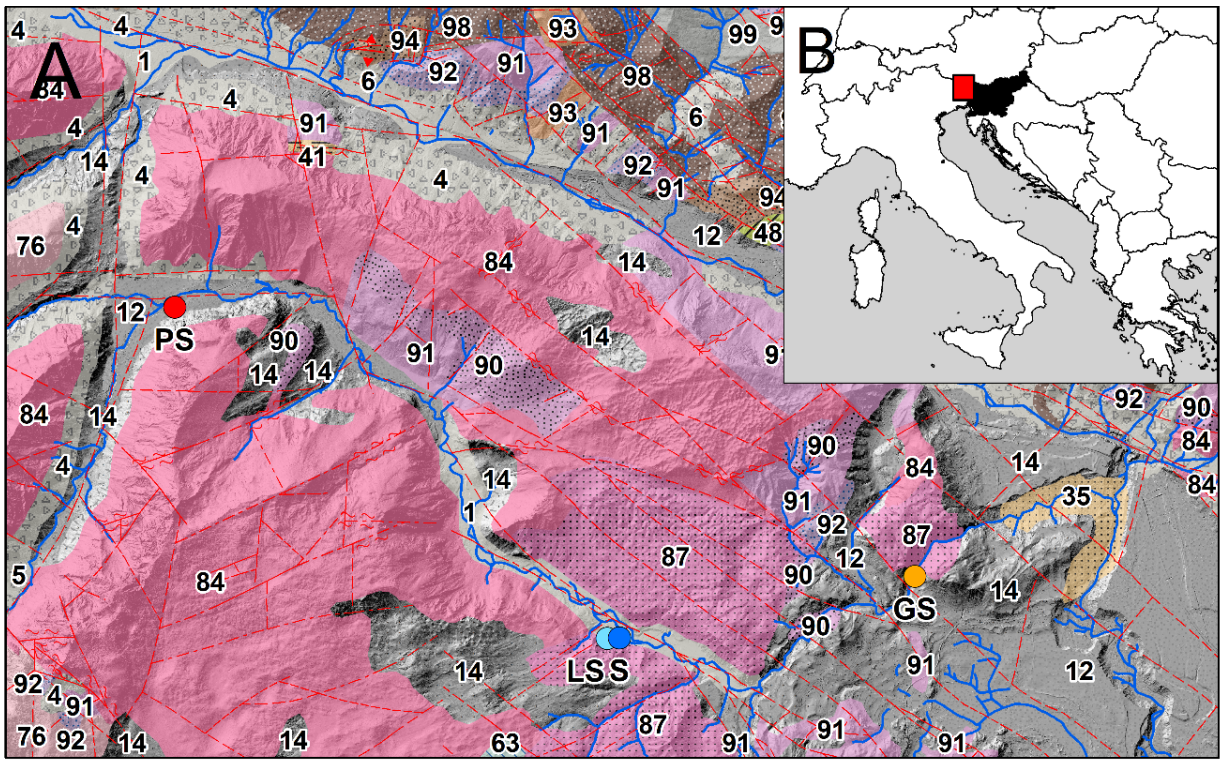

Legend

Geological map

Lithology class

- 1 Fluvial sediments (gravel, sand, silt and clay)
- 4 Rubble
- 5 Alluvial fan (rubble, gravel and silt)
- 6 Deluvium (mostly clay with various rock fragments)
- 12 Loose fluvial deposits; terraces
- 14 Till; moraine
- 35 Marly clay - Sivica
- 41 Marlstone, sandstone, reef limestone - Gornji Grad beds
- 43 Marlstone, sandstone, claystone and coal - Socka beds
- 48 Thick-bedded micritic limestone - Vreme and Kozina beds
- 63 Platy Biancone limestone with chert
- 68 Limestone of Ammonitico Rosso type, limestone breccia, marlstone and claystone
- 76 Thick-bedded Dachstein Limestone, dolomite
- 84 Massive coarse-crystalline dolomite and limestone
- 87 Platy micritic limestone with chert nodules
- 90 Shale, siltstone, limestone with chert, marlstone, sandstone, conglomerate, breccia, tuff
- 91 Thick-bedded and massive dolomite
- 92 Dolomite, siltstone, sandstone, claystone, oolitic limestone
- 93 Thick-bedded dolomite, subordinately limestone
- 94 Sandstone, shale and conglomerate
- 97 Light-gray to red limestone
- 98 Alternation of shale, quartz sandstone and conglomerate, limestone intercalations
- 99 Alternation of shale and quartz sandstone, quartz conglomerate
- 100 Alternation of shale, quartz sandstone and conglomerate, limestone intercalations

Measuring locations

Name

- PS - Gornja Radovna
- LS - Permanent Lipnik spring
- S - Stream
- GS - Podhom

N

0 1 2 3 4 5 km

Fig. 1. A. Geological map with sampling location (S - stream recharged from permanent Lipnik spring, LS – Lipnik spring, PS – precipitation station Zgornja Radovna, GS – gauging station Podhom). B. Position of research catchment area (red square) in the broader region (Slovenia is filled with black color). Geological map is in the original scale of 1:250,000 (Buser & Komac, 2002).

groundwater sources in some areas. Hydrological data from Environment Agency of the Republic of Slovenia indicate a hydrological station on the Radovna River upstream of the Lipnik spring (1953-1972) and another downstream (1957–1966), with a significant difference of approximately 2 m^3/s between their average flows, which exceeds the expected discharge of the Lipnik spring. No other significant groundwater withdrawals occur within the catchment area (Internet 1). The investigated stream is fed by the permanent Lipnik spring (Fig. 1) through groundwater recharge, subsurface flow, and surface flow.

Numerous studies have previously examined both the permanent Lipnik spring (LS, Fig. 1) and the two temporary spring outlets of the Lipnik spring in the context of water geochemistry and aquatic fauna research (Kanduč et al., 2012; Mori & Brancelj, 2013; Mori et al., 2015; Opalički, 2015; Serianz et al., 2020). Investigation of $\delta^{18}O$ and ^3H tracers in Lipnik springs recharging investigated headwater stream indicated that springs are recharged from precipitation. The value of $\delta^{18}O$ ranged from -10.7 to -8.1 ‰ Main conclusions considering $\delta^{18}O$ and ^3H were that spring water did not differ between investigated springs. $\delta^{18}O$ of the spring water was lowest during spring due to melting of snow. Concentrations of tritium ranged from 5.5 to 6.9 TU for perennial spring and 4.0 to 7.5 TU for the temporary spring, which also indicated that spring water originated from precipitation (Mori et al., 2015). From the decay of tritium, the age of the spring water was estimated to be around 3.8 years (Kanduč et al., 2012) indicating a highly permeable aquifer with fast flowing water, which is typical of karst-fissured aquifers.

Methods

Sampling

Sampling was performed during different sampling seasons e.g. three times in summer (20/07/2023, 31/08/2023, 29/09/2023), autumn (24/10/2023, 29/11/2023), winter (18/03/2024) and spring (13/05/2024). Monthly sampling throughout the year is presented in Figure 2. The distance from the Lipnik spring to the sampling point is 160 m (Fig. 1), and the width of the stream at the sampling point (Fig. 2) is 4 m. Sampling was performed in the middle of the stream (Fig. 2). Associated precipitation and discharge data are provided in Table 1.

Fig. 2. Sampling of the stream recharging from the permanent Lipnik spring in different sampling months in August 2023 (photo by Nataša Mori).

Temperature (T), electrical conductivity, dissolved oxygen (DO) and pH of stream water were measured *in-situ* using a digital multiparameter portable meter (WTW, MultiLine® 3630 IDS). The measurement errors are as follows: for temperature ±0.1 °C, for pH ±0.004 units, and for dissolved oxygen (DO) ± 0.5 %. Samples for total alkalinity were filtered through a 0.45 µm VPDF filter and stored in 30 mL High Density Polyethylene (HDPE) bottles. Samples for $\delta^{13}C_{POC}$ analyses were collected in 5 L Low Density Polyethylene (LDPE) bottles, while samples for $\delta^{13}C_{DIC}$ analyses were filtered through 0.45 µm VPDF filter and stored in 12 mL glass serum bottles filled with no headspace to prevent gas exchange. Total alkalinity and $\delta^{13}C_{DIC}$ were analysed within 24 hours of sample collection.

Total alkalinity and isotopic analyses of carbon

The total alkalinity was measured using Gran titration, as described in detail by Zuliani et al. (2020). The stable isotope composition of dissolved inorganic carbon ($\delta^{13}C_{DIC}$) was determined using a Europa Scientific 20–20 continuous flow isotope ratio mass spectrometer (IRMS) with an ANCA–TG preparation module. The method is fully described in Zuliani et al. (2020). Filters used for determination of total suspended solids (m_{TSS}) mass and for $\delta^{13}C_{POC}$ analysis were preweighed. Five liters of stream water were filtered through a

Whatman GF/F glass fiber filter (0.7 μm pore size). The filters, coated with suspended matter, were dried at 60 °C and reweighed to calculate the total suspended solids (TSS) by comparing the pre- and post-filtration weights. After weighing, the filters were treated with 3 M HCl to remove carbonate material, dried again at 60 °C in a Memmert UN 55 oven and stored until analysis. Approximately 1 mg of particulate matter was scraped from the filters for $\delta^{13}C_{POC}$ analysis (Kanduč et al., 2012).

To calibrate the $\delta^{13}C_{POC}$ measurements, we used 0.05 mg of the IAEA CH-3 (-24.72‰±0.04) and IAEA CH-7 (-32.15 ‰±0.05) reference materials, along with a weighed sample of commercially available table sugar ($\delta^{13}C$ = -27.1‰±0.2) used as a working standard. The stable isotope composition of particulate organic carbon ($\delta^{13}C_{POC}$) was measured using a Europa Scientific 20-20 continuous flow isotope ratio mass spectrometer (IRMS) equipped with an ANCA–SL preparation module. The weighing of certified materials was performed using a Mettler AE240 scale.

A mass balance calculation for three months representing low, high, and intermediate discharge conditions (July 2023, October 2023, and May 2024) was performed to evaluate in-stream biogeochemical processes, including equilibration with atmospheric CO2, degradation of organic matter, and dissolution of carbonates, using equations (1)–(4) described below.

The mass flux (F_{ex}) between the stream and the atmosphere can be calculated using the following equation (Broecker, 1974):

$$F_{ex} = D \cdot ([CO_2]_{eq} - [CO_2])/z \quad (1)$$

Where:

D - represents the diffusion coefficient of CO_2 in water, with values of 1.26 10^{-5} cm^2 /s at 10 °C and 1.67 10^{-5} cm^2 /s at 20 °C (Jähne et al., 1987).

$[CO_2]_{eq}$ and $[CO_2]$ indicate concentrations of dissolved CO_2 at equilibrium with the atmosphere and the sampled water [mol·cm^{-3}], respectively.

z – empirical thickness of the water surface layer [cm]; this boundary layer is a thin film located at the interface between air and water, and its thickness varies depending on wind speed (Broecker et al., 1978) and water turbulence (Holley, 1977).

D/z represents thin gas transfer velocity, reflecting the height of the water column that equilibrates with atmospheric CO_2 over time. Based on an average wind speed of 4 m/s characteristic for Sava River watershed in Slovenia, D/z is 8 cm/h for calm waters, 18 cm/h and 115 cm/h very turbulent conditions.

Mass balance concentrations of dissolved inorganic carbon (DIC) in stream:

$$F_s = \pm F_{ex} + F_{org} + F_{carb.} \quad (2)$$

Where:

F = Q · [DIC] (mol/s)

F_s (mol/s) – mass flow of dissolved inorganic carbon at stream sampling point

Q (m^3/s) – measured discharge at gauging station Podhom; the flow rate was taken from the nearest gauging station (Podhom, Fig. 1), which is not active within in stream itself. In the mass balance calculation, we consider the general hydrological conditions in the catchment area and calculate the individual contributions of biogeochemical processes in the mass balance. The stream sampling point has similar hydrographic characteristics as nearest gauging station.

[DIC] (mmol/L) – measured total alkalinity in stream samples

F_{ex} (mol/s) – the mass flux of dissolved inorganic carbon between the stream and the atmosphere calculated according to equation (1)

F_{org} (mol/s) – the mass flux of dissolved inorganic carbon due to degradation of organic matter

F_{carb} (mol/s) – the mass flux of dissolved inorganic carbon due to dissolution of carbonates

$F_{org.}$ and $F_{carb.}$ are unknowns in equation (2)

Isotopic mass balance, which includes mass flow and isotopic composition of individual biogeochemical processes (ex – equilibration with atmospheric CO_2, org - degradation of organic matter and carb - dissolution of carbonates), influencing $\delta^{13}C_{DIC}$ is expressed as follows:

$$F_s \cdot \delta^{13}C_s = \pm F_{ex} \cdot \delta^{13}C_{ex} + F_{org} \cdot \delta^{13}C_{org.} + F_{carb} \cdot \delta^{13}C_{carb} \quad (3)$$

$\delta^{13}C_s$ – isotopic composition of dissolved inorganic carbon in stream

$\delta^{13}C_{ex.}$ – isotopic composition of dissolved inorganic carbon if solely equilibration of CO_2 would influence DIC values, calculated according to eq. (4)

$\delta^{13}C_{org.}$- average isotopic composition of carbon in particulate organic matter in stream with value of -27.1‰

$\delta^{13}C_{carb.}$ – average isotopic composition of carbon in carbonates composing the stream catchment with value of 3.3 ‰ (Kanduč et al., 2012)

Isotopic composition of DIC due to equilibration with atmospheric CO_2 (Levin et al., 1987)

$$\delta^{13}C_{DIC} = -(0.141 \cdot T) + 10.78 + (-7.8) \quad (4)$$

$\delta^{13}C_{DIC}$ –isotopic composition of DIC in water that forms due to equilibrium with atmospheric CO_2; the isotopic composition of atmospheric CO_2 is -7.8 ‰ (Levin et al., 1987), T – water temperature [°C]

PHREEQC for Windows software (Parkhurst & Appelo, 1999) was used to calculate partial pressure of CO_2 (pCO_2). Following parameters of the water were used as input parameters: temperature (T), pH and total alkalinity (TA).

Spearman correlations (Table SM1) between measured quantities at $p<0.050$ were performed with a program Statistica 14.0.0.15, while scatterplots were performed with Excel version 2016 and Python program.

GIS Map Preparation

Visual presentation and distance measurements were performed in ESRI ArcMap 10.5.1 software. We used a geological map at a scale of 1:250,000 (Buser & Komac, 2002). Only the geological units, outcropping in the map extent, are presented on the map. Coordinates of sampling locations were determined in the field using the GNSS and were transformed from WGS84 coordinate system into the local Gauss-Krüger metric coordinate system. Location of the gauging station Podhom was obtained from the Environment Agency of the Republic of Slovenia (Internet 2). As a base map, we used a high-resolution (1 × 1 m) digital elevation model (DEM) of Slovenia obtained by laser scanning (lidar) in 2014–2015 and changed the geological map to being slightly transparent, to preserve the visualization of relief surface.

Results and discussion

The results for temperature, pH, electrical conductivity, and dissolved oxygen (DO) are reported in Table 1. Measured and calculated variables (T, pH, EC, DO, m_{TSS}, total alkalinity, log pCO_2, $\delta^{13}C_{DIC}$, $\delta^{13}C_{POC}$) versus time (date) in our study are presented in Supplementary material (SM).

The temperature ranged from 6.6 to 8.6 °C, pH from 7.9 to 8.1, and electrical conductivity from 275 to 318 µS/cm (Table 1, SM Figs. A, B, C). The temperature was the highest in June 2024. pH was higher during autumn months, and lower during spring. The highest electrical conductivity was in October 2024, while the lowest during spring. The stream water was oversaturated with oxygen (Table 1, SM Fig. D), as the saturation point is reached at 8.3 mg/l at 25 °C (Atkins, 1994). DO was the lowest in autumn month, and the highest in spring 2024 (SM Fig. D). Electrical conductivity was typical for pristine carbonate catchment at their source (Kanduč et al., 2007a). Further, we compared electrical conductivity measured in the stream with the measurements in the Radovna River during the other studies (Torkar & Brenčič, 2015; Torkar et al., 2016). Seasonal measurements conducted in February 2006, February 2008, September 2008, and March 2009 revealed lower electrical conductivities in the Radovna River, ranging from 213 to 287 µS/cm, along the entire stretch from its source to its confluence with the Sava River (Torkar & Brenčič, 2015). In a later study by (Torkar et al., 2016) electrical conductivity showed a wider range due to more intensive sampling, spanning the period from May 2005 to December 2007, with values ranging from 222 to 325 µS/cm.

Daily precipitation (P_{daily}) ranges from 0-20.6 mm (Internet 1), while daily discharge at Podhom on the River Radovna (Q_{daily}) ranges from 4 to 18.2 m^3/s (Table 1) during the investigated period. The mass of total suspended solids ranged from 0.05 to 0.2 mg/L (Table 1, SM Figure E) on a monthly basis, being higher in September 2023 due to higher discharge and precipitation, and lower in March 2023 when there was no precipitation. In this study, the mass of suspended matter ranged from 0.1 to 0.8 mg/L, which, according to Meybeck (1981), classifies it within the first class. The mass of total suspended matter in the River Sava catchment in Slovenia ranged from 0.5 to 313 mg/L, as measured in late summer 2004 and in spring, 2005 (Kanduč et al., 2007b) placing it in the fourth class according to Meybeck (1981).

Total alkalinity ranges from 2.2 to 2.7 mM being lower in summer months due to lower discharges (Table 1, SM Fig. F).

Log pCO_2 ranged from -3.4 to -2.8, $\delta^{13}C_{DIC}$ from -11.8 to -9.7 ‰, while $\delta^{13}C_{POC}$ from -29.4 to -24.9 ‰, respectively (Table 1, SM Figs. G, H, I).

Table 1. Results of measured variables in the headwater stream recharged by Lipnik springs (July 2023 - May 2024).

Lab ID	year-month--day	P_{daily}* (mm) at Zg. Radovna	Q_{daily}* (m^3/s) at Podhom	T (°C)	pH	Electrical conductivity (µS/cm)	Dissolved oxygen (mg/L)	m_{TSS} (mg/L)	Total alkalinity (mM)	log pCO_2	$\delta^{13}C_{DIC}$ (‰)	$\delta^{13}C_{POC}$ (‰)
23-208	2023-07-20	20.6	4.0	8.6	8.0	297	11.0	0.2	2.5	-2.9	-9.8	-29.4
23-306	2023-08-31	4.6	10	n.d.	8.0	n.d.	n.d.	0.2	2.5	-2.8	-11.8	-26.1
23-352	2023-09-29	4.0	5.4	7.0	7.9	318	11.1	0.8	2.7	-2.8	-11.2	-28.2
23-383	2023-10-24	0.5	18.2	7.2	7.9	300	11.3	0.5	2.2	-2.9	-11.8	-27.1
23-428	2023-11-29	0	5.3	6.6	8.1	308	11.8	0.2	2.2	-3.1	-10.7	-28.2
24-192	2024-03-18	0	7.8	7.7	8.0	300	12.0	0.05	2.3	-2.9	-11.1	-24.9
24-265	2024-05-13	5.1	7.0	8.5	7.9	275	11.0	0.3	2.6	-3.4	-9.7	-26.3

n.d. – not determined, pCO_2 – partial pressure of CO_2, $\delta^{13}C_{DIC}$ – isotopic composition of dissolved inorganic carbon, $\delta^{13}C_{POC}$ – isotopic composition of particulate organic carbon, m_{TSS} – mass of total suspended solids *data provided by EARS (Environmental Agency of the Republic of Slovenia)

Log pCO_2 values indicate that during all sampling period, the CO_2 was releasing to the atmosphere (Figure 3, SM Fig. G). Calculated log pCO_2 is one to four times higher than recent atmospheric value of pCO_2 (Lan et al., 2024). pH is approximately 8, which is typical for investigated stream and also for waters draining carbonate rocks. When waters interact with these rocks, a buffering reaction occurs, typically leading to a neutral to slightly alkaline pH. HCO_3^- acts as a buffer and helps maintaining pH in the range of 7 to 8.

Figure 4 shows $\delta^{13}C_{DIC}$ versus total alkalinity. Changes in-stream indicate processes affecting $\delta^{13}C_{DIC}$, e.g. respiration of organic matter, carbonate mineral dissolution, and equilibration with atmospheric CO_2 (Barth et al., 2003). Therefore, the $\delta^{13}C_{DIC}$ of the headwater stream is controlled by bedrock lithology, the degradation of organic matter (vegetation), and equilibration with atmospheric CO_2. The headwater stream is surrounded by narrow hill slopes covered with mixed forest composed of C_3 plants (Kanduč et al., 2012) growing over carbonate bedrock. Runoff events flush vegetation and soil material with different $\delta^{13}C$ values into the stream.

The prevailing forest communities in the Sava River watershed are various types of European beech (*Fagus sylvatica* L.) forests. At higher altitudes (900–1500 m), European beech is associated with Norway spruce (*Picea abies* (L.) Karst.), silver fir (*Abies alba* P. Mill.), and European larch (*Larix decidua* P. Mill.) (Kanduč et al., 2007b). *Fagus sylvatica* has a $\delta^{13}C$ value of –34.8 ‰ (Kanduč et al., 2007b). The leaves and needles of *Picea abies* and *Fagus sylvatica* have $\delta^{13}C$ values of –30.4 ‰ (Kanduč et al., 2025).

Measured $\delta^{13}C_{POC}$ in the headwater stream has an average value of –27.1 ‰. We measured an average $\delta^{13}C_{soil}$ of -26.2 ‰ for the Sava River Basin (Kanduč et al., 2007b). The carbonate bedrock in the catchment area has a $\delta^{13}C$ value of 3.3‰ (Kanduč et al., 2012).

An average $\delta^{13}C_{POC}$ of –27.1 ‰ was assumed to calculate the isotopic composition of DIC derived from in-stream respiration. Open system equilibration of DIC with CO_2 enriches DIC in ^{13}C by about 9 ‰ (Mook et al., 1974), thus yielding the estimate of –18.1 ‰ shown in Figure 4 (line 4). Nonequilibrium dissolution of carbonates with one part of DIC originating from soil CO_2 (–27.1 ‰), and the other from carbonates with an average $\delta^{13}C_{Ca}$ of 3.3 ‰, produces an intermediate $\delta^{13}C_{DIC}$ value of –11.9 ‰ (line 3 in Fig. 4). Given the isotopic composition of atmospheric CO_2 (–7.8 ‰ Levin et al., 1987) and the equilibrium fractionation with DIC of +9 ‰, DIC in equilibrium with the atmosphere should have a $\delta^{13}C_{DIC}$ of about -1.2 ‰ (line 2 in Fig. 4). Dissolution of carbonates provides 1 ‰ enrichment with ^{12}C isotope (Romanek et al., 1992) and gives a value of 2.3 ‰ (line 1, Fig. 4). Stream samples (Fig. 4) fall around fractionation line (3), which presents nonequilibrium carbonate dissolution by carbonic acid produced from soil zone with a $\delta^{13}C_{CO2}$ of -27.1 ‰.

By solving equations (2) and (3), we calculated F_{DICorg} (molC/day) and $F_{DICcarb}$ (molC/day) (Table 2), and subsequently determined the contribution of biogeochemical processes in the stream. The dominant biogeochemical process in the stream is the dissolution of carbonates (from 50.3 to 57.3 %), followed by the degradation of organic matter (from 42.8 to 49.7 %), while the

smallest contribution comes from equilibration with atmospheric CO_2 (from 0.01 to 0.11 %) (Table 2). Other investigated rivers in Slovenia with diverse flow regimes—such as the Sava River (Alpine rain-snow regime), Krka River (Dinaric-Alpine rain-snow regime) (Zavadlav et al., 2013), Kamniška Bistrica River (Alpine high-mountain nival-pluvial regime), and Idrijca River (nival-pluvial karstic flow regime) (Kanduč et al., 2017)—also exhibit similar contributions of biogeochemical processes. Among these, carbonate dissolution is the most dominant, followed by organic matter degradation, while atmospheric exchange represents the least significant process. The lowest $\delta^{13}C_{DIC}$ with value of -11.8 ‰ is observed in August and October 2023 (SM Fig. H) due to higher discharge condition in stream, while the lowest (-9.7 ‰) in May 2024 meaning that nonequilibrium dissolution of carbonates with one part of DIC originating from soil CO_2 and the other from carbonates is dominant. Completely different $\delta^{13}C_{DIC}$ was found in McMurdo Cry Valley streams. The $\delta^{13}C$ values from McMurdo Dry Valley (Lyons et al., 2013) streams span a range of greater than 14 ‰, from -9.4 ‰ to +5.1 ‰, with the majority of samples falling between -3 ‰ and +2 ‰, suggesting that inorganic in source. Because there are no vascular plants on this landscape and no groundwater input to these streams, atmospheric exchange is the dominant control on $\delta^{13}C_{DIC}$. For example, the latest study indicates that $\delta^{13}C_{DIC}$ ranges from -13.3 to -8.0 ‰ in silicate River Oplotnica catchment, meaning that only equilibration of CO_2 and degradation of organic matter influence $\delta^{13}C_{DIC}$ values (Kanduč et al., 2025), which suggests that biogeochemical processes within the specific catchment area have an effect on the $\delta^{13}C_{DIC}$ values. The $\delta^{13}C_{DIC}$ values investigated in the study of the Varaždin alluvial aquifer, which is characterized by overfertilization (Karlović et al., 2022), are compared to $\delta^{13}C_{DIC}$ values found in a headwater stream. The $\delta^{13}C_{DIC}$ values varied seasonally from –13.6 ‰ to –0.5 ‰ in surface water samples and from –14.5 ‰ to –10.7 ‰ in groundwater samples. The $\delta^{13}C_{DIC}$ values in both surface water and groundwater from the Varaždin aquifer span a wider range than those in the headwater stream ($\delta^{13}C_{DIC}$ from –11.8 ‰ to –9.7 ‰), due to different biogeochemical processes influencing the $\delta^{13}C_{DIC}$ signature. In the Varaždin aquifer study, the highest oscillations of $\delta^{13}C_{DIC}$ and other tracers (DIC, DOC) were observed in the gravel pit. More negative $\delta^{13}C_{DIC}$ values were detected during the warmer months, attributed to increased degradation of organic matter leached from terrestrial sources. In shallow groundwater, more negative $\delta^{13}C_{DIC}$ values were measured compared to deeper groundwater.

We find no correlation between $\delta^{13}C_{POC}$ and $\delta^{13}C_{DIC}$ (Fig. 5). More positive $\delta^{13}C_{POC}$ values are associated with highly degradable soil matter, while plant debris exhibits more negative $\delta^{13}C_{POC}$ values (Fig. 5). Suspended organic matter in rivers is mostly derived from soil and plant material. Therefore, the isotopic composition of suspended organic matter ($\delta^{13}C_{POC}$) in rivers has been used to determine the contribution of terrestrial vegetation and soil matter in the river ecosystems (Ittekot, 1988). The $\delta^{13}C$ values of C3 plants range from -32.0 to -20.0 ‰, while C4 plants range from -15 ‰ to -9.0 ‰ (Deines, 1980). C3 plants in the Sava River catchment in Slovenia have $\delta^{13}C$ values ranging from -34.8 ‰ (*Fagus sylvatica*) to -29.2 ‰ (*Clematis vitalba*) (Kanduč et al., 2007b). The $\delta^{13}C_{POC}$ values in the Lipnik stream range more widely, from -29.4 to -24.9 ‰ (SM Fig. 1), while for the Sava River (2004-2005), $\delta^{13}C_{POC}$ values range from -29.2 to -25.1 ‰ (Kanduč et al., 2007b). The $\delta^{13}C_{POC}$ values (Table 1, Fig. 5) in our study indicate that the particulate organic matter is composed of degraded soil material derived from plant

Table 2. Results of mass balance calculation for evaluation of biogeochemical processes based on total alkalinity and isotopic composition of dissolved inorganic carbon ($\delta^{13}C_{DIC}$) at three different discharge conditions (July 2023, October 2023, May 2024).

year-month-day	F_{DICex} [molC/day]	F_{DICorg} [molC/day]	F_{DICCa} [molC/day]	F_{DICex} [%]	F_{DICorg} [%]	F_{DICCa} [%]
2023-07-20	$9.5 \cdot 10^{2}$	$3.7 \cdot 10^{5}$	$4.8 \cdot 10^{5}$	0.11	43.1	56.8
2023-10-24	$1.1 \cdot 10^{3}$	$1.7 \cdot 10^{6}$	$1.7 \cdot 10^{6}$	0.03	49.7	50.3
2024-05-13	$9.2 \cdot 10^{1}$	$6.8 \cdot 10^{5}$	$9.1 \cdot 10^{5}$	0.01	42.8	57.2
Range	$9.2 \cdot 10^{1}$-$1.1 \cdot 10^{3}$	$3.7 \cdot 10^{5}$-$1.7 \cdot 10^{6}$	$4.8 \cdot 10^{5}$-$1.7 \cdot 10^{6}$	0.01-0.11	42.8-49.7	50.3-57.2
Average	$7.2 \cdot 10^{2}$	$9.2 \cdot 10^{5}$	$1.0 \cdot 10^{6}$	0.05	45.2	54.8

F_{DIC} – the mass flux of dissolved inorganic carbon, ex – equilibration of CO_2 between atmosphere and water, ca – dissolution of carbonates, org – degradation of organic matter.

litter leached from slopes (Fig. 6). More negative $\delta^{13}C$ values suggest less degraded organic matter, while more positive values indicate more degraded organic matter. A schematic overview of carbon cycling dynamics with $\delta^{13}C$ in different carbon storage compartments in a headwater stream is presented in Figure 6.

No significant correlations were found between the measured parameters at $p<0.05$, except strong negative correlations between electrical conductivity and water temperature (-0.91), which are both connected with discharge and residence time of water in the aquifer among other, m_{TSS} and pH (-0.84), and $\delta^{13}C_{DIC}$ versus log pCO_2 (-0.77).

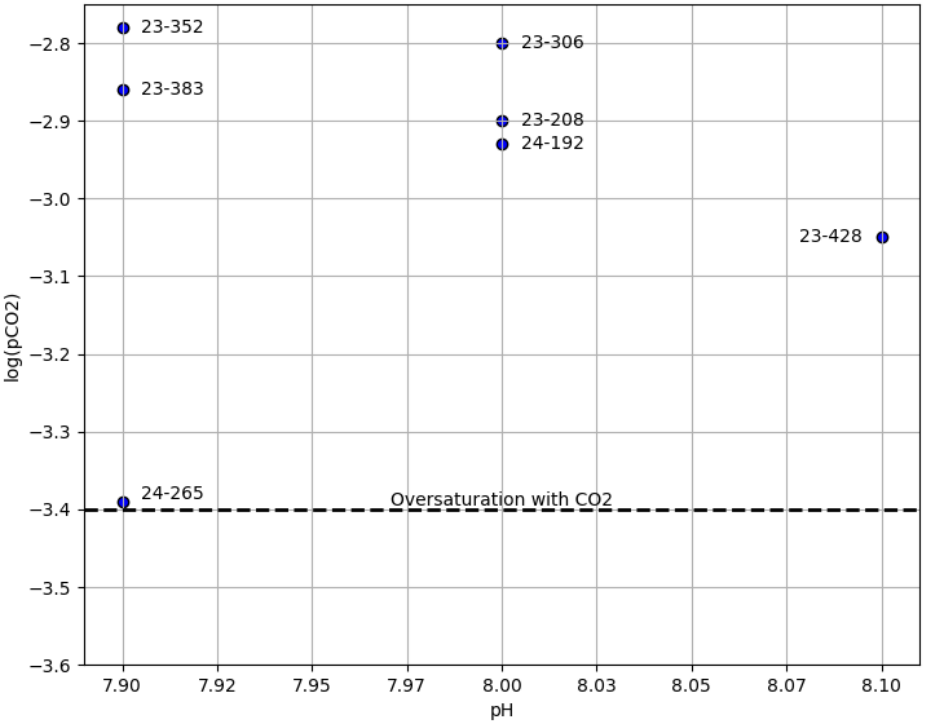

Fig. 3. log pCO_2 versus pH.

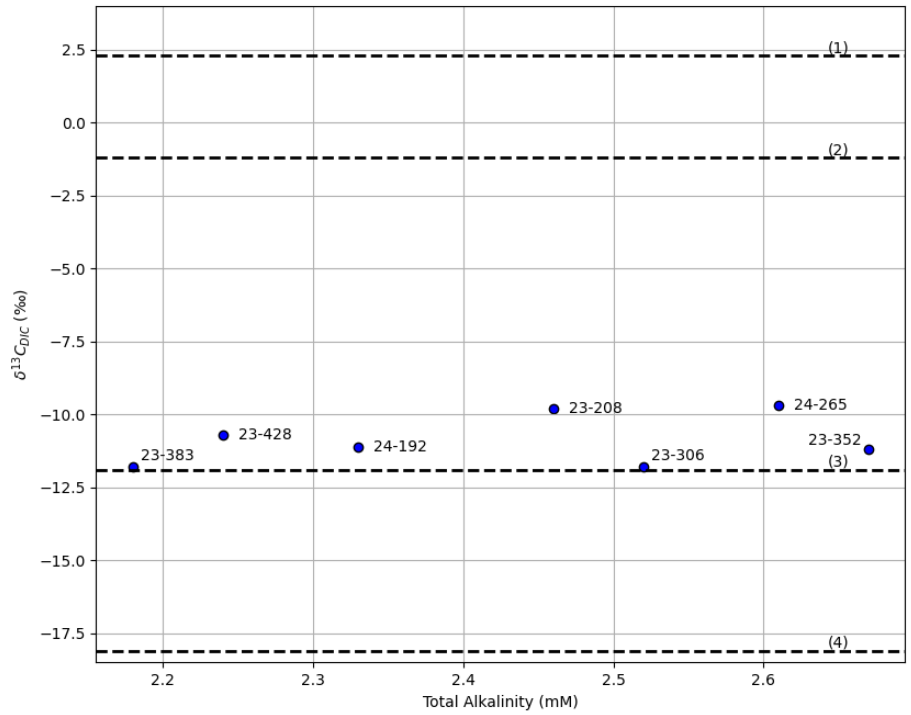

Fig. 4. $\delta^{13}C_{DIC}$ versus total alkalinity; 1 – equilibration with atmospheric CO_2 with value of 1.2 ‰, 2 – dissolution of carbonate with average $\delta^{13}C_{CaCO3}$ of 3.3 ‰, 3 – nonequilibrium carbonate dissolution by carbonic acid produced from soil zone with a $\delta^{13}C_{CO2}$ of -27.1 ‰, 4 – open system equilibration of DIC with soil CO_2 originating from degradation of organic matter with a $\delta^{13}C_{CO2}$ of -27.1 ‰.

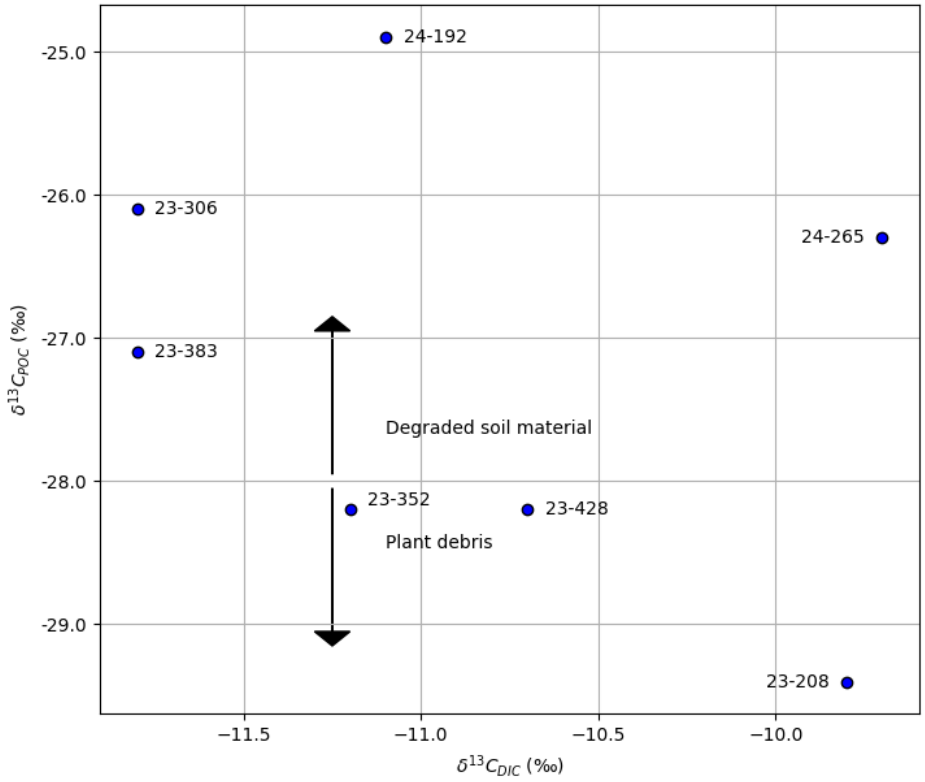

Fig. 5. $\delta^{13}C_{POC}$ versus $\delta^{13}C_{DIC}$.

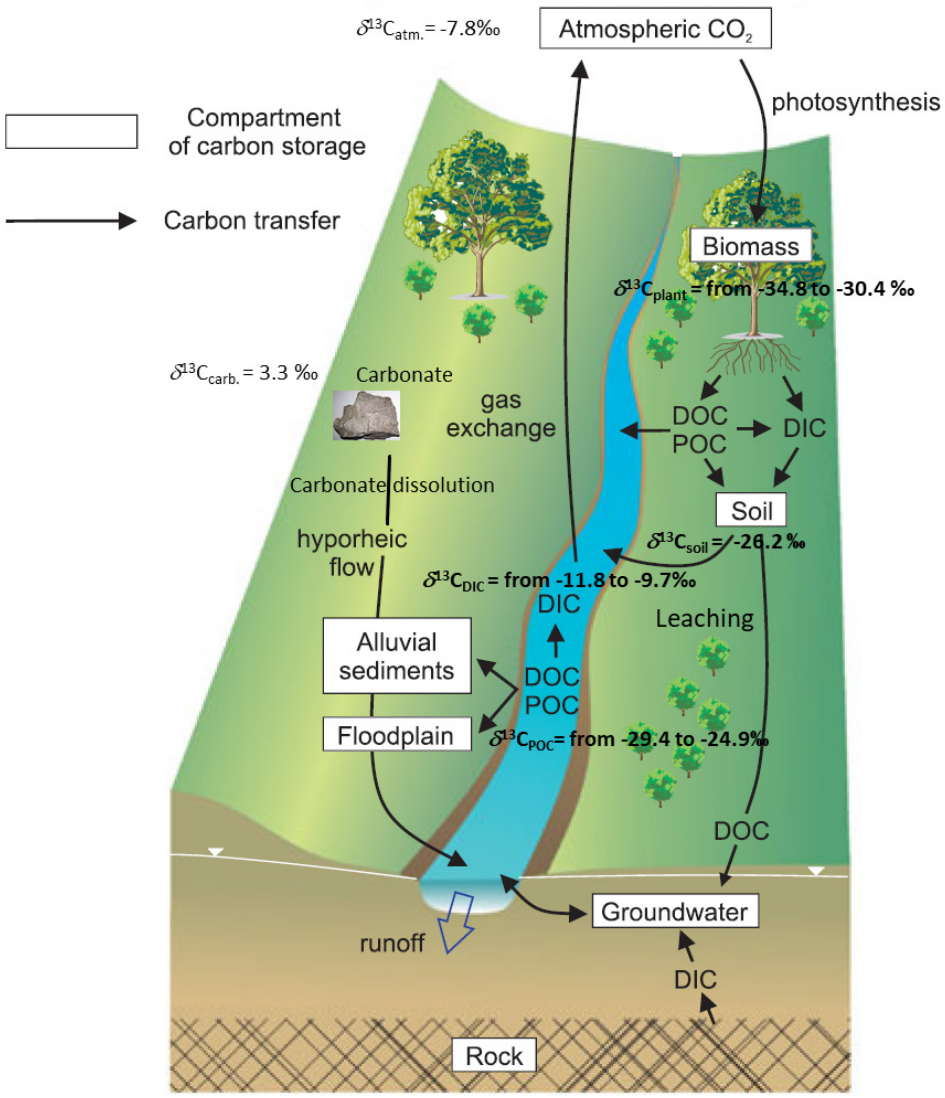

Fig. 6. Schematic overview of carbon cycling dynamics with $\delta^{13}C$ in a headwater stream (adapted from Marx et al., 2017 , reproduced with permission). $\delta^{13}C_{plant}$ – isotopic composition of carbon in plant litter (data from Kanduč et al., 2007b), $\delta^{13}C_{soil}$ – isotopic composition of carbon in soil (data from Kanduč et al., 2007b), $\delta^{13}C_{POC}$ – isotopic composition of carbon in particulate organic matter, $\delta^{13}C_{DIC}$ – isotopic composition of carbon in dissolved inorganic carbon, $\delta^{13}C_{carb.}$ – isotopic composition of carbon in carbonate (data from Kanduč et al., 2012), $\delta^{13}C_{atm.}$ – isotopic composition of carbon in atmospheric CO_2 (data from Levin et al., 1987).

Conclusion

This study confirmed the role of headwater streams as important contributors of CO_2 to the atmosphere, as well as the importance of groundwater recharge and soil leaching for the geochemical processes in such streams. Total alkalinity ranged from 2.2 to 2.7 mM, which is typical for carbonate pristine catchment. The sampled stream water was supersaturated with CO_2 in all months, and represents a source of CO_2 into the atmosphere. Seasonal variations in the stable isotope composition of carbon ($\delta^{13}C_{DIC}$) were due to differences in discharge conditions, being lower during high discharge conditions due to dilution with precipitation and higher during low discharge conditions.

The biogeochemical processes affecting total alkalinity and $\delta^{13}C_{DIC}$ (ranging from -11.8 to -9.7 ‰) indicate that carbonate dissolution has the most significant impact on $\delta^{13}C_{DIC}$ in the carbonate catchment, contributing 50.3–57.0 %, followed by the degradation of organic matter, contributing 42.8–49.7 %. Equilibration with atmospheric CO_2 has a minimal impact (ranging from 0.01 % to 0.11 % in our study) under all three-discharge conditions, as the water does not stagnate and does not reach equilibrium with atmospheric CO_2.

Both isotopic compositions ($\delta^{13}C_{DIC}$ and $\delta^{13}C_{POC}$) are considered powerful tools for tracing biogeochemical cycles in freshwater systems. $\delta^{13}C_{DIC}$ is particularly valuable for investigating instream biogeochemical processes (e.g. degradation of organic matter, dissolution of carbonates, and equilibration with atmospheric CO_2).

Acknowledgements

We thank the ARIS research programme P1-0143, P1-0255, P1-0195 for funding, Mr. Stojan Žigon who performed stable isotopic analyses and Mr. Patrik Kušter for creation of scatter plots in Python. The research was conducted in the area of Triglav National Park with their permission and the consent of the landowners.

Author contribution

Tjaša Kanduč, Nataša Mori contributed to conceptualization. Tjaša Kanduč, Nataša Mori, Timotej Verbovšek were responsible for methodology, software, formal analysis, investigation, writing, original draft preparation. Review, editing, funding acquisition and supervisions were performed by Tjaša Kanduč, Nataša Mori, Timotej Verbovšek.

References

Atekwana, E.A. & Krishnamurthy, R.V. 1998: Seasonal variations of dissolved inorganic carbon and $\delta^{13}C$ of surface waters: application of a modified gas evaluation technique. Journal of Hydrology, 205: 260–278.

Atkins, P.W. 1994: Physical Chemistry. Oxford University press, Oxford, 5th Edition: 1031 p.

Barth, J.A.C., Cronin, A.A., Dunlop, J. & Kalin, R.M. 2003: Influence of carbonates on the riverine carbon cycle in an anthropogenically dominated catchment basin: evidence from major elements and stable carbon isotopes in the Lagan River (N. Ireland). Chemical Geology, 200: 203–216.

Battin, T.J., Kaplan, L.A., Newbold, D., Cheng, X. & Richter, A. 2008: Biological and geochemical controls on organic carbon turnover in streams and rivers. Nature Geoscience, 1/11: 665–669. https://doi.org/10.1038/ngeo325

Broecker, W.S. 1974: Chemical oceanography. In: Leeder, MR (ed.): Sedimentology and sedimentary basins. Harcout-Brace-Jovanovich, New York: 592.

Broecker, H.C, Peterman, J. & Siems, W. 1978: The influence of wind on CO_2–exchange in a wind–wave tunnel, including the efects of monolayers. Journal of Marine Research, 36: 595–610.

Buser, S. & Komac, M. 2002: Geological map of Slovenia 1:250,000. Geologija, 45/2: 335–340. https://doi.org/10.5474/geologija.2002.029

Deines, P. 1980: The isotopic composition of reduced organic carbon. In: Fritz, P. & Fontes J.C. (eds.): Handbook of Environmental isotopic Geochemistry, 329–406.

Doctor, D.H., Kendall, C., Sebestyen, S.D., Shanley, J.B., Ohte, N. & Boyer, E.W. 2008: Carbon isotope fractionation of dissolved inorganic carbon (DIC) due to outgassing of carbon dioxide from a headwater stream. Hydrological Processes, 22/14: 2410–2423. https://doi.org/10.1002/hyp.6833

Evans, M.L., Raymond, P.A. & Bauer, J.E. 2024: Tracing sources of stream DIC using $\delta^{13}C$ and $\delta^{14}C$ isotopes. Environmental Research, 244: 117209. https://doi.org/10.1016/j.envres.2024.117209

Gammons, C.H., Babcock, J.N., Parker, S.R. & Poulson, S.R. 2011: Diel cycling and stable isotopes of dissolved oxygen, dissolved inorganic carbon, and nitrogenous species in a stream receiving treated municipal sewage. Chemical geology, 283: 44–55.

Holley, E.H. 1977: Oxygen transfer at the air–water interface. In: Gibbs, R.J. (ed.): Transport

processes in lakes and oceans, Proc. Symp. On Transp. Processes in the Ocean held at the 2nd Nat. Meet Of the AICE, Atlantic City, N. J. Aug. 29.–Sep. 1, 1976, 117–150.

Ittekkot, V. 1988: Global trends in the nature of organic matter in the river suspensions. Nature, 332: 436–438. https://doi.org/10.1038/332436a0

Jähne, B., Heinz, G. & Dietrich, W. 1987: Measurments of the Diffusion Coefficients of Sparingly soluble gases in water. Journal of Geophysical Research, 92: 10767–10776.

Kanduč, T., Szramek, K., Ogrinc, N. & Walter, L.M. 2007a: Origin and cycling of riverine inorganic carbon in the Sava River watershed (Slovenia) inferred from major solutes and stable carbon isotopes. Biogeochemistry, 86: ^{13}7–184.

Kanduč, T., Ogrinc, N. & Mrak, T. 2007b: Characteristics of suspended matter in the River Sava watershed, Slovenia. Isotopes in Environmental and Health Studies, 43/4: 369–385.

Kanduč, T., Mori, N., Kocman, D., Stibilj, V. & Grassa, F. 2012: Hydrogeochemistry of Alpine springs from North Slovenia: insights from stable isotopes. Chemical geology, 300–301: 40–54. https://doi.org/10.1016/j.chemgeo.2012.01.012

Kanduč, T., Kocman, D. & Verbovšek, T. 2017: Biogeochemistry of some selected rivers (Kamniška Bistrica, Idrijca and Sava in Slovenia): insights into river water geochemistry, stable carbon isotopes and weathering material flows. Geologija, 60/1: 9–26. https://doi.org/10.5474/geologija.2017.001

Kanduč, T., Vrabec, M., Verbovšek, T., McIntosh, J., Žlindra, D. & Vilhar, U. 2025: Assesing silicate catchment dynamics of the Oplotnica River (Slovenia) through stable carbon and nitrogen isotopes. Aquatic geochemistry, 31/5: 1–33. https://doi.org/10.1007/s10498-025-09439-w.

Karlović, I., Marković, T., Kanduč, T. & Vreča, P. 2022: Assessment of Seasonal Changes on the Carbon Cycle in the Critical Zone of a Surface Water (SW)-Groundwater (GW) system. Water, 14/21: 3372. https://doi.org/10.3390/w14213372

Kendall, C. & McDonell, J.J. 1998: Isotope tracers in catchment hydrology. Elsevier: 794 p.

Knoll, L.B., Hotchkiss, E.R., Hall, R.O. & Sponseller, R.A. 2024: Groundwater-derived carbon stimulates headwater stream CO2 emissions. Water Research, 259: 120741. https://doi.org/10.1016/j.watres.2024.120741

Lan, X., Tans, P. & Thorning, K.W. 2024: Trends in globally –averaged CO_2 determined from NOAA Global Monitoring Laboratory measurements. Version Tuesday, 05-Nov-2024 13: 17:54 MST. https://doi.org/10.15138/9N0H-ZH07

Levin, I., Kromer, B., Wagenback, D. & Minnich, K.O. 1987: Carbon isotope measurements of atmospheric CO_2 at a coastal station in Antarctica. Tellus, 39B: 89–95.

Lyons, W.B., Leslie, D.L., Harmon, R.S., Neumann, K., Welch K.A., Bisson, K.M. & McKnight, D.M. 20^{13}: The carbon stable isotope biogeochemistry of stream. Taylor Valley Antratctica. Applied geochemistry, 32: 26–36.

Marx, A., Dusek, J., Jankovec, J., Sanda, M. Vogel, T., van Geldern, R., Hartmann, J. & Barth, J.A.C. 2017: A Review of CO_2 and Associated Carbon Dynamics in Headwater Streams: A Global Perspective. Reviews of Geophysics, 55/2: 560–585. https://doi.org/10.1002/2016RG000547

Meybeck, M. 1981: River transport of organic carbon to the ocean. In Flux of Organic Carbon to the Oceans, G.E. Likens, F.T. Mackenzie, Richey J.R., Seddell K.K., Turekian K.K. (eds.): U.S. D.O.E. CONF-8009140, Nat. Tech. Ing. Serr. Springfield: 219–269.

Mori, N., Kanduč, T., Opalički, M. & Brancelj, A. 2015: Groundwater drift as a tracer for identifying sources of spring discharge. Groundwater, 53: 123–132. https://doi.org/10.1111/gwat.12314

Mori, N. & Brancelj, A. 20^{13}: Differences in aquatic microcrustacean assemblages between temporary and perennial springs of an alpine karstic aquifer. International journal of speleology, 42/3: 257–266. https://doi.org/10.5038/1827-806X.42.3.9

Mook, W.G., Bommerson, J.C. & Staverman, W.H. 1974: Carbon isotope fractionation between dissolved bicarbonate and gaseous carbon dioxide. Earth Planetary Science Letters, 22: 169–176.

Opalički, M. 2015: Patterns in invertebrate drift from an alpine karst aquifer over a one year period = Dinamika plavljenja vodnih nevretenčarjev iz alpskega kraškega vodonosnika v obdobju enega leta. Acta Carsologica, 44/2: 265–278.

Raymond, P.A., Hartmann, J., Lauerwald, R., Sobek, S., McDonald, C., Hoover, M., Butman, D., Striegl, R., Mayorga, M., Humborg, C., Kortelainen, P., Dürr, H., Meybeck, M., Ciais, P. &

Guth, P. 2013: Global carbon dioxide emissions from inland waters. Nature, 503: 355–359.

Richardson, J.S. 2019: Headwater streams in book: Reference Module in Earth System and Environmental Sciences, Elsevier. https://doi.org/10.1016/B978-0-12-409548-9.11957-8

Romanek, C.S., Grossman, E.L. & Morse, J.W. 1992: Carbon isotopic fractionation in synthetic aragonite and calcite: effects temperature and precipitation rate. Geochimica et Cosmochimica Acta, 46: 419–430.

Serianz, L., Rman, N. & Brenčič, M. 2020: Hydrogeochemical Characterization of a Warm Spring System in a Carbonate Mountain range of the Eastern Julian Alps, Slovenia. Water, 12/5: 1427. https://doi.org/10.3390/w12051427

Torkar, A. & Brenčič, M. 2015: Spatio-temporal distribution of discharges in the Radovna River valley at low water conditions = Prostorska-časovna porazdelitev pretokov v dolini reke Radovne v obdobju nizkih vod. Geologija, 58/1: 47–56. https://doi.org/10.5474/geologija.2015.003

Torkar, A., Brenčič, M. & Vreča, P. 2016: Chemical and isotopic characteristics of groundwater-dominated Radovna River (NW Slovenia). Environmental Earth Science, 75: 1296. https://doi.org/10.1007/s12665-016-6104-5

Utsumi, G.S.A., He, D., Berelson, W.M., Castelao, R.M., Yager, P.L. & Medeiros, P.M. 2025: Influence of the Amazon River on the composition of particulate organic carbon in the western tropical Atlantic Ocean. Geochimica et Cosmochimica Acta, 389: 84–99.

Waldron, S., Lansdown, J.M. & Scott, E.M. 2018: Stable Carbon Isotopes Reveal Soil-Stream DIC Linkages in Headwater Catchments. Journal of Geophysical Research: Biogeosciences, 123/2: 383–399. https://doi.org/10.1002/2017JG004083

Zavadlav S., Kanduč T., McIntosh J.C. & Lojen, S. 2013: Isotopic and chemical constraints on the biogeochemistry of dissolved inorganic carbon and chemical weathering in the karst watershed of Krka River (Slovenia). Aquatic geochemistry, 19/3: 209–230.

Zuliani, T., Kanduč, T., Novak, R. & Vreča, P. 2020: Characterization of bottled waters by multielemental analysis, stable and radiogenic isotopes. Water, 12/9: 2454. http://doi.org/10.3390/w12092454

Electronic sources:

Internet 1: https://meteo.arso.gov.si/uploads/probase/www/hidro/watercycle/text/sl/observation_sites/springs/Lipnik.pdf (15.3.2025).

Internet 2: https://www.arso.gov.si/en/ (7.4.2025).

Supplementary table

Table SM 1: Results of Spearman correlations (significant at p<0.

	P_{daily}	Q_{daily}	Temperature (°C)	pH	Electrical Conductivity (µS/cm)	Dissolved oxygen (mg/L)	m_{TSS}	TA (mM)	log pCO_2	$\delta^{13}C_{DIC}$ (‰)	$\delta^{13}C_{POC}$ (‰)
P_{daily}	1.0	-0.27	0.70	-0.31	-0.609	-0.61	0.34	0.55	0.09	0.34	-0.318
Q_{daily}	-0.27	1.0	0.17	-0.38	-0.28	0.52	0.25	-0.25	0.25	-0.79	0.73
T	0.70	0.17	1.0	0.0	**-0.91***	0.018	-0.11	0.28	0.07	0.04	0.31
pH	-0.31	-0.38	0.0	1.0	-0.019	0.48	**-0.84***	-0.38	-0.27	0.13	-0.06
Cond.	-0.60	-0.28	**-0.91***	-0.019	1.0	-0.05	0.12	-0.14	0.18	-0.1	-0.40
DO	-0.61	0.52	0.018	0.48	-0.05	1.0	-0.39	-0.32	0.23	-0.65	0.61
m_{TSS}	0.34	0.25	-0.107	**-0.84***	0.12	-0.39	1.0	0.42	0.53	-0.32	-0.23
TA	0.55	-0.25	0.28	-0.38	-0.14	-0.32	0.42	1.0	0.25	0.21	-0.02
log pCO_2	0.09	0.25	0.07	-0.27	0.18	0.23	0.53	0.25	1.0	**-0.77***	-0.13
$\delta^{13}C_{DIC}$	0.34	-0.70	0.03	0.13	-0.1	-0.65	-0.32	0.21	**-0.77***	1.0	-0.29
$\delta^{13}C_{POC}$	-0.31	0.73	0.3	-0.05	-0.4	0.61	-0.23	-0.02	-0.12	-0.29	1.0

*Spearman correlations marked as bold are significant at p<0.050, m_{TSS} – mass of total suspended solids, TA – total alkalinity, pCO_2 – partial pressure of CO_2, $\delta^{13}C_{DIC}$ – isotopic composition of dissolved inorganic carbon, $\delta^{13}C_{POC}$ – isotopic composition of particulate organic carbon

Supplementary figures

Figure SM Fig. A: T (°C) versus sampling date
Figure SM Fig. B: pH versus sampling date
Figure SM Fig. C: Electrical conductivity versus sampling date
Figure SM Fig D: DO versus sampling date
Figure SM Fig. E: m_{TSS} versus sampling date
Figure SM Fig. F: TA versus sampling date
Figure SM Fig. G: log pCO_2 versus sampling date
Figure SM Fig. H: $\delta^{13}C_{DIC}$ versus sampling date
Figure SM Fig. I: $\delta^{13}C_{POC}$ versus sampling date

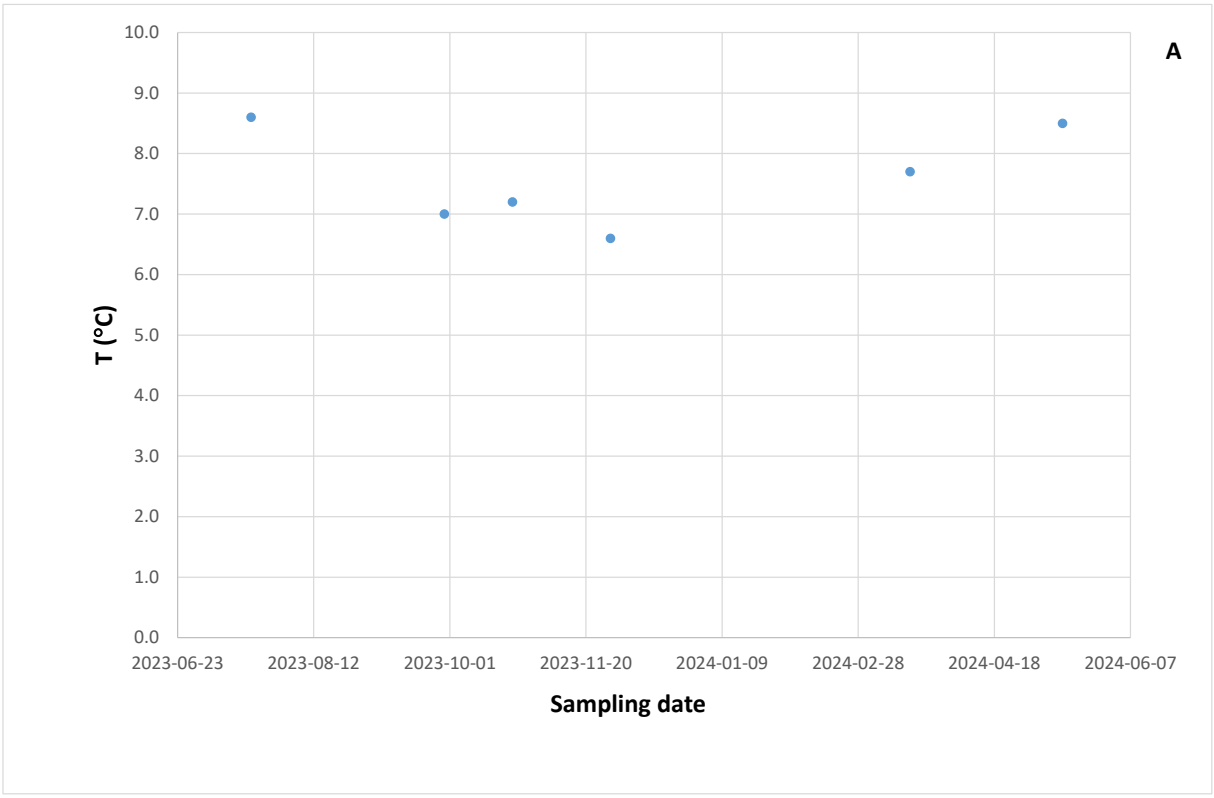

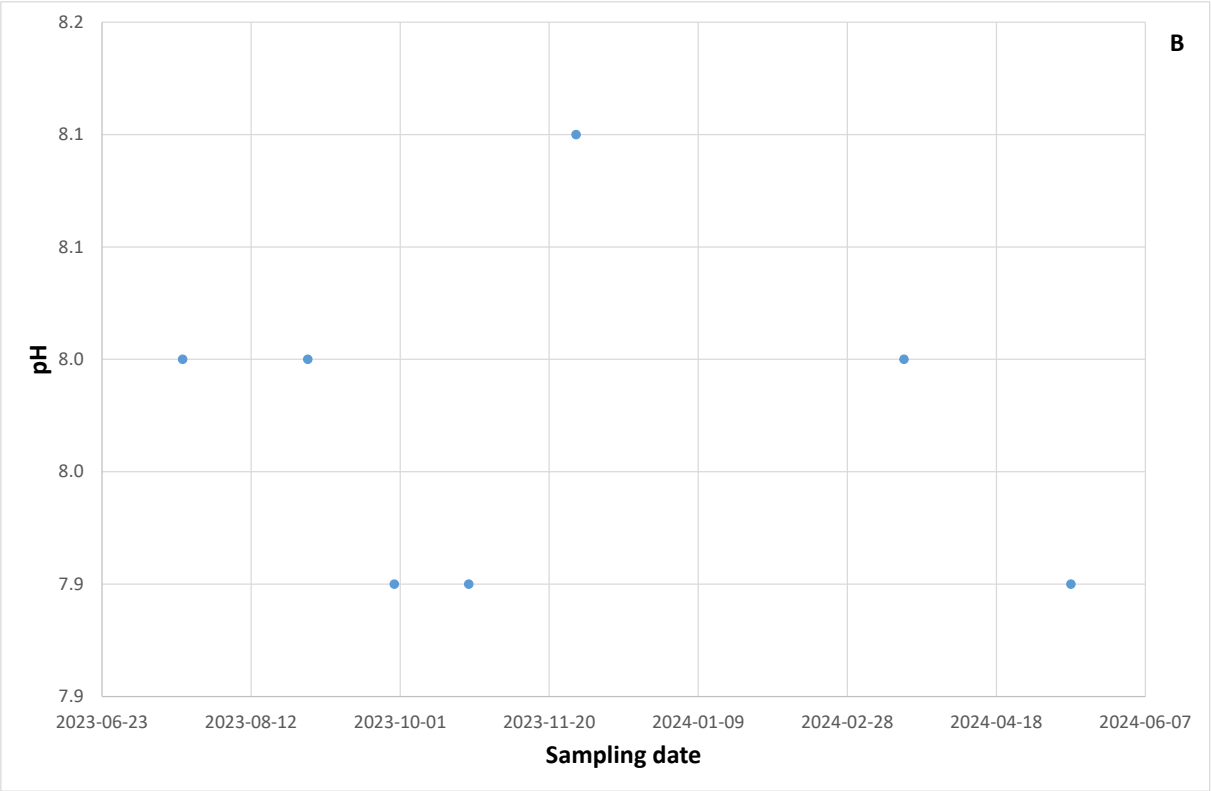
B
pH
8.2
8.1
8.1
8.0
8.0
7.9
7.9
2023-06-23
2023-08-12
2023-10-01
2023-11-20
2024-01-09
2024-02-28
2024-04-18
2024-06-07
Sampling date

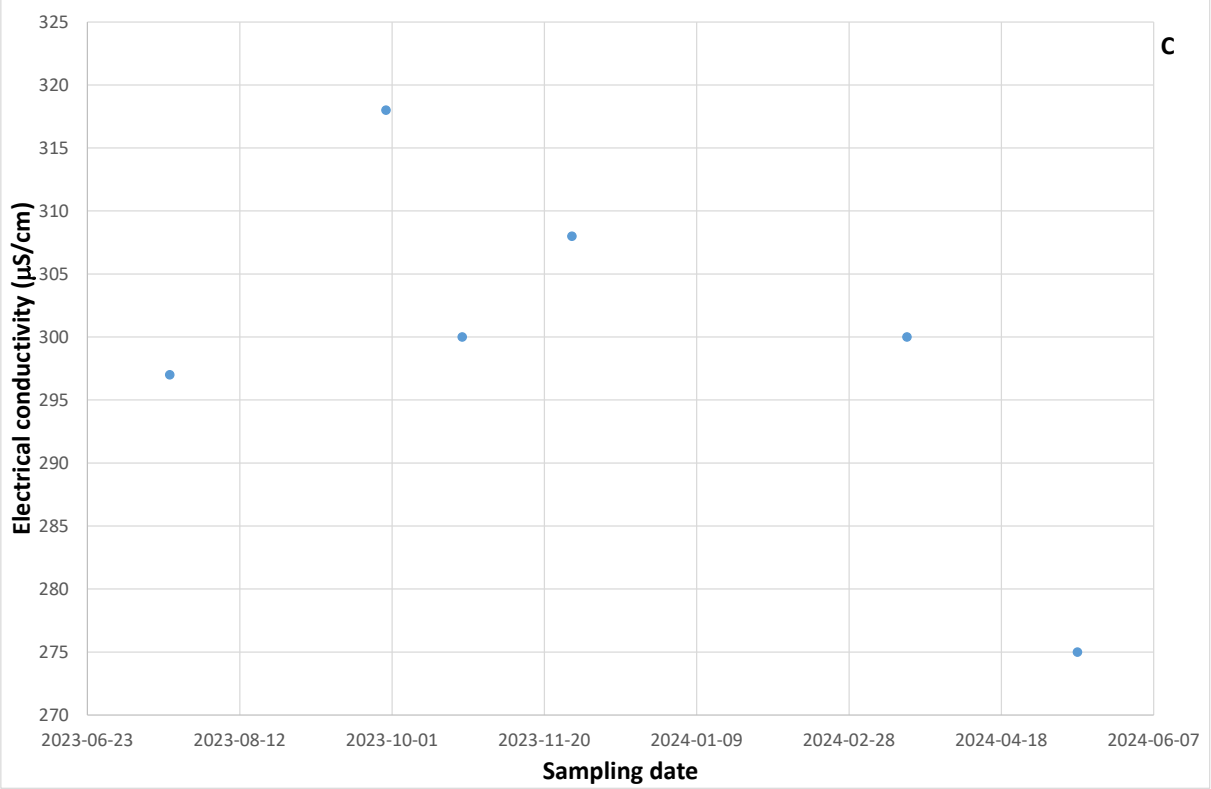
C
Electrical conductivity (µS/cm)
325
320
315
310
305
300
295
290
285
280
275
270
2023-06-23
2023-08-12
2023-10-01
2023-11-20
2024-01-09
2024-02-28
2024-04-18
2024-06-07
Sampling date

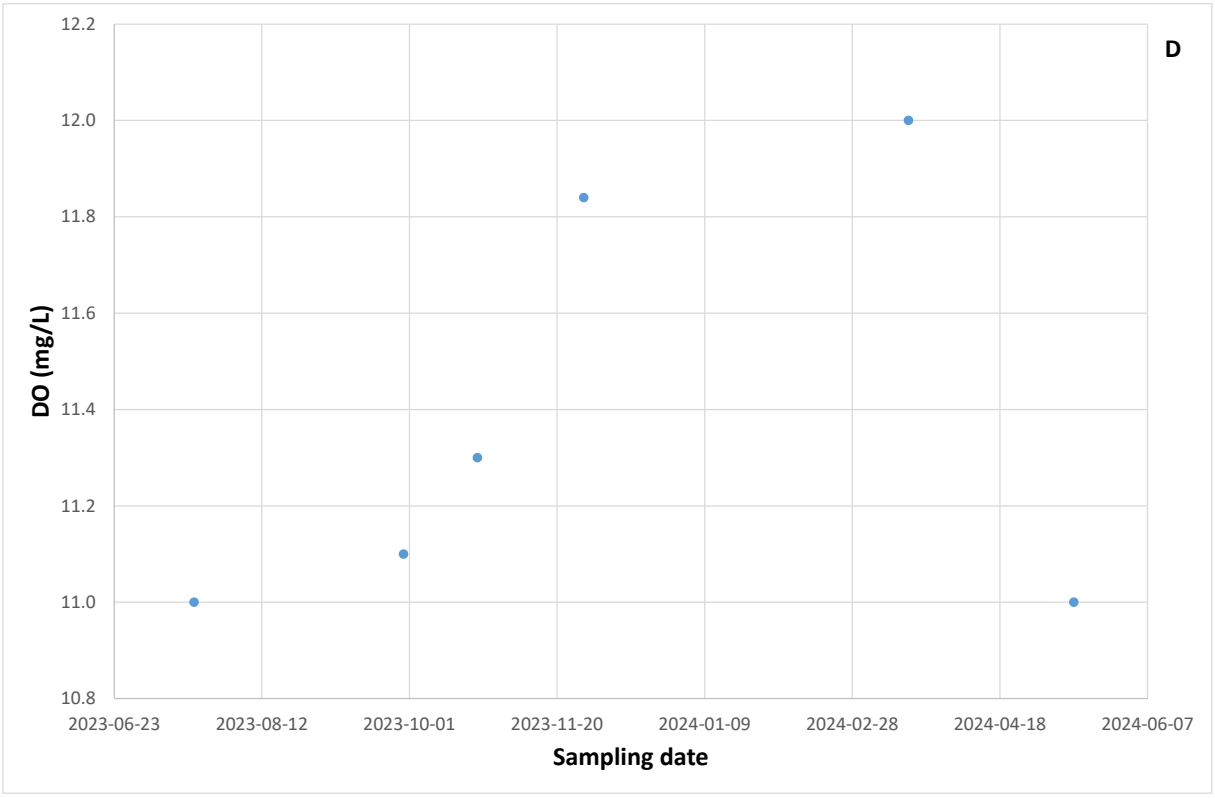
D
12.2
12.0
11.8
11.6
11.4
11.2
11.0
10.8
DO (mg/L)
2023-06-23
2023-08-12
2023-10-01
2023-11-20
2024-01-09
2024-02-28
2024-04-18
2024-06-07
Sampling date

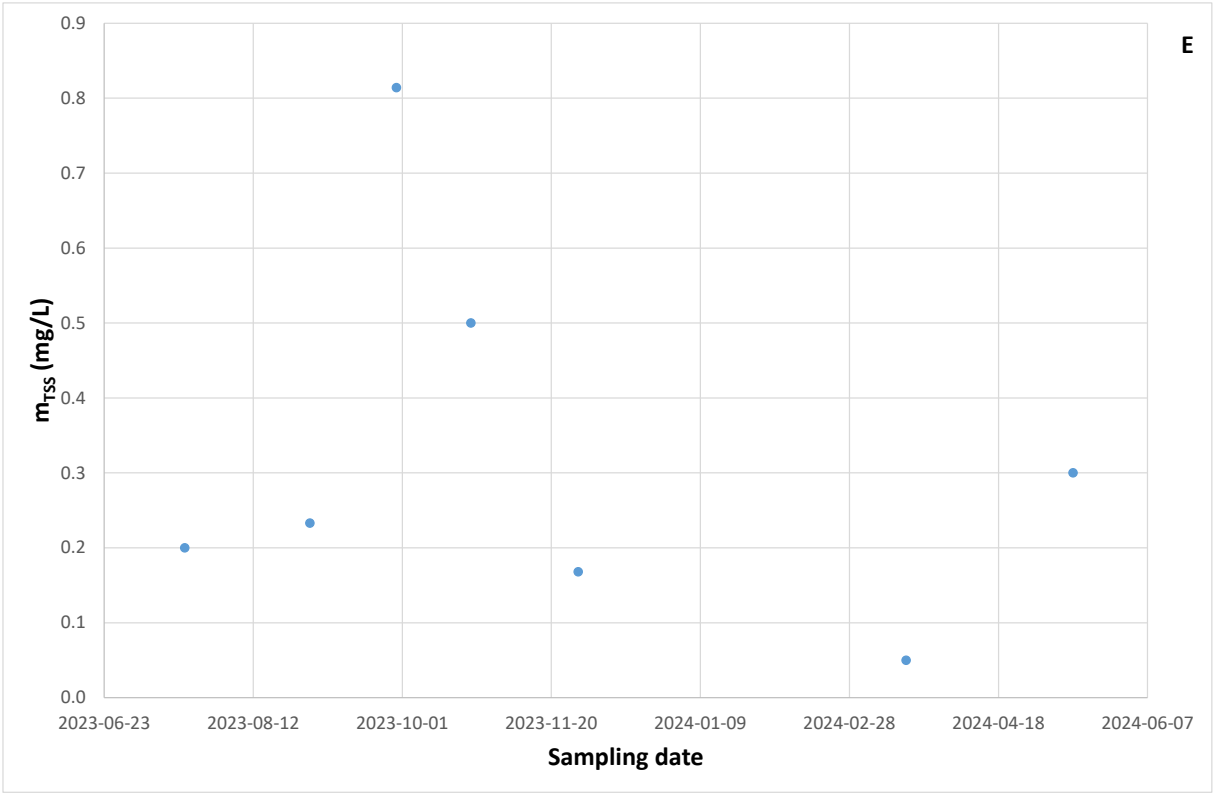
E
0.9
0.8
0.7
0.6
0.5
0.4
0.3
0.2
0.1
0.0
m_{TSS} (mg/L)
2023-06-23
2023-08-12
2023-10-01
2023-11-20
2024-01-09
2024-02-28
2024-04-18
2024-06-07
Sampling date

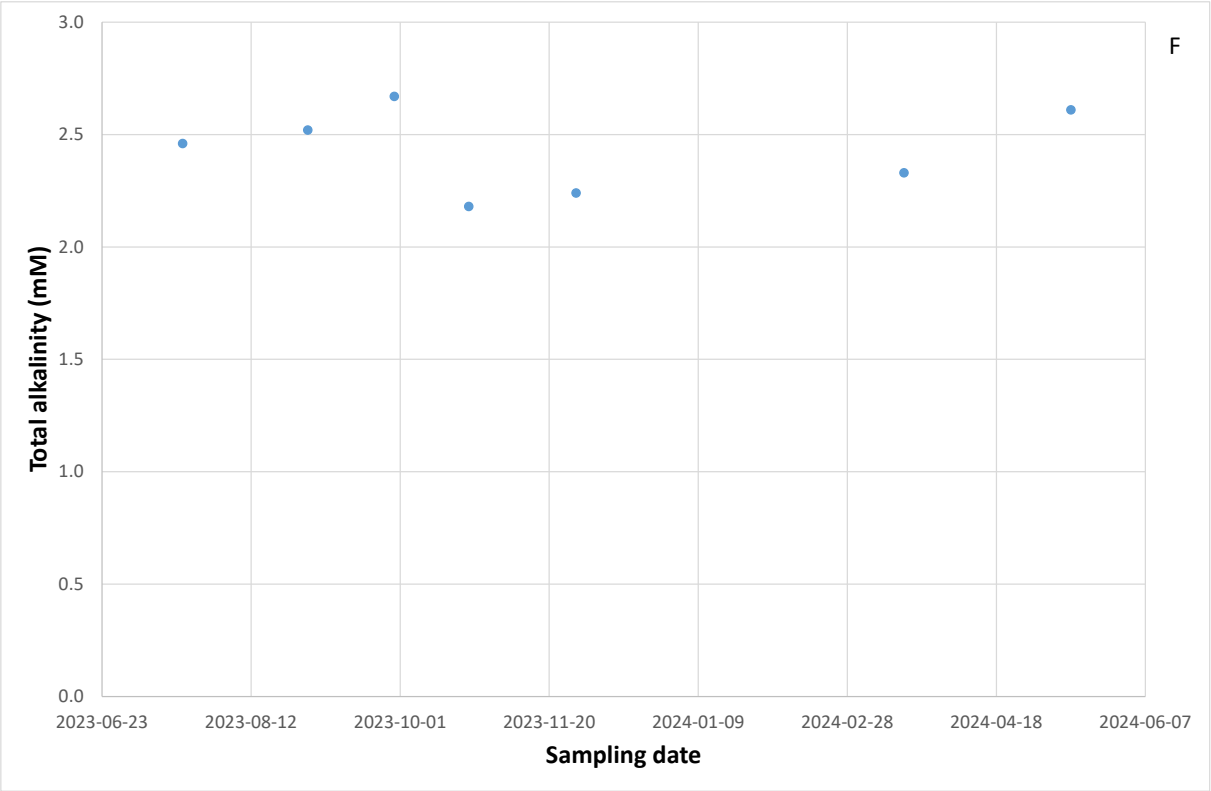
F
Total alkalinity (mM)
3.0
2.5
2.0
1.5
1.0
0.5
0.0
2023-06-23
2023-08-12
2023-10-01
2023-11-20
2024-01-09
2024-02-28
2024-04-18
2024-06-07
Sampling date

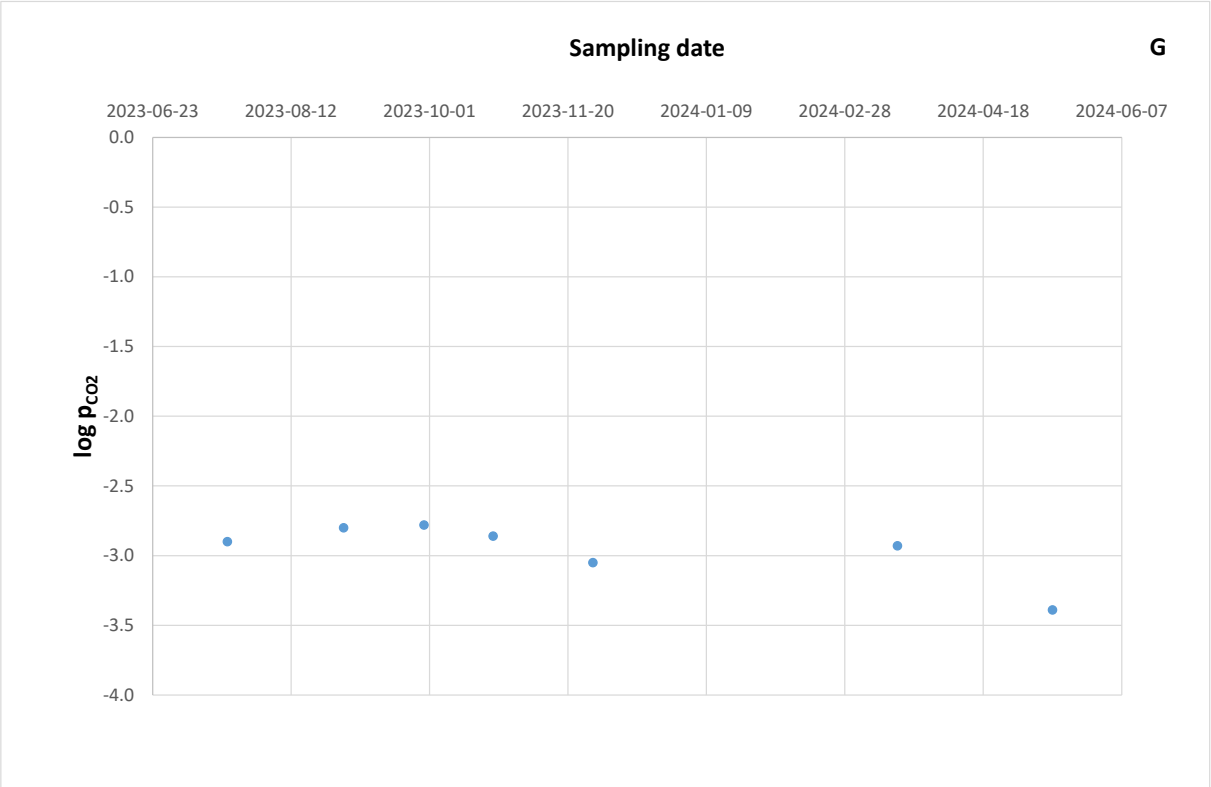
Sampling date
G
2023-06-23
2023-08-12
2023-10-01
2023-11-20
2024-01-09
2024-02-28
2024-04-18
2024-06-07
0.0
-0.5
-1.0
-1.5
-2.0
-2.5
-3.0
-3.5
-4.0
log pCO2

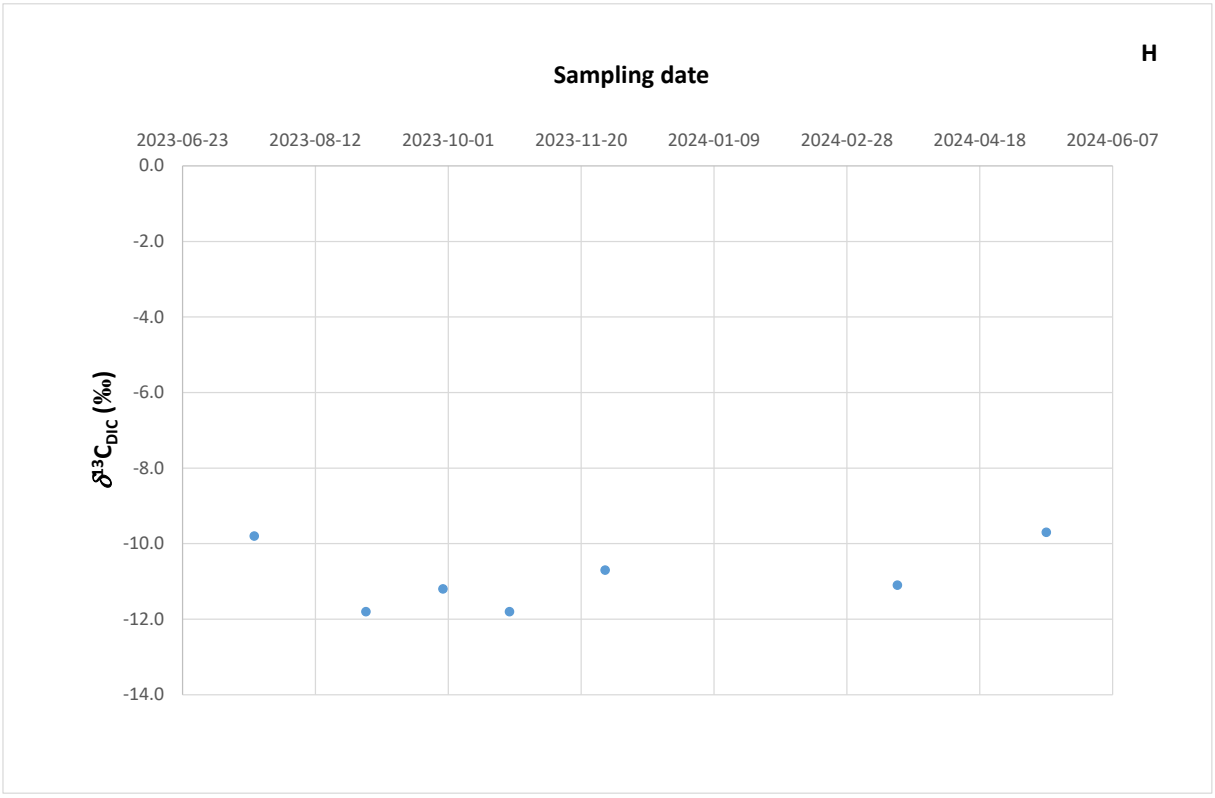
H
Sampling date
2023-06-23
2023-08-12
2023-10-01
2023-11-20
2024-01-09
2024-02-28
2024-04-18
2024-06-07
0.0
-2.0
-4.0
-6.0
-8.0
-10.0
-12.0
-14.0
δ13CDIC (‰)

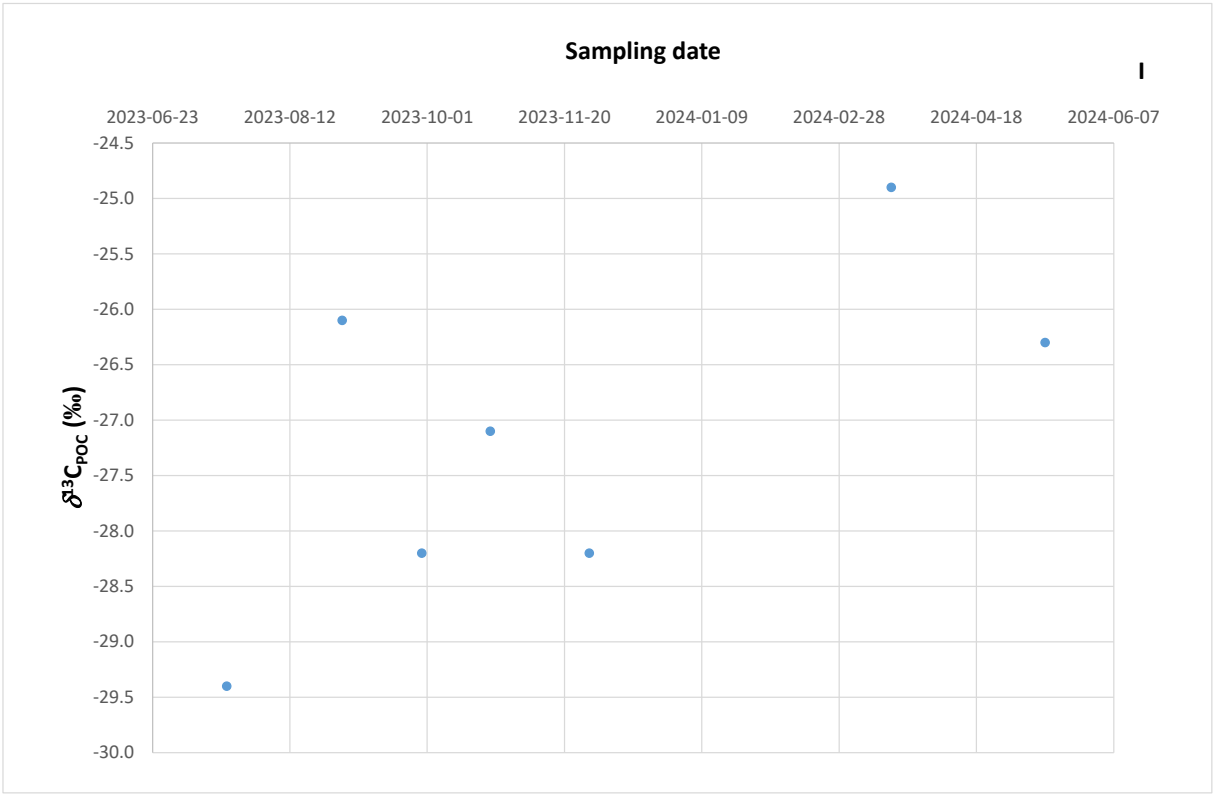
Sampling date
I
2023-06-23
2023-08-12
2023-10-01
2023-11-20
2024-01-09
2024-02-28
2024-04-18
2024-06-07
-24.5
-25.0
-25.5
-26.0
-26.5
-27.0
-27.5
-28.0
-28.5
-29.0
-29.5
-30.0
δ13CPOC (‰)

GEOLOGIJA 68/2, 221-241, Ljubljana 2025

https://doi.org/10.5474/geologija.2025.009

Article

Landslides on Glaciers: from a literature collection towards a detection strategy

Plazovi na ledenikih: od pregleda literature do strategije za njihovo prepoznavanje

Gisela DOMEJ

Geological Survey of Slovenia, Dimičeva ulica 14, SI-1000 Ljubljana, Slovenia; e-mail: gisela.domej@geo-zs.si

Prejeto / Received 10. 6. 2025; Sprejeto / Accepted 25. 7. 2025; Objavljeno na spletu / Published online 25. 9. 2025

Key words: glaciers, landslides, debris, rockslides, rock avalanches, glacier dynamics
Ključne besede: ledeniki, plazovi, drobir, skalni zdrs, skalni plazovi, dinamika ledenikov

Abstract

Glacial environments are extremely sensitive to climate change and associated phenomena such as deglaciation and changes in snowfall patterns affecting the glacial mass balance globally. However, as an essential part of the Earth's water storage, glaciers are of significant importance for the geo-biologic stability.

As documented in many locations, landslides on glaciers can trigger altered glacier responses, i.e., glacial advance or glacial surges, which is approached via a literature collection in three categories: cases, inventories, and detection. This publication presents the complexity of landslides on glaciers, statistics based on the literature collection, and a possible index stacking approach towards pattern and shape recognition.

Izvleček

Ledeniška okolja so izjemno občutljiva na podnebne spremembe in z njimi povezane pojave, kot so taljenje ledenikov in spremembe v vzorcu snežnih padavin, ki vplivajo na masno bilanco ledenikov po vsem svetu. Vendar pa so ledeniki, ki predstavljajo bistveni del Zemljinih zalog vode, izjemnega pomena za geo-biološko stabilnost.

Kot je dokumentirano na številnih lokacijah, lahko plazovi na ledenikih sprožijo spremenjene ledeniške odzive, kot sta napredovanje ledenikov ali ledeniški sunki. To je obravnavano s pomočjo pregleda literature, razdeljene v tri kategorije: primeri, popisi in zaznavanje. Ta objava predstavlja kompleksnost plazov na ledenikih, statistične podatke, ki temeljijo na zbrani literaturi in možen pristop slojenja indeksov za prepoznavanje vzorcev in oblik.

Introduction

Glacial environments are endangered due to climate change and global warming, leading to general rapid deglaciation, reduced snowfall because of changes in precipitation preventing glacier growth and mass balance stability, and glacier calving at tidewater glaciers. Shrinking of ice surfaces results in a reduced albedo, which enhances the absorption of solar radiation and faster melting processes. The mechanism is of crucial importance for the Earth's water household as glaciers act as natural reservoirs, as well as for the geo-biologic balance, the sea level, climate self-regulation, and seasonality around the globe (e.g., Böhm et al., 2007).

One phenomenon that is impacting glacial dynamics is landslides on glaciers (LSGL), i.e., landslides coming to rest or traveling over glacial surfaces. This publication provides an overview of the topic, its importance explained by classic examples, and a collection of literature divided into three categories: LSGL cases, inventories, and detection. Existing databases and mapping tools are compared, and statistics on the literature collections are presented. Drawing on the publications in the category of LSGL detection, a possible index stacking approach towards LSGL pattern and shape recognition is showcased.

Landslides on glaciers

In order to approach the topic of LSGL, a correct terminology is essential, which concerns glaciers on the one hand, and the rather inconsistently used term "landslide" throughout literature on the other hand.

Glaciers are, by definition, large ice and snow masses that commonly exhibit strong dynamic down-slope behaviors caused by their weights. Glacial environments are characterized by mean annual temperatures allowing for perennial snow and ice conservation, usually around and below the freezing point. Glaciers may be distinguished by thermal regime (i.e., cold glaciers, temperate glaciers) as well as by size (i.e., ice fields/sheets, valley glaciers, cirque glaciers, piedmont glaciers, tidewater glaciers, ice caps, etc.), but categories vary throughout literature (e.g., Hagg, 2022; Huggett, 2011; Martini et al., 2001; NSDIC, 2025).

Depending on authors' preferences, however, the term "landslide" can refer to a multitude of mass movement types ranging from various forms of slides, flows, and falls (Fig. 1) typical for distinct speeds and levels of water saturation (e.g., Cruden & Varnes, 1996; Hungr et al., 2014; Hutchinson, 1968; Varnes, 1978). In glacial environments, dry mass movement types are most common – i.e., rockslides, rock avalanches, and rockfalls (Fig. 2a–b), amongst which an exact distinction is likewise difficult as one type might transform into another. For simplicity, this publication describes all concerned phenomena as "landslides".

Generally, climate change and global warming have a worldwide negative effect on the cryosphere (e.g., Bolch et al., 2012; Herreid & Pellicciotti, 2020; Rabatel et al., 2013; Sorg et al., 2012; Zemp et al., 2020) causing glacial retreat (Figure 3a) and associated processes such as, for instance, (classic) landslides and glacial lake outburst floods (GLOFS). Confirmed and predicted further global ice losses attributed to climate change draw a dramatic picture, in which glacial mass balances do not expose positive trends (e.g., Bliss et al, 2014; Shannon et al., 2019). In contrast to glacial retreat, which is considered a normal glacier response to global warming, the phenomenon of altered glacial response can be observed at different locations around the globe (Fig. 3b). Here, LSGL provide a debris cover on top of the ice, which – according to its extent – may have two effects:

- Insulation – the debris acts like a thermal insulator preserving the underlying ice masses; the debris cover, hence, slows down the process of ablation (e.g., Bessette-Kirton et al., 2018; Bull & Marangunić, 1966; Deline, 2005; Deline et al., 2015; Herreid & Pellicciotti, 2020; Shugar et al., 2012; Reznichenko et al., 2010; Reznichenko et al., 2011; Vacco et al., 2010)
- Load increase – the weight of the debris entails a vertical and/or lateral kinematic constraint and thermodynamic energy transformation; ice flow rates rise as it is considered to be proportional to driving stress to the power of three (Bons et al., 2018)

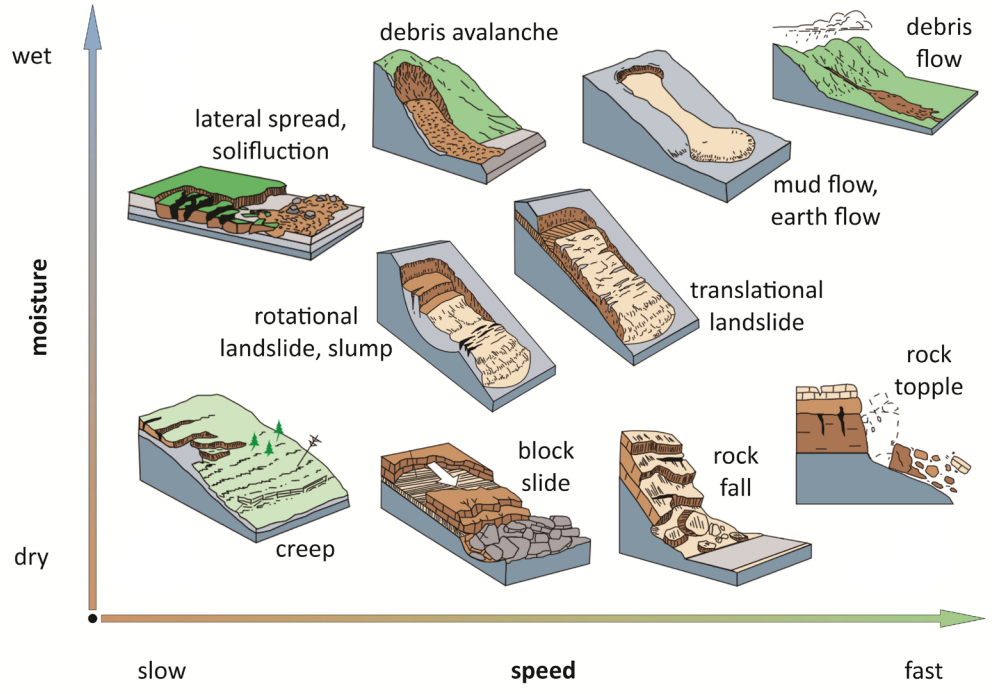

Fig. 1. Various mass movement types with gradual transition (after USGS, 2004).

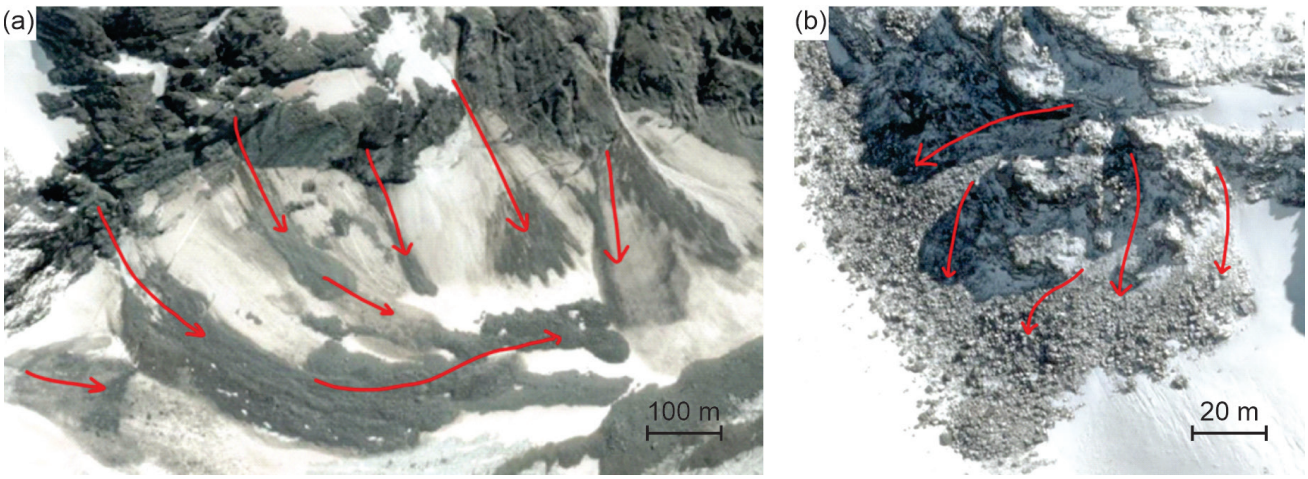

Fig. 2. Examples of rockslides and rock avalanches (**a**) and rockfalls (**b**); the exact distinction is difficult in glacial environments (photos: project internal source).

Both settings may condition glacial expansion in the direction of the least resistance (i.e., down-slope) as well as glacial advances with considerable speeds. The phenomenon might become distinctly pronounced, as LSGL often depict a far wider runout and deposit area than their non-glacial counterparts, due to considerably different friction mechanisms one ice surfaces (e.g., Delaney & Evans, 2014; Ekström & Stark, 2013).

Moreover, the formation of mixed ice-rock flows similar to debris flows is possible at glacier toes, as thermodynamic alterations might increase the formation of meltwater.

It is essential to note that besides the effect of LSGL, conditional changes in hydrological as well as thermal regimes in cold environments are known to cause rapid glacier advances or cyclic surges. They are, however, more widely discussed and documented (e.g., Björnsson, 1998; Eisen et al., 2005, Fatland & Lingle, 2002; Fowler et al., 2001; Harrison et al., 1994; Kamb et al., 1985; Kamb, 1987; Lingle & Fatland, 2003; Murray et al., 2003; Murray & Porter, 2001; Raymond, 1987) than LSGL.

The danger potential of LSGL is underlined by the event at Blatten, Switzerland, that occurred on 28th of May 2025, right at the finalization of this publication. Weathered rock from Kleines Nesthorn accumulated for years on the Birch Glacier, and a major collapse took place from 19th to 20th of May 2025, accelerating the glacial movement under additional load from several to about ten meters per day, before finally coming loose as an avalanche of millions of cubic meters of rock and ice. Large parts of the village of Blatten were destroyed and later flooded by the dammed Lonza River (Farinotti et al., 2025).

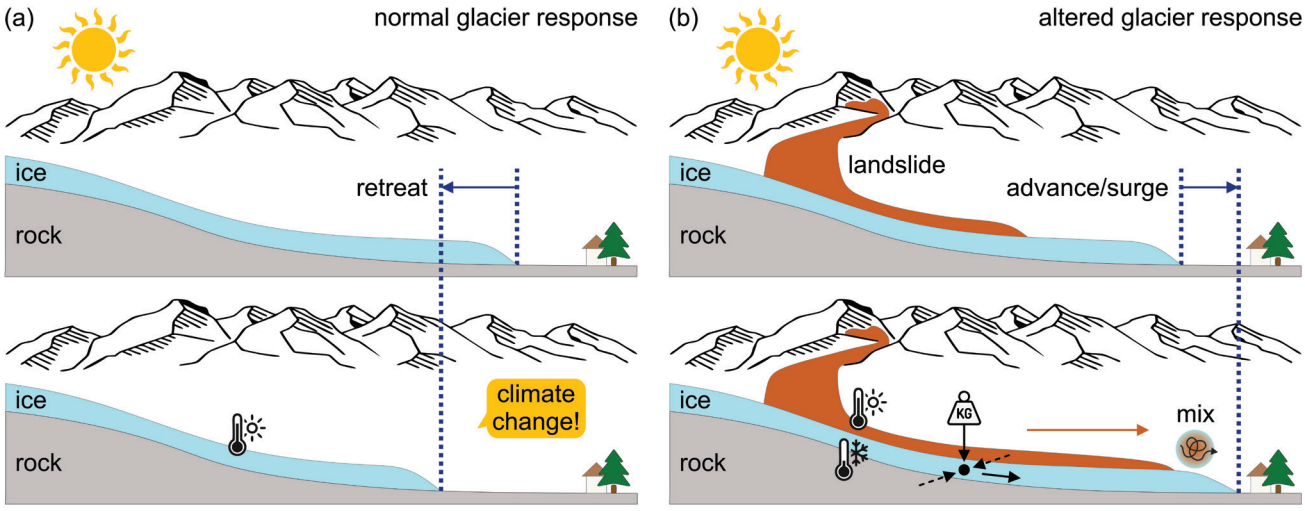

Fig. 3. Normal glacier response to climate change (**a**) and altered glacier response (**b**) due to landslide cover, resulting thermal insulation, and additional vertical load and lateral compression entailing a kinematic regime change.

Classic examples

Several prominent cases of LSGL are listed in Table 1 and shown in Figure 4a–f. It is apparent that the extent of the debris cover is not proportional to the displacement speed of the entire LSGL underlining the complexity of the phenomenon and its conditioning factors such as – amongst others – the topographic and hydrogeologic setting, local geomorphology, seasonality, and insolation, etc.

Intriguingly, one of the most striking examples of an altered glacier response to debris cover is the tailing management at the Kumtor Gold Mine in Kyrgyzstan, where starting in 1999, excavation residues were deposited on Lysii Glacier and Davidov Glacier (Jamieson et al., 2015; Evans et al., 2016). Strictly speaking, the setting is, therefore, not a classic landslide or LSGL scenario. Nonetheless, it is considered a textbook example, as glacier advances took on speeds ranging from meters to hundreds of meters per year destroying mining facilities and covering worth-to-excavate pits.

All images (Fig. 4a–f) are created with the Google Earth Engine code CataEx by Domej et al. (2025; Section 2.2.) and consist of an overlay of two layers. The RGB (red-green-blue = true-color) image components represent the extent of the Randolph Glacier Inventory 6.0 (RGI; RGI Consortium, 2017) and appear in gray scales due to rather sparse cryospheric vegetation patterns. The images underlying the RGI 6.0 polygon are false-color images carrying values between -1 and 1 of the Normalized Difference Moisture Index (previously named "water index" by Gao, 1996):

$$NDMI = \frac{NIR - SWIR1}{NIR + SWIR1} \quad \text{(Eq. 1)}$$

where ***NIR*** is the near-infrared band and ***SWIR1*** is the first short-wave infrared band of different satellite sensors.

The blue extremity (i.e., NDMI = 1) indicates very moist conditions (e.g., open waters), while the red extremity (i.e., NDMI = -1) represents extremely dry surfaces (e.g., bare rock); the latter can be mistaken for shadows.

All images (Fig. 4a–f) have the same scale emphasizing the differences in dimension of LSGL. This aspect evokes the following (non-exhaustive) series of questions, which should be the focus of data evaluation based on the here-presented literature collection throughout the runtime of the concerned scientific project (cf. Acknowledgments):

(i) location & and frequency of LSGL
- Which glaciers experience/experienced LSGL?
- Are LSGL uniformly distributed throughout glaciated regions or are they clustered?
- What is the magnitude-frequency distribution of LSGL over time?
- Is there a correlation between climate change, global warming, and a possible increase in overall landslide activity?

Table 1. Prominent cases of LSGL around the globe. The debris cover on Lysii Glacier and Davidov Glacier at the Kumtor Gold Mine, Kyrgyzstan, are artificial deposits of mine tailings (Jamieson et al., 2015; Evans et al., 2016).

Name of Glacier	Country	Occurrence between	Debris cover increase until 2022	Debris cover displacement
Morsárjökull	Iceland	2006/08 – 2007/07	3.2 km² – 7.4 km²	182 m/year
Svinafellsjökull	Iceland	2012/06 – 2013/07	± 7.7 km²	284 m/year
Lamplugh	Alaska/USA	2015/09 – 2016/08	74.1 km² – 74.3 km²	165 m/year
Kumtor Lysii Kumtor Davidov	Kyrgyzstan	deposit start 1999	[advance 1.2 km] [advance 3.2 km]	m/year to 100s of m/year
Leones 1 Leones 2	Chile	2014/03 – 2015/01 2015/01 – 2017/01	2.8 km² – 10.6 km² (combined)	500 m/year (combined)
Tasman	New Zealand	2022/01 – 2022/02	± 0.4 km²	n. d.

Table 2. Satellite image data referring to Figure 4a–f. All images originate from different collections but are categorized as Collection 2 (C2), Tier 1 (T1), and Top-of-Atmosphere (TOA). The last number sequence of the image ID indicates the date of image acquisition.

Name of Glacier	Latitude (dec°)	Longitude (dec°)	Landsat Mission	Landsat Image ID
Morsárjökull	64.09917	-16.89346	LS5	LT05_218015_20090830
Svinafellsjökull	64.01489	-16.82946	LS7	LE07_217015_20130522
Lamplugh	58.79244	-136.88199	LS8	LC08_059019_20160807
Kumtor Mine	41.877575	78.205832	LS8	LC08_148031_20140701
Leones (1 & 2)	-46.78430	-73.27296	LS8	LC08_232092_20170416
Tasman	-43.57460	170.17477	LS8	LC08_075090_20220213

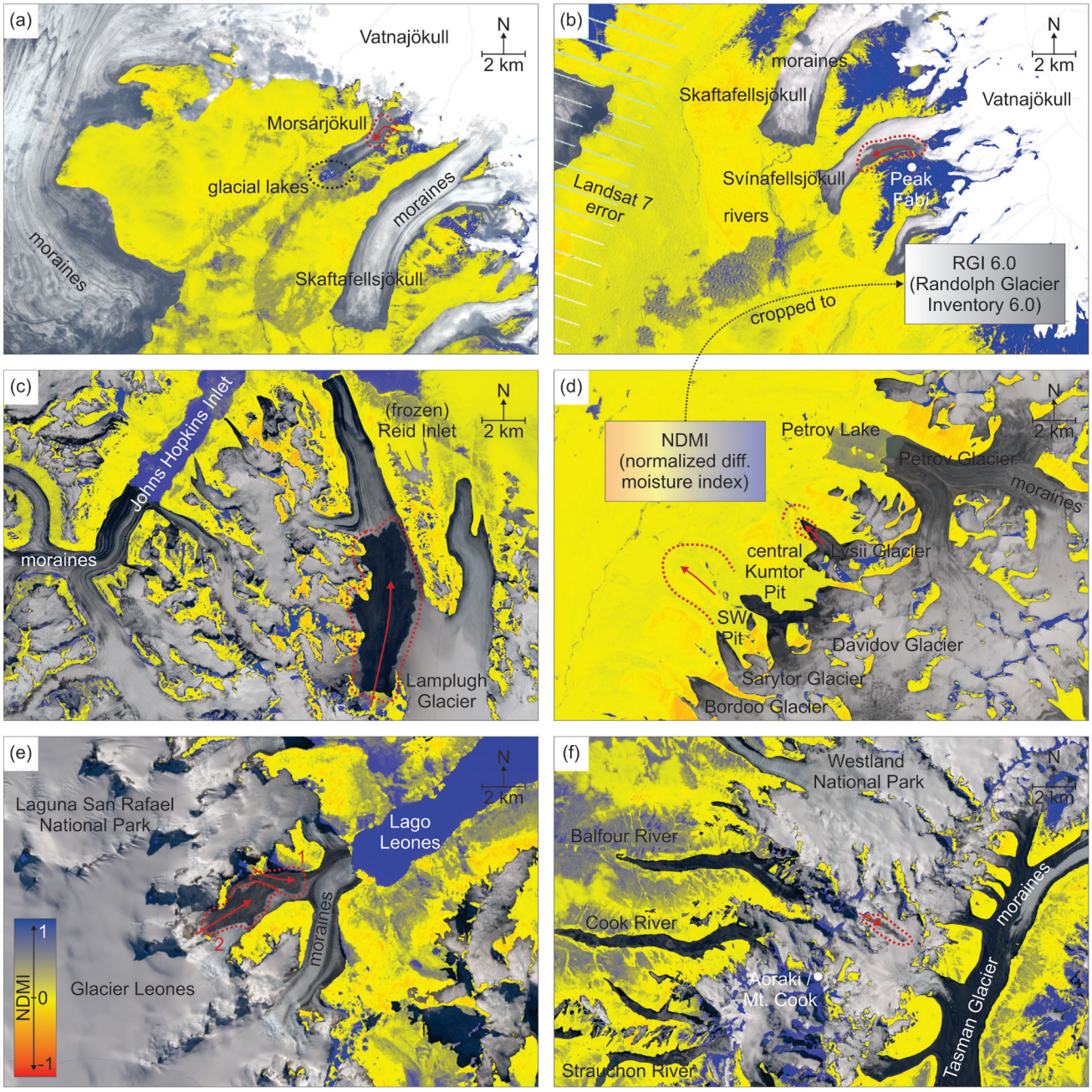

Fig. 4. Prominent cases of LSGL around the globe – on Morsárjökull, Iceland (**a**), on Svinafellsjökull, Iceland (**b**), on Lamplugh Glacier, Alaska/USA (**c**), on glaciers around the Kumtor Mine, Kyrgyzstan (**d**), on Glacier Leones, Chile (**e**), on Tasman Glacier, New Zealand (**f**). Images display NDMI exports obtained with the Google Eart Engine code CataEx (Domej et al., 2025) cropped to the RGI 6.0 (RGI Consortium, 2017) showing glaciated surfaces. Satellite image data is listed in Table 2.

(ii) processes of LSGL

- How do LSGL behave in terms of kinematics?
- How can LSGL be characterized in their dimensions?
- What mass thresholds can be considered relevant to entail an altered glacier response?
- After what time does an altered response become visible, and for how long does an altered response last?
- How can advance or cyclic surge scenarios be characterized in a dynamic, kinematic, and temporal manner?
- Are altered responses dependent on glacier regimes (i.e., cold or temperate glaciers) and/or landslide types (i.e., rockslides, rock avalanches, or rockfalls)?
- Are altered responses dependent on the extent ratio of LSGL area to glacier area, and what ratio is of critical relevance?

Literature sources and methodology

The literature collection is strongly framed by the initially very specific project goal of establishing a new global database of LSGL reaching back in time as far as (primarily) free-of-cost remote sensing

data is available. The first strategic step was, therefore, to understand from literature, which detection methods are commonly employed in the tracing process of LSGL over time. The following libraries, publishers, and platforms were searched up to March 2023 (i.e., corresponding roughly to the first year of the post-doctoral assignment of the author):

- Scopus (https://www.scopus.com/)
- Wiley Online Library (https://onlinelibrary.wiley.com/)
- ScienceDirect (https://www.sciencedirect.com/)
- Springer Nature Link (https://link.springer.com/)
- Taylor & Francis Online (https://www.tandfonline.com/)
- GeoScienceWorld (https://pubs.geoscienceworld.org/)
- ICE Virtual Library (https://www.icevirtuallibrary.com/)
- MDPI (https://www.mdpi.com/)
- ResearchGate (https://www.researchgate.net/)
- Google Scholar (https://scholar.google.com/)

For the topic of detection of LSGL, references of the publications identified as relevant were followed through until redundant. While screening publications, and with the redundant-reference approach, publications on distinct LSGL cases and LSGL inventories turned up, which were eventually collected separately (Fig. 5). It is essential to note that the collections of LSGL cases and inventories were not treated with the redundant-reference approach and, hence, reflect an overview without claiming exhaustiveness up to March 2023. Likewise, the collection of LSGL detection publications is supposedly not complete, as it is common for literature collections in general. The identified literature is listed in Appendix 2.

From Figure 5, it becomes apparent that case studies on LSGL reach back to earlier dates (even if sparsely, though), while publications on detection and inventories of LSGL significantly increased in numbers after the year 2000 when satellite imagery became considerably better and easier to access. Exemplarily, only Landsat missions of the National Aeronautics and Space Administration and the United States Geological Survey (NASA & USGS), Sentinel missions of the European Space Agency (ESA), and SPOT (French: Satellite Pour l'Observation de la Terre) of the Centre National d'Études Spatiales (CNES) are shown, reflecting only a small spectrum of spectral and radar imagery suppliers. Due to the obvious difficulty tracing LSGL back in time for reasons of image quantity and quality (Section 2.2.), the initial goal of establishing a global database of LSGL was modified into an assessment of LSGL inventories and detection methods to

(i) assemble a database from existing inventories and homogenize the data,

(ii) and study techniques to potentially fill gaps in the database.

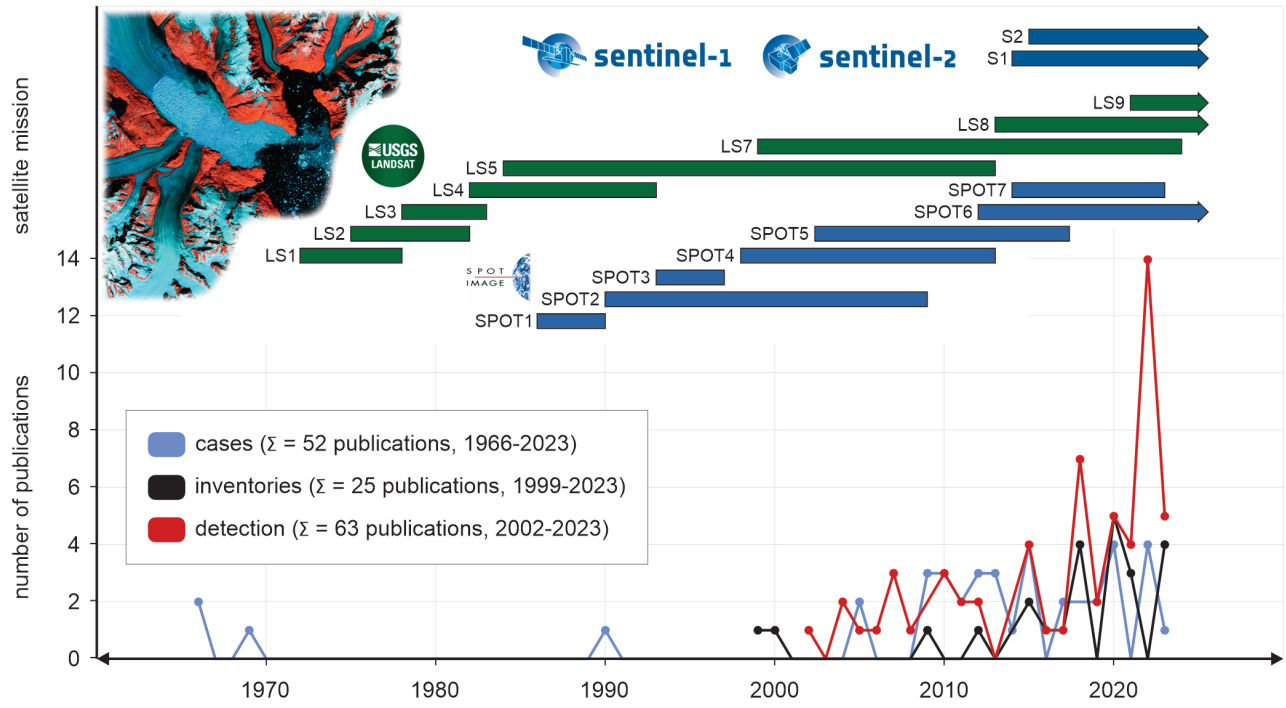

Fig. 5. Numbers of publications per year included in the here-presented literature collection and chronology of satellite missions (satellite image: after Bouchard, 2022).

Existing databases

Particularly for the task of filling gaps and detecting LSGL in areas where no inventories are established, but also to verify and complete existing inventories, several existing databases are of essential interest. As they reach back in time and/or are being updated regularly by the providing institutions and authors, they can assist in tracking both glacier extents (which condition the existence of LSGL) and debris cover across glaciers caused by LSGL.

- The World Glacier Inventory (WGI) is a global glacier database with information of more than 130,000 glaciers based on aerial photographs and maps, with most entries being non-multitemporal. By the time of establishment, it included about 85 % of the Earth's glaciers providing a static snapshot of the glaciation in the second half of the 20th century (WGMS, 1989).
- To continue the efforts of the WGI with remote sensing techniques, the initiative Global Land Ice Measurements from Space (GLIMS) was launched between the National Snow and Ice Data Center (NSIDC) and the World Glacier Monitoring Service (WGMS). GLIMS mainly relies on spectral satellite imagery such as ASTER data and several others. It globally covers more than 20,000 glaciers and 750,000 km² excluding the ice sheets in Greenland and Antarctica, with some of the glaciers having multi-temporal coverage (Kargel et al., 2014).
- Integrating GLIMS into new formats, the RGI (i.e., in all its versions) provides global coverage of single glacier outlines as polygons together with attributes and auxiliary data starting approximately from the year 2000. RGI data is available currently in its 7th version and provides a static snapshot as by the year 2023 for glaciers excluding ice sheets; it is sectioned in Global Terrestrial Network for Glaciers (GTN-G) Glacier Regions and freely available (RGI 7.0 Consortium, 2023).

A strong reference for assessing LSGL on a global scale is the dataset on Supraglacial Debris Cover provided by the GFZ (Helmholtz Centre for Geosciences) Data Services in its version 1.0 (Scherler et al., 2018b). Based on the RGI 6.0 and a remote sensing identification technique for ice and snow, Scherler et al. (2018a) mapped and analyzed the global distribution of supraglacial debris using Landsat 8 and Sentinel-2 satellite imagery with resolutions of 30 m and 10 m, respectively. The dataset includes shapefiles (SHP-file) and auxiliary data but has the drawback that areas that belong to glaciers without being ice or snow are classified as debris cover, while they could in reality be – for instance – nunataks. As the dataset draws on the RGI 6.0, information on debris cover on the ice sheets of Greenland and Antarctica is sparse. This aspect is, however, not critical for mapping LSGL, as ice sheets are usually not dissected by topographic ridges from which landslides could originate.

The tools GERALDINE, GEEDiT, and CataEx

Popular concepts and algorithms discriminating between ice, snow, and areas not containing either of them (i.e., ice-snow-free areas) are commonly based on the pixel-wise processing of satellite data combining ratios, indexes, and thresholds. Indexes refer to normalized-difference operations such as – for instance – the one for the NDMI (Equation 1); a variety of sensor band combinations result in distinct indexes, of which the most commonly used are:

- NDVI (normalized-difference vegetation index; Kriegler et al., 1969) using the NIR and red bands to differentiate open waters from healthy vegetation
- NDWI (normalized-difference water index; McFeeters, 1996) using the green and NIR bands to differentiate open waters from dry areas
- NDSI (normalized-difference snow index; Dozier, 1989) using the green and SWIR1 bands to differentiate snow and ice from bare rock and vegetation

Herreid et al. (2015), Mölg et al. (2018), and Scherler et al. (2018a) used a similar method to map ice, snow, and other areas; other authors developed comparable sequences of algorithms involving most commonly the NDVI, NDWI, and NDSI (Table A1 in the Appendix). Worth mentioning is the work of Keshri et al. (2009), who demonstrate how ice, snow, debris, and a mix of ice and debris can be distinguished in the Himalayas using the NDSI, the NDGI (normalized difference glacier index using green and red sensor bands; Keshri et al., 2009), and the NDSII (equal to the NDWI by McFeeters, 1996).

For all remote sensing-based approaches to map LSGL remains the general question, of whether areas classified as debris indeed represent LSGL; many algorithms are only designed for ice-snow-free areas, which can well locate nunataks, exposed rock cliffs, or simply areas that previously were covered by glaciers and affected by glacial

retreat. The latter discrepancy is particularly frequent when working with polygons of an older RGI version or even within the most recent version as glacial retreat can take place with striking speed. Shadow effects and cloud cover in remote sensing imagery can likewise hinder algorithms from performing properly and result in misclassifications.

Other options to outline LSGL are traditional and/or assisted mapping strategies, which can be supported by different tools such as GEEDiT (Lea, 2018) and GERALDINE (Smith et al., 2020) implemented as ready-to-run JavaScript routines in the Google Earth Engine (Gorelick et al., 2017).

GEEDiT (Google Earth Digitisation Tool) was designed by Lea (2018) to map and trace margin changes of environmental processes over time on satellite imagery of Landsat 4–8 and Sentinel-1 and -2. The complementary MaQiT (Margin Quantification Tool) allows for rapid quantification of the mapped margins (e.g., of glacier margin changes).

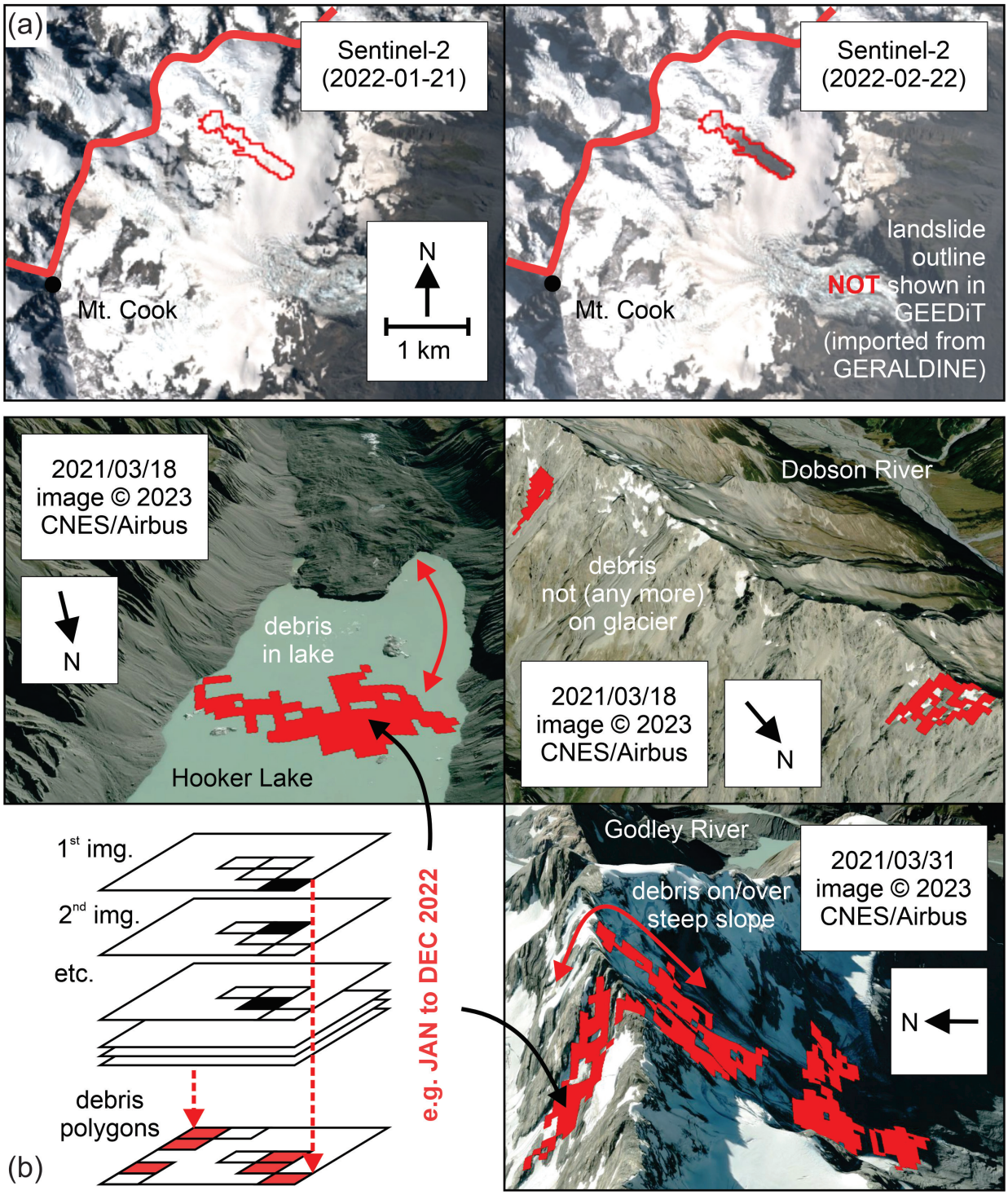

Fig. 6. Manual mapping with GEEDiT (Lea, 2018) of the LSGL on Tasman Glacier (Table 2) and assisted mapping with GERALDINE (Smith et al., 2020). Communication between GEEDiT and GERALDINE is implemented by Domej & Pluta (2022–2024).

GEEDiT alone can also be used as a catalog viewer for screening purposes to identify LSGL and their occurrence windows, which is – nonetheless – a subjective and time-consuming task (Fig. 6a).

GERALDINE (Google Earth Engine supRagl-AciaL Debris INput dEtector) is likewise a JavaScript routine for the Google Earth Engine (Smith et al., 2020) that computes large debris covers on glaciers such as LSGL (with areas >0.05 km²) via a pixel-stacking and comparison approach (Fig. 6b). For a given area and timeframe, GERALDINE stacks Landsat 4–9 satellite images on top of each other to filter for pixels that fulfill the condition of "not containing debris" and turning into "containing debris" in more recent images; for this purpose, the spectral NDSI imprint is decisive with a threshold of 0.4 is below which material is classified as debris. Excluded from this algorithm are areas outside the RGI 6.0 and areas that were marked as cloudy before the launch of the algorithm (i.e., with a degree of cloudiness of 20 %). The result of each computation is a mosaic of red pixels indicative of debris input onto glaciers, which, however, is not solely sensitive to LSGL (Fig. 6b). False positives such as debris on open water bodies, debris located (not anymore) on glaciers, and/or debris on/over steep slopes are no reasonable locations for LSGL and are usually caused by a combination of reasons: (i) seasonality and glacial retreat, (ii) shadow effects, and (iii) avalanches exposing bare rock being misinterpreted as debris input, and (iv) unlikely deposit locations for LSGL in steep terrain.

To ease the process, Domej & Pluta (2022–2024) developed a code communication between both routines importing mosaics as unfilled polygons from GERALDINE into GEEDiT so that catalog screening (e.g., for the assessment of occurrence windows) would become more efficient. Furthermore, Domej & Pluta (2022–2024) introduced an image ID display into GEEDiT to keep track of distinct satellite images displaying features of particular interest or to use them in different routines where image IDs are required.

A third tool assisting in the visualization of LSGL is the Google Earth Engine code CataEx (Domej et al., 2025). Although not exclusively designed for glacial environments, Domej & Pluta (2022–2024) developed a multi-functional JavaScript routine to filter satellite image collections (i.e., Landsat and Sentinel-2 imagery), mask clouds, compute indexes and pixel-based histograms, create and visualize layers, and export images as GeoTIFFs. Besides the frequently used indexes of the NDVI, NDSI, NDWI, and NDMI, CataEx also computes the NDGI (Keshri et al., 2009), two false-color images, and several RGB images, of which one is tailored to the RGI 6.0. Figure 4a–f is an example of possible exports of CataEx via traditional GIS software (e.g., ArcGIS® Pro or QGIS).

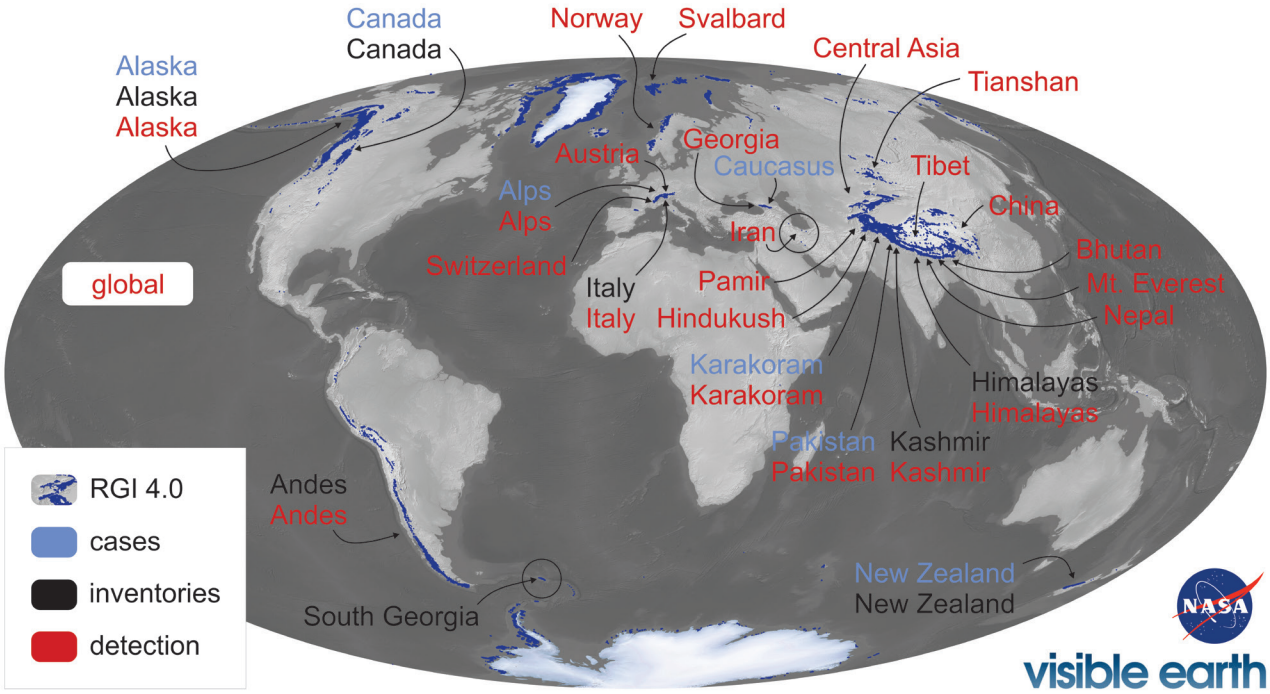

Fig. 7. Locations mentioned in publications on LSGL cases, inventories, and detection. The underlying map (after NASA visible earth, 2025) depicts the RGI 4.0 (Pfeffer et al., 2014). Distributions coincide well with the supraglacial debris cover map by Scherler et al. (2018a).

Insights into the literature collection

The collection of literature on the topic of LSGL comprises 140 publications sorted into three categories (Fig. 5): LSGL cases (#52), inventories (#25), and detection (#63). This tripartition originates from the initial ambition to (i) apprehend the worldwide distribution and/or clustering, (ii) the accomplished work on inventories and potential gaps, and (iii) strategies on how to effectively detect LSGL using satellite imagery.

A worldwide phenomenon

From an overview of collected literature, the question of global LSGL distribution can be straightforwardly answered. Referring to geographical information from the collection sections of LSGL cases and inventories, documentation of LSGL can be associated with the locations given in Figure 7. Additionally, the areas where LSGL detection was studied and/or performed are marked on the map, which is closely comparable with another map by Scherler et al. (2018a), who globally estimated supraglacial debris cover extents in percent for 1°×1° tiles from Landsat 8 imagery from 2013–2015.

Detailed quantitative and qualitative analyses on relevant contents shedding light on the questions mentioned above should be the subject of the ongoing scientific project based on this literature collection.

Detection strategies of LSGL

From Figure 8 it is apparent that both traditional and/or assisted mapping approaches as well as automated detection methods were in use over the last two decades, but within the last decade a strong tendency towards detection approaches using learning methods (Table A1 in the Appendix) became visible. Various methods appear throughout the publications and can be classified as machine learning techniques (Figure 8); they are listed in the last column of Table A1 (in the Appendix) in alphabetical order.

Several essential aspects emerge from the literature collection. Spectral satellite imagery is more popular than radar imagery, and from spectral missions, bands ranging over the visible and infrared spectrum are more frequently used than low-frequency thermal bands.

From band combinations (i.e., mostly form the green, red, NIR, and SWIR1 bands), indexes are calculated according to the example Equation 1, with the NDVI, NDSI, NDMI, and MDWI being the most recently cited in the collection of publications of LSGL detection.

Ideal information

The ideal information for the assessment of LSGL and glacial co-dynamics would consist of a clear characterization of LSGL in their spatial extent over time for comparison with the kinematic behavior of their underlying glaciers. Relevant parameters are (Fig. 9b):

L length of landslide (m)
ΔL advance of landslide (m)
G length of glacier (m)
ΔG advance of glacier (m)

$$speed_L = \frac{\Delta L - L}{\Delta t - t} \quad \text{(Eq. 2)}$$

$$speed_G = \frac{\Delta G - G}{\Delta t - t} \quad \text{(Eq. 3)}$$

where t and Δt are not necessarily the same for the landslide and the glacier but simply describe the considered time interval.

For length (and likewise width) estimations, a reference and a direction of measurement should

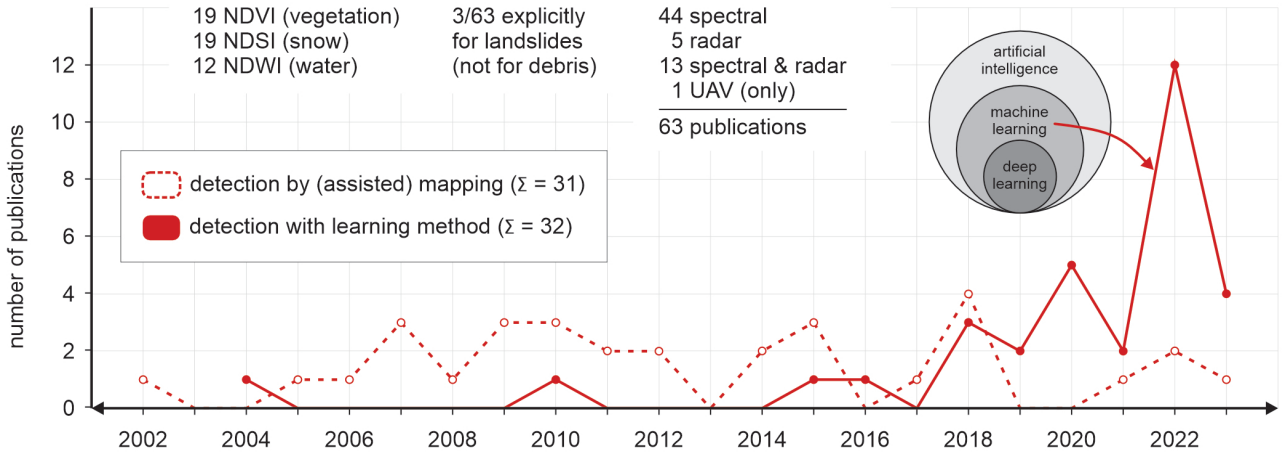

Fig. 8. Comparison of numbers of publications that used traditional and/or assisted mapping approaches for LSGL with those using automated detection with learning methods (i.e., machine learning methods).

be set, which is, however, problematic (Fig. 9b–c). Often LSGL slide into corners or hollows, which raises the question of whether an area (independently of direction-related entities) is more suitable for LSGL quantification. The question about LSGL thicknesses and volumes is even more complicated, but ultimately the most crucial for LSGL and glacial co-dynamics, as volumes give clues on additional vertical load and lateral compression entailing kinematic regime changes (Fig. 3b) and resulting enhanced ablation rates and mass balance alterations.

An aspect that significantly impedes the quantification of LSGL and glacial co-dynamics is the fact that strategies for their assessment and recorded units vary considerably between authors. For a meaningful comparison of LSGL and their effects on glaciers, the most essential step would, therefore, have to be the introduction of a standardized formats of relevant parameters and assessment strategies.

Stacking indexes strategy

Drawing on the popularity of indexes throughout different publications and acknowledging the trend towards machine learning in recent years, Domej & Pluta (2022–2024) designed a MATLAB® routine that extracts a debris mask after index stacking with the aim of exploring suitable pre-stages of datasets for pattern and shape recognition and object-based image analysis (OBIA). The ambition is to calculate debris masks, that would ideally outline shapes typical for LSGL, which could assist in training machines in pattern and shape recognition as well as assisted and automated mapping of LSGL.

As the first step, the layers containing the five indexes of the NDVI, NDSI, NDMI, NDWI, NDGI, one RGB image, and the RGI 6.0 image are exported as GeoTIFFs from the Google Earth Engine with the cote CataEx (Domej et al., 2025) for an area of interest containing an LSGL. The images each contain an n×m grid with pixel values ranging from -1 to 1 and, therefore, appear grey in any

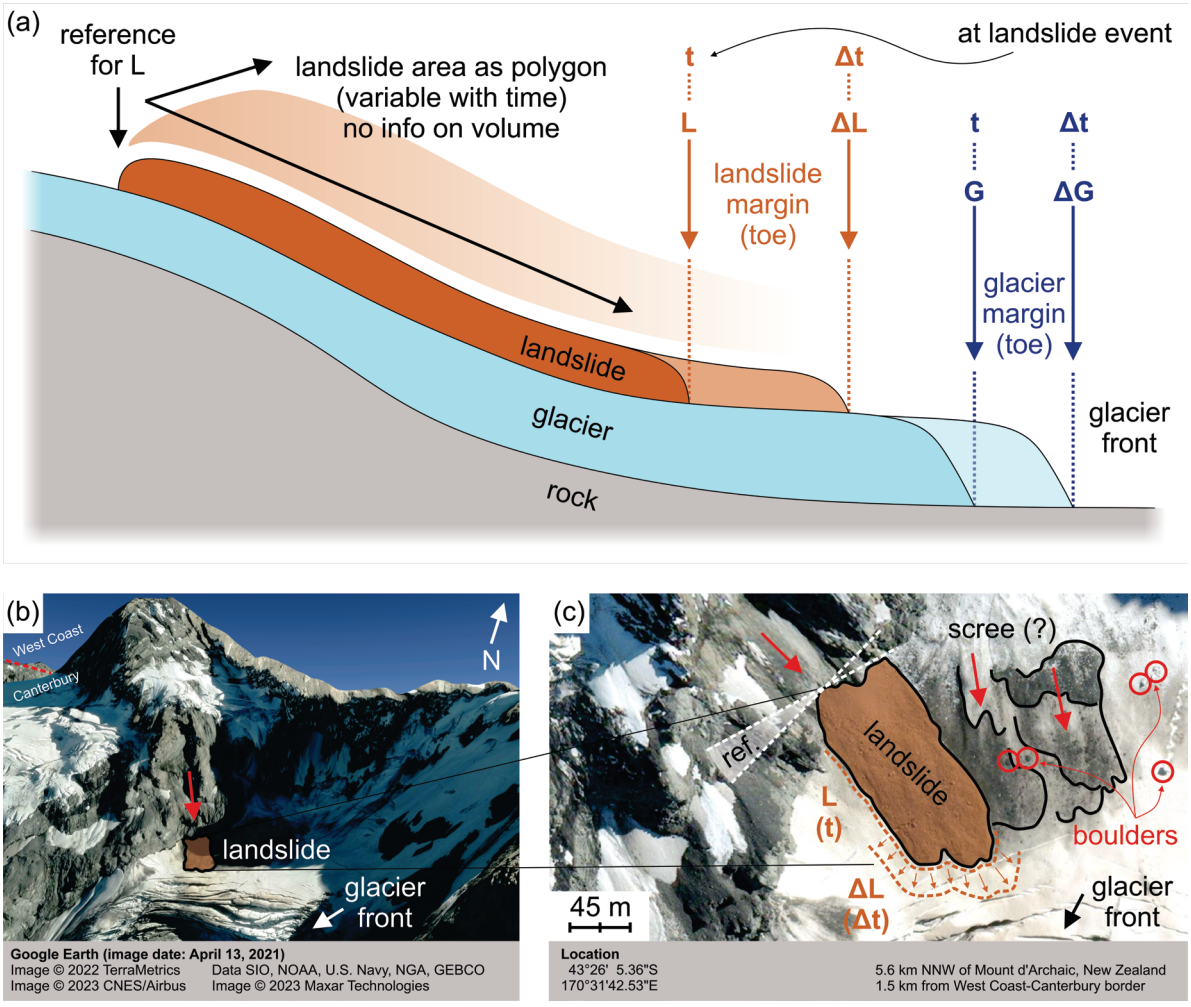

Fig. 9. Idealized LSGL sketch from which dynamic information could be calculated provided that the elevation contrast is not too pronounced (**a**), example LSGL in New Zealand (**b**), and reference discrepancies (**c**).

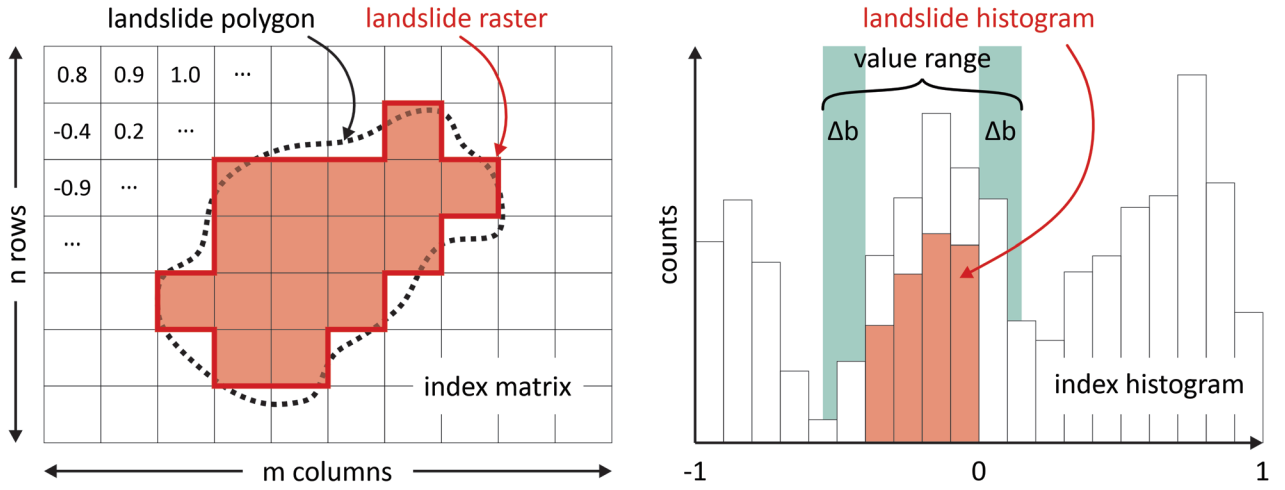

Fig. 10. Histogram calculation based on an entire index matrix and for the area included in the LSGL polygon.

software capable of displaying TIF-files. Color coding is re-applied after importing the respective grids as matrices into MATLAB®; however, color maps are different from common usage per index, as color maps in MATLAB® are not easily customizable. The RGI 6.0 image does not need a color map, as it will be used only as a stencil in the routine.

The index layer with the (subjectively) best contrast between a LSGL and the surrounding glacier and the RGB image are read in ArcGIS® Pro to outline an LSGL reference polygon, which is first rasterized and then likewise imported as TIF-file into MATLAB® where the TIF-files are treated as n×m matrices with cells holding pixel-values.

In the second step, cell value histograms are computed for all entire index matrices and for the area included in the LSGL polygon (Fig. 10).

Eventually, the MATLAB® routine performs the following sequence of operation:

1. From the histogram (per index matrix), the range of values within the LSGL polygon is retrieved (i.e., a range between min. -1 and max. 1) and a bonus (±Δb) is added to account for border cells (Fig. 10).
2. All values in cells that are not included in the identified range (including ±Δb) are eliminated (per index matrix; first four columns in Fig. 11a–c).
3. All four perforated index matrices are stacked to create a debris mask; if at least one of the four superimposed cell locations is empty, the debris mask matrix also contains an empty cell, and only if all four cell locations contain a value, the debris mask contains the value 1 and appears black (last column in Fig. 11a–c).
4. Finally, the debris mask is truncated with the RGI 6.0 matrix, to eliminate cells that do not belong to glaciers, and, hence, cannot contain debris on glaciers. It is likely, that by drawing the LSGL reference polygon manually, after the rasterization of the polygon in ArcGIS® Pro, and with the histogram bonus (±Δb), some cells enter the debris mask as "intruders"; the truncation using the RGI 6.0 can limit this problem.

The routine is somewhat functional, as the examples of three of the LSGL of Table 1 show. It must be noted that the routine is in a preliminary phase, as discussed in Section 5.

Results and discussion of the first examples of debris masks

Exemplarily, the MATLAB® routine stacking indexes and computing a debris mask was applied to Lamplugh Glacier in Alaska/USA (Fig. 11a), Glacier Leones in Chile (Fig. 11b), and Tasman Glacier in Australia (Fig. 11c). The three were chosen, as their LSGL shapes let assume straightforward, medium-successful, and difficult outlining, respectively.

For all three LSGL, the NDVI, NDSI, NDWI, NDMI, and NDGI were computed with the routine. However, the NDGI does not reveal any particular information content, as cell value ranges do not vary a lot and the image appears almost monochrome with very little perforations. The NDGI is, therefore, not displayed in Figure 11a–c, but – strictly mathematically – its matrix is included and processed in the routine alongside the other four index matrices. For all three LSGL, a bonus (±Δb) of 0.01 was added to the landslide histograms (Fig. 10).

Although indexes carry specific names, they are not limited in use to distinct contexts. For in-

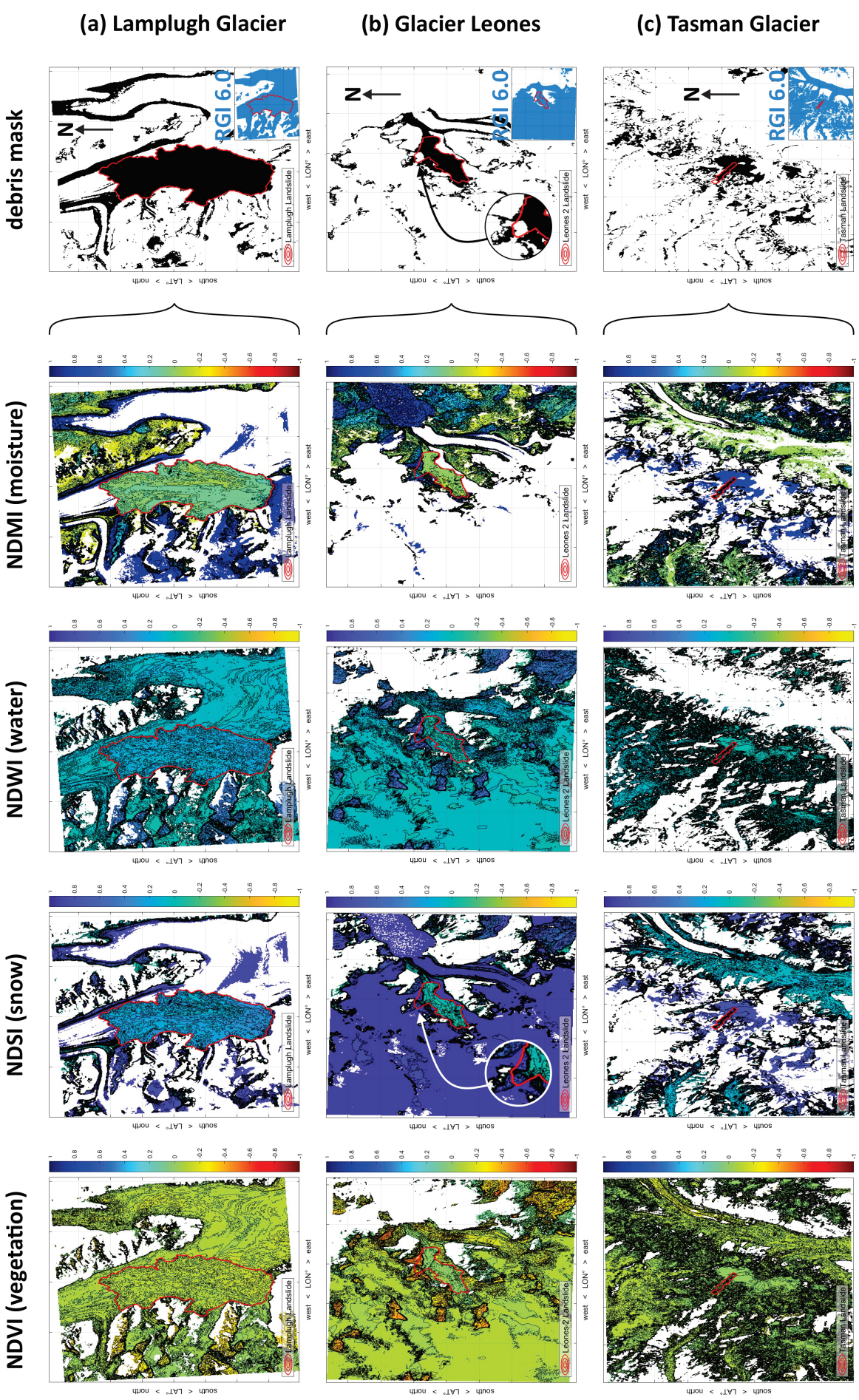

Fig. 11. Comparison of the NDVI, NDSI, NDWI, and NDMI for Lamplugh Glacier (**a**), Glacier Leones (**b**), and Tasman Glacier (**c**) and the resulting debris mask. The blue insert refers to the RGI 6.0 (RGI Consortium, 2017). Images are due north but vertically and horizontally distorted since computed and plotted in MATLAB®.

stance, the NDVI was initially developed for the discrimination between different degrees of plant health and density. Effectively, it is based on red light and NIR, from whose content conclusions can be drawn in different (e.g., glacial) environments. For the LSGL on Lamplugh Glacier, the perforated NDVI index matrix returns values around 0, which are caused by the fact that the glacier is humid compared to bare rock and open waters; in analogy, the NDWI index matrix shows a similar setting for the same reason. The index matrices of the NDSI and NDMI are likewise similar in terms of perforation due to their more pronounced sensitivity to moisture; however, the NDMI index matrix shows the best contrast between the LSGL and other surroundings. The RGI 6.0 does not significantly change the debris mask.

In addition to a similar interpretation of the setting around the two LSGL on Glacier Leones, the problem of accidental value inclusion within the LSGL polygon becomes apparent. When drawing the reference in ArcGIS® Pro, a northern corner was added to the first LSGL, which seemed to belong to it based on the RGB image. Particularly from the NDSI and NDMI index matrices, this looks, however, unlikely, and probably the additional northern corner is an artifact due to shadow effects. Also, the RGI 6.0 excludes this corner, as it is not part of a glaciated surface.

Tasman Glacier is located between cragged mountainous terrain, and rock avalanches and rockfalls are frequent and repeatedly associated with seismic activity. As the events are rather small in size compared to the LSGL on Lamplugh Glacier and Glacier Leones, it is already difficult to draw a meaningful reference polygon, which contributes to accidental value inclusion and subsequent difficulties at perforation and the creation of the debris mask.

In summary, the three examples show that by stacking index matrices, debris masks can be created, but their significance depends strongly on the correctness of the reference polygon; here, the impact of shadow and cloud effects are to be considered as well. In the course of the routine, the NDMI usually displays the strongest contrast in its index matrix, and after stacking, debris masks depict the LSGL and typical moraine structures well. The larger the LSGL and the more discriminative the surrounding environment is, the better is the routine performance; and the smaller and more cragged the terrain is, the less efficient is the debris mask as it produces too many false positives.

It is essential to keep in mind that the last column of Figure 11a–c with the coincidence of the reference polygon with the black LSGL shape cannot be seen as proof for a successful computation, as the reference polygon serves as input itself. Simply speaking, it is logical that it proves itself as LSGL. Considering, however, that the mask clearly identifies debris in the form of moraines in the immediate vicinity, it stands to reason that – at least within a certain periphery – the routine performs a correct scrutinization of debris and non-debris areas based on the spectral content of the five indexes.

In the next stage, the approach should be tested in wider areas and with a greater variety of LSGL. Moreover, the aspect of time series should be taken into account, as seasonality is a strong factor that could disturb the routine; particularly in glacial environments, snow cover can create false readings. Ideally, one or several LSGL in an area would be used as references, while some others should be (re-)identified with the debris mask according to typical shapes different from moraine deposits.

If the approach can be automated, the reference polygons could serve as learning sets for machine learning techniques in pattern and shape recognition and OBIA, offering a new strategy for mapping debris on glaciers and distinguishing LSGL from other debris covers. The latter would considerably contribute to the initial project question of whether – and if yes, how – LSGL influence glacier dynamics in terms of altered glacier responses (Fig. 3b).

Conclusion

Glacial environments are amongst the Earth's most affected by climate change. One of the many phenomena present in such environments are LSGL, which can evoke – under certain circumstances – an altered glacier response, i.e., glacial advances and/or surges, which in return can cause severe damage to life and infrastructure, as the most recent event at Blatten, Switzerland, has demonstrated in May 2025.

The causes for altered glacial responses after LSGL are the isolating effect of the debris cover protecting the underlying ice masses from melting and even benefiting ice accumulation and the increase of vertical load and lateral compression on the ice masses pushing them down-slope.

In order to apprehend the phenomenon, a comprehensive literature collection was established in three categories: LSGL cases, inventories, and detection. From those, statistics on contents of publications are presented, and drawing on the category

of LSGL detection, a strategy towards pattern and shape recognition based on index stacking is showcased. It turned out that from the NDVI, NDSI, NDWI, and NDMI a debris mask can be computed, that logically returns areas across glaciers that are covered by debris, from which patterns typical for moraines and LSGL can be distinguished. The approach is at its very initial stage, but – if developed further – it can lead to the development of machine learning techniques in pattern and shape recognition and OBIA, offering a new strategy for mapping debris on glaciers and distinguishing LSGL from other debris covers.

Funding

This work is part of the project "Global Assessment of Glacier-Landslide Interactions and Associated Geo-Hazards" (2021/42/E/ST10/00186), funded by the Polish National Science Center (NCN) and running from 2022–2027.

Data & code availability

The literature collection for this publication is available via the references given in Appendix 2. The code CataEx (Domej et al., 2025) was developed by G. D. during her post-doctoral assignment at Adam Mickiewicz University, Poznan, Poland, and can be downloaded free of charge from https://doi.org/10.5281/zenodo.8407940 (Domej et al., 2023).

References

Bessette-Kirton, E.K., Coe J.A., Zhou, W. 2018: Using Stereo Satellite Imagery to Account for Ablation, Entrainment, and Compaction in Volume Calculations for Rock Avalanches on Glaciers: Application to the 2016 Lamplugh Rock Avalanche in Glacier Bay National Park, Alaska. Journal of Geophysical Research: Earth Surface, 123/4: 622–641. https://doi.org/10.1002/2017jf004512

Björnsson, H. 1998. Hydrological characteristics of the drainage system beneath a surging glacier. Nature, 395, 6704: 771–774. https://doi.org/10.1038/27384

Bliss, A., Hock, R. & Radić, V. 2014: Global response of glacier runoff to twenty-first century climate change. Journal of Geophysical Research: Earth Surface, vol. 119/4: 717–730. https://doi.org/10.1002/2013jf002931

Böhm, R., Auer, I., Schöner, W., Hynek, B., Kroisleitner, C. & Weyss, G. 2007: Gletscher im Klimawandel - Vom Eis der Polargebiete zum Goldbergkees in den Hohen Tauern. Zentralanstalt für Meteorologie und Geodynamik, Wien: 116 p. (in German) https://austria-forum.org/web-books/gletscherimklim00de2007kfu

Bolch, T., Kulkarni A., Kaab, A., Huggel, C., Paul, F., Cogley, J.G., Frey, H., Kargel, J.S., Fujita, K., Scheel, M., Bajracharya, S. & Stoffel, M. 2012: The State and Fate of Himalayan Glaciers. Science, 336, 6079: 310–314. https://doi.org/10.1126/science.1215828

Bons, P.D., Kleiner, T., Llorens, M.G., Prior, D.J., Sachau, T., Weikusat, I. & Jansen, D. 2018: Greenland Ice Sheet: Higher Nonlinearity of Ice Flow Significantly Reduces Estimated Basal Motion. Geophysical Research Letters, 45/13: 6542–6548. https://doi.org/10.1029/2018gl078356

Bouchard, M. 2022: Landsat 9 Image of Kangerdlugssuaq Glacier, Greenland. USGS. https://www.usgs.gov/media/images/landsat-9-image-kangerdlugssuaq-glacier-greenland (accessed in June 2025)

Bull, C. & Marangunić, C. 1966: The Earthquake-Induced Slide on the Sherman Glacier, South-Central Alaska, and Its Glaciological Effects. Institute of Polar Studies, Ohio State University Publication, 108/395–408. https://eprints.lib.hokudai.ac.jp/dspace/bitstream/2115/20314/1/1_p395-408.pdf

Cruden, D.M., Varnes, D.J. 1996 : Landslide types and processes. In: Turner A.K. & Shuster R.L. (eds.): Landslides: Investigation and Mitigation. Transportation Research Board, Special Report, 247: 36–75. https://onlinepubs.trb.org/Onlinepubs/sr/sr247/sr247-003.pdf

Delaney, K.B. & Evans, S.G. 2014: The 1997 Mount Munday landslide (British Columbia) and the behaviour of rock avalanches on glacier surfaces. Landslides, 11/6: 1019–1036. https://doi.org/10.1007/s10346-013-0456-7

Deline, P. 2005: Change in surface debris cover on Mont Blanc massif glaciers after the"Little Ice Age" termination. The Holocene, 15/2: 302–309. https://doi.org/10.1191/0959683605hl809rr

Deline, P., Hewitt, K., Reznichenko, N. & Shugar, D. 2015: Rock Avalanches onto Glaciers. In: J.F. Shroder & Davies, T. (eds.): Landslide Hazards, Risks and Disasters: 263–319. https://doi.org/10.1016/b978-0-12-396452-6.00009-4

Domej, G. & Pluta, K. 2022–2024: JavaScrip and MATLAB code development for GERALDINE-GEEDiT communication, GEEDiT functionality upgrades, and preparation for OBIA integration concepts. Various unpublished reports.

Domej, G., Pluta, K. & Ewertowski, M. 2023: CataEx - Export Code for Google Earth Engine

(version 1.0). Zenodo. https://doi.org/10.5281/zenodo.8407940

Domej, G., Pluta, K. & Ewertowski, M. 2025: CataEx: a multi-task export tool for the Google Earth Engine data catalog. Environmental Modelling & Software, 183: 17 p. https://doi.org/10.1016/j.envsoft.2024.106227

Dozier, J. 1989: Spectral signature of alpine snow cover from the landsat thematic mapper. Remote Sensing of Environment, 28: 9–22. https://doi.org/10.1016/0034-4257(89)90101-6

Eisen, O., Harrison, W.D., Raymond, C.F., Echelmeyer, K.A., Bender, G.A. & Gorda, J.L.D. 2005; Variegated Glacier, Alaska, USA: a century of surges. Journal of Glaciology, 51/174: 399–406. https://doi.org/10.3189/172756505781829250

Ekström, G. & Stark, C.P. 2013: Simple Scaling of Catastrophic Landslide Dynamics. Science, 339/6126: 1416–1419. https://doi.org/10.1126/science.1232887

Evans, D.J.A., Ewertowski. M., Jamieson. S.S.R. & Orton, C. 2015: Surficial geology and geomorphology of the Kumtor Gold Mine, Kyrgyzstan: human impacts on mountain glacier landsystems. Journal of Maps, 12/5: 757–769. https://doi.org/10.1080/17445647.2015.1071720

Farinotti, D., Huss, M., Jacquemart, M., Werder, M., Knutti, R. & Seneviratne, S. 2025: Fact sheet for the now-collapsed Birchgletscher, Switzerland. ETH Zürich, 5 p. https://polybox.ethz.ch/index.php/s/eazXqWn8z6rPNwo

Fatland, D.R. & Lingle, C.S. 2002: InSAR observations of the 1993–95 Bering Glacier (Alaska, U.S.A.) surge and a surge hypothesis. Journal of Glaciology, 48/162: 439–451. https://doi.org/10.3189/172756502781831296

Fowler, A.C. 1987: A theory of glacier surges. Journal of Geophysical Research, 92/B9: 9111–9120. https://doi.org/10.1029/jb092ib09p09111

Gao, B.C. 1996: NDWI—A normalized difference water index for remote sensing of vegetation liquid water from space. Remote Sensing of Environment, 58/3: 257–266. https://doi.org/10.1016/s0034-4257(96)00067-3

Gorelick, N., Hancher, M., Dixon, M., Ilyushchenko, S., Thau, D. & Moore, R. 2017. Google Earth Engine: Planetary-scale geospatial analysis for everyone. Remote Sensing of Environment, 202: 18–27. https://doi.org/10.1016/j.rse.2017.06.031

Hagg, W. 2022. Glaciology and Glacial Geomorphology. Springer Berlin-Heidelberg, ed. 1, IX+186 p. https://doi.org/10.1007/978-3-662-64714-1

Harrison, W.D., Echelmeyer, K.A., Chacho, E.F., Raymond, C.F. & Benedict, R.J. 1994: The 1987–88 surge of West Fork Glacier, Susitna Basin, Alaska, U.S.A. Journal of Glaciology, 40/135: 241–254. https://doi.org/10.3189/s0022143000007334

Herreid, S. & Pellicciotti, F. 2020: The state of rock debris covering Earth's glaciers. Nature Geoscience, 13/9: 621–627. https://doi.org/10.1038/s41561-020-0615-0

Herreid, S., Pellicciotti, F., Ayala, A., Chesnokova, A., Kienholz, C., Shea, J. & Shrestha, A. 2015: Satellite observations show no net change in the percentage of supraglacial debris-covered area in northern Pakistan from 1977 to 2014. Journal of Glaciology, 61/227: 524–536. https://doi.org/10.3189/2015jog14j227

Huggett, R.J. 2011: Fundamentals of Geomorphology (Routledge Fundamentals of Physical Geography. Routledge, ed. 3: 536 p. https://sudartomas.wordpress.com/wp-content/uploads/2012/11/fundamentalsofgeomorphology_routledgefundamentalsofphysicalgeography.pdf

Hungr, O., Leroueil, S. & Picarelli, L. 2014: The Varnes classification of landslide types, an update. Landslides, 11: 167–194. https://doi.org/10.1007/s10346-013-0436-y

Hutchinson, J.N. 1968. Mass movement. In: Fairbridge R.W. (ed.): Encyclopedia of Geomorphology. Reinhold Publishers, 688–695.

Jamieson, S.S.R., Ewertowski, M.W. & Evans, D.J.A. 2015: Rapid advance of two mountain glaciers in response to mine-related debris loading. Journal of Geophysical Research: Earth Surface, 120/7: 1418–1435. https://doi.org/10.1002/2015jf003504

Kamb, B. 1987: Glacier surge mechanism based on linked cavity configuration of the basal water conduit system. Journal of Geophysical Research, 92/B9: 9083–9100. https://doi.org/10.1029/jb092ib09p09083

Kamb, B., Raymond, C.F., Harrison, W.D., Engelhardt, H., Echelmeyer, K.A., Humphrey, N., Brugman, M.M. & Pfeffer, T. 1985: Glacier Surge Mechanism: 1982–1983 Surge of Variegated Glacier, Alaska. Science, 22/, 4686: 469–479. https://doi.org/10.1126/science.227.4686.469

Kargel, J.S., Leonard, G.J., Bishop, M.P., Kääb, A. & Raup, B.H. 2014: Global Land Ice Measurements from Space. In: Kargel J.S., Leonard G.J., Bishop M.P., Kääb, A. & Raup, B.H.

(eds.). Springer Nature, ed. 1, p. LXXIX+876 p. https://doi.org/10.1007/978-3-540-79818-7

Keshri, A., Shukla, A. & Gupta, R.P. 2009: ASTER ratio indices for supraglacial terrain mapping. International Journal of Remote Sensing, 30/2: 519–524. https://doi.org/10.1080/01431160802385459

Kriegler, F.J., Malila, W.A., Nalepka, R.F. & Richardson, W. 1969: Preprocessing transformations and their effect on multispectral recognition. In: American Meteorological Society (ed.): Proceedings of the 6th International Symposium on Remote Sensing of Environment, 97–132.

Lea, J.M. 2018: The Google Earth Engine Digitisation Tool (GEEDiT) and the Margin change Quantification Tool (MaQiT) – simple tools for the rapid mapping and quantification of changing Earth surface margins. Earth Surface Dynamics, 6/3: 551–561. https://doi.org/10.5194/esurf-6-551-2018

Lingle, C.S. & Fatland, D.R. 2003: Does englacial water storage drive temperate glacier surges? Annals of Glaciology, 36/1: 14–20. https://doi.org/10.3189/172756403781816464

Martini, I.P., Brookfield, M.E. & Sadura, S. 2001: Principles of Glacial Geomorphology and Geology. Pearson College Division, ed. 1., 381 p.

McFeeters, S.K. 1996: The use of the Normalized Difference Water Index (NDWI) in the delineation of open water features. International Journal of Remote Sensing, 17/7: 1425–1432. https://doi.org/10.1080/01431169608948714

Mölg, N., Bolch, T., Rastner, P., Strozzi, T. & Paul, F. 2018: A consistent glacier inventory for Karakoram and Pamir derived from Landsat data: distribution of debris cover and mapping challenges. Earth System Science Data, 10/4: 1807–1827. https://doi.org/10.5194/essd-10-1807-2018

Murray, T. & Porter, P.R. 2001: Basal conditions beneath a soft-bedded polythermal surge-type glacier: Bakaninbreen, Svalbard. Quaternary International, 86/1: 103–116. https://doi.org/10.1016/s1040-6182(01)00053-2

Murray, T., Strozzi, T., Luckman, A., Jiskoot, H. & Christakos, P. 2003: Is there a single surge mechanism? Contrasts in dynamics between glacier surges in Svalbard and other regions. Journal of Geophysical Research: Solid Earth, 108(B5): 15 p. https://doi.org/10.1029/2002jb001906

NASA (National Aeronautics and Space Administration) visible earth, 2025: Randolph Glacier Inventory. NASA. https://visibleearth.nasa.gov/images/83826/randolph-glacier-inventory (accessed in June 2025)

NSDIC (National Snow and Ice Data Center), 2025: Glaciers. NSDIC. https://nsidc.org/learn/parts-cryosphere/glaciers/science-glaciers (accessed in June 2025)

Pfeffer, W.T., Arendt, A.A., Bliss, A., Bolch, T., Cogley, J.G., Gardner, A.S., Hagen, J.O., Hock, R., Kaser, G., Kienholz, C., Miles, E.S., Moholdt, G., Mölg, N., Paul, F., Radić, V., Rastner, P., Raup, B.H., Rich, J. & Sharp, M.J. 2014: The Randolph Glacier Inventory: a globally complete inventory of glaciers. Journal of Glaciology, 60/21: 537–552. https://doi.org/10.3189/2014jog13j176

Rabatel, A., Francou, B., Soruco, A., Gomez, J., Cáceres, B., Ceballos, J.L., Basantes, R., Vuille, M., Sicart, J.E., Huggel, C., Scheel, M., Lejeune, Y., Arnaud, Y., Collet, M., Condom, T., Consoli, G., Favier, V., Jomelli, V., Galarraga, R. & Ginot, P. 2013: Current state of glaciers in the tropical Andes: a multi-century perspective on glacier evolution and climate change. The Cryosphere, 7/1: 81–102. https://doi.org/10.5194/tc-7-81-2013

Raymond, C.F. 1987: How do glaciers surge? A review. Journal of Geophysical Research, 92(B9): 9121–9134. https://doi.org/10.1029/jb092ib09p09121

Reznichenko, N.V., Davies, T.R.H. & Alexander, D.J. 2011: Effects of rock avalanches on glacier behaviour and moraine formation. Geomorphology, 132/3–4: 327–338. https://doi.org/10.1016/j.geomorph.2011.05.019

Reznichenko, N., Davies, T., Shulmeister, J. & McSaveney, M. 2010: Effects of debris on ice-surface melting rates: an experimental study. Journal of Glaciology, 56/197: 384–394. https://doi.org/10.3189/002214310792447725

RGI 7.0 Consortium, 2023: Randolph Glacier Inventory - A Dataset of Global Glacier Outlines, Version 7.0. NSDIC. https://doi.org/10.5067/f6jmovy5navz

RGI Consortium, 2017: Randolph Glacier Inventory - A Dataset of Global Glacier Outlines, Version 6. NSDIC. https://doi.org/10.7265/4m1f-gd79

Scherler, D., Wulf, H. & Gorelick, N. 2018a: Global Assessment of Supraglacial Debris-Cover Extents. Geophysical Research Letters, 45/21: 11798–11805. https://doi.org/10.1029/2018gl080158

Scherler, D., Wulf, H. & Gorelick, N. 2018b: Supraglacial Debris Cover. v.1.0. GFZ Data Services. https://doi.org/10.5880/GFZ.3.3.2018.005

Shannon, S., Smith, R., Wiltshire, A., Payne, T., Huss, M., Betts, R., Caesar, J., Koutroulis, A., Jones, D. & Harrison, S. 2019: Global glacier volume projections under high-end climate change scenarios. The Cryosphere, 13/1: 325–350. https://doi.org/10.5194/tc-13-325-2019

Shugar, D.H., Rabus, B.T., Clague, J.J. & Capps, D.M. 2012: The response of Black Rapids Glacier, Alaska, to the Denali earthquake rock avalanches. Journal of Geophysical Research: Earth Surface, 117/F1: 14 p. https://doi.org/10.1029/2011jf002011

Smith, W.D., Dunning, S.A., Brough, S., Ross, N. & Telling, J. 2020: GERALDINE (Google Earth Engine supRaglAciaL Debris INput dEtector): a new tool for identifying and monitoring supraglacial landslide inputs. Earth Surface Dynamics, 8/4: 1053–1065. https://doi.org/10.5194/esurf-8-1053-2020

Sorg, A., Bolch, T., Stoffel, M., Solomina, O. & Beniston, M. 2012: Climate change impacts on glaciers and runoff in Tien Shan (Central Asia). Nature Climate Change, 2/10: 725–731. https://doi.org/10.1038/nclimate1592

USGS (United States Geological Survey), 2004: Landslide Types and Processes. USGS Fact Sheet, no. 2004-3072(-), 4 p. https://pubs.usgs.gov/fs/2004/3072/

Vacco D.A., Alley R.B. & Pollard D. 2010: Glacial advance and stagnation caused by rock avalanches. Earth and Planetary Science Letters, 294/1–2: 123–130. https://doi.org/10.1016/j.epsl.2010.03.019

Varnes, D.J. 1978: Slope Movement Types and Processes. In: Schuster, R.L. & Krizek, R.J. (eds.): Landslides, Analysis and Control. Transportation Research Board, Special Report, 176: 11–33.

WGMS (World Glacier Monitoring Service), 1989: World Glacier Inventory, status 1988 (p. 459). IAHS/UNEP/UNESCO. https://wgms.ch/downloads/wgi_1988_small.pdf

Zemp, M., Gärtner-Roer, I., Nussbaumer, S. U., Bannwart, J., Rastner, P., Paul, F. & Hoelzle, M. 2020: Global Glacier Change Bulletin, 3 (2016–2017). WGMS, 3: 289. https://wgms.ch/downloads/WGMS_GGCB_03.pdf

APPENDIX

Appendix 1

Year	Author(s)	Target area	Debris type	Indexes (mentioned)	Image type	Mapping approach	Method(s)
2023	**Ganerød** et al.	Norway	LS	NDVI	SP & RAD	LM	CCDC, CNN, U-Net
2023	**Khan** et al.	Pakistan	D	NDVI, NDWI	SP	LM	CNN, RF, SVM
2023	**Panwar & Singh**[G:D:S]	Himalayas	D		RAD	LM	DNN, SVM
2023	**Peng** et al.	China	D	NDVI, NDSI, NDWI	SP	LM	LGT & LGCB
2023	**Sharma** et al.	Himalayas	D	NDVI, NDWI, [...]	RAD	assisted	
2022	**Barella** et al.	Alps	D		SP & RAD	LM	SVM
2022	**Hu** et al.	Tibet	D	snow, cloud	SP	LM	RF
2022	**Kaushik** et al.	Himalayas, Karakoram	D		SP	LM	ANN
2022	**Lin** et al.	China	D	NDSI	SP	LM	ANN, CNN, OBIA, [...]
2022	**Lindsay** et al.	Norway	LS	NDVI	SP & RAD	assisted	
2022	**Lu** et al.	Tibet	D	NDVI, NDSI, NDWI	SP & RAD	LM	RF
2022	**Mitkari** et al.	Himalayas	D	NDWI, [...]	SP	LM	OBIA
2022	**Sharda** et al.	Karakoram	D	NDSI	SP	LM	[...]
2022	**Shukla** et al.	Himalayas	D	NDSI	SP	mapping	
2022	**Sood** et al.[G:D:S]	Himalayas	D	NDSI	SP	LM	ANN, U-Net
2022	**Tian** et al.	Pamir	D		SP	LM	U-Net
2022	**Xie** et al. (a & b)	Himalayas, Karakoram	D	NDVI, water	SP	LM	CNN
2022	**Yao** et al.	Tibet	D		RAD	LM	SVM, [...]
2021	**Holobâcă** et al.[G:D:nG]	Georgia	D	NDVI, NDSI	SP & RAD	assisted	
2021	**Xie** et al.	Karakoram	D	7 different	SP	LM	CNN, U-Net
2021	**Yan** et al.	Tibet	D	NDSI	SP	LM	U-Net
2020	**Alifu** et al.	Pakistan, China	D		SP & RAD	LM	RF, SVM, [...]
2020	**Barella** et al.	Italy, Austria	n. d.	snow, cloud	SP & RAD	LM	SVM
2020	**Khan** et al.	Pakistan	D	NDVI, NDSI, NDWI, [...]	SP	LM	ANN, RF, SVM
2020	**Lu** et al.	Pamir	D	NDVI, NDSI, NDWI	SP	LM	RF
2020	**Xie** et al.	Karakoram	D	NDWI, [...]	SP	LM	CNN
2019	**Yan** et al.	Tibet	D		SP	LM	U-Net
2019	**Zhang** et al.	Tibet	D	NDVI, NDSI, NDWI	SP	LM	RF
2018	**Azzoni** et al.	Italy	D		SP & UAV	mapping	

2018	**Lippl** et al.	Karakoram	D		SP & RAD	assisted	
2018	**Mölg** et al.	Karakoram, Pamir	D		SP & RAD	mapping	
2018	**Nijhawan** et al.	Himalayas	D		SP	LM	CNN, RF
2018	**Sahu & Gupta**	global	D		SP	LM	OBIA
2018	**Winsvold** et al.	Norway, Svalbard	n. d.		SP & RAD	mapping	
2018	**Xie** et al.	Himalayas, Karakoram	D		SP	LM	CNN
2017	**Huang** et al.	Tianshan	D		SP & RAD	mapping	
2016	**Kraajenbrink** et al.	Nepal	D	NDWI, blue index	UAV	LM	OBIA
2015	**Alifu** et al.	China	D	NDSI	SP	mapping	
2015	**Khan** et al.[G:D:S]	Himalayas, Karakoram, Hindukush	D	NDSI	SP	mapping	
2015	**Robson** et al.[G:D]	Nepal	LS	NDVI, NDSI, NDWI, [...]	SP & RAD	LM	OBIA
2015	**Smith** et al.[G:D]	Central Asia	D	NDSI	SP	assisted	
2014	**Gosh** et al.	Himalayas	D	NDSI	SP	mapping	
2014	**Huang** et al.	Tienshan	D		SP & RAD	mapping	
2012	**Karimi** et al.	Iran	D		SP	mapping	
2012	**Racoviteanu & Williams**	Himalayas	D	NDVI, NDSI	SP	mapping	
2011	**Bhambri** et al.	Himalayas	D		SP	mapping	
2011	**Jiang** et al.	China	D		RAD	mapping	
2010	**Atwood** et al.	Alaska/USA	D		RAD	mapping	
2010	**Lu** et al.	Pamir	D	NDVI, NDSI, NDWI	SP	LM	CNN, RF
2010	**Shukla** et al. (a & b)	Himalayas, Kashmir	D		SP	mapping	
2009	**Keshri** et al.[I:S:D:M]	Himalayas	D	NDSI, NDGI, NDSII	SP	mapping	
2009	**Ranzi** et al.	Italy	D	NDVI	SP	mapping	
2009	**Shukla** et al.	Himalayas, Kashmir	D		SP	mapping	
2008	**Mihalcea** et al.	Italy	D		SP	mapping	
2007	**Bolch** et al.	Everest	D		SP	assisted	
2007	**Buchroithner & Bolch**	Everest	D		SP	assisted	
2007	**Suzuki** et al.	Everest, Bhutan	D	thermal resistance	SP	mapping	
2006	**Bolch & Kamp**	Tianshan, Alps	D	NDVI	SP	mapping	
2005	**Bolch** et al.	Himalayas, Andes	D		SP	mapping	
2004	**Paul** et al.	Switzerland	D	NDVI	SP	LM	ANN
2002	**Taschner & Ranzi**	Italy	D	NDVI	SP	mapping	

Table A1: Publications related to LSGL detection (#63). References are listed in Appendix 2.

Abbreviations:

LS	–	landslides explicitly
D	–	debris
SP	–	spectral imagery
RAD	–	radar imagery
UAV	–	unmanned aerial vehicle (i.e., drones)
mapping	–	traditional mapping
assisted	–	assisted mapping
LM	–	learning method (i.e., any of machine learning)
[...]	–	other elements
ANN	–	artificial neural network
CCDC	–	continuous change detection and classification
CNN	–	convolutional neural network
DNN	–	deep neural network
LGCB	–	local global GNN (graph neural network) blocks
LGT	–	local global transformer
OBIA	–	object-based image analysis
RF	–	random forest
SVM	–	support vector machine
U-Net	–	U-shaped CNN (convolutional neural network)

Footnotes on distinction algorithms:

G:D:S	–	mapping of glacier vs. debris vs. snow
G:D:nG	–	mapping of glacier vs. debris vs. no glacier
G:D	–	mapping of glacier vs. snow
I:S:D:M	–	mapping of ice vs. snow vs. debris vs. ice-debris-mix

Appendix 2

Appendix 2 is a separate document and can be downloaded as PDF.

GEOLOGIJA 68/2, 243-250, Ljubljana 2025

https://doi.org/10.5474/geologija.2025.010

Article

Transmission electron microscopy analysis of shock veins in the meteorite Jesenice

Presevna elektronska mikroskopija udarnih žil v meteoritu Jesenice

Bojan AMBROŽIČ[1], Sašo ŠTURM[2,3] & Mirijam VRABEC[3]*

[1]Center of Excellence on Nanoscience and Nanotechnology – Nanocenter, Jamova c. 39, SI-1000 Ljubljana, Slovenia; e-mail: bojan.ambrozic@nanocenter.si
[2]Jožef Stefan Institute, Jamova c. 39, SI-1000 Ljubljana, Slovenia; e-mail: saso.sturm@ijs.si
[3]*Faculty for Natural Sciences and Engineering, Department for Geology, Aškerčeva cesta 12, SI-1000 Ljubljana, Slovenia; *corresponding author: mirijam.vrabec@ntf.uni-lj.si

Prejeto / Received 27. 8. 2021; Sprejeto / Accepted 9. 10. 2025; Objavljeno na spletu / Published online 10. 12. 2025

Key words: chondrite, shock stage, shock veins, metal-sulfide globules, tetrataenite, transmission electron microscopy
Ključne besede: hondrit, udarna metamorfoza, udarne žile, kovinsko-sulfidne globule, tetrataenit, presevna elektronska mikroskopija

Abstract

Meteorite Jesenice is a weakly (S3) shocked ordinary chondrite from Slovenia. The shock event was violent enough to cause localized partial melting of the meteorite and the formation of shock veins. Inside the shock veins, metal-sulfide globules were found, which provided evidence for a post-shock cooling rate of $2.2{\cdot}10^5$ Ks^{-1} – $7.4{\cdot}10^3$ Ks^{-1}. From the mineral paragenesis of the shock veins, shock pressure and peak shock temperature were deduced as 2.5–15 GPa and 1500–2150 °C, respectively. We provide evidence that shock veins were formed via a shear and friction mechanism. Furthermore, the confirmed presence of ordered FeNi metal (tetrataenite) found in the matrix indicates that the shock occurred in the parent body of the meteorite Jesenice.

Izvleček

Meteorit Jesenice je šibko udarno metamorfoziran (S3) navadni hondrit iz Slovenije. Udarni dogodek je bil dovolj silovit, da je povzročil delno taljenje meteorita in s tem nastanek udarnih žil. V udarnih žilah so bile najdene kovinsko-sulfidne globule, s katerimi smo določili hitrost ohlajanja na $2.2{\cdot}10^5$ K s^{-1} – $7.4{\cdot}10^3$ K s^{-1}. Iz mineralne združbe udarnih žil smo določili najvišji udarni tlak in najvišjo temperature na 2.5–15 GPa oz. 1500–2150 °C. Sklepamo, da je do nastanka žil prišlo z mehanizmom strižnega trenja. V meteoritu smo potrdili tudi obstoj minerala tetrataenita, kar nakazuje, da je do dogodka udarne metamorfoze prišlo znotraj starševskega telesa meteorita Jesenice.

Introduction

Meteorite Jesenice fell on April 9, 2009 on the Mežakla Plateau near the town of Jesenice as a spectacular fireball, frightening the residents (Bischoff et al., 2011). Three stones with a total mass of 3.67 kg were later recovered. Analyses carried out by Bischoff et al. (2011) showed that it is a weakly shocked ordinary (L6 S3) chondrite. The shock stage of the meteorite is a fundamental property because it reflects the intensity of impact processes that shaped the meteorite's parent body and provides essential information on solar system collisional evolution (Stoffler et al., 1992). There are several studies on shock veins and the effects of local melting in moderately and strongly shocked chondrites (Acosta-Maeda et al., 2013; Guo et al., 2020; Kong & Xie, 2003). However, local melting in weakly shocked chondrites has been poorly studied (Owocki & Muszyński, 2012; Xie et al., 2006). In the following paper, we study in detail the shock veins and the ordered FeNi phase (tetrataenite) in order to better understand the conditions of shock metamorphism in the weakly shocked meteorite Jesenice, specifically the mechanism of shock vein formation and the subsequent thermal history recorded by the preservation of tetrataenite.

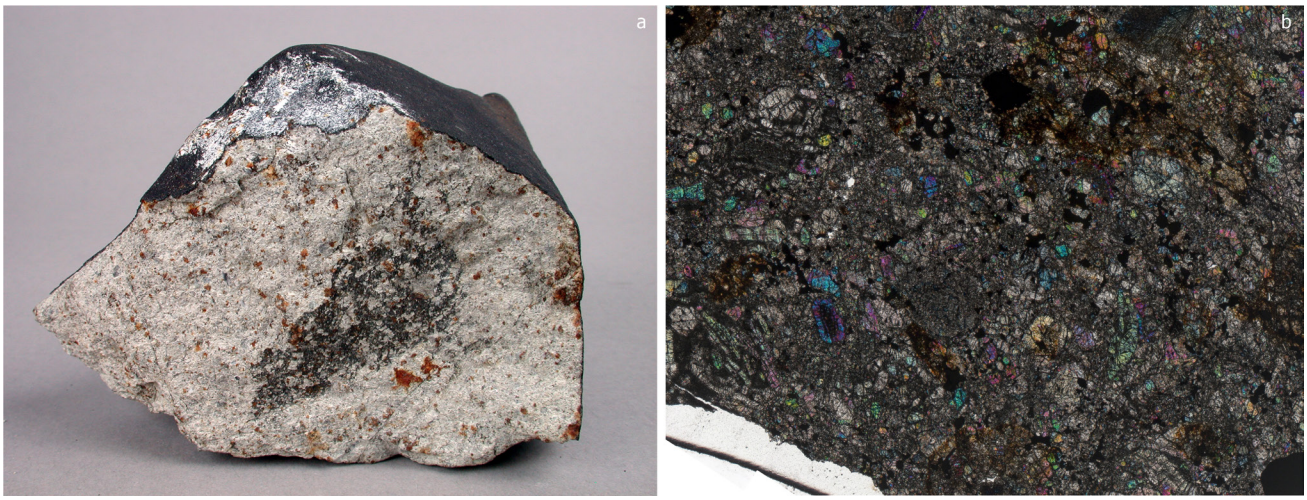

Fig. 1. Meteorite Jesenice, which fell on 9 April 2009 on the Mežakla Plateau: (a) hand specimen (photo: Miha Jeršek), and (b) polished thin section 1M.

Experimental section

Sample preparation

Polished thin sections, 30 μm thick, were prepared from the meteorite Jesenice (Fig. 1). For scanning electron microscope observations, the sections were coated with a 3 nm layer of amorphous carbon to ensure electrical conductivity.

Analytical methods

Polished thin sections were examined with a Zeiss Axio Z1-m optical microscope (Jožef Stefan Institute, Ljubljana) in transmitted and reflected light under crossed and parallel polarizers at magnifications 100–1000×.

Scanning electron microscopy (SEM) imaging was performed using JEOL JSM-5800, JEOL JSM-7600F, FEI Helios NanoLab 650, JEOL JIB-4601F, and JEOL JSM-840 at facilities in Slovenia (Jožef Stefan Institute, Nanocenter), Turkey (Sabanci University Nanotechnology Center), and Slovakia (SGIDS, Bratislava). Images were collected using backscattered electrons (BSE), secondary electrons (SE), scanning transmission electron microscopy (STEM), and secondary ion imaging (SI), with accelerating voltages of 0.2–30 kV. The maximum spatial resolution of the Helios NanoLab 650 was 1.1 nm at 15 kV.

Quantitative EDS microanalyses were performed on a JEOL JSM-5800 SEM at 20 kV. Spectra were acquired for 100 s at a detector dead time of 25–30 % and quantified using mineral standards recalculated to oxides. Calibration was regularly checked against a cobalt standard.

WDS analyses were conducted with a CAMECA SX-100 electron microprobe and a JEOL JSM-840 SEM (SGIDS, Bratislava) at 15 kV, 20 nA. Spot analyses determined the chemistry of olivine, pyroxenes, plagioclase, apatite, kamacite, taenite, chromite, and troilite in the meteorite Jesenice. Elements analyzed included F, Na, Si, Al, Mg, Cl, K, Ca, Ti, Fe, Mn, Cr, Ni, and P, along with trace elements in apatite (Y, U, Sr, Ba, REEs, Th, Zn, and V). Calibration standards included LiF (F), albite (Na), orthoclase and wollastonite (Si), orthoclase (K), $Al2O_3$ (Al), NaCl (Cl), wollastonite (Ca), TiO_2 (Ti), fayalite (Fe), rhodonite (Mn), forsterite and MgO (Mg), metallic Cr (Cr), metallic Ni (Ni), apatite (P), UO_2 (U), barite (Ba, S), $CePO_4$ (Ce), $LaPO_4$(La), $NdPO_4$ (Nd), $SmPO_4$ (Sm), $EuPO_4$ (Eu), $GdPO_4$ (Gd), $TbPO_4$ (Tb), $DyPO_4$ (Dy), $HoPO_4$(Ho), $ErPO_4$ (Er), $TmPO_4$ (Tm), $YbPO_4$ (Yb), ThO_2 (Th), willemite (Zn), and metallic V (V).

TEM analyses were carried out with JEOL JEM-2010F, JEM-ARM200F, and JEM-2100 instruments at 200 kV. TEM foils were prepared from selected regions of the meteorite Jesenice. Techniques included high-resolution TEM (HR-TEM), selected area electron diffraction (SAED), STEM, EDS, and bright-/dark-field imaging. The highest resolution (JEM-ARM200F, Sabanci University) was 0.08 nm. SAED patterns were indexed against the Inorganic Crystal Structure Database (ICSD).

Results

Petrography and mineral chemistry of shock veins

Optical analysis revealed the presence of 1–2 shock veins per thin section, each measuring approximately 5 × 10 mm. The shock veins in meteorite Jesenice are up to 1500 μm long and up to 30 μm thick (Fig. 2a). The distribution of the phases present in the shock veins is heterogeneous. Shock veins consist of metallic taenite (FeNi)/troilite (FeS) globules, nanocrystalline silicate melt,

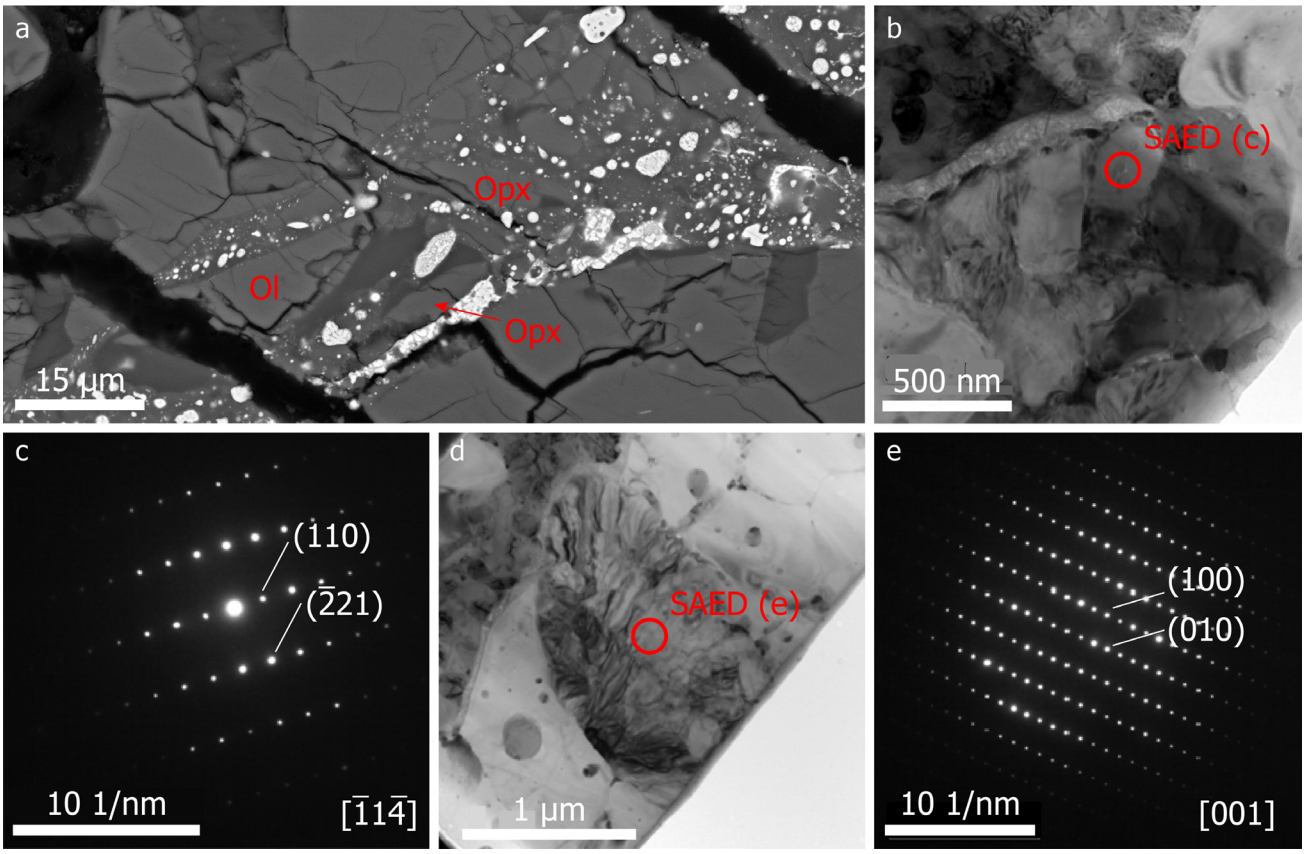

Fig. 2. Silicates in shock vein: (a) SEM image of a shock vein with marked silicate fragments (Opx – orthopyroxene, Ol – olivine); (b) TEM image of Opx; (c) SAED pattern of Opx; (d) TEM image of an olivine grain with a large number of dislocations; (e) SAED pattern of olivine.

and large fragments of silicate minerals. Metallic globules, together with the silicate melt occupy a thicker central part of the shock veins.

Fragments of silicate minerals in shock veins are mostly grains of olivine and orthopyroxene (Fig. 2b,c), with grain diameters ranging from 5 to 30 µm. The analyzed olivines are very homogeneous and predominantly forsteritic (Fo_{74-75}) (Table 1). Orthopyroxenes have enstatite compositions, with X_{Ca} = 0.01, X_{Mg} = 0.77, and X_{Fe} = 0.21. Transmission electron microscopy analysis of the olivine grains showed the presence of a large concentration of dislocations (Fig. 2d,e). However, the simultaneous shock and shear were sufficient to cause these grains to be pulled out of their original position and moved (possibly a few tens of microns to a few millimeters) along the shock vein.

Around large silicate grains, smaller metal-sulfide globules and submicrometer- to nanocrystalline silicate grains were found. Smaller metal-sulfide globules are usually scattered around these grains. Submicrometer-sized silicate grains are usually orthopyroxene, which acts as cement. The size of these grains ranges from 0.5–1 µm. Between the orthopyroxene grains, a cluster of 50 nm rounded olivine grains was observed. Round troilite blebs of 10–500 nm in size (similar to metallic globules) are also present (Fig. 2a).

Globules

Many different types of FeNi/FeS globules occur in the meteorite Jesenice (Fig. 3), which occupy about 50 vol.% of the shock veins. SEM analyses revealed the presence of four different types of FeNi/FeS globules (Fig. 3). The first type is globules of FeNi/FeS intergrowth (Fig. 3b), which are the largest type of globules that were found in the shock veins of the meteorite Jesenice. They occur in two different sizes: 3–15 µm and 100–200 nm. These globules form an almost perfect spherical shape. Some globules are elongated, possibly in the direction of flow (Fig. 3e–f). Secondary dendrites, reported in many other different chondrites (Scott, 1982), are not present. The average width of dendritic elongated FeNi cells is 0.1–1 µm. The second type are globules with dendritic/cellular structure (Fig. 3c), which are rare in this meteorite. The third type are irregular globules (Fig. 3d), which are common and can be up to several 10 µm in size. They have a similar internal composition to other types of globules but differ in their irregular shape, which merges with the silicate matrix of the shock vein. The fourth type is deformed globules (Fig. 3e), which were deformed by the shock process and indicate the direction of the melt flow.

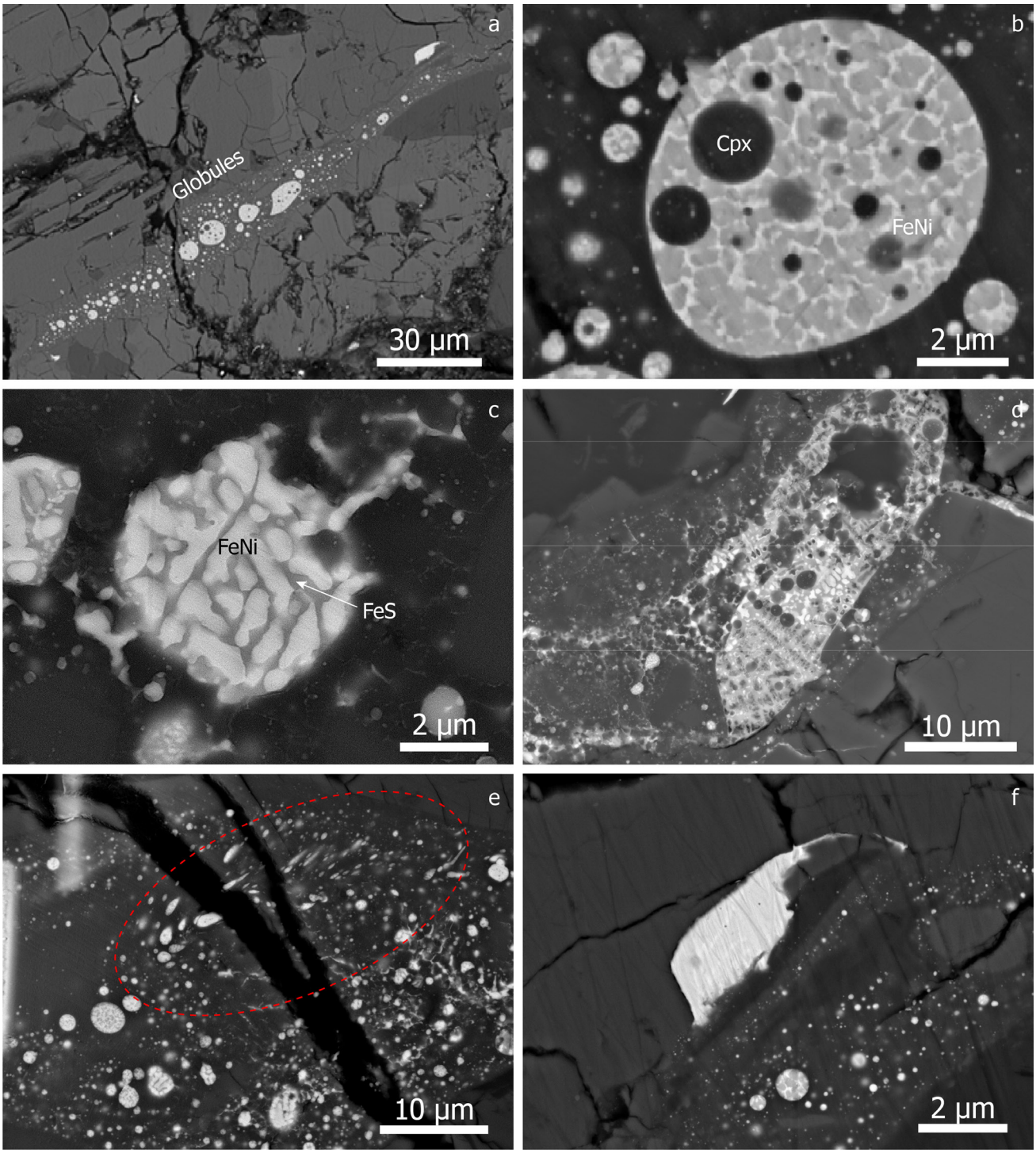

Fig. 3. SEM images of globules in shock veins in the meteorite Jesenice: (a) shock vein in the meteorite with globules; (b) globules of FeNi/FeS intergrowth; (c) globules with dendritic/cellular structure; (d) irregular globules; (e) elongated, oval-shaped globule (delineated by a dashed line); (f) heavily deformed FeNi mineral at the edge of the shock vein.

Globules of FeNi/FeS intergrowth were studied in detail with high-angle annular dark-field (HAADF) scanning transmission electron microscopy (STEM) analysis, which revealed a complex internal structure (Fig. 4). The main part of the globule consists of the eutectic intergrowth of FeNi/FeS minerals (Fig. 4a–c). Selected area electron diffraction (SAED) analysis revealed that all minerals occur in the same crystallographic orientation. Within the main globule many smaller, 1–2 µm sized, spherical subglobules occur (Fig. 4a). EDS analysis (Fig. 4d–f) showed that they consist of clinopyroxene with diopsidic composition (X_{Ca} = 0.45, X_{Mg} = 0.47, and X_{Fe} = 0.08), completely different from the orthopyroxenes found outside the shock veins in the host rock. Within the pyroxene subglobules, many smaller (10–200 nm) troilite blebs with the same crystallographic orientation are found. The main globule is surrounded by a 50–100 nm thick rim (Fig. 4g),

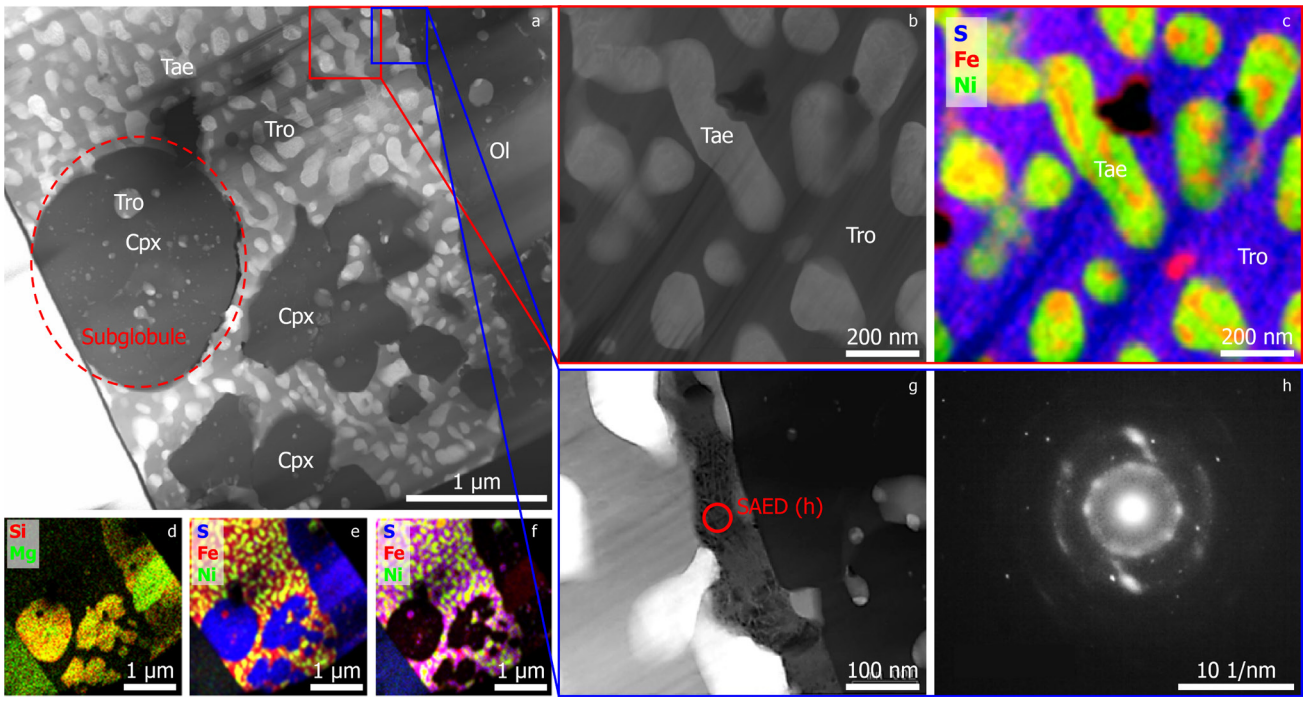

Fig. 4. STEM analysis of structures inside of FeNi/FeS globule: (a) HAADF-STEM image of a cross-section of the globule (Tae – taenite, Tro – troilite, Ol – olivine, Cpx – clinopyroxene); (b) detail of taenite/troilite intergrowth; (c) EDS map of taenite/troilite intergrowth; (d–f) EDS maps of a FeNi/FeS globule; (g) detail of globule rim; (h) SAED pattern of globule rim marked on figure g.

which consists of partially crystallized grains of clinopyroxene, as indicated in the corresponding SAED pattern (Fig. 4h).

The cooling rate of FeNi/FeS globules

To estimate cooling rates based on solid-state dendritic microstructures in the metallic phase for pre-shock or parent-body cooling, we used an equation proposed by (Scott, 1982):

$$R = 5.3\ 10^{5} d^{-2.9}$$

where R is cooling rate in Ks^{-1} and d is diameter of the dendrites (or in our case the width of the elongated cells in micrometers, as noted by (Blau & Goldstein, 1975), we estimated the cooling rate at $5.3 \cdot 10^{5}$ Ks^{-1} – $4.2 \cdot 10^{8}$ Ks^{-1}.

From the size of the globules observed in the meteorite Jesenice we have estimated the post-shock cooling rate, using the equation for a crystallizing melt sphere (Tsuchiyama et al., 1980):

$$R = \frac{3\varepsilon\sigma}{rp\left(C_p + \frac{\Delta H_c}{\Delta T_c}\right)}\left(T^4 - T_a^4\right)$$

where R is cooling rate (Ks^{-1}), σ is Stefan-Boltzmann constant (5.704×10^{-12} $Jcm^{-2}s^{-1}K^{-1}$), ε is emissivity, C_p is specific heat ($Jg^{-1}K^{-1}$), ΔH_c is enthalpy of crystallization (Jg^{-1}), ΔT_c is temperature interval of crystallization (K), T_a is ambient temperature (K), ρ = density (gcm^{-3}), and r is radius of the sphere (in this case FeNi/FeS globules) (cm).

We have used the following parameters, which have been adopted from (D'orazio et al., 2009): ε = 0.28 (emissivity of molten iron), C_p = 0.66 $Jg^{-1}K^{-1}$ (average Cp for FeS and FeNi at 1400 K), ΔH_c = 298 Jg^{-1} (average ΔHc for FeS and FeNi at 1400 K), (cooling from 1623 K to 1223 K), T_a = 200 K, ρ = 6.12 gcm^{-3} and r_1 = 0.5 µm in r_2 = 15 µm (minimum and maximum diameter of globules present in the meteorite Jesenice). The calculations show a cooling rate of $2.2 \cdot 10^{5}$ Ks^{-1} – $7.4 \cdot 10^{3}$ Ks^{-1}.

Discussion

The presence of shock veins filled with FeNi/FeS metal-troilite intergrowth grains indicate that shock veins formed by shock-induced melting followed by rapid quenching. Rounded olivine grains, together with a high frequency of dislocations, indicate that the olivine was severely damaged during the shock. For this reason, we have considered the melting temperature of olivine at a given shock pressure as the highest possible temperature during shock metamorphism. On the other hand, the chemical composition of clinopyroxenes in melt veins and the host rock is significantly different, implying the crystallization of clinopyroxenes in veins from the melt during shock metamorphism. Therefore, we propose the crystallization temperature of pyroxene as the lowest possible temperature during shock metamorphism. TEM analyses have shown that FeNi/FeS minerals and clinopyroxene present in globules crystallized from melt and

olivine did not melt during shock. This indicates that the peak temperature of shock metamorphism is 1500–2150 °C (Gasparik, 2014). Clinopyroxenes in globules are enriched with FeO compared to clinopyroxenes in the matrix and chondrules, which implies oxidation of the meteorite Jesenice parent body during the impact (Chen et al., 2002). The presence of olivine and Ca-pyroxene and the absence of plagioclase in the shock veins indicate shock pressures of 2.5–15 GPa (Agee et al., 1995). This is in agreement with the previously reported (Bischoff et al., 2011) classification of the meteorite Jesenice as an S3 chondrite. Our calculations showed a rapid after-shock cooling rate of $2.2{\cdot}10^{5}$ Ks^{-1} – $7.4{\cdot}103$ Ks^{-1}.

Our study showed that taenite in the globules is not surrounded by kamacite, which has been frequently reported in similar systems (Scott, 1982). This can be explained by the still ongoing thermal metamorphosis inside the meteorite Jesenice's parent body (Scott, 1982) after the shock metamorphic event had occurred for a limited time. The absence of kamacite around taenite in the globules is most readily explained if parent-body thermal metamorphism continued after the shock event; this scenario would imply that the impact preceded a period of longer-duration heating, although additional chronological or thermal-history data are required to confirm this sequence. Troilite inclusions in silicates in globules indicate exsolution of troilite during the shock. FeNi/FeS globules are a consequence of the immiscibility of metal-sulfide melt and silicate melt (Chen et al., 2002).

The oval shape of some globules could indicate the shear direction and that melting by a shear-friction mechanism, as noted by Xie et al. (2011), is the main reason for the formation of shock veins in the meteorite Jesenice and that crystallization took place during the shock.

We identified an ordered FeNi phase (tetrataenite) in the meteorite matrix (Fig. 5) with an approximately stoichiometric composition of 50 at.% Ni and 50 at.% Fe. The chemical composition of tetrataenite typically ranges from 46 to 56 at.% Ni (Clarke & Scott, 1980), in agreement with the values observed in the meteorite Jesenice (42–50 at.% Ni). The presence of tetrataenite in the matrix indicates that this ordered FeNi phase most likely formed after the shock event, under low-temperature and slow-cooling conditions, and was therefore not affected by shock. Together with the absence of kamacite in FeNi globules—which suggests that thermal metamorphism continued after the shock but before disruption of the parent body—the occurrence of tetrataenite further supports the interpretation that extended parent-body metamorphism followed the shock event. Our analyses indicate that the meteorite Jesenice cooled from the peak temperature of thermal metamorphism at a slow cooling rate of 1–100 K/Ma. The presence of tetrataenite supports this interpretation, as it is known to form only in slow-cooled meteorites (Clarke & Scott, 1980), further implying that meteorite Jesenice originated deep within its parent body (Wittmann et al., 2010). To constrain its thermal history, we applied two complementary approaches, each addressing different processes. First, we estimated cooling rates from the solid-state FeNi dendritic microstructures in the metallic phase (Scott, 1982), reflecting the long-term cooling within the parent body prior to any shock events. This provides insight into the slow thermal evolution in a deep, insulated environment. Second, we estimated the cooling rates of FeNi/FeS globules formed during the shock event, accounting for heat loss from individual molten globules, their size, latent heat of crystallization, and radiative cooling (Tsuchiyama et al., 1980).

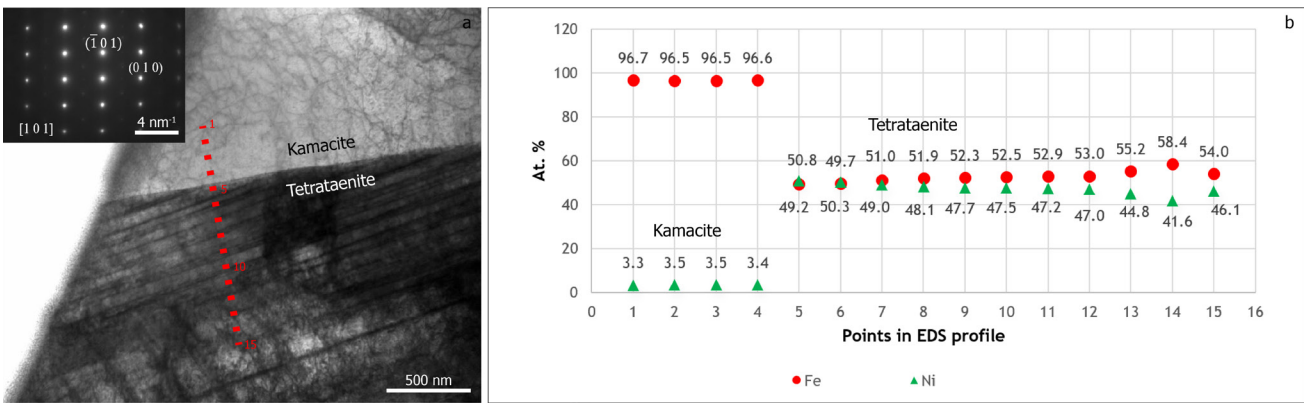

Fig. 5. TEM analysis of tetrataenite in meteorite Jesenice: (a) STEM image of kamacite – tetrataenite grain boundary with SAED pattern of tetrataenite in [1 0 1] (ICSD = 103556); (b) EDS profile of kamacite – tetrataenite grain boundary. The chemical composition of tetrataenite varies between 42 and 50 at.% of Ni.

This yields a realistic estimate of post-shock melt solidification, which occurs over a much shorter timescale than parent-body cooling. Together, these methods allow us to distinguish between slow pre-shock cooling and rapid post-shock solidification, providing a more complete picture of the thermal history of the meteorite Jesenice. Some parts of the shock veins show a partially melted transition zone, indicating that the shock melting took place *in situ*.

Conclusions

The presence of shock veins in the meteorite Jesenice indicates that the shock event was violent enough to cause partial melting of the meteorite. The presence of oval-shaped globules indicates the formation of shock veins as a consequence of shear friction melting. Peak pressure and temperature during shock were 2.5–15 GPa and 1500–2150 °C, respectively. The presence of tetrataenite in the meteorite Jesenice indicates, that the FeNi metal experienced slow cooling at temperatures below ~320 °C (Wasilewski, 1988), reflecting the low-temperature thermal history within the parent body, but it does not directly constrain the timing or location of the shock event.

Meteorite Jesenice is a good example of a weakly shocked chondrite, which provides the evidence for the hypothesis that local melting is not a result of severe shock, but a consequence of very locally increased pressure and temperature, most likely due to the shear-fracture mechanism, during shock.

Acknowledgments

We are thankful to the curator of the Slovenian museum of Natural History Miha Jeršek for providing samples of the meteorite Jesenice. This work was financially supported by the Slovenian Research and Innovation Agency (ARIS): Research Core Funding Nos. P2-0084 and P1-0195.

References

Acosta-Maeda, T.E., Scott, E.R.D., Sharma, S.K. & Misra, A.K. 2013: The pressures and temperatures of meteorite impact: Evidence from micro-Raman mapping of mineral phases in the strongly shocked Taiban ordinary chondrite. American Mineralogist, 98/5–6: 859–869. https://doi.org/10.2138/am.2013.4300

Agee, C.B., Li, J., Shannon, M.C. & Circone, S. 1995: Pressure–temperature phase diagram for the Allende meteorite. Journal of Geophysical Research, 100: 17725–17740.

Bischoff, A., Jeršek, M., Grau, T., Mirtič, B., Ott, U., Kučera, J., Horstmann, M., Laubenstein, M., Herrmann, S., Řanda, Z., Weber, M. & Heusser, G. 2011: Jesenice – A new meteorite fall from Slovenia. Meteoritics and Planetary Science, 46/6: 793–804. https://doi.org/10.1111/j.1945-5100.2011.01191.x

Blau, P.J. & Goldstein, J.I. 1975: Investigation and simulation of metallic spherules from lunar soils. Geochimica et Cosmochimica Acta, 39/3: 307–324. https://doi.org/10.1016/0016-7037(75)90199-4

Chen, M., Xie, X., Wang, D. & Wang, S. 2002: Metal-troilite-magnetite assemblage in shock veins of Sixiangkou meteorite. Geochimica et Cosmochimica Acta, 66/17: 3143–3149. https://doi.org/10.1016/S0016-7037(02)00903-1

Clarke, R.S. & Scott, E.R.D. 1980: Tetrataenite-ordered FeNi, a new mineral in meteorites. American Mineralogist, 65/1959: 624–630.

Gasparik, T. 2014: Phase Diagrams for Geoscientists. An Atlas of the Earth's Interior. Springer, New York: 462 p.

Guo, Z., Li, Y., Liu, S., Xu, H., Xie, Z., Li, S., Li, X., Lin, Y., Coulson, I.M. & Zhang, M. 2020: Discovery of nanophase iron particles and high pressure clinoenstatite in a heavily shocked ordinary chondrite: Implications for the decomposition of pyroxene. Geochimica et Cosmochimica Acta, 272: 276–286. https://doi.org/10.1016/j.gca.2019.10.036

Kong, P. & Xie, X. 2003: Redistribution of elements in the heavily shocked Yanzhuang chondrite. Meteoritics and Planetary Science, 38/5: 739–746. https://doi.org/10.1111/j.1945-5100.2003.tb00038.x

Owocki, K. & Muszyński, A. 2012: Shock veins in the Sahara 02500 ordinary chondrite. Geologos, 18/2: 111–118. https://doi.org/10.2478/v10118-012-0006-0

Robie, R., Hemingway, B. & Fisher, J. 1978: Thermodynamic properties of minerals and related substances at 298.15 K and 1 bar (105 pascals) pressure and at higher temperatures (Report No. 1452), Bulletin. https://doi.org/10.3133/b1452

Scott, E.R.D. 1982: Origin of rapidly solidified metal-troilite grains in chondrites and iron meteorites. Geochimica et Cosmochimica Acta, 46/5: 813–823. https://doi.org/10.1016/0016-7037(82)90032-1

Stoffler, D., Keil, K. & Scott, E.R.D. 1992: Shock Classication of Ordinary Chondrites: New Data and Interpretations. Meteoritics, 27/3: 292. http://ads.nao.ac.jp/cgi-bin/nph-bib_

query?bibcode=1992Metic..27R.292S&db_key=AST

Tsuchiyama, A., Nagahara, H. & Kushiro, I. 1980: Experimental reproduction of textures of chondrules. Earth and Planetary Science Letters, 48/1: 155–165. https://doi.org/10.1016/0012-821X(80)90178-8

Wasilewski, P.J. 1988: Magnetic characterization of the new magnetic mineral tetrataenite and its contrast with isochemical taenite. Physics of the Earth and Planetary Interiors, 52: 150–158. https://doi.org/10.1016/0031-9201(88)90063-5

Wittmann, A., Swindle, T.D., Cheek, L.C., Frank, E.A. & Kring, D. A. 2010: Impact cratering on the H chondrite parent asteroid. Journal of Geophysical Research: Planets, 115/7: E07009. https://doi.org/10.1029/2009JE003433

Xie, X., Sun, Z. & Chen, M. 2011: The distinct morphological and petrological features of shock melt veins in the Suizhou L6 chondrite. Meteoritics and Planetary Science, 46/3: 459–469. https://doi.org/10.1111/j.1945-5100.2011.01168.x

Xie, Z., Sharp, T.G. & De Carli, P.S. 2006: Estimating shock pressures based on high-pressure minerals in shock-induced melt veins of L chondrites. Meteoritics and Planetary Science, 41/12: 1883–1898. https://doi.org/10.1111/j.1945-5100.2006.tb00458.x

GEOLOGIJA 68/2, 251-267, Ljubljana 2025

https://doi.org/10.5474/geologija.2025.011

Article

Prostorski razvoj sivega dela Grödenske formacije na Žirovskem vrhu

Spatial development of the grey part of the Val Gardena Formation on Žirovski vrh

Franci ČADEŽ[1]* & Ivan GANTAR[2]

[1]Gorje 7, SI-5282 Cerkno, Slovenia; *corresponding author: fcadez@gmail.com
[2]Rožna 7, SI-5280 Idrija, Slovenia; e-mail: ivan.gantar@gmail.com

Prejeto / Received 10. 9. 2025; Sprejeto / Accepted 9. 10. 2025; Objavljeno na spletu / Published online 10. 12. 2025

Ključne besede: sedimentacijski razvoj, orudenje, grödenske klastične kamnine, Žirovski vrh
Key words: sedimentary horizons, mineralization, Val Gardena clastic rocks, Žirovski vrh

Izvleček

Raziskave in odkopavanje se je na Rudniku urana Žirovski vrh opravljalo med leti 1960 in 1990. Ivan Mlakar (2000) je razdelil celotno Grödensko formacijo na 6 členov in poimenoval najstarejši Brebovniški člen v katerem je poznano orudenje z uranom. Že pred tem je Tomaž Budkovič (1980) ta sivi del Grödenske formacije razčlenil na 10 horizontov na osnovi barve, zrnavosti in prodniških združb in sicer po podatkih kartiranja podkopa P-10 in njegovega nadaljevanja. V tem članku smo prikazali razvoj Brebovniškega člena na celotnem prostoru rudišča, tako jame kot tudi njenega nadaljevanja proti JV in SZ. Prvotno razdelitev Budkoviča smo spremenili tako, da smo zgornji del 3. horizonta z intraformacijskimi konglomerati in nekdanji 4. peščeni horizont združili v enoten 5. konglomeratni horizont. Dragomir Skaberne je namreč v svojem doktoratu (1995) Brebovniški člen razdelil na 2 megaritma pri čemer se vsak pričenja s konglomerati, zaključi pa z drobnozrnatimi sedimentnimi kamninami. Zato je ustrezneje, da se 3. horizont zaključi z drobnozrnatimi sedimenti in je hkrati zaključek 1. megaritma, intraformacijski konglomerati, ki so bili prej še zgornji del 3. horizonta pa so po novem že del enotnega konglomeratnega horizonta, ki podrejeno vsebujejo še peščenjake.

Debelina celotnega Brebovniškega člena je največja v osrednjem delu odprte jame, kjer znaša 410 m in se proti robovom bazena zmanjšuje. Na območju Golega vrha proti JV, do kamor sežejo pojavi orudenja, se njegova debelina zmanjša na 50 m. Debelina posameznih horizontov pa se, razen 2. in 5. horizonta, zmanjša z nekaj 10 metrov le na nekaj metrov oziroma se posamezni horizonti celo izklinjajo. V SZ smeri od nekdanjih jamskih del ni več ekonomsko pomembnih orudenj z uranom. V to smer se izklinjajo pisani konglomerati, spreminja se tudi značaj peščenih horizontov, ki so bili v jami glavni nosilci orudenja. Njihova barva se spreminja iz sive in temnosive v zelenosivo, v njih je manj drobcev antracitizirane organske snovi, ki je pogojevala nastanek redukcijskih sredin, kjer se je lahko izločal uran. V pisanih konglomeratih je pomembna prisotnost prodnikov kislih magmatskih predornin, ki imajo povišan clark urana glede na druge skupine kamnin. Z njihovo erozijo so se površinske vode ter podtalnica obogatile z uranom že na površju, dodatno pa še pri precejanju skozi plasti pisanega konglomerata. V oksidacijskih pogojih se je uran raztapljal, v redukcijskih pa izločal v vezivu peščenih klastitov. Od celotne dolžine pojavljanja plasti sivega Brebovniškega člena, ki meri po geološki karti 18 km, znaša območje s pogojno ekonomskim orudenjem le dobrih 5,5 km in približno na ta del je omejeno tudi pojavljanje pisanih konglomeratov.

Abstract

The Uranium Mine Žirovski vrh was actively being researched and excavations took place between 1960 and 1990. Ivan Mlakar (2000) divided the entire Val Gardena Formation into 6 members and named the oldest one the Brebovnica member. This is the only member with uranium ore mineralization. Previously, Tomaž Budkovič (1980) subdivided the gray part of the Val Gardena formation into ten horizons based on colour, grain size, and pebble associations. He did that by mapping of undercut P-10 and its continuation. In this article, we have shown the development of the Brebovnica member in the entire area of the ore deposit, both the mining area and its continuations to the SE and NW. We have modified Budkovič's original division by combining the upper part of the 3rd horizon with intraformational conglomerates and the former 4th sandy horizon into a single 5th conglomerate horizon. In his doctoral thesis (1995), Dragomir Skaberne divided the Brebovnica member into 2 megarhythms, each of which begins with conglomerates and ends with fine-grained sediments. Therefore, it is more appropriate that the 3rd horizon ends with fine-grained sediments and is at the same time the end of the 1st megarhythm, while the intraformational conglomerates, which were previously the upper part of the 3rd horizon, are now part of a single conglomerate horizon, which sometimes also contains sandstones.

The total thickness of the Brebovnica member is greatest in the central part of the mine area, where it reaches 410 meters and decreases towards the edges of the basin. Towards Goli vrh in the southeast, where the last uranium mineralization occurs, its thickness decreases to 50 meters. The thickness of individual horizons, except the second and fifth, decreases from tens of meters to only a few meters, and some horizons even wedge out. To the northwest from the former mining area there are no economically significant uranium ores. In that direction, the colorful conglomerates wedge out, and the nature of sandy horizons, which were the main carriers of uranium mineralization in the mining area, changes. Their colour changes from gray and dark gray to greenish gray, with fewer fragments of anthracitized organic matter that created reducing environments necessary for uranium precipitation. The colourful conglomerates contain important

pebbles of acidic magmatic rocks with higher uranium contents compared to other rock groups. Their erosion enriched surface and groundwater with uranium already at the surface and additionally during percolation through the layers of colorful conglomerate. Uranium dissolved under oxidizing conditions, while under reducing conditions it precipitated in the binder of sandy grains. Of the entire 18 km length of the gray Brebovnica member as shown on the geological map, only 5.5 km show conditionally economic uranium mineralization, which approximately corresponds to the area where colorful conglomerates occur.

Uvod

Tridesetletna aktivna zgodovina rudarjenja na rudniku urana Žirovski vrh (1960–1990), je poznala celo paleto raziskovanj od radiometrične in geokemične prospekcije, površinskega geološkega kartiranja, izdelave razkopov, vrtanja s površine, raziskovalnih rovov in vrtalnih del iz jame ter geološkega kartiranja teh del do poskusnih in nazadnje rednega odkopavanja uranove rude. Pri teh delih se je nabralo ogromno podatkov o razvoju klastičnih sedimentnih kamnin v katerih so se v geološki preteklosti nakopičili uranovi minerali. Na prostoru jame, kjer se je pričelo z raziskavami, odpiranjem in odkopavanjem, se je v dolžini 1,9 km v treh desetletjih izdelalo preko 60 km rovov, 64 km strukturnih in 380 km udarnih vrtin. Ta osrednji del rudišča se je raziskoval v prečnih prerezih, ki so si sledili od P-0 na JV do P-37 na skrajnem SZ (sl. 1).

V južnih podaljških pa je bilo s površinskimi vrtinami raziskano in dokazano nadaljevanje orudenja še na dolžini 3,8 km, to je do Golega vrha, najvišje vzpetine Žirovskega vrha. Brebovniški člen se po geološki karti nadaljuje še naprej od Golega vrha proti jugu na dolžini 3 km, vendar je vse tanjši, zaradi poševnega reza ob narivu vse ožji in brez poznanih mineralizacij. Zato se v tem zadnjem delu ni več vrtalo raziskovalnih vrtin. Za južne podaljške kot tudi SZ nadaljevanje smo prečne prereze in njihove oznake povzeli po Mlakarju (2000). Še večji obseg kakor proti jugovzhodu, zavzemajo sivi grödenski klastiti proti severozahodu oziroma zahodu, kjer se po Mlakarjevi geološki karti (sl. 1) nadaljujejo do Fužin (4,2 km), naprej proti Sovodnju (še preko 5 km) pa že v močno zmanjšanih debelinah. V tej smeri pa v njih ne nastopa več ekonomsko zanimivih uranskih orudenj saj se ta končajo v zadnjih prerezih odprtega dela jame (prerezi P-35 do P-37). Orudenja z uranom se tako pojavljajo v sivih klastitih na dolžini preko 5,5 km, celotna dolžina njihovega pojavljanja pa znaša po geološki karti I. Mlakarja 18 km. V članku podajamo značilnosti razvoja posameznih horizontov sivega dela Grödenske formacije na celotnem prostoru Žirovskega vrha. Na območju jame je ta zgradba potrjena z mnogimi rudarskimi deli, v južnih in severnih podaljških je interpretirana na osnovi geološke karte in strukturnih vrtin s površine.

Litološke značilnosti razvoja Brebovniškega člena na prostoru jame

Starejši raziskovalci tega prostora so Grödenske plasti delili na spodnji sivi in zgornji rdeči del (Marinković, 1961, Omaljev, 1967, Grad & Ferjančič, 1976, Budkovič, 1980). Šele Mlakar pa je na osnovi kartiranja celotnega območja Žirovskega vrha grödenske sedimentne kamnine razčlenil na 6 členov in jih poimenoval: Brebovniški, Hobovški, Zalški, Koprivniški, Škofješki in Dobračevski. Sivi, najstarejši del Grödenske formacije, ki ga je Mlakar (2000) poimenoval Brebovniški člen, je za nas najzanimivejši saj se le v njem pojavljajo orudenja z uranom. Budkovič ga je že pred tem še podrobneje razčlenil na osnovi kartiranja podkopa P-10, prečnika H-74 v nadaljevanju podkopa in vrtine B-63. Na osnovi zrnavosti, barve in prodniških združb je sivi del Grödenske formacije delil na 10 litostratigrafskih horizontov (Budkovič, 1980). Rdeči del Grödenske formacije, kakor so ga imenovali starejši raziskovalci, je Mlakar delil še na več členov na osnovi prevladujoče zrnavosti (muljevci, peščenjaki in konglomerati). Vsi so prevladujoče rdeče barve, razen Škofješkega člena v katerem prevladujejo sivi peščenjaki, v tem členu pa je nastalo bakrovo rudišče Škofje.

Mnogi raziskovalci rudišča so poudarjali hitro spremenljivost sedimentnih razmer, zlasti obliko in vsebnost orudenja. Podrobna kartiranja rovov in vrtin, ki so se zlasti intenzivno izvajala v zadnjem desetletju delovanja rudnika so pokazali, da se podobne zakonitosti pojavljanja posameznih horizontov javljajo na širšem prostoru. Ugotovljene značilnosti posameznih horizontov, ki so bile ugotovljene v P-10 in njegovem nadaljevanju (Budkovič, 1980), predstavljajo le en presek teh plasti v prostoru. Z izdelavo podkopa P-11 ter nanj navezujočih se ramp, ki ležijo skoraj v istem prečnem prerezu le 60 m višje, smo imeli priložnost vzporejanja teh horizontov med obema podkopoma. Primerjava je pokazala, da so se podobni horizonti, kakor so bili ugotovljeni v P-10, pojavljali tudi v podkopu P-11 (sl, 2). Povezovanje horizontov je bilo torej uspešno, povezovanje posameznih sekvenc, ki gradijo horizonte pa ne, zato so se tudi v debelinah pojavljale določene razlike. Med obema podkopoma se je lahko povezalo horizonte 1, 2, 3 in 5 ter seveda karbonsko podlago, ki smo jih v

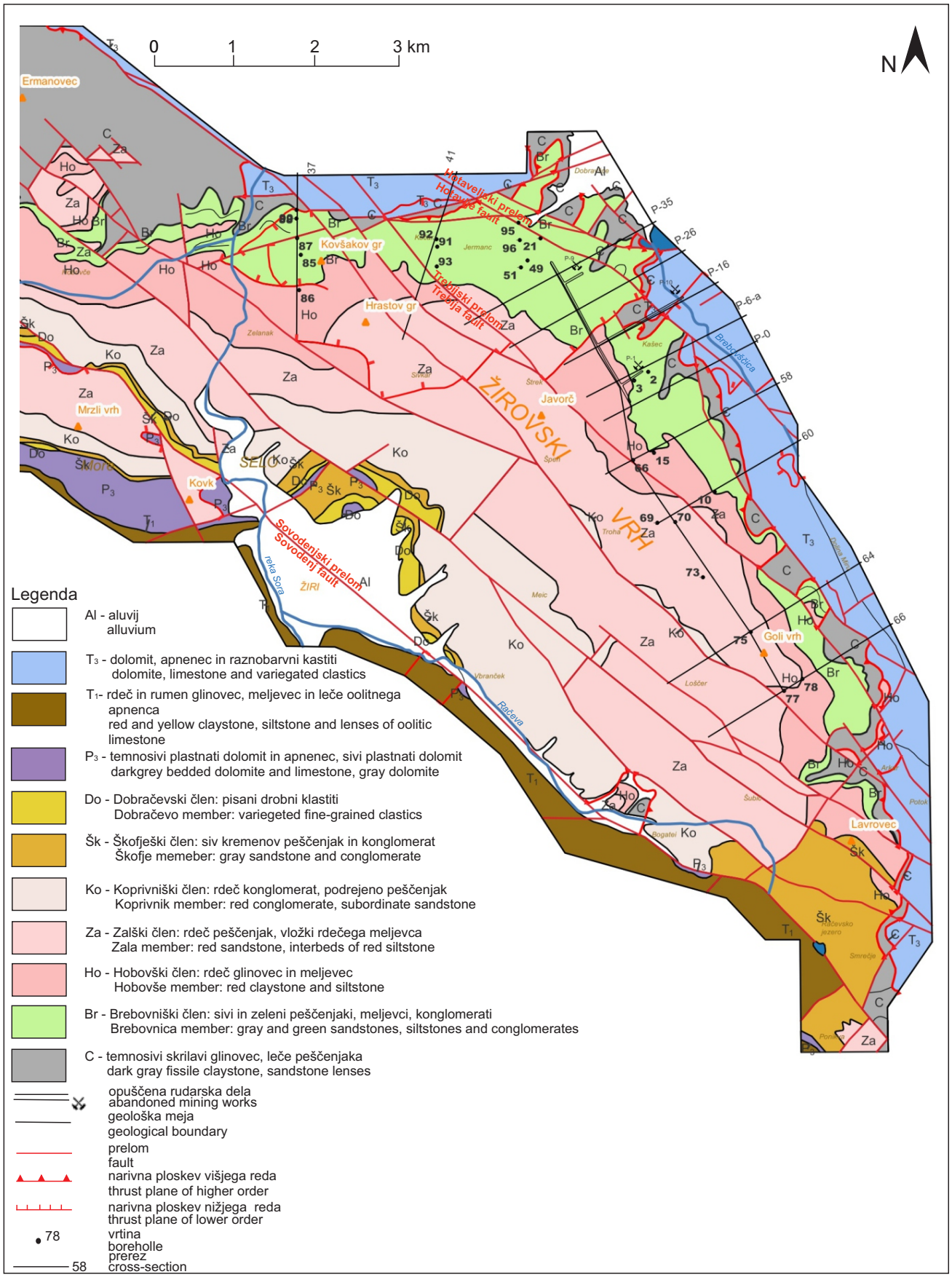

Sl. 1. Geološka karta Žirovskega vrha (po I. Mlakarju, 2000).
Fig. 1. Geological map of Žirovski vrh (after I. Mlakar, 2000).

drugih raziskovalnih objektih le bolj poredko srečali. Poglejmo si sedaj značilnosti posameznih horizontov v P-10 kakor jih je podal Budkovič (1980) v primerjavi s P-11 in predvsem razlike s to delitvijo v ostalem prostoru, kakor smo jih spoznavali tekom izvajanja rudarskih del.

Karbonska podlaga je bila kartirana tako na površini kot tudi v mnogih raziskovalnih delih. Zastopajo jo črni do temnosivi glinovci in meljevci z redkimi polami sivih peščenjakov, v okolici Fužin je Mlakar kartiral tudi do 30 m debele plasti skrilavih laporovcev in lapornatega apnenca. Glinovci in meljevci so skrilavi, v njih pa ni bilo najdenih fosilov. Glede na podobne litološke razvoje, kakor so jih ugotovili v vzhodnih Posavskih gubah, kjer so dokazali njihovo karbonsko starost, jim Mlakar tudi tu pripisuje karbonsko starost čeprav dopušča možnost, da so v zgornjem delu lahko že tudi spodnjepermske starosti (Mlakar & Placer, 2000).

1. horizont leži v podkopu P-10 diskordantno na karbonskih skrilavih muljevcih (sl. 2). Nad diskordanco je bila odložena najprej 2 m debela plast zelenosivega peščenjaka s precej pirita in klasti črnega muljevca. Ti pripadajo karbonskim muljevcem podlage. Nad tem je sledil peščen konglomerat sive in zelene barve, v njem so klasti belega kremena in lidita. V zgornjem delu so bili posamezni prodniki tudi iz rožnatega kremena, rdečih kislih predornin in rdečega apnenca. Posamezne sekvence so v zgornjem delu imele še peščenjake (Budkovič, 1980, Skaberne, 1995). V podkopu P-11 je bil v zgornjem delu podkopa še ohranjen del diskordance, ki se navezuje na enak kontakt v podkopu P-10, v spodnjem delu rova je bil odrezan ob prelomu. Tu se nad diskordanco pričenja siv do temnosiv muljevec, ki predstavlja presedimentirano karbonsko podlago, navzgor postane zelen in rdeč. Na muljevcih je bilo odloženega najprej 2 m pisanega konglomerata z rdečkastimi klasti, nato pa 15 m sivega konglomerata. Podrejeno v konglomeratnih sekvencah nastopata še siv in zelen peščenjak ter muljevec. Tudi tu je bilo značilno pojavljanje pirita. Skupna debelina tega pretežno konglomeratno razvitega horizonta je bila v P-10 45 m, v P-11 pa 25 m.

Ta horizont je bil na prostoru jame navrtan še v površinskih vrtinah B-2 in B-3 v prerezu P-5, kjer je bilo nad karbonskim skrilavim muljevcem ugotovljeno 12 m oz. 20 m sivega konglomerata, v B-2 pa je bilo pod njim še 30 m zelenih, rdečih in sivih peščenjakov in muljevcev. V prerezu P-6a je vrtina V-960 nad karbonsko podlago navrtala 15 m sivega peščenega konglomerata z več polami peščenjaka in muljevca (sl. 4). Med prevladujočimi klasti

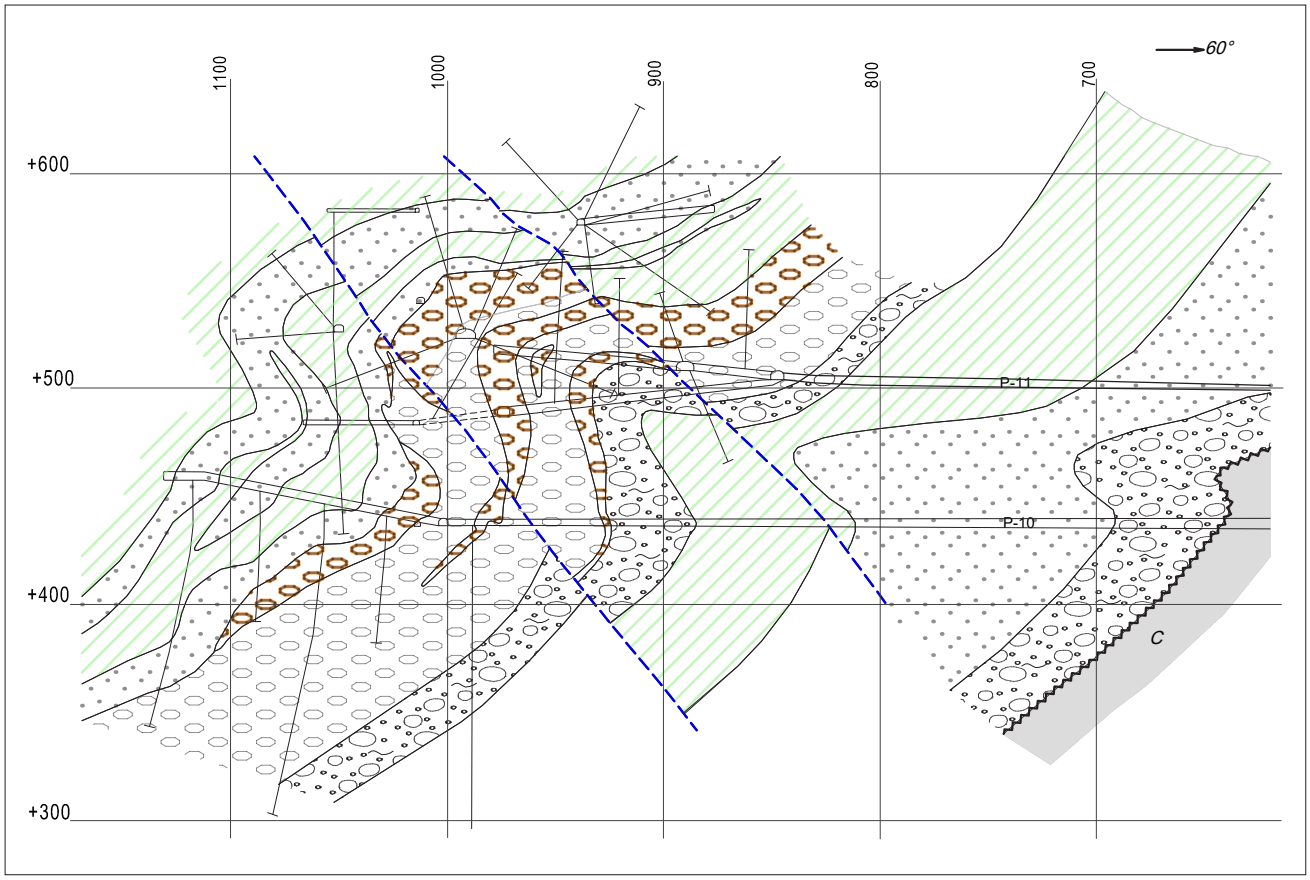

Sl. 2. Geološki prečni prerez P-16.
Fig. 2. Geological cross section P-16.

kremena so bili tudi klasti sivega apnenca, gomolji pirita in antracitni drobci. Karbonske skrilave muljevce so navrtali še v jamski vrtini V- 975, prerez P-0 (sl. 3). V njej so se nad podlago pojavljali sivi peščeni konglomerati, konglomeratični peščenjaki in zeleni ter sivi muljevci. Med prodniki so bili tudi rožnati klasti. V vrtini V-973 v istem prerezu (slika 3) pa so bili sivi in zeleni peščeni konglomerati in konglomeratični peščenjaki, v zgornjih delih sekvenc pa še sivi debelo do drobnozrnati in zeleni drobnozrnati peščenjaki. Debelina horizonta je znašala v prvi vrtini 16 m, v drugi vsaj 10 m saj vrtina še ni navrtala karbonske podlage.

2. horizont je značilen po nastopanju dokaj enoličnih sivih debelo do srednje zrnatih peščenjakov. Konglomeratov v njem ni, ponekod se javljajo tanjše pole sivih do temnosivih muljevcev, ki zaključujejo posamezne peščene sekvence. V njem se dobijo tudi pole in gomolji pirita ter drobci organske snovi. Debelina horizonta je v podkopu P-10 znašala 100 m, v P-11 pa le 50 m (sl. 2). Debelina horizonta je zaradi gubanja že deformirana. Razen v profilu P-16 oziroma obeh podkopih, smo na sedimente tega horizonta naleteli še v prerezu P-0. V vrtini V-975 so bili nad 1. horizontom sivi peščenjaki debeli 30 m, v vrtini V-973 pa 25 m (sl. 3).

3. horizont je značilen po pisani sedimentaciji rdečih in zelenih muljevcev ter drobnozrnatih peščenjakov s karbonatnimi konkrecijami, v spodnjem delu sta bili v obeh podkopih še dve ločeni sekvenci sivega peščenjaka. V zgornjem delu tega horizonta kakor ga je opredelil Budkovič (1980) pa se v podkopu P-10 pojavijo sedimenti korit s konglomerati in peščenjaki v katerih so pogostni klasti muljevcev in apnencev. Šele Skaberne (1995) pa je tem sedimentom korit dal drugi pomen. Na osnovi podrobnega kartiranja istega podkopa P-10 je sedimente 1., 2. in spodnjega dela 3. horizonta uvrstil v I. makroritem, sedimente preostalih horizontov Brebovniškega člena po Budkoviču in spodnji del Hobovškega člena s prevladujočimi rdečimi muljevci pa v II. makroritem grödenske formacije. V nadaljni sedimentaciji grödenske formacije na prostoru med Smrečjem in Cerknom je ločil še 2 makroritma, skupaj torej 4 (Skaberne, 1995). Prodniki apnencev v konglomeratih na bazi I. in II. makroritma so sivih, rožnatih do mesnato rdečih barv in večinoma ekstrabazenski, del njih pa je nastajal v lagunah na poplavnih ravnicah in so bili erodirani iz podlage skupaj s klasti in celo bloki muljevcev in odloženi v koritih, ki so jih reke vrezovale v podlago ob poplavah (Skaberne, 1995). V 3. horizont moremo potemtakem šteti le pisane

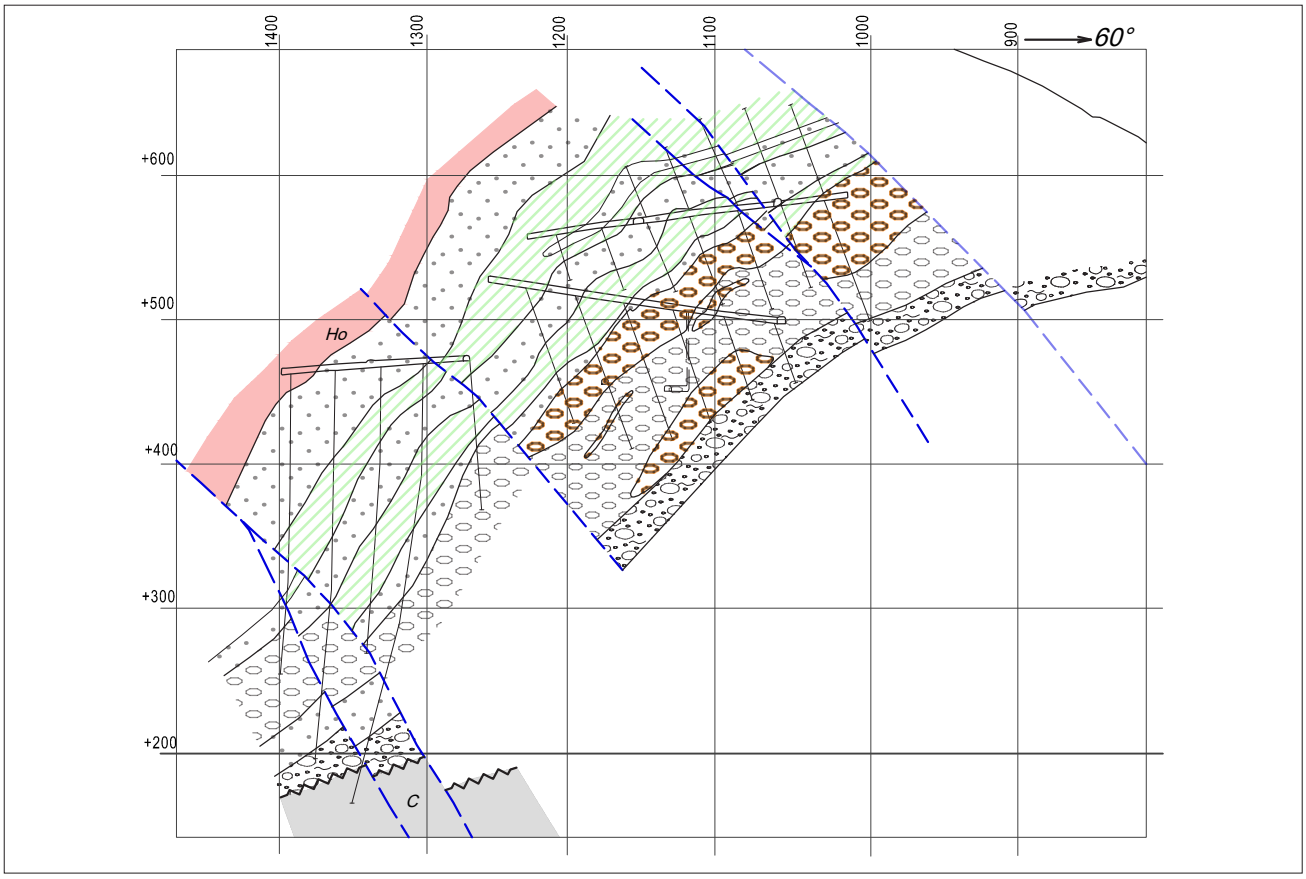

Sl. 3. Geološki prečni prerez P-0.
Fig. 3. Geological cross section P-0.

muljevce in drobnozrnate peščenjake, sedimenti korit nad njimi pa so že del naslednjega makroritma po Skabernetu (1995) oziroma jih moramo uvrstiti že v 5. horizont po Budkoviču (1980). Debelina 3. horizonta je potem v P-10 le 60 m, v P-11 pa 50 m.

4. horizont so v P-10 po Budkoviču (1980) sestavljali sivi debelozrnati peščenjaki z vmesno plastjo konglomerata in dvema plastema temnosivega in zelenega muljevca. V podkopu P-11 so bili kot ekvivalent tega horizonta razviti predvsem sivi in zelenkastosivi konglomeratni peščenjaki, le v zgornjem delu sekvenc so nastopali debelozrnati peščenjaki. Vendar bomo z opisom naslednjega 5. horizonta po Budkoviču videli, da ta v širšem prostoru še večkrat vsebuje partije debelozrnatih peščenjakov znotraj konglomeratičnih peščenjakov in pravih peščenih konglomeratov. Zato imenovani "4. horizont" uvrščamo sedaj v 5. horizont za katerega so značilni debelozrnati sedimenti rečnih korit. Pod njim ležijo konglomerati s prodniki apnencev in klasti muljevcev, ki pričenjajo 5. horizont oziroma so začetek drugega makroritma po Skabernetu (1995). Četrti horizont smo zato črtali kot samostojnega, številke naslednjih horizontov pa obdržali saj je vsa obsežna geološka dokumentacija o rudišču vezana na tako oštevilčenje horizontov.

5. horizont je Budkovič (1980) opredelil kot sivi konglomerat z dvema vmesnima plastema pisanega konglomerata, debeline 5 in 10 m ter v skupni debelini 55 m. Z razširitvijo tega horizonta z zgornjim konglomeratnim delom 3. horizonta in celotnim 4. horizontom se je njegova debelina precej povečala. V prerezu P-16, kjer sta podkopa P-10 in P-11 znaša njegova debelina 90 m, proti SZ se spreminja od 50 do 90 m proti JV pa med 85 in 120 m (sl. 2 do 6). Pogled na geološki karti nivojev 440 in 530 in prečne prereze pokaže na mestih, kjer imamo dovolj pogostne podatke, precej bolj razgibano sliko pojavljanja tega horizonta. Prevladujoči različek je še vedno sivi peščeni konglomerat in konglomeratični peščenjak. Sestavo prodnikov, ki nastopajo v sivih, pisanih in intraformacijskih konglomeratih je v svoji doktorski disertaciji najpopolneje razčlenil Skaberne (1995). V sivih konglomeratih nastopajo prodniki sivih, belih in zelenkastih odtenkov po sestavi pa pripadajo večinoma sivemu in belemu kremenu, sivim in zelenim predorninam, liditu, tufom in intraklastom muljevca. V sivih konglomeratih, konglomeratičnih in debelozrntih peščenjakih je značilno tudi nastopanje drobcev antracitizirane organske snovi katerih velikost sega od manj kot mm do več dm in celo več metrov dolgih ostankov drevesnih debel. Na mestih z večjo ali manjšo

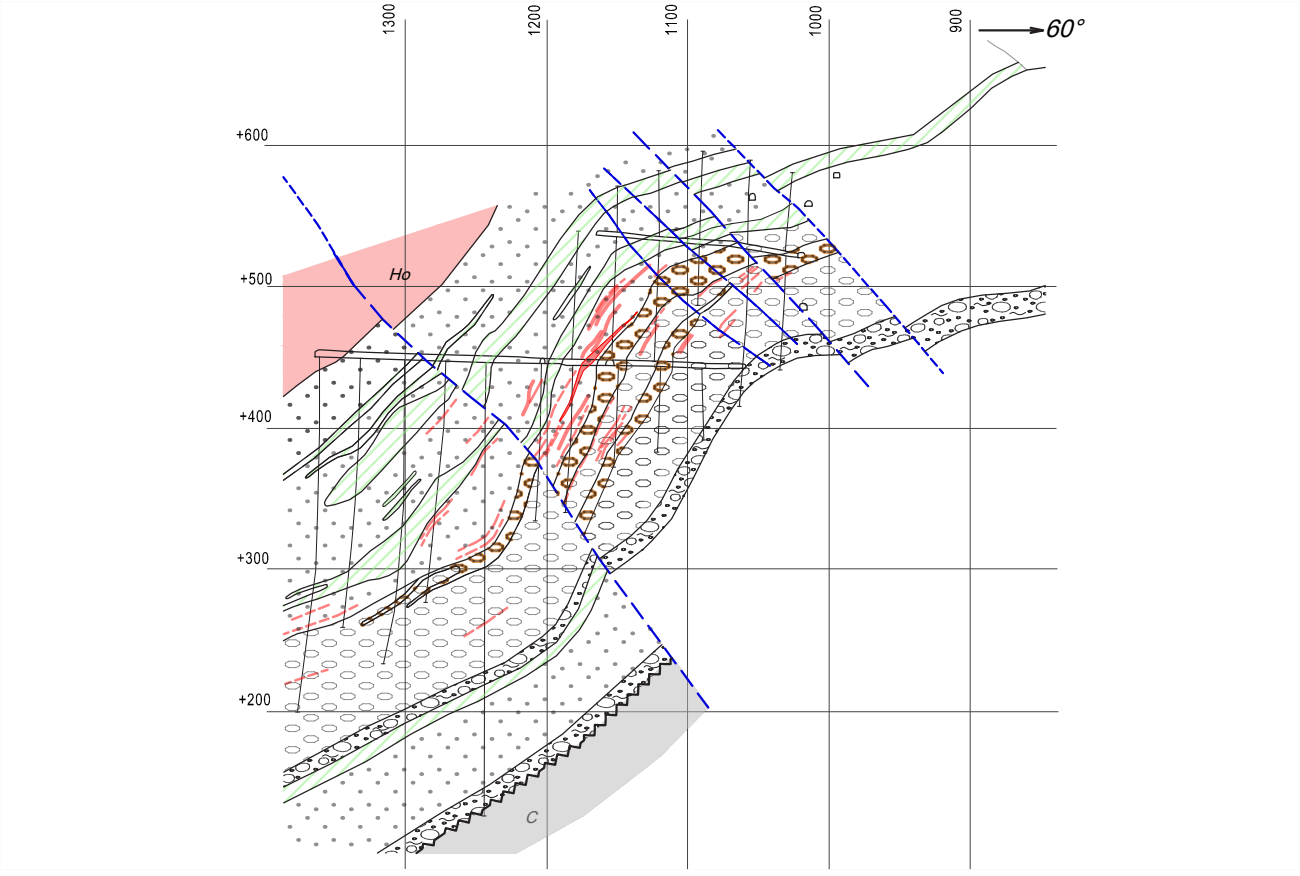

Sl. 4. Geološki prečni prerez P-6a.
Fig. 4. Geological cross section P-6a.

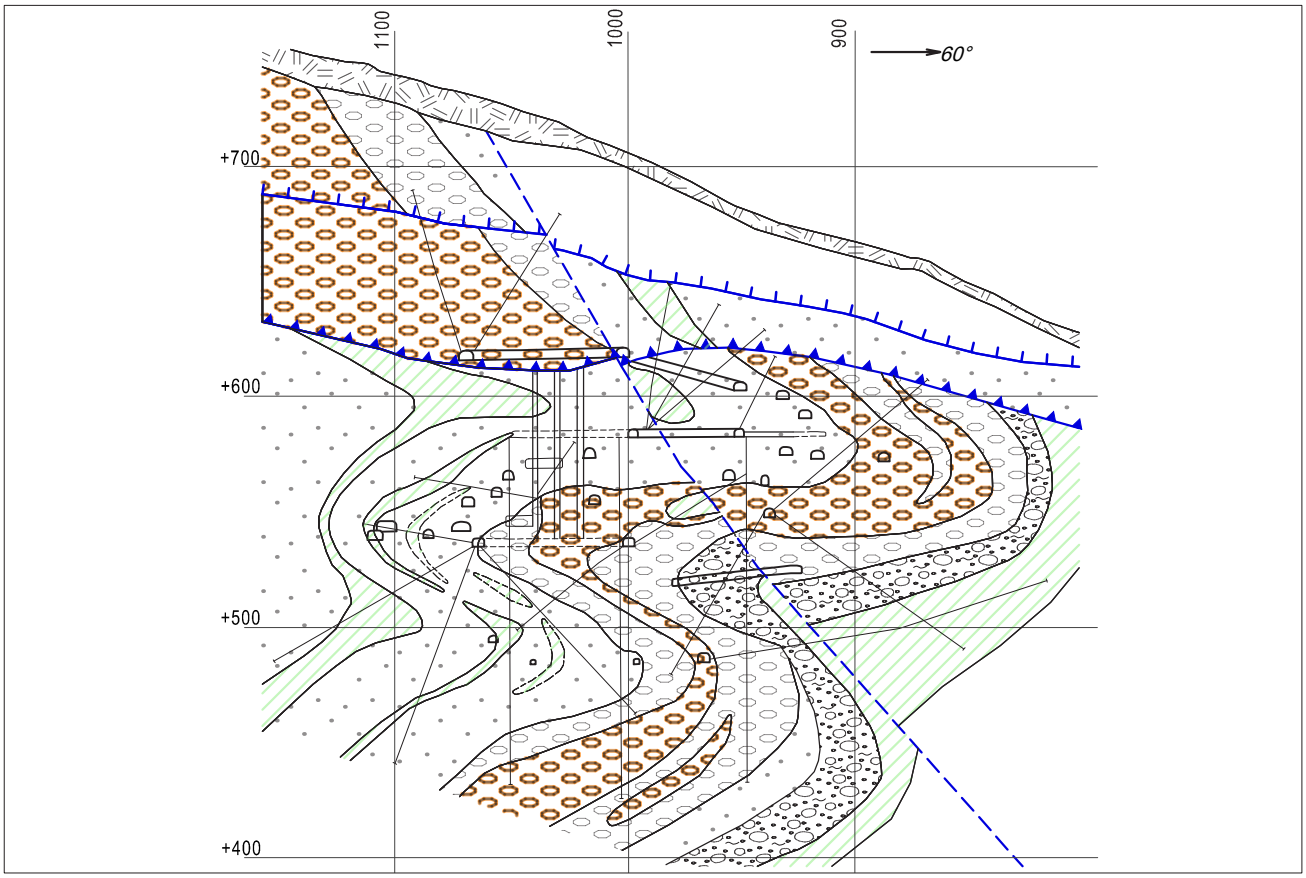

Sl. 5. Geološki prečni prerez P-26.
Fig. 5. Geological cross section P-26.

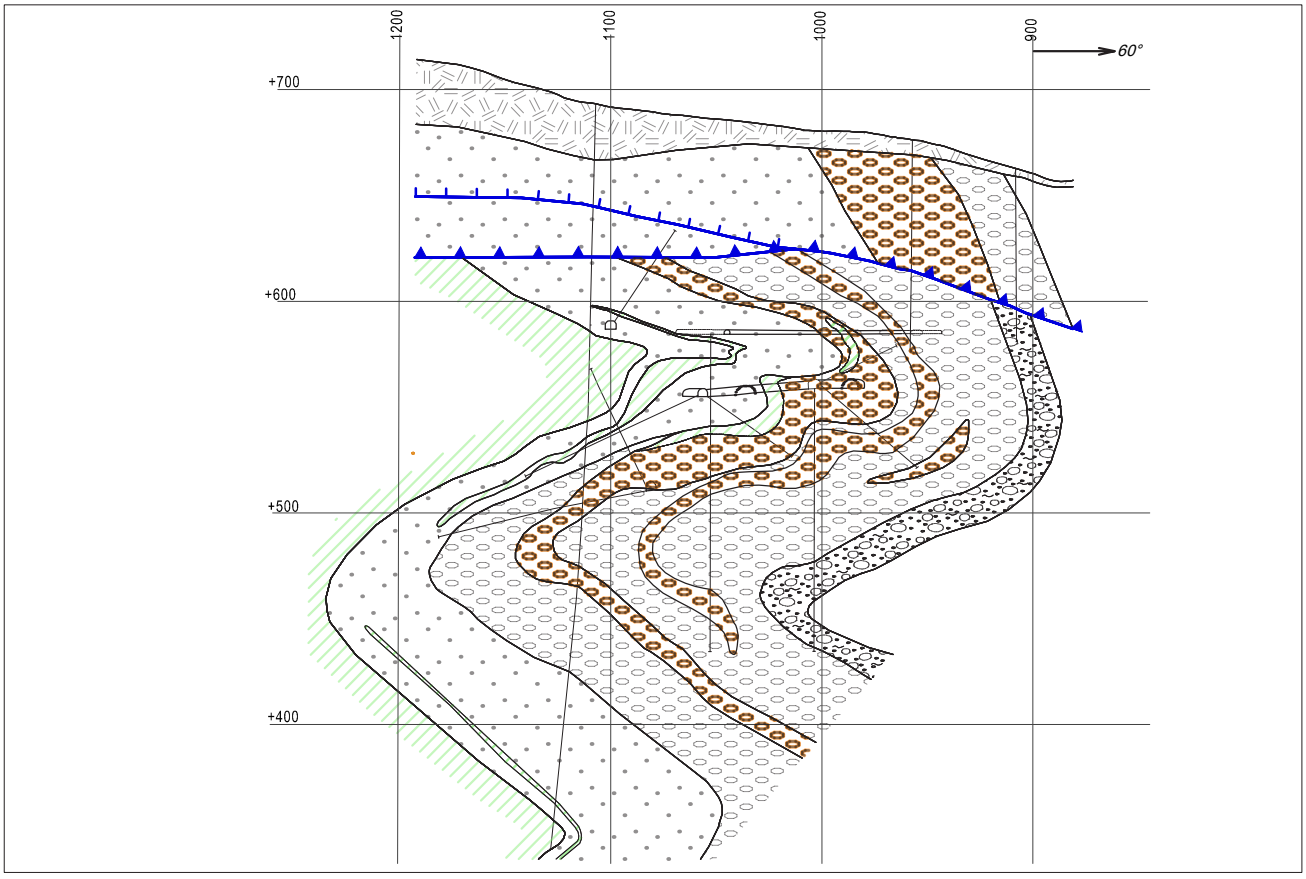

Sl. 6. Geološki prečni prerez P-35.
Fig. 6. Geological cross section P-35.

koncentracijo organske snovi pa se lahko pojavljajo že tudi povišane vsebnosti urana. Najvišje vsebnosti in obseg orudenja se pojavljajo v debelozrnatih in konglomeratičnih peščenjakih in sicer na mestih, kjer nad njimi ni več pisanih konglomeratov. V sivih konglomeratih je značilno tudi pojavljanje leč oziroma zaključevanje sekvenc z debelozrnatimi peščenjaki. Ena takih je bila v podkopu P-10 potem napačno uvrščena kot samostojen horizont. Prehodi iz sivih peščenih konglomeratov in konglomeratičnih peščenjakov v sive debelozrnate peščenjake znotraj 5. horizonta so bili pogosto kartirani na spodnjem nivoju 440 (sl. 8).

V pisanih konglomeratih je poleg prodnikov, ki se pojavljajo v sivih konglomeratih značilno še nastopanje kremenovih prodnikov rožnatih odtenkov, jaspisa ter prodnikov rožnatih predornin in apnenca (Skaberne, 1995). V vezivu prevladujejo zeleno obarvani peščenjaki, ki skupaj z rožnatimi odtenki prodnikov dajejo kamnini značilen pisani videz. V JV delu jame velja v večjem delu podobna razdelitev pisanih in sivih konglomeratov kot jo je podal Budkovič (1980) s tem, da so pod njimi sedaj še pisani peščenjaki in muljevci ter apnenčevi konglomerati in intraformacijski konglomerati, ki so bili prej del 3. horizonta. Pisani konglomerat se v vzdolžni smeri na prostoru jame spreminja tako, da sta večinoma prisotni po dve plasti ponekod celo tri, v vmesnih delih pa tudi le po ena. V večjem delu jame je pisani konglomerat zaključeval ta horizont. V prečni smeri je pisani konglomerat najdebelejši med nivojema 530 in 580 v SZ delu jame, kjer ponekod celo prevladuje nad sivim (sl. 5 in 6). Na nivoju 530, med P-16 in P-22, je bilo v konglomeratih izdelanih precej prog, kjer ugotavljamo, da so meje in prehodi med pisanim in sivim konglomeratom zelo nepravilne. Tak izgled njihovih meja najlepše dokazuje režim prepletajoče reke, ko so se med seboj ločeno odlagali sedimenti iz dveh izvornih območij (sl. 7). Navzdol oziroma proti JZ se pričenja debelina pisanega konglomerata zmanjševati in izklinjati, kar je vidno v prečnih prerezih.

O intraformacijskem konglomeratu z apnenimi prodniki in klasti muljevca na bazi tega horizonta je bilo v začetku, razen v obeh podkopih, bolj malo podatkov. V sklopu zapiralnih del pa so se vrtale tudi odvodnjevalne vrtine s katerimi smo ugotovili, da se konglomerati z apnenimi prodniki in/ali apnenim vezivom (sl. 8) ter konglomerati, ki jih lahko sestavljajo pretežno le klasti rdečkastih muljevcev, pojavljajo praktično na celi dolžini jame. V starejših vrtinah so te intraformacijske konglomerate s prevladujočimi klasti muljevcev napačno popisovali kot muljevce ali peščenjake. Prodniki apnencev so rožnatih, rdečih in sivih odtenkov. Klasti muljevcev so v tem delu pretežno rdečkaste barve, po obliki ploščati in lahko dosegajo velikosti blokov večmetrskih dimenzij.

6. horizont se razprostira preko celotnega odprtega dela jame vendar njegova debelina precej niha. V njem prevladujejo sivi do temnosivi debelozrnati peščenjaki, v posameznih delih sekvenc prehajajo tudi v drobnejše različke. Nad erozijskimi površinami nastopajo tudi konglomeratični peščenjaki, ki jih sestavljajo klasti črnega in sivega muljevca ter drobni kremenovi prodniki. V paleokoritih reke najdemo poleg klastov črnega muljevca še številna antracitizirana zrnca netopne organske snovi, lahko celo ostanke debel. Te intraformacijske površine so navadno kar številne in predstavljajo le manjše prekinitve v sedimentaciji med posameznimi poplavnimi obdobji prepletajoče reke v primerjavi z erozijsko diskordanco, ki ločuje karbonske in grödenske plasti.

Debelina horizonta je na skrajni SZ strani jame (blok 1) znašala 20–30 m, v naslednjih blokih 2, 3 in 4 se je ponekod lahko še povečala, v bloku 5 pa je bilo opaziti, da se je debelina tega horizonta močno zmanjšala in je peščenjak postajal zelenosiv. To se je dogajalo s tem peščenjakom tudi nad temenom zgornje gube. S to spremembo v litološki sestavi v bloku 5 je bilo povezano tudi orudenje, ki se je vleklo skorajda neprekinjeno od bloka 1 do 5, največji obseg je imelo v bloku 3. V bloku 5 pa so se z zmanjšanjem debeline sivega peščenjaka izklinjala tudi rudna telesa. Navedeni bloki so segali do nivoja 530. Tudi v nadaljevanju jame med prerezi P-16 in P-0 je nad nivojem 530 ta horizont slabo razvit, kakor se je dogodilo v bloku 5. Zanimivo je, da se v smeri proti površju ta horizont tanjša oziroma spreminja po barvi iz temnosive in sive v zelenosivo in zeleno in ga zato potem na prerezih izklinjamo (sl. 2 do 6). Ta horizont se v JV delu jame ponovno odebeli šele pod nivojem 530, pod bloki 1–5 v SZ delu jame pa je podobno razvit kakor zgoraj. Tu so v njem pogostna rudna telesa in horizont je najpomembnejši nosilec zalog uranove rude na prostoru odprte jame.

7. horizont sestavljajo zeleni in rdeči peščenjaki ter muljevci. Njihova debelina se spreminja med 15 in 35 m in se povečuje v smeri proti SV, povečanje debeline pa gre na račun zmanjševanja debeline 6. horizonta kakor smo omenili zgoraj. Proti JZ kjer postaja ta horizont vse tanjši pa opazujemo prevladovanje zelenega peščenjaka in rdečega muljevca, rdeči peščenjak pa se tanjša in izklinja. Ponekod se ti pisani klastiti lahko v celoti izklinjajo in ne ločujejo več sivih peščenjakov 6. in 8. horizonta, kar smo opazovali predvsem v zgornjih blokih (1–5) v SZ delu rudišča.

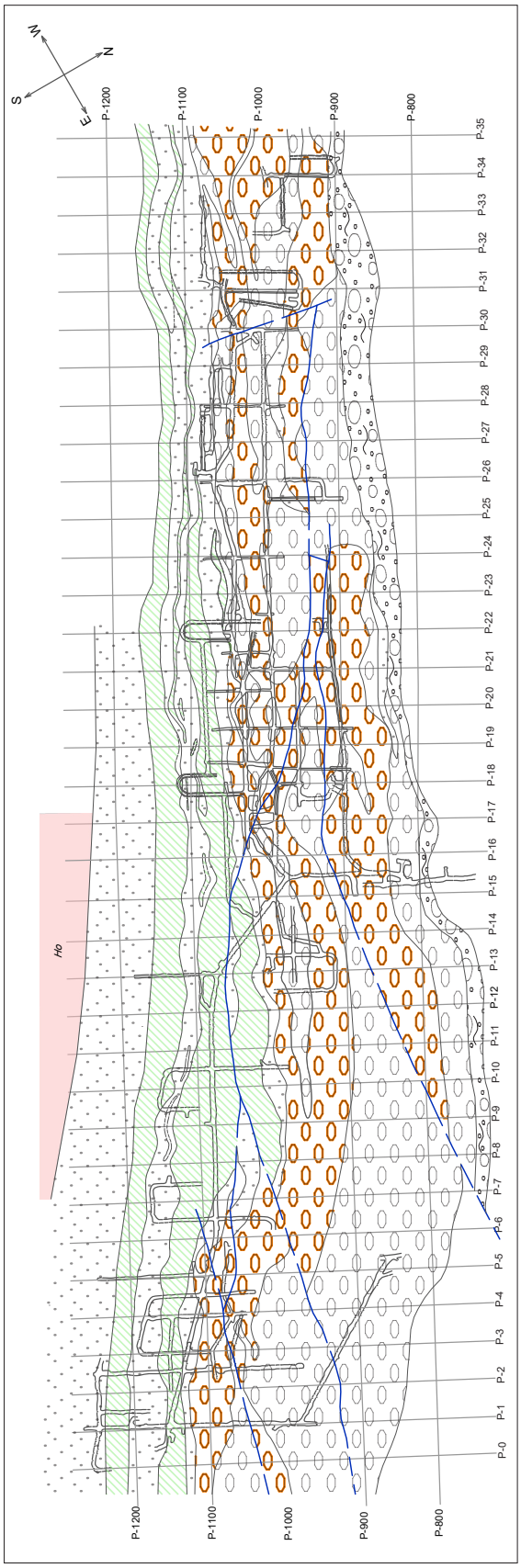

Sl. 7. Geološka karta nivoja 530.
Fig. 7. Geological map of level 530.

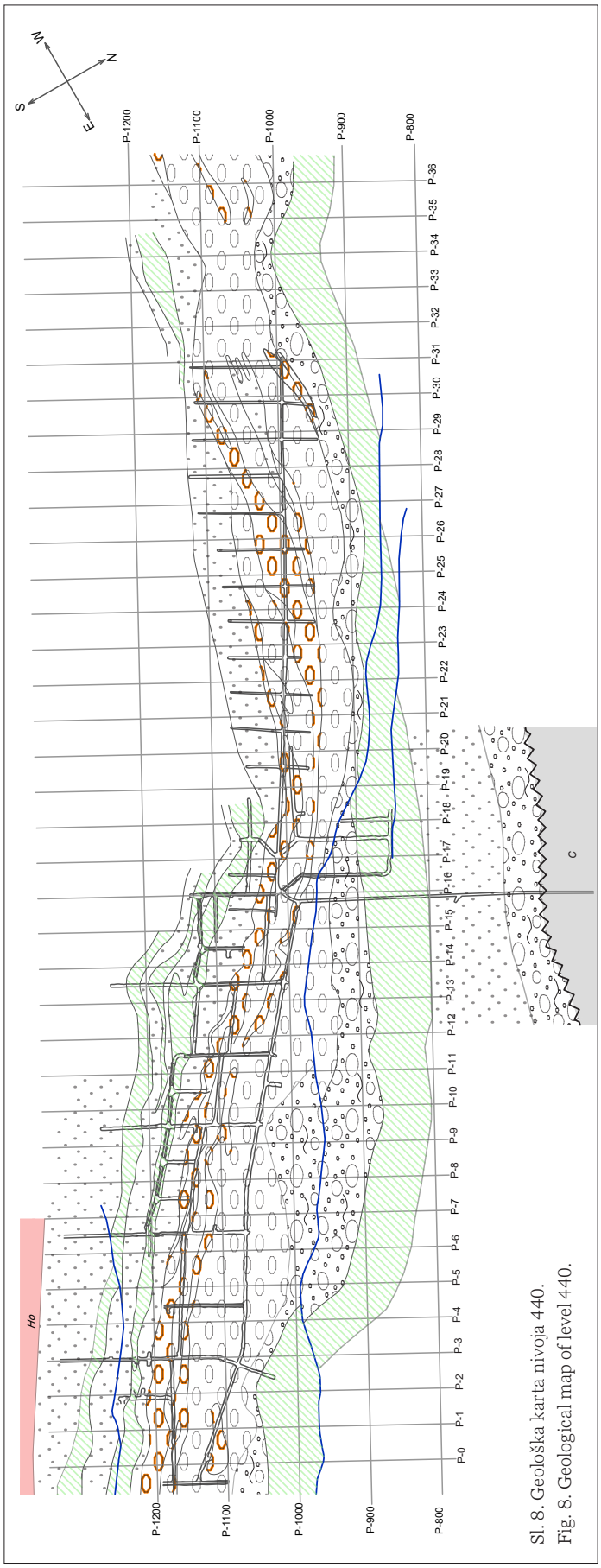

Sl. 8. Geološka karta nivoja 440.
Fig. 8. Geological map of level 440.

8. horizont označuje pojavljanje sivih do temnosivih peščenjakov v katerih dobimo ob erozijskih površinah klaste črnega ter sivega muljevca in drobce antracita, redkeje silificirana antracitna debla. Navzgor v sekvencah običajno debelozrnat peščenjak prehaja v srednjezrnatega, ob zaključku sekvenc lahko še v drobnozrnatega in muljevce. 8. horizont deli v večjem delu do 4 m debela plast zelenega peščenjaka na dva dela. Debelina horizonta je dokaj stalna in znaša skupaj okrog 30 m. V SZ delu jame je ta horizont vseboval le siromašna orudenja z uranom, proti JV pa so se tudi tu pojavljala ekonomsko zanimiva rudna telesa, ki pa so bila omejena le na spodnji del horizonta pod vmesno plastjo zelenega peščenjaka.

9. horizont je po barvi podobno razvit kot 7. horizont. Gradijo ga rdeči in zeleni muljevci ter peščenjaki s tem, da je muljevcev več kakor peščenjakov, s čimer se razlikuje od klastitov 7. horizonta. Njegova debelina znaša 20–25 m. Horizont je predstavljal krovnino rudonosne cone saj v njem, kot tudi naslednjem horizontu, ni bilo več ugotovljenih povišanih vsebnosti urana.

10. horizont je bil podrobneje raziskan šele v zadnjem letu obratovanja rudnika. Takrat so bile v JV delu jame izdelane 4 prečne proge iz katerih se je nameravalo raziskati razvoj in orudenje pod najnižjim nivojem 430. Vse proge so se pričenjale v 8. horizontu in presekale 9. in 10. horizont ter se zaključile že v rdečih muljevcih Hobovškega člena. Iz podatkov kartiranj teh prog povzemamo njihovo sestavo. Horizont se pričenja z erozijsko površino nad katero leži sivi debelozrnati do srednjezrnati peščenjak s klasti črnega muljevca, ki hitro prevlada, v njem zasledujemo vzporedno in navzkrižno plastovitost. Naslednja sekvenca se ponovno pričenja s sivim debelozrnatim peščenjakom s klasti muljevca, drobci organske snovi in piritnimi gomolji. Navzgor se ponovijo srednjezrnati in nato že drobnozrnati peščenjaki, barve so sive do temnosive zaradi pogostih drobcev organske snovi (antracita). Na drobnozrnatem peščenjaku je bila v prerezu P-0 odložena še 3–5 m debela plast zelenega drobnozrnatega peščenjaka z rožnatimi karbonatnimi konkrecijami. V ostalih prerezih je bilo takih zelenih vložkov še več in imajo lečast značaj. Do konca horizonta je bilo zatem odloženih še več sekvenc debelih od 2–6 m, v njih prevladujejo sivi drobnozrnati peščenjaki, ki prehajajo že v muljevce. Poleg antracitnih drobcev je značilno pojavljanje piritnih gomoljev, podrobnejše mineraloške preiskave bi zanesljivo pokazale še prisotnost bakrovih mineralov, ki jih v tem delu Brebovniškega člena omenjata, po podatkih površinskih vrtin, Skaberne (1995) in Mlakar (2000). V ostali jami je bila v tem horizontu najdena mineralizacija z bakrovimi minerali le na enem mestu (prečnik H-35). Skupna debelina horizonta se spreminja med 25 in 55 m.

Skupna debelina Brebovniškega člena je največja prav v osrednjem delu jame okrog prereza P-16 (sl. 14), kjer imamo največ podatkov. Zaradi gubanja so sicer debeline posameznih horizontov, kot tudi skupno, navidezno povečane, vendar menimo, da je prava debelina podobna, kakor sta jo navajala že Budkovič (1980) in Skaberne (1995, 2000, 2002) in znaša 410 m.

Razvoj Brebovniškega člena v JV podaljšku

V nadaljevanju jamske zgradbe proti JV se podobne razmere, kakor smo jih opisali na prostoru odprte jame še nadaljujejo, vendar opazujemo postopno zmanjševanje debelin posameznih členov predvsem pa skupne debeline in še izklinjanje posameznih horizontov. V mejnem prerezu P-0 znaša skupna debelina horizontov Brebovniškega člena še 300 m, dokazano razviti pa so še vsi horizonti.

Kot reperni horizont se je v rudišču predvsem pa pri površinskih raziskavah izdvajal 5. horizont, ki je bil prevladujoče konglomeratno razvit. Na prostoru jame je bil največkrat zastopan z dvema nivojema sivega in dvema nivojema pisanega konglomerata ter po novem na bazi z nivojem intraformacijskega in apnenega konglomerata. Proti JV se takoj za prerezom P-0 izklini najprej spodnja plast pisanega konglomerata, ki se je sicer tanjšala in prekinjala že v zadnjih jamskih prerezih, po 1000 m pa še druga (v prerezu P-61 in naprej ga ni več, ga pa že pred tem ni bilo v posameznih vrtinah). V tem delu se na zadnjih prerezih z orudenjem tudi zmanjša njegova debelina s 50–70 na 40–10 m. Že pred tem se je izklinil 3. horizont (pisani drobnozrnati klastiti) oziroma v podaljških drugi horizont postaja bolj pestro razvit, s sivimi, različno zrnatimi peščenjaki in muljevci, ki nadomeščajo pisane klastite 3. horizonta. V njih se nahajajo tudi pojavi orudenja. Prvi horizont je večinoma še povsod razvit, značilen je po nastopanju tanjših slojev konglomerata, tudi z apnenimi prodniki, pa tudi različno obarvanimi muljevci, kar smo poznali že na prostoru prereza P-16 oziroma podkopov P-10 in P-11.

Nad konglomeratnim horizontom se med prerezom P-0 in prerezom 58 (sl. 9) začne pojavljati, med 5 in 6. horizontom, nivo rdečkastih in zelenih peščenjakov, kar se je ponekod ugotavljalo že tudi na območju obstoječe jame. Za horizonte nad konglomeratom je v JV nadaljevanju rudišča tudi značilno, da se zmanjšuje njihova debelina in da se v njih ponekod odebelijo vložki rdečkastih in zelenih

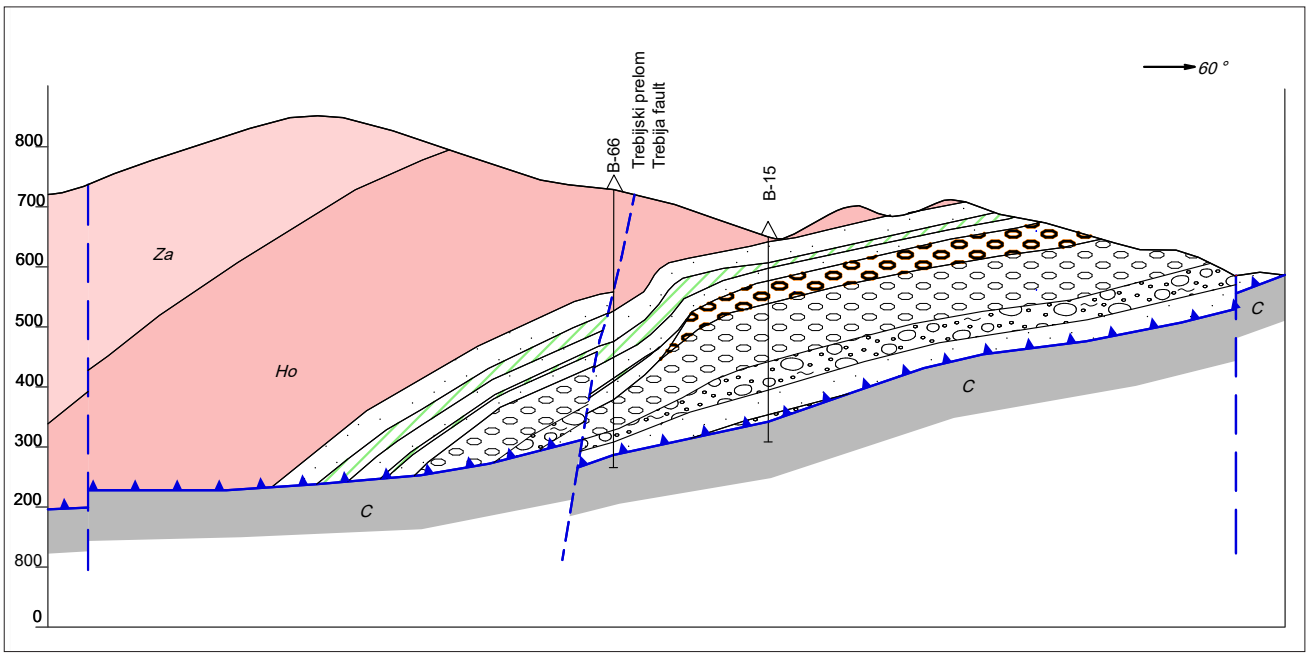

Sl. 9. Geološki prečni prerez 58 (dopolnjeno po I. Mlakarju).
Fig. 9. Geological cross section 58 (supplemented after I. Mlakar, 2000).

peščenjakov ter muljevcev, ki lahko celo presegajo debelino sivih. Debeline sicer znašajo v začetku od nekaj 10 m za posamezen horizont do samo nekaj metrov v zadnjih orudenih prerezih 65 in 66. Od prereza 60 do 64 je še značilno da se v 8. in 10. horizontu pojavljajo tudi debelozrnati in celo konglomeratični peščenjaki, kar na prostoru jame ni bilo poznano. Tam smo opažali striktno zmanjševanje velikosti zrn v mlajših horizontih nad 5. konglomeratnim. Medtem ko so v 6. horizontu prevladovali debelozrnati peščenjaki, na začetku sekvenc tudi konglomeratični peščenjaki s klasti muljevcev in drobnimi prodniki so bili v 8. horizontu na bazi sekvenc še odloženi debelozrnati peščenjaki tudi še s klasti muljevcev, sicer pa so že prevladovali srednjezrnati peščenjaki. V 10. horizontu so prevladovali srednje in drobnozrnati peščenjaki ter muljevci. Pojav debelozrnatih in konglomeratičnih peščenjakov v 8. in 10. horizontu v južnih podaljških, lahko razlagamo le z bočnim transportom. Na območju Golega vrha, kjer so zadnji prerezi s pojavi orudenja, se zmanjša debelina Brebovniškega člena na 50 m. Naprej se ta člen po geološki karti še nadaljuje na dolžini 3000 m, vendar se njegova debelina in širina še naprej zmanjšujeta in zaradi odsotnosti orudenja z uranom za podrobnejše raziskave ni bil več zanimiv.

Širina ohranjenega Brebovniškega člena znaša na območju Golega vrha še 900 m in se potem skupaj z debelino še naprej zmanjšuje, oz. po 3 km izklini ali pa je odrezan ob Sovodenjskem prelomu. Na drugo stran proti odprti jami se širina ohranjenega Brebovniškega člena povečuje in znaša v prerezu P-0 vsaj 1300 m. Do prereza P-14, kjer se pričenja jamska zgradba gubati, se taka širina ohranja. Prvotno je bila še večja vendar so bile te plasti na SV strani, torej proti površini, v preteklosti že deloma erodirane. Proti SZ se potem ohranjena širina zaradi nagubanosti lahko celo povečuje vendar so podatki v globino pod nivojem 430 zelo redki. S približno izravnavo gub smo dokazano širino ocenili na 900 m lahko pa znaša do 1200 m. Zaradi redkih podatkov pod nivojem 440 v JZ smeri rudišča, podrobnejše razmere v to smer niso poznane, vendar po podatkih razvoja 5. konglomeratnega horizonta vemo, da se le-ta v to smer izklinja (najprej pisani konglomerat) kar kaže na to, da se bodo zaključevali tudi ostali horizonti oziroma je bila tolikšna širina rečne doline, kjer so se odlagali njeni nanosi. Ker se debelina tega horizonta zmanjšuje tako v SV kot JZ smeri lahko rečemo, da je v celoti ohranjen osrednji del doline z največjo debelino konglomeratov. Obrobni del doline pa je deloma erodiran na SV strani, oziroma mestoma tektonsko odrezan na JZ strani.

Značilnosti Brebovniškega člena v SZ nadaljevanju

Tudi za profilom P-37, ki je mejni prerez v SZ smeri na prostoru jame, se Brebovniški člen še nadaljuje. Vendar smo že pri poskusnem odkopavanju v bloku 1 opazili, da se je rudonosni 6. horizont med P-35a in P-37 še pojavljal vendar v njem ni bilo več ekonomsko zanimivega orudenja. Pred

tem sklenjeno rudno telo se je začelo tanjšati, izklinjati in zmanjševala se je njegova vsebnost. Na oko je bilo opaziti, da so peščenjaki 6. horizonta, kot glavni nosilci orudenja v tem bloku, prehajali iz temnosivih do sivih odtenkov v zelenkastosive (Čadež, 2023). Zelenosivi in rjavkasti odtenki so potem značilni za kamnine Brebovniškega člena v severozahodnem nadaljevanju. V osrednjem delu jame in tudi južnem podaljšku je značilno često prevladovanje sivih in temnosivih različkov na katere je potem vezano tudi orudenje z uranom. Sivi in temnosivi različki peščenjakov se sicer pojavljajo tudi v nekaterih delih v SZ nadaljevanju jame saj so bili v njih kartirani tudi drobci in celo debla organske snovi, katerih prisotnost v veliki meri povzroča temno obarvanost. Z njimi je povezan nastanek redukcijskega okolja (Drovenik et al., 1980 ; Dolenec, 1983 ; Palinkaš, 1986; Skaberne, 1995), ki je na prostoru jame in v južnih podaljških vodilo do obarjanja uranilnih kompleksov in nastanka rudnih teles, v SZ nadaljevanju teh istih členov pa je le ponekod prihajalo do šibkih uranskih mineralizacij. Zaradi gubanja in nastanka nariva v SZ zgornjem delu jame, o čemer bomo več pisali v naslednjem poglavju, so plasti v tem delu medsebojno ločene še z več narivnimi enotami nižjega reda, kar onemogoča podrobnejše spremljanje horizontov v severnem nadaljevanju saj so bile kamnine marsikje močno tektonsko pregnetene. Poleg spremembe barve sivih klastitov je druga pomembna značilnost tega prostora še izklinjanje pisanih konglomeratov. V zadnjem prerezu odprte jame (P-37) so pisani konglomerati nastopali v dveh slojih nad sivimi s tem, da se je spodnji izklinjal malo pod nivojem 500, zgornji, ki leži pod 6. horizontom pa se nadaljuje še pod nivojem 400. Na njih so bili zelenosivi debelozrnati peščenjaki 6. horizonta, ki so le poredko vsebovali še tanjše leče siromašnega orudenja z uranom. V nadaljevanju se plast pisanega konglomerata reducira na leče. Podobno smo opazovali na prostoru jame že v zadnjih prerezih na spodnjem nivoju 440, dočim je bil ta horizont na višjih nivojih še enovit. Po podatkih vrtin so v SZ nadaljevanju posamezne vrtine imele, med prevladujočimi zelenosivimi in rjavosivimi konglomerati, še posamezne leče pisanih konglomeratov. Tako so bili kartirani pisani konglomerati še v vrtinah B-21, B-49, B-51, B-96 ter B-91 najdlje proti zahodu (profil 41, sl. 12), vse ostale vrtine pa jih niso ugotovile ali pa so bili opisi vrtin premalo natančni. Običajno so se v teh vrtinah pojavljali le še tanjši, nekaj meterski odseki konglomeratov s pisanimi ali rdečimi klasti. Zadnji sklenjen profil vrtin na Kovšakovem griču je bil že zanesljivo brez njih (sl. 13).

Strukturna lega plasti

Na prostoru jame je bila v sedemdesetih letih ugotovljena dvojna S struktura (Lukacs & Florjančič, 1976) in sicer v njenem SZ delu. Z nadaljnimi raziskovalnimi deli smo dokazali, da v JV delu jame in celotnih južnih podaljških grödenske plasti le malo povijajo in enotno vpadajo proti JZ pod koti 20 do 50° (sl. 3 in 4). V prerezih P-12 do P-16 (sl. 2) se postopno oblikujeta spodnja in srednja guba, v prerezih P-17 do P-20 pa še zgornja guba.

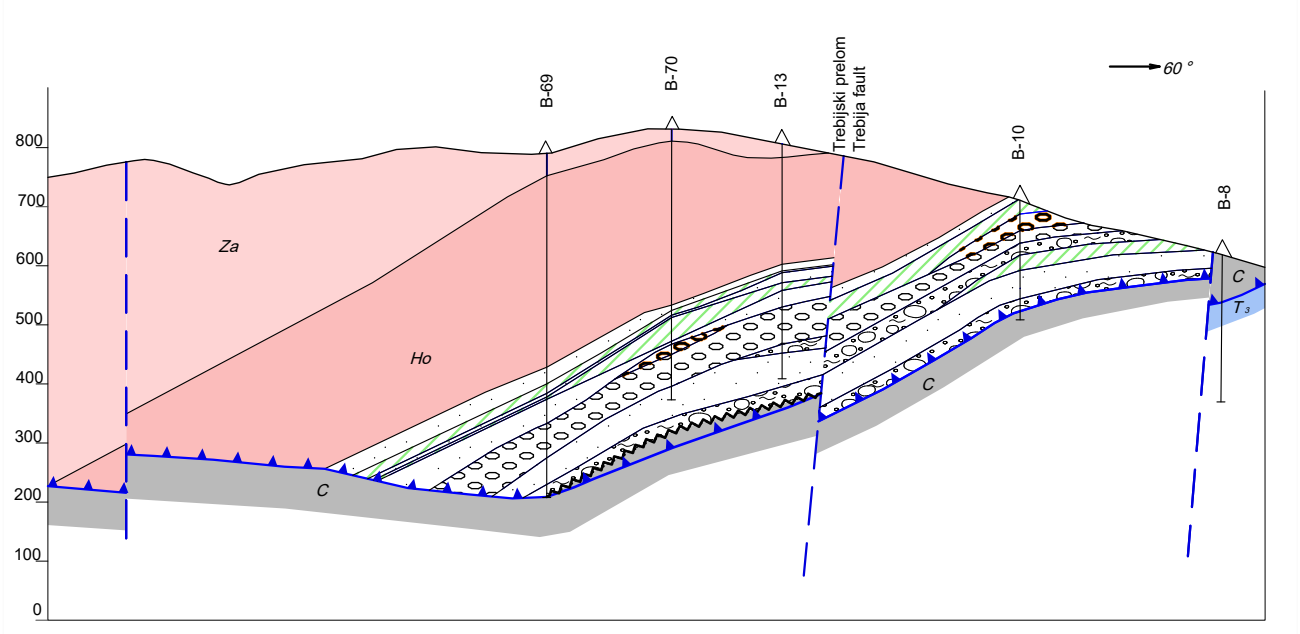

Sl. 10. Geološki prečni prerez 60 (dopolnjeno po I. Mlakarju).
Fig. 10. Geological cross section 60 (supplemented after I. Mlakar, 2000).

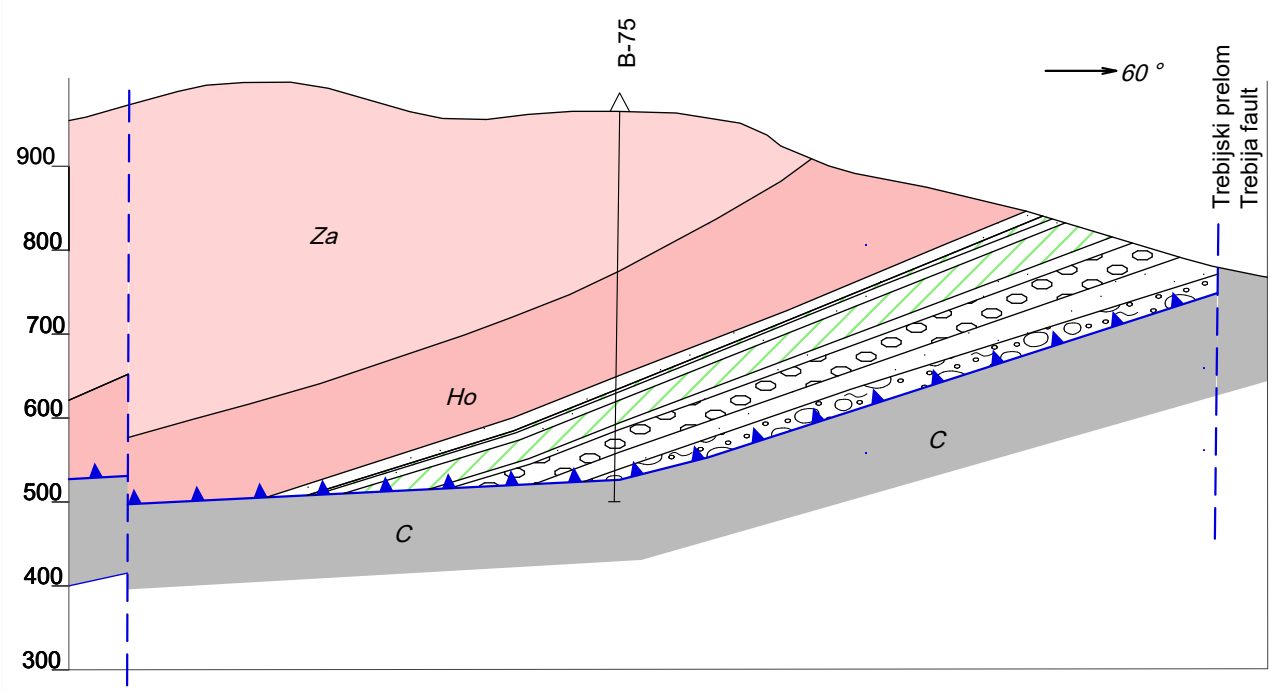

Sl. 11. Geološki prečni prerez 64 (dopolnjeno po I. Mlakarju).
Fig. 11. Geological cross section 64 (supplemented after I. Mlakar, 2000).

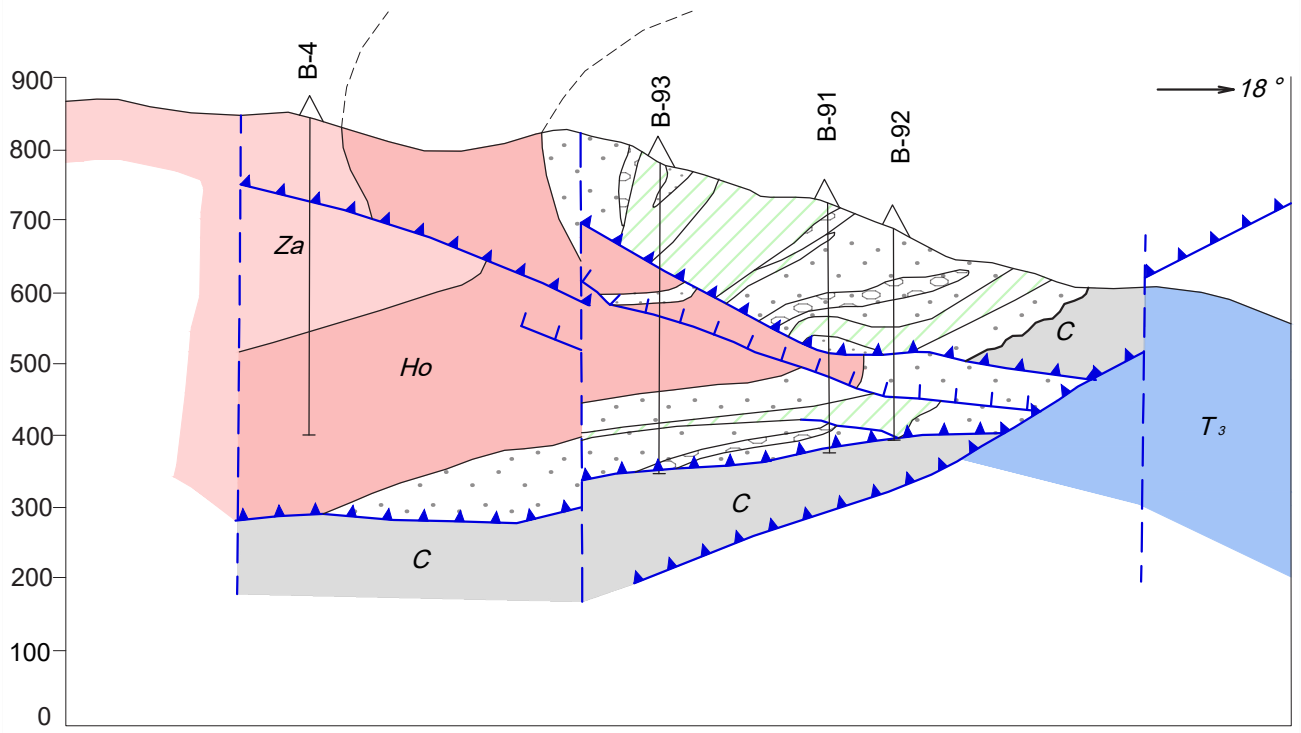

Sl. 12. Geološki prečni prerez 41 (po I. Mlakarju, 2000).
Fig. 12. Geological cross section 41 (after I. Mlakar, 2000).

Pri reintepretaciji podatkov globokih vrtin smo v zadnjih prerezih med P-27 in P-31 domnevali še pojavljanje dodatnih dveh gub pod nivojem 430 m. Že v zadnjih prerezih jamske zgradbe smo opažali vse bolj stisnjene gube, kar je še dlje proti severu vodilo v njihov prestrig in narivanje. Nastala je Kovšakova narivna enota (KNE) iz prevrnjene sinklinale in antiklinale, kakor jo je poimenoval Mlakar, njen nastanek pa sta s Placerjem pripisala posledicam narivanja Južnih Alp na Trnovski pokrov Zunanjih Dinaridov (Mlakar in Placer, 2000). V jami smo to narivno cono kartirali in potrdili na najvišje ležečih progah (sl. 5) in nekaterih jaških, ki so segali do površine. Preboje narivne cone v jaških so navadno spremljali zruški in/ali vdori vode.

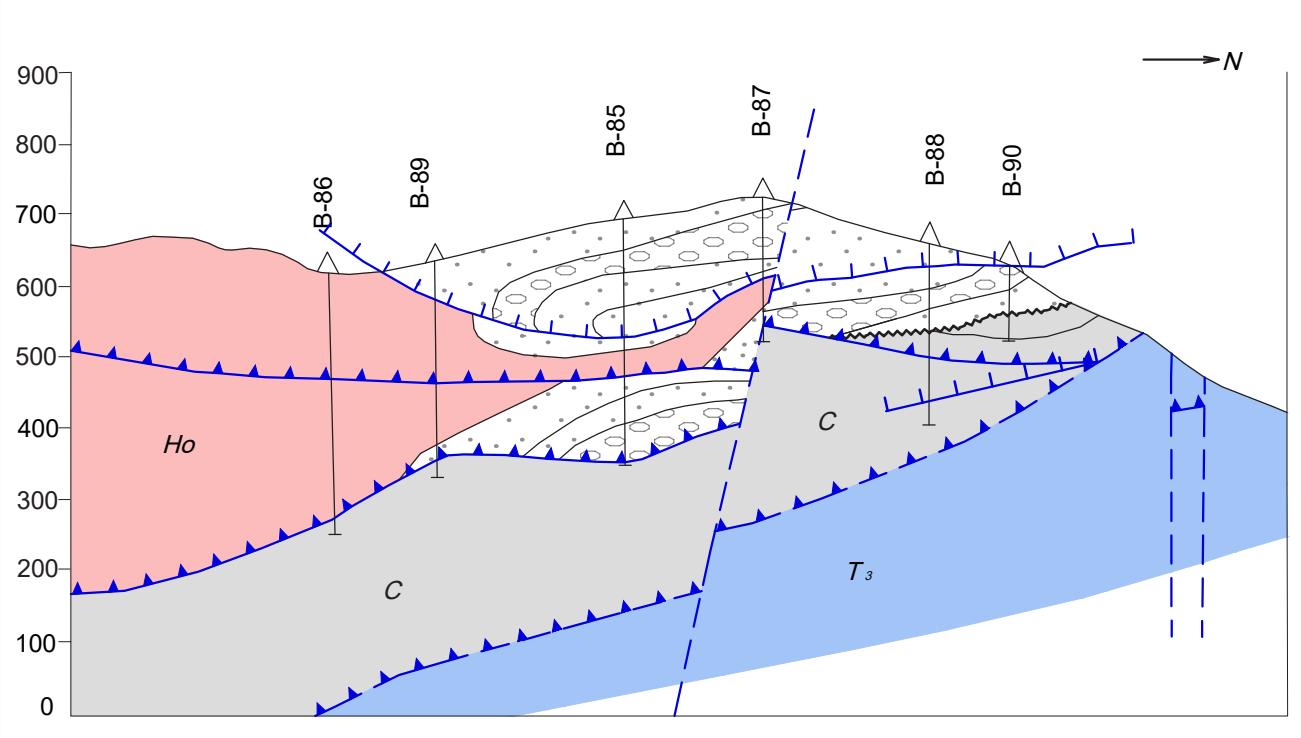

Sl. 13. Geološki prečni prerez 37 (po I. Mlakarju, 2000).
Fig. 13. Geological cross section 37 (after I. Mlakar, 2000).

Na geološki karti nivoja 440 (sl. 8) je razvidno, da v JV delu jame posamezni horizonti slemenijo približno v smeri 160–340°, med prerezi P-14 in P-20 pa postopno spreminjajo smer in za prerezom P-20 nato slemenijo v smeri 120–300°. Sprememba smeri je najizrazitejša na spodnjem nivoju, navzgor se zmanjšuje. Opazna je tudi na geoloških kartah površine (Kossmat, 1910, Grad in Ferjančič, 1976 in Mlakar, 2000). Omaljev (1967) jo je interpretiral kot zavoj reke, Mlakar in Placer (2000) pa menita, da je nastala kot posledica narivanja Julijskih Alp na Idrijsko žirovsko ozemlje. Z ugotovitvijo, da se v tem delu spreminja značaj sedimentacije (izklinjanje oziroma pojavljanje pisanih konglomeratov, ki jih je prinašal dotok iz severne do severovzhodne smeri) in da se v jami spreminja smer slemenitve teh plasti je verjetnejša razlaga, da se je na tem mestu dejansko spreminjal tok glavne reke. Pri tem je potrebno upoštevati še, da se po Mlakarjevi geološki karti in tektonski interpretaciji na površju pojavljajo plasti, ki pripadajo Kovšakovi narivni enoti, kar pomeni da so bile nagubane in narinjene v današnjo lego. Njihova slemenitev poteka približno v smeri vzhod-zahod. Plasti v tem delu jame, tudi spreminjajo smer iz predhodno dinarske proti smeri V-Z, vendar to z jamskimi deli ni bilo širše potrjeno, ker so se ta prej zaključila.

Med 200–2000 m JV od prereza P-0, ki zaključuje prostor odprte jame, poševno seče rudonosno strukturo Trebijski prelom (sl. 10 in 11). Trebijski prelom je edini regionalni prelom z Mlakarjeve geološke karte, ki preseče orudene grödenske sklade. Prostor jame sicer seče še Hotaveljski prelom katerega smo kartirali v podkopu P-10, a tam preseče le karnijske plasti. Oba sta subvertikalna, premik ob njima pa je le nekaj 10 m (Mlakar & Placer, 2000). Ob Hotaveljskem prelomu je bil ugotovljen vertikalni premik 40 m. Ob Trebijskem prelomu Mlakar njegov premik ocenjuje na 100 m v horizontalni in 30 m v vertikalni smeri. Na JV koncu Žirovskega vrha strukturo rudišča odreže Sovodenjski prelom, ob katerem znaša premik po Mlakarju več 100 m. Prelom pa nima vpliva na rudišče saj se orudenje v sivih plasteh Brebovniškega člena izklinja že pred tem. Vsi ostali prelomi z Mlakarjeve geološke karte površine so od orudenega dela še bolj oddaljeni.

V sami jami pa smo kartirali še nekaj prelomov, ki imajo dinarsko smer in vpadajo proti SV. Prikazani so na prečnih prerezih (sl. 2 do 6) in obzornih geoloških kartah (sl. 7 in 8). Ugotovljeni premiki so znašali od nekaj metrov do 20 m, SV krilo je bilo vedno pogreznjeno. Ti prelomi imajo podobno smer kakor klivaž, ki so ga že starejši avtorji smatrali za najizrazitejši tektonski element rudišča (Omaljev, 1967; Lukacs & Florjančič, 1976; Budkovič, 1980; Dolenec, 1983; Skaberne, 1995). Njegov vpad znaša okrog 60/40°, Placer navaja vpad 67/33°, Skaberne 64/37. Nastanek tektonske zgradbe je pojasnil Placer (Mlakar & Placer, 2000). Klivaž in ti prelomi so nastali kot posledica napetostnega stanja pri narivanju Žirovsko Trnovskega

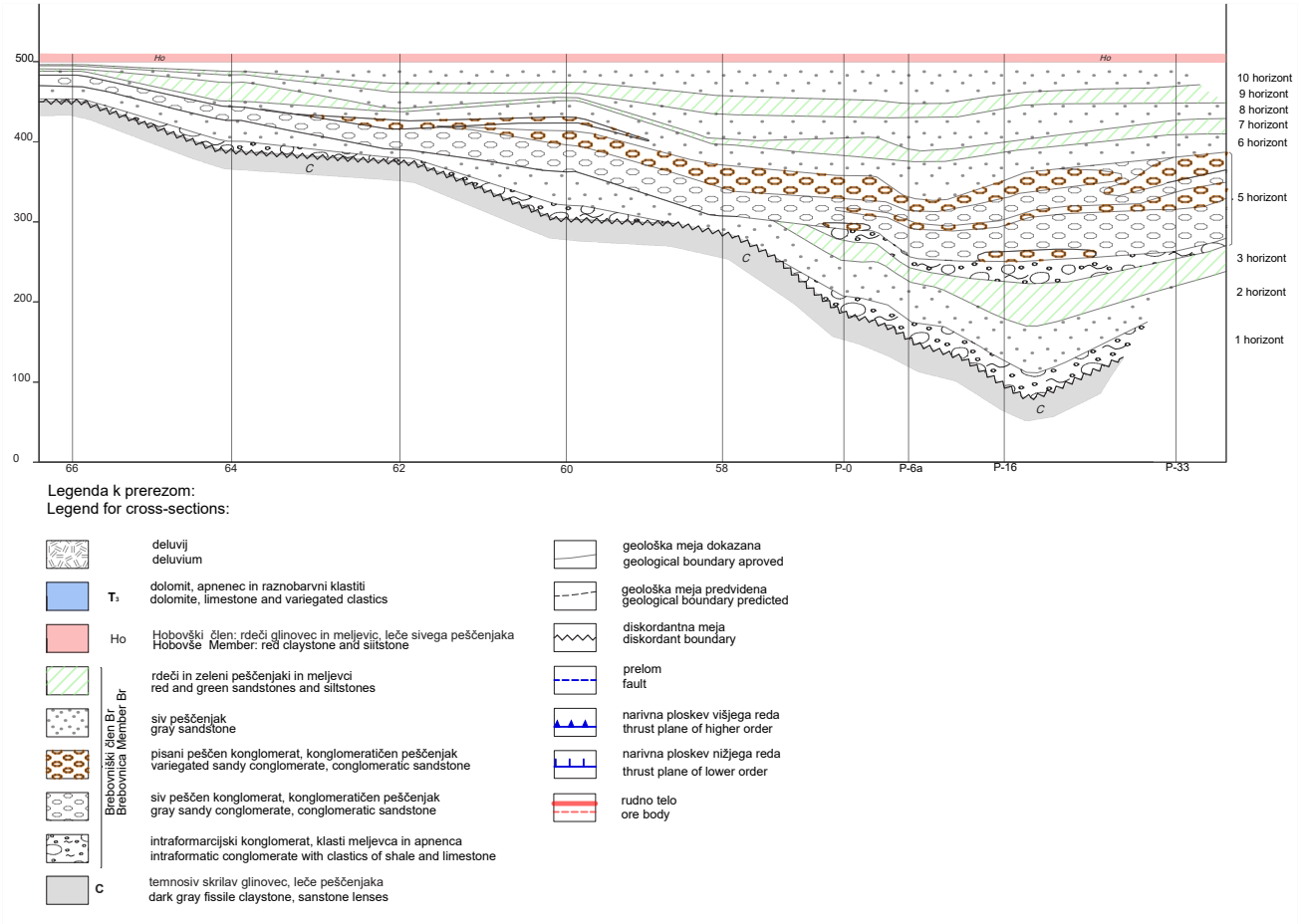

Sl. 14. Shematski vzdolžni prerez rudišča.
Fig. 14. Schematic longitudional section of the ore deposit.

ozemlja, ko se je SZ del rudišča nagubal. V bloku 1 je odkopna proga O-1/3 potekala prav po osi zgornje gube, ki je slemenila v smeri 150–330°, plasti so vpadale v smeri 60°. Nagubana zgradba v SZ delu jame je torej nastala kot posledica narivanja idrijsko trnovskega pokrova (Mlakar, 1969). V Kovšakovi narivni enoti pa plasti in gube slemenijo najprej v smeri 120–300° (profili P-21 in P-35) nakar se zelo hitro obrnejo v smer 100–280° (P-36 in P-37). Med Gorenjo vasjo in Trebijo Mlakar navaja spremenjen vpad klivažnih razpok (0/50), kar kaže na spremenjene napetostne razmere, ki pa so bile posledica narivanja Julijskih Alp na Idrijsko žirovsko ozemlje.

O orudenju

Vse raziskave rudišča so imele predvsem namen ugotoviti, kje se nahaja in pod kakšnimi zakonitostmi nastopa orudenje z uranovimi minerali. Tudi tu je bilo v preteklosti opravljenih in objavljenih kar nekaj del. Pomen in prisotnost kislih magmatskih kamnin kot izvoru urana je navajal že Drovenik s sod. (1980), še prej je Omaljev (1967) že poznal pomen organske snovi in redukcijskega okolja pri nastajanju orudenja. Največ se je z mikroskopskimi preiskavami orudenja v svojem doktoratu ukvarjal T. Dolenec (1983), ki je podal tudi razlago njegovega nastanka. Glede izvora urana je smatral, da je bodisi prihajal s kopnega z izluževanjem iz prodnikov kislih magmatskih kamnin ali pa je bilo na kopnem celo erodirano neko uransko nahajališče, kot izvor urana v podtalnici. Uranilni ioni so bili v začetni fazi transporta v oksidni obliki, v redukcijskem okolju, ki je v začetku diageneze prevladalo v horizontih z ostanki organskega materiala, lahko pa tudi z minerali glin, so se vezali in izločali v vezivu med klastičnimi zrni (Dolenec, 1983). Podobne razmere so bile dokazane v ploščastih penekonkordantnih rudiščih urana na Koloradskem platoju, le da na Žirovskem vrhu ni prišlo do obogatitev roll type. Skaberne pa je v svojem doktoratu podrobno preučil sedimentacijsko okolje pri usedanju grödenskih klastitov. Dokazal je, da so pisani konglomerati imeli drugačno sestavo in drugo izvorno območje kot sivi konglomerati in da so nastajali kot aluvialni vršaji. Njihova smer transporta naj bi bila s SV dočim je bila glavna smer transporta s SZ (Skaberne, 1995, 2000, 2002). V pisanih konglomeratih je bila oksidacijska porna voda, ki je prinašala raztopljen uran v sredine, kjer je bilo redukcijsko okolje in tam se je uran pričenjal izločati (Skaberne, 1995).

Pogled na prikazane prečne prereze in geološki karti dveh nivojev nam kaže, da je v predelu, kjer se pojavlja uransko orudenje, pomembna prisotnost pisanega konglomerata. Ta sicer ni nikoli oruden, v njem pa je bila dokazana prisotnost rdečkasto obarvanih klastov, ki pripadajo tudi kislim magmatskim kamninam. Skaberne (1995) je v njih določil kisle predornine riolite, kremenove riolite in trahite, med globočninami pa granite, ki se pojavljajo tudi v sivem polimiktnem konglomeratu, le da med njimi prevladujejo sivi in zelenkasti odtenki. Povprečne vsebnosti urana se od ultrabazičnih (0,003 ppm) in bazičnih magmatskih kamnin (0,5 ppm) povečujejo proti srednjim (1,8 ppm) in so najvišje pri kislih (3 ppm). Znotraj teh povprečnih vrednosti pa so na primer za granite z različnih lokacij navajali precejšnje razpone v njihovih povprečnih vrednostih od 1 do 32 ppm (Rossler & Lange, 1972). V tem članku se ne ukvarjamo podrobneje z orudenjem, pri preiskavi prostorskega razvoja posameznih horizontov pa smo prišli do naslednjega zaključka. Pri 18 km dolgem odseku Brebovniškega člena se pogojno ekonomsko orudenje, ki je bilo v preteklosti raziskovano in odkopavano, pojavlja le na 5,5 km njegove dolžine. V tem delu je značilno tudi nastopanje pisanega konglomerata oziroma se proti JV pisani konglomerati izklinijo že 1–2 km prej. Tok podtalnice je moral biti vzporeden toku reke od SZ proti JV saj v isto smer visijo tudi plasti. Zato se je po koncu odlaganja pisanih konglomeratov podtalnica premikala še naprej v tej smeri. Iz nje so se izločali v okolne sive klastite uranonosni minerali, ker je tu vladalo redukcijsko okolje. Izvorno območje urana so torej morale biti kisle magmatske kamnine, ki jih je v pisanih konglomeratih največ. Pri eroziji teh kislih predornin so pri oksidacijskih pogojih že površinske vode raztapljale uran, še dodatno pa so se z njim obogatile, ko so se kot podtalnica precejale skozi pisane konglomerate. Glavni tok reke zahodno od Gorenje vasi ni prinašal pisanih prodnikov, torej tudi površinske vode niso vsebovale bistveno povečanih koncentracij urana. Od Gorenje vasi proti zahodu zato nimamo ekonomsko povečanih vsebnosti urana v grödenskih klastitih. Pritok reke severno do severovzhodno od Gorenje vasi pa je prinašal pisane klaste in je tudi že sama površinska voda pritoka vsebovala povečane vsebnosti urana. SZ od odprte jame se pisani konglomerati pojavljajo le v lečasti obliki, nad njimi pa so peščenjaki 6. horizonta zelenosivo obarvani in zato tu še ni obstajalo zadostno redukcijsko okolje ugodno za obarjanje urana. V prerezu P-37 poznamo že sklenjene pasove pisanega konglomerata. S spremembo barve peščenjakov 6. horizonta okrog prereza P-36 iz zelenosive v sivo in temnosivo, kar pomeni povečan delež organske snovi in nastopanje redukcijskega okolja, se tudi pojavijo prva rudna telesa z večjo vsebnostjo in debelino, ki se nadaljujejo praktično skozi celoten prostor odprte jame in še naprej v južne podaljške. Ko se za prerezom P-0 izklini najprej spodnji nivo pisanega konglomerata in za prerezom 60 (sl. 10) še zgornji nivo pa se rudna telesa v sivih horizontih še pojavljajo. Podtalnica je torej morala še vsebovati in nositi uranilne komplekse, ki so se v redukcijskih sredinah še lahko izločali čeprav novega raztapljanja potem ni bilo več.

Sl. 15. Orudenje z uranovimi sekundarnimi minerali, odkop v bloku 4 (foto: Marko Miklavčič).

Fig. 15. Mineralization with uranium secondary minerals, stope in block 4 (photo: Marko Miklavčič).

Na prerezu P-6a (sl. 4) smo poleg litostratigrafskih enot za ponazoritev vrisali še mesta pojavljanja uranskih orudenj. Ta nastopajo večinoma vzporedno s pojavljanjem pisanega konglomerata, ki se večinoma izklinja na globinah okrog 400 m, kar je v času usedanja predstavljalo lateralno smer. Vrtanja z najnižjega prečnika na nivoju 450 m navzdol pod nivojem 400 m v peščenjakih, ki so višje orudeni, ugotavljajo le siromašne pojave orudenja (pod 300 gU3O8/t). V tem delu se pisani konglomerati izklinjajo. Tudi v severnih podaljških smo ugotavljali le pojave siromašnega orudenja. Tu se sicer S in SZ od jame manjše leče pisanega konglomerata že pojavljajo, od prereza 37 proti zahodu pa jih ni več, večji obseg in debelino pa dobijo šele s pričetkom odprtega dela jame. Zato menimo, da je bil izvor urana lahko vezan na pojavljanje pisanega konglomerata s kislimi magmatskimi kamninami, kjer se je izluževal, v ugodnih redukcijskih sredinah, ki so mejile na nivoje s pisanim konglomeratom pa izločal. Največja rudna telesa se pojavljajo v peščenjakih 6. horizonta, ki v večjem delu mejijo prav na zgornji nivo pisanega konglomerata. Rudna telesa v sivih konglomeratih so potem vezana na sive konglomeratične peščenjake ob pisanih konglomeratih, rudna telesa v peščenjakih 8. hori-

zonta pa so navadno nastala tam, kjer peščenjaki 6.horizonta niso nudili ugodnih pogojev za izločanje urana. Redukcijska podtalnica je iz 6.horizonta lahko prehajala tudi v 8. horizont na mestih, kjer se je vmesni slabše prepustni 7. horizont izklinjal. Primarno uranovo orudenje je sive barve kakor kamnina zato s prostim očesom ni vidno. V zgornjih delih rudišča pa je bila ruda že oksidirana, sekundarni uranovi minerali so bili pestrih pisanih barv in so nazorno kazali na orudena mesta (sl. 15).

Zahvala

Strokovni pregled članka je opravil dr. Dragomir Skaberne. Za njegove pripombe se mu najlepše zahvaljujeva. Grafične priloge je izdelala Maryna Malova za kar se ji prav tako lepo zahvaljujeva.

Literatura

Budkovič, T. 1980: Sedimentološka kontrola uranove rude na Žirovskem vrhu. Geologija, 23/2: 221–226.

Čadež, F. 2023: Geološka spremljava poskusnega odkopa uranove rude na Žirovskem vrhu. Geologija, 66/1: 73–85. https://doi.org/10.5474/geologija.2023.002

Dolenec, T. 1983: Nastanek uranovega rudišča Žirovski vrh. Doktorska disertacija. Univerza v Ljubljani, Ljubljana: 2 zv. 287 str. + 48 tabel.

Drovenik, M., Pleničar, M. & Drovenik, F. 1980: Nastanek rudišč v Sloveniji. Geologija, 23/1: 1–157.

Grad, K. & Ferjančič, L. 1974: Osnovna geološka karta 1:100000 List Kranj. Zvezni geološki zavod, Beograd.

Kossmat, F. 1910: Erlauterungen zur Geologische Karte Bischoflack-Idria, Wien.

Lukacs, E. & Florjančič, A.P. 1974: Uranium ore deposites in the Permian sediments of Northwest Yugoslavia. Formation of Uranium Ore Deposites, Proceedings of a Symposium, Athens, 6–10 May 1974, International Atomic Energy Agency, Wienna.

Marinković, P. 1961: Radiometrijska prospekcija i geološko kartiranje u oblasti Žirovski vrh 1961. godine. Fond strokovne dokumentacije Geoinstituta, Beograd.

Mlakar, I. 1969: Krovna zgradba idrijsko žirovskega ozemlja. Geologija, 12: 5–72.

Mlakar, I. & Placer, L. 2000: Geološka zgradba Žirovskega vrha in okolice. In: Florjančič, A.P. (ed.): Rudnik urana Žirovski vrh, 34–45.

Omaljev, V. 1967: Razvoj gredenskih slojeva i uranove mineralizacije u ležištu urana Žirovski vrh. Radovi IGRI, 3: 33–65.

Palinkaš, L.A. 1986: Geochemical facies analysis of gröden sediments and ore forming processes in Žirovski vrh uranium mine, Slovenia, Yugoslavia. Acta Geologica, Jugosl. akad. znan. i umjet., 16/2: 43–82.

Rössler, H.J. & Lange, H. 1972: Geochemical Tables. Edition Leipzig, Leipzig.

Skaberne, D. 1995: Sedimentacijski in postsedimentacijski razvoj grödenske formacije med Cerknim in Žirovskim vrhom. Doktorska di-sertacija. Univerza v Ljubljani, Ljubljana: 1. del 500 str., 2. del 192 str. + 46 prilog.

Skaberne, D. 2000: Sedimentacijsko okolje Brebovniškega (uranonosnega) člena. In: Florjančič, A.P. (ed.): Rudnik urana Žirovski vrh, 46–52.

Skaberne, D. 2002: Faciesi, razvoj in interpretacija sedimentacijskega okolja uranonosnega Brebovniškega člena Grödenske formacije na območju Žirovskega vrha. Geologija, 45/1: 163–188. https://doi.org/10.5474/geologija.2002.014

GEOLOGIJA 68/2, 269-286, Ljubljana 2025

https://doi.org/10.5474/geologija.2025.012

Article

Petrography and geothermobarometry of quartz diorite from Pohorje Mountains, Slovenia

Petrografija in geotermobarometrija kremenovega diorita s Pohorja

Tim SOTELŠEK[1], Simona JARC[1], Andreja PAJNKIHER[2] & Mirijam VRABEC[1]*

[1]University of Ljubljana, Faculty of Natural Sciences and Engineering, Department of Geology, Aškerčeva cesta 12, SI-1000 Ljubljana, Slovenia; e-mail: tim.sotelsek@ntf.uni-lj.si; simona.jarc@ntf.uni-lj.si;
*corresponding author: mirijam.vrabec@ntf.uni-lj.si
[2]ELEA IC projektiranje in svetovanje, Dunajska cesta 21, SI-1000 Ljubljana, Slovenia; e-mail: andreja.pajnkiher@gmail.com

Prejeto / Received 5. 9. 2025; Sprejeto / Accepted 21. 11. 2025; Objavljeno na spletu / Published online 10. 12. 2025

Key words: quartz diorite, "cizlakite", petrography, clinopyroxene geothermobarometry, amphibole geothermobaromery, amphibole–plagioclase thermometry, Pohorje Mountains
Ključne besede: kremenov diorit, "čizlakit", petrografija, klinopiroksenova geotermobarometrija, amfibolova geobarometrija, amfibol–plagioklaz termometrija, Pohorje

Abstract

The mineral composition and pressure–temperature conditions of Pohorje quartz diorite were investigated to reconstruct crystallization sequence and integrate the results with previous data on the Pohorje igneous complex, providing insights into its petrogenesis. Pohorje quartz diorite has phaneritic texture and is medium- to coarse-grained. The major minerals include light green clinopyroxene, dark green amphiboles, and white feldspars; the first two give the rock its characteristic colour. The proportion of dark- to light-colored minerals is approximately 4:1. Clinopyroxene predominates and correspond to diopside (X_{Ca} = 0.47–0.51, X_{Mg} = 0.41–0.49, X_{Fe} = 0.05–0.09). Amphiboles are Ca-amphiboles and are divided into two types: Type I amphiboles occur as single grains with distinctive core and rim zones, whereas Type II amphiboles replace clinopyroxene grains. Type I amphibole cores are classified as magnesiohornblende, tschermakite, edenite, pargasite, or magnesiohastingsite; Type I amphibole rims are classified as magnesiohornblende and actinolite; and Type II amphiboles are classified as magnesiohornblende. The dominant feldspars are oligoclase to andesine (X_{Ab} = 0.61–0.73), often replaced by potassium feldspar orthoclase. Minor minerals include quartz, biotite group minerals, apatite group minerals, titanite, epidote group minerals (allanite), and magnetite, while secondary minerals comprise chlorite group minerals and calcite. Various thermometers and barometers were applied to reconstruct the crystallization history of the quartz diorite and link it to the evolution of the host granodiorite intrusion. Thermobarometric data indicate that clinopyroxene in the quartz diorite, which is considered the earliest cumulate product from basaltic melts, crystallized under the highest P–T conditions (840–905 °C; 6.70–7.70 kbar), consistent with petrographic evidence. Subsequent crystallization of Type I amphibole cores occurred at 675–730 °C and 6.45–6.50 kbar, conditions comparable to those of the less evolved granodiorite, suggesting coeval formation. Later stages involved the formation of Type I amphibole rims at 585–640 °C and ~2.00 kbar, Type II amphiboles at 615–680 °C and 2.59–2.79 kbar, and biotites at 670–690 °C, associated with the emplacement of more evolved granodiorite at shallower crustal levels.

Izvleček

Proučili smo mineralno sestavo in tlačno-temperaturne pogoje nastanka pohorskega kremenovega diorita, z namenom določitve zaporedja kristalizacije posameznih mineralov. Dobljene rezultate smo povezali z objavljenimi podatki o pohorski granodioritni intruziji, kar omogoča dodaten vpogled v petrogenzo kremenovega diorita. Pohorski kremenov diorit ima faneritsko strukturo in je srednje do debelozrnat. Glavne minerale predstavljajo svetlozeleni klinopirokseni in temnozeleni amfiboli, ki dajo kamnini značilno barvo, ter beli glinenci. Razmerje med temnimi in svetlimi minerali je približno 4:1. V kamnini prevladuje klinopiroksen, ki ustreza diopsidu (X_{Ca} = 0,47–0,51, X_{Mg} = 0,41–0,49, X_{Fe} = 0,05–0,09). Amfiboli so Ca-amfiboli in jih lahko razdelimo na dve vrsti: amfiboli tipa I se pojavljajo kot posamezna zrna z značilno različno sestavo jedra in robnih delov, medtem ko amfiboli tipa II nadomeščajo zrna klinopiroksenov. Jedra amfibolov tipa I pripadajo magnezijski-rogovači, tschermakitu, edenitu, pargasitu ali magneziohastingsitu; robni deli amfibolov tipa I pripadajo magnezijski-rogovači in aktinolitu; amfiboli tipa II so po klasifikaciji vsi magnezijska-rogovača. Med glinenci prevladujejo plagioklazi sestave oligoklaz do andezin (X_{Ab} = 0,61–0,73), ki so pogosto nadomeščeni z ortoklazom. Med manj zastopanimi minerali se pojavljajo kremen, biotiti, apatiti, titanit, minerali epidotove skupine (allanit) in magnetit, od sekundarnih mineralov so prisotni kloriti in kalcit. Da bi rekonstruirali zgodovino kristalizacije kremenovega diorita in ga povezali z razvojem glavnega granodioritnega intruziva smo uporabili različne geotermometre in geobarometre. Rezultati geotermobarometrije kažejo, da so klinopirokseni v kremenovem dioritu, ki velja za najzgodnejši kumulat bazaltnih talin, kristalili pri najvišjih P–T pogojih (840–905 °C; 6,70–7,70 kbar), kar je skladno s petrografskimi dokazi. Sledila je kristalizacija jeder amfibolov tipa I, ki je potekala pri 675–730 °C in 6,45–6,50 kbar, kar ustreza pogojem kristalizacije manj razvitega granodiorita in nakazuje njihov sočasni nastanek. Kasnejše faze so vključevale nastanek robnih delov amfibolov tipa I pri 585–640 °C in ~2,00 kbar, amfibolov tipa II pri 615–680 °C in 2,59–2,79 kbar, ter biotitov pri 670–690 °C in so povezane z intruzijo bolj razvitega granodiorita v višje nivoje skorje.

Introduction

Quartz diorite, in the past also known as "cizlakite" is an intrusive igneous rock. It consists of dark green amphiboles, light green pyroxene, white feldspars and quartz, with minor biotite group minerals (in continuation biotite), titanite, epidote group minerals (allanite), apatite group minerals (in continuation apatite), chlorite group minerals (in continuation chlorite), calcite and opaque minerals, mainly magnetite. In Slovenia, it occurs in only one location – on Pohorje, near the village of Cezlak, forming large enclave within granodiorite host rock. In the past, both granodiorite and quartz diorite were extracted. The quarry of quartz diorite had a significant economic value for the natural stone industry and at the same time represents an important natural heritage site (ARSO, 2018).

The first studies of the igneous rocks of Pohorje were carried out by Benesch (1917). He drew attention to a smaller outcrop of "green stone", analysed it and described it as quartz hornblende augite diorite, and thus classified it as diorite. Dolar-Mantuani (1935) analysed samples of quartz diorite, which were subsequently named by Nikitin & Klemen (1937) as tylaite, a rock with a transitional composition between gabbro and peridotite. Nikitin & Klemen (1937) described quartz diorite more precisely as a quartz hornblende augite diorite containing 70–80% mafic minerals (hornblende, augite, biotite, apatite, titanite) and 20–30% salic minerals (quartz, plagioclases). As the existing name was not suitable, Nikitin (1939) carried out a detailed classification and defined the rock as a separate igneous rock according to the CIPW system, which he named "cizlakite" after the village of Čizlak (now Cezlak). Rock was considered as a product of the early gravitational differentiation during crystallization of granodioritic magma (Nikitin & Klemen, 1937; Nikitin, 1939; Faninger, 1965).

Later investigations confirmed the characteristic mineral composition with dominant augite, hornblende and an anorthite component in the plagioclases between 34 and 52% (Dolar-Mantuani, 1935, 1940; Nikitin, 1939; Faninger, 1973). Faninger (1973) suggested that quartz diorite is a product of hybridisation of ultramafic magma with magma from the Pohorje main igneous rock, while Dolenec et al. (1987) concluded, that quartz diorite is classified as a gabbroic rock based on the isotopic composition of oxygen. Činč (1992) showed that quartz diorite was formed by fractional crystallization of tholeiitic magma and that the samples fall into the gabbro or quartz gabbro field according to Streckeisen's classification. Dolenec (1994) determined the Miocene age of the quartz diorite (18.7 ±0.7 Ma) using the radiometric K–Ar method, confirming that it is slightly older than granodiorite, which Nikitin (1939) had already surmised. Poli et al. (2020) claimed that mixing and fractional crystallization were responsible for the formation of rocks from the Pohorje Igneous Complex (PIC) including granodiorite, tonalite and quartz diorite. The geodynamic sequence involves mantle metasomatism, crustal thickening, and mantle melt production in response to tectonic events.

The objective of this study is to characterize the mineral composition of quartz diorite and to reconstruct the crystallization sequence and pressure–temperature conditions using optical microscopy, cold cathodoluminescence, electron microprobe analysis, and geothermobarometric calculations. The results are integrated with previously published data on the Pohorje igneous complex to provide a more comprehensive understanding of its petrogenesis.

Geological setting

Pohorje is part of the Eastern Alps, which consist of Cretaceous nappes, collectively known as the Austroalpine nappes, or Austroalpine for short. The Eastern Alps include Kobansko, Pohorje, the northern Karawanke, and Strojna. The Pohorje Mountains are bounded to the west and southwest by the Labot Fault, which separates them from the Southern Alps; to the north, the Ribnica trough separates them from the lithologically similar structures of Strojna and Kozjak; and to the east and southeast, they sink beneath the Plio–Quaternary sediments of the Pannonian Basin (Fig. 1) (Mioč, 1978; Mioč & Žnidarčič, 1989).

The sequence of Cretaceous nappes in Pohorje begins with the structurally deepest Pohorje nappe, composed of medium to high metamorphic rocks. This is followed by two further nappes, namely the first, structurally higher nappe with low-grade metamorphic rocks, mainly schists and phyllites, and the second nappe composed of clastic sedimentary rocks (Janák et al., 2004). The entire sequence is overlain by Miocene sediments of the Pannonian Basin (Fodor et al., 2003, 2008).

The metamorphic rocks from the Pohorje nappe are mainly gneisses, and, less commonly, micaschist, containing lenses of eclogite, amphibolite, marble, quartzite, and a somewhat larger ultrabasic body with remnants of garnet peridotite (Hinterlechner-Ravnik, 1971, 1973; Hinterlechner-Ravnik & Moine, 1977; Hinterlechner-Ravnik

et al., 1991a, b) (Fig. 1a). These rocks underwent intracontinental subduction during the Cretaceous orogeny, descending to depths over 100 km (Janák et al., 2004). At these depths, they experienced ultrahigh pressure metamorphic conditions at pressures up to 4.0 GPa and temperatures of 750–940 °C (e.g., Vrabec et al., 2012; Janák et al., 2015).

The Pohorje nappe is folded into an antiform (Pohorje antiform; Kirst et al., 2010), with an axis trending east–southeast to west–northwest. Its central part is occupied by the Pohorje Igneous Complex (Poli et al., 2020), which intruded metamorphic rocks during the Miocene (ca. 18 Ma; Zupančič, 1994; Altherr et al., 1995; Fodor et al., 2008; Trajanova et al., 2008). The PIC comprises three main rock groups: (1) granodiorite, tonalite (GDT), and quartz diorite; (2) dacite dykes and stocks intruding both metamorphic rocks and GDT, particularly in western Pohorje, together with porphyritic microgranodiorite (DAMG); and (3) andesitic dykes (AD), which mainly cut metamorphic rocks and less commonly GDT (Poli et al., 2020). Magmatic activity in the PIC occurred in multiple pulses (Poli et al., 2020). The first pulse (ca. 20 Ma) involved the ascent of small mafic magma batches to middle-crustal level chambers, where cumulus processes produced the quartz diorite body. During the second pulse (ca. 18 Ma, 6.2 kbar), hybridized magmas rose into middle-crustal level chambers and crystallized to form less evolved GDT that enclosed the earlier quartz diorite. Continued magma–felsic interaction during the third pulse (ca. 17 Ma, 4.2 kbar) generated more evolved GDT, with chamber depths decreasing in response to rapid uplift. The fourth pulse (ca. 16 Ma, 2–3 kbar) was characterized by magmas that evolved through mixing and fractional crystallization (MFC), ascended into subvolcanic-level chambers, and were emplaced as Ga-rich DAMG dykes and sheet-like intrusions. The fifth pulse (ca. 17 Ma) introduced small batches of mantle-derived melts into middle-crustal levels, producing dykes and crosscutting intrusions of Ga-poor DAMG. In the final stages of crystallization, residual granitic melts (~20%) intruded GDT and quartz diorite as aplitic and pegmatitic bodies, cutting the main intrusion in multiple directions; these late-stage intrusions occur both at the pluton margins and, locally, within the surrounding metamorphic rocks (Poli et al., 2020).

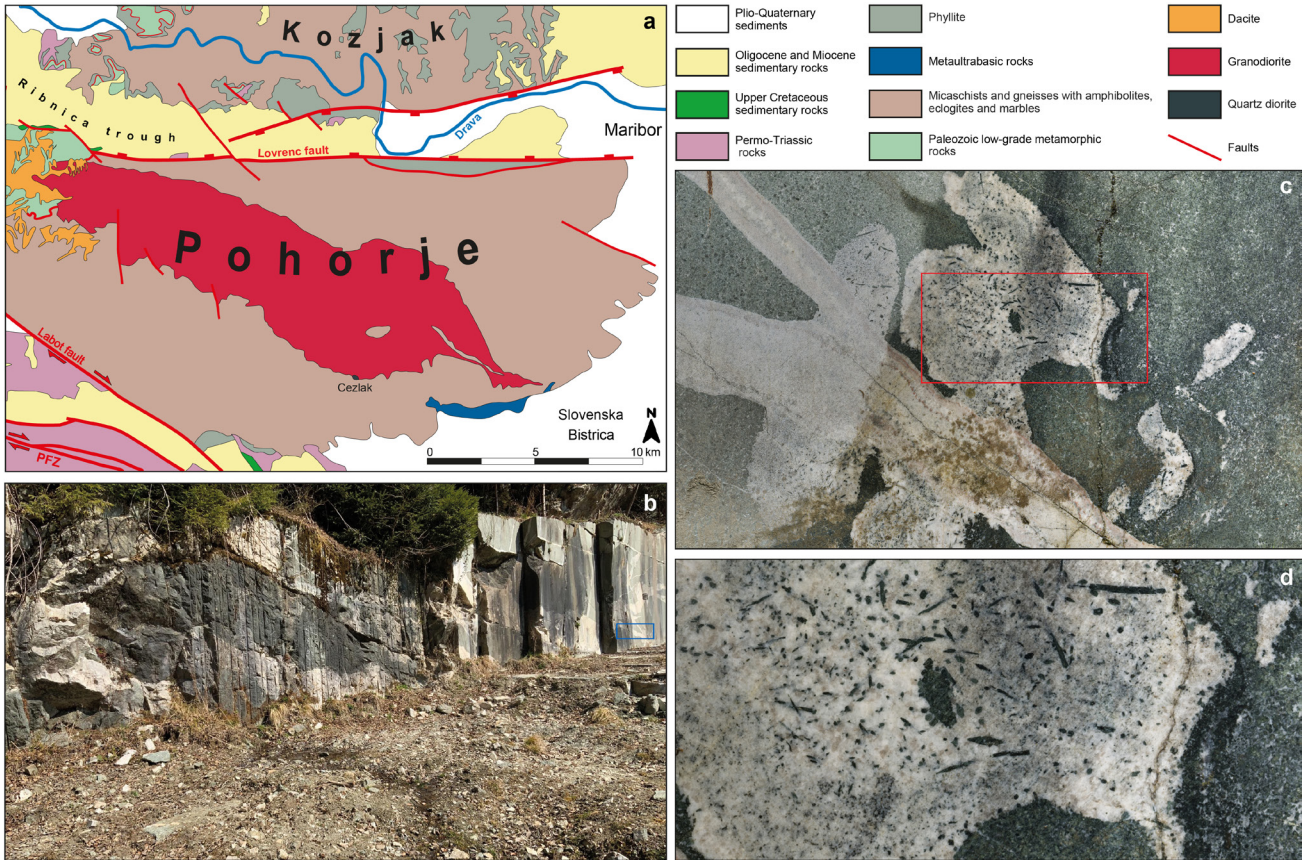

Fig. 1. (a) Simplified geological map showing the position of the quartz diorite body (modified after Mioč & Žnidarčič, 1977). (b) Present-day view of the Cezlak II quarry. (c) Close-up of a quarry wall section, where pegmatite veins clearly cutting through the quartz diorite (marked with a blue rectangle in panel b). (d) Elongated amphibole crystals (up to 5 cm) visible within the pegmatite vein (marked with a red rectangle in panel c).

Table 1. List of quartz diorite samples from Cezlak II quarry.

Sample number	Sample description	Thin section number
C1	Quartz diorite	C1-1
C2	Quartz diorite	C2-1
C3	Quartz diorite	C3-1, C3-2, C3-3, C3-4
C4	Quartz diorite in contact with pegmatite vein	C4-1
C5	Quartz diorite in contact with pegmatite vein	C5-1, C5-2
C6	Quartz diorite in contact with pegmatite vein	C6-1, C6-2
C7	Quartz diorite in contact with pegmatite vein	C7-1, C7-2, C7-3
C8	Quartz diorite in contact with pegmatite vein	C8-1, C8-2, C8-3
C9	Quartz diorite	C9-1
C10	Quartz diorite	C10-1

Sotelšek (2019) determined pressures and temperatures of granodiorite intrusion using conventional amphibole and biotite geothermobarometers. Calculated pressures decrease from southeast to northwest from 6.6 kbar to 2 kbar, suggesting that the intrusion was tilted after emplacement. Temperatures follow the same decreasing trend from 724 °C in the southeast to 670 °C in the northwest.

Materials and methods

Samples and sample preparations

Available fresh rock samples were collected in the abandoned Cezlak II quarry (Fig. 1b), from which 19 thin sections were prepared. The samples, thin sections, and corresponding labels are presented in Table 1.

Optical microscopy

Polished thin sections were examined with a Nikon Eclipse E200 optical polarising microscope. A Nikon DS-Fi1 camera and the NIS-Elements Basic Research software were used for photo documentation of individual areas under parallel and crossed polars. A method of point counting was used to determine the relative proportions between minerals in thin sections. Between 400 and 600 points were counted per sample, depending on the grain size and texture.

Optical cathodoluminescence with cold cathode

Cathodoluminescence (CL) imaging was performed on polished thin sections of selected samples in order to examine mineral textures, zoning, and phase relations. The measurements were conducted using a CITL 8200 Mk3 cold-cathode CL stage attached to an Olympus BH2 petrographic microscope. Analytical conditions were kept stable, with a vacuum of ~0.05–0.1 mbar, an accelerating voltage of 14–15 kV, and a beam current of 200–300 μA.

Images were captured using a digital camera under constant operating parameters to ensure comparability between minerals. With this method, clear distinction between potassium feldspar, plagioclases, quartz, amphiboles, and accessory phases such as apatite, was possible based on their characteristic luminescence colours. Luminescence colours were used qualitatively to recognize textural features and were processed only for brightness and contrast adjustment, without modification of the original colour information.

Electron microprobe analyses (EPMA) with wavelength dispersive spectroscopy (WDS)

Electron microprobe analyses (EPMA) with wavelength dispersive spectroscopy (WDS) were carried out using a CAMECA SX-100 microprobe, operating at an electron acceleration voltage of 15 kV, a beam current of 20 nA, and a peak counting time of 20 s. All analyses were spot measurements using an electron beam with cross-section of 5 μm. Raw counts were corrected using a PAP routine. A total of 45 amphibole grains, 30 clinopyroxene grains, 30 plagioclase grains, 20 potassium feldspar grains, and 3–5 grains of minor mineral phases were measured. Within individual grains 4–6 spot measurements were conducted.

The contents of the following oxides were measured: SiO_2, TiO_2, Al_2O_3, Cr_2O_3, Na_2O, K_2O, FeO, MnO, MgO, and CaO, using the following standards: LiF for F, albite for Na, orthoclase for Si, orthoclase for K, Al_2O_3 for Al, NaCl for Cl, wollastonite for Ca, TiO_2 for Ti, fayalite for Fe, rhodonite for Mn, forsterite for Mg, Cr for Cr, and Ni for Ni. The chemical composition of minerals — including clinopyroxene, amphiboles, plagioclases, biotite, potassium feldspar, quartz, chlorite, and

epidote group minerals — was determined on samples C1-1, C3-1, C4-1, C7-3, and C8-3.

Content of Fe^{2+} and Fe^{3+} in amphiboles and pyroxene was determined by stoichiometric calculations. The presented ferric iron content in amphiboles was estimated based on averaged normalization to 15 cations excluding Na, K ((15eNK + 15eK)/2) (Yavuz & Döner, 2017). Where needed, the normalizations were recalculated considering the required calculation steps for the specific thermobarometer. The calculation of ferric iron in pyroxene was determined as the average of Fe^{3+} content calculated using the models of Droop (1987) and Papike et al. (1974). All iron in other minerals was considered as Fe^{2+}.

Geothermobarometric calculations

Pressures and temperatures are key parameters for determining the emplacement sequence of plutons. To constrain the pressure and temperature conditions of quartz diorite crystallization, we applied several geothermobarometers, which are listed in Table 2.

For geothermobarometric calculations involving amphiboles, understanding the specific site-related reactions within the amphibole structure can provide valuable insight. A substitution analysis is commonly used to check for the major substitution types. A Tschermak molecule substitution is thought to be a function of temperature and pressure (Anderson and Smith, 1995; Hammarston and Zen, 1986; Helz, 1982). Al-Tschermak exchange is pressure sensitive and can be written as $^{C}(Mg,Fe) + {}^{T}Si = {}^{VI}Al + {}^{IV}Al$, where Al in tetrahedral coordination (^{IV}Al) replaces ^{T}Si and Al in octahedral coordination (^{VI}Al) replaces Mg and Fe in C sites. Ti-Tschermak exchange is a temperature-sensitive coupled substitution, where ^{C}Ti replaces ^{B}Mg, which leads to ^{T}Si being replaced by ^{IV}Al. At higher temperatures it can be expressed as $^{B}Mg + {}^{T}Si = {}^{C}Ti + {}^{IV}Al$. Another temperature sensitive substitution is edenite substitution written as $^{A}vacancy + {}^{T}Si = {}^{A}(Na + K) + {}^{IV}Al$, where higher $^{A}(Na + K)$ is accommodated by the exchange of ^{T}Si with ^{IV}Al (Helz, 1982; Hammarstrom & Zen, 1986; Anderson & Smith, 1995). Plagioclase substitution can also play an important role in the content of ^{IV}Al in amphiboles as variations in albite and anorthite components in coexisting plagioclase can affect Al incorporation at the T site (Blundy & Holland, 1990; Holland & Blundy, 1994) and can be expressed as $^{B}Na + {}^{T}Si = {}^{B}Ca + {}^{IV}Al$.

Results

Macroscopic description

Quartz diorite has phaneritic structure and is medium- to coarse-grained with a grain size of up to 8 mm (Figure 2a,b). It is heterogeneous both in grain size and in the proportion of individual minerals. It consists of dark green amphiboles, light green pyroxene, white feldspars, and greyish quartz. Visually, the green colour dominates, which is due to the main minerals, pyroxene 4–7 mm in size, and amphiboles up to 8 mm in size. The ratio between the proportion of mafic and salic minerals determined using picture analysis of scanned polished hand specimens is about 4:1 in most cases. Samples are often intersected by pegmatite veins (Fig. 1c,d and Fig. 2c,d). The pegmatite is uniform and medium-grained with a grain size of up to 5 mm. It contains white feldspars, greyish quartz, a small amount of elongated green amphibole minerals occasionally reaching 5 cm in length, calcite and rare beryl.

Table 2. Selected geothermobarometers and their calibrations applied to calculate the P–T conditions of quartz diorite crystallization.

Geothermobarometer	Estimated uncertainty	Reference	Abbreviation
Clinopyroxene barometer	± 1.70 kbar	Nimis & Ulmer (1998)	NU98
Clinopyroxene barometer	± 1.10 kbar	Nimis (1999)	N99
Fe^{2+}–Mg exchange Clinopyroxene thermometer	Not reported	Dal Negro et al. (1982)	DN82
Fe^{2+}–Mg exchange Clinopyroxene thermometer	Not reported	Molin & Zanazzi (1991)	MZ91
Fe^{2+}–Mg exchange Clinopyroxene thermometer	Not reported	Bertrand & Mercier (1985)	BM85
Al-in-Amphibole barometer	± 0.6 kbar	Schmidt (1992)	S92
Al-in-Amphibole barometer	± 0.6 kbar	Anderson & Smith (1995)	AS96
Amphibole–Plagioclase thermometer	± 30 °C	Blundy & Holland (1990)	BH90
Amphibole–Plagioclase thermometer	± 30 °C	Holland & Blundy (1994)	HB94
Ti-in-Amphibole thermometer	± 25 °C	Otten (1984)	O84
Biotite thermometer	± 23 °C	Luhr et al. (1984)	L84
Biotite thermometer	± 24 °C	Henry et al. (2005)	H05

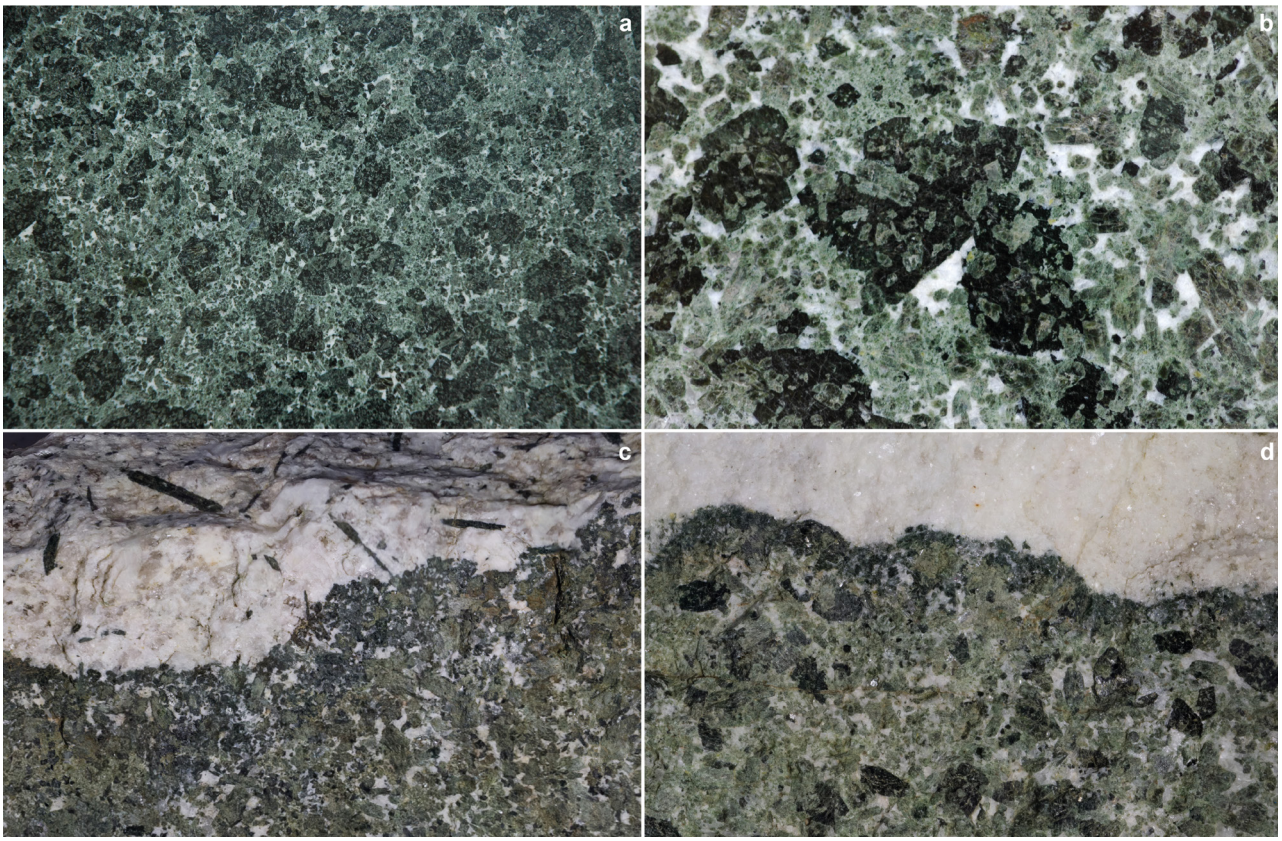

Fig. 2. Close-up of the polished surface of a quartz diorite hand specimens. (a) The prevailing green colour of the rock is a result of the combination of pale green clinopyroxene and dark green amphiboles. (b) Amphibole replacing pyroxene is forming an uralitic structure. The white minerals are feldspars, and the grey mineral (lower left corner) is quartz. (c, d) Samples are often cut by pegmatitic veins, composed of quartz, feldspars and common elongated amphibole grains. The lower border of each picture measures 12 cm.

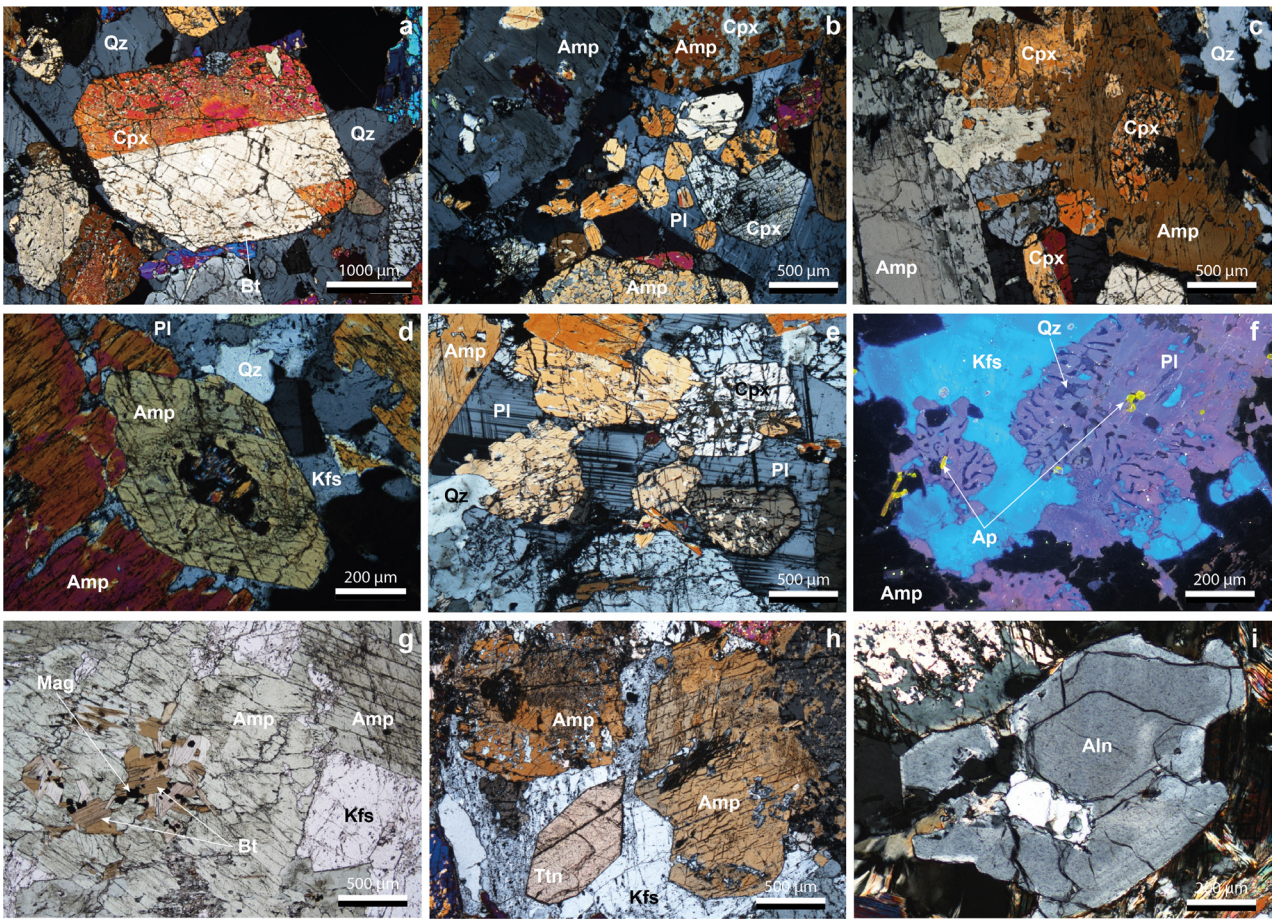

Fig. 3. (figure caption on next page)

Table 3. Representative microprobe analyses of the main mineral phases identified in quartz diorite. Analyses (in wt%) include amphiboles (Amp), clinopyroxene (Cpx), plagioclases (Pl), potassium feldspar (Kfs), biotite (Bt), chlorite (Chl), and epidote (Ep). Amp I_C – Type I amphibole core, Amp I_R – Type I amphibole rim, Amp II – Type II amphibole. Elements in the lower part of the table are calculated values per formula unit, based on the corresponding number of oxygens. An. No. denotes the analysis number.

Sample	C3-1	C4-1	C4-1	C7-3	C4-1	C7-3	C4-1	C7-3	C3-1	C4-1	C7-3	C7-3	C3-1	C1-1
Mineral	Amp I_C	Amp I_C	Amp I_R	Amp I_R	Amp II	Amp II	Cpx	Cpx	Pl	Pl	Kfs	Bt	Chl	Ep
An. No.	12	5	6	4	4	3	2	2	10	9	6	8	5	10
SiO_2	44.36	44.35	53.12	51.91	51.91	50.69	54.04	54.23	63.13	61.03	64.36	36.36	28.31	36.94
TiO_2	0.99	1.01	0.21	0.30	0.60	0.71	0.24	0.11	0.27	0.00	0.11	2.72	0.05	1.08
Al_2O_3	10.91	12.71	4.78	5.30	6.04	6.50	1.92	1.42	22.84	25.00	18.91	14.14	19.13	21.76
Cr_2O_3	0.06	0.00	0.00	0.00	0.00	0.00	0.00	0.00	0.42	0.00	0.00	0.07	0.00	1.40
FeO	13.69	9.31	6.64	7.13	6.77	7.90	3.38	3.35	0.10	0.11	0.07	21.38	18.66	10.62
MnO	0.50	0.15	0.21	0.17	0.20	0.14	0.12	0.11	0.12	0.02	0.06	0.25	0.39	0.13
MgO	11.63	14.32	18.69	17.97	18.03	17.25	15.36	15.58	0.01	0.00	0.01	11.81	19.61	0.22
CaO	12.21	12.20	12.61	12.67	12.81	12.42	24.05	24.08	4.48	6.25	0.04	0.01	0.09	23.24
Na_2O	1.17	1.80	0.49	0.49	0.56	0.55	0.39	0.32	7.52	7.92	0.88	0.07	0.02	0.01
K_2O	1.25	0.60	0.26	0.29	0.27	0.39	0.00	0.00	0.35	0.36	14.76	9.83	0.03	0.01
BaO	0.00	0.25	0.00	0.04	0.05	0.06	0.01	0.00	0.00	0.03	1.49	0.00	0.00	0.00
Total	96.77	96.70	97.01	96.27	97.23	96.62	99.49	99.18	99.22	100.73	100.67	96.63	86.29	95.41
Oxygens	23	23	23	23	23	23	6	6	8	8	8	22	28	12.5
Si	6.56	6.39	7.48	7.39	7.31	7.23	1.98	1.99	2.81	2.70	2.98	5.56	2.29	3.08
Ti	0.11	0.11	0.02	0.03	0.06	0.08	0.01	0.00	0.01	0.00	0.00	0.32	0.00	0.07
Al	1.90	2.16	0.79	0.89	1.00	1.09	0.08	0.06	1.20	1.30	1.03	2.54	1.83	2.14
Cr	0.01	0.00	0.00	0.00	0.00	0.00	0.00	0.00	0.01	0.00	0.00	0.00	0.00	0.09
Fe^{3+}	0.51	0.55	0.18	0.21	0.21	0.23	0.00	0.00	0.00	0.00	0.00	0.00	0.00	0.00
Fe^{2+}	1.18	0.58	0.63	0.64	0.61	0.72	0.10	0.10	0.00	0.00	0.00	2.74	1.26	0.74
Mn	0.06	0.02	0.03	0.02	0.02	0.02	0.00	0.00	0.00	0.00	0.00	0.04	0.03	0.01
Mg	2.56	3.07	3.92	3.82	3.79	3.67	0.84	0.85	0.00	0.00	0.00	2.70	2.37	0.03
Ca	1.93	1.88	1.90	1.93	1.93	1.90	0.94	0.95	0.21	0.30	0.00	0.00	0.01	2.08
Na	0.34	0.50	0.13	0.14	0.15	0.15	0.03	0.02	0.65	0.68	0.08	0.02	0.00	0.00
K	0.24	0.11	0.05	0.05	0.05	0.07	0.00	0.00	0.02	0.02	0.87	1.92	0.00	0.00
Ba							0.00	0.00	0.00	0.00	0.00	0.00	0.00	0.00
Total	15.41	15.38	15.14	15.12	15.15	15.15	3.99	3.99	4.91	5.00	4.97	15.82	7.79	8.24

Petrography and mineral chemistry

Under the optical microscope, the rock exhibits a heterogeneous texture. Clinopyroxene is the dominant mineral, accounting for approximately 35–40% of the rock (Fig. 3). The average grain size of clinopyroxene is 3.4 mm, with the largest crystals reaching 7.6 mm. Amphiboles are the second most abundant mineral phase, comprising up to 30% of the sample. Plagioclases makes up 10–15% of the rock, with an average grain size of 1.63 mm and maximum grains reaching 5.6 mm. Potassium feldspar (i.e., orthoclase) represents about 10% of the quartz diorite; its average grain size is 1.57 mm, with the largest grains measuring up to 5.2 mm.

Minor mineral phases include quartz, biotite, titanite, apatite, magnetite, and epidote group minerals (allanite) with average grain sizes ranging from 0.08 mm (apatite) to 1.1 mm (quartz). Together, these minerals account for 10–15% of the sample. Secondary minerals identified include chlorite, and calcite.

The remaining microscopic and microchemical characteristics are described below for individual minerals. Representative mineral analyses are presented in Table 3.

Fig. 3. Microphotographs of quartz diorite. (a) An idiomorphic, twinned clinopyroxene grain surrounded by smaller clinopyroxene and anhedral quartz grains. Sample C7-3. (b) Amphibole replaces clinopyroxene in an irregular patchy pattern (upper right). Clinopyroxene grains form small clusters enclosed in plagioclase, producing a poikilitic texture. Sample C7-3. (c) Amphibole replacing clinopyroxene completely envelops the grain, producing an uralitic texture. Sample C7-3. (d) An idiomorphic amphibole grain is surrounded by quartz, plagioclase and orthoclase grains. Sample C6-2. (e) Clinopyroxene, quartz and biotite grains enclosed in plagioclase with polysynthetic twins forming a poikilitic texture. Amphibole is visible in the upper-left corner. Sample C8-3. (f) Potassium feldspar (orthoclase) replacing plagioclase forms a myrmekitic texture at their contact. Small apatite inclusions in plagioclase are clearly visible. Sample C3-1. (g) Inclusions of biotite and magnetite occur within amphibole. Sample C5-2. (h) Idiomorphic titanite and amphibole grains surrounded by orthoclase. Sample C10-1. (i) A large allanite grain. Sample C8-3. Abbreviations: Aln–Allanite, Amp–amphiboles, Bt–biotite, Cpx–clinopyroxene, Kfs–potassium feldspar (orthoclase), Mag–magnetite, Pl–plagioclases, Qz–quartz, Ttn–titanite. Crossed polars (a–e, h, i); parallel polars (g); cathodoluminescence (f).

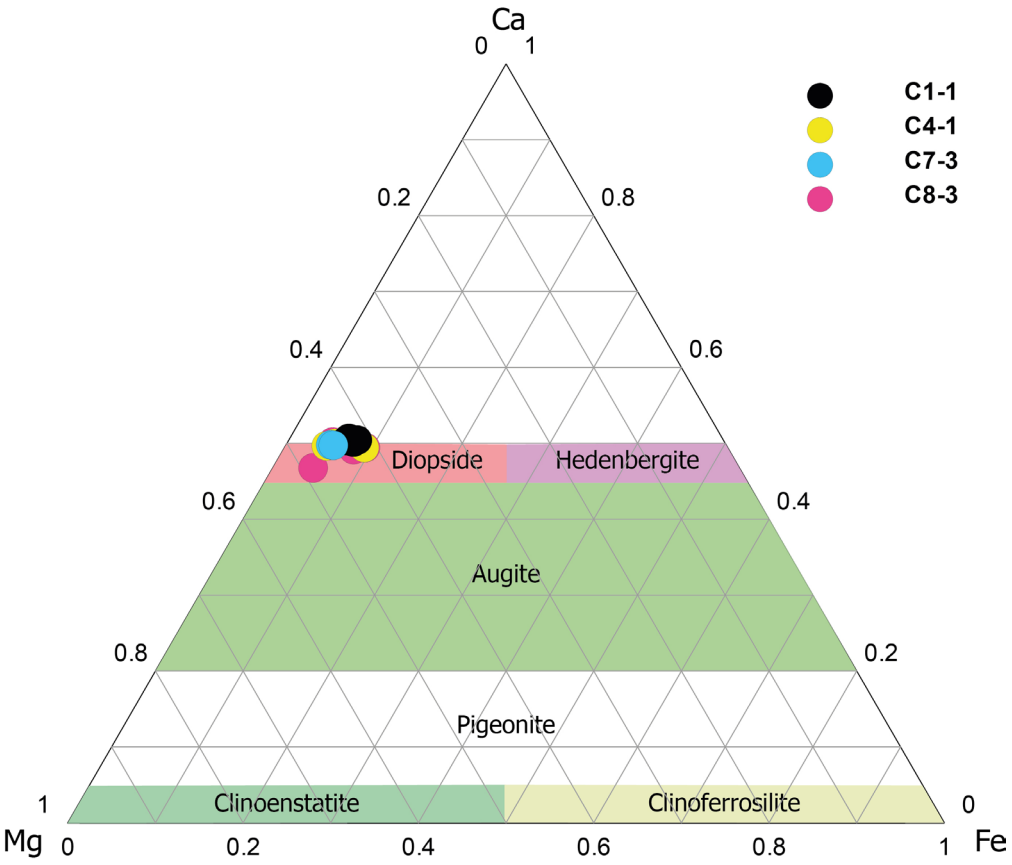

Fig. 4. Classification of clinopyroxene grains in a triangular diagram, following Poldervaart & Hess (1951).

Clinopyroxene

They occur in hypidiomorphic to idiomorphic forms. They often occur as simple twins (Fig. 3a). In some places, idiomorphic pyroxene grains are clustered in one area (Fig. 3b). They are often overgrown by amphiboles (Fig. 3c), which is a result of the uralitization process. They correspond in composition to diopside (Fig. 4) and have values of X_{Ca} = 0.47–0.51, X_{Mg} = 0.41–0.49, and X_{Fe} = 0.05–0.09.

Amphiboles

Two types of amphiboles can be distinguished. Type I amphibole occurs as xenomorphic individual grains (Fig. 5a) and only rarely form hypidiomorphic (Fig. 5b) to idiomorphic shapes (Fig. 3d). Their average size is approximately 4.15 mm. In Type I amphibole core and rim parts have slightly different composition (Fig. 5c). The average core/rim compositions are as follows: X_{Ca} = 0.31/0.30, X_{Mg} = 0.44/0.56, X_{Fe} = 0.25/0.14, and Ti = 0.11/0.03 atoms per formula unit (apfu). Biotite inclusions are very common in Type I amphibole. Type II amphibole replaces clinopyroxene grains (Figs. 3d and 5b), sometimes forming uralitic texture (Fig. 3e). Their average composition corresponds to X_{Ca} = 0.30, X_{Mg} = 0.55, X_{Fe} = 0.15, and Ti = 0.06 apfu.

According to the nomenclature of Leake et al. (1997) all amphiboles are calcic (^{B}Ca>1.5 apfu; with an average Ca content of 1.9 apfu). Type I amphibole cores are classified as magnesiohornblende, tschermakite, edenite, pargasite, or magnesiohastingsite. Type I amphibole rims are classified as magnesiohornblende and actinolite. All Type II amphibole grains belong to magnesiohornblende (Fig. 6).

Based on their Al content, amphiboles can be grouped into two distinct clusters, as shown in the graphs in Figure 7. Amphiboles with higher Al content correspond to Type I amphibole cores, while those with lower Al content belong to Type I amphibole rims and Type II amphibole grains. A positive correlation of Al in T sites with ^{A}(Na + K) for both groups indicates the importance of the edenite exchange (Fig. 7a). Only a slight positive correlation between ^{IV}Al and ^{C}Ti indicates that the Ti-Tschermak exchange substitution is not significant (Fig. 7b). Calcium at the B site shows a slightly positive correlation in the Type I amphibole rims and Type II amphibole grains and a slightly negative one in the Type I amphibole cores; however, the plagioclase exchange is insignificant in both cases (Fig. 7c). The Al-Tschermak substitution is reflected in

the relationship between ^{VI}Al and ^{IV}Al and shows a good positive correlation in the Type I amphibole rims and Type II amphibole grains. In the Type I amphibole cores, however, no correlation is observed (Fig. 7d).

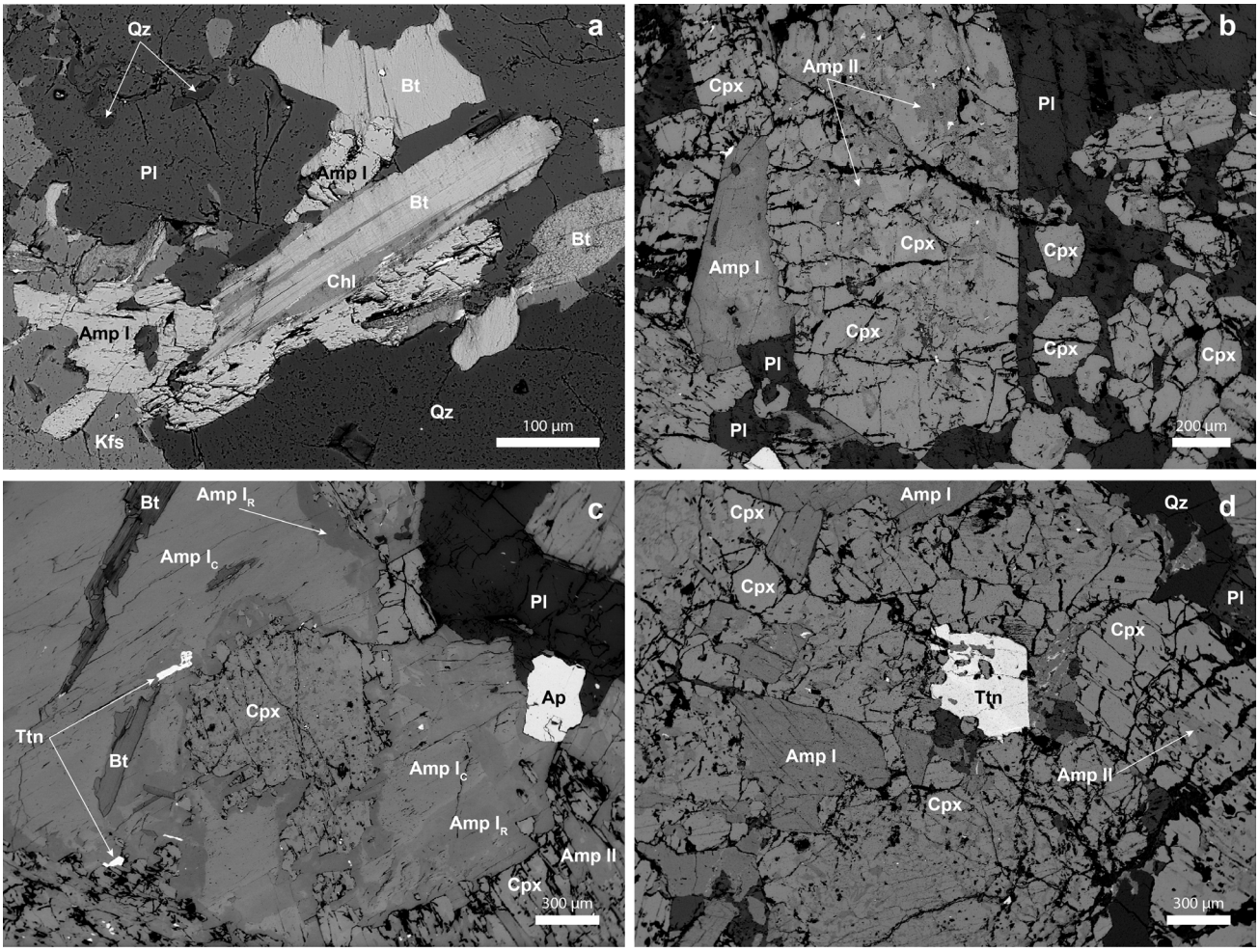

Fig. 5. Backscattered electron images of quartz diorite. (a) Type I amphibole grains are often heavily replaced. Together with plagioclase, quartz, and potassium feldspar (orthoclase), they form a paragenesis suitable for Al-in-amphibole barometry. Biotite grain in the centre is partly chloritized (darker parts). Sample C7-3. (b) A large clinopyroxene grain is partly replaced by Type II amphibole. Type I amphibole is hypidiomorphic and has different core and rim compositions. A large plagioclase grain is enveloping numerous smaller clinopyroxene grains forming a poikilitic texture. Sample C4-1. (c) Type I amphibole grains with well-distinguished core (pale–IC) and rim (dark–IR) parts, clinopyroxene, plagioclase, small titanite, and an apatite grain next to plagioclase are visible. Sample C8-3. (d) A large titanite inclusion in clinopyroxene, Type I amphibole, and Type II amphibole replacing clinopyroxene grains. Sample C7-3. Abbreviations: Amp–amphiboles, Bt–biotite, Cpx–clinopyroxene, Kfs–potassium feldspar (orthoclase), Pl–plagioclases, Qz–quartz, Ttn–titanite.

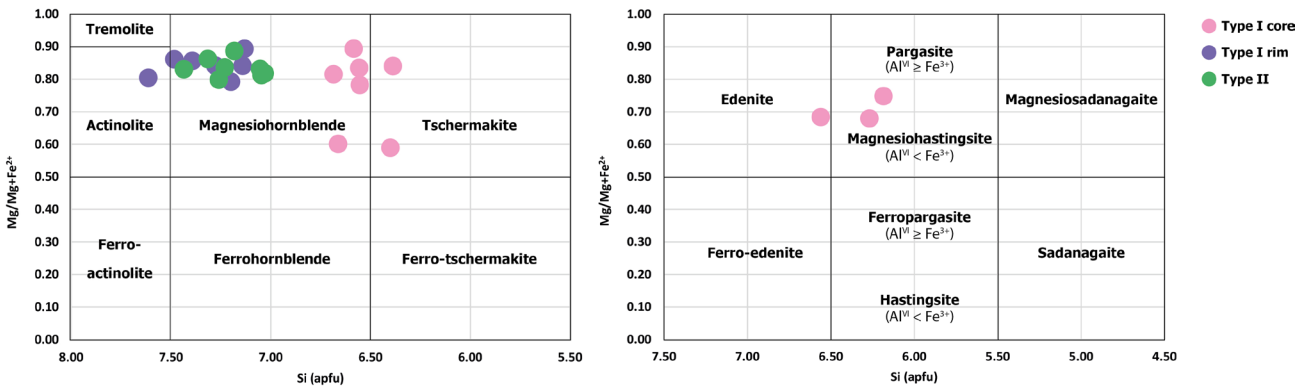

Fig. 6. The composition of Type I and Type II amphibole is shown in the calcic amphibole classification diagram (adapted from Leake et al., 1997).

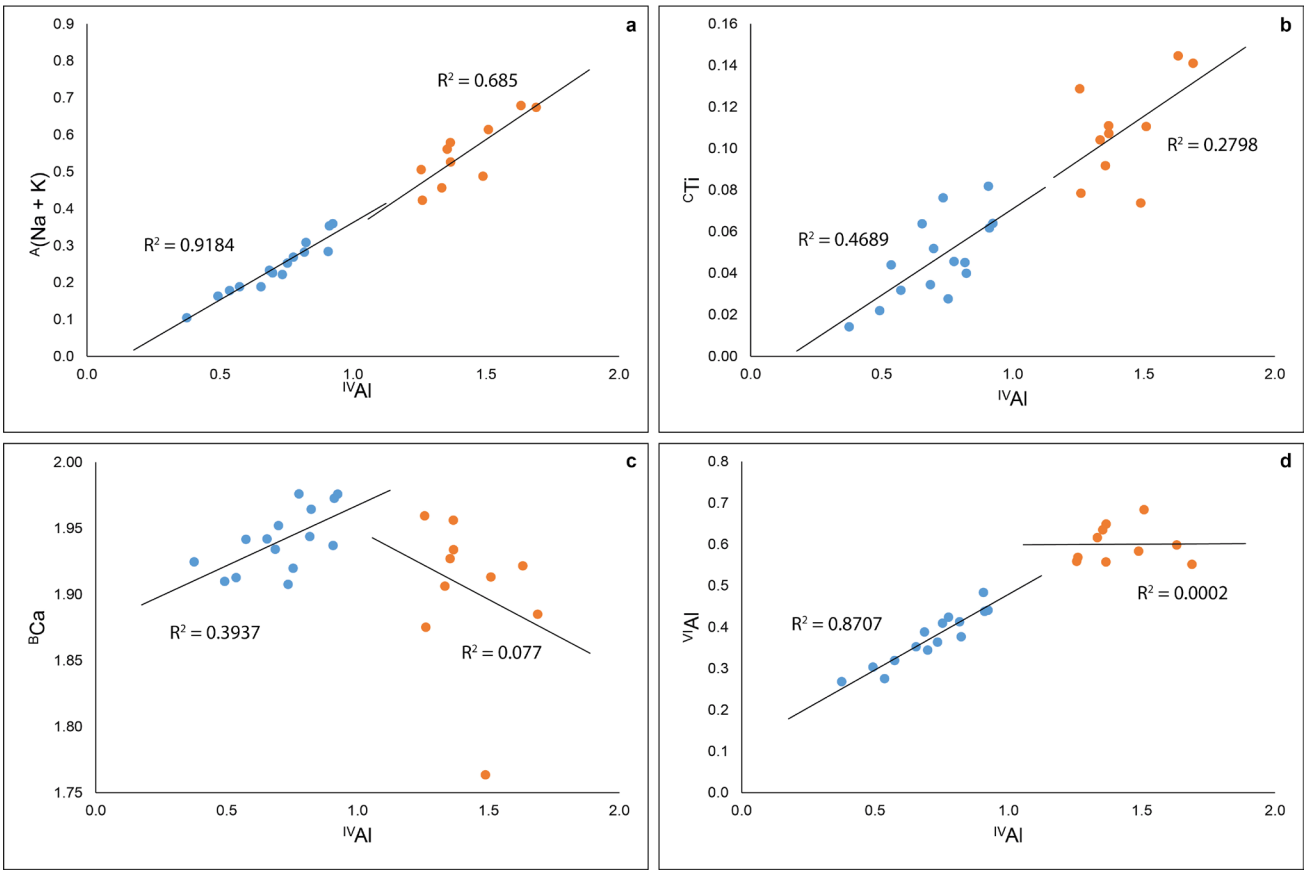

Fig. 7. Site occupancies and exchange mechanisms in amphiboles: (a) edenite exchange, (b) Ti–Tschermak exchange, (c) plagioclase exchange, and (d) Al–Tschermak exchange. Note that scales on the x- and y-axes are not equal.

Feldspars

Plagioclases are usually quite homogeneous; however, in some grains, zoning and polysynthetic twinning (Fig. 3e) can be recognised. Occasionally, a poikilitic texture is present, where grains of other minerals, such as clinopyroxene, quartz, and biotite, are enclosed within larger plagioclase grains (Fig. 3b). A myrmekitic texture at the boundary between plagioclase and orthoclase may also be observed, formed as a result of reaction between these two minerals (Fig. 3f). Plagioclases are intermediate in composition, with X_{Ab} = 0.61–0.73, corresponding to the feldspar series from oligoclase to andesine (Fig. 8), with a low proportion of orthoclase (up to ~2.56 mol%).

Potassium feldspars are represented by orthoclase commonly forming characteristic perthitic structure. It mostly fills the spaces between the femic minerals. In some places, orthoclase grains replace plagioclases (Fig. 3f). The measured composition of potassium feldspar shows 85.43–91.72 mol% orthoclase, 8.12–14.32 mol% albite, and 0.16–0.32 anorthite. Some potassium feldspar grains contain BaO, with an average content of 1.49 wt%.

Minor mineral phases

Quartz occurs in all samples. It typically occurs as small grains, with larger individual crystals observed only occasionally. The average grain size is 1.1 mm, and the largest measured grain is 6 mm. Quartz makes up 5–10% of the total rock. It occurs as small inclusions in minerals but mostly forms xenomorphic grains filling the spaces between larger crystals (Figs. 3a and 5a). **Biotite** is also present among the femic minerals, but in subordinate amounts not exceeding 3%. The average grain size is 0.67 mm, and the largest measured grain is 0.84 mm. It is brown in colour and exhibits strong pleochroism. It occurs in hypidiomorphic grains. Biotite most frequently appears as inclusions in amphiboles (Fig. 3g), or as individual grains (Fig. 5a). It is partly replaced by chlorite (Fig. 5a).

Accessory mineral phases include apatite, titanite, and epidote group minerals. **Titanite** is present as idiomorphic grains (Figs. 3h and 5d). The average grain size is 0.74 mm, and the largest measured grain is 1.4 mm. It usually accounts for 1–2% of the total rock. It often occurs as an inclusion in plagioclases, orthoclase, clinopyroxene, and amphiboles (Fig. 5c). **Apatite** occurs as small

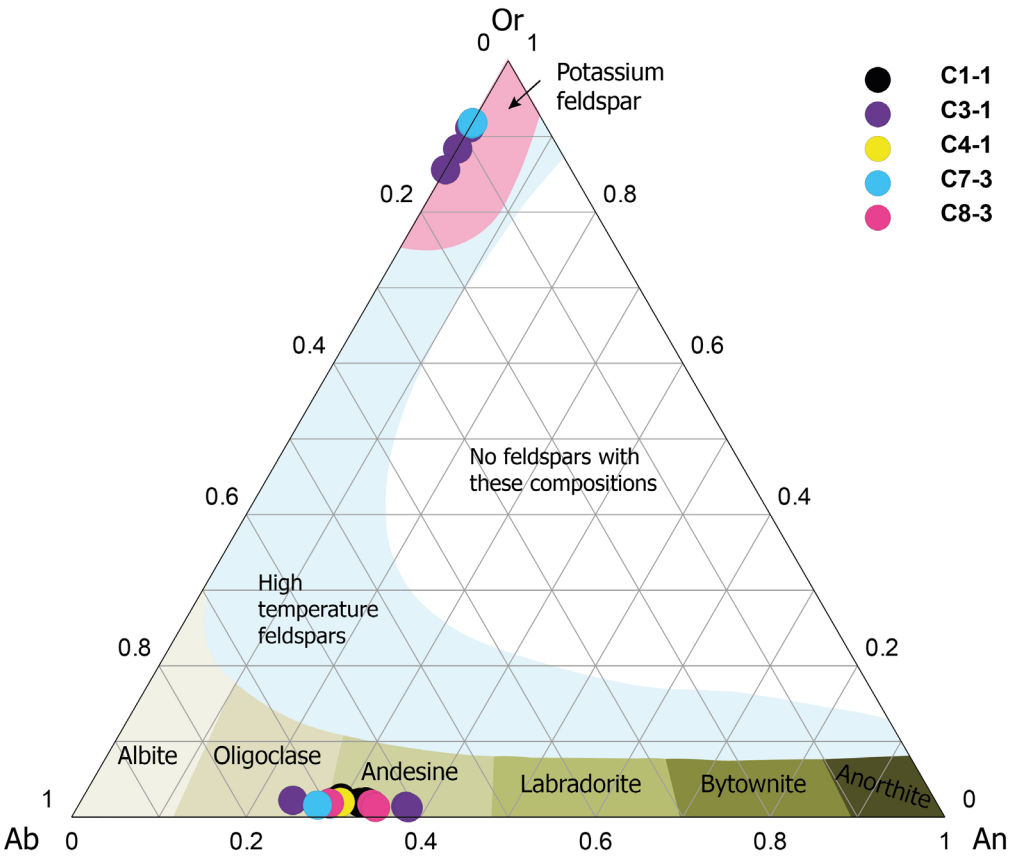

Fig. 8. Composition of feldspars shown in the classification diagram of orthoclase (Or), albite (Ab), and anorthite (An) (adapted from Deer et al., 2001).

grains; the average grain size is 0.08 mm, while the largest measured grain is 0.13 mm. Apatite grains account for up to 1% of the total rock. They occur as rod-shaped grains, often as inclusions in plagioclases, and orthoclase (Fig. 3f). **Epidote group minerals** (most probably allanite) are very rare and enriched in REEs (Fig. 3i). **Magnetite** occurs as small grains included in amphiboles, often accompanied by biotite (Fig. 3g).

Secondary minerals are abundant in more intensely differentiated and/ or metasomatically altered samples and are mainly **chlorite** replacing biotite and amphibole grains (Fig. 5a) and **calcite** replacing clinopyroxene and feldspar grains.

Geothermobarometry

Data selection and validation for geothermobarometric calculations

Nimis (1995) developed a crystal-structure–based clinopyroxene barometer. This calibration is restricted to C2/c clinopyroxene crystallized from basaltic melts. Because the alumina content of the parental magma strongly influences clinopyroxene chemistry, it is not applicable to high-alumina magmas. Later revision by Nimis and Ulmer (1998) produced a new calibration valid only for clinopyroxene that satisfy the following conditions: (Ca + Na) > 0.5 apfu, $Mg/(Mg + Fe^{2+}) > 0.7$, and Al_2O_3/SiO_2 (wt%) < 0.375 (i.e., Al2O3 < 18 wt%).

All investigated clinopyroxene grains are classified as diopside, which belongs to the C2/c space group, therefore meeting the crystal-structure criterion. Furthermore, all the measured clinopyroxene grains satisfy the chemical restrictions. (Ca + Na) contents vary between 0.9 and 1.0, $Mg/(Mg + Fe^{2+})$ values are 0.8–0.9 and Al_2O_3/SiO_2 ranges from 0.012 to 0.039. Therefore, we find all the measurements to meet the requirements for applying geothermobarometric calculations.

The amphibole composition varies not only with pressure, temperature and coexisting mineral assemblage, but also with oxygen fugacity (fO_2) in melt, which controls the Fe# and Fe^{3+}/Fe_{TOT} ratios. Spear (1981) and Anderson & Smith (1995) classify Fe# values in the range from 0 to 0.6 as high, between 0.6 and 0.8 as medium, and 0.8 to 1 as low oxygen fugacity. Low fO_2 favours the insertion of Fe^{2+} in the amphibole lattice, which promotes the substitution of Mg by Al during the Tschermak exchange. A low oxygen fugacity therefore leads to high contents of aluminium in amphibole. Therefore, Anderson & Smith (1995) recommends using only amphiboles with Fe# ≤ 0.65. On the other hand, a high fO_2 leads to a preferred incorporation of Fe^{3+} into the lattice, which

preferably substitutes Al, thus keeping the content of aluminium in amphibole low. Anderson & Smith (1995) recommend using amphiboles with Fe^{3+}/Fe_{TOT} ratio ≥ 0.25, while Schmidt (1992) sets this ratio at ≥ 0.2. Presence of accessory minerals can, according to Ishihara (1977), suggest conditions of oxygen fugacity. Magnetite and titanite in igneous rocks point to a high oxygen fugacity, while ilmenite indicates a low oxygen fugacity. In general, amphibole crystallizing under high fO_2 gives better and more reliable geothermobarometry results than those growing under low fO_2 as experimental calibrations were carried out under medium to high oxygen fugacity (Stein & Dietl, 2001).

Measured amphibole grains in our case show different ratios of Fe^{3+}/Fe_{TOT} and Fe#, which can be seen in Figure 9. All grains have Fe# well below 0.65, which according to Spear (1981) and Anderson & Smith (1995) indicates high oxygen fugacity. Fe^{3+}/Fe_{TOT} ratio of all grains are within the recommended values apart from grains Amp6 (sample C8-3, analysis no. 10) and Amp8 (sample C8-3, analysis no. 16). Therefore, these measurements are excluded from further calculations. However, it is important to stress that the Fe^{3+} content is based on stoichiometric calculations and not on direct measurements of the amount of Fe^{3+} and Fe^{2+} in amphiboles. In addition, magnetite and titanite were found as accessory minerals, which point to high fO_2 as well, suggesting the overall suitability of the measured amphibole samples for geothermobarometry.

The empirical biotite thermometer equation of Henry et al. (2005) is strictly valid only for X_{Mg} = Mg/(Mg + Fe) = 0.275–1.000 and Ti = 0.04–0.60 apfu calculated on the basis of 22 oxygen atoms, with temperatures in the range 480–800 °C. All our measured biotite grains meet the required criteria (X_{Mg} = 0.496–0.799 and Ti = 0.16–0.34 apfu, so we were able to apply the thermometer.

Clinopyroxene thermobarometry

Results of thermobarometric calculations of clinopyroxene are presented in Table 4, where pressures and temperatures of all considered samples are shown, as well as averages and standard deviations of individual thermobarometers. Calculated crystallization temperatures using the pressure-uncorrected thermometers of Dal Negro et al. (1982) and Molin & Zanazzi (1991) yielded values of approximately 900 °C. Pressure-dependent thermometer of Bertrand & Mercier (1985), calculated at 7 kbar results in lower temperatures, averaging around 842 °C, though with standard deviation of 61 °C.

Pressures of crystallization based on barometer of Nimis (1999) result in an average of 7.73 kbar. Temperature corrected barometer of Nimis & Ulmer (1998) at 900 °C on average shows 6.73 kbar. Standard deviations in calculated pressures are 0.94 and 0.79 kbar for Nimis (1999) and Nimis & Ulmer (1998), respectively. Positions of thermobarometers calculated for the representative clinopyroxene grain Cpx9 (sample C4-1, analysis no. 5) in the P–T diagram are shown in Figure 10.

Amphibole thermobarometry

Results of thermobarometric calculations using the above-listed thermometers and barometers applied to selected amphiboles are summarized in Table 4. Type I amphibole cores crystallized at av-

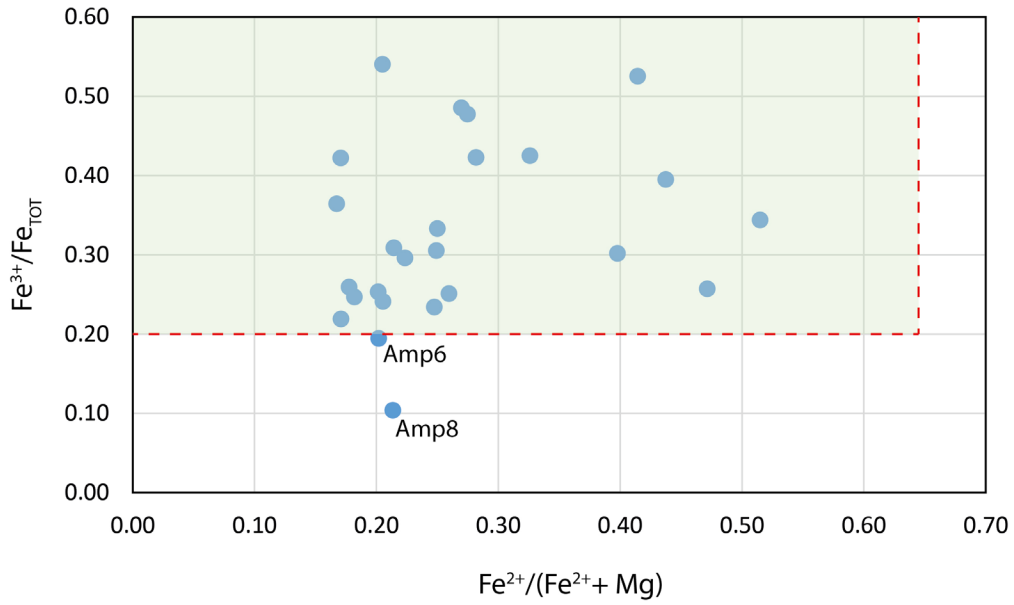

Fig. 9. Ratios of Fe^{2+}/Fe_{TOT} plotted against Fe# [$Fe^{2+}/(Fe^{2+}$ + Mg)] for analysed amphiboles. Amp6 (sample C8-3, analysis no. 10) and Amp8 (sample C8-3, analysis no. 16) fall outside the recommended values, so we excluded them from further calculations.

Table 4. Temperatures T(°C) and pressures P(kbar) calculated for selected clinopyroxene, amphibole and biotite grains. The applied geothermobarometers are listed in Table 2, along with their corresponding abbreviations. The assumed pressure for the calculation of temperatures with the BM85 thermometer was 7.0 kbar. The assumed temperature for the calculation of pressures with the NU98 barometer was 900 °C.

Grain	An. No.	Sample	T(DN82)	T(BM85)	T(MZ91)	P(NU98)	P(N99)
Clinopyroxene							
Cpx2	8	C8-3	907	750	906	6.75	7.05
Cpx3	3	C8-3	897	835	904	6.54	7.21
Cpx4	5	C8-3	901	854	905	5.51	6.82
Cpx6	18	C8-3	897	883	904	5.86	7.33
Cpx7	10	C7-3	899	918	904	7.38	8.43
Cpx8	11	C7-3	907	848	906	6.42	7.86
Cpx9	5	C4-1	903	930	906	8.27	9.18
Cpx10	4	C1-1	901	818	905	8.07	8.63
Cpx12	12	C1-1	909	746	907	5.76	7.04
Average			902	842	905	6.73	7.73
Standard deviation			4	61	1	0.94	0.79

			T(O84)	T(BH90)	T(HB94)	P(S92)	P(AS95)	Grain	An. No.	Sample	T(L84)	T(H05)
Type I amphibole core								Biotite				
Amp2	3	C8-3	669	673	634	6.16	6.23	Bt1	11	C8-3	697	698
Amp 4	5	C8-3	654	674	671	6.33	6.56	Bt2	12	C8-3	674	673
Amp10	18	C8-3	672	673	659	6.47	6.50	Bt3	8	C7-3	638	677
Amp13	10	C7-3	632	695	804	6.69	7.12	Bt4	9	C7-3	658	694
Amp14	11	C7-3	638	668	773	5.60	5.93	Bt5	12	C7-3	651	685
Amp17	5	C4-1	676	688	842	7.26	7.25	Bt6	13	C7-3	695	697
Amp20	4	C1-1	699	664	803	5.56	5.25					
Amp22	3	C3-1	711	719	775	7.44	6.86					
Amp23	12	C3-1	677	678	654	6.04	6.02					
Amp24	13	C3-1	716	705	709	7.44	6.76					
Average			675	684	732	6.50	6.45				669	687
Standard deviation			28	18	75	0.70	0.61				24	11
Type I amphibole rim												
Amp3	4	C8-3	586	605	587	2.08	2.18					
Amp5	7	C8-3	599	624	707	2.81	3.03					
Amp9	17	C8-3	578	615	587	2.49	2.60					
Amp12	4	C7-3	583	591	664	1.22	1.20					
Amp18	6	C4-1	571	575	596	0.77	0.61					
Amp21	11	C1-1	593	624	696	2.67	2.87					
Average			585	606	640	2.01	2.08					
Standard deviation			10	20	56	0.83	0.97					
Type II amphibole												
Amp1	2	C8-3	600	616	575	2.67	2.88					
Amp7	15	C8-3	607	610	691	1.92	2.08					
Amp11	3	C7-3	636	613	649	2.19	2.36					
Amp15	3	C4-1	643	629	730	3.57	3.78					
Amp16	4	C4-1	621	601	688	1.76	1.92					
Amp25	16	C1-1	622	634	758	3.45	3.72					
Average			622	617	682	2.59	2.79					
Standard deviation			17	12	64	0.77	0.81					

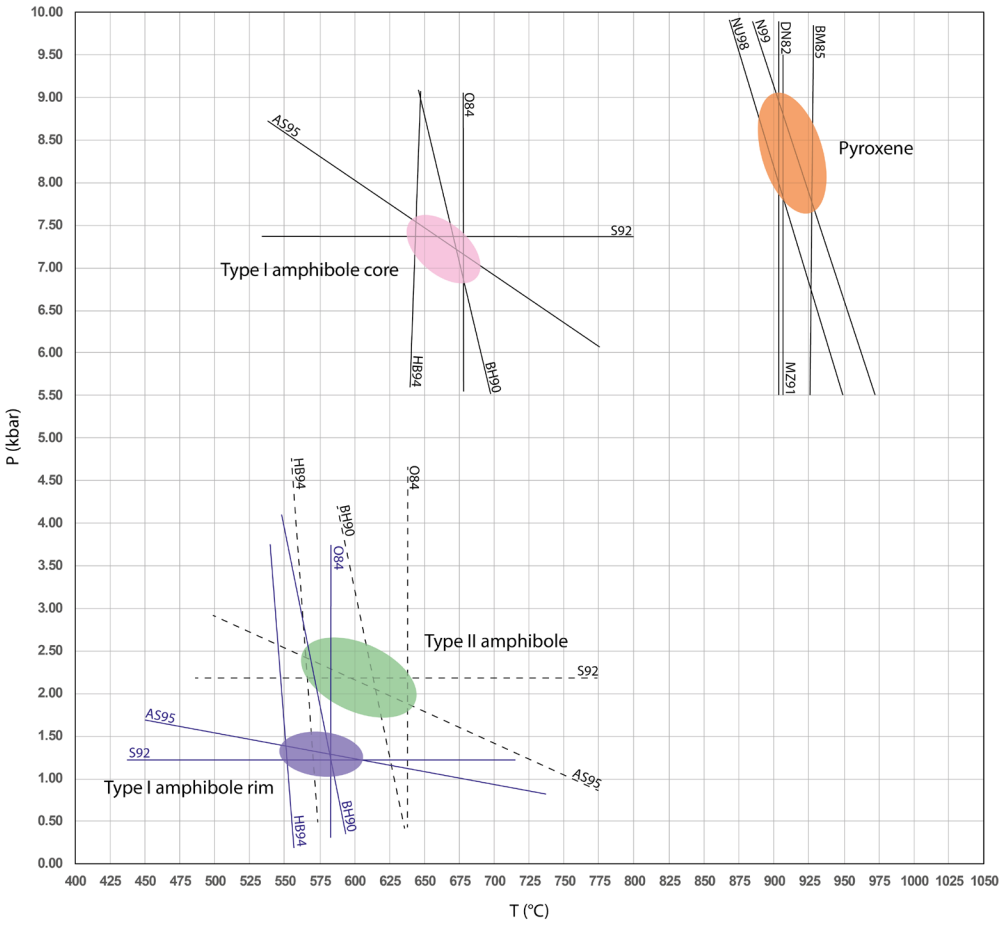

Fig. 10. Positions of thermobarometers for representative clinopyroxene grain Cpx9 (sample C4-1, analysis no. 5), Type I amphibole core – Amp23 (sample C3-1, analysis no. 12), Type I amphibole rim – Amp12 (sample C7-3, analysis no. 4), and Type II amphibole replacing clinopyroxene – Amp11 (sample C7-3, analysis no. 3). The applied geothermobarometers are listed in Table 2, along with their corresponding abbreviations.

erage temperatures of 675 °C, 732 °C, and 684 °C calculated by equations of Otten (1984), Holland & Blundy (1994), and Blundy & Holland (1990), respectively. The latter two thermometers are pressure-corrected using pressures derived from Schmidt (1992) and thus considered more reliable. Average pressures at the time of equilibrium are calculated to be 6.50 kbar and 6.45 kbar based on barometers of Schmidt (1992) and temperature-corrected Anderson & Smith (1995), respectively.

Type I amphibole rims show temperatures of 585 °C, 640 °C, and 606 °C based on calibrations of Otten (1984), Holland & Blundy (1994), and Blundy & Holland (1990), respectively. Average pressures from Schmidt (1992) and Anderson & Smith (1995) are estimated at 2.01 kbar and 2.08 kbar, respectively. These amphiboles show high variations in calculated pressures within both barometers used. Standard deviations are 0.83 kbar and 0.97 kbar for Schmidt (1992) and Anderson & Smith (1995), respectively. Consequently, this is also reflected in the pressure-corrected temperatures calculated using Holland & Blundy (1994) and Blundy & Holland (1990).

Type II amphibole grains show average temperatures of 622 °C, 682 °C, and 617 °C, which were determined based on calibrations of Otten (1984), Holland & Blundy (1994), and Blundy & Holland (1990), respectively. Determined average pressures are calculated to be 2.59 kbar and 2.79 kbar with standard deviations of 0.77 kbar and 0.81 kbar using barometers of Schmidt (1992) and Anderson & Smith (1995), respectively.

Thermobarometers applied to representative amphibole grains are shown in Figure 10. The Type I amphibole core is represented by grain Amp23 (sample C3-1, analysis no. 12); the Type I amphibole rim, by grain Amp12 (sample C7-3, analysis no. 4); and the Type II amphibole replacing clinopyroxene, by grain Amp11 (sample C7-3, analysis no. 3). Crystallization conditions of the Type I amphibole cores are clearly distinguishable from those of the Type I amphibole rims and Type II amphibole grains. On the other hand, pressures and temperatures of the latter two groups are very similar and fall close to the estimated errors of pressure determination, making them indistinguishable based on calculations alone.

Biotite thermometry

The analysed biotite grains yielded average temperatures of 669 °C and 687 °C according to the thermometers of Luhr et al. (1984) and Henry et al. (2005), respectively. The calculated temperatures are shown in Table 4. The measured biotite grains were petrographically associated with Type I amphibole cores. They were in contact with amphiboles or completely enclosed within Type I amphibole in the core regions (Fig. 5a, c).

Discussion

Quartz diorite body is part of the larger PIC; therefore, we should consider its crystallization in the light of the PIC formation. Poli et al. (2020) explain its formation as a series of chemically diverse melt pulses intruding different crust levels, leading to a variety of observed lithologies. Quartz diorite is considered the first to form from basaltic melts by cumulus processes. Modelling of the cumulus process of quartz diorite has shown that the most important cumulus mineral was clinopyroxene, whereas amphiboles plus plagioclases were subordinate (Poli et al., 2020). Our thermobarometric calculations show that the clinopyroxene formed first, at the highest pressures and temperatures ranging from 840–900 °C and 6.70–7.70 kbar. This is consistent with modelled cumulus process as well as with petrographic observations, which indicate that amphiboles crystallized later, replacing the early-formed pyroxene and sometimes forming uralitic texture.

The first amphiboles to crystallize were Type I amphibole cores. They crystallized at 670–730 °C and 6.45–6.50 kbar. These conditions are consistent with calculations of amphiboles crystallization in the less evolved GDT. Poli et al. (2020) determined average temperatures of 666 °C and pressures of 6.08 kbar. Similar averages of 695 °C and 6.91 kbar were obtained by Sotelšek (2019). These similarities in pressures and temperatures of amphiboles from quartz diorite and the less evolved GDT suggest their coeval formation. Temperatures derived from biotite grains and Type I amphibole cores are consistent, confirming the accuracy of the calculations and supporting the interpretation that these amphiboles crystallized contemporaneously with the less evolved GDT.

Type I amphibole rims were formed at lower P–T conditions near 585–640 °C and ~2.00 kbar. Slightly higher conditions of 617–682 °C and 2.59–2.79 kbar were calculated from Type II amphibole grains. The distinctly different chemical composition of the Type I amphibole rims and the replacement and assimilation of pyroxene by Type II amphibole grains compared to Type I amphibole cores clearly point to their later formation. These results can be related to the emplacement of the shallower parts of the GDT pluton (more evolved granodiorite sensu Poli et al., 2020). Sotelšek (2019) reports pressures from the shallower NW parts of the pluton in the range of 2–3 kbar and temperatures of 635–699 °C, which is comparable to the Type I amphibole rims and Type II amphibole growth conditions. Therefore, amphiboles from these two groups are assumed to have formed contemporaneously with the emplacement of more evolved GDT.

Conclusions

Based on the presented data, we can relate all observations and calculations to the evolution of the whole PIC. Quartz diorite body formed in several stages recorded in the pressures and temperatures of formation of clinopyroxene, amphiboles, and biotite. Pyroxene grains were the first to form by cumulus processes at 840–905 °C and 6.70–7.70 kbar, followed by Type I amphibole cores at 675–730°C and 6.45–6.50 kbar, which corresponds to the formation conditions of the less evolved GDT. Coeval with the formation of the more evolved GDT was the formation of Type I amphibole rims and Type II amphibole at 585–640 °C and ~2.00 kbar and 615–680 °C and 2.59–2.79 kbar, respectively. Biotite records similar temperatures of 670–690 °C.

Acknowledgements

The authors acknowledge the financial support of the Slovenian Research and Innovation Agency (ARIS): Research Core Funding No. P1-0195, Young Researchers Program No. 55758, and UNESCO IGCP 637 (Heritage Stone Designation).

References

Altherr, R., Lugović, B., Meyer, H.P. & Majer, V. 1995: Early Miocene postcollisional calc-alkaline magmatism along the easternmost segment of the Periadriatic fault system (Slovenia and Croatia). Mineralogy and Petrology, 54: 225–247. https://doi.org/10.1007/bf01162863

Anderson, J.L. & Smith, D.R. 1995: The Effects of Temperature and f_{O2} on the Al-in-Hornblende Barometer. American Mineralogist, 80/5–6: 549–559. https://doi.org/10.2138/AM-1995-5-614

ARSO, 2018: Varstvo naravnih vrednot. Ljubljana: Agencija Republike Slovenije za okolje. Inter-

net: https://zrsvn-varstvonarave.si/kaj-varujemo/naravne-vrednote/ (18. 9. 2018).

Benesch, F. 1917: Beiträge zur Gesteinskunde des östlichen Bachergebirges (Südsteiermark). Mitteilungen des Alpenländischen Geologischen Vereines, 10: 161–183.

Bertrand, P. & Mercier, J.-C.C. 1985: The mutual solubility of coexisting ortho- and clinopyroxene: toward an absolute geothermometer for the natural system? Earth and Planetary Science Letters, 76/1–2: 109–122. https://doi.org/10.1016/0012-821X(85)90152-9

Blundy, J.D. & Holland, T.J.B. 1990: Calcic amphibole equilibria and a new amphibole-plagioclase geothermometer. Contributions to Mineralolgy and Petrology, 104: 208–224. https://doi.org/10.1007/BF00306444

Činč, B. 1992: Mineraloške in geokemične značilnosti aplitnih in pegmatitnih žil v pohorskem tonalitu in čizlakitu. Magistrsko delo. Univerza v Ljubljani, Fakulteta za naravoslovje in tehnologijo, Ljubljana: 106 p.

Dal Negro, A., Carbonin, S., Molin, G.M., Cundari, A. & Piccirillo, E.M. 1982: Intracrystalline cation distribution in natural clinopyroxenes of tholeiitic, transitional, and alkaline basaltic rocks. In: Saxena, S.K. (ed.): Advances in Pyhsical Geochemistry, 2: 117–150.

Deer, W.A., Howie, R.A. & Zussman, J. 2001: Rock-forming minerals. 4A, framework silicates, feldspars, 2. ed. Geological Society, London: 972 p.

Dolar-Mantuani, L. 1935: Razmerje med tonaliti in apliti pohorskega masiva. Geološki Anali Balkanskog Poluostrva, 12: 1–165.

Dolar-Mantuani, L. 1940: Diferencijacija magmatskih kamnin na Pohorju. Ljubljana. Razprave matematično-prirodoslovnega razreda: 1–13.

Dolenec, T. 1994: Novi izotopski in radiometrični podatki pohorskih magmatskih kamnin. Rudarsko-metalurški zbornik, 41/3–4: 147–152.

Dolenec, T., Pezdič, J. & Strmole, D. 1987: Isotopic composition of oxygen in igneous rocks of Pohorje = Izotopska sestava kisika v pohorskem tonalitu in čizlakitu). Geologija, 30/1: 231–244.

Droop, G.T.R. 1987: A general equation for estimating Fe^{3+} concentrations in ferromagnesian silicates and oxides from microprobe analyses, using stoichiometric criteria. Mineralogical Magazine, 51: 431–435.

Faninger, E. 1965: Čizlakit v novejši petrografski klasifikaciji. Geologija, 8/1: 263–278.

Faninger, E. 1973: Pohorske magmatske kamenine. Geologija, 16/1: 271–315.

Fodor, L., Balogh, K., Dunkl, I., Pécskay, Z., Korokanai, B., Trajanova, M., Vrabec, M., Vrabec, M., Horváth, P., Janák, M., Lupták, B., Frisch, W., Jelen, B. & Rifelj, H. 2003: Structural evolution and exhumation of the Pohorje-Kozjak Mts., Slovenia. Annales Universitatis Scientiarum Budapestinensis. Sectio Geologica, Tom. 35: 118–119.

Fodor, L.I., Gerdes, A., Dunkl, I., Koroknai, B., Pécskay, Z., Trajanova, M., Horváth, P., Vrabec, M., Jelen, B., Balogh, K. & Frisch, W. 2008: Miocene emplacement and rapid cooling of the Pohorje pluton at the Alpine-Pannonian-Dinaridic junction, Slovenia. Swiss Journal of Geosciences, 101: 255–271. https://doi.org/10.1007/978-3-7643-9950-4_15.

Hammarstrom, J.M. & Zen, E. 1986: Aluminum in hornblende: An empirical igneous geobarometer. American Mineralogist, 71/11-12: 1297–1313.

Helz, R.T. 1982: Chapter 2, Experimental studies of amphibole stability; Phase relations and compositions of amphiboles produced in studies of the melting behavior of rocks. Reviews in Mineralogy & Geochemistry, 9B:279–346. https://pubs.geoscienceworld.org/msa/rimg/article/9B/1/279/87635/Chapter-2-Experimental-studies-of-amphibole

Henry, D.J., Guidotti, C.V. & Thomson, J.A. 2005: The Ti–saturation surface for low–to–medium pressure metapelitic biotites: Implications for geothermometry and Ti–substitution mechanisms. American Mineralogist, 90/2–3: 316–328. https://doi.org/10.2138/am.2005.1498

Hinterlechner-Ravnik, A. 1971. Pohorske metamorfne kamnine = The metamorphic rocks of Pohorje. Geologija, 14/1: 187–226.

Hinterlechner-Ravnik, A. 1973: Pohorske metamorfne kamnine II = The metamorphic rocks of Pohorje mountains II. Geologija, 16/1: 245–270.

Hinterlechner-Ravnik, A. & Moine, B. 1977: Geochemical Characteristics of the Metamorphic Rocks of the Pohorje Mountains. Geologija, 20/1: 107–140.

Hinterlechner-Ravnik, A., Sassi, F.P. & Visona, D. 1991a: The Austridic eclogites, metabasites and metaultrabasites from the Pohorje area (Eastern Alps, Yugoslavia): 1. The eclogites and related rocks. Rendiconti Fisiche Accademia Lincei, 2: 157–173.

Hinterlechner-Ravnik, A., Sassi, F.P. & Visona, D. 1991b: The Austridic eclogites, metabasites and metaultrabasites from the Pohorje area

(Eastern Alps, Yugoslavia): 2. The metabasites and metaultrabasites, and concluding considerations. Rendiconti Fisiche Accademia Lincei, 2: 175–190.

Holland, T. & Blundy, J. 1994. Non-ideal interactions in calcic amphiboles and their bearing on amphibole-plagioclase thermometry. Contributions to Mineralogy and Petrology, 116: 433–447. https://doi.org/10.1007/BF00310910

Ishihara, S. 1977: The magnetite series and ilmenite series granitic rocks. Mining Geology, 27: 293–305. https://doi.org/10.11456/SHIGENCHISHITSU1951.27.293

Janák, M., Froitzheim, N., Lupták, B., Vrabec, M. & Krogh Ravna, E.J. 2004: First evidence for ultrahigh – pressure metamorphism of eclogites in Pohorje, Slovenia: Tracing deep continental subduction in the Eastern Alps. Tectonics, 23: TC5014. https://doi.org/10.1029/2004TC001641

Janák, M., Froitzheim, N., Yoshida, K., Sasinková, V., Nosko, M., Kobayashi, T., Hirajima, T. & Vrabec, M. 2015: Diamond in metasedimentary crustal rocks from Pohorje, Eastern Alps: A window to deep continental subduction. Journal of Metamorphic Geology, 33: 495–512. https://doi.org/10.1111/jmg.12130

Kirst, F., Sandmann, S., Nagel, T.J., Froitzheim, N. & Janák, M. 2010: Tectonic evolution of the southeastern part of the Pohorje Mountains (Eastern Alps, Slovenia). Geologica Carpathica, 61: 451-461. https://doi.org/10.2478/v10096-010-0027-y

Leake, B., Woolley, A.R., Arps, C.E.S. et al. 1997: Nomenclature of Amphiboles: Report of the Subcommittee on Amphiboles of the International Mineralogical Association Commission on New Minerals and Mineral Names. Mineralogical Magazine, 61: 295–321.

Luhr, J.F., Carmichael, I.S.E. & Varekamp, J.C. 1984: The 1982 eruptions of El chichon volcano, Chiapas, Mexico: mineralogy and petrology of the anhydrite-bearing pumices. Journal of volcanology and geothermal research, 23: 69–108. https://doi.org/10.1016/0377-0273(84)90057-X

Mioč, P. 1978: Osnovna geološka karta SFRJ 1:100 000. Tolmač lista Slovenj Gradec. Zvezni geološki zavod, Beograd: 74 p.

Mioč, P. & Žnidarčič, M. 1977. Osnovna geološka karta SFRJ 1:100 000. List Slovenj Gradec. Zvezni geološki zavod, Beograd.

Mioč, P. & Žnidarčič, M. 1989: Osnovna geološka karta SFRJ 1:100 000. Tolmač lista Maribor in Leibnitz. Zvezni geološki zavod, Beograd: 60 p.

Nikitin, V. 1939: Čizlakit – nova kamnina s Pohorja. Ljubljana. Zbornik Priorodoslovnega Društva, 1: 32–36.

Nikitin, V. & Klemen, R. 1937: Diorit-pirokseniti v okolici Čizlaka na Pohorju. Geološki Anali Balkanskog Poluostrva, 14/2: 149–198.

Nimis, P. 1995: A clinopyroxene geobarometer for basaltic systems based on crystal-structure modeling. Contributions to Mineralogy and Petrolgy, 121: 44–125. https://doi.org/10.1007/s004100050093

Nimis, P. 1999: Clinopyroxene geobarometry of magmatic rocks. Part 2. Structural geobarometers for basic to acid, tholeiitic and mildly alkaline magmatic systems. Contributions to Mineralogy and Petrolgy, 135: 62–74. https://doi.org/10.1007/s004100050498

Nimis, P. & Ulmer, P. 1998: Clinopyroxene geobarometry of magmatic rocks Part 1: An expanded structural geobarometer for anhydrous and hydrous, basic and ultrabasic systems. Contributions to Mineralogy and Petrology, 133: 122–135. https://doi.org/10.1007/s004100050442

Otten, M.T. 1984: The origin of brown hornblende in the Artfjället gabbro and dolerites. Contributions to Mineralogy and Petrology, 86: 189–199. https://doi.org/10.1007/BF00381846

Papike, J.J., Cameron, K.L. & Baldwin, K. 1974: Amphiboles and pyroxenes: characterization of other than quadrilateral components and estimates of ferric iron from microprobe data. Geological Society of America Abstract Program, 6: 1053–1054.

Poldervaart, A. & Hess, H.H. 1951: Pyroxenes in the Crystallization of Basaltic Magma. Journal of Geology, 59/5: 472–489. https://doi.org/10.1086/625891

Poli, G., Christofides, G., Koroneos, A., Trajanova, M. & Zupančič, N. 2020: Multiple processes in the genesis of the Pohorje igneous complex: Evidence from petrology and geochemistry. Lithos, 364–365: 105512. https://doi.org/10.1016/j.lithos.2020.105512

Schmidt, M.W. 1992: Amphibole composition in tonalite as a function of pressure: an experimental calibration of the Al-in-hornblende barometer. Contributions to Mineralogy and Petrology, 110/2–3: 304–310. https://doi.org/10.1007/BF00310745

Sotelšek, T. 2019: Globina kristalizacije pohorskega granodiorita. Diplomsko delo. Univerza v Ljubljani, Naravoslovnotehniška fakulteta, Ljubljana: 67 p.

Spear, F.S. 1981: Amphibole-plagioclase equilibria: an empirical model for the reaction albite

+ tremolite = edenite + 4 quartz. Contributions to Mineralogy and Petrology, 77: 355–364. https://doi.org/10.1007/BF00371564

Stein, E. & Dietl, C. 2001: Hornblende thermobarometry of granitoids from the Central Odenwald (Germany) and their implications for the geotectonic development of the Odenwald. Mineralogy and Petrology, 72: 185–207. https://doi.org/10.1007/s007100170033

Trajanova, M., Pécskay, Z. & Itaya, T. 2008: K-Ar geochronology and petrography of the Miocene Pohorje Mountains batholith (Slovenia). Geologica Carpathica, 59: 247–260.

Vrabec, M., Janák, M., Froitzheim, N. & De Hoog, J.C.M. 2012: Phase relations during peak metamorphism and decompression of the UHP kyanite eclogites, Pohorje Mountains (Eastern Alps, Slovenia). Lithos, 144–145: 40–55. https://doi.org/10.1016/j.lithos.2012.04.004

Yavuz, F. & Döner, Z. 2017: WinAmptb – A Windows program for calcic amphibole thermobarometry. Periodico di Mineralogia, 86: 135–167. https://doi.org/10.2451/2017PM710

Zupančič, N. 1994: Petrološke in geokemične značilnosti pohorskih magmatskih kamnin. Doktorska disertacija. Univerza v Ljubljani, Fakulteta za naravoslovje in tehnologijo, Ljubljana: 126 p.

GEOLOGIJA 68/2, 287-306, Ljubljana 2025

https://doi.org/10.5474/geologija.2025.013

Article

Stratigraphic-genetic complexes of the bedrock of Lviv city and their geotechnical properties

Stratigrafsko-genetski kompleksi kamninske podlage mesta Lviv in njihove geotehnične lastnosti

Pavlo ZHYRNOV[1] & Petro VOLOSHYN[2]

1Faculty of Natural Sciences, Comenius University in Bratislava, str. Ilkovičova 6, 842 15 Bratislava, Slovakia;
*corresponding author: zhyrnov1@uniba.sk
2Geological Department of Ivan Franko National University of Lviv, str. Hrushevskoho, 4, 79005 Lviv, Ukraine;
e-mail: petro.voloshyn@lnu.edu.ua

Prejeto / Received 22. 9. 2025; Sprejeto / Accepted 6. 11. 2025; Objavljeno na spletu / Published online 10. 12. 2025

Key words: stratigraphy, genetic complexes, facies, geotechnical properties, soils, Lviv
Ključne besede: stratigrafija, genetski kompleksi, facies, geotehnične lastnosti, tla, Lviv

Abstract

The geological basis of engineering geological surveys is based on age and genetic factors. The age is determined by the regional stratigraphic scheme. Identification of specific features and criteria of genetic subdivisions of rocks is the main task of studying the geological structure of the territory of Lviv city for geotechnical purposes. Stratigraphic and genetic complexes should be identified for this purpose based on the stratigraphic-genetic scheme of bedrock dissection. The bedrock of the Cretaceous and Neogene systems was separated into independent stratigraphic-genetic complexes by this principle and dissected into engineering-geological elements based on the application of stratigraphic and geotechnical research methods. The article describes each engineering-geological element with characteristic geotechnical properties and concludes their use as a basis for foundations of buildings and structures. The soils that are the most difficult in geotechnical terms are also analyzed, recommendations on foundation construction on problematic soils are given, and a set of engineering preparation measures aimed at improving the general engineering-geological situation in Lviv city are defined.

Izvleček

Geološka podlaga inženirsko-geoloških raziskav temelji na starosti in genetskih dejavnikih. Starost se določa z regionalno stratigrafsko shemo. Opredelitev specifičnih značilnosti in meril genetske delitve kamnin je glavna naloga pri preučevanju geološke zgradbe območja mesta Lviv za geotehnične namene. V ta namen je treba, na podlagi stratigrafsko-genetske sheme razčlenitve kamnin, opredeliti stratigrafske in genetske komplekse. Kamnine krednega in neogenskega sistema so bile po tem načelu razdeljene na samostojne stratigrafsko-genetske komplekse in razčlenjene na inženirsko-geološke elemente na podlagi uporabe stratigrafskih in geotehničnih raziskovalnih metod. Članek opisuje vsak inženirsko-geološki element z značilnimi geotehničnimi lastnostmi ter podaja zaključke o njihovi uporabi kot osnovi za temeljenje stavb in objektov. Analizirana so tudi tla, ki so v geotehničnem smislu najzahtevnejša, podana so priporočila glede gradnje temeljev na problematičnih tleh in opredeljen je nabor inženirskih pripravljalnih ukrepov, namenjenih izboljšanju splošnega inženirsko-geološkega stanja v mestu Lviv.

Introduction

Lviv is one of the most dynamically developing cities in Ukraine in terms of construction, in connection with which there is a need for a detailed study of the geotechnical properties of soils as the basis for the foundations of buildings and structures.

The territory of Lviv city is geostructurally located within the Lviv Paleozoic Trough, corresponding to a deeply submerged section of the crystalline basement of the southwestern margin of the East European Platform. Paleozoic, Mesozoic, and Cenozoic rocks take part in the geological structure of the area. Of the extensive rock complexes developed within the study area, three different-aged and different-genesis rock complexes are of decisive importance for prospective construction: Upper Cretaceous, Neogene and Quaternary. We will focus on the description of the bedrock Upper Cretaceous and Neogene rocks in this paper and their geotechnical properties.

Geotechnical characterization of soils is based on the identification and mapping of stratigraphic-genetic complexes of rocks, accordingly, the geological basis of engineering-geological surveys should be based on two factors – age (stratigraphic) and genetic. If the age factor with sufficient completeness to fulfill the tasks is strictly regulated by regional stratigraphic schemes adopted by the Interdepartmental Stratigraphic Committee, there is no accepted scheme for the genetic division of rocks. The main task of studying the geological structure of Lviv city from the point of view of geotechnical use and development of the territory was to identify specific features and criteria of the genetic division of rocks corresponding to the specialization of works.

This article presents the results and bases of the adopted stratigraphic-genetic scheme of bedrock dissection, necessary for the allocation of stratigraphic-genetic complexes of the territory of Lviv city. Therefore, this scheme, especially in its genetic part, cannot have regional significance but is only adapted to a specific area according to the intended purpose of the works (Gruzman, 1980).

Study area

Lviv is located in the central part of the Lviv Region between Yavoriv, Zhovkva and Pustomyty Districts, in the Eastern European time zone at the 24th meridian. The city is located approximately 540 km west of Kyiv, at a distance of about 70 km from the border with Poland (Fig. 1).

Bedrocks are confined to certain geomorphological units, so it makes sense to briefly present the geomorphological zoning of the territory of Lviv city. It is also necessary to designate individual landforms that will be encountered in the text of this article. Lviv city belongs to the Volhynian-Podolian Region of strata-denudation upland by the map of geomorphological zoning. The territory of the Lviv city is located within two geomorphological subregions – the Podolian structural-denudation upland on Cretaceous and Neogene deposits and the Lower Polissia strata-accumulative plain on Cretaceous deposits. Geomorphological subregions are further divided into districts and subdistricts (Gruzman, 1980) (Figs. 2, 3).

Fig. 1. Administrative location of the Lviv city.

COUNTRY	REGION	SUBREGIONS	DISTRICTS	SUBDISTRICTS		
				NAME OF SUBDISTRICTS		CHARACTERISTIC OF SUBDISTRICTS
EASTERN EUROPEAN POLYGENIC PLAIN	VOLHYNIAN-PODOLIAN REGION OF STRATO-DENUDATION UPLAND	A. PODOLIAN STRUCTURAL-DENUDATION UPLAND	I. LVIV PLATEAU	I_1	LVIV PLATEAU	GENTLY-DELUVIAL, GENTLY-WAVOUS, WEAKLY DISSECTED
				I_2	LVIV-BOBYRSK HILLY UPLAND	STRUCTURAL-EROSIONAL, STRONGLY DISSECTED EASTERN PART OF LVIV PLATEAU
				I_3	DISSECTED NORTHERN SLOPE PART OF LVIV PLATEAU	EROSIONAL CAPE PROTRUSIONS OF LVIV PLATEAU, THAT BEND AROUND POLTVA VALLEY
			II. ZUBRA VALLEY	II_1	BOTTOM OF ZUBRA VALLEY	ALLUVIAL FLAT AND CANOPY CONCAVE CHANNEL AND FLOODPLAIN SURFACES OF ZUBRA VALLEY
				II_2	SLOPES OF ZUBRA VALLEY	EROSIONAL-DELUVIAL, GENTLE
			III. HILLY RIDGE ROZTOCZE	III_1	HILLY RIDGE ROZTOCZE	HIGHLY EROSIONAL, HILLY RIDGE UPLANDS
				III_2	SOUTHERN-WESTERN SPURS OF HILLY RIDGE ROZTOCZE	AEOLIAN-DELUVIAL, GENTLY-WAVED AND SMALL-RIDGY, GENTLY-DISSECTED
				III_3	RESIDUAL HIGHS	STRUCTURAL-DENUDATION, OUTLIER, GENTLY-SUMMIT, TERRACED HILLS AND UPLANDS
			IV. BILOHIRIA-MALCHYTSKA VALLEY	IV_1	BILOHIRIA STRUCTURAL BASIN	ACCUMULATIVE, FLAT BOTTOM WITH GENTLY SLOPES, SWAMPED (BILOHIRIA STREAM VALLEY)
				IV_2	RYASNA VALLEY	ACCUMULATIVE, FLAT BOTTOM WITH GENTLY SLOPES, HEAVILY SWAMPED
		B. LOWER POLISSIA STRATIFIED-ACCUMULATIVE PLAIN	V. POLTVA VALLEY	V_1	FLOODED TERRACED SURFACES OF POLTVA RIVER	ACCUMULATIVE, FLAT
				V_2	UNDERFLOODED TERRACED SURFACES OF POLTVA RIVER	
			VI. UPLANDS OF RIDING LANDS OF BUH	VI	VYNNYKY RIDGE	EROSIONAL RIDGE WITH GENTLY SLOPES AND RIDGY CRESTS

Fig. 2. Scheme of geomorphological zoning of Lviv city.

Materials and methods

The basis for the genetic dissection of rocks was the available facies-ecological studies of the Paleogene and Neogene of Lviv city (Kudrin, 1966) and the experience of large-scale (1:50 000) geological survey. To describe the stratigraphic-genetic complexes of Lviv city's bedrock deposits we used the works on the stratigraphy of the loess formation of Ukraine (Veklych, 1968), stratotypes and biostratigraphy of Miocene deposits of the Volhynian-Podolian plate (Venglinsky & Horetsky, 1979), stratigraphy of the Tortonian deposits of Volhynia-Podolia (Vyalov & Horetsky, 1965), Stratigraphic Code of Ukraine (Hozhyk, 2012), stratigraphic schemes and legends for the Carpathian region (Biryuleva et al., 1972), geological atlas of Lviv city and its surroundings (Lomnicki, 1897), stratigraphy of the Middle Miocene deposits of Opillia (Kazakova, 1952).

As for geotechnical studies of the territory of Lviv city, the existing information is based on the materials of reports on engineering-geological surveys for residential-civil and industrial objects. 357 geotechnical reports were analyzed, and those materials were collected and systematized

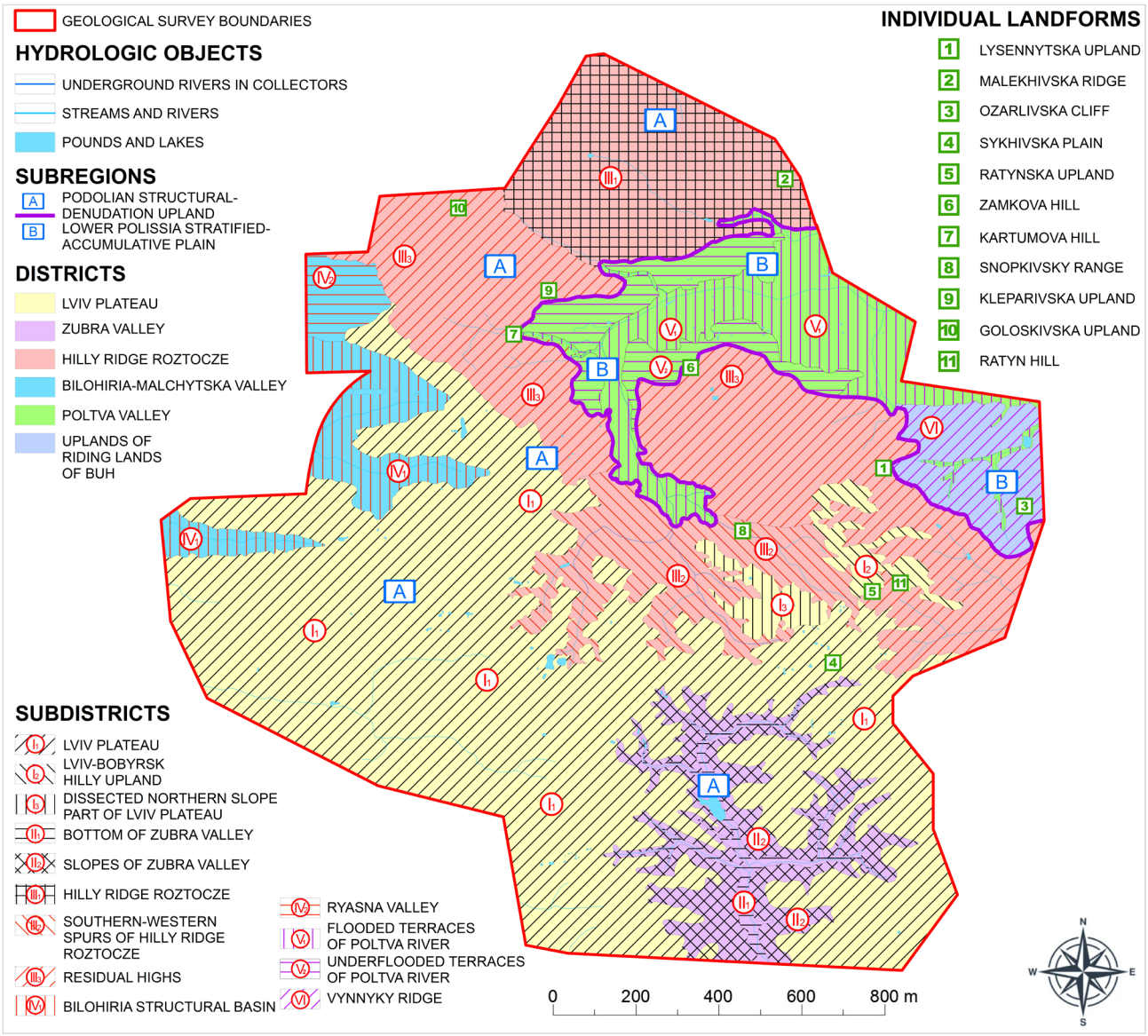

Fig. 3. Geomorphological zoning and individual landforms of Lviv city.

at the Lviv Branch of the "Ukrainian Institute of Engineering Technical Exploration for Construction" (SE "LF UKRIINTR"). Also the main ideas on engineering-geological assessment of stratigraphic-genetic complexes were taken from several scientific works of Ukrainian (Mokritskaya, 2012, 2019; Budkin & Cherkez, 2000) and foreign scientists (Hataullin, 1991; Kopylov & Melchakova, 2020; Arkhipov et al., 1980; Slavinskaya & Lyubimova, 2008; Bogomolov, 2011).

Lithological, paleontological and chronostratigraphic research methods were applied in the study of the stratigraphy of the bedrock of Lviv city. The group of lithological methods included dissection and correlation based on visual features (establishing sediment types, colour, density, strength, structure, texture, presence of inclusions, secondary alteration, signs of cyclicity, etc.). Mineralogical-petrographic methods included microscopic diagnosis of the minerals that make up the rocks and structural analysis using X-rays.

The paleontological method was used to determine the relative ages, stratigraphic separations and correlations of sedimentary rocks based on the sequence of fossil assemblages contained within them, as a result of biological evolution and changes in environmental conditions. For the paleontological method the groups of organisms with high abundance, rapid evolution and wide distribution, whose remains are well preserved, in our case these were red algae and several shell cephalopod mollusks, were of greatest importance.

The use of chronostratigraphic methods solved the problem of comparing sections (private and composite) with the general stratigraphic scale and global correlation of sedimentary strata. The

method is based on a comprehensive substantiation of the age of the lower strata boundary, linking it to the anchored "golden nail" tier boundary, and tracing this "isochronal boundary" within the basin and beyond based on a guiding correlation event (Zorina, 2015) (Fig.4).

Geotechnical research methods included borehole drilling and mining, field and laboratory studies of the soils (engineering-geological elements) identified within each stratigraphic-genetic complex. All strength and deformation characteristics of both rocks and soils were determined in the field. The compressibility of soils was studied by die methods, pressiometers, and dynamic and static probing.

To realize die loads in the borehole, boreholes with a diameter of more than 320 mm were drilled. Soil testing was carried out by special installations, which make it possible to work at a borehole depth of up to 20 m. A 600 cm^2 die was lowered to the bottom of the borehole. The load on the die was transmitted through a rod on which a platform with a load was placed. The modulus of deformation was determined by the formula.

Pressiometric studies were carried out in clayey soils using exploratory boreholes. The pressiometer is a rubber cylindrical chamber that is lowered into the borehole to a predetermined depth. The chamber is expanded by liquid or gas pressure. In the process, radial ground displacement and pressure are measured in the borehole walls. This makes it possible to determine the modulus of deformation of the soils.

Probing was used to study rock strata up to a depth of 15–20 m. The essence of the method was to determine the resistance to penetration of the probe into the ground. Probing gave an idea of the density and strength of soils at a certain depth and characterized changes in the vertical section.

The shear resistance of soils in the field was assessed in both rocks and soils. The shear resistance of soils was determined by the stress limits at which they begin to fracture.

In rocks, the experiments were carried out in construction pits, in which the pillars of undisturbed soil of columnar type are left. A horizontal shear force was applied to the pillars. At the same time, the experiments were carried out on at least three columnar pillars for the correct determination of internal friction and specific cohesion. Shifting in soils was performed in two ways: 1) on targets; 2) using rotary shears with impeller torsion. The operation on targets is similar to rocks. The impeller is a paddle device and is used to determine shear resistance in dusty clay soils. A four-bladed impeller probe was lowered into the borehole bottom, pressed into the soil and rotated. The torque was measured and the shear resistance was calculated (Ananyev & Potapov, 2005).

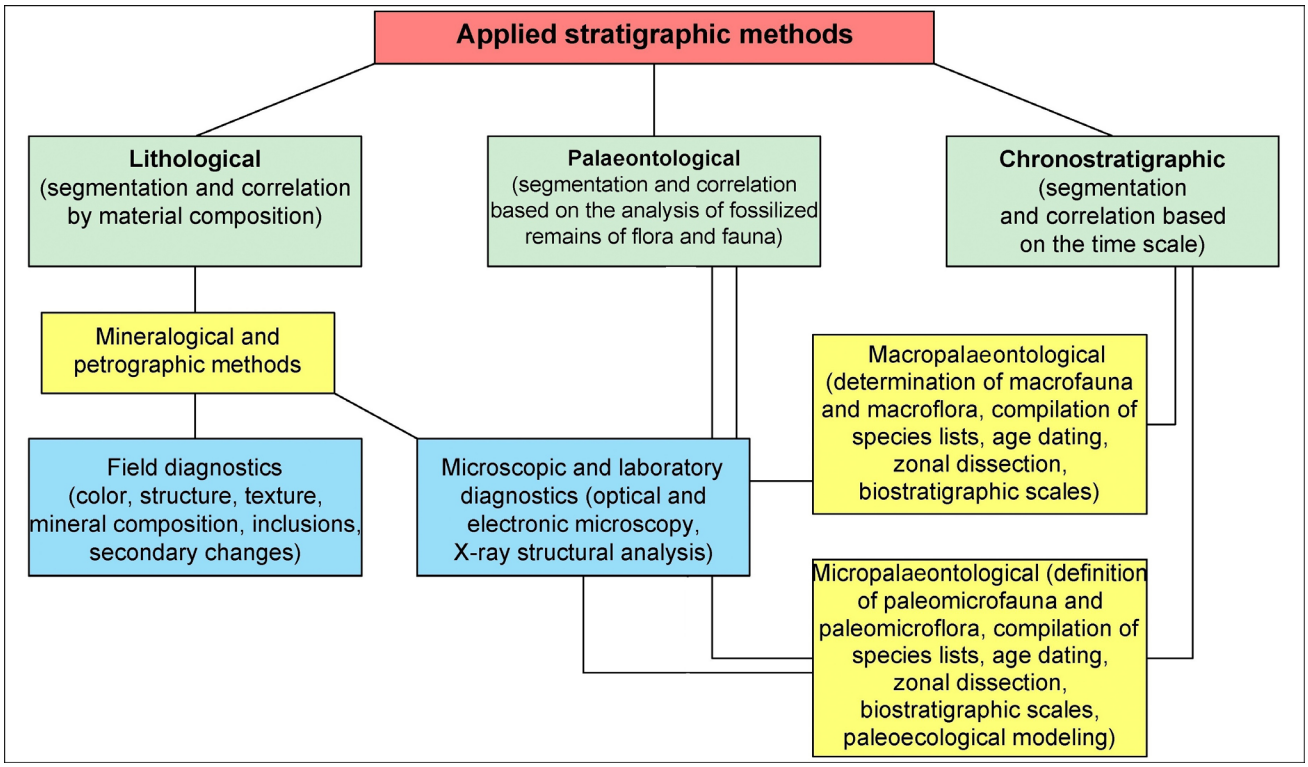

Fig. 4. Stratigraphic methods of the current study.

Laboratory soil testing is also an important geotechnical method. Soil samples for laboratory investigations were collected from soil layers in boreholes located at the construction sites under investigation. Soil samples were delivered to the laboratory as monoliths or loose samples.

All physical-mechanical and physical-chemical properties of soils can be determined in laboratory conditions. Each characteristic of these properties is defined according to its SSU, e.g. physical-mechanical, physical-chemical characteristics are defined according to SSU B V.2.1-3-96, particle size distribution is defined according to SSU ISO 11277:2005, tensile strength is defined according to SSU B V.2.1-4-96, etc. (Fig. 5).

Geotechnical research methods included borehole drilling and mining, field and laboratory studies of the soils (engineering-geological elements) identified within each stratigraphic-genetic complex. All strength and deformation characteristics of both rocks and soils were determined in the field. The compressibility of soils was studied by die methods, pressiometers, and dynamic and static probing. In-situ and laboratory investigations were performed using Ukrainian standards

Today laboratory tests remain the main type of determination of physical-mechanical and physical-chemical properties of soils. A number of characteristics, for example, natural moisture content, density of soil particles and some others are determined only in laboratory conditions and with high enough accuracy. The names and values of indicators of geotechnical properties of soils will be displayed further in the article in the relevant tables (Trofimov et al., 2005).

Results

The Upper Cretaceous complex (k_2m_2) developed within the city of Lviv is part of the so-called Lviv Cretaceous trough, composing the uppermost part of the Cretaceous rocks (Figs. 6, 7, 8). It is covered everywhere by Neogene and Quaternary deposits, exposed on the daytime surface only on the sides of deeply incised ravines in the southeast of the territory within the Lysennytska Upland. Cretaceous rocks reach the subquaternary surface in the areas of the Poltva River valley, where they form the bottom of the valley, and also form the bedrock base of the loess cover of the Vynnyky ridge and eastern spurs of hilly ridge Roztocze. Cretaceous rocks are lithologically represented by gray, light-gray, and greenish-gray marls, weakly sandy, weakly layered with interlayers of marly limestone, in some areas with a high content of sponge opicules, fragments of inoceramol shells and other detritus. The bulk of the rock under a microscope is composed of the finest silty particles of carbonate-clayey composition, their size does not exceed 0.01 mm, which determines its pelitomorphic structure. Structurally, the rock is characterized by the alternation of thin layers enriched to varying degrees in the detrital eleuritic component, which determines the eleuritic-pelitic structure and thin-layered texture of the rock. Clastic material (up to 17 %) whose grain size does not exceed 0.1 mm is represented mainly by quartz and glauconite, with minor amounts of feldspars, sericite, zircon, and rutile.

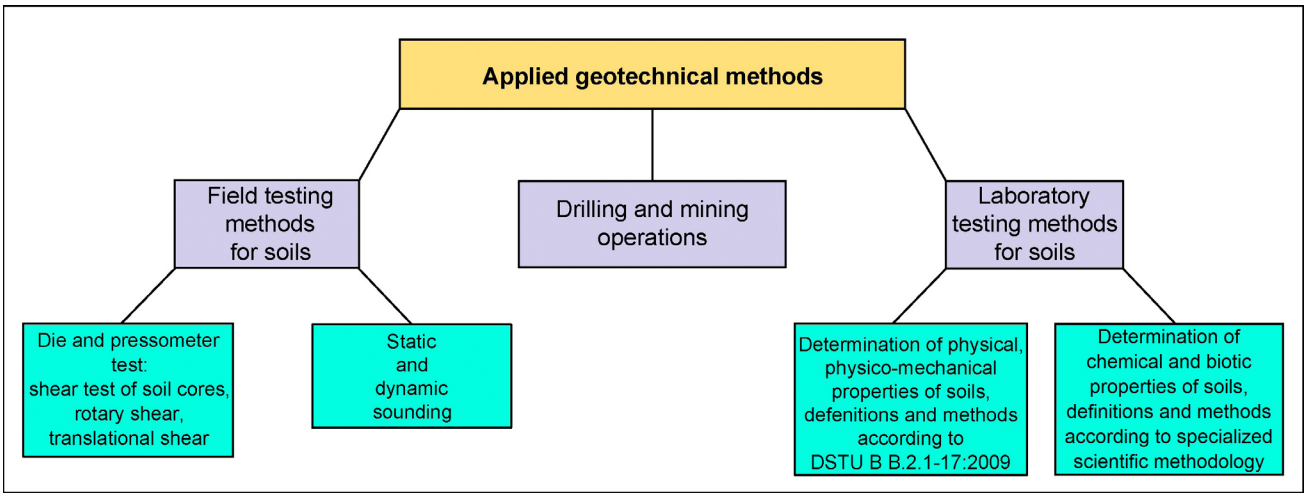

Fig. 5. Geotechnical methods of the current study.

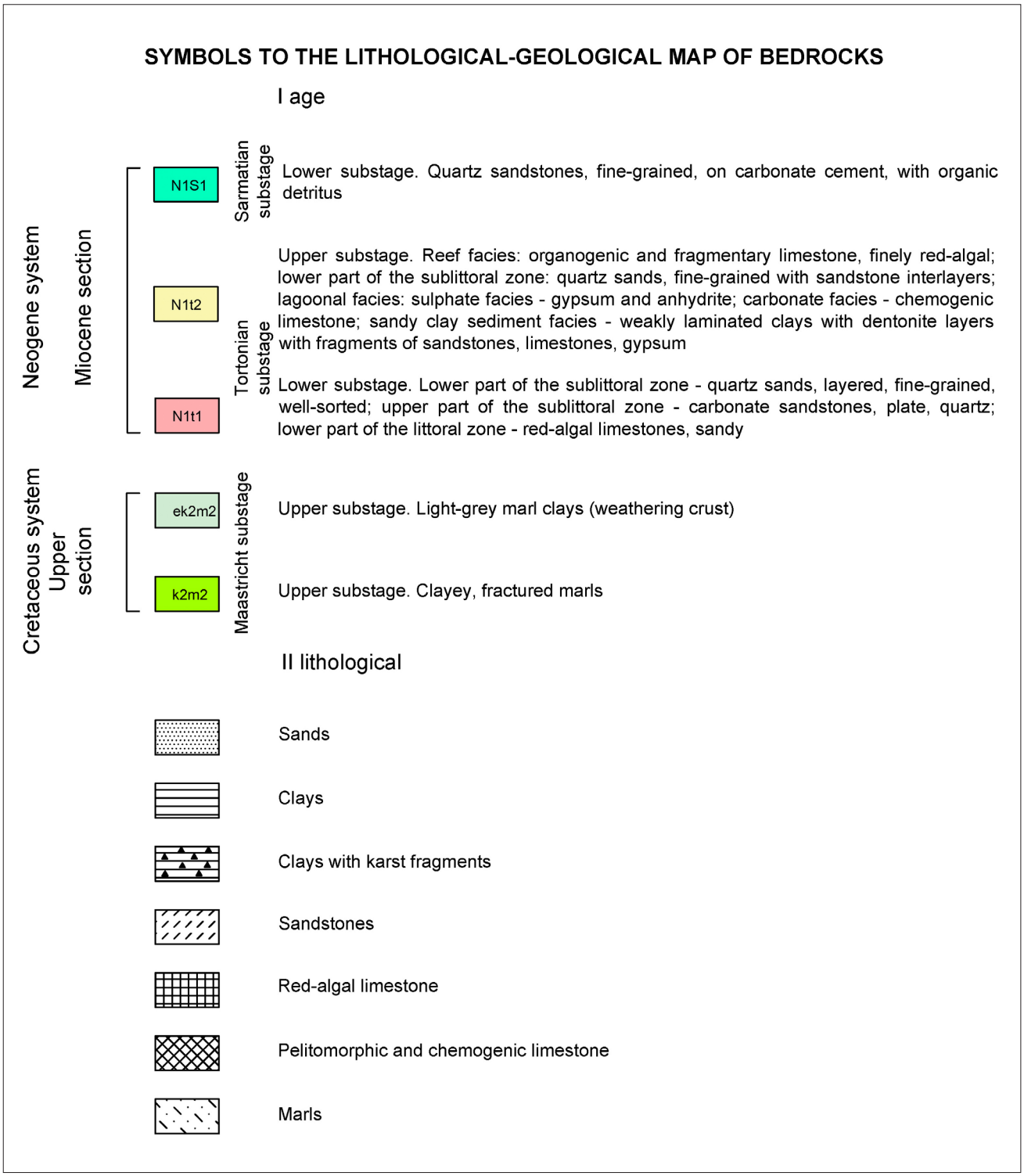

Fig. 6. Symbols for the lithological-geological map of the bedrock of Lviv city.

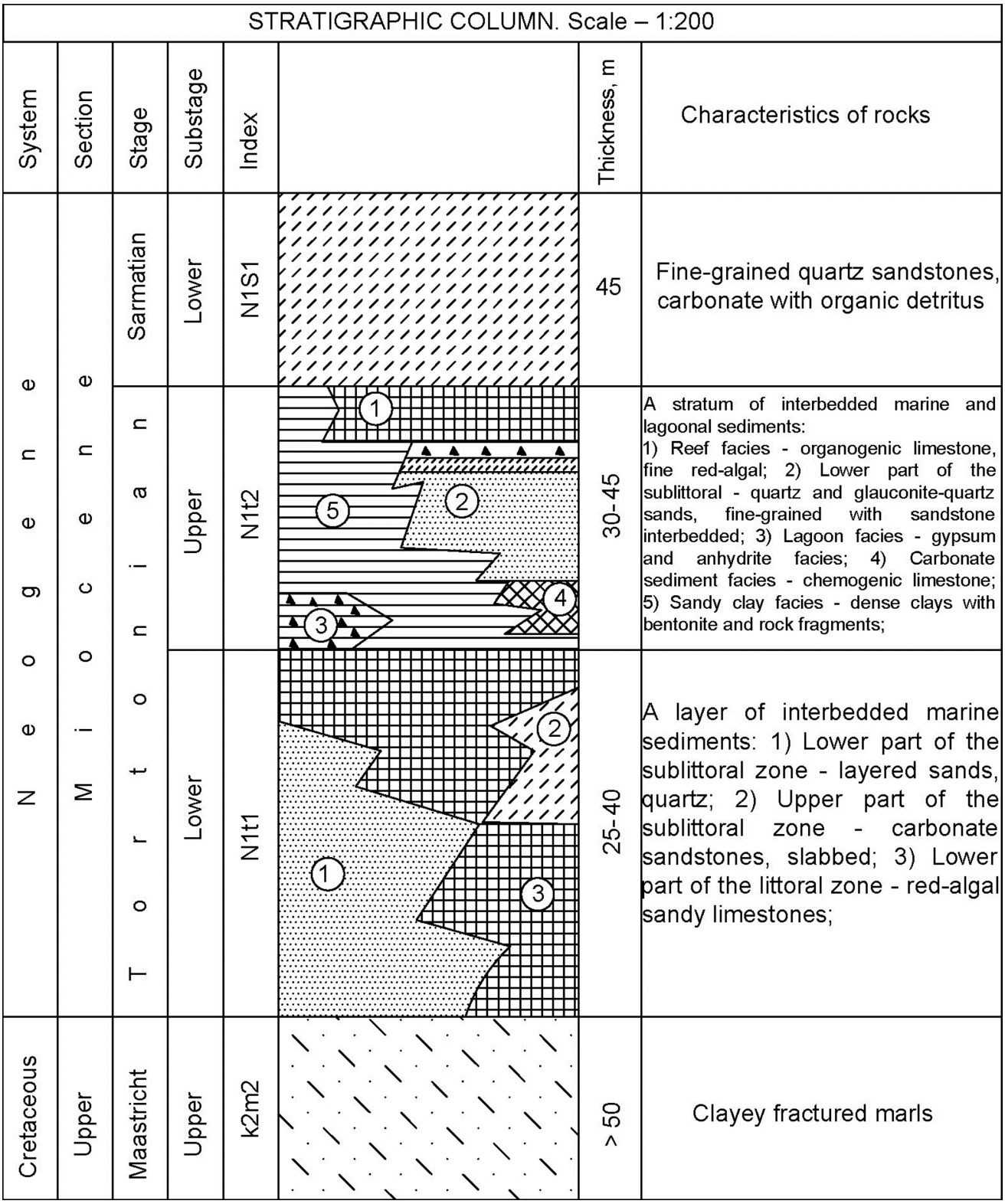

Fig. 7. Stratigraphic column.

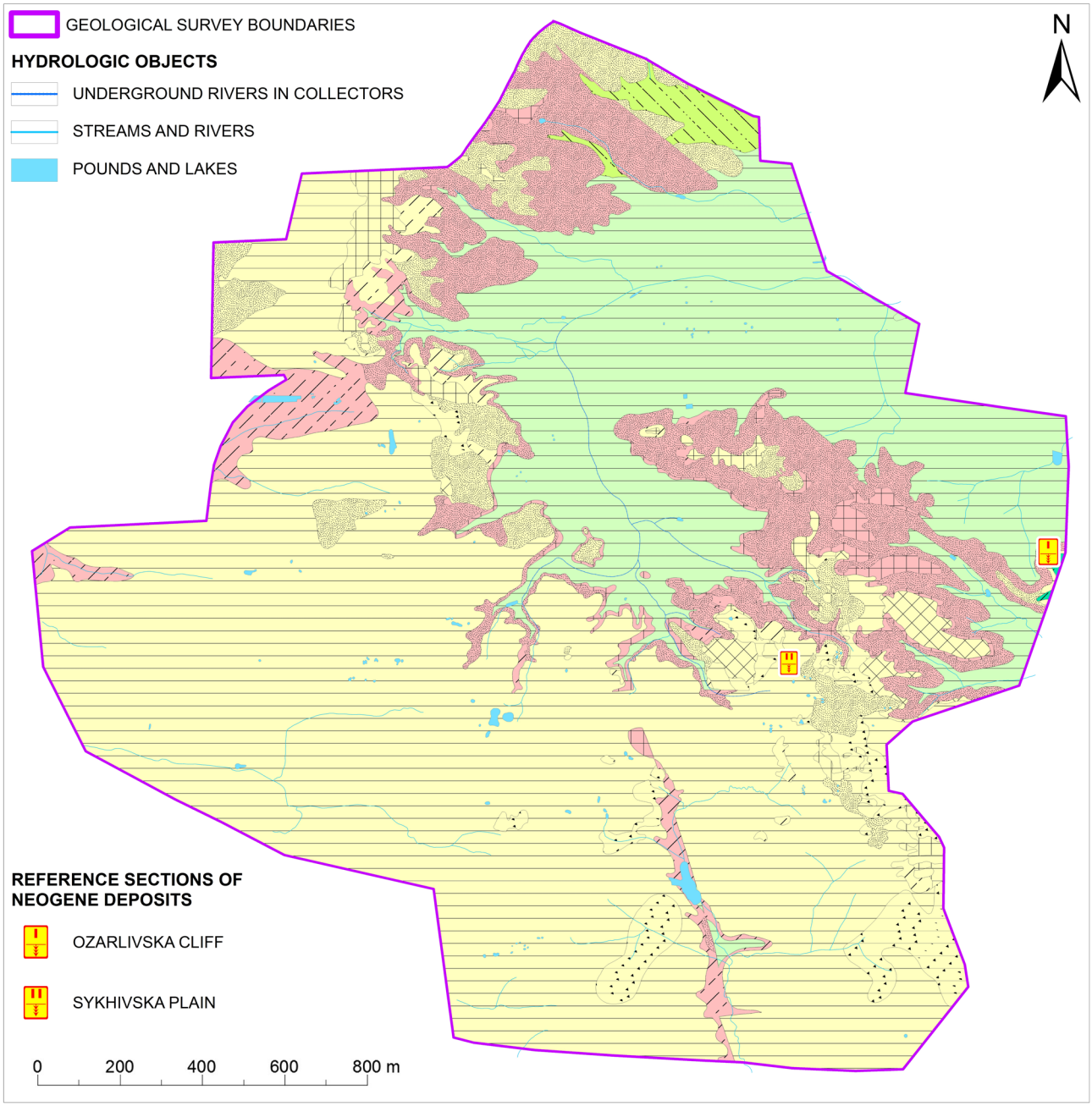

Fig. 8. Lithological-geological map of the bedrock of the city of Lviv.

The marls of Lviv contain an extensive complex of micro- and macrofauna, based on which it has been established that they belong to the upper part of the Maastricht stage, and the so-called ***Belemnitella junior*** zone. (Gruzman, 1980).

The described Cretaceous complex stands out as an independent stratigraphic-genetic complex in engineering-geological terms. Its importance for future construction is especially great in the vast valley of the Poltva River, where intensive civil and residential construction is currently taking place, and where it forms a bearing base (up to 20 m deep) for all types of foundations. The Cretaceous age marls composing this complex have several specific geotechnical properties, which are the object of study during engineering-geological surveys in the Poltva River valley. It has no impact on design and survey work in other areas due to the deep burial of this complex.

Table 1. Engineering-geological elements of the Upper Cretaceous complex.

EGE	Description
Marl	The sedimentary rocks is grey, weakly weathered, low-strength, softening, swelling, fractured, fractures without filler, fracture walls tinny, massive texture, fracture smooth, and mostly watered. The marl often delaminates and disintegrates when saturated with water.

Table 2. Geotechnical properties of rocks of the Upper Cretaceous complex.

№	Indicators of geotechnical properties	Marl
1	Density, γ_o (t/m^3)	2.63
2	Bulk density, γ_c (t/m^3)	2.12
3	Soil carbonate, (%)	48
4	Tensile strength in uniaxial compression at water-saturated state, R_c (MPa)	7
5	Tensile strength in uniaxial compression at natural water content, R_c (MPa)	9
6	Tensile strength in uniaxial compression at air-dried state, R_c (MPa)	15
7	Weathering coefficient	0.90
8	Softening coefficient	0.15
9	Degree of saturation, S_r (%)	0.89
10	Swelling coefficient, (%)	3.7

Clay complex of the weathering crust (ek$_2$m$_2$). This complex is widespread in the northern and central parts of Lviv (Figs. 6, 7, 8). This is the Poltva River valley and the dissected northern slope part of the Lviv plateau according to the taxonomy of geomorphological zoning. The thickness of sediments is mainly 1-2 m and only at the sides of the Poltva valley, and in some cases of the valley itself, it increases up to 10-11 m. This is explained by the fact that from the valley sides, the sediments were partially swept away by denudation processes, while in the Poltva Valley, they are developed and preserved intact in the near-slope areas and some parts of the valley. The deposits are characterized by the content of clastic material, which varies from single inclusions in the roof to 30-40 % at the bottom. Different $CaCO_3$ content in soils determines their different dispersibility and plasticity, and consequently their classification indices. It was not possible to establish any regularity in the spatial distribution of hard and half-hard loams, and hard and half-hard clays. The geotechnical properties of the selected nomenclature soil types are described below (Gruzman, 1980).

The Neogene complex (N) is lithologically the most complex and consists of a motley mix of a significant number of sedimentary rocks from different facies zones of the open sea. Neogene rocks are ubiquitously developed within the Lviv Plateau, the Roztocze Ridge, the Bilohiria-Malchytska Valley, the Zubra River Valley, and are absent in the Poltva River valley and on the loess Vynnyky and Malekhivska ridges.

Table 3. Geotechnical properties of clayey soils of the weathering crust.

№	Indicators of geotechnical properties	Half-hard loam	Hard loam	Half-hard clay	Hard clay
1	Bulk density, γ_c (t/m^3)	1.93	1.85	1.89	1.92
2	Porosity, e	–	0.80	–	–
3	Degree of saturation, S_r (%)	0.28	0.22	0.29	0.25
4	Modulus of deformation, E_o (MPa)	4.9	6.4	5.3	6.9
5	Specific adhesion, C (KPa)	39.2	41.1	37.5	38.2

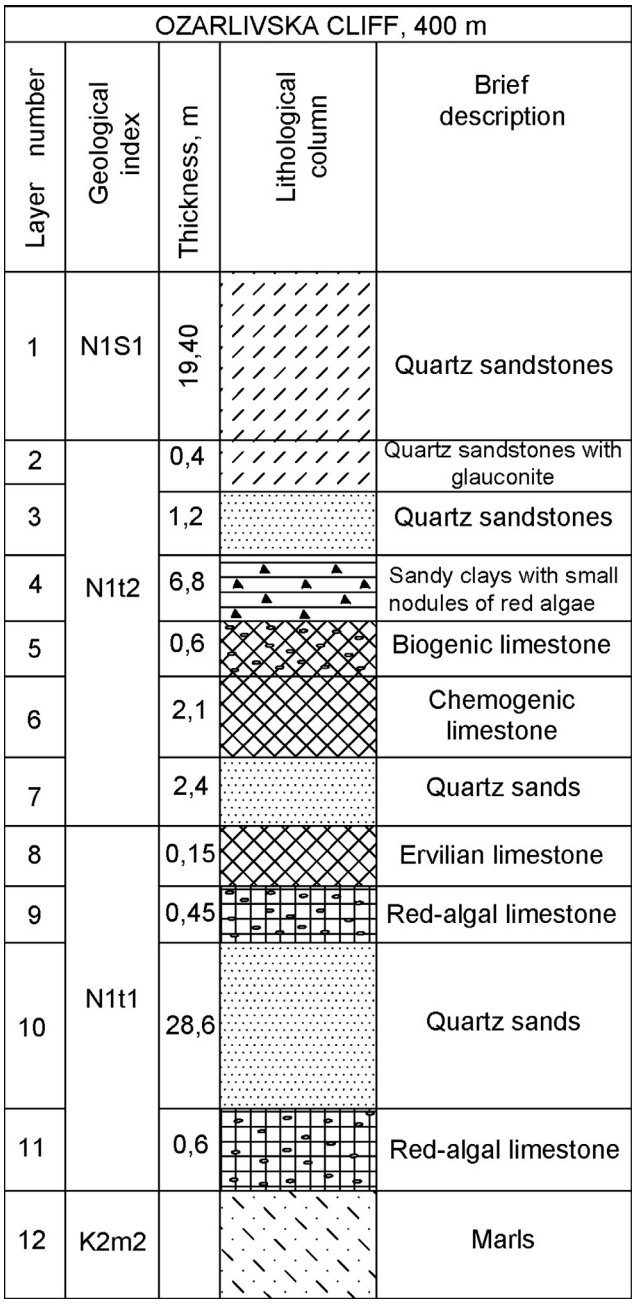

Fig. 9. Reference section of the Neogene strata of the Lviv city "Ozarlivska Cliff".

The Neogene complex is traditionally divided in age into two parts, corresponding to the supra-Ervilian and sub-Ervilian layers of the Lomnicki Formation (Lomnicki, 1897). The lower part belonging to the Lower Tortonian Substage is combined into the Opolian horizon, and the upper part comprising the Upper Tortonian Substage is allocated to the Tyrassic horizon. These strata are separated by a peculiar Ervilian horizon, which in the conditions of Lviv city serves as a marking age reference. However, it should be noted that the position of this horizon in the regional plan for the Neogene complex of the Ciscarpathian region contradicts many factors and its marking position was not recognized by several geologists. The most complete section of the Neogene complex was uncovered by a borehole on the Ozarlivska Cliff (Fig. 9) and this section was the reference for mapping the Neogene strata of the Lviv city.

The Lower Tortonian deposits (N_1t_1) on the territory of Lviv city include deposits of the following facies zones (Figs. 6, 7, 8):

- The lower part of the sublittoral zone of the sea – quartz sands;
- The upper part of the sublittoral zone of the sea is quartz sandstones;
- The lower part of the littoral zone of the sea – lithothamnium sandstones and limestones;
- Deposits of the desalinated sea – sandstones and limestones with Ervilia pusilla Phil.

1. Deposits of the lower part of the subtidal zone, known in previous schemes as the Mykolaev or Opillia layers, are represented by sands of various grain sizes and make up most of the lower Tortonian section. The greatest thickness of sandy sediments is confined to the eastern and south-eastern parts of the territory – on the Sykhivska Plain, it reaches 32–40 m (Fig. 10).

Geologist Leonid Kudrin divided the entire thickness of sandy sediments into two parts, formed in different facies conditions: the facies of sandy sediments of the open sea and the complex of submarine deltaic facies (Kudrin, 1966). The Lower Tortonian sands on the territory of the city of Lviv are considered by many researchers as submarine deltaic deposits. The basis for this conclusion is the presence of cross-bedding and fragments of silicified wood, devoid of bark, which is considered a sign of river transport of sands. However, a more or less detailed study of cross-bedding in numerous quarries in Lviv city showed that the layered formations of sublittoral sandy sediments are distinguished by internal structure features that contradict their classification as submarine deltaic textures. Vertical alternation of a series of different thicknesses without visible or significant changes in the granulometry and thickness of the constituent layers is quite common for cross-bedded deposits. The rule is a subparallel horizontal occurrence of serial seams. Although there are relatively frequent cases of displacement of the boundaries of obliquely layered series, in which the series has the appearance of concave, less often convex inclined lenses with a larger or smaller radius of curvature. Bedding is either unidirectional or alternately multidirectional; S-shaped cross-bedding is widespread along the direction of layers in adjacent series. All these features are not characteristic of deltaic layering,

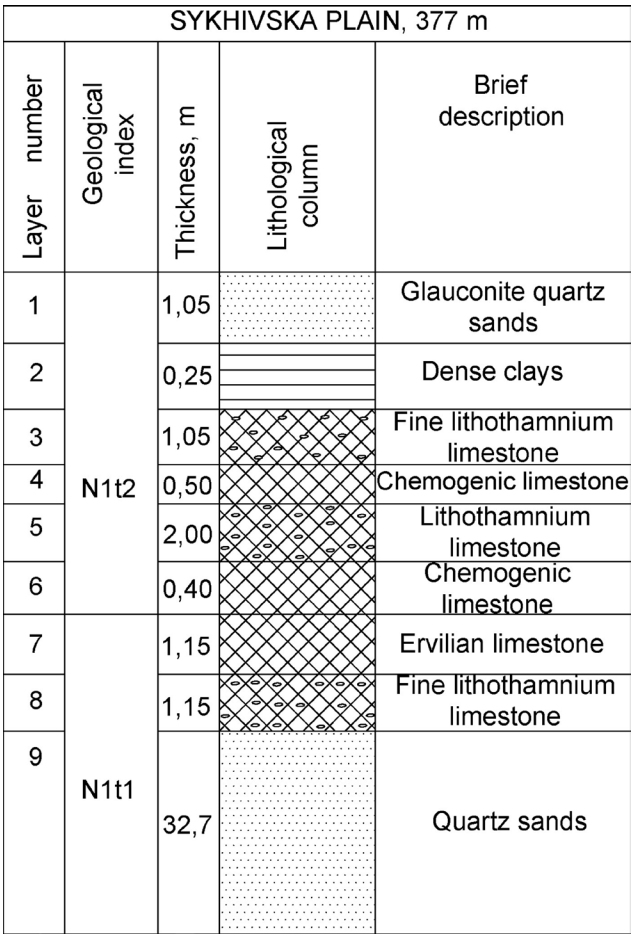

Fig. 10. Reference section of Neogene strata of Lviv city "Sykhivska Plain".

and even in the description of the latter, which is given by geologist Leonid Kudrin, one of the main features of submarine deltaic accumulation is missing – the cross, imbricated shape of serial sutures of cross-bedded units. There were no cases of confinement to the surfaces of the boundaries of a series of plant detritus, so common for the layering of river fans. Also unusual for deltaic formations is a typical detail of the internal structure of the Lower Tortonian sands: the separation of layers of the same order in thickness into packs or series, which alternate with non-layered strata, sometimes reaching impressive thicknesses of 12–15 m.

Thus, the nature of the internal structure of the Lower Tortonian sands on the territory of Lviv city makes us consider this entire sequence to be a single genetic formation, formed under conditions of quiet sedimentation of the open sea, in some areas of which the bottom currents arose with the formation of an inclined-layered texture. Bottom sediments reach their greatest thickness in the south and southeast of the territory, where they are 35–40 m.

Among the sands of the Sykhivska Plain, the light fraction is about 99.9 %, and the heavy fraction is 0.1 %. The light fraction is practically monomineral: the quartz content ranges from 99.4 to 100 %. Glauconite, feldspars, and carbonates with a total content of 0 to 0.6 % are present as impurities. Particles of carbonate material and fractions with a grain size of up to 0.5 mm are absent or present in negligible quantities in the form of a cementing mass. Feldspars contained in sands are essentially potassium in composition.

The lithologic-facies isolation of sandy deposits as part of the Lower Tortonian cycle made it possible to identify them as an engineering-geological element of the Lower Tortonian stratigraphic-genetic complex.

2. The upper part of the sublittoral zone includes quartz sandstones, which in some areas form rock and bedrock outcrops such as armored surfaces. They make up the Lower Tortonian section within the Western planning area, replacing a thick layer of sand. They are covered everywhere by Upper Tortonian clays and gypsum. In all other sections, they occur in the form of frequent interlayers of varying thickness (from 0.1 m to 10 m) among the quartz sands of the lower Tortonian.

The colour of the rocks varies from light yellow, and gray to greenish-gray. Studies of sandstones in thin sections using the immersion method showed that their composition is monomineral sandstones. The grain size is 0.01–0.1 mm, which determines the silty structure of the rocks. The composition of the clastic part includes glauconite. Fine- and medium-grained sandstones predominate according to mechanical analyses.

A feature of the rocks of this facies is the almost universal, but extremely uneven content of coarse clastic material of black chert. In some areas, there is a spotty alternation of interlayers and lenses of different sorting of grains, up to the identification of gravel packs. Quite often in sandstones, there is an accumulation of broken shells or large fragments of thick-walled fauna, as well as single fibrous concretions of red algae. As the amount of the latter increases, the sandstones are replaced by shallower formations compared to the previously described sands and were deposited in the intermediate zone between the sublittoral (quartz sands) and littoral (lithothamnium limestones) facies.

Sublittoral sandstones stand out as a strong engineering-geological element in engineering-geological terms. Their importance in this regard is increased by the fact that in several places they emerge on the daylight surface and can serve as a rock foundation for building structures.

3. The main feature of the deposits of this facies zone is the presence of organic remains from the class of red algae. The traditional name of these rocks (lithothamnium limestones and sandstones) is because it was initially believed that the red algae in them were represented only by the Lithothamnium species. But later, geologist Vladimir Maslov showed the widespread distribution of other representatives of red algae – Lithophyllum and Mesophyllum. Therefore, geologists began to call them red-algal limestones and sandstones. Red-algal rocks occupy very different positions in the sections of the Lviv Tortonian – at the base of the Opillia horizon (the central part of the Lviv plateau), at the top of the horizon (Roztocze ridge), sometimes completely composing the section of the Lower Tortonian (eastern part of the Lviv plateau). Red-algal rocks are present both at the base and at the top of the Lower Tortonian in the most complete Neogene section (in the borehole near the Ozarlivska Cliff). Three layers of lithothamnium limestones were found in sections of the Northern planning area. The thickness of the rocks is generally small (up to 4 m), except for those sections where red-algal rocks entirely compose the Lower Tortonian section, and then their thickness increases to 18 m.

The sediments of this facies are composed of concretionary red-algal limestones and sandstones. Coarse layering is often observed in them due to the different nature of cementation of the underlying nodules or their coarseness. Massive varieties occur besides concretionary varieties, connected by gradual transitions. The rocks are generally light grey to yellowish grey in colour, usually coarsely slabbed. The diameter size of red-water nodules reaches sometimes 10 cm. The histological structure of the algae, consisting of pelitomorphic calcite and characterized by sheaf-like arrangements of sieve-like rows, is visible in the splits. The bottom rocks are characterized by a constant admixture of clastic material consisting of poorly sorted and variously fossilized sandy fragments of quartz, glauconite, feldspars, and flints.

Red algal rocks were formed in areas of shallow water, in the zone of tidal action at a depth of not more than 60 m, accessible to the influence of solar radiation, as evidenced by the lithological composition of rocks and ecological features of red algae. In addition, the red-algal rocks were deposited on uplands of the chalk substrate, where sunlight penetrated and in this case, they are characterized by the presence of uncemented or weakly cemented nodule varieties. Red-algal (lithothamnium) limestones along with the described sandstones form another class of rocks in the Lower Tortonian complex. Although they are connected by various transitions, their engineering-geological properties are sharply different, which necessitates their separation.

Sandy-calcareous rocks with a massive accumulation of internal cores and shells of Ervilia pussila Phil belong to the deposits of a desalinated, regressive basin. These sediments have been given an important stratigraphic position since Lomnický's time and are usually isolated as an independent stratum. Certain facts emerged in the process of large-scale surveying that contradict the marking significance of the layers with the Ervilian fauna. These rocks occur everywhere on the boundary of the Upper and Lower Tortonian on the territory of the Lviv city and therefore they were considered as a separate horizon during the works. Ervilian deposits are distributed only in the eastern part of the studied area – on the Lysennytska and Ratyn uplands and the northern planning area. The maximum thickness of Ervilian deposits was recorded in the section of Zamkova Hill (1.1 m), in other places it varies between 0.1–0.7 m. The poverty and specificity of the species composition of the fauna of the Ervilian layers indicate unfavorable living conditions associated with the sharp shallowing and significant desalination of the basin at the end of the Lower Tortonian time. The water salinity was no lower than 17 ‰. The lithological composition of the deposits and the large accumulation of remains of sessile benthos indicate a slow rate of sediment accumulation and conditions of sea regression. Deposition of the Ervilian layers ends the Lower Tortonian sedimentation cycle (Gruzman, 1980).

The identified lithological-facial features of the Lower Torton sediments allowed the engineering-geological survey to segregate them into a separate stratigraphic-genetic complex consisting of several engineering-geological elements. Although the Lower Tortonian soils act directly as a bearing basement in a limited area (mainly on the slopes of uplands), they are involved in the sphere of the impact of engineering structures in most of the territory of Lviv, which predetermined the need for stratigraphic and lithological-facial study of these rocks for geotechnical purposes.

Upper Torton (N_1t_2). The next cycle of sedimentation in the study area is associated with the Upper Tortonian transgression, which completely covered the studied area of Lviv and had the greatest development here (Figs. 6, 7, 8). On the territory of Lviv city, there are several reference sections, which formed the basis of the classical scheme of stratification of the Upper Torton – Ratynska Upland, Kartumova Hill, Zamkova Hill, and Snopkivsky Range.

Table 4. Engineering-geological elements of the Lower Torton deposits.

EGE	Description
Limestone	Organogenic, organogenic-clastic, strong, fractured, cavernous, white with a greenish tinge, 8-10 m thick.
Sandstone	Sandstones are fine-grained, greenish grey on clayey cement, carbonate, and fractured, with the inclusion of freshwater fauna in the southwest. Sandstones are grey and light grey, weathered, and fractured, with interbeds of strongly fractured sandstone within the Kleparivska Upland. Sandstones can be used as a natural foundation for buildings and structures.
Fine sand	Sand is fine with thin interlayers and nests of dusty and medium, low-moisture, medium density, yellowish-grey, and light grey, quartz, in the lower part of the layer with crushed limestone and sandstone up to 40 %, up to 8.5 m thick. The sands can serve as a natural foundation for buildings and structures, as well as a bearing layer for pile foundations.
Dusty sand	The sands are greenish and light yellow, weakly yellow, medium to dense, homogeneous, low-moisture, up to 5.1 m thick. The sands can be used as a natural foundation for structures.
Medium sand	The sands are yellowish and bluish-grey, water-saturated, medium density, quartz-feldspar, semi-calcareous, and homogeneous. The sands can be used as a natural base for buildings and structures.

Table 5. Geotechnical properties of rocks of the Lower Torton.

№	Indicators of geotechnical properties	Limestone	Sandstone
1	Coefficient of non-uniformity, C_u	0.11	0.19
2	Density, γ_o (g/cm^3)	2.72	2.67
3	Bulk density, γ_c (g/cm^3)	2.39	2.4
4	Porosity, e	12.5	8.3
5	Water absorption, w_{abs} (%)	5.05	–
6	Tensile strength in uniaxial compression at dry state, R_c (MPa)	15.8	13.7
7	Tensile strength in uniaxial compression at water-saturated state, R_c (MPa)	13.8	10.8

Table 6. Geotechnical properties of sandy soils of the Lower Torton.

№	Indicators of geotechnical properties	Fine sand	Dusty sand	Medium sand
1	Coefficient of non-uniformity, C_u	0.24	0.25	0.25
2	Water content, W (%)	–	26	–
3	Degree of saturation, S_r (%)	0.28	0.30	0.83
4	Theoretical resistance index, R_o (MPa)	13.8	–	–
5	Porosity, e	0.7	0.64	0.59
6	Internal friction's angle, φ (°)	35	26	35
7	Bulk density, γ_c (g/cm^3)	1.70	1.91	1.99
8	Specific adhesion, C (KPa)	1.96	1.72	1.98
9	Modulus of deformation, E_o (MPa)	24.5	14.3	17.2

The dissection of the Upper Torton deposits in the area of Lviv city is presented as follows:

I. Facies of the open sea:

- Upper part of the sublittoral – reefogenic facies: shallow lithothamnium limestones,
- The lower part of the sublittoral – quartz and glauconite-quartz sands.

II. Lagoon facies:

- The phase of sulfate sediments – gypsums, anhydrite.
- Carbonate sediments – chemogenic limestones.

III. Transitional facies:

- Sandy-clayey sediments - dense clays with interlayers and nests of sandstones, with fragments of karst rocks (limestone, gypsum).

1. The presence of reefogenic deposits in the Upper Torton in the territory of Lviv city confirmed the existence of a reef ridge in the southwest of the East European Platform. In the area of works, this facies is represented mainly by fine concretionary lithothamnium limestones of grey colour on clay cement and consists of a heterogeneous accumulation of small nodules and their fragments

of 0.5 to 5 mm size cemented by clay-carbonate mass. Occasionally, limestones gradually change to layered grey and greenish-grey clays and small nodule red algae. Under the microscope it can be seen that the rock consists of small nodules and fragments of red algae, to which foraminifer shells and fragments of corals and mollusks are mixed in subordinate quantities. The thicknesses of these deposits vary from 1.0 to 5–6 meters.

These rocks compose the most elevated parts of the relief and can be traced in a discontinuous band, starting in the south-east of the territory (Sykhivska Plain and Ratynska Upland) at 360–370 m and ending in the northern spurs of Kleparivska Upland at 350–380 m. The width of the strip in the widest part reaches 2.5–2.8 kilometers and the narrowest (Zamkova Hill and the western part of the Northern planning area) is 0.5–0.8 kilometers.

A large deposit of bioherm-type riffogenic rocks was identified during the works, located within the northern spurs of the Kleparivska Upland and the western part of the Goloskivska Upland and confined to an anticlinal uplift of the Cretaceous substrate. The central part of the bioherm, located at the maximum elevations of the territory, forms an armored site. It is composed of slabby recrystallized fine lithothamnium limestones with subhorizontal positions of planes of separateness.

The identification of reefogenic deposits in the cycle of the Upper Tortonian transgression makes geotechnical sense in that in several places they serve as a rock base for housing and civil engineering. Therefore, the geotechnical properties of these soils due to genetic features are important for the engineering-geological characterization of these areas.

2. As a single genetic formation, the Upper Tortonian sublittoral sediments consist of a variegated combination of essentially clastic sediments. The main role in this complex is played by multigrain quartz sands, always well pelletized, greyish-green due to insignificant but notable admixture of glauconite. Compacting, the sands are replaced by sandstones of the same composition, which in some cases represent the entire section of the sublittoral zone. Often the composition of sandstones changes towards an increase in carbonateness and an increased role of cement in the rock texture. These varieties are distinguished by an increased content of organic and plant detritus and an accumulation of internal lamellar gill nuclei. Rapidly disappearing interlayers and lenses of gravel and pebble material are observed in some sections.

Having a similar material composition, the Upper Tortonian sands on the territory of Lviv city differ in the conditions of occurrence. They have a continuous area distribution in the east of the territory, on the elevated side of the Lysennytska tectonic zone. In the central part of the district, in the area enclosed between two faults (Lysennytsky and Zubrovsky), sands lie in a complex interlacing with reefogenic lithothamnium limestones and lagoonal "ratynsky" limestones, nevertheless quite often forming independent fields. In the western part of the studied area, sands have no independent position and are subordinate to the clayey stratum, forming more or less extended and thick interlayers.

3. Sulfate deposits of gypsums and anhydrites are of particular importance for the assessment of the area for prospective construction. Long-term studies of sulfate rocks in the Precarpathian region have revealed a great variety of petrographic varieties: anhydrites, gypsums, gypsoanhydrites, sulphate-carbonate rocks, sulphur-bearing and ore-free limestones. Even greater diversity is revealed in the morphological structure of rocks – up to 12 types of structures are distinguished.

The sulfate strata on the territory of Lviv are spread in the west and south: starting at the headwaters of the Bilohiria-Malchytska valley it covers the western and southern outskirts of the city in a giant semicircle, composing the territory of the South-Western planning district, the Southern planning district and the outskirts of the Sykhivska Plain. In its composition anhydrites are dominant, and gypsums and transitional varieties – gypsoanhydrites – are much less widespread. There are no indications of other petrographic varieties. The thickness of sulfate rocks naturally increases to the west, where it reaches 13 meters.

There is no zoning of lithological and petrographic types of gypsum-bearing formations and data of specialized studies of sulfate rocks on the territory of Lviv city. It follows from descriptive works that of petrographic varieties gypsums have the greatest predisposition to karst formation, and of textural-structural types – coarse-crystalline types – columnar, sheaf-shaped, radial-radiate, needle-shaped, twin-like. But at the same time, anhydrides are subject to hydration processes, which can also cause karst formation.

4. The studied area contains a stratotypic section of sediments of lagoonal carbonate facies, the location of which gave the name to these rocks – Ratyn Hill. Here the greatest thickness of these limestones on the territory of Lviv (14 m) was uncovered. Ratyn limestones form dense hard rocks

of grey, creamy- and brownish-grey colour, often with significant clay admixture, detectable by dark grey colouring and the earthy surface of fresh chipping. Very often they bear traces of marked calcification. Limestones are characterized by a pelitomorphic structure and their grain size does not exceed 0.01 mm. Very often limestones reveal various kinds of clotted structures characterized by sometimes complex textural patterns. The usual clot structure consists of the presence of pelitomorphic lumpy clots with vague outlines of calcite. Sometimes the clots have the character of vein-like formations, intricately branching in the rock mass. Connecting, they form a fine-mesh network, the cells of which are made of fine-grained calcite.

5. The characteristics and conditions of sandy-clay deposits have been reported previously. It should be added that under the microscope the main mass of these rocks is composed of clayey material with an admixture of carbonate and is characterized by a pelitic structure. It contains thin phenocrysts of pyrite and carbonized plant detritus. The sulphate component gives lenticular and rounded formations revealing an aggregate structure. At the same time, the carbonate-clay matter of the main mass seems to flow around anhydrite inclusions, which determines the glass structure of clays (Gruzman, 1980).

Genetic peculiarities and stratigraphic independence allowed the described rocks to be identified as an independent stratigraphic-genetic complex. The lithological diversity of the Upper Tortonian rocks ensured the separation of a large number of engineering-geological elements with different geotechnical properties in this complex. The Upper Tortonian marine stratigraphic-genetic complex is not only the most complex, where all engineering-geological types of soils are combined, except for peat soils but also has the largest area distribution on the territory of Lviv.

Table 7. Engineering-geological elements of the Upper Torton deposits.

EGE	Description
Sandy limestone	Moderately weathered, strongly fractured, fractures 0.1–1 cm in size are randomly orientated and filled with sandy-clayey material with faunal remains. The thickness of sandy limestone is 1.8–2.8 m.
Chemogenic limestone	Low-strength, homogeneous, fractured, on clay cement, whitish grey. The thickness is from 0.8 to 4.0 m.
Gypsum	Crystalline, smoky, moderately weathered, and fractured – fractures up to 5 cm wide, watered along the fractures, karst phenomena are developed. Caverns are sometimes filled with tight and soft plastic clay with lenses of dusty sand. Gypsum thickness ranges from 1.8 to 13 meters. Fractured pressure waters are found in gypsums. Gypsum under load can cause uneven settlement of foundations due to uneven cavernousness in the plan.
Sandstone	Fine-grained, dense, on clay and lime cement, fractured, fractures of different densities, mainly vertical. Fractures of different widths – hair-like and thin up to 1 mm, less often 2-5 mm, and single fracture 5–20 mm. The fractures are closed, and some are filled with clayey material. The thickness of sandstones is up to 8.2 m. It is a water-bearing rock, fractured water is present. Sandstones occur below the active zone of buildings.
Medium sand	Medium-sized, water-saturated, medium-density, heterogeneous, yellowish-grey sands. They occur in the roof of Upper Tortonian deposits, and underlying gypsums, occur among gypsums. It can serve as a natural foundation for buildings and structures.
Fine sand	Sands are yellowish and light grey, fine with thin interlayers and nests of dusty and medium, low-moisture, medium density. The sands can serve as a natural foundation for buildings and structures, as well as a bearing layer for pile foundations.
Dusty sand	The sands are greenish-yellow, dense, water-saturated, glauconite-quartz, with interlayers and lenses of sandy loam up to 10 cm thick. The sands are water-bearing rocks. Underground waters are not aggressive in all types of corrosion. The sands can be used as a natural foundation for buildings and structures.
Hard clay	The clay is greenish-grey, lumpy with sandstone fragments. Clays can serve as a natural foundation for buildings and structures.
Half-hard clay	Clays are greenish and bluish-grey, strongly sandy, with interlayers of weakly cemented sandstone, with fragments of limestone, with nests of bentonite. The clays can serve as a natural foundation for buildings and structures.
Stiff-plastic clay	Medium compressible clays of greenish-grey colour, lumpy, heterogeneous in composition, with frequent bentonite inclusions. The clays can serve as a natural foundation for buildings and structures.
Hard loam	Loams can serve as a natural foundation for buildings and structures.
Half-hard loam	
Stiff-plastic loam	

Table 8. Geotechnical properties of rocks of the Upper Torton.

№	Indicators of geotechnical properties	Sandy limestone	Chemogenic limestone	Gypsum	Sandstone
1	Tensile strength in uniaxial compression at air-dried state, R_c (MPa)	–	–	–	0.4
2	Tensile strength in uniaxial compression at dry state, R_c (MPa)	–	18.5	13.0	24.5
3	Tensile strength in uniaxial compression at water-saturated state, R_c (MPa)	28.4	12.6	8.2	0.15
4	Softening coefficient	–	–	–	0.50

Table 9. Geotechnical properties of sandy soils of the Upper Torton.

№	Indicators of geotechnical properties	Medium sand	Fine sand	Dusty sand
1	Degree of saturation, S_r (%)	–	0.24	–
2	Porosity, e	–	0.63	0.59
3	Natural slope's angle dry (°)	32	33	39
4	Natural slope's angle underwater (°)	29	32	35
5	Bulk density, γ_c (g/cm³)	1.65	–	2.0
6	Specific adhesion, C (KPa)	1.96	1.96	4.0
7	Modulus of deformation, E_o (MPa)	27.9	–	23.6

Table 10. Geotechnical properties of clayey soils of the Upper Torton.

№	Indicators of geotechnical properties	Hard clay	Half-hard clay	Stiff- plastic clay	Hard loam	Half-hard loam	Stiff- plastic loam
1	Plasticity index, P_I	–	25	–	11	13	13
2	Water content, W (%)	–	27.4	23.8	18.8	22.6	
3	Density, γ_o (g/cm³)	1.89	1.95	1.95	2.02	2.03	1.90
4	Bulk density, γ_c (g/cm³)	1.44	1.54	1.60	1.70	1.63	1.49
5	Porosity, e	0.9	0.5	0.7	0.6	0.6	0.81
6	Degree of saturation, S_r (%)	0.96	0.93	–	0.87	0.95	0.93
7	Soil compaction index, k_{com} (KPa)	2.3	2.0	2.5	–	–	
8	Modulus of deformation, E_o (MPa)	9.1	9.9	9.6	9.8	–	–
9	Internal friction's angle, φ (°)	15	19	18	21	18	19
10	Specific adhesion, C (KPa)	42.9	42.5	43.7	54.9	32.6	27.5

Lower Sarmatian (N_1S_1). Sarmatian deposits are known only on the Ozarlivska Cliff, where they form rock outcrops up to 30 m high. In general, their thickness here is up to 50 m and they are represented by quartz sandstones of light grey colour, dense, multigrained with individual large quartz grains. The cement of the rocks is carbonate, the character of basal-type cementation (Figs. 6, 7, 8).

Discussion

Having characterized the geotechnical properties of stratigraphic-genetic complexes of bedrock in Lviv, it is proposed to discuss the most difficult in geotechnical respect engineering-geological elements, which require certain measures during construction development and organization of engineering preparation of the territory.

The Upper Cretaceous complex is represented by marl, whose geotechnical properties include a tendency to swell. The peculiarity of swelling soils is their ability to decompact and increase in volume when moistened. Subsequent decrease of humidity in such soils leads to shrinkage. Deformations of the foundation soil as a result of swelling and shrinkage may cause damage to construction objects. Water protection measures are implemented first of all to eliminate the negative impact of swelling soil on structures: site planning for drainage of rain and melt water and organized drainage of water from the roof of buildings. One method of eliminating swelling properties of the soil is pre-soaking, which results in raising the soil before construction to a level above which swelling deformations are eliminated. It is also allowed to

build compensating sand cushions, for which sand of any coarseness is used, except for dusty sand. The compaction of sand in the cushions is carried out to the dry density (γ_o = 1.6 t/m³).

The weathering crust is represented by clayey soils characterized by low values of deformation modulus (E_o = 4.9-6.9 MPa). In addition, these types of soils are mainly confined to flooded and non-flooded terraces of the Poltva River, which are characterized by high levels of groundwater table from the day surface. Sand cushions and slab foundations are recommended for these soils (Shutenko et al., 2015).

The gypsum column is identified among the engineering-geological elements of the Upper Torton deposits, which have a propensity for karst formation. Special engineering surveys for karst were carried out in the southern planning area of Lviv in 2020. Gypsum was found to be present in the geological section of the southern part of the city and saucer-shaped waterlogged depressions of karst origin were found on the surface. In this connection, the possibility of deformation of the earth's surface as a result of the collapse of karst cavity vaults or suffusion of loose material of overlying deposits into the cavity and expansion of fractures in gypsum is not excluded, especially if the natural regime of groundwater is disturbed. However, there is little evidence of karst on the earth's surface. No karst failures have been observed in the Southern planning area. Complications in the construction and operation of buildings and structures related to karst in Lviv and its immediate vicinity are practically unknown. Therefore, the following activities are recommended:

1. Do not locate buildings and structures over identified underground cavities of significant size or grout these cavities, do not locate buildings and structures on or near identified surface and buried sinkholes;
2. It is necessary to choose to strip monolithic or prefabricated monolithic reinforced concrete foundations, to use foundations with support on rocks below the karst zone, to use pile-stocks and deep piles when supporting non-karst rocks (Tolmachev, 1986);
3. To prevent the activation of karst-suffosion phenomena it is extremely important to organize a thorough drainage of the storm and waste water from the construction area, to effectively control water leaks from utilities and to eliminate all boreholes exploiting the Neogene horizon, the zones of influence of which cover the territory of the southern planning area, as well as to prohibit the operation of new boreholes in the future (Gruzman, 1980).

Conclusions

1. Geotechnical characterization of soils is based on the identification and mapping of stratigraphic-genetic complexes of rocks, accordingly, the geological basis of engineering-geological surveys should be based on two factors – age (stratigraphic) and genetic. The age factor is regulated by regional stratigraphic schemes, there is no accepted scheme of genetic division of rocks. The main task of studying the geological structure of Lviv for geotechnical purposes is to identify specific features and criteria of the genetic division of rocks, corresponding to the specialization of works. It is necessary to distinguish stratigraphic-genetic complexes based on the adopted stratigraphic-genetic scheme of bedrock dissection.

2. Bed rocks are confined to certain geomorphological units, in connection with which at the primary stage it is necessary to geomorphological zoning of the territory of Lviv. Lviv belongs to the Volhynian-Podolian Region of strata-denudation uplands, in turn, within Lviv city there are two geomorphological subregions - Podolian structural-denudation upland on Cretaceous and Neogene deposits and Lower Pollisia strata-accumulative plain on Cretaceous deposits. These subregions are divided into 6 geomorphological districts and 13 subdistricts.

3. Lithological, paleontological and chronostratigraphic research methods were applied in the study of the stratigraphy of the bedrock of Lviv. Geotechnical methods included drilling and sinking of mine workings, field tests, and laboratory studies of soils.

4. The Cretaceous system is represented by rocks of the Upper Cretaceous complex (k_2m_2): clayey fractured marls with a high content of sponge spicules, fragments of inoceram shells and other detritus. The marls contain an extensive complex of micro- and macrofauna, based on which it was established that they belong to the upper part of the Maastricht Stage, and the so-called *Belemnitella junior* zone. The marl has specific swelling properties, therefore, rain and meltwater drainage, sand cushions, and preliminary soaking are necessary to eliminate this phenomenon. The clay complex of the weathering crust (ek_2m_2) lithological complex is represented by loams and clays. Clay soils are characterized by a small deformation modulus value and occurrence in waterlogged conditions, which requires sand cushions and the choice of slab foundations.

5. The Neogene system is represented by rocks of the Lower Torton, (N_1t_1) Upper Torton (N_1t_2), and Lower Sarmatian (N_1S_1). The Lower Torton

rocks are a thickness of interchangeable marine sediments: the lower part of the sublittoral zone is lithologically represented by laminated, quartz sands; the upper part of the sublittoral zone is represented by carbonate plate sandstones; the lower part of the littoral zone is represented by red-algal sandy limestones. The geotechnical characteristic of the rocks of the Lower Torton is satisfactory, all soils can serve as a natural base for buildings and structures. The rocks of the Upper Torton are a thickness of intermixed marine and lagoonal sediments: reef facies are represented by organogenic fine-lithothamnium limestones; the lower part of the sublittoral is represented by quartz and glauconite-quartz sands, fine-grained with sandstone interbeds; lagoonal facies is represented by gypsum and anhydrite facies; carbonate sediments facies is represented by chemogenic limestones; sandy-clay sediments facies is represented by dense clays with bentonite and rock fragments. Geotechnical characteristics of the rocks of the Upper Torton are as follows: gypsum is characterized by karst formation; sandstones lie below the active zone of buildings; sands, clays, and loams can serve as natural foundations for buildings and structures. The Lower Sarmatian rocks are represented by quartz fine-grained carbonate sandstones with organic detritus, which may well serve as natural foundations for buildings and structures, as they are quite strong.

6. Gypsum is the most problematic rock in geotechnical terms, as it is prone to karst formation. Surveys of buildings and structures that are located in the conditions of these types of rocks have not revealed any deformation, settlement, or emergency condition. However, avoidance measures, special types of foundations, and measures to prevent water leakage from utilities and liquidation of boreholes exploiting the Neogene aquifer are recommended for the Southern planning area of the city.

Acknowledgments

The authors express their gratitude to the leadership of the Lviv branch of Ukrainian Institute of Engineering Scientific and Technical Exploration (LF UKRIINTR) for the provided geotechnical reports and corresponding graphic materials.

References

Ananyev, V.P. & Potapov, A.D. 2005: Engineering geology. Moscow, Vysshya Shkola: 575 p.

Arkhipov, S.A., Vorobyev, A.I., Martynov V.A., Sukhorukova, S.S, Chernousov, S.I. & Shatsky, S.B. 1980: Engineering-geological characteristics of the main stratigraphic-genetic complexes of Cenozoic deposits in the south of Western Siberia. Engineering Geology, 6: 43–50.

Biryuleva, L.V., Polonsky, B.T. & Ismalkova, S.P. 1972: Stratigraphic charts and legends for 1:50000 scale maps of the Carpathian region. Lviv, Lviv Geological Expedition: 177 p.

Bogomolov, A.N. 2011: Engineering-geological characteristics of loess rocks of the Prut-Dniester interfluves. Bulletin of Volgograd State University of Architecture and Civil Engineering. Series: Construction and Architecture, 24: 33–45.

Budkin, B.V. & Cherkez, E.A. 2000: Analysis of engineering-geological efficiency of anti-landslide measures in Odesa, Ukraine. Landslides in Research, Theory and Practice: Proceedings of the 8th International Symposium on Landslides held in Cardiff on 26–30 June 2000: 189–194.

Gruzman, G.G. 1980: Large-scale engineering-geological atlas of Lviv city. Lviv, LF UKRIINTR: 352 p.

Hataullin, V.N. 1991: Marresale formation of the Western Yamal – deposits of the Pra-Ob delta. Bulletin of the Commission on Quaternary Research, 60: 53–61.

Horetsky, V.A. 1977: To the stratigraphy of the Miocene territorial strata of the Outer Zone of the Precarpathian Trough. Paleontological collection, 14: 56–72.

Hozhyk, P.F. 2012: Stratigraphic Code of Ukraine. Kyiv, NASU: 66 p.

Kazakova, V.P. 1952: Stratigraphy and fauna of plate-gill mollusks of Middle Miocene deposits of Opillia. Moscow, Moscow Geological Prospecting Institute: 241 p.

Kopylov, I.S. & Melchakova, N.P. 2020: Engineering-geological assessment and zoning of the central part of Perm Krai for gas pipelines design. Geoecology, engineering geodynamics, geological safety, 5: 216–230.

Kudrin, L. N. 1966: Stratigraphy, facies and ecological analysis of the fauna of Paleogene and Neogene deposits of the Precarpathians. Lviv, Lviv State University: 49 p.

Lomnicki, M.A. 1897: Geology of Lviv and surroundings. Geological atlas of Galicia. Krakow, Krakow Scientific Society: 105 p.

Mokritskaya, T.P. 2012: Aspects of systematization of engineering-geological data on soil properties in the Middle Dnieper region. Sergeev Readings, 14: 55–60.

Mokritskaya, T.P. 2019: Microaggregate composition and other features of the loesses of Kryvyi Rih. Journal of Geology, Geography and Geoecology, 28/1: 133–139. https://doi.org/10.15421/111914

Ogonochenko, V.P., Grinchenko, N.F., Knysh, M.V. & Sapuzhak, A.V. 2020: Engineering-geological characteristics of karst on the territory of IV microdistrict in the Southern planning district of Lviv city. Lviv, LF UKRIINTR: 242 p.

Shabliy, O.I. 2012: Lviv: comprehensive atlas. Kyiv, SSME "Kartographiya": 192 p.

Shutenko, L.N., Rud, A.G. & Kichaeva, O.V. 2015: Soil mechanics, bases and foundations. Kharkiv, Kharkiv National University of Urban Economy: 501 p.

Slavinskaya, M.Y. & Lyubimova, T.V. 2008: Engineering-geological complexes of the Black Sea coast of the North-West Caucasus. Sergeev Readings, 12: 79–83.

State standard of Ukraine 11277:2005, 2005: Determination of soil particle size distribution. Sieving method. Kyiv, Minregion: 34 p.

State standard of Ukraine B V.2.1–3:96, 1997: Soils. Classification. Kyiv, State Committee of Ukraine for Urban Planning and Architecture: 47 p.

State standard of Ukraine B. V.2.1-4-96, 1997: Bases and foundations of buildings and structures. Soils. Methods of laboratory determination of strength and deformation characteristics. Kyiv, State Committee of Ukraine for Urban Planning and Architecture: 107 p.

Tolmachev, V.V., Troitsky, G.M. & Khomenko, V.P. 1986: Engineering-construction development of karst territories. Moscow, Stroyizdat: 176 p.

Trofimov, V.T., Korolev, V.A., Voznesensky, E.A., Golodkovskaya, G.A., Vasylchuk, Y.K. & Ziangirov R.S. 2005: Soil science. Moscow, Moscow State University: 1024 p.

Veklych, M.F. 1968: Stratigraphy of the loess formation of Ukraine and neighboring countries. Kyiv, Naukova dumka: 238 p.

Venglinsky, I.V. & Horetsky V.A. 1979: Stratotypes of Miocene deposits of the Volhynian-Podolian plate, Precarpathian and Transcarpathian troughs. Kyiv, Naukova dumka: 176 p.

Vyalov, O.S. & Horetsky, V.A. 1965: To the stratigraphy of the Tortonian deposits of Volhynia and Podolia. Report of the USSR Academy of Sciences, 1: 86–125.

Zorina, S.O. 2015: Methods of stratigraphic studies. Kazan, Kazan Federal University: 40 p.

GEOLOGIJA 68/2, 307-310, Ljubljana 2025

https://doi.org/10.5474/geologija.2025.004

Data Article

Geochemical dataset of environmental samples from Idrija urban area, Slovenia

Geokemični podatkovni niz okoljskih vzorcev iz urbanega območja Idrije, Slovenija

Špela BAVEC* & Mateja GOSAR

Geološki zavod Slovenije, Dimičeva ulica 14, SI-1000 Ljubljana, Slovenija; *corresponding author: spela.bavec@geo-zs.si

Prejeto / Received 20. 2. 2025; Sprejeto / Accepted 28. 3. 2025; Objavljeno na spletu / Published online 30. 7.2025

Key words: data, urban geochemistry, soil, stream sediment, road sediment, household dust, mining
Ključne besede: podatki, urbana geokemija, tla, potočni sediment, cestni sediment, hišni prah, rudarjenje

Abstract

This paper presents a dataset containing the results of geochemical analyses of three different urban materials- soil, sediment and household dust from the urban area of Idrija town (Slovenia). Topsoil, subsoil and garden soil were collected on the urban green surfaces. Sediments were collected in the gully pots of the urban drainage system (road sediments) and local streams flowing through Idrija's urban area (stream sediments). Household dust was collected from the vacuum cleaner bags, which were provided by the residents. The geochemical analyses carried out were: (1) multi-elemental analysis (determination of element contents after modified aqua regia digestion by inductively coupled plasma (ICP) mass spectrometry and ICP emission spectrometry (ES) and (2) solid phase Hg thermo-desorption technique (determination of the relative amount of Hg binding forms). These two methods were applied to all investigated materials. Water leaching tests were carried out to determine the water-soluble Hg content in the urban soil by ICP-MS. A modified simulated stomach acid extraction in vitro tests were carried out to determine the bioaccessible Hg content in topsoil and household dust by ICP-MS. The dataset has a fundamental scientific value and is useful for local soil, sediment and household dust quality research, mitigation of pollution evaluation over time and assessment of environmental exposure and related health impacts.

Izvleček

Ta članek predstavlja podatkovni niz, ki vsebuje rezultate geokemičnih analiz treh različnih urbanih materialov – tal, sedimentov in hišnega prahu iz poseljenega območja Idrije. Na urbanih zelenih površinah so bili vzorčeni zgornji in spodnji sloj tal ter vrtna tla. Sedimenti so bili vzorčeni iz obcestnih jarkov drenažnega sistema (cestni sedimenti) in lokalnih potokov, ki tečejo skozi urbano območje Idrije (potočni sedimenti). Hišni prah je bil vzorčen iz vrečk sesalnikov, ki so jih posredovali prebivalci Idrije. Geokemične analize vključujejo (1) več-elementno analizo (določitev vsebnosti elementov po modificirani zlatotopki z induktivno sklopljeno plazmo (ICP) masno spektrometrijo (MS) in ICP emisijsko spektrometrijo (ES)) in (2) termično desorpcijsko analizo oblik vezave Hg (določitev relativne količine Hg oblik vezave). Ti dve metodi sta bili uporabljeni za vse preiskovane materiale. Izvedeni so bili vodni izluževalni testi za določitev vodotopne vsebnosti Hg v izlužkih urbanih tal z ICP-MS ter in vitro izluževalni testi z modificirano simulirano želodčno kislino za določitev biološko dostopne vsebnosti Hg v zgornjem sloju tal in hišnem prahu z ICP-MS. Podatkovni niz ima temeljno znanstveno vrednost in je uporaben za lokalne raziskave kakovosti tal, sedimentov in hišnega prahu, vrednotenje onesnaženosti skozi čas ter oceno izpostavljenosti okolju in s tem povezanih vplivov na zdravje.

Background

The presented dataset is a result of a research work carried out during the preparation of a PhD thesis entitled “Geochemical investigation in Idrija urban area with emphasis on mercury” (Bavec, 2015a). Idrija urban area was selected as a case study. In Idrija and surroundings severe pollution and contamination with mercury exist due to historical mining activity (about 500 years). Idrija is Slovenia’s oldest mining town and was the second largest mercury mine in the world after the mine in Almadén, Spain. The mine was closed in 1995. However, Idrija town was successfully transitioned from a mining town to an industrial town. The goals of the research work were to identify enrichments of elements in the studied materials and investigate the potential sources of elements by using the tools of statistical and spatial analysis (Bavec et al., 2014, 2015, 2017; Bavec, 2015b, 2017). Due to the strong mercury contamination

of the investigated area, it was important to examine the properties of Hg in the studied materials, which would help to better understand the fate of mercury in the urban area of Idrija. Hg binding forms were determined to quantify the fraction of mercury, which is more susceptible to the transformations in the environment (Bavec et al., 2014, 2017; Bavec and Gosar, 2016). Water soluble fraction of Hg in urban soil was determined to indicate the portion of mercury in the soil that is relevant to affect the local water cycle, since surface and/or rainwater can leach and mobilize mercury from the contaminated soils to the deeper soil layers and to the groundwater (Bavec and Gosar, 2016). The bio-accessible fraction of Hg in the soil and household dust was determined to perform risk assessment (Bavec et al., 2018).

Value of the data

- A comprehensive dataset is provided to assess the extent and distribution of urban contamination, especially potentially toxic elements in environmental matrices. Furthermore, the dataset includes geochemical characteristics of Hg to better understand its behavior in different urban matrices, including binding forms, bioaccessibility and water solubility.
- Specific to local authorities, the dataset has high relevance for addressing local environmental issues and can help establish tailored mitigation strategies. The data supports evidence-based decision-making for environmental monitoring, public health, and land use management.
- While focused on Idrija, the dataset provides insights into urban geochemistry that can be extrapolated or adapted to similar urban areas worldwide, particularly those with industrial legacies. It can be used to compare geochemical pollution levels between Idrija and other urban or industrial areas, offering insights into specific pollution sources and patterns.
- The pollution of environmental matrices is related with increasing human health risks. The knowledge about chemical elements distribution in environmental matrices of urban areas helps to develop and improve assessment of environmental exposure and related health impacts.

Experimental design, materials, methods, data validation

Altogether 45 soil, 16 road sediment, 14 stream sediment and 16 household dust sampling locations were established. Regarding soil, 45 topsoil (0-10 cm), 45 subsoil (10-20 cm), 12 duplicate soil (6 topsoil and 6 of subsoil), 4 garden soil and 1 duplicate garden soil sample were collected (sum of all samples = 153). Duplicate soil samples were collected randomly within a radius of 10 m from the primary soil samples to estimate sampling variance. Soil samples were pre-treated in the laboratory only for multi-elemental analysis after aqua regia digestion and soil pH analysis. For all other chemical analyses (soil water content analysis, Hg thermo-desorption technique, water leaching test and bioaccessibility leaching test according to the European Standard Toy Safety Protocol) fresh samples were used. To determine the soil pH, dry samples were gently crushed in a ceramic mortar and sieved through a 2 mm mesh sieve. For multi-elemental analysis after aqua regia digestion the samples were additionally ground in an agate mill. To obtain road and stream sediment (<0.125 mm and <0.04 mm) and household dust (<0.125 mm) analytical fractions, dry sieving was carried out. For sediments, the particle size distribution according to the standard (EN ISO 14688-1:2002) was determined. For Hg thermo-desorption technique, fresh soil and sediment samples and dry household dust samples (<0.125 mm) were used. Further details of sampling and sample preparation were already presented in research papers, that is for soil (Bavec et al., 2015; Bavec and Gosar, 2016, Bavec, 2017; Bavec et al., 2018), road and stream sediments (Bavec et al., 2014; Bavec, 2015b) and household dust (Bavec et al., 2017, 2018). Chemical analytical method procedures applied in each sampled material are described in previously cited papers and are also summarized in detail in the Table 3 together with quality control.

Data description

The dataset includes three separate tables. The number of samples within the dataset is higher (n = 183) than that of actually sampled (n = 153). This is because, for road sediments (n = 16) and stream sediments (n = 14), element contents were measured in two analytical fractions (<0.125 mm and <0.063 mm). This is why the number of sediment samples in the dataset is doubled (60 instead of 30).

Table 1 entitled *"Urban Idrija dataset"* is a catalogue of all collected samples and related data. Each sample has a unique identifier (ID), a type, a name and GPS coordinates (D48/GK, D96/TM and WGS84). However, for household dust samples, GPS coordinates are not shared. Due to the sensitive nature of household dust data and its

associated geographic location (which could potentially reveal a resident's identity if coordinates were shared), participants providing household dust samples were assured that raw data would remain confidential. Researchers or experts interested in using this data for research purposes should contact the authors of this paper to explore the possibility of obtaining household sample coordinates. The rest of the data attributes in the dataset describe a characteristic of a sample determined either during field work (e.g. depth) or in a laboratory during sample preparation (e.g. analytical fraction) or with a specific analytical method (e.g. pH). Altogether, the table consists of 81 attributes.

Table 2 entitled *"The description of attributes within the Urban Idrija dataset (the abbreviation n.d. means no data)"* provides a clear definition of each attribute of a given sample within the Urban Idrija dataset, which is presented in Table 1.

Table 3 entitled *"Chemical and physical method procedures carried out to obtain data, which are included in the Urban Idrija dataset"* provides a detailed description of chemical and physical analytical methods, which were carried out to determine pH, particle size distribution, soil water content, element contents, relative amount of mercury binding forms, water soluble Hg contents and bioaccessibe Hg contents according to the European Standard Toy Safety Protocol.

Data format

Table 1: Microsoft Excel file (.csv format)

Table 2–3: Portable document format (.pdf format)

Data accessibility

The data described is open-source data and has been deposited in DiRROS repository. License: CC-BY 4.0. Data are accessible using the link: to be done. Repository name: DiRROS

Direct URL to data: https://dirros.openscience.si/IzpisGradiva.php?id=23021&lang=slv

Acknowledgement

This work was co-funded by the Slovenian Research and Innovation Agency (ARIS) in the frame of the research programme Groundwater and Geochemistry under the grant number (P1-0020) carried out at the Geological Survey of Slovenia. Additional financial support was provided by the Slovene human resources development and scholarship fund in the frame of the Ad futura programme, which enabled a five-month-long research exchange at the Technical University of Braunschweig (TUB), Germany. The authors are honoured and thankful to have had the opportunity of doing the comprehensive laboratory work reported in this study at the TUB, under the supervision of Prof. Dr. Harald Biester, who offered professional guidance and support during geochemical analyses and interpretation of the results. The authors would also like to thank Prof. Dr. Helena Grčman for professional guidance, the authorities of the Idrija municipality and the staff of the Idrija Mercury mine in liquidation (Mr. Bojan Režun and Mrs. Tatjana Dizdarević) and the staff of Komunala Idrija for their support during sampling of the urban soil.

References

AOAC 2016: AOAC official methods of analysis. Guidelines for standard method Performance requirements. Appendix F. Internet: https://www.aoac.org/resources/guidelines-for-standard-method-performance-requirements/ (28.1.2015).

Bavec, Š. 2015a: Geochemical Investigations in Idrija Urban Area with Emphasis on Mercury: Dissertation Thesis. University of Ljubljana, Ljubljana:180 p.

Bavec, Š. 2015b: Geochemical investigations of potentially toxic trace elements in urban sediments of Idrija. Geologija, 58/2: 111–120. https://doi.org/10.5474/geologija.2015.009

Bavec, Š. 2017: Geochemical baseline for chemical elements in top- and subsoil of Idrija. Geologija, 60/2: 181–198. https://doi.org/10.5474/geologija.2017.013

Bavec, Š. & Gosar, M. 2016: Speciation, mobility and bioaccessibility of Hg in the polluted urban soil of Idrija (Slovenia), Geoderma, 273: 115–130. https://doi.org/10.1016/j.geoderma.2016.03.015

Bavec, Š., Biester, H. & Gosar, M. 2014. Urban sediment contamination in a former Hg mining district, Idrija, Slovenia. Environmental Geochemistry and Health, 36/3: 427–439. https://doi.org/10.1007/s10653-013-9571-6

Bavec, Š., Gosar, M., Biester, H. & Grčman, H. 2015. Geochemical investigation of mercury and other elements in urban soil of Idrija (Slovenia), Journal of Geochemical Exploration, 154: 213–223. https://doi.org/10.1016/j.gexplo.2014.10.011

Bavec, Š., Gosar, M., Miler, M. & Biester, H. 2017. Geochemical investigation of potentially harmful elements in household dust from a mercury-contaminated site, the town of Idrija (Slovenia). Environmental Geochemistry and Health, 39: 443–465. http://dx.doi.org/10.1007/s10653-016-9819-z

Bavec, Š., Biester, H. & Gosar, M. 2018: A risk assessment of human exposure to mercury-contaminated soil and household dust in the town of Idrija (Slovenia), Journal of Geochemical Exploration, 187: 131–140. https://doi.org/10.1016/j.gexplo.2017.05.005

Biester, H. & Scholz, C. 1996: Determination of mercury binding forms in soils: mercury pyrolysis versus sequental extraction. Environmental Science & Technology, 31/1: 233–239. https://doi.org/10.1021/es960369h

Biester, H. & Nehrke, G. 1997: Quantification of mercury in soils and sediments – acid digestion versus pyrolysis. Fresenius' Journal of Analytical Chemistry, 358: 446–452. https://doi.org/10.1007/S002160050444

EGS 2016: Urban Geochemistry Project (URGE): EuroGeoSurveys 2015 annual report. EuroGeoSurveys, Brüssels, 17–18. Internet: https://eurogeosurveys.org/egs-publications/urban-geochemistry-project-urge-eurogeosurveys-2016-annual-report/ (28.1.2025)

EN71–3:2002. Safety of toys - Part 3: Migration of certain elements; German version EN 71-3:1994 + A1:2000 + AC:2002. European Committee for Standardization, Brussels, Belgium.

EN ISO 14688–1:2002: Geotechnical investigation and testing — Identification and classification of soil. Part 1: Identification and description.

EPA 2002: Environmental Protection Agency [online]. Method 1631, Revision E: Mercury in Water by Oxidation, Purge and Trap, and Cold Vapor Atomic Absorption Fluorescence Spectrometry, 2002. Internet: https://www.epa.gov/sites/default/files/2015-08/documents/method_1631e_2002.pdf (28.1.2025)

ISO 9001:2008 Quality management systems — Requirements.

SIST ISO 10390:1996 - Soil quality - Determination of pH.

GEOLOGIJA 68/2, 311-322, Ljubljana 2025

https://doi.org/10.5474/geologija.2025.005

Data Article

Podatkovna baza za določanje izvora rimskodobnih kamnitih izdelkov z Ižanskega

Database for provenance determination of Roman-time stone products from Ig area

Rok BRAJKOVIČ[1]*, Petra ŽVAB ROŽIČ[2] & Luka GALE[1,2]

[1]Geološki zavod Slovenije, Dimičeva ulica 14, SI-1000 Ljubljana, Slovenija; *corresponding author: rok.brajkovic@geo-zs.si
[2]Oddelek za geologijo, Naravoslovnotehniška fakulteta, Aškerčeva 12, 1000 Ljubljana, Slovenija

Prejeto / Received 17. 3. 2025; Sprejeto / Accepted 28. 5. 2025; Objavljeno na spletu / Published online 30. 7.2025

Ključne besede: Podatkovni set, geološka karta, sedimentološki profil, mikrofacies, foraminifere, katodoluminiscenca, mineralogija, geokemija, izotopi, izvor

Key words: Dataset, geological map, sedimentological log, microfacies, foraminifera, cathodoluminescence, mineralogy, geochemistry, isotopes, provenience

Izvleček

Rimskodobni kamniti izdelki najdeni na Ižanskem so bili pretežno izdelani iz mikritnega in peloidnega apnenca. Izvor teh izdelkov je bil do sedaj le ohlapno definiran, zlasti zaradi pomanjkanja podrobnih opisov mikrofaciesov, študije mikrofosilov in manjkajočih geokemičnih analiz iz do sedaj prepoznanih ali predlaganih območij rimskih kamnolomov. Podatkovna baza zapolnjuje to vrzel in nudi podroben vpogled v litološko in geokemično sestavo apnenca, ki izdanja pri Podutiku, Stajah, Igu, v Podpeči, Jezeru pri Podpeči, na hribu Sv. Ana in pri Ledenici v bližini Planince. Profili predstavljajo dele spodnjejurske Podbukovške formacije, natančneje člene E1 – plastnat mikritni in ooidni apnenec, E2 – fosiliferni apnenec, E3 – krinoidni apnenec, ki pripadajo Podbukovški formaciji in E4 – ooidni apnenec in dolomit, ki pripada Lazenski formaciji. Z namenom primerjave so bili z enakimi metodami proučeni tudi dostopni kamniti izdelki z Ižanskega. Uporabljena metodologija vključuje geološko kartiranje, detajlno sedimentološko profiliranje sedimentnih zaporedij in makroskopski pregled vzorcev, optično mikroskopijo za analizo litofaciesov, mikrofaciesov in bentoških foraminifer, katodoluminiscenčno analizo, analizo vrednosti izotopskega razmerja stroncija, vrednosti izotopskega razmerja stabilnih izotopov ogljika in kisika, določitev mineralne sestave in vsebnosti glavnih, stranskih ter slednih elementov.

Abstract

The stone products from the Roman-time found in the Ig area were mainly made from micritic and peloidal limestone. The provenance of these products has been only roughly defined so far, mainly due to the lack of detailed microfacies descriptions, study of microfossils and missing geochemical analyses from the previously identified or proposed areas of Roman quarries. This database fills this gap and provides a detailed insight into the lithological and geochemical composition of the limestone found in Podutik, Staje, Ig, Podpeč, Jezero near Podpeč, on the hill of St. Ana and at Ledenica near Planinca. The sedimentological logs represent parts of the Lower Jurassic Podbukovje Formation, specifically the members E1 – laminated micritic and oolitic limestone, E2 – fossiliferous limestone, E3 – crinoid limestone belonging to the Podbukovje Formation, and E4 – oolitic limestone and dolomite belonging to the Laze Formation. For purposes of comparison, accessible stone products from the Ig area were studied using the same methods. The applied methodology includes geological mapping, detailed sedimentological description of sediment sequences and macroscopic examination of samples, optical microscopy for the analysis of lithofacies, microfacies and benthic foraminifera, cathodoluminescence analysis, analysis of strontium isotope ratio values, stable carbon and oxygen isotope ratio values, determination of mineral composition and content of major, minor and trace elements.

Izhodišče

Raziskava je vezana na severovzhodno območje nekdanje rimske regije X – Venetia et Histria (sl. 1a), natančneje na antično (rimskodobno) naselbino Emona (sl. 1b) oziroma njeno ruralno obrobje (sl. 1c). Do sedaj je bil izvor apnenca kot naravnega kamna v kamnitih izdelkih emonskega agra opredeljen na podlagi litofaciesa in mikrofaciesnega tipa ter z uporabo bentoških foraminifer, ki so omogočili vsaj delno biostratigrafsko korelacijo proučenih kamnitih izdelkov z izvorno formacijo ali členom na podlagi obstoječih geoloških podatkov (Šmuc et al., 2017; Visočnik et al., 2017; Žvab Rožič et al., 2022). Spodnjejurski apnenci so bili v Emoni uporabljeni v prevladujočem deležu (Djurić et al., 2022), na Ižanskem pa je raba apnenca vezana izključno na spodnjejurske litofaciese. Dodatno so Djurić in sodelavci (2022) na primeru Emone pokazali, da z uporabo zgolj petroloških metod utemeljena določitev provenience ni mogoča za kar 42,7 % v študijo vključenih izdelkov, izdelanih iz spodnjejurskega apnenca. Apnenec, uporabljen za izdelavo izdelkov na Ižanskem, je po do sedaj veljavnih interpretacijah prihajal iz spodnjejurskega zaporedja Podbukovške formacije (Žvab Rožič et al., 2022).

V tem delu predstavljeni podatki dopolnjujejo do sedaj predlagano litostratigrafsko razdelitev spodnjejurskih apnencev (Dozet & Strohmenger, 2000; Dozet, 2009) ter prispevajo k boljši korelaciji členov Podbukovške formacije, ki so bili do sedaj že delno proučeni na obrobju Ljubljanskega barja (Buser & Debeljak, 1994, 1997; Miler & Pavšič, 2008; Ogorelec, 2009; Gale, 2015; Gale & Kelemen, 2017). Z geoarheološkega vidika sta poznavanje in natančna ločitev spodnjejurskega zaporedja nujna, saj vsi najdeni kamniti izdelki na Ižanskem izvirajo iz tega dela zaporedja (Brajkovič et al., 2019a; Žvab Rožič et al., 2022). Z namenom vzpostavitve jasnih ter preverljivih meril za stratigrafsko ločevanje izvora apnenca, uporabljenega v Emoni in na Ižanskem, objavljamo podatke, ki so bili do sedaj že uporabljeni v več kongresnih prispevkih (Brajkovič et al., 2019a, 2019b, 2021, 2022a, 2022b) in znanstvenih člankih (Brajkovič et al., 2022c; Djurić et al.. 2022) ter doktorski nalogi (Brajkovič, 2025).

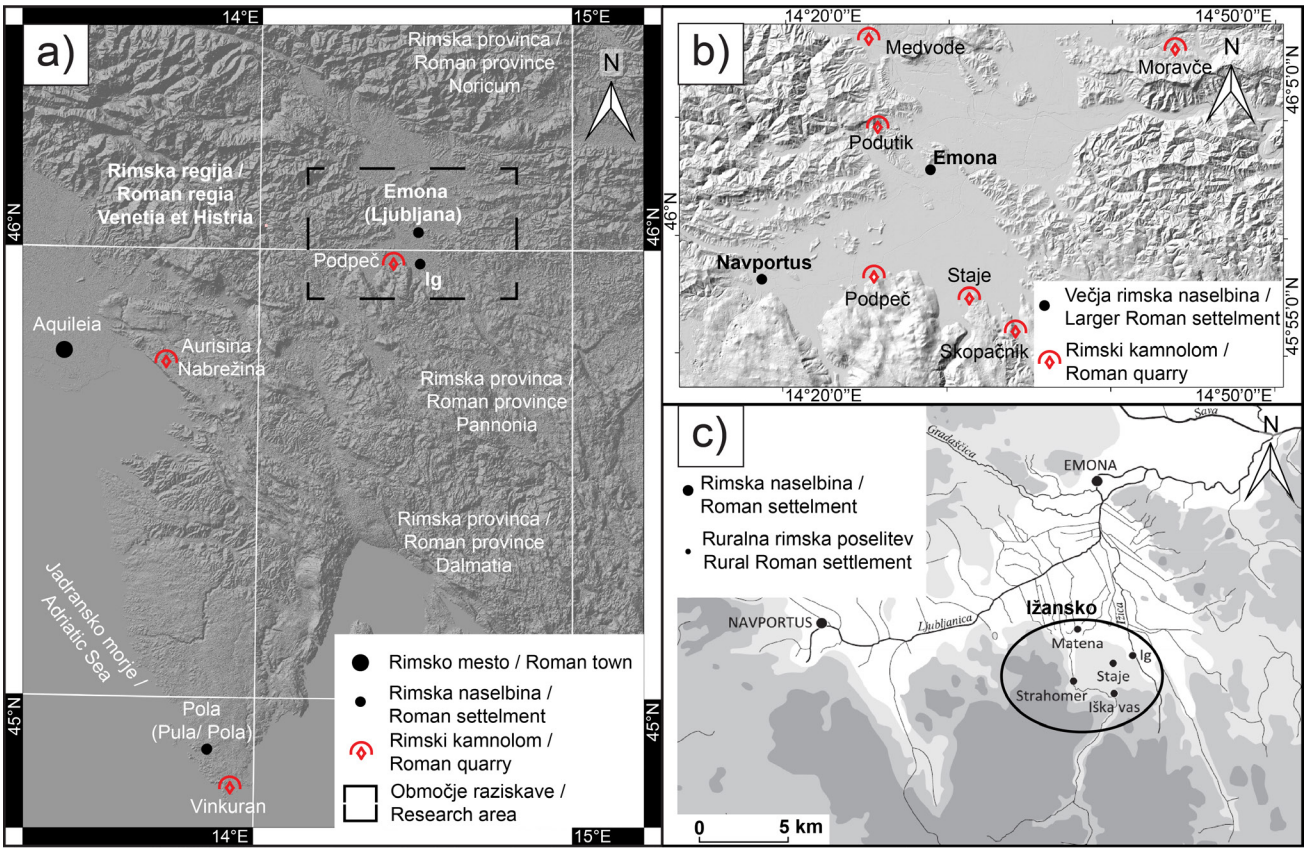

Sl. 1. Predstavitev območja raziskav. a) Širša geografsko-zgodovinska umestitev z glavnimi rimskimi mesti/naselbinami ter njihovimi najpomembnejšimi potrjenimi rimskodobnimi kamnolomi. b) Emona in njena bližnja okolica s potrjenimi in domnevnimi lokacijami rimskodobnih kamnolomov (Russell, 2013). c) Lokacija ruralnega območja Ižansko (povzeto po Lozić, 2009).

Fig. 1. Presentation of the research area. a) Broader geographical-historical setting with the main Roman towns/settlements and their most important quarries. b) Emona and its immediate surroundings with confirmed and presumed locations of Roman quarries (Russell, 2013). c) Location of the rural Ig area (after Lozić, 2009).

Tabela 1. Izvor proučenih kamnitih izdelkov z najdiščem na Ižanskem, opredeljenih po izvornih (litostratigrafskih) enotah. Zaporedne številke kamnitih izdelkov (IV) temeljijo na katalogu Lozić (2008).

Table 1. Provenance of studied stone products from the Ig area determined in source (lithostratigraphic) units. The consecutive numbers of the stone artifacts (IV) are based on the catalogue by Lozić (2008).

Litostratigrafske enote / Lithostratigraphic unit	Inventarne številke / Inventory numbers	
Spodnjejurski apnenci / Lower Jurassic limestones – J_1	IK-3; IV 16; IV 23; IV 34; IV 5; IV 42; IV 2; IV 6; IV 9; IV 10; IV 11; IV 14; IV 19; IV 36; IV 40; IV 45; IV 46-1; IK-4; IK-5; IK-6; IV 20; IV 26; IV 29; IV 33; IK-1	
Spodnje- do srednjesinemurijski apnenci / Lower to Middle Sinemurian Limestones – E1 – $J_1^{1,2}$	Makroskopski in mikroskopski pregled ter biostratigrafija / Macroscopic and microscopic examination and biostratigraphy	Večmetodni pristop / Multi-method approach
	/	IV 39; IV 8
Zgornjesinemurijski–spodnjepliensbachijski apnenci / Upper Sinemurian–Lower Pliensbachian limestones – PE2.1 – $J_1^{2,3}$	Makroskopski in mikroskopski pregled ter biostratigrafija / Macroscopic and microscopic examination and biostratigraphy	Večmetodni pristop / Multi-method approach
	IV 24; IV 25; IV 32; IV 41; IV 43; IV 44; IV 7; IV 17; IV 37; IV 22; IV 46-2; IV 21	IV 27; IV 28; IV 12; IV 35; IV 18; IK-2
Pliensbachijski apnenci / Pliensbachian limestones – PE2.2 – J_1^3		IV 13; IV 15; IV 1; IV 3
Toarcijski apnenci / Toarcian limestones – E3 – J_1^4	IV 30	IV 31; IV 38; IV 4

Kljub pomembni vlogi nagrobnih spomenikov z Ižanskega v slovenski arheologiji (Šašel, 1975a, 1975b; Vuga, 2000a, 2000b; Lozić, 2009; Veranič & Repanšek, 2016; Ragolič, 2016; Grahek & Ragolič, 2020), so bili ti do sedaj opredeljeni zgolj kot lokalni apnenec brez dodatne litostratigrafske ali geografske opredelitve izvora. Geološke študije kamnitih izdelkov iz nahajališča Marof (Ig) in sedimentnih zaporedij, ki izdanjajo v okolici, so pokazale ujemanje v makro- in mikroskopskih značilnostih in s tem na lokalen izvor kamnine (Žvab Rožič et al., 2016, 2022), izvor mikritnih in peloidnih apnencev pa je ostal odprt. To vrzel zapolnjujemo s podatki, ki jih predstavljamo v pričujočem delu.

Za predlagane določitve izvora posameznih kamnitih izdelkov, najdenih na Ižanskem (Tabela 1), so uporabljeni kriteriji za določitev, ki so predstavljeni v delu Brajkoviča in sodelavci (2022b).

Materiali

Proučeni vzorci zajemajo primarne vzorce iz sedimentoloških profilov ter vzorce arhitekturnih, votivnih in sepulkralnih kamnitih izdelkov. Na vseh vzorcih so bile izvedene enake analize po enakem metodološkem pristopu. Skupna površina kartiranega ozemlja znaša okoli 20 km^2. Sedimentološko so bile natančno opredeljene le litostratigrafske enote, ki predstavljajo potencialen izvor apnenca za Emono ali Ižansko. V teh litostratigrafskih enotah smo posneli okoli 400 m sedimentoloških profilov v merilu 1 : 100. Za analize stabilnih izotopov kisika, ogljika ter izotopov stroncija je bila iz vzorcev primarnih zaporedij in kamnitih izdelkov uporabljena le mikritna osnova. Le-ta je bila natančno vzorčena iz sveže kamnine. Za analize mineralne in elementne sestave iz primarnih zaporedij in proučenih kamnitih izdelkov so bili pripravljeni vzorci iz celokupne kamnine, pri čemer je bila pozornost namenjena dovoljšni globini vzorčenja, da smo se izognili preperelemu in potencialno z meteorno vodo spremenjenemu delu kamnine. Vsi vzorci so bili homogenizirani v ahatni terilnici in presejani skozi 100 μm sito v laboratoriju Geološkega zavoda Slovenije. Nadaljnji postopek priprave vzorcev za analize je bil opravljen v laboratorijih, kjer je bila opravljena meritev. V Tabeli 2 so opredeljene analize, oznake vzorcev in njihovo število ter merilo izbire vzorca za nadaljnje preiskave.

Tabela 2. Število in oznake vzorcev ter kriterij izbire.

Table 2. Number and labels of samples and selection criteria.

ANALIZA / ANALYSIS	OZNAKA / LABEL	ŠTEVILO VZORCEV / NUMBER OF SAMPLES	MERILO IZBIRE / SELECTION CRITERIA
Geološka karta Podutik / Geological map Podutik	K-P - zaporedna oznaka vzorca / consecutive sample number	18	Izbrani tipični litofaciesi definiranih litostratigrafskih enot / Selected typical lithofacies of defined lithostratigraphic units
Geološka karta Ig / Geological map Ig	K-IG - zaporedna oznaka vzorca / consecutive sample number	15	Izbrani tipični litofaciesi definiranih litostratigrafskih enot / Selected typical lithofacies of defined lithostratigraphic units
Geološka karta Podpeč / Geological map Podpeč	K-POD - zaporedna oznaka vzorca / consecutive sample number	19	Izbrani tipični litofaciesi definiranih litostratigrafskih enot / Selected typical lithofacies of defined lithostratigraphic units
Optične preiskave vzorcev – sedimentološki profil Podutik 1 / Optical examination of samples – sedimentological section Podutik 1	P1 - oznaka vzorca po metraži / sample label by metrage	126	Vzorci vseh lito- in mikrofaciesov ob upoštevanju minimalne gostote vzorčenja (1 plast – vsaj 1 vzorec). S katodoluminiscenco pregledani reprezentativni zbruski vsakega litofaciesa ter vsi vzorci, namenjeni za nadaljnje preiskave vrednosti $^{87}Sr/^{86}Sr$ / Samples of all lithofacies and microfacies, taking into account the minimum sampling density (1 bed – at least 1 sample). Representative sections of each lithofacies examined by cathodoluminescence and all samples intended for further investigation of $^{87}Sr/^{86}Sr$ values..
Mineraloške analize sedimentološki profil Podutik 1 / Mineralogical analyses sedimentological section Podutik 1	P1 - oznaka vzorca po metraži / sample label by metrage	7	Izbrani vzorci mikritnih apnencev (LF1) približno enakomerno razporejeni po sedimentološkem profilu / Selected samples of micrite limestones (LF1) approximately evenly distributed across the sedimentological section
Geokemične analize sedimentološki profil Podutik 1 / Geochemical analyses sedimentological section Podutik 1	P1 - oznaka vzorca po metraži / sample label by metrage	7	Izbrani vzorci mikritnih apnencev (LF1) približno enakomerno razporejeni po sedimentološkem profilu / Selected samples of micrite limestones (LF1) approximately evenly distributed across the sedimentological section
Analize izotopov $\delta^{18}O_{total}$ in $\delta^{13}C_{total}$ sedimentološki profil Podutik 1 / Isotope analyses $\delta^{18}O_{total}$ and $\delta^{13}C_{total}$ sedimentological section Podutik 1	P1 - oznaka vzorca po metraži / sample label by metrage	7	Izbrani vzorci mikritnih apnencev (LF1) približno enakomerno razporejeni po sedimentološkem profilu / Selected samples of micrite limestones (LF1) approximately evenly distributed across the sedimentological section
Analize izotopov $^{87}Sr/^{86}Sr$ sedimentološki profil Podutik 1 / Isotope analyses $^{87}Sr/^{86}Sr$ sedimentological section Podutik 1	P1 - oznaka vzorca po metraži / sample label by metrage	7	Izbrani vzorci mikritnih apnencev (LF1) približno enakomerno razporejeni po sedimentološkem profilu / Selected samples of micrite limestones (LF1) approximately evenly distributed across the sedimentological section
Optične preiskave vzorcev – sedimentološki profil Podutik 3 / Optical examination of samples – sedimentological section Podutik 3	P3 - oznaka vzorca po metraži / sample label by metrage	13	Vzorci vseh lito- in mikrofaciesov ob upoštevanju minimalne gostote vzorčenja (1 plast – vsaj 1 vzorec) / Samples of all litho- and microfacies, taking into account the minimum sampling density (1 bed – at least 1 sample)
Optične preiskave vzorcev – sedimentološki profil Podutik 4 / Optical examination of samples – sedimentological section Podutik 4	P4 - oznaka vzorca po metraži / sample label by metrage	5	Vzorci vseh lito- in mikrofaciesov ob upoštevanju minimalne gostote vzorčenja (1 plast – vsaj 1 vzorec) / Samples of all litho- and microfacies, taking into account the minimum sampling density (1 bed – at least 1 sample)
Optične preiskave vzorcev – sedimentološki profil Dedec / Optical examination of samples – sedimentological section Dedec	D - oznaka vzorca po metraži / sample label by metrage	86	Vzorci vseh lito- in mikrofaciesov ob upoštevanju minimalne gostote vzorčenja (1 plast – vsaj 1 vzorec). S katodoluminiscenco pregledani reprezentativni zbruski vsakega litofaciesa ter vsi vzorci, namenjeni za nadaljnje preiskave vrednosti $^{87}Sr/^{86}Sr$ / Samples of all lithofacies and microfacies, taking into account the minimum sampling density (1 bed – at least 1 sample). Representative sections of each lithofacies examined by cathodoluminescence and all samples intended for further investigation of $^{87}Sr/^{86}Sr$ values..
Mineraloške analize – sedimentološki profil Dedec / Mineralogical analyses sedimentological section Dedec	D - oznaka vzorca po metraži / sample label by metrage	9	Izbrani vzorci mikritnih apnencev (LF1) približno enakomerno razporejeni po sedimentološkem profilu / Selected samples of micrite limestones (LF1) approximately evenly distributed across the sedimentological section
Geokemične analize – sedimentološki profil Dedec / Geochemical analyses sedimentological section Dedec	D - oznaka vzorca po metraži / sample label by metrage	9	Izbrani vzorci mikritnih apnencev (LF1) približno enakomerno razporejeni po sedimentološkem profilu / Selected samples of micrite limestones (LF1) approximately evenly distributed across the sedimentological section
Analize izotopov $\delta^{18}O_{total}$ in $\delta^{13}C_{total}$ – sedimentološki profil Dedec / Isotope analyses $\delta^{18}O_{total}$ and $\delta^{13}C_{total}$ sedimentological section Dedec	D - oznaka vzorca po metraži / sample label by metrage	16	Izbrani vzorci mikritnih apnencev (LF1) približno enakomerno razporejeni po sedimentološkem profilu / Selected samples of micrite limestones (LF1) approximately evenly distributed across the sedimentological section
Analize izotopov $^{87}Sr/^{86}Sr$ – sedimentološki profil Dedec / Isotope analyses $^{87}Sr/^{86}Sr$ sedimentological section Dedec	D - oznaka vzorca po metraži / sample label by metrage	5	Izbrani vzorci mikritnih apnencev (LF1) približno enakomerno razporejeni po sedimentološkem profilu / Selected samples of micrite limestones (LF1) approximately evenly distributed across the sedimentological section

Optične preiskave vzorcev – sedimentološki profil Ig / Optical examination of samples – sedimentological section Ig	IG - oznaka vzorca po metraži / sample label by metrage	45	Vzorci vseh lito- in mikrofaciesov ob upoštevanju minimalne gostote vzorčenja (1 plast – vsaj 1 vzorec). S katodoluminiscenco pregledani reprezentativni zbruski vsakega litofaciesa ter vsi vzorci, namenjeni za nadaljnje preiskave vrednosti $^{87}Sr/^{86}Sr$ / Samples of all lithofacies and microfacies, taking into account the minimum sampling density (1 bed – at least 1 sample). Representative sections of each lithofacies examined by cathodoluminescence and all samples intended for further investigation of $^{87}Sr/^{86}Sr$ values.
Analize izotopov $^{87}Sr/^{86}Sr$ – sedimentološki profil Ig / Isotope analyses $^{87}Sr/^{86}Sr$ sedimentological section Ig	IG - oznaka vzorca po metraži / sample label by metrage	4	Izbrani vzorci mikritnih apnencev (LF1) ali vzorcev z mikritno osnovo (LF10 – litiotidni apnenec) razporejeni po sedimentološkem profilu / Selected samples of micrite limestones (LF1) or samples with micrite groundmass (LF10 – lithiotid limestone) approximately evenly distributed across the sedimentological section
Optične preiskave vzorcev – sedimentološki profil kamnolom Jezero / Optical examination of samples – sedimentological section Jezero	JEZ - oznaka vzorca po metraži / sample label by metrage	19	Vzorci vseh lito- in mikrofaciesov ob upoštevanju minimalne gostote vzorčenja (1 plast – vsaj 1 vzorec) / Samples of all litho- and microfacies, taking into account the minimum sampling density (1 bed – at least 1 sample)
Optične preiskave vzorcev – kompozitni sedimentološki profil Podpeč / Optical examination of samples – composite sedimentological section Podpeč	POD (arheo, 1, 2, 3, 4, 5,) zaporedna oznaka profila in vzorca po metraži / conaecutive section mark and sample markin by metrage	250	Vzorci vseh lito- in mikrofaciesov ob upoštevanju minimalne gostote vzorčenja (1 plast – vsaj 1 vzorec). S katodoluminiscenco pregledani reprezentativni zbruski vsakega litofaciesa ter vsi vzorci, namenjeni za nadaljnje preiskave vrednosti $^{87}Sr/^{86}Sr$ / Samples of all lithofacies and microfacies, taking into account the minimum sampling density (1 bed – at least 1 sample). Representative sections of each lithofacies examined by cathodoluminescence and all samples intended for further investigation of $^{87}Sr/^{86}Sr$ values.
Mineraloške (XRD) analize – kompozitni sedimentološki profil Podpeč / Mineralogical analyses composite sedimentological section Podpeč	POD (arheo, 1, 2, 3, 4, 5) zaporedna oznaka profila in vzorca po metraži / conaecutive section mark and sample markin by metrage	23	Izbrani vzorci mikritnih apnencev (LF1) približno enakomerno razporejeni po sedimentološkem profilu / Selected samples of micrite limestones (LF1) approximately evenly distributed across the sedimentological section
Geokemične analize – kompozitni sedimentološki profil Podpeč / Geochemical analyses composite sedimentological section Podpeč	POD (arheo, 1, 2, 3, 4, 5) zaporedna oznaka profila in vzorca po metraži / conaecutive section mark and sample markin by metrage	29	Izbrani vzorci mikritnih apnencev (LF1) približno enakomerno razporejeni po sedimentološkem profilu / Selected samples of micrite limestones (LF1) approximately evenly distributed across the sedimentological section
Analize izotopov $\delta^{18}O_{total}$ in $\delta^{13}C_{total}$ kompozitni sedimentološki profil Podpeč / Isotope analyses $\delta^{18}O_{total}$ and $\delta^{13}C_{total}$ composite sedimentological section Podpeč	POD (arheo, 1, 2, 3, 4, 5) zaporedna oznaka profila in vzorca po metraži / conaecutive section mark and sample markin by metrage	151	Izbrani vzorci opredeljenih litofaciesov približno enakomerno razporejeni (+/– 90 cm) po sedimentološkem profilu / Selected samples of defined lithofacies approximately evenly distributed (+/– 90 cm) along the sedimentological section
Analize izotopov $^{87}Sr/^{86}Sr$ –kompozitni sedimentološki profil Podpeč / Isotope analyses $^{87}Sr/^{86}Sr$ composite sedimentological section Podpeč	POD (arheo, 1, 2, 3, 4, 5) zaporedna oznaka profila in vzorca po metraži / conaecutive section mark and sample markin by metrage	13	Izbrani vzorci mikritnih apnencev (LF1) približno enakomerno razporejeni po sedimentološkem profilu / Selected samples of micrite limestones (LF1) approximately evenly distributed across the sedimentological section
Optične preiskave vzorcev – kompozitni sedimentološki profil Ledenica Planinca / Optical examination of samples – composite sedimentological section Ledenica Planinca	LP - zaporedna oznaka vzorca po metraži / sample label by metrage	112	Vzorci vseh lito- in mikrofaciesov ob upoštevanju minimalne gostote vzorčenja (1 plast – vsaj 1 vzorec). S katodoluminiscenco pregledani reprezentativni zbruski vsakega litofaciesa / Samples of all lithofacies and microfacies, taking into account the minimum sampling density (1 bed – at least 1 sample). Representative sections of each lithofacies examined by cathodoluminescence
Analize izotopov $\delta^{18}O_{total,}$ $\delta^{13}C_{total}$ in $\delta^{13}C_{ogr}$ – sedimentološki profil Ledenica Planinca / Isotope analyses $\delta^{18}O_{total}$ and $\delta^{13}C_{total}$ – sedimentological section Ledenica Planinca	LP - zaporedna oznaka vzorca po metraži / sample label by metrage	67	Izbrani vzorci opredeljenih litofaciesov približno enakomerno razporejeni (+/– 20 cm) po spodnjem delu sedimentološkega profila / Selected samples of defined lithofacies approximately evenly distributed (+/– 20 cm) along the lower part of sedimentological section
Optične preiskave vzorcev – kompozitni sedimentološki profil Sv. Ana / Optical examination of samples – composite sedimentological section Sv. Ana	SV.A-zaporedna oznaka vzorca po metraži / sample label by metrage	115	Vzorci vseh lito- in mikrofaciesov ob upoštevanju minimalne gostote vzorčenja (1 plast – vsaj 1 vzorec). Z katodoluminiscenco pregledani reprezentativni zbruski vsakega litofaciesa / Samples of all lithofacies and microfacies, taking into account the minimum sampling density (1 bed – at least 1 sample). Representative sections of each lithofacies examined by cathodoluminescence
Optične preiskave vzorcev – kamniti izdelki hranjeni v lapidariju v cerkvi Sv. Mihaela v Iški vasi / Optical examination of samples – stone products kept in the lapidary in the church of St. Michael in Iška vas	IV zaporedna številka po katalogu Lozić (2008) / sample label according to the Lozić catalogue (2008)	47	Dostopnost po izbiri kustosa oziroma soglasodajalca. Zagotovljeno vzorčenje vseh zaznanih litofaciesov. S katodoluminiscenco pregledani vsi zbruski / Accessibility at the discretion of the curator or approver. Sampling of all detected lithofacies ensured. All thinsections examined with cathodoluminescence

Mineraloške (XRD) analize – kamniti izdelki hranjeni v lapidariju v cerkvi Sv. Mihaela v Iški vasi / Mineralogical analyses – stone products kept in the lapidary in the church of St. Michael in Iška vas	IV zaporedna številka po katalogu Lozić (2008) / sample label according to the Lozić catalogue (2008)	9	Analiza opravljena glede na ostanek vzorca po pripravi petrografskega preparata (nizka prioriteta) / Analysis performed based on the sample residue after preparation of the petrographic preparation (low priority)
Geokemične analize – kamniti izdelki hranjeni v lapidariju v cerkvi Sv. Mihaela v Iški vasi / Geochemical analyses – stone products kept in the lapidary in the church of St. Michael in Iška vas	IV zaporedna številka po katalogu Lozić (2008) / sample label according to the Lozić catalogue (2008)	14	Analiza opravljena glede na ostanek vzorca po pripravi petrografskega preparata (srednja prioriteta) / Analysis performed based on the sample residue after preparation of the petrographic preparation (medium priority)
Analize izotopov $\delta^{18}O_{total}$ in $\delta^{13}C_{total}$ v cerkvi Sv. Mihaela v Iški vasi / Isotope analyses $\delta^{18}O_{total}$ and $\delta^{13}C_{total}$ – stone products kept in the lapidary in the church of St. Michael in Iška vas	IV zaporedna številka po katalogu Lozić (2008) / sample label according to the Lozić catalogue (2008)	14	Analiza opravljena glede na ostanek vzorca po pripravi petrografskega preparata (srednja prioriteta) / Analysis performed based on the sample residue after preparation of the petrographic preparation (medium priority)
Analize izotopov $^{87}Sr/^{86}Sr$ – kamniti izdelki hranjeni v lapidariju v cerkvi Sv. Mihaela v Iški vasi / Isotope analyses $^{87}Sr/^{86}Sr$ – stone products kept in the lapidary in the church of St. Michael in Iška vas	IV zaporedna številka po katalogu Lozić (2008) / sample label according to the Lozić catalogue (2008)	14	Analiza opravljena glede na ostanek vzorca po pripravi petrografskega preparata (visoka prioriteta) / Analysis performed based on the sample residue after preparation of the petrographic preparation (high priority)
Optične preiskave vzorcev – kamniti izdelki najdeni na arheološkem najdišču Ig krožišče / Optical examination of samples – stone products found at the Ig roundabout archaeological site	IK interna zaporedna številka / internal sample lable	6	Pregledani vsi najdeni kamniti izdelki. S katodoluminiscenco pregledani vsi zbruski / All found stone products were examined. All thinsections were examined with cathodoluminescence
Geokemične analize – kamniti izdelki najdeni na arheološkem najdišču Ig krožišče / Geochemical analyses – stone products found at the Ig roundabout archaeological site	IK interna zaporedna številka / internal sample lable	1	Analiza opravljena glede na ostanek vzorca po pripravi petrografskega preparata (srednja prioriteta) / Analysis performed based on the sample residue after preparation of the petrographic preparation (medium priority)
Analize izotopov $\delta^{18}O_{total}$ in $\delta^{13}C_{total}$ – kamniti izdelki najdeni na arheološkem najdišču Ig krožišče / Isotope analyses $\delta^{18}O_{total}$ and $\delta^{13}C_{total}$ – stone products found at the Ig roundabout archaeological site	IK interna zaporedna številka / internal sample lable	1	Analiza opravljena glede na ostanek vzorca po pripravi petrografskega preparata (srednja prioriteta) / Analysis performed based on the sample residue after preparation of the petrographic preparation (medium priority)
Analize izotopov $^{87}Sr/^{86}Sr$ – kamniti izdelki najdeni na arheološkem najdišču Ig krožišče / Isotope analyses $^{87}Sr/^{86}Sr$ – stone products found at the Ig roundabout archaeological site	IK interna zaporedna številka / internal sample lable	1	Analiza opravljena glede na ostanek vzorca po pripravi petrografskega preparata (visoka prioriteta) / Analysis performed based on the sample residue after preparation of the petrographic preparation (high priority)

Metode

Terensko delo

Geološko kartiranje

Osnovo geološkega kartiranja je obsegala priprava topografskih osnov z visoko ločljivostjo ter LIDAR-modelov površja (Tarolli, 2014), ki so predstavljali podlago za natančno geološko kartiranje (terenski popis) v merilu 1:2.500. Podatki so bili pridobljeni iz spleta (Internet). Kartiranje je potekalo po metodi sledenja geoloških mej, na pokritih terenih pa po metodi vseh izdankov (Compton, 1985). Geološke karte Podutik, Ig in Podpeč so bile izdelane v merilu 1:5.000. Izrisane so bile v program AutoCAD MAP 3D 2019 in pripravljene za arhiviranje v programu ArcGIS PRO ter se v podatkovni bazi nahajajo v mapi G*eološke karte*.

Makroskopski opis vzorcev sedimentoloških profilov in kamniti izdelkov

Vsi makroskopski popisi so zajemali opis debelin plasti, litologije, strukturnih in teksturnih značilnosti ter barve po standardni barvni lestvici (Geological Rock-Color Charts, 2011). Profili so zajeli lokacije predlaganih rimskodobni kamnolomi (Russel, 2013), ki zajemajo območja Podutika (sedimentološki profili Podutik: P1, P3, P4), Staj (sedimentološki profil Dedec, oznaka D), Jezera pri Podpeči (sedimentološki profil Jezero, oznaka JEZ), Iga (sedimentološki profil Ig, oznaka IG), Podpeči (kompozitni sedimentološki profil Podpeč, oznake POD Arheo, POD1, POD2, POD3, POD4 in POD5) in Sv. Ana (sedimentološki profil Sv. Ana, oznaka SV.A). Območje Ledenica – Planinca (sedimentološki profil Ledenica – Planinca, oznaka LP) je bilo dodano za predstavitev toarcijskega člena E3 – krinoidni apnenec (po Dozet

& Strohmenger, 2000 – marogasti apnenec), ki v precej krajšem profilu izdanja tudi neposredno nad današnjim kamnolomom v Podpeči (Djurić idr., 2022). Iz vsake plasti je bil odvzet vsaj po en vzorec. V makroskopski popis so zajeti vsi vzorci iz sedimentoloških profilov (št. vzorcev 742) ter kamniti izdelki lapidarija v Iški vasi (št. vzorcev 47, kataloške številke IV privzete po Lozić, 2008) ter nahajališča Ig krožišče (št. vzorcev 6, oznaka IK z dodano označbo interne zaporedne številke).

Laboratorijsko delo

Petrografske analize

Zbruski (velikosti 47 × 28 mm) so bili izdelani v laboratoriju Geološkega zavoda Slovenije iz reprezentativnih vzorcev vsakega litofaciesa iz sedimentoloških profilov (300 zbruskov) ter iz vseh vzorčenih kamnitih izdelkov (40 zbruskov). Za določitev vsebnosti dolomita so bili zbruski obarvani z barvilom Alizerin-Red S. Zbruski so bili optično prebrani z digitalnim mikroskopom z visoko ločljivostjo Keyence VHX 7100-S750E. Mikrofaciesni tipi apnenca so bili poimenovani v skladu s posodobljeno klasifikacijo po Dunhamu (Lokier & Al Junaibi, 2016). Dolomiti so bili klasificirani skladno s klasifikacijo po Sibley in Gregg (1987). Iz tega dela v podatkovni bazi izhajajo podatki arhivirani v mapi *Optično prebrani zburski*, ki zajema tako zbruske iz sedimentološki profilov kot tudi zbruski kamnitih izdelkov.

Biostratigrafija

Spodnjejurska zaporedja so bila biostratigrafsko opredeljena z bentoškimi foraminiferami. Foraminifere so bile določene na podlagi presekov v zbruskih. Starostni razpon posamezne foraminiferne združbe je bil določen na podlagi relevantnih objav (Fugagnoli & Loriga Broglio, 1998; Fugagnoli, 2004; Velić, 2007; Gale, 2014; Gale & Kelemen, 2017; Gale et al., 2018; Sevillano et al., 2020; BouDagher-Fadel, 2018). Kamniti izdelki so bili obravnavani posamično, saj se litofaciesi in mikrofaciesni tipi, določeni v kamnitih izdelkih, pogosto pojavljajo v več litostratigrafskih enotah. V podatkovni bazi podatkov arhivirani v mapi *Paleontologija – foraminifere*.

Katodoluminiscenca

Analize so bile izvedene na ZRC SAZU, Inštitutu za raziskovanje krasa v Postojni. Zbruski za preiskavo s katodoluminiscenco so bili polirani z diamantno pasto zrnavosti 1 μm. Meritve so bile opravljene na mikroskopu Nikon Eclipse E 600, opremljenem s hladno katodo CITL CL8200/MK4, proizvajalca Cambridge Image Technology Ltd. Mikroskopija je bila opravljena pri standardni napetosti 16 kV, električnem toku 450 mA in 15 μA toka v vakuumu. Rezultati so bili dokumentirani z digitalnim fotoaparatom DXM1200F pri 50-kratni povečavi in 4-sekundni izpostavljenosti zaslonke ter so arhivirani v podatkovni bazi v mapi *Katodoluminiscenca*. Opis katodoluniscenčnih lastnosti za sedimentološke profile je podan v mapi *Opisi lito- in mikrofaciesov (dokument Opisi lito- in mikrofaciesov),* katodoluminiscenčne lastnosti proučenih kamnitih izdelkov pa so podane individualno za posamezen vzorčen v mapi *Kamniti izdelki* (*Katodoluminiscenca → Kamniti izdelki →* dokument *Katodoluminiscenčne lastnosti proučenih kamnitih izdelkov*).

Mineraloške analize

Mineraloške rentgenske analize vzorcev so bile opravljene v laboratoriju Oddelka za geologijo Naravoslovnotehniške fakultete Univerze v Ljubljani. Mineralna sestava vzorcev (39 primarnih vzorcev ter 9 proučenih kamnitih izdelkov) je bila izmerjena z metodo rentgenske praškovne difrakcije na rentgenskem difraktometru Philips PW3710 s sevanjem CuKα1 in sekundarnim grafitnim monokromatorjem. Podatki so bili zbrani pri 40 kV s tokom 30 mA s hitrostjo 3,4° 2θ na minuto v območju snemanja od 2 do 70° (2θ). Difrakcijski vzorci so bili identificirani s programsko opremo X'Perth Highscore Plus 4.6 za difrakcijo z uporabo podatkovne baze PAN-ICSD in metode popolnega prileganja vzorca (Rietveld) za kvantitativno analizo mineralnih faz. Minerali pod 0,1 masnega % niso bili zaznani. V podatkovni bazi so podatki vključeni v mapi *Mineralogija*.

Geokemične analize

Vsebnosti glavnih, stranskih in slednih elementov so bile izmerjene v laboratoriju Actlabs (Kanada). Analize so bile opravljene na 43 vzorcih iz sedimentoloških profilov ter na 15 vzorcih iz kamnitih izdelkov z metodo fuzijske induktivno sklopljene masne spektroskopije (Fusion-ICP-MS). Vsak vzorec je tehtal 5 g. Za analizo je bil izbran modul 4litho (Activation Laboratories Ltd.). Točnost meritev je bila zagotovljena s certificiranimi laboratorijskimi standardi, natančnost pa s ponovljenimi meritvami laboratorijskih standardov. Navedene vrednosti odstopajo od ponovljenih za manj kot 2,15 %. Podatki so arhivirani v podatkovni bazi v mapi Litogeokemija (*Geokemija → Litogeokemija →* dokumenta *Podatki geokemičnih meritev analiziranih vzorcev za okside in element nad mejo zaznavanja*).

Stabilni izotopi kisika in ogljika

Meritve so bile izvedene v laboratoriju GeoZentrum Nordbayern na Univerzi v Erlangnu v Nemčiji. Analize so bile izvedene za primarne vzorce (216 vzorcev) ter dodatno tudi za vzorce kamnitih izdelkov (15 vzorcev), na katerih je bilo izmerjeno tudi izotopsko razmerje stroncija. Vrednosti izotopskega razmerja celokupnega kisika ($\delta^{18}O_{carb}$) in ogljika ($\delta^{13}C_{carb}$) so bile izmerjene z uporabo naprave Gasbench II, povezane z masnim spektrometrom ThermoFisher Delta V Plus. Rezultati so podani v zapisu δ‰ (promil) glede na standard Vienna Peedee Belemnite. Poročana ponovljivost kalibracijskih standardov je bila 0,05 SD za meritve izotopov $\delta^{13}C_{carb}$ in 0,04 SD za meritve izotopov $\delta^{18}O_{carb}$.

Na izbranem sedimentološkem profilu Ledenica Planinca so bile dodano izmerjene tudi vrednosti izotopskega razmerja organskega ogljika ($\delta^{13}C_{ogr}$; 67 vzorcev). Analize vrednosti izotopskega razmerja organskega ogljika so bile opravljene na istih vzorcih kot analize $\delta^{13}C_{carb}$ z namenom dodatne karakterizacije in interpretacije pričakovanih ekskurzij v ogljikovem ciklu. Dekarbonatizacija in homogenizacija vzorcev sta bili opravljeni v laboratorijih Geološkega zavoda Slovenije, meritve pa so bile opravljene na GeoZentrum Nordbayern na Univerzi v Erlangnu v Nemčiji. Analize ogljikovih izotopov organskega ogljika so bile opravljene z elementnim analizatorjem Flash EA 2000, povezanim z masnim spektrometrom ThermoFinnigan Delta V Plus. Natančnost in točnost analiz sta bili preverjeni s ponovljenimi analizami laboratorijskih standardov, dodatno umerjenih po mednarodnih standardih USGS 40 in 41. Poročana ponovljivost kalibracijskih standardov za meritve izotopov $\delta^{13}C_{org}$ je bila 0,06 SD. Rezultati meritev so arhivirani v mapi *C - O_Sr (Geokemija → C - O_Sr → dokumenta Podatki δ18Ocarb_ δ13Ccarb_Corg_ Sr).*

Izotopi stroncija

Meritve so bile izvedene z multikolektorskim masnim spektrometrom na induktivno sklopljeno plazmo (MC-ICP-MS) na Oddelku za vede o Zemlji Univerze v Oxfordu. Analize so bile opravljene za primarne vzorce (29 vzorcev) in vzorce kamnitih izdelkov (15 vzorcev). Približno 6 mg karbonata na vzorec je bilo stehtanega in raztopljenega v 5 ml 2M HNO_3. Pred meritvami $^{87}Sr/^{86}Sr$ je bilo odvzeto 1 ml raztopine za izvedbo prečiščenja stroncija (Sr) s kolono ESI PrepFast-MC Sr-Ca (Romaniello et al., 2015). Masna frakcionacija instrumenta je bila notranje umerjena na $^{86}Sr/^{88}Sr$ = 0,1194. Vsa navedena razmerja $^{87}Sr/^{86}Sr$ so bila normalizirana na SRM 987 $^{87}Sr/^{86}Sr$ = 0,710248 (McArthur et al., 2012; McArthur et al., 2016). Zunanja ponovljivost $^{87}Sr/^{86}Sr$ v SRM 987 je dala vrednost 0,710251 ± 0,000025 (2SD, št. meritev = 30). Za primerjavo so bili izmerjeni tudi trije standardi USGS (G-2, BCR-1 in BHVO-2), katerih vrednosti so skladne z referenčnimi vrednostmi, navedenimi v prejšnjih študijah (Weis et al., 2006). Vsak vzorec je bil analiziran trikrat. Rezultati meritev so arhivirani v mapi *C - O_Sr (Geokemija → C - O_Sr → dokumenta Podatki δ18Ocarb_ δ13Ccarb_Corg_ Sr).*

Struktura podatkovne baze

- *Geokemija*
  - *C - O_Sr*
  - *Litogeokemija*
- *Geološke karte*
- *Katodoluminiscenca*
  - *E1*
    - *Profil Dedec*
    - *Profil Podutik*
  - *E2*
    - *Profil Podpeč 3*
  - *E3*
    - *Profil Podpeč 4*
    - *Profil Sv. Ana*
  - *E4*
  - *Kamniti izdelki*
- *Mineralogija*
  - *E1*
    - *Profil Podutik*
    - *Profil Dedec*
  - *E2*
    - *Profil Podpeč arheo in Podpeč 1, 2, 3*
  - *E3*
    - *Profil Podpeč 4*
  - *Kamniti izdelki*
- *Opisi lito- in mikrofaciesov*
- *Paleontologija - foraminifere*
  - *E1*
    - *Profil Dedec*
    - *Profil Podutik*
  - *E2*
    - *Profil Ig*
    - *Profil kamnolom Jezero*
    - *Profili Podpeč*
      - *Profil Podpeč 2*
      - *Profil Podpeč 3*
  - *E3*
    - *Kamniti izdelki*
      - *Lapidarij Iška vas*
      - *Nahajališče Ig krožišče*
    - *Profil Ledenica-Planinca*
    - *Profil Podpeč 4*
    - *Profil Sv. Ana*

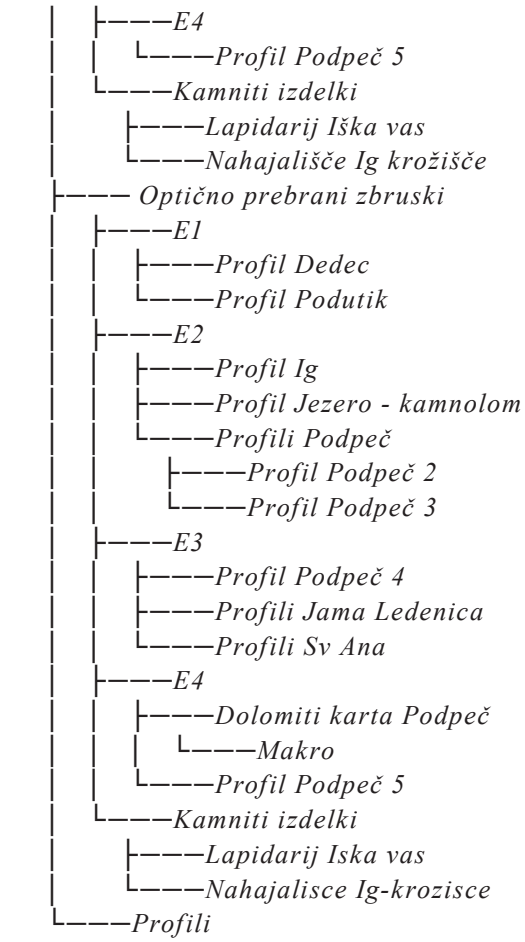

Tip podatkov

Primarni podatki so arhivirani v obliki rentgenogramov, makroskopskih fotografij, optično prebranih zbruskov in njihovih fotografij. Interpretirani podatki so podani v obliki tekstovnih datotek in obliki .jpg za sedimentološke profile, vektorski podatki geoloških kart pa v .shp obliki. Metapodatki so za geološke karte podani v pdf datoteki.

Opis podatkov

Zbrani podatki so arhivirani v podatkovni bazi, ki je strukturirana v mape in podmape. V končnih podmapah se nahajajo ustrezni podatki, ki jih podrobneje predstavljam v nadaljevanju.

Datoteka z naslovom *Podatki δ18Ocarb_ δ13Ccarb_Corg_δSr* vsebuje podatke o meritvah stabilnih izotopov $\delta^{18}O_{carb}$ in $\delta^{13}C_{carb}$ (skupaj 231 vzorcev) ter meritve razmerja izotopov $^{87}Sr/^{86}Sr$ (skupaj 44 meritev). Datoteka *Podatki geokemičnih meritev analiziranih vzorcev za okside in elemente nad mejo zaznavanja* vključuje podatke o geokemični sestavi za skupno 58 vzorcev.

V mapi *Geološke karte* so shranjeni digitalni podatki treh geoloških kart. Za vsako karto so na voljo tri datoteke v formatu .*shp* – za točkovne, linijske in poligonske podatke ter avtorsko oblikovane verzije v formatu .pdf. Vsi podatki so organizirani enotno in imajo enako atributno tabelo. Poleg tega sta v podatkovni bazi dostopna dva tekstovna dokumenta: eden z opisom litostratigrafskih enot (*Geološke karte izvornih območij spodnjejurskega apnenca*) in drugi z metapodatki izdelanih geoloških kart (*Metapodatki - geološke karte*).

Končne podmape mape *Katodoluminiscenca* vsebujejo naslednje sklope:

Profil Dedec (10 vzorcev, 20 slik),
Profil Podutik (6 vzorcev, 12 slik),
Profil Podpeč 3 (4 vzorci, 8 slik),
Profil Podpeč 4 (4 vzorci, 8 slik),
Profil Sv. Ana (2 vzorca, 4 slike),
E4 (6 vzorcev, 12 slik),
Kamniti izdelki (18 vzorcev, 38 slik in en tekstovni dokument z naslovom *Katodoluminiscenčne lastnosti proučenih kamnitih izdelkov*).

Mineraloški podatki so predstavljeni v tekstovni datoteki *Mineraloške analize* ter v izvornih podatkih, razdeljenih v naslednje podmape:

Profil Podutik (7 rentgenogramov),
Profil Dedec (9 rentgenogramov),
Profil Podpeč arheo in Podpeč 1, 2, 3 (15 rentgenogramov),
Profil Podpeč 4 (8 rentgenogramov),
Kamniti izdelki (9 rentgenogramov).

Opis lito- in mikrofaciesov je podan v ločeni tekstovni datoteki.

Optično prebrani zbruski so arhivirani v obliki fotografij in razdeljeni v naslednje podmape:

Profil Dedec (44 skenov),
Profil Podutik (62 skenov),
Profil Ig (23 skenov),
Profil Jezero – kamnolom (21 skenov),
Profil Podpeč 2 (14 skenov),
Profil Podpeč 3 (7 skenov),
Profil Podpeč 4 (9 skenov),
Profil Jama Ledenica (52 skenov),
Profil Sv. Ana (52 skenov),
Dolomiti – karta Podpeč (4 mikroskopske slike),
Makro (4 fotografije),
Profil Podpeč 5 (13 skenov),
Lapidarij Iška vas (35 skenov),
Nahajališče Ig – krožišče (5 skenov).

Paleontološki podatki so predstavljeni v obliki fotografij foraminifer iz pozitivnih vzorcev. Za vsako končno podmapo je navedeno število slik:

Profil Dedec (29 slik),
Profil Podutik (109 slik),
Profil Ig (61 slik),
Profil Jezero – kamnolom (35 slik),
Profil Podpeč 2 (123 slik),
Profil Podpeč 3 (30 slik),
Profil Podpeč 4 (30 slik),

Profil Ledenica – Planinca (103 slike),
Profil Sv. Ana (127 slik),
Profil Podpeč 5 (38 slik),
Kamniti izdelki (en tekstovni dokument),
Lapidarij Iška vas (57 slik),
Nahajališče Ig – križišče (47 slik).

Sedimentološki profili so arhivirani v mapi *Profili*, ki vsebuje šest dokumentov z izrisanimi profili ter en tekstovni dokument z koordinatami profilov in opisom zaporedja.

Oblika zapisa

Besedilne datoteke so arhivirane v formatu .pdf. Popisi sedimentoloških profilov, optično prebrani zbruski ter fotografije foraminifer in katodoluminiscenčnih lastnosti vzorcev so shranjeni v formatu .jpg. Rentgenogrami so podani v izvorni obliki v formatu .rd. Geološke karte so v podatkovni bazi shranjene v formatu .shp. V formatu .csv so podani geokemični podatki.

Dostopnost podatkov

Analizirani podatki so javno dostopni v repozitoriju DiRROS, skladno z licenco CC BY 4.0 (Creative Commons Attribution 4.0 International). Do podatkov je mogoče dostopati prek naslednje povezave: https://dirros.openscience.si/IzpisGradiva.php?id=22946&lang=slv

Vsi vzorci, odvzeti na terenu, so shranjeni v arhivu Geološkega zavoda Slovenije in so po predhodnem dogovoru na voljo za nadaljnje raziskave.

Zahvala

Za pomoč pri terenskem delu in laboratorijski pripravi vzorcev se zahvaljujemo Petri Škrap, Nini Valand in Blažu Puciharju ter Mladenu Štumergarju (Geološki zavod Slovenije). Za vse nasvete se zahvaljujemo prof. dr. Boštjanu Rožiču (Oddelek za geologijo, Naravoslovnotehniška fakulteta) in prof. dr. Bojanu Djuriću (Oddelek za arheologijo, Filozofska fakulteta). Za dostop do raziskovalne opreme se zahvaljujem dr. Bojanu Otoničarju (ZRC SAZU, Inštitut za raziskovanje krasa), prof. dr. Mateju Dolencu (Oddelek za geologija, Naravoslovnotehniška fakulteta UL), prof. dr. Michaelu Joachimskemu (GeoZentrum Nordbayern) ter prof. Yu-Te Hsiehu (Department of Earth Sciences, University of Oxford). Za dostop do vzorčenja kamnitih izdelkov na Ižanskem se za odobritve zahvaljujem Borisu Vičiču (Zavod za varstvo kulturne dediščine – OE Ljubljana), kustosinji dr. Bernardi Županek (Muzej in galerije mesta Ljubljane) ter župniku Janezu Avseniku (Župnija Ig). Za temeljito recenzijo se zahvaljujem anonimnemu recenzentu, ter recenzentki dr. Petri Gostinčar, ki sta s temeljitim pregledom povišala konsistentnost navedb in opisa pridobljenih podatkov. Te raziskave so bile sofinancirane s strani Javne agencije za znanstvenoraziskovalno in inovacijsko dejavnost Republike Slovenije (projekti št. P1-0195, P1-0011 in P1-0025), Slovenski nacionalni komisiji za UNESCO (SNUK) in IGCP/IGGG projektoma IGCP 637 – Heritage Stone Designation ter IGCP 710 – Western Tethys meets Eastern Tethys – geodynamical, paleoceanographical and paleobiogeographical events.

Viri in literatura

Activation Laboratories Ltd. (n.d.): Lithogeochemistry & litho. Activation Laboratories Ltd. Retrieved March 8, 2018, from https://actlabs.com/geochemistry/lithogeochemistry-and-whole-rock-analysis/lithogeochemistry-litho/

BouDagher-Fadel, D.M.K. 2018: Evolution and Geological Significance of Larger Benthic Foraminifera. University College London. https://doi.org/10.2307/j.ctvqhsq3

Brajkovič, R., Žvab Rožič, P., Djurić, B., Rožič, B. & Gale, L. 2019a: Source areas of antique artefacts in the Ig area. In: B. Rožič (ed.): Geološki zbornik, 25: 24-28. Razprave - poročila = Treatises, reports, 24. Posvetovanje slovenskih geologov = 24th Meeting of Slovenian Geologists, Univerza v Ljubljani, Naravoslovnotehniška fakulteta, Oddelek za geologijo.

Brajkovič, R., Gale, L. & Djurić, B. 2019b: Rock types of Roman stonemason workshops on the southern outskirts of Emona (present-day Ljubljana) - Ig area. Geophysical Research Abstracts, 21. EGU General Assembly 7-12 April 2019 Vienna. https://meetingorganizer.copernicus.org/EGU2019/EGU2019-9957.pdf

Brajkovič, R., Žvab Rožič, P. & Gale, L. 2021: Methodological approach to provenance determination of stone products made from micritic and fine-grained limestones. In: Rožič, B. (ed.): Razprave, poročila = Treatises, reports: 25. posvetovanje slovenskih geologov = 25th Meeting of Slovenian Geologists, Geološki zbornik, 26: 5-10. Univerza v Ljubljani, Naravoslovnotehniška fakulteta, Oddelek za geologijo.

Brajkovič, R., Žvab Rožič, P. & Gale, L. 2022a: Lower to Middle Jurassic limestone succession at the margin of the Ljubljana Moor: From microfacies to the Romans: fieldtrip D. in: Rožič, B. & Žvab Rožič P. (eds.): 15th Emile Argand Conference on Alpine Geological Studies: 12–14: Abstract book & fieldtrip guide: 128–137.

Faculty of Natural Sciences and Engineering, Department of Geology.

Brajkovič, R., Žvab Rožič, P., Djurić, B., Županek, B., Cvetko Tešović, B., Holocová, K. & Gale, L. 2022b: Stratigraphic database for the determination of provenance of limestone used in Colonia Iulia Emona (Regio X, Italia). 13th International Conference of the Association for the Study of Marble and other Stones of Antiquity: Vienna: 19-24 September 2022: Book of abstracts: 28–29. Austrian Archaeological Institute, Austrian Academy of Sciences.

Brajkovič, R., Gale, L. & Djurić, B. 2022c: Multi-method study of the Roman quarry at Podpeč sedimentary succession and stone products. Geologija, 65/1: 101–121. https://doi.org/10.5474/geologija.2022.007

Brajkovič, R. 2025: Stratigrafska karakterizacija antičnih kamnolomov apnenca in primerjava s kamnitimi artefakti iz Emone. Doktorska disertacija. Univerza v Ljubljani, Fakulteta za gradbeništvo in geodezijo & Naravoslovnotehniška fakulteta. https://repozitorij.uni-lj.si/IzpisGradiva.php?id=168738

Buser, S. & Debeljak, I. 1994: Lower Jurassic beds with bivalves in south Slovenia. Geologija, 37/1: 23–62. https://doi.org/10.5474/geologija.1995.001

Buser, S. & Debeljak, I. 1997: Lithiotid Bivalves in Slovenia and Their Mode of Life. Geologija, 40/1: 11–64. https://doi.org/10.5474/geologija.1997.001

Compton, R.R. 1985: Geology in the Field. Wiley.

Djurić, B., Gale, L. & Brajkovič, R. 2022: Kamnolom apnenca v Podpeči pri Ljubljani in njegovi izdelki = Limestone quarry at Podpeč near Ljubljana (Slovenia) and its products. Arheološki Vestnik,73:155–198. https://doi.org/10.3986/AV.73.06

Dozet, S. & Strohmenger, C. 2000: Podbukovška formacija, osrednja Slovenija = Podbukovje Formation, Central Slovenia. Geologija, 43/2: 197–212. https://doi.org/10.5474/geologija.2000.014

Dozet, S. 2009: Lower Jurassic carbonate succession between Predole and Mlačevo, Central Slovenia = spodnjejursko karbonatno zaporedje med Predolami in Mlačevim, osrednja Slovenija.RMZ – Materials and Geoenvironment, 56/2, 164–193. http://www.dlib.si/details/URN:NBN:SI:DOC-2YNYNFUC

Fugagnoli, A. & Loriga Broglio, C. 1998: Revised biostratigraphy of Lower Jurassic shallow water carbonates from the Venetian Prealps (Calcari Grigi, Trento Platform, Northern Italy). Studi trentini di scienze naturali. Acta geologica, 73/1: 35–73.

Fugagnoli, A. 2004: Trophic regimes of benthic foraminiferal assemblages in Lower Jurassic shallow water carbonates from northeastern Italy (Calcari Grigi, Trento Platform, Venetian Prealps). Palaeogeography, Palaeoclimatology, Palaeoecology, 205/1–2: 111–130. https://doi.org/10.1016/j.palaeo.2003.12.004

Gale, L. 2014: Lower Jurassic foraminiferal biostratigraphy of Podpeč limestone (external Dinarides, Slovenia) = Spodnjejurske foraminifere podpeškega apnenca (zunanji Dinaridi, Slovenija). Geologija, 57/2: 119–146. https://doi.org/10.5474/geologija.2014.011

Gale, L. 2015: Microfacies characteristics of the Lower Jurassic lithiotid limestone from northern Adriatic Carbonate Platform (central Slovenia). Geologija, 58/2: 121–138. https://doi.org/10.5474/geologija.2015.010

Gale, L. & Kelemen, M. 2017: Early Jurassic foraminiferal assemblages in platform carbonates of Mt. Krim, central Slovenia. Geologija, 60/1: 99–115. https://doi.org/10.5474/geologija.2017.008

Gale, L., Barattolo, F. & Rettori, R. 2018: Morphometric approach to determination of lower jurassic siphovalvulinid foraminifera. Rivista Italiana Di Paleontologia e Stratigrafia, 124/2: 265–282. https://doi.org/10.13130/2039-4942/9984

Geological rock-color charts with genuine Munsell color chips, 2011. Munsell Color.

Grahek, L. & Ragolič, A. 2020: Ig. In: Horvat, J., Lazar, I. & Gaspari, A. (eds.): Manjša rimska naselja na slovenskem prostoru, 173–186. Založba ZRC. https://omp.zrc-sazu.si/zalozba/catalog/view/1890/7848/1025-2

Lokier, S.W. & Al Junaibi, M. 2016: The petrographic description of carbonate facies: are we all speaking the same language? Sedimentology, 63/7: 1843–1885. https://doi.org/10.1111/sed.12293

Lozić, E. 2008: Rimski lapidarij v Iški vasi v kontekstu krajinskega parka Barje. Diplomsko delo. Univerza v Ljubljani, Filozofska fakulteta, Oddelek za arheologijo.

Lozić, E. 2009: Roman stonemasonry workshops in the Ig area. Arheološki Vestnik, 60: 207–221. http://www.dlib.si/details/URN:NBN:SI:DOC-DYJSFIKD

McArthur, J.M., Howarth R.J. & Shields, G.A. 2012: Strontium isotope stratigraphy. In: Gradstein, F.M., Ogg, J.G., Schmitz, M.D. & Ogg, G.M. (eds.): A Geologic Time Scale, 127–144.

https://doi.org/10.1016/B978-0-444-59425-9.00007-X

McArthur, J.M., Steuber, T., Page, K.N. & Landman, N.H. 2016: Sr-Isotope Stratigraphy: Assigning Time in the Campanian, Pliensbachian, Toarcian, and Valanginian. The Journal of Geology, 124/5: 569–586. https://doi.org/10.1086/687395

Miler, M. & Pavšič, J. 2008: Triassic and Jurassic beds in Krim Mountain area (Slovenia) = Triasne in jurske plasti na območju Krima. Geologija, 51/1: 87–99. https://doi.org/10.5474/geologija.2008.010

Ogorelec, B. 2009: Spodnje jurske plasti v Preserju pri Borovnici = Lower Jurassic beds at Preserje near Borovnica (Central Slovenia). Geologija, 52/2: 193–204. https://doi.org/10.5474/geologija.2009.019

Ragolič, A. 2016: The funerary stele of Petto from Ig = Nagrobna stela za Petona z Iga. Arheološki Vestnik, 67: 277–296.

Romaniello, S.J., Field, M.P., Smith, H.B., Gordon, G.W., Kim, M.H. & Anbar, A.D. 2015: Fully automated chromatographic purification of Sr and Ca for isotopic analysis. Journal of Analytical Atomic Spectrometry, 3/9: 196–1912. https://doi.org/10.1039/c5ja00205b

Russell, B. 2013: Gazetteer of Stone Quarries in the Roman World. http://oxrep.classics.ox.ac.uk/docs/Stone_Quarries_Database.pdf

Sevillano, A., Septfontaine, M., Rosales, I., Barnolas, A., Bádenas, B. & López-García, J.M. 2020: Lower Jurassic benthic foraminiferal assemblages from shallow-marine platform carbonates of Mallorca (Spain): stratigraphic implications. Journal of Iberian Geology, 46/1: 77–94. https://doi.org/10.1007/s41513-019-00117-9

Sibley, D.F. & Gregg, J.M. 1987: Classification of dolomite rock textures. Journal of Sedimentary Petrology, 57/6: 967–975. https://doi.org/10.1306/212F8CBA-2B24-11D7-8648000102C1865D

Šašel, J. 1975a: Ig. In: Gabrovec, S. (ed.): Arheološka najdišča Slovenije. Državna založba Slovenije: 180–181.

Šašel, J. 1975b: Iška vas. In: Gabrovec, S. (ed.): Arheološka najdišča Slovenije. Državna založba Slovenije 182.

Šmuc, A., Dolenec, M., Lesar-Kikelj, M., Lux, J., Pflaum, M., Šeme, B., Županek, B., Gale, L. & Kramar, S. 2017: Variety of Black and White Limestone Tesserae Used in Ancient Mosaics in Slovenia. Archaeometry, 59/2: 205–221. https://doi.org/10.1111/arcm.12250

Tarolli, P. 2014: High-resolution topography for understanding Earth surface processes: Opportunities and challenges. Geomorphology, 216: 295–312.

Velić, I. 2007: Stratigraphy and Palaeobiogeography of Mesozoic Benthic Foraminifera of the Karst Dinarides (SE Europe). Geologia Croatica, 60/1: 1–113.

Veranič, D. & Repanšek, L. 2016: Rimski kamniti spomeniki iz cerkve sv. Janeza Krstnika v Podkraju pri Tomišlju = Roman stone monuments in the Church of St. John the Baptist in Podkraj near Tomišelj. Arheološki Vestnik, 67/1: 297–320.

Visočnik, J., Županek, B., Jarc, S. & Gale, L. 2017: Rimski fragmenti z napisi v Mestnem muzeju Ljubljana. Studia Universitatis Hereditati, 5/2: 9–20. https://doi.org/10.26493/2350-5443.5(2)9-20

Vuga, D. 2000a: Stari Dedec pri Stajah: lapis sepulcralis gentis Laepiae. Kras, 42/1: 10–11.

Vuga, D. 2000b: Ižanski lapidarij. Rodna Gruda: revija za Slovence po svetu, 47/7: 48.

Weis, D., Kieffer, B., Maerschalk, C., Barling, J., de Jong, J., Williams, G.A., Hanano, D., Pretorius, W., Mattielli, N., Scoates, J.S., Goolaerts, A., Friedman, R.M. & Mahoney, J.B. 2006: High-precision isotopic characterization of USGS reference materials by TIMS and MC-ICP-MS. Geochemistry, Geophysics, Geosystems, 7/8: 1–30. https://doi.org/10.1029/2006GC001283

Žvab Rožič, P., Gale, L. & Rožič, B. 2016: Analiza kamnin rimskih nagrobnih stel iz Podkraja in z Iga = Rock analysis of Roman tombstones from Podkraj and Ig near Ljubljana. Arheološki Vestnik, 67/1: 359–369. http://www.dlib.si/details/URN:NBN:SI:doc-FQSHAUMU

Žvab Rožič, P., Rožič, B., Gale, L. & Brajkovič, R. 2022: Provenance analysis of Roman limestone artefacts from Colonia Iulia Emona (Marof archaeological site, Slovenia). Archaeometry, 64/5: 1057–1078. https://doi.org/10.1111/arcm.12771

Elektronski viri:

Internet: https://gis.arso.gov.si/evode/profile.aspx?id=atlas_voda_Lidar@Arso (21.5.2020)

GEOLOGIJA 68/2, 323-330, Ljubljana 2025

Poročila in ostalo - Reports and More

Unveiling Portugal's Geothermal Landscape: Insights from the IGCP636 Annual Meeting 2023

Fernando GUTIÉRREZ-SOLEIBE[1]*, Mafalda M. MIRANDA[2], Mariana GOLDONI DE SOUZA[2], Fiona M. CHAPMAN[2], Abra R. GOLD[2], Victoria M. LEE[2], Violaine GASCUEL[2], Garen J. THOMAS[2], Michaël THIBAULT[2], Jasmin RAYMOND[2], Daniela BLESSENT[3], Michel MALO[2], Nina RMAN[4], Jacqueline LOPEZ-SANCHEZ[3], Linda DANIELE[5], Mar ALCARAZ[6] & Renato SOMMA[7]

[1]University of Neuchâtel, 2000 Neuchâtel, Switzerland, *Corresponding author: fernando.gutierrez@unine.ch
[2]Institut national de la recherche scientifique Centre Eau Terre Environnement, Québec, QC G1K 9A9 Canada; e-mail: mafalda_alexandra.miranda@inrs.ca, mariana.goldoni_de_souza@inrs.ca, fiona.chapman@inrs.ca, abra.gold6@gmail.com,victoria.lee@inrs.ca, violaine.gascuel@ete.inrs.ca, gthomas2490@gmail.com, michael.thibault@inrs.ca, jasmin.raymond@inrs.ca
[3]Environmental Engineering Program, Universidad de Medellín, 050026 Medellín, Colombia
[4]Geological Survey of Slovenia, 1000 Ljubljana, Slovenia; e-mail: nina.rman@geo-zs.si
[5]Departamento de Geología-Centro de Excelencia en Geotermia de los Andes, Universidad de Chile, Santiago de Chile, Chile; e-mail: ldaniele@uchile.cl
[6]Universidad Politécnica de Cartagena, Departamento de Ingeniería Minera y Civil, Pza. del Cronista Isidoro Valverde, Edif. La Milagrosa, C.P. 30202 Cartagena; e-mail: mar.alcaraz@upct.es
[7]Osservatorio Vesuviano-Sez, Napoli Istituto Nazionale di Geofisica e Vulcanologia, Via Diocleziano, 328-80124 Napoli, Italy; e-mail: renato.somma@ingv.it

Introduction

The Geothermal Resources for Energy Transition project, identified by the acronym IGCP636, is a collaborative effort involving research institutes worldwide, supported by the International Geoscience Programme (IGCP) of UNESCO. The IGCP programme has partnered since 1972 with the International Union of Geological Sciences (IUGS) and, since 2018, with the Jeju Province Development Corporation (JPDC) of the Republic of Korea.

The main goal of the UNESCO IGCP636 Project is to strengthen scientific to promote the use of geothermal resources as a clean, low-carbon, baseload, and renewable energy. The project has three main targets: increasing knowledge and understanding of deep geothermal reservoirs; conducting outreach activities with focus groups and communities; promoting the installation of geothermal heat pumps. The activities proposed by this research team include engaging local authorities, civil society, and other stakeholders, paying attention to local needs and concerns, enabling co-design of new strategies and measures for the development of green energy solutions.

Alongside the IGCP636 research team, students from the Geothermal Research Group at the *Institut national de la recherche scientifique* (INRS) in Quebec City, Canada, organized a research expedition in Portugal mainland and in Azores from October 21st to November 1st 2023. The primary aim of this expedition was to offer an enriching educational experience, particularly for graduate students specializing in geothermal energy, within the occasion of the annual meeting for the IGCP636 project. The focus was on providing the participants with insights into the utilization of geothermal resources in Portugal, along with attending the annual group meeting at the University of Coimbra (UNESCO World Heritage Site).

The INRS students wrote an itinerary guidebook[1], providing information to enrich the exploration of the visited sites. The guidebook offers in-depth insights into the geological features of Portugal and provides information about the geothermal energy exploration in the visited sites.

Additionally, it included details about the local culture, history, and attractions, widening the overall experience for the participants. This fieldtrip not only enhanced the overall group dynamics, but also provided the students and researchers (around 20 participants) with a unique opportunity to gain insights into geothermal resources in Portugal.

Geological context of Portugal

Portugal's continental territory is located in the Iberian Peninsula, where 63 % of the total geothermal occurrences are linked to the Central-Iberian Zone, associated with the *Variscan* granitic units and large deep regional faults and their conjugates; mainly the *Penacova-Regua-Verin* and *Manteigas-Vilarica-Bragança* fault systems in the north of the country (Julivert et al., 1980). In the West-

ern Meso-Cenozoic margin, geothermal occurrences are associated with faulting and diapirism, most importantly around the *Nazare-Caldas da Rainha-Vimeiro* fault; and detrital sedimentary aquifers, such as the lower Cretaceous aquifer in the Lisbon region. Finally, a small number of occurrences can be seen in the *Ossa-Morena* and *South-Portuguese* zones and the *Algarve* basin (Fig. 1). There are, in total, 30 low-enthalpy geothermal occurrences, with temperatures between 30 and 76 °C; 36 very-low enthalpy geothermal occurrences, temperatures between 20 and 29 °C; and 24 springs, officially used in balneotherapy, with temperatures from 25 to 76 °C (DGEG, 2020).

Itinerary and visited sites

Alfama Springs

The very first activity on the itinerary was organized at *Alfama* Springs, now a recognized cultural geoheritage site in Lisbon, served multiple purposes for locals, including bathing and water provisioning. Lisbon is situated in the Lusitanian Basin, characterized by Mesozoic and Cenozoic sediments, including aquifer formations. Consequently, Alfama Springs exhibit hydrochemical facies indicating low salinity and temperatures between 24 and 34 °C, with geothermometers suggesting groundwater rises quickly from depths

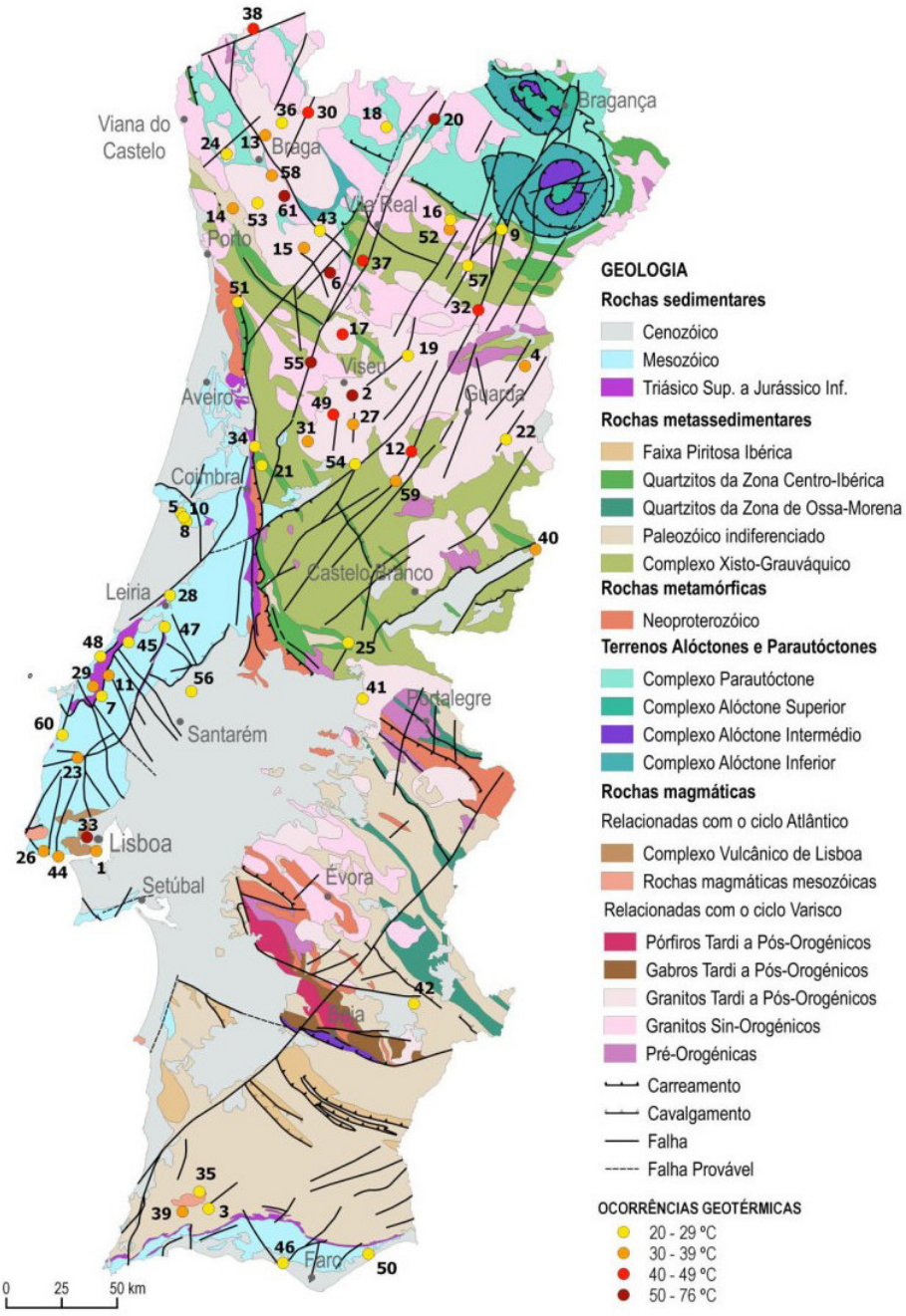

Fig. 1. Geological map of Portugal Mainland and thermal occurrences (DGEG, 2020).

of 565 to 2957 m, showing significant geothermal energy potential influenced by the Alfama fault (Ramalho et al., 2020; Marrero-Diaz et al., 2021).

This site was chosen as the first day visit because it represents a significant case study for geothermal energy. The analysis enhances the understanding of water temperature at depth and the reservoir depth in the Alfama Springs region, providing valuable insights into the geothermal potential of this historical site.

Vila Velha de Rodão

After Lisbon, the group drove to *Vila Velha de Rodão* for a guided visit of the region consisting of a field trip to recognize the geomorphological features of the *Naturtejo* Geopark and its relation to the Tagus River, as well as a visit to historical sites seeing prehistoric engravings and ancient roman olive oil production. During the day, the main sighting was the imponent *Portas de Ródão*, a gorge formed by the Tagus River in the quartzite crest of the *Perdigão* mountain range, featuring a 45-meter-wide bottleneck, and where Pleistocene terraces to the sides, comprising conglomeratic and silty sediments, showcase the fluvial evolution of the Tagus River over 2-3 million years, highlighting various stages of settlement.

Fronteira

On October 23rd, the itinerary continued towards the municipality of *Fronteira*, including the villages of *Cabeço de Vide* and *Alter do Chão*. Starting in Fronteira's cultural center, Dr. Carla Rocha presented the local geothermal occurrences, highlighting the local hydrogeological conditions, where mineral waters emerge from boreholes and natural springs located at the junction of the Alter do Chão pluton and Cambrian carbonate metasediments of Elvas, as part of the prior mentioned Ossa Morena zone. She also showed practical examples for methods used to quickly assess the geochemical composition of the water (Fig. 2). The thermal waters in Cabeço do Vide have been used since 119 B.C. for medicinal purposes and are used nowadays in the Termas da Sulfúrea balneary. They have a unique geochemical composition with a pH of 11.55 and being sulfuric, hyposaline, and hyperalkaline with sodium and calcium, oxidized. No other water in the country is simultaneously oxidized and hyposaline. The group was able to explore the surroundings of the thermal baths and observe the extraction wells and learn more about the functioning of the balneary and its relation to the geological and tectonic context.

Fig. 2. Application of experimental methods to local groundwater samples.

A visit to Alter do Chão was done after the thermal baths to learn about the history of the town and the region, given by a guided tour through the Casa do Álamo and to the Casa da Medusa museums.

To finish the day, a trip was done to the Alter Pedroso castle (Fig. 3) to learn about the 120 history of the Alentejo region and its importance in the Portuguese restoration war.

Fig. 3. Group picture in front of the Alter Pedroso castle.

Castelo de Vide

On October 24th, the group moved towards the municipality of *Castelo de Vide*. The historical relation between water and local Jewish ancestry since the 13th century and how the groundwater and thermal springs helped shape the town's rich history and culture were explained.

A short drive then took the group to the town of Marvão, located on a ridge of the Serra de Sã Mamede mountain range, to take a better look at the geological context of the region, where the ridge

is part of a synclinal structure with local quartzite and dolomite series. The day was finished with a visit to the municipality of Nisa, where the local tourism office presented their unique pottery techniques using quartz fragments, with a demonstration by local craftsmen and craftswomen, before heading to the city of Coimbra.

Coimbra: Annual IGCP636 Meeting 2023

The Earth Science Department and the Geosciences Center from the University of Coimbra, which is a UNESCO World Heritage Site, hosted the IGCP636 Annual Group Meeting on October 25th. The morning session was committed to introducing the IGCP636 project, featuring keynote talks on geothermal resources and case studies in Portugal. These talks were led by representatives from various pertinent institutions, including the Earth Science Department; Portugal's General Directorate of Energy and Geology, presenting the current state of geothermal energy use throughout the country; *SYNEGE,* showcasing different-scale projects for low to medium enthalpy geothermal applications; and the National Laboratory of Energy and Geology, introducing their work regarding research on new resources and the collaboration to unify geological data with multiple European geological surveys. In the afternoon, presentations were delivered by representatives from the Bureau of Economic Development, U.S.A., the Geological Survey of Slovenia, and Canada's National Institute for Scientific Research (Fig. 4).

Posters, listed in Table 1, were also presented after the meeting, where students and collaborators from the INRS exhibited their most recent research work in the field of geothermal energy.

São Pedro do Sul

São Pedro do Sul Hydromineral and Geothermal Field consists of two main zones: the *Termas* and *Vau* poles, both within the junction of São Pedro do Sul-Ribamá Fault, Termas Fault, and Fataunços Fault, in highly fractured granite and metasedimentary aquifers, and separated by approximately 1.2 km (Almeida et al., 2022). As a place of great interest for its hydrothermal activity, the group arrived at Rainha D. Amélia thermal bath where they had the opportunity

Fig. 4. Annual meeting at University of Coimbra.

Chapman, F.M., Klepikova, M., Bour, O., Soucy La Roche, R., & Raymond, J., 2023. Heat flow assessments in southwestern Yukon using fibre-optics.
Gasguel, V., Raymond, J. & Rivard, C. 2023. Repurposing idle wells for the heat transition: Dynamic modelling of a deep borehole heat exchanger system.
Goldoni de Souza, M., Bordeleau, G., Lacombe, S., Raymond, J. & Comeau, F. A., 2023. Geothermal and geochemical considerations in open-loop systems in Quebec's former open-pitmines.
Thibault, M., Rajaobelison, M. M., Comeau, F. A., Raymond, J., Terklay, V. & Newson, J. 2023. Geothermal potential of the South Slave Region, Northwest Territories, Canada.
Gold, A., Miranda, M.M., Raymond, J., & Asbjornsson, E.J., 2023. Minimiser le dégel du pergélisol et maximiser le stockage souterrain de la chaleur à Baker Lake (Nunavut).
Lee, V., Raymond, J., Rivard, C., Parent, M., Comeau, F.-A., & Newson, J., 2023. The potential of groundwater heat pump systems for urban heat island mitigation: aquifer suitability assessmentin Canada's major cities.
Thomas, G., Rajaobelison, M. M., Comeau, F. A. & Raymond, J. 2023. Geothermal Reservoir Analysis of the Fort Liard region, Northwest Territories, Canada.

Table 1. Works presented during the poster session at IGCP636 Annual Meeting in University of Coimbra.

to observe the exploitation network for the thermal waters. Both an artesian thermal spring and a 500 m deep artesian well are used to feed the direct geothermal systems in place. They have a flowrate of 10 l/s and outflow temperatures of 68.7 °C and 69 °C respectively, being bicarbonated, carbonated, fluoridated, sulfhydrated, sodic and strongly silicate waters, although weakly mineralized, with around 300 mg/L (Almeida et al., 2022). After the technical visit, the group spent the afternoon visiting the ancient roman baths and museum, learning about the historical importance of thermal waters in the region, concluded by paying a last visit to the thermal baths in the hotel to enjoy their health benefits.

Guimarães

The visit of Guimarães started at the Laboratório da Paisagem, where sustainability projects are proposed to promote and innovate in environmental and territorial practices, and where the group got to see first-hand many projects implemented in the city. Later, a trip to the Taipas Termal thermal baths was made to learn more about the local hydrogeological conditions and how the heat has been used since Roman times for balneotherapy. Within mostly granitic lithology, the hydrothermal waters are weakly mineralized and with low temperatures of around 32 °C (Fig. 5), where the exploitation well for the thermal baths was drilled on a fault and to a depth of less than 200 m, to get better temperatures and a pumping rate of 7.3 l/s. The afternoon consisted in a guided tour around the city's historical center to learn more about the importance of the city in Portugal's national history as a republic, followed by a visit to the Gimnastics Academy, where the coupled use of low-enthalpy groundwater, surface water, air, photovoltaic, thermal and passive solar, and adequate construction materials (special concrete, cork, etc.) contribute to a energy efficient and architecturally beautiful building. This building, during parts of the year, is a net producer of electricity to the grid, thus making a positive energy balance from sustainable practices.

Fig. 5. Temperature measurement at a thermal water outlet in the Taipas Thermal baths.

Porto to Lisbon

On October 28th, a road trip back to Lisbon from Porto was planned to prepare for the upcoming flight to the Azores Islands the next day, but not before a stop at the city of Nazaré, on the western coast, to see the very notable sedimentary cliffs and the enormous waves generated by Nazaré's undersea canyons, place that serves as one of the main spots worldwide for big-wave surfing competitions

Azores - São Miguel Island

The Azores archipelago consists of nine volcanic islands located in the North Atlantic. São Miguel, the largest island, is the most volcanically active with three dormant volcanoes: Sete Cidades, Fogo, and Furnas, and numerous scoria cones, given the location of the island on the mid-Atlantic ridge are where the Eurasian, African (Nubian), and North American lithospheric plates meet, resulting also in significant seismic activity. After landing on Ponta Delgada, São Miguel Island, on October 29th, the group immediately proceeded to visit one of the main dormant volcanic complexes, Sete Cidades. This site es most active volcano in the archipelago, with 17 explosive eruptions that displayed predominantly hydromagmatic character (Queiroz et al., 2015). A short hike was done through Grota Do Inferno to the panoramic view of the ancient calderas in the zone. A small discussion about the local geomorphology took place regarding the evolution of the volcano, its features, and their relation to the tectonic context. To continue learning more about the influence of volcanic activity on the morphology of the island, the group drove to the *Escalvado* viewpoint to observe the pumice, tuff, and other pyroclastic deposits that originated from ancient eruptions.

The next day, the University of Azores and its volcanology center received the group for a guided visit, to show their research work and laboratories around understanding of volcanic processes in the island and identifying possible threats to the population related to seismicity and eruptions. Hydrochemistry, petrology, meteorology, seismicity, and cartography are the main topics investigated. In the afternoon, the group moved towards the *Pico Vermelho* Geothermal Power Station, located

on the Ribeira Grande geothermal field, which, together with the *Ribeira Grande* Geothermal plant, provides around 44 % of the electricity needs of São Miguel Island, 23 Mwe net. The field is located in the northern flank of Fogo Volcano, the largest among the three dormant stratovolcanoes of the island, characterized as a 245 °C two-phase reservoir hosted in volcanic rocks intersected by 1 to 1.5 km deep wells. A guided visit through the installations was made (Fig. 6) and the operation team explained the details of the exploitation system, both advantages and challenges presented along the history of the plant. Currently, the operation runs five producing and three reinjecting wells, working with a fluid at 161 °C and 5 bar, with an installed production capacity of 10 MW with a binary ORC plant. Residual heat from the operation is not used for any other application, although the 90 °C reinjection temperatures could represent an interesting opportunity for low to intermediate enthalpy geothermal applications.

Fig. 6. Visit to the Pico Vermelho powerplant's installations (São Miguel Island).

Back to the University of Azores, the Geotalk workshop took place with the help of Department of Volcanology. The researchers presented their most recent work and a brief overview of the status of geothermal energy in their respective countries. The event was concluded by a discussion about the newest challenges geothermal energy is facing as an emerging renewable source and getting insights from recent experiences.

On October 31st, the day started with a visit to the *Gorreana* tea factory, known to be the oldest in Europe, and of significant importance in the economy of the island. Later, a series of sightseeing stops were included in the fieldtrip, to look at the region around the Furnas volcano, which has had 10 moderately explosive trachytic eruptions of sub-Plinian character. Two of these have taken place since the island was settled in the mid-fifteenth century, and where several craters, domes, maars, and pumice cones can be observed. The group then headed to the *Terra Nostra* park, located next to the Furnas Lake and inside the ancient caldera, where fumarole fields and hot springs can be seen (Fig. 7). A local dish is prepared here by burying a hot pot in the ground to let the high temperature fluids cook the meat and vegetables at temperatures from 66 °C to 93°, for 6 to 8 hours. There are also thermal baths, which are characterized by temperatures around 40°C, and high iron content.

Fig. 7. Visit to the Furnas volcano's fumaroles in Terra Nostra park.

The final day in Sao Miguel of Azores was spent visiting the rest of the island, diving the group in two teams: one that went to the *Salto Do Cabrito* trail, near the *Ribeira Grande* area to better observe the surrounding features of Fogo volcano; and the other team headed to see the impressive cliffs made from mafic pyroclastic rocks and thermal water discharging in the sea at *Ponta da Ferraria,* on the western most point of the island.

Main Results and Outcome of Annual Meeting 2023

A relevant involvement of graduate students at Master and Doctorate level (half of the group) was achieved: they gave more than 10 talks. They also presented posters (Table 1) and wrote a field guidebook for all planned activities with all due technical, scientific, and logistical aspects (Miranda et al., 2023).

The activities benefited from the contribution of local experts in geothermal energy (e.g.: Direção de Serviços de Recursos Hidrogeológicos e Geotérmicos, Synege and TARH companies) and the new contacts with professors and researchers from the Research Institute for Volcanology and Risk Assessment of the University of Azores.

It is worth mentioning the participation of professionals from Geothermal Canada, as well as the visibility of the IGCP636 activities in international bulletins (Cariaga, 2024).

The Annual Meeting and the fieldtrip were an excellent opportunity to strengthen and create collaborations between researchers, to encourage the participation of graduate students, and to lay the foundations for future joint research activities, while continuing to comply with the IGCP program mission.

Conclusion

Exploring Portugal's geothermal resources proved to be an enriching educational journey, marking yet another successful chapter for the IGCP636 Geothermal Resources for Energy Transition research group. The most important experiences in the immersion of young researchers, both from the INRS and the IGCP636 groups, was the opportunity to get into networking and the sharing of knowledge, having academic discussions with professionals in geothermics, and presenting their work to the universities of Coimbra, Azores, and governmental institutions interested in their research. As part of the third objective of the IGCP636 project, based on promoting educational resources and outreach around geothermal energy, the experience from the joint annual meeting and academic expedition proved to be a highly successful activity that can be taken as an example for further geosciences related events.

Acknowledgments

The International Geoscience Programme (IGCP), the United Nations Educational, Scientific and Cultural Organization (UNESCO), and the International Union of Geological Sciences (IUGS) are acknowledged since they supported the project "IGCP636 Geothermal Resources for Energy Transition". The *Institut national de la recherche scientifique* (INRS) is acknowledged for the support given to the students through INRS Foundation. The municipalities of Cabeço de Vide, Vila de Alter do Chao, Notável Vila de Castelo de Vide, Fronteira, Termas de Sao Pedro do Sul, Guimaraes, the institutions of Department Earth Sciences from University of Coimbra (DCT.UC), International Association of Hydrogeologists (IAH), Center of Geosciences from University of Coimbra, University of Azores, Institute of Agricultural and Environmental Research and Technologies (IITAA), IVAR, Laboratório da Paisagem, Terra Nostra Park, EDA Renováveis (EDA Group), Early Career Hydrogeologists Network, and the companies Deep corp, Geomax Forage – Drilling, Intragaz, ENKI GeoSolutions Sustainable geological solutions, Geonatour, Versaprofiles, Geothermal Canada, Puitbec Group, Derena Geosciences are acknowledged for sponsoring this expedition.

This trip was made possible by Mafalda Miranda who worked tirelessly with the IAH, academic institutions, and municipalities to ensure that this field excursion was accessible to all and informative. Special thanks to Manuel Abrunhosa – President IAH-Portuguese Chapter, Carla Rocha, Instituto Superior Tecnico, Paulo Borges, University of Azores, Fátima Saraiva and Luis Gomes – Termalistur, Maria do Rosário Carvalho – University of Lisbon, Antonio Trota and Maria João Trota University of Azores, Bruno Teixeira – Geonatour, Maria Helena Henriques – Geosciences Center,University of Coimbra, Pedro Dinis – Dep. Earth Sciences, University of Coimbra, Carlos Ribeiro –Landscape Laboratory, C.M. Guimarães, João Botelho and Carlos Ponte – EDA Renovaveis for theirsignificant contributions to the planning and success of this trip.

References

Almeida, S., Gomes, L., Oliveira, A. & Carreira, P. 2022: Contributions for the Understanding of the São Pedro do Sul (North of Portugal) Geohydraulic and Thermomineral System: Hydrochemistry and Stable Isotopes Studies. Geosciences, 12/2, 84. https://doi.org/10.3390/geosciences12020084

Cariaga, C. 2024: Think Geoenergy. https://www.thinkgeoenergy.com/unesco-igcp636-project-holds-annual-meeting-in-portugal/ (accessed 14 May 2024)

DGEG 2020: Geotermia - Energia Renovável em Portugal. DGEG - Direção Geral de Energia e Geologia. Electronic Edition, 54 p.

Marrero-Diaz, R., Ramalho, E.C., Carvalho, J., Dias, R., Ramada, A. & Pinto, C. 2021: 3D Modelling of a Hydrothermal System in a Densely Populated Urban Area–the Alfama Springs Case-Study (Lisbon, Portugal).

Julivert, M., F.J. Martinez & Ribeiro A. 1980: The Iberian segment of the European Hercynian foldbelt. Geology of Europe from Precambrian to the post-Hercynian sedimentary basins.

Bureau de Recherches Gélogiques et Minières Société Géologique du Nord. 132–158.

Miranda, M.M., M. Goldoni de Souza, F.M. Chapman, A.R. Gold, V.M. Lee, V. Gascuel, J.T., Garen & Thibault, M. 2023: IGCP636 & INRS Discover Portugal guide. Retrieved from:

https://inrsigcp636portugal.wixsite.com/inrsigcp636portugal (accessed 14 May 2024).

Queiroz, G., J.L. Gaspar, J.E. Guest, A. Gomes & M.H. Almeida 2015: Eruptive history and evolution of Sete Cidades Volcano, São Miguel Island, Azores. In Geological Society Memoir (44/1; 87–104). Geological Society of London. https://doi.org/10.1144/M44.7

Ramalho, E.C., Marrero-Diaz, R., Leitao, M., Dias, R., Ramada, A. & Pinto, C. 2020. Alfama springs, Lisbon, Portugal: Cultural geoheritage throughout the centuries. Geoheritage, 12: 1–14.

GEOLOGIJA 68/2, 331-336, Ljubljana 2025

Reports and More

Izobraževalne delavnice za osnovnošolske učence na Geološkem zavodu Slovenije

Rada PETERNEL RIKANOVIĆ, Teja ČERU, Katja KOREN PEPELNIK, Blaž PUCIHAR & Marjana ZAJC

Geološki zavod Slovenije, Dimičeva ulica 14, SI–1000 Ljubljana, Slovenija; e-mail: rada.peternel-rikanovic@ geo-zs.si; teja.ceru@geo-zs.si; katja.koren@geo-zs.si; blaz.pucihar@ geo-zs.si; marjana.zajc@ geo-zs.si

Uvod

V prostorih Geološkega zavoda Slovenije so nas 13. februarja 2025 obiskali učenci OŠ Križe in OŠ Tržič.

Skupina zaposlenih na Geološkem zavodu Slovenije je zanje pripravila dva tematska sklopa delavnic: izobraževalne delavnice *Podzemna voda in njeno onesnaževanje* ter izobraževalno-ustvarjalno delavnico *Kamnine in barvni pigmenti*. Program se je pričel s krajšo predstavitvijo izvajalcev in delovanja Geološkega zavoda Slovenije. Poudarili smo, da je to osrednja raziskovalna ustanova s področja geologije v Sloveniji ter na kratko opisali, s čim vse se geologija ukvarja, kje vse so se že srečali z geologijo in zakaj je pomembna za naše vsakdanje življenje.

Delavnic se je udeležilo 35 učencev od 5. do 9. razreda s statusom nadarjenih učencev, od tega 18 iz OŠ Križe in 17 učencev OŠ Tržič.

Pri zasnovi in izvedbi delavnic smo skušali slediti naslednjim ciljem:

- spodbujanje povezovanja geologije z drugimi vedami oz. znanjem pridobljenim pri šolskih predmetih, ki so del obveznega učnega načrta (geografija, kemija, biologija, fizika...);
- seznanitev s perečimi družbenimi in okoljskimi problemi (npr. prekomerna raba naravnih virov, negativni vplivi človekovih dejavnosti na okolje...); razmišljanje o vplivu geoloških procesov na posameznika (npr. geološke nevarnosti, kot so plazovi, kamninski podori, poplave...);
- spodbujanje radovednosti – učenec se uči postavljati vprašanja in spoznava nove, manj znane teme ter aktivno sodeluje v procesu pridobivanja novega znanja.

Izobraževalne delavnice Podzemna voda in njeno onesnaževanje

Tematski sklop Podzemna voda in njeno onesnaževanje je bil sestavljen iz med seboj povezanih in dopolnjujočih se podtem, ki smo jih predstavili v okviru štirih delavnic:

- podzemna voda je glavni vir pitne vode v Sloveniji – delavnica Model vodonosnika (Rada Peternel Rikanović);
- izkoriščanje podzemne vode – delavnica Vrtina (Blaž Pucihar);
- laboratorijske analize kakovosti podzemne vode – delavnica Hidrogeološki laboratorij (Katja Koren Pepelnik);
- skrita okoljska bremena – delavnica Georadar (dr. Marjana Zajc).

Skozi sosledje izbranih delavnic so učenci dobili vpogled v raziskovalno delo geologa na različnih nivojih (raziskovanje procesov, terensko in laboratorijsko delo). Učence smo zaradi različne starosti in različnega predhodnega znanja o obravnavani tematiki ter potrebnih prilagoditev razlage razdelili v štiri manjše skupine. Prva skupina so bili učenci 5. razredov, druga skupina učenci 6. razredov. Učenci 7., 8. in 9. razredov so bili razdeljeni v dve mešani skupini. Vsaka delavnica je trajala približno 20–25 minut, skupaj so pokrile približno dve šolski uri. Skupine učencev so med delavnicami krožile, vse skupine so se udeležile vseh delavnic. Delavnici Vrtina in Georadar sta potekali pred stavbo Geološkega zavoda, drugi dve v notranjih prostorih.

Učencem 5. razreda, ki se šele seznanjajo s temo podzemne vode, smo želeli pojasniti nekaj osnovnih pojmov, zato smo delavnice organizirali tako, da so se ti učenci udeležili najprej delavnice Model vodonosnika, kjer smo jim najprej pojasnili, kaj podzemna voda sploh je in zakaj je pomembna. Tako so pridobili osnovno znanje in v nadaljevanju lažje sledili ostalim delavnicam. Vsi učenci so si v sklopu te delavnice najprej ogledali kratki film Vodni krog (https://www.cicfilm.com/sl/film/36-video/jame/158-vodni-krog), ob katerem smo skupaj ugotavljali, da človek s svojimi dejanji neposredno vpliva tako na količinsko kot kakovostno stanje podzemne vode. Poudarili smo, da je to najpomembnejši vir pitne vode v Sloveniji. Na modelu medzrnskega vodonosnika smo pojasnili pomen vodonosnika in katere vrste vodonosnikov poznamo, ter razložili nekaj osnovnih pojmov, kot so gladina in tok podzemne vode. Preverili smo njihovo znanje o kroženju vode v naravi in ali vedo v kakšnem odnosu sta površinska voda in podzemna voda. S pomočjo modela vodonosnika ter

opazovanj in izkušenj iz domačega okolja so ugotovili, da so glavni viri onesnaževanja predvsem kmetijske dejavnosti in pomanjkljivo odvajanje odpadnih voda iz naših domov oz. neobstoječe kanalizacijsko omrežje. Tudi občasni, izredni dogodki, kot so prometne nesreče, lahko zaradi izpusta nevarnih snovi močno ogrozijo podzemno vodo. Skupaj smo ugotavljali, da je v naših domovih veliko nevarnih snovi, ter opozorili na njihovo pravilno shranjevanje oz. odlaganje med nevarne odpadke. Na karti zajetij in vodovarstvenih območij občine Tržič smo pogledali, katero zajetje je vir pitne vode v njihovem domu, ob tem so nas nekateri učenci seznanili, da njihov dom ni priključen na vodovod, temveč imajo lastna manjša zajetja. Spoznali so, da moramo zajetja zaščititi z vodovarstvenimi pasovi, tako zavarujemo zajetje pred nedovoljenimi posegi in dejavnostmi v njegovem zaledju in s tem pred potencialnim onesnaženjem. Učence je presenetilo, da hidrogeologi raziskujemo tudi onesnaževanje podzemne vode z mikroplastiko, le-ta predstavlja izredno pereč problem, katerega najhujše posledice se bodo pokazale šele v prihodnosti.

Za Slovenijo pravimo, da je preluknjana kot švicarski sir, kar ne velja zgolj zaradi številnih jam, ampak tudi zaradi številnih vrtin, ki nas obdajajo. Z učenci smo se zbrali ob vrtini pred Geološkim zavodom Slovenije, kjer smo pričeli z na videz zelo enostavnim vprašanjem: "Ali v okolju, v katerem bivate, obstajajo vrtine in za kakšen namen se jih uporablja?" Ob začetni dilemi smo z učenci hitro prišli do ugotovitve, da nas na vsakem koraku obdajajo vrtine, ki pa jih težje opazimo, saj je le manjši del le-teh viden in tudi takrat ne vemo, čemu služi "štrleča cev", ki gleda iz zemlje. Če je bil prvi del vprašanja nekoliko bolj zapleten, pa je drugi del postregel s številnimi odgovori. Učenci so povedali, da vrtine uporabljamo za črpanje (pitne) vode, nafte in plina. Namembnosti vrtin je več, saj služijo tudi za opazovanje in vzorčenje podzemne vode, z geomehanskimi vrtinami pa spremljamo morebitne premike zemljine in hribine. Spregovorili smo tudi o vzrokih za onesnaževanje podzemne vode. Tu so učenci predstavili številne dejavnike in vzroke, ki slabšajo kakovost podzemne vode (promet, razlitje snovi, požari, prekomerna raba fitofarmacevtskih sredstev v kmetijstvu...). Ob osvojenih osnovah vrtin smo od besed prešli k dejanjem. Učencem smo predstavili scenarij terenskega delavca, ki mora na terenu vzeti vzorec podzemne vode iz vrtine in ga predati sodelavcem v laboratoriju. Pred odhodom na teren je potrebno poskrbeti za vso potrebno opremo in pripomočke, ki jih bomo uporabili. V našem primeru smo potrebovali nivometer za meritev gladine nivoja podzemne vode, Hanno S za meritev kemijskih parametrov vode ter ročni vzorčevalnik za zajemanje vode iz vrtine. Sledil je praktičen prikaz uporabe prej omenjene terenske opreme, nato pa so jo učenci še sami preizkusili in uspešno izmerili nivo gladine podzemne vode ter z vzorčevalnikom zajeli vzorec vode. Z meritvijo parametrov zajete vode smo predstavitev vrtine zaključili. Sledil je še kratek ogled novo postavljenih lizimetrov, kjer se bo v kratkem pričelo spremljati novodobno onesnaževalo - mikroplastiko.

V sklopu laboratorijskih analiz kakovosti podzemne vode smo v hidrogeološkem laboratoriju Geološkega zavoda Slovenije učencem predstavili delo v laboratoriju. S prikazom instrumentov za določanje motnosti vode in prisotnosti bakterij v vzorcih vode smo jim želeli predstaviti povezavo med motnostjo vode in prisotnostjo določenih bakterij v vodi ter merilno metodo motnosti vode v primerjavi z opisno oceno videza vode. V ta namen smo učencem pokazali merilnik motnosti. Motnost vode je pokazatelj prisotnosti delcev v vodi. Ta je večinoma povišana na območjih kraških oz. kraško-razpoklinskih vodonosnikov, za katere je značilen hiter odtok podzemne vode po kanalih in razpokah. V takih sistemih se v vodi plavajoči delci (npr. glineni delci, organske snovi) ne zadržijo med zrni, kot je to v primeru medzrnskih vodonosnikov. Motnost vode je zato zlasti ob velikih nalivih in poplavah predvsem problem kraških vodonosnikov. V medzrnskih vodonosnikih se ti plavajoči delci zadržijo med zrni sedimentov. Tok podzemne vode je zaradi toka med zrni počasnejši kot v primeru kraško-razpoklinskih vodonosnikov, motnost pa je manjša. Večja količina plavajočih delcev zmanjšuje prosojnost vode. Motnost lahko spremljamo na primeru rek in potokov ter podzemnih voda. Spremljamo, kako se le-ta spreminja predvsem v odvisnosti od vremenskih dogodkov (obilne padavine in poplave) ali zaradi vpliva človekovih dejavnosti (izpusti odpadnih voda). Višja motnost je velikokrat povezana s povišanim številom bakterij v vodi. Plavajoči delci predstavljajo dodatno površino, na katero se lahko pritrdijo različne bakterije, kot npr. bakterije E. coli, ki so pokazatelj prisotnosti fekalnih odplak. Organski plavajoči delci so lahko tudi vir hranil za razvoj in rast bakterij. Učencem smo predstavili napravo za določanje prisotnosti in števila E. coli in koliformnih bakterij v vzorcu vode ter pokazali, kako se voda obarva, če so le-te prisotne v njej. Pojasnili smo tudi, kakšne so zahteve za kakovost pitne vode in kaj je potrebno storiti, ko distributerji opozorijo na neprimernost uporabe pitne vode zaradi prisotnosti bakterij v vodovodnem sistemu.

Sl. 1. Izobraževalne delavnice (fotografije: Petra Buh).

V sklopu delavnice Georadar je dr. Marjana Zajc predstavila meritve z georadarjem in kaj vse lahko z njim odkrijemo. Gre za neinvazivno geofizikalno metodo, s katero na Geološkem zavodu Slovenije raziskujemo podpovršje brez neposrednega poseganja v okolje. Tako lahko na okolju prijazen način ugotovimo lokacije in globine, kjer nastopajo različni geološki pojavi (npr. kraške jame, spremembe v litologiji, drsne ploskve plazov, razpoke in prelomi) ali pa so zakopani različni predmeti/objekti antropogenega izvora (npr. podzemna infrastruktura – cevi, kabli, tuneli in odprti podzemni prostori). Ker je bil na delavnici poudarek na pomembnosti virov pitne vode, smo si z učenci pogledali, kako lahko s pomočjo georadarja pripomoremo k ohranjanju kakovosti podzemne vode. Najprej smo jim predstavili raziskovalno opremo ter prikazali, kako meritve izgledajo na terenu. Razlaga o delovanju georadarja je bila prilagojena starosti posameznih skupin, kjer so učenci nižjih razredov poslušali precej bolj poenostavljeno razlago, medtem ko so učenci 8. in 9. razredov slišali tudi nekaj fizikalnih izrazov (valovanje, merjenje hitrosti, pretvorba časovne lestvice v globinsko ipd.). Pri možnostih uporabe georadarja smo se osredotočili predvsem na problematiko starih bremen in divjih odlagališč, ki so prepoznana kot resen okoljski problem povsod po svetu, tako v razvitih državah kot tudi v državah v razvoju. V preteklosti se je zaradi bolj ohlapne zakonodaje ter manj restriktivnega nadzora marsikatero onesnaževalo namreč preprosto zakopalo v tla, oziroma zasulo z zemljino. Danes nelegalno odvrženi in zakopani odpadki zaradi neposrednega vnosa onesnaženja ogrožajo kvaliteto podzemnih vod in s tem virov pitne vode. Tveganje predstavljajo tudi sicer legalno zakopana bremena, kjer so nevarne snovi odložene v embalaži, ki z leti razpada in prične spuščati nevarne snovi v okolje. Lokacijo takšne podzemne kontaminacije je možno odkriti z georadarskimi meritvami, prav tako pa pridejo te meritve prav v primerih, ko se želi odkriti mesta odtekanja vode iz poškodovanih vodovodnih cevi v tleh. Učenci so izvedeli še, da se s pomočjo georadarja za potrebe iskanja novih vodnih virov lahko določi tudi globina do gladine podzemne vode, če je le-ta v globinskem dosegu uporabljene opreme. Po predstavitvi opreme in razlagi njenega delovanja so se učenci lahko sprehodili z georadarjem po parkirišču in na ekranu sproti opazovali, kaj se dogaja pod površjem. Videli so posamezne plasti asfaltiranega parkirišča, kaj vidimo, če z opremo zapeljemo čez jašek ter kaj se nam izriše na ekranu, ko prečkamo podzemno vodovodno cev in električno napeljavo. Interes učencev, da sami poizkusijo izvajati meritve, je bil večji pri mlajših generacijah, medtem ko je bilo samo razumevanje o delovanju opreme večje pri starejših učencih.

Izobraževalno-ustvarjalna delavnica Kamnine in barvni pigmenti

Za popestritev geoloških delavnic so učenci v sklopu zadnje delavnice pod vodstvom dr. Teje Čeru svoje vtise iz prej predstavljenih delavnic prenesli na papir. Delavnica je bila zasnovana iz začetnega interaktivnega teoretičnega uvoda, v katerem so bili učenci spodbujeni k razmišljanju, iz česa vse lahko izdelamo pigmente in kako izdelamo barve. Skozi uporabnost različnih geoloških materialov za izdelavo pigmentov so spoznavali lastnosti posameznih mineralov in kamnin, kje jih lahko najdemo v svetu in pri nas in katere so še druge uporabne vrednosti različnih mineralov. Predstavitev je potekala zelo spontano, z vprašanji smo spodbujali otroke k razmišljanju in radovednosti. Pogledali smo si katere kamnine, minerali in tla so primerni za pridobivanje posamezne barve in kako so jih uporabljali že v prazgodovini pri jamskih poslikavah. Otroci so bili seznanjeni o tem, kaj je pigment, kaj vezivo in kakšna veziva so se uporabljala skozi čas. Kako na koncu izdelamo barvo, je bilo prikazano na demonstracijski mizi. Tu so bili predstavljeni kamnine/minerali in pigmenti iz Slovenije (hematit, limonit, tuf, kalcit, blestnik/gnajs) ter nekaj pigmentov od drugod po svetu. Učenci so bili s pomočjo slikovnega gradiva seznanjeni z različnimi materiali iz Slovenije, ki jih lahko srečajo med pohajkovanji po naravi. Kar nekaj jih je že poznalo različne minerale in razliko med mineralom in kamnino, saj imajo svoje lastne zbirke, nekateri pa so presenetili z znanjem o uporabnosti nekaterih mineralov (npr. hematit kot železova ruda). Med spoznavanjem različnih mineralov smo si pogledali tudi tiste, ki so se v preteklosti uporabljali, a se je njihova uporaba v 19. stoletju zaradi toksičnosti opustila (npr. cinabarit, realgar, avripigment). Po uvodnem delu so bili otroci razporejeni v skupine, kjer so na plakate z naravnimi barvami slikali utrinke geološko obarvanega dne. Najbolj navdušeni so bili nad modrim pigmentom iz azurita, saj je bil ta na njihovi paleti tudi najbolj redek – modri naravni pigmenti so namreč že od nekdaj veljali za ene najbolj redkih in zato tudi najdražjih pigmentov. V tem delu so imeli učenci čas za sprostitev in prikaz novo osvojenega znanja z likovnim izražanjem. Ustvarjene plakate otrok smo za nekaj časa izobesili na naše hodnike, da jih malo popestrijo in vnesejo nekaj otroškega duha tudi v naše vsakodnevno delo.

Sl. 2. Izobraževalno-ustvarjalna delavnica (fotografije: Petra Buh, Rada Peternel Rikanović, Teja Čeru).

Zaključki

Na koncu so učenci izpolnili ankete, ki smo jih pripravili zato, da pridobimo povratne informacije o izvedbi, vsebini, jasnosti in razumljivosti predstavljenih delavnic. Na podlagi tega bomo v prihodnje lažje snovali in načrtovali ter izpopolnjevali geološke delavnice za otroke različne starosti. Naši vtisi po delavnici so bili pozitivni, otroci so pokazali kar nekaj interesa za geološke vsebine in so bili med potekom delavnic aktivno vključeni z vprašanji. Kljub dokaj velikemu starostnemu razponu učencev, se da delavnice z nekaj prilagoditvami uspešno izvesti. So pa bile seveda nekatere vsebine primernejše za mlajše in nekatere za starejše otroke. Na motivacijo posameznika vpliva njegovo lastno zanimanje za posamezno področje, zato smo pri snovanju delavnic pokrili različne vsebine, da bi vsak v dnevu našel kaj zase in odnesel delček geologije s seboj v svoje vsakdanje življenje.

GEOLOGIJA 68/2, 337-340, Ljubljana 2025

Reports and More

From Point Clouds to CAD Objects: Workflow manual accompanying the case study of the Sabereebi Cave Monastery, Georgia

Gisela DOMEJ[1] & Kacper PLUTA[2]

[1]Geološki zavod Slovenije, Dimičeva ul. 14, 1000 Ljubljana, Slovenija; e-mail: gisela.domej@geo-zs.si
[2]Université Gustave Eiffel, CNRS, LIGM, 2 bd. Blaise Pascal, 77454 Marne-la-Vallée, France; e-mail: kacper.pluta@esiee.fr

Geotechnical stability models of the Sabereebi Cave Monastery

For the underground Sabereebi Cave Monastery a comprehensive analysis of static stability was conducted (Domej et al., 2022a; reprints: Domej et al., 2022b, 2022c; Pluta & Domej, 2021). Caverns, chapels, and churches were carved into a five-layered sequence of weak sedimentary rock—all of which bear a considerable failure potential (Fig. 1a–b, Fig. 2a–d).

Based on point cloud data from drone photogrammetry as well as from laser scanners acquired in- and outside the caves, a 3D geometry was established which was then used for static elasto-plastic stability models (Fig. 3).

Besides the goal of assessing various geomechanical scenarios through numerical modelling, the case also led to the development of a pilot scheme of numerical model compilation for very large structures without compromising on morphological details, which are most critical for stress concentration and failure.

Workflow manual accompanying the case study

As a matter of custom, the main article (Domej et al., 2022a) does not contain details on the model compilation, hence, the phase of processing point clouds of the caves and the slope into high-resolution CAD objects which – as composite – constitute the base for the numerical model.

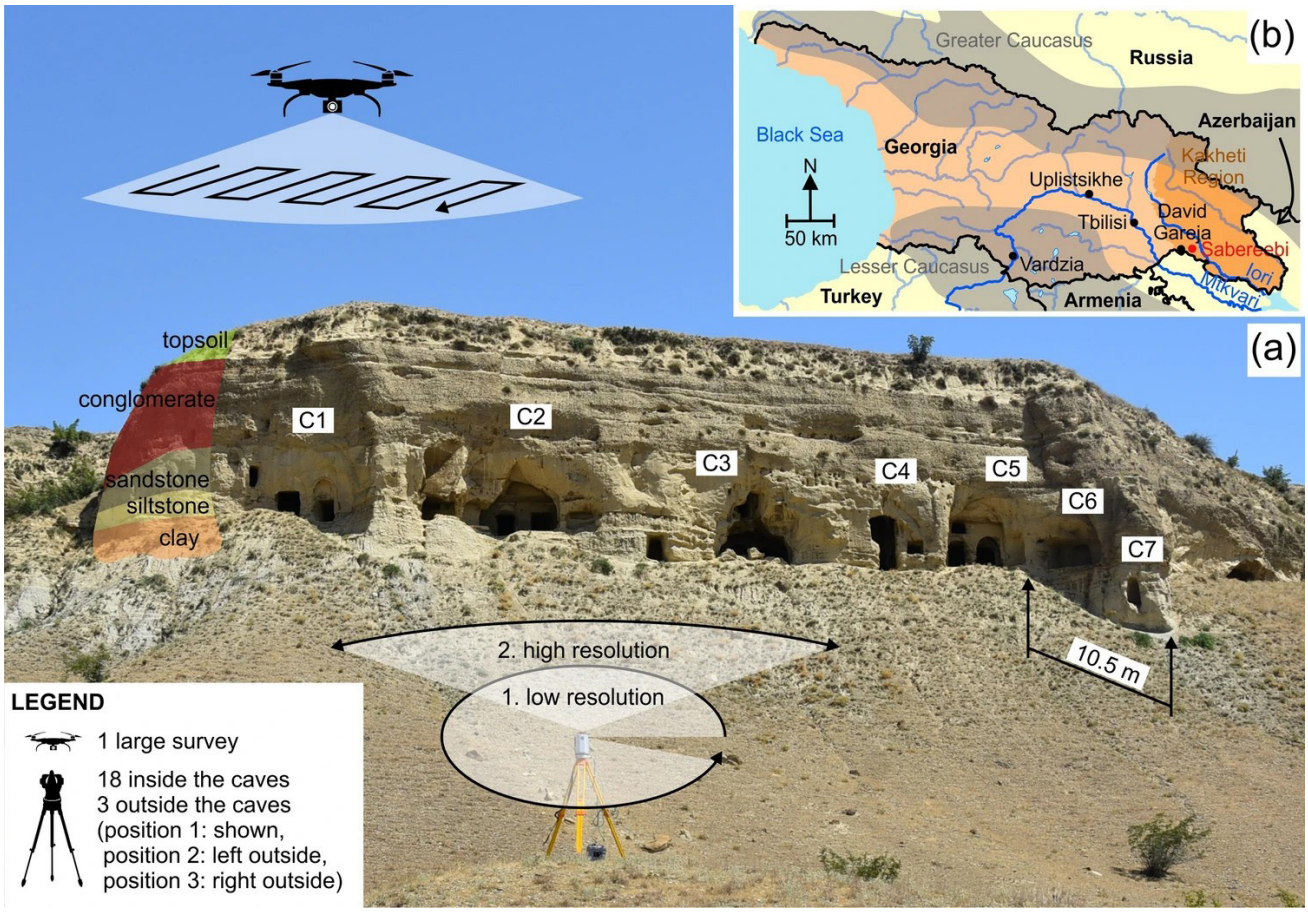

Fig. 1. The Sabereebi Cave Monastery (**a**) in the Kakheti Region of Eastern Georgia (**b**). The representation of the map of Georgia does not reflect political views of the authors nor of the institutions they are/were affiliated to (Domej et al., 2022a).

However, since the transformation of a point cloud into a CAD object is not trivial, we have provided a step-by-step workflow manual for the employed software chain, whose only purpose is to share an efficient procedure. It is designed for a point cloud recorded by a laser scanner inside one of the caves resembling a church with several niches and passages to the outside of the hill slope (Figs. 4 and 5). Following our procedure is, therefore, recommended only for similar projects.

The workflow manual was initially made available at ResearchGate with the former affiliations of the authors:

Domej G., Pluta K., 2020. From Point Clouds to CAD Objects: Overview on a case study. Workflow description for open source use, ver. 1, 21 p. http://dx.doi.org/10.13140/RG.2.2.11452.67208

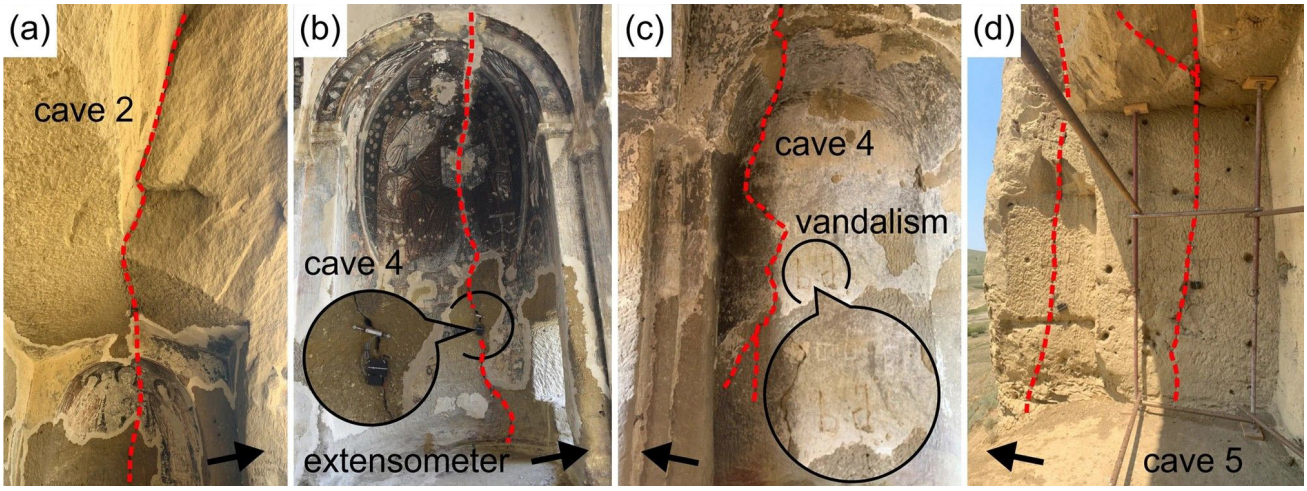

Fig. 2. Fractures at the entrances and in cave 2 (**a**), in cave 4 through a religious fresco monitored by an extensometer (**b**), in cave 4 next to traces of vandalism (**c**), and in cave 5 (**d**). The black arrow points outwards (Domej et al., 2022a).

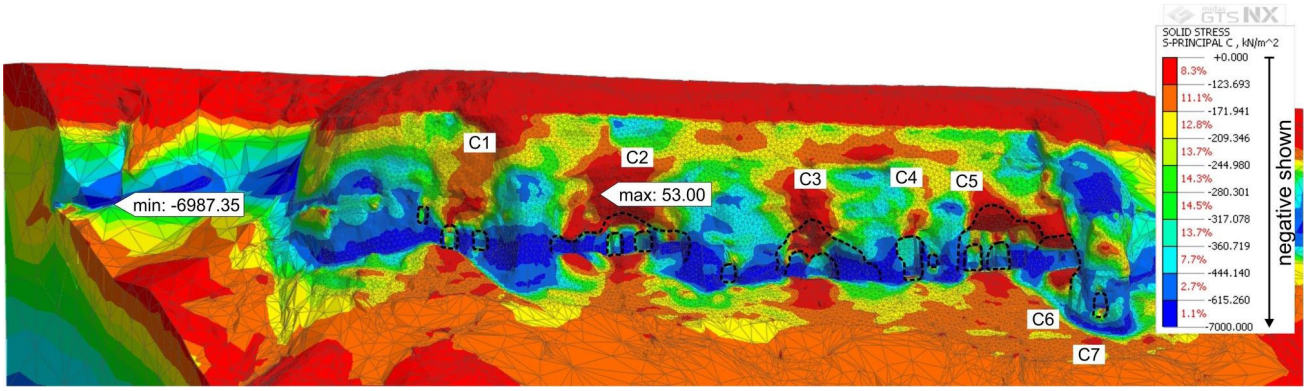

Fig. 3. Zones of compressive stress affecting cave walls, floors, and pillars in particular. Color coding is auto-scaled (Domej et al., 2022a).

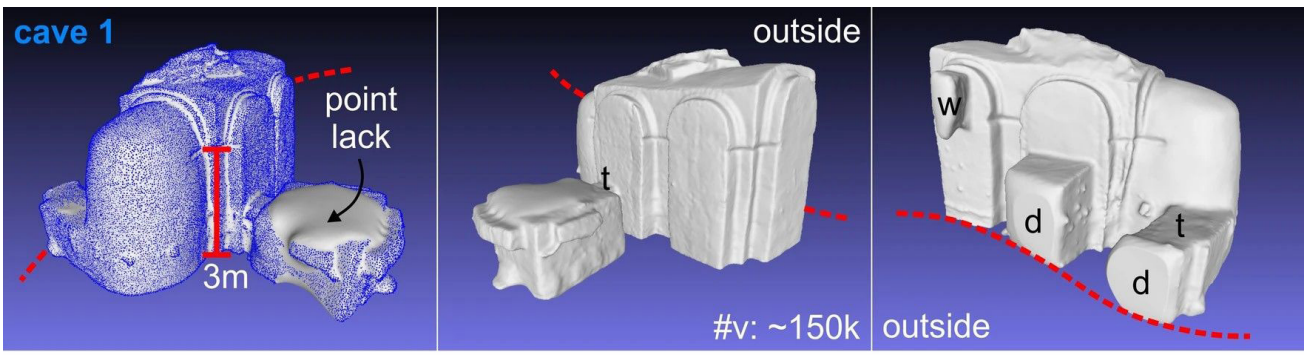

Fig. 4. Envelopes for cave 1 derived from point clouds. The approximate numbers of vertices (per point) for the creation of mesh envelopes are given in thousands. Abbreviations are as follows: ***d*** – doors, ***t*** – tunnel, and ***w*** – window (Domej et al., 2022a).

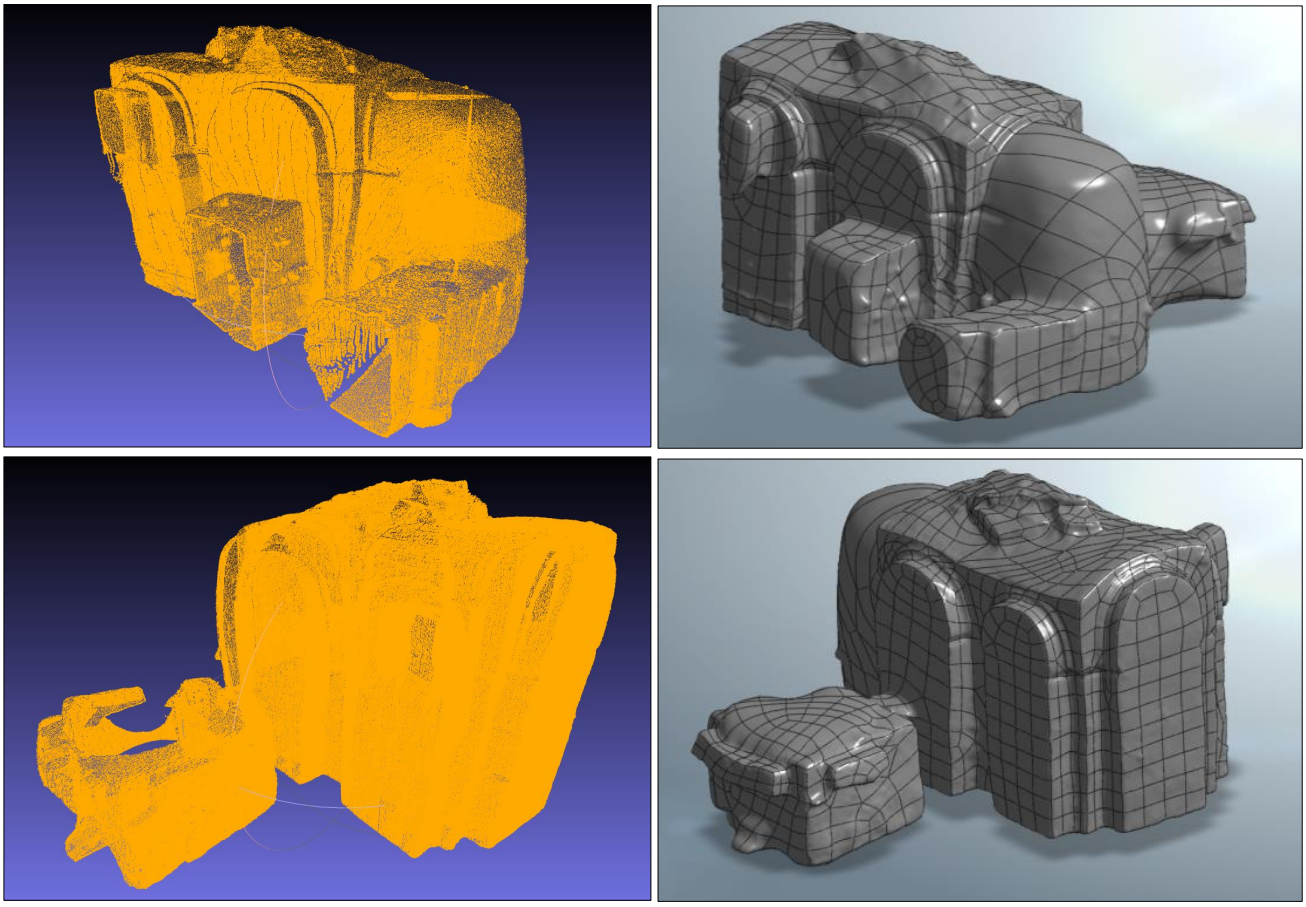

Fig. 5. Cave structure from the front and the back side as point cloud and NURBS (Non-Uniform Rational Basis Splines (Domej & Pluta, 2020).

Acknowledgements

We express our acknowledgement to Romain Carriquiry Borchiari from Ubisoft Film & Television, Montreuil, France, for assistance and advice with the software Houdini.

Funding

The project was conducted within the framework of "Multidisciplinary Survey and Monitoring of the Gareja Rock Cut Complex, the Monument of National Value" funded by the National Agency for Cultural Heritage Preservation of Georgia and managed by the Ilia State University, Georgia, together with the Italian Institute for Environmental Protection and Research, Italy, and the support of the University of Milano-Bicocca, Italy. Data used in this work was jointly acquired and, accordingly, belongs to all three institutions.

The presented workflow was created independently; it is not part of a funded project.

References

Domej, G. & Pluta, K. 2020: From Point Clouds to CAD Objects: Overview on a Case Study. Workflow description for open source use, 1: 21 p. https://doi.org/10.13140/RG.2.2.11452.67208

Domej, G., Previtali, M., Castellanza, R., Spizzichino, D., Crosta, G.B., Villa, A., Fusi, N., Elashvili, M. & Margottini, C. 2022a: High-resolution 3D FEM stability analysis of the Sabereebi Cave Monastery, Georgia. Rock Mechanics and Rock Engineering, 55: 5139–5162. https://doi.org/10.1007/s00603-022-02858-z

Domej, G., Previtali, M., Castellanza, R., Spizzichino, D., Crosta, G.B., Villa, A., Fusi, N., Elashvili M. & Margottini, C. 2022b: Reprint (1/2): High-resolution 3D FEM stability analysis of the Sabereebi Cave Monastery, Georgia. Геоинфо, 2022/10:22–32. (in Russian) https://www.researchgate.net/publication/383870570_RUSSIAN_COPY_part_1_High-Resolution_3D_FEM_Stability_Analysis_of_the_Sabereebi_Cave_Monastery_Georgia

Domej, G., Previtali, M., Castellanza, R., Spizzichino, D., Crosta, G.B., Villa, A., Fusi, N., Elashvili, M. & Margottini, C. 2022c: Reprint (2/2): High-resolution 3D FEM stability analysis of the Sabereebi Cave Monastery, Georgia. Геоинфо, 2022/11: 24–38. (in Russian) https://www.researchgate.net/publication/383870576_RUSSIAN_COPY_part_2_High-Resolution_3D_FEM_Stability_Analysis_of_the_Sabereebi_Cave_Monastery_Georgia

Pluta, K. & Domej, G. 2021: From Point Clouds to Surfaces: Overview on a Case Study. EGU General Assembly 2021, Vienna. https://doi.org/10.5194/egusphere-egu21-1523

GEOLOGIJA 68/2, 341-343, Ljubljana 2025

Reports and More

Poročilo Slovenskega nacionalnega odbora za geoznanosti in geoparke (IGGP) za leto 2024

Matevž NOVAK[1, 2]

[1]Geološki zavod Slovenije, Dimičeva ul. 14, SI–1000 Ljubljana, Slovenija; e-mail: matevz.novak@geo-zs.si
[2]Slovenski nacionalni odbor za geoznanosti in geoparke

Mednarodni program za geoznanost in geoparke (*International Geoscience and Geoparks Programme* – IGGP) od leta 2015 združuje dva, prej ločena programa. To sta Mednarodni geoznanstveni program (*International Geoscience Programme* – IGCP) in program Unescovih Globalnih geoparkov (*Unesco Global Geoparks* - UGGp). Program danes povezuje več kot 10.000 geoznanstvenikov iz več kot 150 držav, ki z ekspertizami in mreženjem postavljajo temelje prihodnosti našega planeta. Program se izvaja skozi IGCP projekte, razdeljene v pet glavnih tematskih sklopov: Zemljini viri, Globalne spremembe in evolucija življenja, Geološko pogojene nevarnosti, Hidrogeologija in Geodinamika.

Sodelovanje slovenskih raziskovalcev v programu IGGP koordinira Slovenski nacionalni odbor IGGP, ki deluje kot strokovno in posvetovalno telo Slovenske nacionalne komisije za Unesco (SNKU).

V letu 2024 je Nacionalni odbor IGGP koordiniral aktivnosti, ki so vključevale sodelovanje v IGCP projektih, v dveh delovnih skupinah IUGS, dveh UNESCO Globalnih geoparkov, Idrija in čezmejnega geoparka Karavanke/Karawanken ter mednarodnega dneva geopestrosti.

Glavnino projektov je obsegal sklop IGCP s poudarkom na prioritetah Unesca. Težišče dela je bilo na terenskih raziskavah, laboratorijski analitiki, mreženju in pripravi ter objavi rezultatov v domačih in tujih mednarodno priznanih znanstvenih revijah. Raziskovalci so težili k čim večji vpetosti v mednarodno sodelovanje, popularizacijo geoznanosti, prenos znanja na mlade ter širšo zainteresirano javnost in prenos dobrih praks med geoparki na mednarodnem nivoju. Povezovanje je potekalo preko spletnih in javnih medijev ter mednarodnih srečanj.

Poleg temeljnih znanj prinašajo raziskovalni projekti neposredno uporabno vrednost na področju vodnih virov, geotermalne energije, varstva okolja in naravne dediščine ter geološko pogojenih nevarnosti. Slovenski raziskovalci so v letu 2024 sodelovali v šestih IGCP projektih. Nadaljevale so se aktivnosti v dveh delovnih skupinah IUGS in dveh UNESCO Globalnih geoparkih. Projekti in nosilci nalog so prikazani v Preglednici 1.

V delovnih skupinah IUGS/IACG in IUGS/IFG slovenski raziskovalci sodelujejo pri ugotavljanju naravnega geokemičnega ozadja, razločevanju med geološkimi materiali naravnega in antropogenega

Preglednica 1: Pregled projektov IGGP in nosilcev posameznih nalog v letu 2024

Zap. št.	Prijavljeni projekti	Nosilci projektov, inštitucije
	IUGS/IAGC: Global Geochemical Baselines	dr. Mateja Gosar, GeoZS
	IUGS/IFG: Initiative on Forensic Geology	dr. Martin Gaberšek, GeoZS
	IGCP 636: Geothermal resources for energy transition: direct uses and clean and renewable base-load power	dr. Nina Rman, GeoZS; Simona Adrinek, GeoZS
	IGCP 683: Pre-Atlantic geological connections among northwest Africa, Iberia and eastern North America: Implications for continental configurations and economic resources	doc. dr. Aleš Šoster, NTF
	IGCP 710: Western Tethys meets Eastern Tethys – geodynamical, paleoceanographical and paleobiogeographical events	dr. Katica Drobne, ZRC SAZU; doc. dr. Petra Žvab Rožič, NTF; prof. dr. Boštjan Rožič, NTF
	IGCP 714: 3GEO – Geoclimbing & Geotrekking in Geoparks	Aleksandra Trenchovska, GeoZS; prof. dr. Marko Vrabec NTF
	IGCP 739: The Mesozoic-Palaeogene hyperthermal events	dr. Adrijan Košir, ZRC SAZU
	IGCP 741: Metallogenic prediction, sustainable development and integrated utilization of mineral resources in the Tethys metallogenic domain	prof. dr. Matej Dolenec, NTF
	Geopark Idrija	Mojca Gorjup Kavčič, Zavod za turizem Idrija
	Geopark Karavanke, Slovenija-Avstrija	mag. Suzana Fajmut Štrucl, Podzemlje Pece
	Obeleževanje Mednarodnega dneva geopestrosti	Martina Stupar, ZRSVN

izvora ter ugotavljanju antropogenega geokemičnega odtisa v tleh urbanih območij. Raziskave so pomembne predvsem za ugotavljanje morebitnega negativnega vpliva trdnih delcev na zdravje ljudi.

Projekti IGCP 683, 710 in 739 so temeljne narave. Na podlagi izsledkov terenskih raziskav in laboratorijskih analiz se v teh projektih ugotavlja in usklajuje stratigrafsko zaporednje kamnin, preko katerega se ugotavljajo razmere in dogajanja v okolju in njegove spremembe v geološki zgodovini. Nadgadnja geoloških modelov z novimi ugotovitvami je nujna za ugotavljanje geološkega razvoja posameznih območij, korelacije s sosednjimi območji, usmerjanje nadaljnjih raziskav, predvsem pa za načrtovanje rabe prostora.

Projekta IGCP 636 in 741 sta aplikativne narave. Obravnavata oceno potenciala in rabo plitve geotermalne energije, raziskavah reinjekcije in njenih možnosti v geotermalnih vodonosnikih v Sloveniji ter geokemične analize slabo raziskanih rudnih pojavov v Karavankah. Te raziskave imajo velik družbeno-ekonomski pomen pri prehodu na pridobivanje energije iz obnovljivih virov in pri iskanju kritičnih mineralnih surovin.

Projekt IGCP 714 in aktivnosti obeh Unescovih Globalnih geoparkov, Idrije in Karavank/Karawanken, združujejo interdisciplinarna znanja na osnovi geoznanosti. Njihov cilj je krepitev znanja o vseh vidikih geološke dediščine s širjenjem lastnih izkušenj z vzpostavljanjem in upravljanjem območij Unescove svetovne dediščine, Globalnih geoparkov in drugih zavarovanih območij geološke naravnih vrednot. Oba geoparka sta uspešno opravljala vlogo informiranja, izobraževanja in ozaveščanja šolajoče se mladine in zainteresirane javnosti. Aktivnosti za vzpostavitev upravljavskega načrta in trajnostnega razvoja čezmejnega geoparka Kras-Carso potekajo v sodelovanju z italijanskimi partnerji v okviru projekta INTERREG IT-SI KRAS-CARSO II – Skupno upravljanje in trajnostni razvoj območja Matičnega Krasa. Oddaja aplikacije za članstvo v Unescovi Globalni mreži geoparkov se je žal zamaknila še za eno leto in je načrtovana v letu 2025.

V okviru obeležitve 3. mednarodnega dneva geopestrosti je bilo tudi v letu 2024 s koordinacijo Zavoda RS za varstvo narave in Nacionalnega odbora IGGP pripravljenih več promocijskih gradiv ter izvedenih več aktivnosti in predavanj z namenom osveščanja o mednarodnem dnevu geopestrosti s poudarkom pomena tega dneva. Osrednji dogodek obeležitve je bil 11. oktobra v Ljubljani z okroglo mizo z naslovom »Geologija v šoli in poučevanje o geopestrosti«, ogledom geološke zbirke Oddelka za geologijo NTF in geološkim sprehodom po Ljubljani.

Nacionalni odbor IGGP je nosilcem nalog v posameznih projektih posredoval informacije o aktualnih dogodkih v okviru UNESCO in IUGS. Za širšo geološko javnost smo imeli v okviru predavanj Slovenskega geološkega društva predavanje z naslovom »Kaj so IUGS, IGGP in IGCP – predstavitev in možnosti sodelovanja«. Sledila je predstavitev aktivnosti dr. Nine Rman v projektu IGCP 636: *Geothermal resources for energy transition*. NO IGGP bo v sodelovanju s Slovenskim geološkim društvom tudi v prihodnje spodbujal predstavljanje aktivnosti noslilcev projektov v okviru društvenih predavanj.

Predsednik NO je na redni letni seji NO IGGP predstavil novosti glede sprememb pri izvajanju IGCP projektov. Novica je bila sporočena na "*Open Session of the International Geoscience Programme Council, featuring the presentation of new UNESCO Global Geoparks applicants and to the information meeting on UNESCO Global Geoparks*". Glavne novosti so, da v letu 2024 ne bo razpisov za nove projekte, trenutno aktivni projekti pa se bodo zaključili leta 2026. Nov koncept bo vključeval nov regionalni fokus (prva predlagana je Afrika). Tematske prioritete vključujejo razogličenje in strateške kovine. Vsebine projektov bodo prilagojene fokusnim regijam, hkrati bo aktivnih manj projektov, ki bodo dobili višjo finančno podporo kot do sedaj, obvezna bo sinergija z drugimi komisijami IUGS, delovnimi skupinami, iniciativami, itd. Več informacij pričakujemo po sestanku UNESCA marca 2025 v Parizu in po srečanju v Nairobiju septembra 2025.

Avgusta 2024 je bil član NO, prof. dr. Marko Komac izvoljen za enega od dveh podpredsednikov IUGS.

Novembra 2024 je umrl naš častni član, zaslužni prof. dr. Simon Pirc (1932–2024). Član slovenskega odbora IGCP za UNESCO je bil od ustanovitve leta 1991, leta 1998 je postal njegov predsednik, po tem pa častni član. Za njegov doprinos k delu v tem odboru in uspešnemu mednarodnemu sodelovanju smo mu neizmerno hvaležni.

GEOLOGIJA 68/2, 344-345, Ljubljana 2025

Reports and More

Poročilo o tretji mednarodni poletni geotermalni šoli Ljubljana 30. junij – 5. julij 2025

Nina RMAN[1] & Mihael BRENČIČ[1,2]

[1]Geološki zavod Slovenije, Dimičeva ul. 14, SI-1000 Ljubljana, Slovenija; e-mail: nina.rman@geo-zs.si
[2]Oddelek za geologijo, Naravoslovnotehniška fakulteta, UL, Aškerčeva cesta 12, SI-1000 Ljubljana, Slovenija; e-mail: mihael.brencic@ntf.uni-lj.si

Geotermalna energija postaja vse bolj pomembna. Leta 2024 sprejeti resoluciji Evropskega parlamenta o geotermalni energiji so sledile tematske konference med predsedovanjem EU s strani Madžarske (2024) in Poljske (2025) in vsi s tem povezani dogodki so poudarjali pomen izobraževanja in usposabljanja. Tudi zato smo na Oddelku za geologijo Naravoslovnotehniške fakultete Univerze v Ljubljani (NTF UL) v okviru predmeta Termogeologija na magistrski stopnji z veseljem že tretjič organizirali mednarodno poletno geotermalno šolo. Tokrat je bil poudarek na plitvi geotermiji. Šola je potekala pod naslovom »Spajanje in integracija energetskih pilotov z drugimi geotermalnimi tehnologijami«. Izvedli smo jo med 30. junijem in 5. julijem 2025 pretežno v Ljubljani, v organizaciji partnerstva COST projekta CA21156 FOLIAGE, Geološkega zavoda Slovenije (GeoZS), Oddelka za geologijo – Naravoslovnotehniške fakultete Univerze v Ljubljani, Zavoda za gradbeništvo Slovenije (ZAG) in Fakultete za gradbeništvo, prometno inženirstvo in arhitekturo Univerze v Mariboru (UM FGPA).

Na šoli je sodelovalo enajst predavateljev iz šestih držav: prof. dr. Mihael Brenčič (NTF UL & GeoZS, Slovenija), doc. dr. Nina Rman (GeoZS & NTF UL, Slovenija) in Dušan Rajver (GeoZS, Slovenija), dr. Hrvoje Dorotić (Energetski institut Hrvoje Požar, Hrvaška), prof. dr. Rao Martand Singh (Norwegian University of Science and Technology, Norveška), Fiona M. Chapman (Institut national de la recherche scientifique, Kanada), izr. prof. dr. Primož Jelušič (UM FGPA, Slovenija), doc. dr. Stanislav Lenart (ZAG, Slovenija), prof. dr. Nikolas Makasis (School of Engineering of University of Surrey, Združeno Kraljestvo), Grzegorz Ryżyński (Polish Geological Institute, Poljska) in Maja Turnšek (Faculty of Tourism of University of Maribor, Slovenija).

Sodelujoče smo seznanili z najnovejšimi tehnologijami energetskih pilotov in geotermalnih toplotnih črpalk in načini povezovanja z drugimi obnovljivimi tehnologijami (fotovoltaika, vetrna energija...), koraki za načrtovanje energetskih pilotov in uspešnimi primeri po svetu, možnostmi podzemnega skladiščenja toplote in hladu, najnovejšimi smernicami v sektorju daljinskega ogrevanja ter okoljsko ustreznim načrtovanjem takšnega načina rabe plitve geotermalne energije.

Med dvodnevno ekskurzijo smo obiskali proizvodnjo toplotnih črpalk KRONOTERM d.o.o. v Trnavi; Medpodjetniški izobraževalni center Šolskega centra Velenje s pasivno hišo z vgrajenimi geosondami in energetskimi košarami ter fotovoltaičnim (PV) sistemom; startup okolje Katapult in visokotehnološko podjetje DEWESoft d.o.o., ki je v Trbovljah postavilo prvo sezonsko podzemno skladiščenje toplote z geosondami (BTES) v Sloveniji. Ogledali smo si tudi neposredno rabo termalne vode v Termah Šmarješke Toplice. V parku slednjih smo izvedli dopoldanske praktične vaje, kjer smo preizkusili različne metode za terensko določanje geotermičnih lastnosti kamnin in sedimentov, primerjali lastnosti termalne in rečne vode ter testirali merilne sonde. Popoldne smo si na ZAG in GeoZS ogledali geotehnični, geotermalni in hidrogeološki laboratorij, karotažno opremo za vrtine in sistem za izvajanje testa toplotnega odziva tal (TRT). Vsi udeleženci so na študentski konferenci predstavili svoje delo - knjiga povzetkov je dostopna na https://www.geo-zs.si/wp-content/uploads/2025/09/202506-GTSS-abstract-book-Ljubljana-1.pdf, sodelovali pri projektnem delu in opravili izpit iz predmeta Termogeologija in s tem pridobili 3 kreditne (ECTS) točke.

Program je uspešno zaključilo 21 udeležencev, od tega 18 študentov (4 magistrskega in 14 doktorskega študija) ter 3 mlajši zaposleni. Predstavnic ženskega spola je bilo 40 %. Udeleženci se trenutno izobražujejo in delujejo v 11 državah: Belgiji, Franciji, Hrvaški, Italiji, Kanadi, Nemčiji, Nizozemski, Poljski, Severni Makedoniji, Sloveniji in Veliki Britaniji. Približno polovica udeležencev prihaja iz okoljskih in geoznanosti, petina iz strojništva in procesne energetike, preostali pa iz geomehanike in/ali energetskega inženiringa.

Naslednjo mednarodno poletno geotermalno šolo načrtujemo čez dve leti, poleti 2027.

Zahvala

Poletna šola je bila podprta preko več projektov. Projekt CA21156 european network for FOstering Large-scale ImplementAtion of energy GEostructure (FOLIAGE) je zagotovil sredstva programa Obzorje 2020 in COST European Cooperation in Science and Technology. Del aktivnosti je bil podprt s strani ARIS programskih skupin P1-0020 Podzemne vode in geokemija, P1-0011 Regionalna geologija, P2-0273 Gradbeni objekti in materiali ter infrastrukturnih programov, I0-0007 Geološki informacijski center in I0-0032 Preizkušanje materialov in konstrukcij. Podporo so zagotovili tudi: Ministrstvo za okolje, podnebje in energijo; ARIS podoktorski projekt TopDISPERZ, projekta INRIGeoTeam in Geo-OPT, ki ju sofinancira ARIS v okviru razvojnega stebra (RSF); CRP projekt V1-2213 GeoCOOL-FOOD, ki ju sofinancirata MKGP in ARIS; in donatorji Atlas Trading d.o.o., DEWESoft d.o.o., KRONOTERM d.o.o., Radenska d.o.o. in Terme Krka Šmarješke Toplice.

Sl. 1. Ogled vrtanja pilotov na gradbišču ZP Ljubljana.

Sl. 2. Terenske vaje iz meritev toplotne prevodnosti tal.

GEOLOGIJA 68/2, 346, Ljubljana 2025

Reports and More

Poročilo o udeležbi na mednarodnem dogodku "The International Workshop on Mesozoic–Palaeogene Hyperthermal Events & Fifth IGCP 739 Workshop"

od 16. do 26. avgusta 2025 na Kitajskem

Tea KOLAR-JURKOVŠEK

Geološki zavod Slovenije, Dimičeva ul. 14, SI-1000 Ljubljana, Slovenija; e-mail: tea.kolar-jurkovsek@geo-zs.si

Skrajni dogodki globalnega segrevanja v geološki zgodovini, znani kot hipertermalni dogodki, ponujajo primerjavo s sodobnim segrevanjem. Omogočajo boljše razumevanje podnebnega sistema na Zemlji. Od mezozoika do paleogena je bilo več kritičnih obdobij, v katerih so se zvrstili značilni hipertermalni dogodki, kot so mejni dogodek med permom in triasom, med juro in kredo, toarcijski oceanski anoksični dogodek, kredni oceanski anoksični dogodki in paleocensko-eocenski termični maksimum. Projekt IGCP 739 (2021–2025) Mednarodnega programa za geoznanost, ki poteka pod pokroviteljstvom Unesca in IUGS, je usmerjen v proučevanje in razrešitev sprožilnih mehanizmov za mezozojsko-paleogenske hipertermalne dogodke, z njimi povezane okoljske spremembe ter posledično biološke odzive. Raziskave konodontov himalajskega orogena se vključujejo v primerjalne paleobiogeografske študije v okviru programske skupine Regionalna geologija na Geološkem zavodu Slovenije. Na povabilo organizatorja in ob finančni podpori matične institucije sem se udeležila omenjene mednarodne delavnice.

Zaradi novih pomembnih spoznanj, doseženih v okviru tega projekta, in boljšega razumevanja hipertermalnih dogodkov, je na Univerzi v Nankingu od 16. do 18. avgusta 2025 potekala "Mednarodna delavnica o mezozojsko-paleogenskih hipertermalnih dogodkih in peta delavnica IGCP 739". V programu se je zvrstilo 52 izvirnih tematski poročil, vezanih na sedimentologijo, stratigrafijo, geokemijo, paleoekologijo in paleontologijo, podprtih s paleoklimatskimi modeli sistema Zemlje na regionalni ali globalni ravni.

Konferenci je sledila terenska ekskurzija v južnem Tibetu. V osemdnevni delavnici, ki se je pričela v Lhasi, nas je vodila proti zahodu do Yarlung Zangbo suturnega ofiolitnega kompleksa. Kasnejša pozornost je bila osredotočena na oglede profilov z zapisi o “okoljskih odzivih na hipertermalne dogodke" paleogenske, kredne in jurske starosti. Zadnji dan terenske delavnice je bil namenjen triasnim plastem, vključno s permsko-triasnim mejnim intervalom, karnijskim pluvialnim dogodkom ter triasno-jurskim mejnim intervalom. Za namene raziskav konodontov v okviru letos osnovane Himalajske akademije sem imela možnost vzorčiti najmlajše triasne plasti. S pomočjo organizatorja smo vzorčili plasti v dveh profilih. Vzorci se nahajajo na inštitutu v Pekingu, kjer so v postopku laboratorijskega prepariranja.

Organizacijski odbor je zagotovil optimalno okolje in odlične prostore za razpravo o najsodobnejših raziskavah hipertermalnih dogodkov. Ustvarjeno je bilo vzdušje za produktivne razprave in sklepanje novih strokovnih sodelovanj.

Sl. 1. Utrinek s predstavitve triasne konodontne conacije v Dinaridih na konferenci v Nankingu. Fotografija: arhiv projekta IGCP 739.

Sl. 2. Udeleženci terenske delavnice v Tibetu. Fotografija: arhiv projekta IGCP 739.

GEOLOGIJA 68/2, 347-352, Ljubljana 2025

Reports and More

Poročilo o aktivnostih Slovenskega geološkega društva v letu 2024

Astrid ŠVARA

Inštitut za raziskovanje krasa ZRC SAZU, Titov trg 2, SI-6230 Postojna, Slovenija;
e-mail: astrid.svara@zrc-sazu.si

V letu 2024 je bila glavna naloga vodstva društva prenova statuta, ki je zaradi sprememb društvenih aktivnosti postal mestoma neskladen z njegovim delovanjem. Slednje smo opravili skladno z Zakonom o društvih (Uradni list RS št. 64/11-ZDru-1-UPB2), z Zakonom nevladnih organizacijah (Uradni list RS št. 21/18) ter po posvetovanju z referentkama iz Upravne enote (UE) Ljubljana ter Ministrstva za vzgojo in izobraževanje, kjer je SGD kot društvo ter nevladna organizacija registrirano. Statut SGD je skupščina 13. 3. 2024 na seji soglasno sprejela, ga z vlogo za registracijo spremembe naslovila na UE, ter po daljšem čakanju prejema predloga k dopolnitvam uredila in ponovno oddala 22. 11. 2024. Vloga je bila v pregledovanju na UE vse do konca koledarskega leta.

V preteklem letu je društvo zbralo veliko prispevkov, ki jih je strnilo v društvenem glasilu Prelom št. 29. Zaradi podražitev postavitve glasila in tiska je društvo sprejelo odločitev, da bo Prelom fizično distribuiralo le njegovim članom, ki redno plačujejo članarino, ki obenem financira izdajanje glasila. S tem spodbujamo njegov obstoj in podporo društvu. Elektronski izvod je prosto dostopen na naši spletni strani: https://www.slovenskogeoloskodrustvo.si/prelom/.

Geološki zavod Slovenije je na svetovni dan Zemlje podelil priznanja za vrhunske znanstvenoraziskovalne dosežke na področju geologije za obdobje 2022-2023, t.i. Lipoldove nagrade. Častno listino Geološkega zavoda Slovenije na področju geološke znanosti je prejelo Slovensko geološko društvo. Podelitev je potekala v Ljubljani 29. 4. 2024.

Zaradi lažjega deljenja informacij o društvu, smo v preteklem letu postavili društveno Facebook stran. Do konca leta, je stran všečkalo 96 oseb, zbrali smo že skoraj 200 sledilcev. Statistika kaže, da si ljudje ogledajo stran povprečno več kot 500 krat mesečno. Največ interakcije na strani predstavljajo delitve dogodkov v so-organizacijah, predvsem z UL NTF Oddelkom za geologijo in Geološkim zavodom RS, reklamiranje društvenih predavanj in drugih dogodkov ter delavnic. Facebook stran SGD je dostopna na strani: https://www.facebook.com/profile.php?id=61556952675516.

Zaradi prekinitve hrambe podatkov na gostujoči GeoZS domeni, je društvo v preteklem letu investiralo v novo domeno, kjer društvena spletna stran od tedaj deluje ažurno in nemoteno.

V preteklem letu smo zelo uspešno izvedli 5 strokovnih predavanj na treh lokacijah: na GeoZS, ZRC SAZU in na UL NTF Oddelku za geologijo. Uvedena predavanja v hibridni obliki so se izkazala kot zelo ugodna oblika širjenja geoloških vsebin predvsem za tiste, ki se zaradi dela izven Ljubljane predavanja pravočasno ne bi mogli udeležiti. Promocija predavanj s povzetki je bila navedena na spletni strani SGD (Aktualne novice, Koledar, Aktualna predavanja), v e-poštni skupini Georg ter na Facebook profilu. Deljenje informacij je potekalo tudi preko institucionalnih (npr. FB stran GeoZS, FB stran OG NTF) portalov in osebnih družabnih omrežjih. Prvo predavanje (“Geologija v šolah – kako je bilo včasih in kako je danes na Hrvaškem”; 30. 1. 2024, Oddelek za geologijo NTF UL) je obeležila dr. Karmen Fio Firi z Oddelka za geologijo, Naravoslovno-matematične fakultete, Univerze v Zagrebu. Gostujoče predavanje smo dopolnili še s kratkim predavanjem dr. Roka Brajkoviča, mag. Mojce Bedjanič, dr. Neže Malenšek Andolšek, dr. Matevža Novaka, dr. Nine Rman in dr. Petre Žvab Rožič (“Geologija v slovenskem šolskem sistemu – aktualno«). Drugo predavanje (»Kaj so IUGS, IGGP in IGCP?« ter »Geotermični viri za energetski prehod«; 28. 2. 2024, Oddelek za geologijo NTF UL) sta vodila dr. Matevž Novak (predsednik nacionalnega odbora IGGP) in dr. Nina Rman z Geološkega zavoda Slovenije. Tretje predavanje (»Metoda spektralno inducirane polarizacije (SIP): osnove, aplikacije in omejitve«; 14. 3. 2024, atrij ZRC SAZU, Ljubljana) je imel dr. Roguer Edmund Placencio-Gómez z Geološkega zavoda Slovenije. Četrto predavanje (»Klasifikacija virov UNFC«; 9. 10. 2024, Geološki zavod Slovenije) sta vodili dr. Duška Rokavec in dr. Meta Dobnikar iz Sekcija za mineralogijo. Peto predavanje (»Geologija na periferiji najglobje točke planeta«; 18. 12. 2024, Oddelek za geologijo NTF UL) so imeli dr. Blaž Miklavič, dr. Boštjan Rožič in dr. Petra Žvab Rožič. Povzetki predavanj so dostopni na spletni strani društva, pod rubriko

Aktualno: https://www.slovenskogeoloskodrustvo.si/predavanja/.

V preteklem letu, je društvo organiziralo dve samostojni strokovni ekskurziji in dve strokovni ekskurziji v so-organizaciji s skupino SINQUA in Geomorfološkim društvom Slovenije (GMDS). Prva ekskurzija v Križno jamo je pod vodstvom vodnika Alojza Trohe potekala 17. 2. 2024. Za geološko, geomorfološko, hidrološko in sedimentološko vodenje po jami sta poskrbela dr. Mitja Prelovšek in dr. Nadja Zupan Hajna z Inštituta za raziskovanje krasa ZRC SAZU. Udeleženci so si ogledali arheološka najdišča, jamske skalne oblike ob reki, se zapeljali s čolnom in ogledali paleontološko zanimiv Medvedji rov. Ekskurziji je sledilo druženje ob kavi v bližnjem baru.

Sl. 1. Udeleženci ekskurzije v Križni jami (Foto: Matija Križnar).

Druga ekskurzija je potekala 6. 4. 2024 v soorganizaciji s SGD skupino SINQUA in GMDS. Dr. Radovan Lipušček (upokojeni prof. geogr. in soc.), dr. Jurij Kunaver (član GMDS, SINQUA, upokojeni prof. FF UL) in dr. Petra Jamšek Rupnik (članica SINQUA SGD, GMDS, GeoZS) so poskrbeli za vodenje po tolminski kotlini, s povdarkom na kvartarnem razvoju – geomorfološke in sedimentne oblike.

Tretja ekskurzija je pod vodstvom dr. Andreja Novaka (GeoZS) potekala 11. 5. 2024 v dolino Planice, v soorganizaciji z GMDS. Na terenski ekskurziji smo si ogledali sledove in posledice delovanja različnih kvartarnih sedimentacijskih procesov, izdanke pleistocenskih ledeniških sedimentov ter jezerske sedimente. Prejeli smo veliko informacij o najmlajši sedimentaciji, dendrogeomorfološkem datiranju, o uporabi brezpilotnega letalnika in o mehanizmu transporta drobirskega toka pod Ciprnikom. Za konec smo si ogledali tudi posledice delovanja snežnih plazov iz leta 2021.

Četrta ekskurzija je potekala 17. 12. 2024 v Selški dolini in je bila namenjena ogledu razstave in spominske sobe prof. dr. Antona Ramovša, ki so jo odprli ob 100-letnici njegovega rojstva. Ob priložnosti je predavanje o profesorju Ramovšu imel tudi njegov učenec geolog Pavle Alojzij Florjančič. Spominska soba je odprta za javnost in si jo je mogoče ogledati po predhodni najavi.

Potujoča fotografska razstava z naslovom “Geopestrost pred domačim pragom” je v preteklem letu gostovala na dveh lokacijah. Fotografije žive in nežive narave so bile posnete v Sloveniji in prikazujejo geopestrost naše države skozi oči geološke strokovne in tudi širše javnosti. S selitvijo želimo razstavo pripeljati širši javnosti na čimbolj raznolikih lokacijah, da bi tako dosegla čimveč zainteresiranih pogledov. Med 14. in 29. 3. 2024 je razstava fotografij krasila atrij ZRC SAZU. Od oktobra do decembra 2024 je bila na voljo obiskovalcem v prostorih občine Poljčane. Društvo je sodelovalo tudi pri pripravi in promociji dveh tematskih razstav. Med 10. in 12. 5. 2024 je na MINFOSu v Tržiču

Sl. 2. Spominska soba prof. dr. Antona Ramovša (Foto: Matija Križnar).

pripravilo tematsko razstavo prof. dr. Anton Ramovš (1924-2012) – 100-letnica rojstva paleontologa in geologa, od 17. 12. 2024 do marca 2025 pa je razstava ob obeležitvi dela prof. dr. Antona Ramovša postavljena tudi na OG NTF UL (v sodelovanju s PMS).

Sl. 3. Potujoča razstava "Geopestrost pred domačim pragom", ZRC SAZU (Foto: Petra Žvab Rožič).

Sekcija za promocijo geološke znanosti je na letnem sestanku 23. 9. 2024 sprejela sklepe: (1) sprejem predhodnega zapisnika in poročila; (2) dogovor o poskusu pridobitve in pregleda nove predloge učnih načrtov (v prihodnje se člani sekcije sestanejo v ožji skupini, oblikujejo medijski dogodek z izpostavitvijo pomena geološke stroke); (3) vzpostavi se kontakt z IUGS in EGU ter odpošlje uradno prošnjo o pridružitvi sekcije h komisijam. Predlaga se člana in koordinatorja sekcije (Rok Brajkovič in Petra Žvab Rožič). Članstvo v mednarodnih komisijah se v prihodnje spreminja, a član naj bo vedno koordinator sekcije ter predstavnik NTF-OG, ki je obenem član SGD-ja ter aktiven član sekcije; (4) geologi se vključujejo v spremembe učnih načrtov (novi predlogi so pri učiteljih praktikih, uradnega odziva ZRSŠ na predloge popravkov in dopolnitev nismo prejeli). Sekcija je organizirala javni dogodek ''Geologija v šolah – kako je bilo včasih in kako je danes na Hrvaškem'', s povabilom predavateljice doc. dr. Karmen Fio Firi iz Zagreba. Sekcija je soorganizirala osrednji dogodek ob mednarodnem dnevu geopestrosti. Izvedli smo okroglo mizo z naslovom »Geologija v šoli in poučevanje o geopestrosti« ter govorili o spremembah poučevanja mladine o geoloških vsebinah v formalnem izobraževanju. Tem izzivom so se na okrogli mizi posvetili govorci: mag. Andreja Bačnik – Zavod RS za šolstvo, izr. prof. dr. Blaž Repe – Oddelek za geografijo FF UL, prof. dr. Gregor Torkar – Oddelek za biologijo, kemijo in gospodinjstvo PEF UL ter predstojnik UNESCO katedre o izobraževanju učiteljev za trajnostni razvoj na Univerzi v Ljubljani, doc. dr. Luka Gale – Oddelek za geologijo NTF UL, mag. Mojca Bedjanič – Zavod RS za varstvo narave in dr. Darja Komar – Podzemlje Pece. Okroglo mizo sta vodila doc. dr. Petra Žvab Rožič – OG NTF in dr. Rok Brajkovič – GeoZS. Koordinator mednarodnega dne geopestrosti je bil Zavod RS za varstvo narave, kot eden izmed soorganizatorjev pa je dogodek podprl tudi člani sekcije za promocijo geološke znanosti. Vabilo in ostale informacije so na voljo na strani: https://www.slovenskogeolosko-drustvo.si/mednarodni-dan-geopestrosti/. Sekcija je izvedla izobraževalne dogodke in sodelovala na številnih javnih dogodkih: (1) Poučevanje in učenje o mineralih in kamninah v učilnici in naravi (PPU delavnica; 12.-13. 4. 2024); (2) Izdelava KamenCheck poučevalnega kompleta; (3) Izvedba delavnice »Vodni krog in vodonosnik, lastnosti vode, kamninski krog, minerali (17. 5. 2024) na OŠ dr. Franceta Prešerna, podružnična šola Dolenja vas, za 4. in 5. Razred; (4) Delavnice za OŠ in SŠ, (5) Delavnica Kamenčkanje (Vrt eksperimentov, Znanstival 2024; 1.-2. 6. 2024); (6) Zgodba o poljedelcu in kamnu (sodelovanje na Koliščarskem dnevu v Dragi pri Igu; 24. 8. 2024); (7) Ali so minerali in kamnine uporabni? (sodelovanje na 17. festivalu znanosti in umetnosti Hokus Pokus s temo »lastnosti snovi«, Pionirski dom – Center za kulturo mladih; 17.-18. 10. 2024).

Geokemična sekcija je sodelovala pri organizaciji 3. spletne brezplačne mednarodne študentske konference o geomedicini in geokemiji okolja »ISCMGEH Europe« (26.-29. 11. 2024). Glavni organizatorki konference sta bili mednarodni združenji "Society for Environmental Geochemistry and Health (SEGH)" in "International Medical Geology Association (IMGA)". Več o konferenci si lahko preberete na povezavi: https://segh.net/blogs/f/2024-iscmgeh-europe-edition-it%E2%80%99s-a-wrap, knjiga povzetkov pa je dostopna na povezavi: https://segh.net/past-conference-abstracts.

Sl. 4. Posnetek udeležencev conference ISCMGEH Europe 2024 (Foto: Martin Gaberšek).

Sekcija za mineralogijo je pomagala organizirati predavanje »Klasifikacija virov UNFC«, kjer sta predavali dr. Duška Rakovec in dr. Meta Dobnikar.

Sekcija za geološko dediščino je izvedlo svoje aktivnosti v koordinaciji Zavoda Republike Slovenije za varstvo narave. V sodelovanju z društvom DPMFS in PMS je 23. 2. 2024 je potekala okrogla miza o varovanju geološke dediščine v Sloveniji. Osrednja aktivnost leta pa je bila soorganizacija Mednarodnega dne geopestrosti (11. 10. 2024). Dogodek »Ohranimo preteklost – podprimo prihodnost« je potekal na Naravoslovnotehniški fakulteti. V sklopu dogodka je potekala tudi okrogla miza »Geologija v šoli in poučevanje o geopestrosti«.

Vzporedno z dogodkom je potekal tudi Dan geologije, kjer so si udeleženci lahko ogledali geološko zbirko, stavbo Montanistike ter se sprehodili po geološko zanimivi Ljubljani. Dogodka so se udeležili dijaki Srednje gradbene, geodetske, okoljevarstvene šole in dijaki strokovne gimnazije Ljubljana.

Ekipa, ki skrbi za podmladek in povezovanje z Društvom študentov geologije skrbi za redno obveščanje študentov o društvenih dogodkih, predvsem o predavanjih, na katere so tudi vabljeni. V preteklem letu je društvo sofinanciralo tisk koledarja Društva študentov geologije za leto 2025.

SGD je članica mednarodnega združenja EFG - European Federation of Geologists, katerega predsednik ostaja član SGD, Marko Komac. Društvo ima tudi 24 aktivnih članov v strokovnih svetovalnih telesih EFG. Društvo je bilo v letu 2024 vključeno v dva Evropska projekta Obzorje 2020 (Horizon 2020). Projekt NVO_CEEGS in CEEGS (2022-2025) – Nov sistem geološkega skladiščenja CO2 s pridobivanjem elektrotermalne energije (*CO2 Based Electrothermal Energy and Geological Storage System*) temelji na razvoju medsektorske tehnologije za energetski prehod. Združuje sistem za shranjevanje obnovljive energije, ki temelji na trans-kritičnem ciklu CO2, geološkem skladiščenju CO2 in pridobivanju geotermalne toplote. Društvo je k projektu pristopilo maja 2023, njegova naloga

Sl. 5. Okrogla miza in ogled razstave v avli na NTF UL OG ob Mednarodnemu dnevu geopestrosti 2024 (Foto: Jana Preradovič)

Sl. 6. Dan geologije 2024 (Foto: Petra Žvab Rožič – levo; Jana Preradovič – desno).

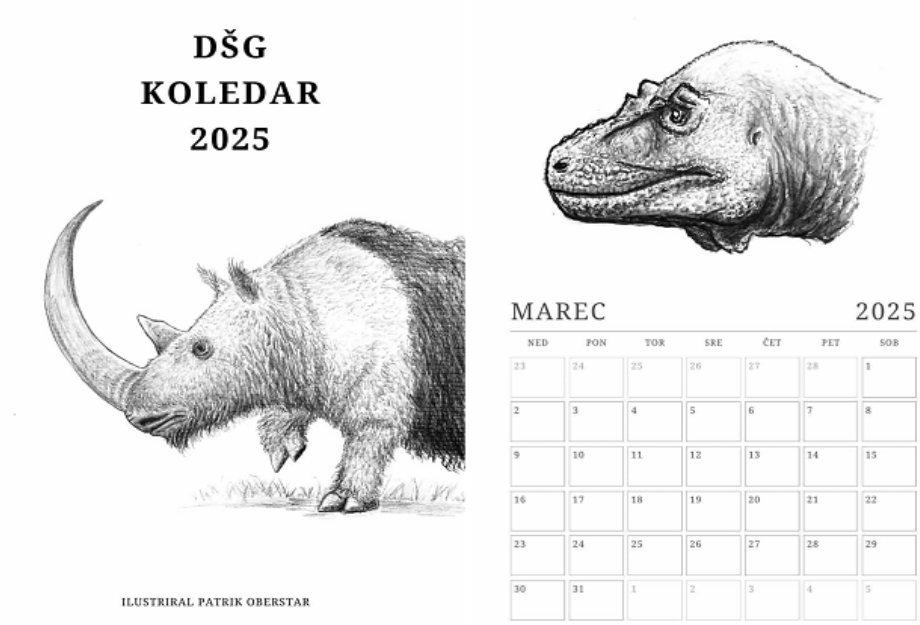

Sl. 7. Koledar Društva študentov geologije za leto 2025 (Arhiv DŠG).

je diseminacija rezultatov projekta. V preteklem letu smo pripravili slovenski prevod vsebin za spletno stran. Več o projektu na povezavi: https://www.slovenskogeoloskodrustvo.si/sodelovanje-v-mednarodnih-projektih/. V preteklem letu sta bila na temo projekta izvedena dva webinarja (“Thermodynamic Modelling & Measurements for the CEEGS Demonstration Loop« in »Challenges and risks of CO2 storage«) ter “CEEGS Coffee Chat”, namenjen neformalnemu mreženju vseh udeležencev. Projekt CRM-GEOTHERMAL (2022-2027) – Surovine iz geotermalnih fluidov (Critical materials from geothermal fluids) razvija inovativne tehnološke rešitve, združuje pridobivanje kritičnih surovin in energije iz geotermalnih tekočin. Ta bo pomagala Evropi izpolniti strateške cilje Zelenega dogovora EU in Agende za trajnostni razvoj, hkrati pa zmanjšala odvisnost od uvoženih CRM-jev. Diseminacija rezultatov je dostopna na spletni strani https://www.geo-zs.si/?option=com_content&view=article&id=1292.

V okviru društva deluje Slovenski nacionalni odbor INQUA (SINQUA), ki povezuje raziskovalce kvartarja in skrbi za pretok informacij med slovensko in mednarodno kvartarno znanstveno sfero. V letu 2024 smo sodelovali v aktivnostih INQUA komisij in fokusnih skupin (na sestankih, volitvah in pri odločanju mednarodnega Sveta INQUA, v aktivnosti komisij CMP, PALCOM, SACCOM in TERPRO). V okviru CMP komisije smo začeli z aktivnostmi v okviru novega INQUA projekta ONSEA (Evolution od Seascapes), ki predstavlja nadgradnjo prejšnjega projekta NEPTUNE. Spomladi in poleti 2024 so pripravili serijo treh predavanj preko spleta na temo morske geoarheologije. Oktobra 2024 so v Montpellierju (Francija) organizirali prvo ONSEA srečanje na tematiko geoarheološkega raziskovanja holocenskih obalnih in morskih okolij. Poročilo o dogodku je bilo objavljeno v decembrski številki INQUA novičnika Quaternary Perspectives. Poleg tega se je v letu 2024 zaključevala posebno številko Quaternary International (Millennial Paleo-landscape Reconstructions of Coastal Areas: From Field Data to Modelling Approaches), ki je vključevala prispevke z NEPTUNE sekcije INQUA srečanja v Rimu. V sodelovanju z Geomorfološkim društvom Slovenije je bila 6. 4. 2024 organizirana ekskurzija v Tolminsko kotlino, na kateri so si udeleženci ogledali nekatere geomorfološko in geološko zanimive točke, ki nam osvetljujejo kvartarni razvoj Tolminske kotline. Skupaj s hrvaškim nacionalnim odborom INQUA smo organizirali 7. regionalno znanstveno srečanje (14.-16. 11. 2024 v Zagrebu na Hrvaškem) za kvartarno geologijo, posvečeno raziskavam krasa. Člani so smo se udeležili 37. svetovnega geološkega kongresa IUGS; kjer smo predstavili napredek na področju IQUAME (International Quaternary Map of Europe 1:2.500.000 and Adjacent Areas) v Sloveniji. Udeležili smo se PANGEO-DEQUA srečanja (23. in 27. 9. 2024 v Innsbrucku), ki je potekalo pod organizacijo avstrijskega in nemškega nacionalnega odbora INQUA. Udeležili smo se srečanja INQUA-SEQS 2024 Meeting “Quaternary stratigraphy and terrestrial carbonates: climate, tectonic and humans driven landscape changes« (28. 9.-2. 10. 2024 v Gavorranu, Italiji). Na srečanju je bila članica dr. Eva Mencin Gale imenovana v odbor SEQS (Section on European Quaternary Stratigraphy) kot tajnica.

Društvo je že peto leto zapored član Mednarodnega združenja ProGEO – The European Association for the Conservation of the Geological Heritage, predstavnica Slovenije je Martina Stupar. V letu 2024 je potekalo srečanje članov skupine preko zoom povezave. Na srečanju smo predstavili priprave 17. simpozija ProGEO, ki bo v letu 2025 v Romuniji. Posredovali smo pri pripravi pisma podpore s strani ProGEO za razglasitev UNESCO-vega mednarodnega dne jam in krasa. Na spletno stran Home | Geodiversity Day smo v koledar aktivnosti ob mednarodnem dnevu geopestrosti objavili osrednji dogodek v Sloveniji.

Društvo je včlanjeno v SIZ – Slovensko inženirsko zvezo. S tem je izpolnjen pogoj o obveznem članstvu SGD v SIZ za pridobitev naziva Evro inženir (EUR ING).

V preteklem letu smo k plačilu članarine pozvali vse člane iz leta 2023. Če v roku 30 dni od poziva članarine niso poravnali, so bili iz društva črtani. Na dan 31. 12 .2024 je društvo tako štelo 101 člana iz plačanih članarin (od tega ena častna članica in štirje študenti). Skladno s 7. členom statuta pa je društvo štelo 112 članov.

Druge aktivnosti društva:

- Plačilo mednarodnih članarin: v preteklem letu je izvršni odbor društva poiskal rešitev za finančni primanjkljaj, ki je nastal kot posledica ARIS-ove prekinitve povračila stroškov za mednarodne članarine. Na redni skupščini 13. 3. 2025 so člani soglasno sprejeli rešitev, da se mednarodna članarina za združenje INQUA razdeli med člane društva po principu 80:20 (80 % članarine plačajo ustanove zaposlenih članov oziroma člani sami, 20 % pa društvo iz lastnih sredstev), članarino za ProGeo v celoti krije društvo (ker je znesek članarine nizek), članarino za EFG krije društvo (iz preostanka sredstev, ki se na društvenem računu nalagajo kot administrativni stroški dela na projektih). Ker se kljub pozivu člani SGD, ki so obenem člani IMU in EMA mednarodnih združenj niso odzvali, se je društvo soglasno odločilo, da do nadaljnjega članarin za ti dve mednarodni združenji ne bo več plačevalo. Ko bodo člani s poročanjem svoje aktivnosti izkazali zanimanje za vključitev društva v IMU in EMA, se članstva aktivira.
- SGD v Evropskem parlamentu: član društva Marko Komac je 27. 11. 2024 predstavil dejavnosti društva v Evropskem parlamentu.

Sl. 8. Predsednik EFG Marko Komac predstavlja v Evropskem parlamentu aktivnosti Slovenskega geološkega društva (Foto: arhiv Marko Komac).

GEOLOGIJA 68/2, 353-354, Ljubljana 2025

In Memoriam

V slovo geologu inženirju Janezu Šternu

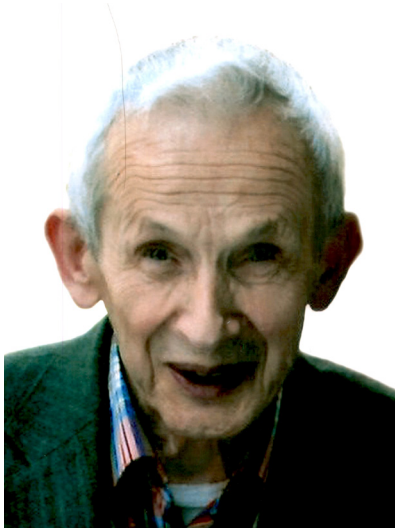

Koncem julija 2025 nas je prizadela vest o smrti našega upokojenega kolega, raziskovalca in mentorja, inženirja Janeza Šterna. Že nekaj let je bil šibkega zdravja in je potreboval pomoč bližnjih, a nas je vest o njegovem dokončnem slovesu vendarle potrla.
Inženir Janez Štern se je rodil v Celju l. 1932 v revni družini, ki jo je leta kot edini skrbnik tudi preživljal. Njegova trnova življenjska pot v mladih letih ga je izklesala v moža, kot smo ga poznali: izredno skromnega, vztrajnega, poštenega in pravičnega.
Obiskoval je znamenito I. gimnazijo v Celju. Po končani gimnaziji se je vpisal na študij geologije na ljubljanski Montanistiki. Študij je zaključil leta 1956 z diplomo na temo feroznega boksita in geologije Grebničke planine na Kosovu. Svoje začetno obdobje profesionalnega dela je tako posvetil raziskavam na Kosovu.
Na Geološkem zavodu se je zaposlil septembra 1960 in mu ostal zvest vse do svoje upokojitve leta 1992. Bil je geolog raziskovalec s srcem in dušo na Oddelku za ekonomsko geologijo Geološkega zavoda Ljubljana, sedaj Oddelku za mineralne surovine in geokemijo na Geološkem zavodu Slovenije. Raziskoval je številna nahajališča mineralnih surovin v nekdanji državi Jugoslaviji, bil udeleženec raziskovalnih odprav v Afriko, v Sloveniji pa je raziskoval predvsem nekovinske mineralne surovine, zlasti zakonitosti pojavljanja, genezo, mineralogijo in tehnološke lastnosti ter uporabne vrednosti raznovrstnih industrijskih kamnin in mineralov, kot so: različne gline, predvsem kaolin, tufi in bentonit, glinasti skrilavci, kalcit, kremenovi peski, pa tudi karbonatne ter magmatske in metamorfne kamnine za različno industrijsko uporabo. Na teh področjih je bil tudi vodja posameznih projektov. Tesno je bil povezan s keramično, steklarsko in kemično industrijo, petrurgijo ter industrijo gradbenih materialov, za katere je iskal, raziskoval in preizkušal lastnosti »novih« surovin. Vzdrževal je številna sodelovanja, od akademije do industrije.
Inženir Janez Štern je bil terenski geolog v pravem pomenu besede. Ker na začetku njegovega službovanja še ni bilo veliko vozil, se je na terene po domovini odpravljal z javnimi prevoznimi sredstvi in peš. Vzorce je nabiral sam, jih vedno prijel v roke in dolgo preučeval in ocenjeval s prostim očesom in z lupo. Na terenu je bil mojster sodelovanja z vrtalci, ki jim je znal spodbuditi delovno vnemo, četudi so bile okoliščine v surovi naravi in neugodnih vremenskih pogojih večkrat vse prej kot prijazne.
Materiale je pogosto tudi sam laboratorijsko preiskoval in uvajal nove metode preiskovanja, ter nas učil priprave posameznih nekovinskih surovin za nadaljnje preiskave.
Izpopolnjeval se je v Nemčiji na Tehnični univerzi v Clausthalu in od tam ter od drugod po Nemčiji prinesel mnogo znanja in odlične povezave, pomembne za številne svoje kolege v domovini. Ker je znal odlično nemško, je tudi prevajal strokovne tekste in pomagal številnim sodelavcem pri njihovih navezavah k sodelovanju in izobraževanju s tujimi raziskovalci, profesorji in strokovnjaki.
V letih 1963-64 je bil vodja geološkega dela znotraj velike ekipe, sestavljene iz strokovnjakov RUDIS-a in tedanjega Geološkega zavoda Ljubljana, ki so raziskovali nahajališča različnih mineralnih surovin, predvsem magnetitov, v Etiopiji in Eritreji. Štern je neumorno vztrajal pri delu v tropskih in drugje spet v puščavskih razmerah do zadnjega moža na delovišču.
Kot rudniški geolog je v 70-ih in 80-ih letih prejšnjega stoletja izvajal geološke raziskave in usmerjal podzemno pridobivanje illitne gline s komercialnim imenom «kaolin« v Črni pri Kamniku, ki so jo uporabljali v papirni in gumarski ter drugih vejah industrije za različna polnila in premaze.
V letih 1974 in 1975 je v reviji Geologija sam ali s soavtorji objavil članke o permokarbonskih skrilavcih v Sloveniji, o glinah in kremenovih peskih v Globokem in pregledno delo z naslovom »Industrijski minerali in kamnine v Sloveniji«. Številne prispevke o nekovinskih surovinah je objavil tudi v raznih drugih strokovnih revijah, na kongresih in srečanjih.
Bil je med prvimi, ki se je na Geološkem zavodu lotil okoljske problematike in onesnaženja sedimentov, predvsem v porečju Save in Bohinjskega jezera, pa tudi Piranskega in Koprskega zaliva. Tako je bil med pionirji na področju geokemije na Geološkem zavodu.
V letih 1976 in 1978 je v reviji Geologija objavil s sodelavci prispevka o težkih kovinah v rečnih usedlinah Save in njenih pritokov in o sestavi in onesnaženju recentnih usedlin Blejskega in Bohinjskega jezera.
Za inženirja Janeza Šterna smo prvič slišali že kot študentje na Naravoslovno tehniški fakulteti. Profesorica dr. Valerija Osterc nam je povedala: »Veste, na Geološkem zavodu je inženir Janez Štern, ki o glinah v Sloveniji vé daleč največ pri nas«.
Ko smo kolegi generacije takratnega »podmladka« v 80-ih let prejšnjega stoletja prišli na Geološki zavod, je v vrsti že renomiranih »zrelih« geologov imel inženir Janez Štern že dobrih 50 let. Bil je tedaj na vrhuncu svojega raziskovalnega ustvarjanja, z izredno širokim znanjem in spektrom interesnih področij, izkušnjami in rezultati svojih del. Bil je izvrsten in iskren raziskovalec, vedno pošten do sebe in do kolegov.
Bil nam je mentor, formalni in neformalni, številnim mlajšim sodelavcem nam je predajal dragocene nasvete o raziskovanju, vzpostavljanju sodelovanj, učil nas je, kaj je pomembno za razvoj raziskav in ravnanje z mineralnimi surovinami pri nas in v svetu.
Prenesel nam je veliko znanja, ki ga je pridobil skozi svojo bogato kariero. Izsledke svojih raziskav je napisal v številnih poročilih, študijah, ekspertizah in objavljenih delih v znanstveni periodiki. Nikoli mu ni šlo za »slavo«, ampak vedno za predajanje svojega znanja na druge, predvsem na mlajše generacije.
Janez je bil znan po svoji, milo rečeno, nečitljivi pisavi, le redkokdo je znal prebrati njegove rokopise. V času, ko še ni bilo računalnikov in so rokopise prepisovale tipkarice, je le eni od njih uspelo dešifrirati njegove »hieroglife«. Še po nečem je bil znan naš mentor, in sicer, da je bil izredno pedanten, natančen in nikoli dovolj zadovoljen s svojimi izdelki, zato je vselej zamujal z oddajo poročil in tako jezil nadrejene. A dobro so ga poznali, predvsem po tem, da so bila njegova dela vedno zanesljiva in imajo še danes trajno vrednost.

Štern je bil deloholik; poglobljen v svoje raziskovalno delo je skozi dolge popoldneve preučeval razne materiale, vzorce in zapise iz terenskih dnevnikov v svoji mali pisarni tja do večera, ko ga je vendarle premagala utrujenost.
Bolj poredko, pa vendarle, se je znal tudi sprostiti in poveseliti v krogu svojih kolegov in sodelavcev. Takrat so še posebej prišli na plan njegova prijaznost, radoživost in smisel za humor.
Tudi ko je bil že dolga leta v pokoju, se je redno udeleževal naših skupnih praznovanj in srečanj. Pripovedoval nam je svoje in svojih kolegov zgodbe, ki smo jih vedno z zanimanjem poslušali in se iz njih tudi marsikaj naučili. Vedno se je veselil tudi naših uspehov, tako službenih kot zasebnih.
Zaradi vsega tega smo ga visoko cenili in imeli radi. Vedno se ga bomo s spoštovanjem spominjali in o njem in njegovih delih rekli še marsikatero besedo.

Duška Rokavec in Miloš Markič

GEOLOGIJA
št.: 68/2, 2025
www.geologija-revija.si

ISSN 0016-7789